

AGARD-R-804

AGARD

ADVISORY GROUP FOR AEROSPACE RESEARCH & DEVELOPMENT
7 RUE ANCELLE 92200 NEUILLY SUR SEINE FRANCE



AGARD REPORT 804

Special Course on Missile Aerodynamics (L'Aérodynamique des Missiles)

The material assembled in this report was prepared under the combined sponsorship of the AGARD Fluid Dynamics Panel, the Consultant and Exchange Programme of AGARD, and the von Kármán Institute (VKI) for Fluid Dynamics. It was presented in an AGARD-FDP-VKI Special Course at the VKI, Rhode-Saint-Genèse, Belgium, 6th-10th June 1994 and at the Middle East Technical University, Ankara, Turkey, 13th-17th June 1994.



NORTH ATLANTIC TREATY ORGANIZATION

19950626 017

Published June 1994

Distribution and Availability on Back Cover

DISTRIBUTION STATEMENT A
Approved for public release
Distribution Unlimited

The Mission of AGARD

According to its Charter, the mission of AGARD is to bring together the leading personalities of the NATO nations in the fields of science and technology relating to aerospace for the following purposes:

- Recommending effective ways for the member nations to use their research and development capabilities for the common benefit of the NATO community;
- Providing scientific and technical advice and assistance to the Military Committee in the field of aerospace research and development (with particular regard to its military application);
- Continuously stimulating advances in the aerospace sciences relevant to strengthening the common defence posture;
- Improving the co-operation among member nations in aerospace research and development;
- Exchange of scientific and technical information;
- Providing assistance to member nations for the purpose of increasing their scientific and technical potential;
- Rendering scientific and technical assistance, as requested, to other NATO bodies and to member nations in connection with research and development problems in the aerospace field.

The highest authority within AGARD is the National Delegates Board consisting of officially appointed senior representatives from each member nation. The mission of AGARD is carried out through the Panels which are composed of experts appointed by the National Delegates, the Consultant and Exchange Programme and the Aerospace Applications Studies Programme. The results of AGARD work are reported to the member nations and the NATO Authorities through the AGARD series of publications of which this is one.

Participation in AGARD activities is by invitation only and is normally limited to citizens of the NATO nations.

The content of this publication has been reproduced directly from material supplied by AGARD or the authors.

Published June 1994

Copyright © AGARD 1994

All Rights Reserved

ISBN 92-835-0752-5



Printed by Specialised Printing Services Limited
40 Chigwell Lane, Loughton, Essex IG10 3TZ

Recent Publications of the Fluid Dynamics Panel

AGARDOGRAPHS (AG)

Design and Testing of High-Performance Parachutes

AGARD AG-319, November 1991

Experimental Techniques in the Field of Low Density Aerodynamics

AGARD AG-318 (E), April 1991

Techniques Expérimentales Liées à l'Aérodynamique à Basse Densité

AGARD AG-318 (FR), April 1990

A Survey of Measurements and Measuring Techniques in Rapidly Distorted Compressible Turbulent Boundary Layers

AGARD AG-315, May 1989

Reynolds Number Effects in Transonic Flows

AGARD AG-303, December 1988

REPORTS (R)

Progress in Transition Modelling

AGARD R-793, Special Course Notes, April 1994

Shock-Wave/Boundary-Layer Interactions in Supersonic and Hypersonic Flows

AGARD R-792, Special Course Notes, August 1993

Unstructured Grid Methods for Advection Dominated Flows

AGARD R-787, Special Course Notes, May 1992

Skin Friction Drag Reduction

AGARD R-786, Special Course Notes, March 1992

Engineering Methods in Aerodynamic Analysis and Design of Aircraft

AGARD R-783, Special Course Notes, January 1992

ADVISORY REPORTS (AR)

Air Intakes for High Speed Vehicles

AGARD AR-270, Report of WG13, September 1991

Appraisal of the Suitability of Turbulence Models in Flow Calculations

AGARD AR-291, Technical Status Review, July 1991

Rotary-Balance Testing for Aircraft Dynamics

AGARD AR-265, Report of WG11, December 1990

Calculation of 3D Separated Turbulent Flows in Boundary Layer Limit

AGARD AR-255, Report of WG10, May 1990

Adaptive Wind Tunnel Walls: Technology and Applications

AGARD AR-269, Report of WG12, April 1990

CONFERENCE PROCEEDINGS (CP)

Computational and Experimental Assessment of Jets in Cross Flow

AGARD CP-534, November 1993

High-Lift System Aerodynamics

AGARD CP-515, September 1993

Theoretical and Experimental Methods in Hypersonic Flows

AGARD CP-514, April 1993

Aerodynamic Engine/Airframe Integration for High Performance Aircraft and Missiles
AGARD CP-498, September 1992

Effects of Adverse Weather on Aerodynamics
AGARD CP-496, December 1991

Manoeuvring Aerodynamics
AGARD CP-497, November 1991

Vortex Flow Aerodynamics
AGARD CP-494, July 1991

Missile Aerodynamics
AGARD CP-493, October 1990

Aerodynamics of Combat Aircraft Controls and of Ground Effects
AGARD CP-465, April 1990

Computational Methods for Aerodynamic Design (Inverse) and Optimization
AGARD CP-463, March 1990

Applications of Mesh Generation to Complex 3-D Configurations
AGARD CP-464, March 1990

Fluid Dynamics of Three-Dimensional Turbulent Shear Flows and Transition
AGARD CP-438, April 1989

Validation of Computational Fluid Dynamics
AGARD CP-437, December 1988

Aerodynamic Data Accuracy and Quality: Requirements and Capabilities in Wind Tunnel Testing
AGARD CP-429, July 1988

Aerodynamics of Hypersonic Lifting Vehicles
AGARD CP-428, November 1987

Aerodynamic and Related Hydrodynamic Studies Using Water Facilities
AGARD CP-413, June 1987

Applications of Computational Fluid Dynamics in Aeronautics
AGARD CP-412, November 1986

Store Airframe Aerodynamics
AGARD CP-389, August 1986

Unsteady Aerodynamics — Fundamentals and Applications to Aircraft Dynamics
AGARD CP-386, November 1985

Aerodynamics and Acoustics of Propellers
AGARD CP-366, February 1985

Improvement of Aerodynamic Performance through Boundary Layer Control and High Lift Systems
AGARD CP-365, August 1984

Wind Tunnels and Testing Techniques
AGARD CP-348, February 1984

Aerodynamics of Vortical Type Flows in Three Dimensions
AGARD CP-342, July 1983

Missile Aerodynamics
AGARD CP-336, February 1983

Prediction of Aerodynamic Loads on Rotorcraft
AGARD CP-334, September 1982

Wall Interference in Wind Tunnels
AGARD CP-335, September 1982

Fluid Dynamics of Jets with Applications to V/STOL
AGARD CP-308, January 1982

Aerodynamics of Power Plant Installation
AGARD CP-301, September 1981

Preface

This volume is a compilation of the edited proceedings of the "Missile Aerodynamics" course held at the von Kármán Institute (VKI) in Rhode-Saint-Genèse, Belgium, 6th–10th June 1994, and at the Middle East Technical University (METU) in Ankara, Turkey, 13th–17th June 1994.

This series of lectures supported by the AGARD Fluid Dynamics Panel and the von Kármán Institute follows previous courses organised at VKI: 1974 (VKI LS67), 1976 (VKI LS88), 1979 (AGARD LS98) and 1987 (AGARD-R-754).

The aim of this special course was to present the current state of the art in some fields of tactical missile aerodynamics. The course begins with an overview of aeromechanical design of modern missiles. It covers system aspects, configurations, physical aspects and methods used in the design phase. This introduction is followed by a lecture on semi-empirical predictive tools which still remain the everyday tools for design engineers. The numerical computation is the subject of two specific notes: Navier-Stokes computation for complete missile configurations and Euler and Navier-Stokes computations for supersonic air intakes. Two other lectures were also included: pyrotechnical lateral jet control and high angle of attack aerodynamics. In addition, and for the first time, an important part of the course is devoted to the analysis and the modelling of missile infrared radiation. Its objective is to provide aerodynamicists with an understanding of IR radiation, useful for low IR signature missile design. Each presentation is illustrated with numerous practical applications.

We want to thank all the speakers for their outstanding work, as well as the organisers of AGARD, VKI and METU,

Préface

Ce volume regroupe les notes concernant le cours "Aérodynamique des Missiles" présenté à l'institut von Kármán (VKI) de Rhode-Saint-Genèse, Belgique, du 6 juin au 10 juin 1994 et à la Middle East Technical University (METU) à Ankara, Turquie, du 13 au 17 juin 1994.

Ce cycle de conférences, conçu et réalisé sous l'égide du Panel de Dynamique des Fluides de l'AGARD et du VKI, fait suite à des cours similaires organisés au VKI en 1974 (VKI LS67), 1976 (VKI LS88), 1979 (AGARD LS98) et 1987 (AGARD-R-754).

L'objet du cours a été de revoir l'état de l'art dans certains domaines de l'aérodynamique des missiles tactiques. Le cours débute par une présentation générale de la conception aérodynamique des missiles modernes avec prise en compte des aspects systèmes, des nouvelles configurations de missiles, des aspects physiques des écoulements et des méthodes de calcul. Cette introduction est suivie par une présentation des outils semi-empiriques qui sont les outils de base de l'ingénieur de conception. Le calcul numérique est traité dans deux notes spécifiques: calcul Navier-Stokes de configurations complètes de missiles, calculs Euler et Navier-Stokes de prises d'air supersoniques. Deux autres sujets ont aussi été inclus: le pilotage par jets latéraux et l'aérodynamique aux grandes incidences. De plus, et pour la première fois, une part importante du cours est consacrée à l'analyse et à la modélisation du rayonnement infrarouge des missiles. Son objectif est de fournir à l'aérodynamicien une bonne compréhension du rayonnement infrarouge, utile pour la conception de missiles à faible émission infrarouge. Chaque présentation est illustrée par de nombreux exemples pratiques.

Nous tenons à remercier tous les conférenciers pour l'excellent travail qu'ils ont accompli ainsi que les organisateurs de l'AGARD, du VKI et du METU.

Special Course Staff

Special Course Director: Mr R.G. Lacau
Aérospatiale Missiles (E/EC/N/A)
Annexe les Gatines
91370 Verrières-le-Buisson
France

LECTURERS

Mr P. Champigny
Direction de l'Aérodynamique
ONERA
BP 72
92322 Chatillon Cédex
France

Dr F.G. Moore
Weapons Systems Department
Naval Surface Warfare Center
Dahlgren Division (Code G04)
Dahlgren Virginia 22448-5000
United States

Dr P. Hennig
VAS 414
Deutsche Aerospace (DASA)
Abwehr und Schutz
Postfach 80 11 49
881663 München
Germany

Mr P. Weinacht
Propulsion & Flight Division, WTD
US Army Research Laboratory
Aberdeen Proving Ground
Maryland 21005-5066
United States

Mr M. Engelhardt
Grumman Corporation
1111 Stewart Avenue (B46-35)
Bethpage NY 11714
United States

HOST NATION COORDINATORS

Professor J.M. Charbonnier
von Kármán Institute for Fluid
Dynamics
Chaussée de Waterloo 72
1640 Rhode-Saint-Genèse
Belgium

Professor C. Çiray
Aeronautical Engineering Department
Middle East Technical University
Inonu Bulvari PK:06531 - Ankara
Turkey

PANEL EXECUTIVE

Mr J.K. Molloy

Mail from Europe:
AGARD-OTAN
Attn: FDP Executive
7, rue Ancelle
92200 Neuilly-sur-Seine
France

Mail from US and Canada:
AGARD-NATO
Attn: FDP Executive
PSC 116, APO AE 09777

Contents

	Page
Recent Publications of the Fluid Dynamics Panel	iii
Preface/Préface	v
Special Course Staff	vi
	Reference
Aeromechanical Design of Modern Missiles by P. Hennig and R.G. Lacau	1
Engineering Codes for Aeroprediction: State-of-the-Art and New Methods by F.G. Moore	2
Lateral Jet Control for Tactical Missiles by P. Champigny and R.G. Lacau	3
Missile Infrared Radiation Analysis by M. Engelhardt	4
Modern Trends in Electro-Optical Technology for use in Missile Detection	4-1
Infrared Radiation Laws and Missile Characteristics	4-6
Missile Infrared Radiation Properties	4-10
Introduction to Missile Thermal Analysis	4-15
Infrared Intensities from Missiles	4-21
High Angle of Attack Aerodynamics by P. Champigny	5
Navier-Stokes Predictions of Missile Aerodynamics by P. Weinacht and J. Sahu	6
Computation of Supersonic Air-Intakes by R.G. Lacau, P. Gamero and F. Gaible	7

AEROMECHANICAL DESIGN OF MODERN MISSILES

P. Hennig
Missile Systems Division
Deutsche Aerospace
Postfach 80 11 49
D-81663 München

P.G. Lacau
Aerospatiale Missiles
Centre des Gatines
F-91370 Verrieres le Buission

SUMMARY

The changes in the political and strategic situation in the world, especially in Europe, result in new kinds of military scenarios and in different approaches to well-known scenarios. In combination with technological advances and with new mathematical and physical solutions for system component design and for improvements in system performance this leads to a request for advanced and new types of missiles with corresponding design goals and criteria. From such more general demands associated with the overall system design new requirements for the aerodynamical and aeromechanical design goals can be derived in correspondence. Advanced experimental and theoretical tools support the project aerodynamicist in coping with these new problems.

Examples for the demands for new missile types and for the new system requirements are given. The most important aeromechanical work packages in the design procedure of modern missiles are identified and methods to get solutions sufficient for qualitative answers in early project phases are presented.

1. INTRODUCTION

The intention of this first lecture of the present series is to give a summary of what seem to be the new and most important aspects of the 'Aeromechanical Design of Modern Missiles'. Some of the topics mentioned here will be discussed in more detail in later lectures, others will be described here in a short survey. In this way the following lectures on special topics are hoped to be put into a conclusive context with the new technological and system requirements of the missile design procedure. Also, the role of the different aeromechanical disciplines and of the technologies and work packages linked to them

for different types of projected missiles will be explained. On the other hand, this is not a summary of system design specialists but of industry aerodynamicists working in a design environment that is much more dominated by very different system requirements and by not purely aerodynamic problems than several years ago.

The new design goals and the advances in different technological fields lead, on one hand, to the fact that the aerodynamic design must be more precise than several years ago, must include more general geometries and must consider new flight conditions, new system components and new types of questions by the system project people. Therefore, a lot of work would have to be done to fulfill all these demands. On the other hand, the design process must be kept very cheap also in its aerodynamic parts, not only since missiles have to be generally much cheaper than, say, airplanes but even more because of the sharply decreasing defense budgets of the last years. In addition to that aerodynamics has lost its former high priority among the most important technologies in the strategy of the MODs of many countries. This leads to even higher cuts for this special field, since in those countries no other support exists any more to promote specific pure and applied research in missile aerodynamics than the also drastically reduced industrial budgets. Although aerodynamics never played a similarly central role in missile design (Ref. 1) as in aircraft design and, therefore, always had to be very cost effective, we have nowadays many difficulties in keeping up with the most urgent needs in advancing our tools. The validation and the extension of existing codes, the transfer of new methods from laboratory state into standard project work and the suitable physical and mathematical modelling of flow phenomena that are of new importance for the project design are in many cases only possible because of very high personal idealism of the aerodynamicists.

The urgency of very cost effective missile design not only leads to the fact that advanced methods implying high effort can be used only in very rare cases, but also that several topics with very close relations to aerodynamic design problems have to be treated by the aerodynamicist in early project phases to guarantee a fast and cost effective optimization process. Since the new system requirements for missiles often lay more stress on these formerly secondary areas, the aerodynamicist has to adopt or to develop suitable tools for this work. This extended area may be called 'aeromechanics'. It is an artificial word and not very well-defined. Within this lecture it covers - besides aerodynamics - general fluid dynamics and hydrodynamics, aerothermodynamics and internal thermodynamics, aeroacoustics, behaviour of structures under aerodynamic loads (aeroelastic effects), flight mechanical aspects and the simulation of signatures of all types (Radar, microwave, infrared, visible, ultra-violet and acoustic). Some of these areas have been foreseen to be subjects of modern missile design some time ago already (Refs. 2-4), others are turning up only in the last time. Therefore, not each field is very elaborated yet. But, anyhow, the close coupling of all these topics with classical aerodynamic design is of high relevance and in many cases quite new.

The present and future requests on these aeromechanical subjects are tried to be presented in this lecture. Therefore, a first reference to existing fast and rather simple project tools is given and an outlook is tried on the problems we have to expect - and to solve - in the next years and for which we have to develop appropriate tools as soon as possible. This is necessarily a very subjective guess which is derived only from the personal project experience and the company environment of the authors.

2. PRECONDITION FOR THE AEROMECHANICAL DESIGN OF MODERN MISSILES

2.1 NEW POLITICAL AND STRATEGIC SITUATION

In the new world-political situation the probability for a mass confrontation between larger armies has decreased drastically, especially for NATO countries. In contrast, there will be a much higher risk of

- local confrontations of limited extent between two nations or with NATO on one side
- UN conflict management missions ('peace enforcement'), often in overseas areas, with a

- limited size of the different national forces
- UN blue helmet missions with peace keeping or humanitarian objectives
- national point defense tasks, for example the defense of objects or small areas against terroristic attacks
- reconnaissance, inspection and control objectives in connection with boycott and disarmament measures or with deescalation actions in domestic conflicts.

For this reason the size of the different national armed forces will decrease probably, while the equipment will be improved much more in quality than in quantity. This latter point had been expected several years ago, already, and is the reason why some outlooks of the past (Refs. 2-4) still are valid partly, although the political situation has changed. For many of the NATO countries (especially for Germany) the possibility of overseas actions is very new. In any case, there will be a need for arms which can be transferred easily into different conflict areas and which are very flexible in mission and can be adapted very easily to different geographical and military environments. Since one has - due to not controllable proliferation - to expect weapons of highest technological standard in the hands of every possible enemy, perhaps only in a limited number, it is in any case still necessary to be able to combat them. Especially in cases of local national conflicts, civil war situations, defense of terror attacks or rather of attempts for black-mailing, highest efficiency and precision are requested because of political reasons.

Many of the possible scenarios for military actions ask for a de-escalating strategy. For this reason, collateral damage, i.e. any harm to humans not involved, damage to infrastructure and to the environment has to be avoided as far as possible. Also, for all countries participating in UN missions there will be high domestic political pressure to avoid casualties of own personnel. This implies that the weapons used have to be of highest precision in hitting their target and in the effect they exercise on it. This implies the use of weapons of high intelligence and autonomy - which also helps to reduce the crews needed - and of arms with minimal side effects, so-called surgical weapons. In many cases non-lethal or less-lethal weapons are required (Refs. 5-8).

Especially for humanitarian missions, but also for high flexibility in geographical engagement with limited troops an accurate and safe delivery of supply is of very high importance. In almost all scenarios an excellent scouting or observation is necessary. Usually, these observers must have a very low signature, in some scenarios they must be as invisible and inaudible as possible.

2.2 NEW TECHNOLOGIES FOR MISSILES

The new demands on modern missiles can be met much easier thanks to the fact that in the last years a lot of new technologies have been developed which can be used for these new tasks. Other well-known missile technologies have been improved or became cheaper and more reliable. Using all the new possibilities for the different components one already would come to an advanced missile design (Fig. 1). Some of the new technologies are only of indirect influence on aeromechanical design, namely by the design requirements or by new system characteristics. Other technologies directly introduce aeromechanical problems or require profound studies in aerodynamics, thermodynamics, aeroelastics or signature simulation to check the realizability of the new concepts.

Despite of the new technologies, the basic components of a missile (Fig. 2) are still the same as formerly. Even their principal relationship to aeromechanics (Ref. 1) is in many cases very similar. Therefore, only a few additional aspects are mentioned here.

Advanced warheads may influence the general design of the frontpart of the missile. Submunition causes aerodynamic problems during separation and by multibody interference effects within the cloud. Missiles that are intended to fight armoured targets like tanks or bunkers often will use penetrators with high L/D at very high velocities (Ref. 9). The start of such projectiles - with a sabot from a high energy gun or from a missile during the endgame - is connected with questions of aerodynamic interference and aeroelastic response.

Modern turbo-propulsion units have reached a price level which makes them attractive for missiles. This leads to new design solutions mainly for low-speed vehicles. New types of fuel make it easier, on one hand, to reach higher velocities which arise problems of high-speed aerodynamics and of aerothermodynamics. On the other hand, smokeless fuels or such of low signature offer the chance of new data link concepts. Novel propulsion systems like ramjets, ramrockets (Fig. 3) and others (Refs. 10-14) ask for new missile geometries and lead to different flight conditions (Fig. 4) that have to be modelled by aeromechanics.

The guidance system (Refs. 15-17) in a more general sense not only consists of the classical types of homing, beam-riding, command and inertial systems (Ref. 1) but also includes data acquisition and transmission by the missile.

The existence of cheap PC's in each unit of the troops, very cheap and very powerful electronic components allow new system features and may

lead to more intelligent and autonomous missiles or to more elaborated launch and guidance units.

New data links like laser beam or glass fibre optics give the opportunity for a more precise homing and for transmission of a lot of data acquired. This gives a better chance for 'surgical strikes'. The same is true due to new possibilities in picture scanning, processing and interpretation. High power television cameras or improved IR, MW or Radar sensors with higher sensitivity, higher spatial resolution and larger range can find or identify a target with much higher precision.

For missiles with higher velocity or larger range the aerodynamic heating of the sensor domes often becomes a problem (Fig. 5). For IR domes active cooling or the use of covers might be a solution. New materials are developed and tested for radomes for such cases. Besides the determination of optical or dielectric parameters to guarantee the necessary sensor performance of the materials and the structures, also aerodynamics, thermodynamics and aeroelastics are needed to check the applicability during the flight of the domes designed.

The use of GPS for navigation has become common and leads also to much higher precision but also to the preference of certain flight manoeuvres. Laser or radar altimeters are of much higher precision and are much more independent of the environment than the classical ones. New concepts of guidance and control (Refs. 19-20) like the observer technique (Ref. 2) or seeker based fusing and new mathematical methods like fuzzy logics (Ref. 21) lead to new challenges in the flight paths aimed at and to the need for more precise aerodynamic models (Fig. 6).

Especially for high velocity missiles the use of classical control surfaces is a problem because of the high temperatures reached by aerodynamic heating, mainly in the wing tips. In such cases, but also for others where it seems favourable, new control mechanisms have been developed. Apart from different types of thrust vector control (Fig. 7) there is mainly the jet reaction control by lateral thrust that is favoured. A new method with still many practical problems to be solved is the bending nose concept (Ref. 23). As for the deflected surfaces or for mechanical spoilers where the forces and moments introduced are aerodynamical in nature, the applicability and the characteristics of the new control methods equally have to be considered by the aerodynamicist. In the case of jets thermodynamic problems may be of importance, too. A new type of deflecting surfaces are the grid fins with their very interesting characteristics. They have been in use already for many years (Ref. 24) but have not found much response in the Western hemisphere.

The general outer design of a missile is traditionally found as a compromise between aeromechanical demands and component needs. The use of new materials like ceramic or fibre reinforced materials (Ref. 25) and the tendency to favour light-weight structures leads to an increase in the importance of an adequate description of their aeroelastic and acrothermodynamic properties.

A lot of new ideas for optimal aerodynamic design of missiles are being produced in system studies but are often disappearing again or have to be modified severely after more detailed research. New geometries introduced by novel control surfaces have been mentioned already. Recently, the ring wing has reappeared as an optimal stabilizing device (Ref. 26). They have been considered in earlier times already (Refs. 27 and 28) but seemed not very favourable at that times in several projects. The fact that they are designed to be deployable now could make a reasonable difference. Variable geometries as movable wings are used for keeping up an optimal value for the stabilization of the missile when a large shift of the center of gravity occurs during the flight.

For high speeds the concept of the waveriders has been developed to give solutions for optimal aerodynamic shape (Refs. 29-32). Today first designs exist that are not only geometric guidelines but are more project oriented (Fig. 8). Nevertheless, these configurations usually are intended rather for hypersonic transport than for tactical missiles.

In general, more integrated designs - integrated intakes (Fig. 9) or sensors or conformal carriage of stores - are considered everywhere because of the wish for reduced drag (Fig. 10) and for higher velocities.

On the other hand, there is a trend to develop 'stealthy' missiles, especially for lower velocities and long ranges. Many of the concepts seem to be in massive contradiction to an optimal aerodynamic shape. Faceted surfaces and a large number of sharp edges lead to highly separated flow and to unfavourable and almost not predictable interference effects of the vortical and turbulent downwash. This makes it necessary to optimize the geometry of low signature missiles in an integrated procedure between aerodynamics and signature simulation. Similar geometry problems - but without the signature restrictions - have been known for a while from dispenser weapons (Figs. 11-12) with their unconventional shapes of non-circular cross section (Ref. 35).

Another 'geometry' that is a challenge for the aerodynamicist are the parachutes and gliders used to decelerate submunition or loads or which shall prolong the flight time or distance. To

simulate the very complicated aerodynamic characteristics of parachutes (Fig. 13) one has to include the behaviour of flexible membranes of irregular shape including the opening procedure, the complex flowfields of semi-permeable walls at a wide speed range and the usually very severe and unsteady aerodynamical and flight mechanical interference between the parachute and the load connected with it. The problems increase if one has to guarantee a controlled flightpath with a parachute or a glider.

2.3 NEW FOCAL POINTS FOR TARGETS, MISSION SCENARIOS, AND OPTIMAL CHARACTERISTICS OF MISSILES

2.3.1 TARGETS AND SCENARIOS

Because of the new geopolitical situation discussed above, new demands in missile characteristics have appeared. If one considers the types of targets involved in possible conflicts one finds out that not too much has changed. This comes from the fact that offensive weapons and military installations are principally the same. But they may be distributed all over the world now and are part of new and very different scenarios. Therefore, the changed conditions of combat situations require new features of future missiles.

The following targets or missions have to be expected as the most important ones. The main requirements for missiles relevant to aeromechanical design are added.

- Little armoured individual targets or formations (trucks, bridges, runways, launchers, infrastructure)
 - short to long range, scattered munition, manoeuvres at low altitudes
- Bunkers and shelters
 - medium to long range, high kinetic energy
- Tanks
 - short to medium range, fast reaction, high kinetic energy, manoeuvres at low altitudes
- Helicopters
 - short and medium range, fast reaction, possibly high kinetic energy
- Fighter airplanes (mostly low-level flight) or offensive missiles of different type
 - short to medium range, fast reaction, high manoeuvrability
- Cruise missiles (terrain-following or low-level flight)
 - short to medium range, fast reaction, high manoeuvrability

- Sea targets (above sea surface)
 - medium to long range, sea-weaving manoeuvres
- Sea targets (below sea surface)
 - medium range, surface effects
- Tactical ballistic missiles (TBM)
 - fast reaction, short to long range, high manoeuvrability
- Radar installations or detectors
 - fast reaction, high manoeuvrability (for moving targets)
- Defense missiles
 - short range, fast reaction, high manoeuvrability
- Highly accurate drop of loads (supply)
 - low cost
- Delivery of non-lethal weapons
 - short range, very high reliability
- Observation of battle fields
 - short range, low signature
- General surveillance (snipers, gun positions, troop movements)
 - short to medium range, low signature, long operation time

In addition to these specific requirements modern missiles have to operate in all geographic and seasonal environments like arctic, tropic, desert, sea-level, high altitude, and in some cases also in the higher atmosphere. In each case a surgical strike should be possible which claims for very high precision and effectiveness. Also because of the demand for low collateral damage and for cost effective actions, high penetrativity is necessary. This can be reached by either very high velocity, by execution of manoeuvres (sea-weaving) or by low detectability of the own missile. The latter can be ensured by terrain-following or by low signature design.

2.3.2 MISSILE TYPES OF CURRENT INTEREST

According to the general demands for new missiles to be developed against the different targets that are listed above, one can define a selection of missile types of special current interest. Most of them are focal points of international studies or development activities as far as it can be derived from recent publications. A selection of project solutions of current interest for different mission and target types and of their corresponding major aerodynamic problems was given in Ref. 4. Here, missiles having modern aeromechanical features are referenced. Their characteristics have to be derived in detail from the new scenarios and can make use of the modern technologies mentioned.

Tactical Ballistic Missiles (TBM)

In Germany, like in most of the NATO countries, missiles of this type are not developed. Nevertheless, to provide reliable data for simulations of TBM targets as a basis for the design of defense systems their aeromechanical data have to be investigated. This includes results like aerodynamic model, stability, probable flight paths and signature levels (plume signature during boost phase and signature of the heated re-entry vehicle).

The long range and the very high velocity in atmospheric heights otherwise unusual for missiles arise aerodynamic problems similar to those of space vehicles. In addition, there will be manoeuvrable TBMs in future introducing the problems of suitable control mechanisms and of the resulting unconventional free flight conditions during manoeuvres.

Hypersonic and High Velocity Missiles (general remarks)

Demands for high kinetic energy, short reaction time and high penetrativity can be satisfied by reaching high velocities. According to the different target and mission types several classes of high velocity missiles can be defined. Besides the aerodynamic behaviour the design aerodynamicist has to consider in this field mainly the aerothermodynamic characteristics. This immediately is connected with the problem of suitable materials withstanding the heat loads and the aerodynamic loads equally. Another severe stress for the surface structure are erosion effects by dust grains and rain. Because of the high missile velocity their impact is of such high kinetic energy that severe damage will occur.

Hypersonic projectiles

Penetrators shot from electro-thermic or electro-magnetic, rail or coil guns (Ref. 9) are mainly intended as anti-tank weapons or last-ditch TBM and air defense as a kind of an improved shell. These kinetic energy (KE) projectiles acquire their high energy by very high velocity (between about Mach 6 to 10) and relatively high mass. Since the velocity decreases fastly, their range is limited to several kilometers. Because of the gun launch, they have a very small inner dead region. The effect of the high kinetic energy impact is utilized by the optimal penetration characteristics of an high L/D core.

The construction of the hypersonic projectiles is very simple: They consist of a long 'rod' penetrator of heavy-weight metal and some aerodynamic appendages for drag-reduction and stabilization (Fig. 14 and Ref. 38). The hit probability - especially for air targets - can be increased

considerably by using guided projectiles. A favourable guidance principle is the collision point oriented line-of-sight guidance (Fig. 15). The control devices may consist of a lateral thrust system or of a bending nose (Fig. 16). The main work packages within the aeromechanical context are the determination of the aerodynamic and acrothermodynamic characteristics (Refs. 37, 38 and 40). A specific problem is the determination of the correct drag coefficients and the correlation of its experimentally found value to the corresponding free-flight one (Ref. 41), especially since these projectiles have relatively large body grooves to hold a sabot (Ref. 42) that functions as a bore rider inside the gun tube and that separates at a short distance from the muzzle of the gun. The effects of internal ballistics and of sabot separation may cause severe initial flight path errors (Fig. 17) and, therefore, must be modelled carefully. But it is often very difficult to simulate the aerodynamic behaviour in those cases because of the high number of parameters involved and because of the multi-body interference during the separation of the sabot fragments (Ref. 43). A similar problem arises when a penetrator follows an advancing projectile in a tandem flight. For projectiles with very high L/D or with special structural designs aeroelastic deformations have to be considered in addition, especially in the launch and the impact phases.

Hypersonic missiles - short range

High velocity missiles for short ranges can be used in complement to projectiles for similar missions. The inner dead region is higher - in the order of several hundred meters - since the acceleration takes place outside the launcher. On the other hand, these missiles can carry their kinetic energy over a higher distance and they are manoeuvrable. This qualifies them for air defense against targets like TBMs (last ditch), missiles and aircraft, but they can be equally used against tanks or helicopters (short reaction at sudden pop-up), see Ref. 44. To reduce the reaction time while keeping the possibility to aim at targets approaching from any direction, vertical launch followed by a fast turn manoeuvre to almost horizontal flight is used in most cases. Again, aerodynamic and acrothermodynamic characteristics of high-speed flight (around Mach 5 to 8) at low altitude have to be determined. Aeroelasticity may be of importance in the case of light-weight structures and for partly or completely burnt-out booster. An additional problem are the characteristics of the control devices as surfaces, lateral thrust, or thrust vector control. The selection of surface materials (maybe ablative) and the guidance unit (radome) are other areas of present research. The data link might be realized by a laser beam. In this case the shape and the transmissivity of the plume in dependence of fuel chemistry and of flight condi-

tions are of high importance and have to be simulated by the aerodynamicist.

Hypersonic missiles - long range

High velocity missiles for medium to long ranges have similar features to those of short range. The speed probably will be a bit lower (around Mach 4 to 6) and the typical cruise height would be between several hundred and several thousand meters (Ref. 44). The main reason to strive for high speed in this case is not so much the necessary kinetic energy anymore in most cases, but the better penetrativity without using stealth features. The aspect of relatively short reaction time will be still of importance in many cases, of course. If the speed is not too high a low signature level will gain increasing importance again with increasing mission ranges. Different control mechanisms will be of interest here probably and different guidance laws, navigation methods and data link systems will be used for these missiles. Although the speed is a bit smaller, aerodynamic heating normally has an even higher priority because of the longer flight time. Structural heating and heat transfer to components have to be considered in this case, too. Materials and acrothermodynamic characteristics of radomes have to be checked (Ref. 45). If air breathing propulsion is used for this type of missiles, geometries with optimized drag characteristics as highly integrated intakes are favourable. This leads to unconventional, non-axisymmetric shapes (Fig. 18) with the corresponding extended aerodynamic models that have to be generated.

Dispensers

The main task of a dispenser is to carry a load and to drop it after some distance. This load may consist of submunitions of different kind, of a penetrator with an acceleration device, of non-lethal agents or of anything that has to be transported and distributed. Since the 'cargo' is covered by the dispenser airframe for almost the complete mission time it may be of quite un-aerodynamic shape. There are dispensers carried only as a store, others with a free-flight phase without propulsion and, therefore, only short range, and long range dispensers with different types of propulsion. The typical flight height is terrain-following up to about 100 meters, the average velocity is transonic but there is the tendency to increase it to the low supersonic regime. For long ranges low signature designs become necessary to assure for a sufficient penetrativity. According to the scenarios to be expected the stand-off feature is of high importance.

A lot of aerodynamic problems arise from the unconventional geometry of the dispensers and even more if a stealth configuration has to be

considered. The large number of inclined edges in combination with lift and control surfaces situated at unconventional positions and perhaps with intakes lead to highly separated flowfields around the missile with severe interaction effects and, therefore, to very complicated aerodynamic models. Store carriage and store separation simulation show an inhomogeneous outer flow additionally. Unsteady effects have to be expected and make it meaningful to execute a coupled aerodynamic/flight mechanic simulation for such flight periods. The same is true for gusts and even more if the dispenser crosses the jet flow behind the airplane. The flight at low altitudes including street tracking or terrain-following manoeuvres asks for high precision aerodynamic inputs into the guidance and control loop. The ejection of the submunition usually is not the problem of the dispenser any more, except in those cases where the distribution takes place over a long distance. In this case open submunition tubes may affect severely the further flight. For long range dispensers with higher velocity or for ones with IR domes aerodynamic heating might become of importance. If low signature design is strived for, a simulation of, mainly, radar cross section (RCS) and IR emission is necessary in the early design process.

Submunitions

There is a wide variety of submunition types. Their targets may be tanks or tank formations, bridges, runways, and other objects of the infrastructure. Also penetrators (bunker busters) or mines and other similar effectuators can be carried as a kind of submunition by a dispenser. In some cases the load has to be distributed regularly over a certain area, in other ones the flight time and range of the submunition has to be extended to allow a longer detection time of a suitable target. Other submunition must be stabilized from their almost completely accidental flight conditions resulting from the irregular interference effects immediately after their ejection, so that their impact angle at the target is reduced to a minimal value which allows a correct operation of the warhead (Fig. 19). All these functions are executed by appropriately adapted retarders, parachutes or gliders (Figs. 20 and 21). The geometry of the submunition may be very simple - often like a can - or may consist of a quite involved system (Fig. 22).

The first aeromechanic difficulty of these submunitions is to model the aerodynamic characteristics of such unaerodynamic objects for subsonic, transonic, supersonic and even hypersonic velocities and for any flow angle. Especially the inhomogeneous flow conditions caused by interference effects are of high importance for the correct flight

simulation. There are first interferences with the dispenser during and shortly after the ejection (Ref. 48) where the body axis of the submunition may be normal or parallel to that of the dispenser. Another type of interference is that between the submunition bodies within the ejected cloud (Ref. 49), also under normal or axial flow conditions. Fig. 23 shows the complicated vortical flow around a set of three interfering bodies at normal flow angle. Another type of interference occurs between a submunition and the different kinds of retarders. Some of them are similar to unconventional control or stabilizing devices, but parachutes or gliders arise additional fundamental problems (Ref. 36). The parachute consists of a membrane deformed by aerodynamic loads (Refs. 51-53). The corresponding aeroelastic effects are of outstanding evidence during the inflation (Fig. 24). Another unconventional aerodynamic feature of the parachutes is the porosity of the material which modifies considerably the flow parameters (Fig. 25). Therefore, the determination of aerodynamic coefficients for parachutes (Ref. 55) and for gliders (Refs. 52 and 56) is rather involved. In addition to that, the interference effects between submunition and the canopy have to be considered (Ref. 57). Fig. 26 shows such a case with separated vortical flow behind a load, modelled by 3D point vortex tracking, and its interaction with a simple spherical canopy with a central hole and with vortex sheets rolling up from the inner and outer edges. Although this simulation is already very expensive with respect to an efficient design process, there are still several important aspects not considered yet. This is not only the porosity and the flexibility of the material and the time-dependence of the flow caused by the unsteady separation, but also the close coupling between the flight mechanical behaviour of the parachute/load system with their internal degrees of freedom (Ref. 59) that should be included, since it leads to an unsteady onset flow.

Fiber optic guided missiles

The new technology of broad band signal transmission by optical fibers over distances up to about 150 kilometers offers the chance to develop systems with completely new features (Ref. 60). The missile carries an IR or visible light camera which transmits the pictures in real time to a screen where the information is used by the launch crew to guide the missile. In this way a very high precision in the flight performance can be reached. This allows surgical strikes with conventional warheads or with non-lethal agents. The missile may be launched from a protected position and can reach protected areas, hidden places or points within narrow streets in cities. The new and cheaper turbo-engines for missiles offer control of thrust and provide adaptable

speed and, therefore, allow for a good coordination of connected missions. Because of the data transmission rate that can be realized at the present time, the flight velocity has to be subsonic. This, on the other hand, makes it easier to reach high manoeuvrability. For long range missions the penetrativity has to be increased by low signature features for all sensor domains to be expected and additionally by sea-weaving or similar manoeuvres. The optical fiber is of high strength and, therefore, produces no severe aeromechanical problems, although a coupling between aerodynamics and elastic behaviour has to be considered in principle (Ref. 61). The determination of the aerodynamic characteristics of the missile should be a standard problem in general. To avoid a contact between the fiber and the hot turbojet the exhausts usually will be situated laterally. This, however, will cause interference effects with the fins and so the control efficiency of the rudders as well as the aerodynamic stability must be assured. Also, the heat of the jet may affect the surface or the structure and thermal protection has to be provided. Therefore, the jet flow has to be simulated and the thermodynamic behaviour of the components involved has to be estimated. For long range missiles the signature of all relevant frequencies (mainly radar and IR) has to be simulated and the geometry has to be optimized accordingly. In this case, similar to the dispensers, an unconventional shape has to be expected. This shape with a lot of relatively sharp edges will also in the subsonic flight regime cause severe separation and correspondingly very difficult vortical interference effects.

Reconnaissance and observation vehicles

Drones of different kind and for different types of missions have been used for a long time. According to the new demands in situations like out-of-area missions, confined and low-level confrontations, disarmament, armistice supervision, inspection, or boycott control, there will be an increasing requirement for vehicles of this type. The design goals imagined by possible users often sound very fabulous: An ideal observation vehicle would be invisible and inaudible, would have unlimited flight range and mission time at co-incidently high manoeuvrability and it would observe and transmit any relevant optical, acoustical and other information from protected and hidden areas, even from the inside of buildings. To meet, at least to some extent these phantastic ideas, one has to develop a vehicle that has an extremely low signature not only in the various electromagnetic frequencies but also in the acoustic regime. It needs a lift producing device capable to carry the necessary sensors and the transmission system. The propulsion system has to be as efficient as possible to save fuel and to stay at a low noise level. In many cases light-weight structures and

unconventional geometries are used in order to realize fold-up wings. Lift and propulsion systems have been realized by balloons, gliders, helicopters or airplanes with propellers or turbo-engines. For aerodynamicists the simulation of such subsonic systems is standard in most cases. A challenge is to optimize the lift and propulsion system in order to produce minimal drag and to assure for an extremely low signature level. In this case aeroacoustics, i.e. the noise produced by the flow, could be of importance, especially if the vehicle carries an acoustic sensor.

Supply gliders

As mentioned before, the safe and accurate delivery of supply or general loads in confined and insecure areas has gained increasing importance in the new scenarios. Several concepts have been developed recently. A possible configuration (Fig. 27) consists of a glider and of different devices to assure for a soft and accurate landing. The freight may have a weight of up to 5 tons. The flight range will be 3 to 5 times the drop altitude which means up to about 50 kilometers. A minimum of manoeuvrability is needed (Fig. 28). Since the system must be as cheap as possible, standard components have to be used. Similar to submunitions with parachutes the aeromechanical challenge consists in the sufficient description of the aerodynamic behaviour of the glider and of the load and in the flight mechanical description of the coupled and heavily interfering unsteady system, especially as far as manoeuvres are to be concerned.

Multi-purpose missiles

A general feature of future missiles has to be emphasized separately since it cannot be derived from a survey table of this kind: There will be an increasing importance of multi-purpose weapons. Because of decreasing budgets, closer international cooperation, smaller independent operational units and higher geographical and seasonal flexibility, troops often don't have the opportunity to be equipped for all eventualities. They rather need missiles that are appropriate against several types of targets and that are fit for all-weather missions. The weapon systems have to be adaptable easily to new or improved components, also of other nations, which means a very modular set-up, and they have to be of good transportability. For missiles an ideal system would be one with exchangeable warheads allowing dosable effects for different missions and perhaps with exchangeable guidance units with sensors that are optimal for different environments and scenarios. In this way the number of different missile systems necessary for different targets should be reduced considerably.

2.3.3 DESIGN AND DEVELOPMENT DEMANDS

From the new targets and scenarios a group of missile types of present interest was derived and listed above. If one summarizes the design and development goals assigned to them one can find several general tactical design and development demands. In many cases technological objectives can be derived directly from them. The major ones are:

High penetrativity means low detectability of the missile or low chance for defense for the attacked target.

This can be realized by

- high velocity which leaves not enough time to an attacked enemy to react properly
- low altitude flight and pop-up manoeuvres which also leads to unawareness
- statistical manoeuvres like sea-weaving or screw-shaped flight that make it difficult for a defensive missile or other measures to find their target
- low signature features (stealthy missile) in all sensor regions that could be relevant for a detection.

High efficiency of the mission means to have a high probability to hit the target with a correctly operating missile and to give the warhead an optimal chance to produce the desired effect. Several aspects are of importance here.

They are

- high precision directly at or after launch asks for small deviations of the thrust vector, of the separation from launcher and of interferences during the start phase and allows an high hit probability for very short distances already (small inner dead region)
- low structural acroclastic or thermic loads during the flight for all components by using suitable materials, by cooling (active or passive) and by optimizing the flight path guarantee the proper operation
- intelligent guidance realized by an autonomous system of a precisely working sensor and advanced software or by integrating the human guide into the loop by using a very good data link
- precisely working control devices allow high precision manoeuvres at the appropriate time and should certify high hit and kill probabilities even for high velocity flight or for long ranges
- high kinetic energy at the target if penetration is planned.

High flexibility of the missile system is of increasing importance because of the new political situ-

ation. It makes possible a wider field of action and reduces the overall costs.

Important aspects are

- adaptability of the system to increased demands or to advanced technologies without a new development phase by using an high modularity of the system
- development of multi-purpose systems, also supported by an high modularity and decreasing costs for acquisition, maintenance and logistics
- high transportability and mobility including flexible installation, modularity of the complete system and low-weight components
- suitability for actions within a wide range of regions, environmental conditions and international cooperations without larger adaptations.

These immediate tactical demands are also the main criteria for the aeromechanical design. To meet these tactical demands the aerodynamicist has to derive special aeromechanical demands which he has to accomplish as well as possible. Consequently, these aeromechanical design criteria are the preconditions within this special technological field to meet the original demands. The core of the aeromechanical know-how is found here. Important points are

- sufficiently exact prediction of all aeromechanical characteristics for all relevant geometries and flight conditions
- sufficiently exact prediction of the aerodynamical and other aeromechanical reactions to (sometimes unsteady) changes in those parameters
- securing a sufficiently high (or low) stability for all flight conditions in spite of changing center of gravity and of unfavourable aerodynamic shapes like submunitions, dispensers or stealth configurations or of aerodynamically optimized but unconventional geometries
- development of relatively optimal aerodynamic shapes for the complete missile or for components (wings, rudders) within the limits set by aeromechanical or other design demands
- optimization of the shape to reach a minimum (or - for retarders - maximum) drag
- description of flow parameters in areas that are of interest for other specialists (afterbody flow, plume, intake).

Some demands have to be met in very close cooperation with other specialists. Such subjects are

- development of control devices with exactly defineable and fastly reachable build-up of lateral forces for all flight conditions
- reaching a fast and high manoeuvrability by bank-to-turn or skid-to-turn control

- integral aerodynamical and flight mechanical simulation of unsteady or other highly time-dependent manoeuvres
- development of methods to reduce the aerodynamical, mechanical and aeroelastical loads of the surface and the structure or development of materials to endure these stresses
- development of methods to reduce the aerothermodynamic loads of surfaces, structures and components by constructive measures, by active or passive cooling, by finding aerothermally optimized flight paths or development of new materials able to stand those stresses
- development of IR domes and of radomes suitable for high velocities
- design of stealthy missiles with low signature levels in all possible domains (this is often already a primary demand)
- simulation of plume emission and transmission characteristics.

2.4 INCREASED DEMANDS TO AEROMECHANICS

A large number of detailed work packages can be derived from the design demands listed above and from the specific questions arising in connection with the different missile types. Some of these subjects have been mentioned above shortly. Here, a more systematic overview is given.

A general remark has to be made here: A survey like the present one easily imposes the impression that all problems in this field are more or less solved and that there are only a few questions open, mostly in coincidence with the present work of the author. In our case this impression would be wrong. Certainly, project aerodynamicists all over the world are able to handle a lot of very difficult problems - often simply because they have to handle them somehow - but there is no doubt that in almost all particular subjects there is a need to improve the fundamental knowledge on physical relations, the experimental and mathematical simulation models and the performance of all design tools.

In addition, there are the new topics where ideas perhaps existing already in other specialized areas have to be transferred and extended to the needs of missile design. For the many questions that are still open we have to find answers in the future or we have at least to prepare methods to produce first qualitative results.

Several of the subjects arising within this context will be discussed later in the present or one of the following lectures in greater detail. In this case only a few key-words are listed here. The same is true for subjects that are still of very high or even increasing importance but that are well established and where, therefore, it seemed not to be necessary to summarize them in detail.

2.4.1 AERODYNAMICS

The standard aerodynamics of the classical missile design has nowadays to be finished in much shorter time, to a much lower price - which automatically excludes expensive wind tunnel tests - and very often with a much smaller error tolerance, which makes it urgently necessary to improve the existing design tools. The new aeromechanical design aspects that are considered in addition to the classical ones have been mentioned before. As can be seen from the lists above the subjects in the following summary will be of very different importance for different missile types.

- General dependence of aerodynamic parameters from the Mach number, especially for the transonic and hypersonic regimes.
- Transonic velocity: increasingly, high precision results in this difficult regime are requested already in the design process. Since many parameters show a high sensitivity to the Mach number close to the speed of sound, design methods have to be improved here.
- Hypersonic velocity: main problems are drag prediction, shock configurations, shock/boundary-layer interactions, surface roughness, interactions between aerodynamics and aerothermodynamics, real gas effects, experimental tools for realistic simulation of missiles (sea-level pressure, temperature, Reynolds number), conversion of experimental data to free-flight conditions, data bases to extend semi-empirical methods.
- Surface roughness: a general investigation for projectile geometries at subsonic (Mach = 0.8) and supersonic (Mach = 2.4) velocities and with different types of rough surfaces was published in Ref. 62.
- Surface roughness because of ablating or ablated coatings: this will affect the boundary-layer and, consequently, the aerothermodynamic behaviour and the drag, in severe cases even the other aerodynamic coefficients. The simulation of this phenomenon is extremely difficult since not only unsteady boundary-layer effects are taking place but also involved, possibly catalytic unsteady chemical reactions under the influence of aerothermodynamic processes. Therefore, for the design aerodynamicist only a very global simulation tool for qualitative predictions would be applicable.
- Shock/boundary-layer interaction: a review of the subject was given in Ref. 63.
- Magnus forces are experienced by a body spinning about an axis which is inclined to the on-

- coming flow. This effect is mainly of importance for fast spinning projectiles and shells. A recent publication (Ref. 64) presents an appropriate test rig. Numerical procedures mainly consider the asymmetric boundary layer introduced by the rotation.
- Deliberate angles of attack may appear in missile flight. This leads to severe separation effects (Fig. 29), but also to the problem that conventional missiles can have very unconventional cross-sections in planes normal to the incident flow. When the incidence increases the slender circular body starts with steady symmetric and later asymmetric separation and goes through an unsteady vortex flow regime to a Karman vortex street at normal incidence. Very complicated separation features may arise in those regions (Ref. 65). For missile wings there will be mainly the problem of $C_{L,max}$ in the region of full separation and lift breakdown. Downwash and vortical interactions are additional problems. A recent review on fundamental problems of separation is given in Ref. 66.
 - Deliberate roll angles may appear, too. Design methods have to take this into account.
 - Bank-to-turn and skid-to-turn manoeuvres lead to different fin deflection configurations and have to be implemented into the design tools.
 - The influence of flight altitude to the aerodynamic characteristics, especially for the drag and, consequently, to the range has to be considered.
 - Unconventional or even 'un-aerodynamic' geometries of missiles are designed more often now (dispensers, stealth geometries, missiles with special sensors or antennas, configurations with highly integrated intakes, wings, radomes, stores and other excrescencies, waveriders, and configurations for conformal carriage). Ref. 35 gives a survey of practical configurations. They show severe separation at the edges, even more difficult to simulate if they are not sharp. Massive interference effects arise between the vortical flow and the different lift and control devices. If there is only one symmetry plane left (as for plane wing configurations) strong coupling effects have to be expected for skid-to-turn manoeuvres.
 - Variable geometries (bending nose, separation of a booster or other components, possibly because of a defect, variable wings, deflecting fins, closed and open intakes) show time-dependent features and lead to the necessity of an integrated aerodynamical and flight mechanical simulation, where in some cases unsteady aerodynamic behaviour might appear.
 - Special geometries for components like grid or ring wings show unconventional characteristics. The results of new design methods for these cases have to be integrated into the simulation of the full configuration.
 - Intakes for air-breathing propulsion are an important component of the missile airframe design. They may improve or decrease the overall aerodynamic behaviour of the missile depending on their shape. Major problems are the quality of the flow at the inlet, the drag induced by the intake, separations from edges or from curvatures and the interferences induced by them. A great variety of different types of intakes have been designed for different applications (Fig. 75). The intakes may appear in unfavourable positions or they may be optimized in shape for varying demands. Reviews are given in Refs. 4 and 67-69. To approach stealth quality, submerged (Ref. 70) or flush intakes are considered sometimes.
 - Aerodynamically optimized shapes ('inverse problem'): This approach has been a desire for many designers. Because of improved numerical methods it has now a broader basis for research. At the moment most investigations are concentrated on optimal wing design (Refs. 71-80), probably since there is a limited number of independent variables that can be optimized with tolerable effort. Only a few papers deal with the optimization of bodies (Ref. 81), often for waverider shapes. But the non-aerodynamic limitations for a body or even more for a complete configuration are by far too many and too strict in most missile design cases to allow such an approach in the near future.
 - Retarders, parachutes and gliders: this subject has been discussed already. The main problems are the flow around flexible membranes, unsteady separation, porosity or semi-porosity, inflation procedures or other flow-dependent behaviour, severe interaction between the vortical flows of the load and the canopy and strong aerodynamic / flight mechanic coupling between both parts and with a high degree of freedom.
 - Severe changes in center of gravity during the flight, mainly because of the burn-out of integrated boosters or propulsion units, cause difficulties in keeping a proper stability of the missile. Some ideas like movable wings or others have to be developed to adapt the center of pressure correspondingly.
 - The afterbody and base flow accounts for several effects in the design of a missile: the base flow may influence the uncoiling of fibers or other processes taking place there. The afterbody flow field may interfere with fixed or deflecting fins

situated closely to the base and may change the forces and moments. The shape of the base itself also may change the performance of a projectile (Ref. 82). But the main influence of the base flow on the missile is that it is responsible for a considerable part of the drag. This part is variable with geometry and speed but will amount to approximately 30% for most missiles and can represent up to 50% for an unpowered projectile at transonic Mach numbers. Therefore, it is no surprise that a lot of effort has been made to predict this characteristics. Surveys are given in Refs. 83-88. The attempts to reduce this base drag are mainly concentrated on using boattail afterbodies which can make an effect of up to 8% and on the base bleeding or base burning techniques (Figs. 30-33) that are often used for artillery projectiles (Refs. 91-95). To predict base pressures within a design context it has turned out that a good approximation is reached by calculating the pressure along the body contour including a simulated plausible dead air region and then to take the value of the body baseline for the base pressure.

- Simulation of jets and plumes (determination of aerodynamical, thermodynamical, chemical and optical parameters of the gaseous constituents including density, velocity and temperature distributions of particles of smoke or solid propellants): this subject is, if taken in full extent, one of the most ambitious tasks of modern aerodynamics, since a lot of difficult problems shortly indicated above are combined here and lead to the necessity of using the most elaborate numerical tools to simulate such a flow. In addition, experimental investigations usually can produce only global results but cannot measure the detailed unsteady structures and parameters. On the other hand, such numerical studies mean a very high effort that is not affordable for design aerodynamics under normal conditions. The background of most of these calculations is the wish to acquire an sufficient basis for the signature simulation of the plume. In this case the flowfield has to be simulated with all details (Fig. 34). There are approximations with two-phase or multi-phase flow, flows with different loads of dust or grains or with smoke (Refs. 96-103). The content and the fraction of particles may have a large influence on the shape and the parameters of the plume (Fig. 35). In particle flow different regimes may be distinguished (Ref. 97). In dense particle flow the mean free path of particles is small compared with characteristic dimensions, while in collisionless particle flow the mean free path length is large compared with a characteristic length. Only if the particle mass flow is small compared with the mass flow of the gas phase, the gas flow may be considered to be unaffected by the particle flow. The particle flow usually will contain particles of different size and velocity. By the collisions occurring between the particles a diffusive motion is induced that is responsible for the spreading of the particles within the plume. According to the high initial temperatures of the particles at the nozzle exit, radiative heat transfer within the plume has to be considered and introduces an high signature level. Particles of different size may have different temperatures which has to be considered in an elaborate model. Even for the simulation of plume signatures or of plume transmissivity for laser beams one should use much cheaper tools within early design phases, which means semi-empirical ones if no other more qualitative model can be found. This is true to an even higher extent if plume models are only used to simulate afterbody flows or interference effects of plumes or jets with the missile itself (for lateral exhausts) or with fins and spoilers, with launchers or airplane components (during store separation). In those cases less expensive theories can be used successfully (Refs. 104-106).
- Thrust vector control: different realistic types of this method can be imagined (Fig. 7), some are realized or in development for modern missiles (Ref. 44). A review of investigations on most of the types and of their virtues and limitations is given in Ref. 107. There are a lot of mechanical problems to be solved to realize such a system. The major task for the aerodynamicist is to predict the lateral forces and moments induced by such a system. In order to do this he has to simulate the original nozzle flow and the one modified by some internal devices (spoilers, injections) and the afterbody flow in the area of the fixed or flexible nozzle. One of the methods to modify the nozzle flow is liquid or hot gas secondary injection. Basic flow studies (Ref. 108) and investigations of side forces that can be reached by single or multiple injections (Ref. 109) have been executed.
- Lateral jet control is one of several control devices applicable for missiles (Ref. 22). It may be situated close to the center of gravity, in the nose or afterbody section or at the wings showing different effects on the flow and the missile in each case. Although this control method has some severe constraints, it is favourable in cases where low speed or high altitude cause low stagnation pressures and where in that way small lateral forces are introduced by control surfaces (Ref. 4). It also allows to reduce the response time of the control and induces additional drag only during the blow time. Lateral jet control may be realized by discretely working pyrotechnical devices, by continuously blowing elements changing the thrust direction mechanically or by fluidics, or by liquid fuel propul-

sion systems similar to those used in space applications. The characteristics of the flow are very complicated (Fig. 36). There have been a lot of early investigations for flat plate conditions, but it turned out that this is a highly three-dimensional problem. General aerodynamic features of a jet in cross-flow are given in Ref. 111. The literature until about 1985 was reviewed in Ref. 112, while information about recent developments in this area may be taken from Ref. 113. The aeromechanical simulation of lateral jet reaction control has to take into account the local interactions between the jet and the external flow around the missile and, secondly, the downstream interactions on the body surface, on adjacent surfaces and on fixed or deflecting fins. The first interaction leads to aerodynamic problems similar to those mentioned for the plume simulation, but with even higher demands because of the asymmetry of the cross flow and because of the adjacent curved 3D body surface. The interaction of the modified flowfield with the missile is conventionally described by an 'amplification factor' defined as the ratio of lateral jet thrust plus interaction forces over the value of the lateral jet thrust if injected into vacuum. Since this coefficient can be smaller than 1 for many practical cases (Figs. 37 and 38), it is favourable to use the neutral term 'jet effectiveness ratio' instead. For the flight mechanical simulation one needs an - at least approximate - value for this coefficient during the design process already. No really sufficient semi-empirical or similar fast and cheap design tools have been developed until now because of the very high number of geometrical (nozzle and missile) and flow (external and jet) parameters involved. The use of advanced CFD methods is not applicable in early design for extended parameter studies but only for a few numerical checks. The wind-tunnel investigations are difficult because of the complicated flowfield interactions taking place and because these interaction forces that one is looking for are only a small fraction of the lateral thrust and even more so of the global forces acting on the missile. The correlation of wind-tunnel results with free-flight data is very complicated because of the fact that many parameters cannot be scaled appropriately, especially for hypersonic speeds. Systematic experimental studies are very expensive, again because of the large number of relevant parameters. Therefore, considerable effort is still necessary nowadays to aeromechanically integrate a lateral jet control system into a missile being designed. Experience shows that only numerical methods are able to produce appropriate results at the moment. Therefore, there is a need to make these tools as effective as possible.

- Interference effects on a missile by an inhomogeneous flowfield can be investigated by generalizing classical aerodynamic methods. External flowfields with velocity vectors variable for different points of the body surface can be modelled by introducing variable incidence angles along the body instead of a fixed one. Many of the aerodynamic tools used in the missile design process - as for example simple potential methods or panel programs - present this possibility. The potentialities of such approximations to get insights into practical aerodynamic effects (Fig. 39) are often underestimated compared with the more spectacular CFD methods. The inhomogeneous flow may arise from the flowfield of a gust, of an airplane, an helicopter or other interfering vehicles, or it may be perceived by the missile during launch or separation.

- Multi-body interference effects have been mentioned already. They appear in a more general sense in most of the examples listed in the preceding paragraph. But within this context we will limit the term to cases where the interaction forces will be noticeable on both interaction partners. This can be the case during the ejection of submunitions (Fig. 40), within clouds of bodies, or for missiles in close formation parallel to each other or in tandem flight following each other. Aeromechanical aspects to be considered are the simulation of the interacting flowfield including severe separations in most cases, interaction of vortical flows and, possibly, an integrated aerodynamical/flight mechanical simulation.

- Unsteady manoeuvres of the missile, time-dependent changes of the outer flow parameters, fast changes in missile geometry and microscopically (turbulent boundary-layer) or macroscopically (unsteady vortex flow) unsteady flow parameters. Strictly spoken, each flow around a missile is 'unsteady' since the flight is time-dependent. But, fortunately, in most practical cases one can consider the problem to be quasi-steady which means that it can be described as a continuous sequence of steady flow conditions. A simple first check of the validity of this approximation is to compare the typical times: The effect of a disturbance peak within the flow expands with the speed of sound, its source propagates with about the free stream velocity. This leads to a period of the order of L/U_∞ where the disturbance affects the flow around the missile.

The description of unsteady flow parameters - which are also the source of aeroacoustical phenomena - is a field of basic research and includes some fundamental questions like turbulence modelling. But even in the case of

quasi-steady conditions there are additional forces and moments compared to purely steady ones. For a pitching motion of a wing or a body an additional external flow is induced resulting in a modified angle of attack distribution along the axis. This additional angle is zero at the pitching axis and varies linearly (Fig. 41). Another distribution is induced by a rolling motion (Fig. 42). From the appropriately modified flow conditions the coefficients for damping forces and moments can be derived (Fig. 43). A lot of experimental, semi-empirical and numerical studies have been executed about this subject (Refs. 116-121).

If the criterion of quasi-steadiness is not fulfilled a completely time-dependent simulation has to be executed. It has to include then all relevant aeromechanical aspects (like aeroelasticity, control deflections or lateral jets, propulsion characteristics, geometry changes as booster separations, flight mechanical parameters or structural heating), at least, if their rate of change is of similar order of magnitude. The force and moment characteristics will show in this case a more or less visible hysteresis which means, for example, that the forces during the pitching-up motion have a different characteristics from the ones of the pitching-down motion. Physically, this means that the separation takes place at another angle of attack than the reattachment. Some studies of these phenomena have been executed (Refs. 122-123), often for wings in pitching motion (Ref. 121), but for most practical cases in missile design such an approach is too expensive compared with the additional information obtained. One case where such an unsteady approach might be justified is a vertical launch combined with a very fast turn to more or less horizontal flight.

2.4.2 FLUID MECHANICS AND HYDRODYNAMICS

Problems in this area may appear in missile design occasionally and often can be solved by using generalized aerodynamic tools. Subjects that are likely to appear are

- Vehicles below sea surface: these may be torpedos, submarines or missiles with a flight path partly underwater as, for example, submerged launch of missiles. The propulsion of submarine vehicles is normally executed by propellers. For some flow conditions cavitation will take place which means that two-phase flow has to be modelled.
- The interface between two phases (water and air) has an influence on the fluid mechanical charac-

teristics of vehicles just above or just below the interface and on the behaviour of their wake.

- Pipe flows or ducted flow of gases or fluids can be summarized here. Multiphase flows, possibly including a fraction of solid particles as for plumes, are quite challenging tasks, especially when chemical reactions (afterburning or intermolecular processes) take place.

2.4.3 AEROTHERMODYNAMICS AND THERMODYNAMICS

Because of the high effort made in hypersonic research for space applications over the last years, aerothermodynamic investigations have abounded in number and width since that time (Ref. 124). Nevertheless, the direct applicability of many of these approaches to specify problems of hypersonic missiles is limited to general verification of methods or to just stipulating new ideas from experimental or numerical research scientists. This comes from the fact that missiles are unmanned one-way articles and that hypersonic missiles - except TBMs which have features similar to space rockets - only fly at much lower Mach numbers, but at zero altitude. Different approximations for the flow are valid here, therefore. In addition to that, missile shapes and components are aerodynamically optimized only to a much lower degree since aspects like high manoeuvrability, warhead or radome shape and function, and even more the aspects of low financial effort for the design are of superior significance. Therefore, special methods and approaches for missiles have been developed (Ref. 125). The importance of aerothermodynamics in the hypersonic speed range can be estimated by a simple sketch showing the stagnation temperatures and the temperature limits for the use of different materials (Fig. 44). One can see easily that there will be a severe problem for the use of radomes at high velocities, although the stagnation temperature is not reached in most real cases. From the limit quoted for IR domes one can see that aerodynamical heating sometimes has to be taken into consideration at velocities much lower than those conventionally called 'high velocity' or 'hypersonic'. In cases of long flight times aerodynamic heating - often in combination with or dominated by heat production of internal sources - can become a severe problem for components like electronic devices or explosives. This is the reason why structural thermodynamics is closely related to aerothermodynamics. On the other hand, thermodynamic parameters of the different materials are needed for suitable design simulations and give access to structural stability (Fig. 45) and to the aeroelastic behaviour under heat loads.

Major problems of aerothermodynamic heating are

- In order to reproduce properly the parameters of hypersonic flowfields one has to consider the effects of aerodynamic heating on the molecules of the air. Different approaches for real gas simulations - in contrast to ideal or perfect gas approximations - can be made (Refs. 126 and 127). These thermochemical models will change the surface temperatures on the missile since some of the energy is transferred to excited rotational-vibrational motions of the molecules or chemical reactions, dissociations or ionizations, depending on the local temperatures.
- Determination of the thermal boundary layer which - as the velocity boundary layer - shows different characteristics depending on if the wall is cooled, insulated or heated (Fig. 46). The temperatures reached here are responsible for a considerable part of the heat transferred from the flow into the wall. The other part is the resulting vector of radiation to and from the surface.
- For some flow conditions a severe interaction between heated wall and boundary layer has to be accounted for. Even catalytic effects at the surface can be of importance for certain flow conditions. The modified boundary layer causes a change of the aerodynamic behaviour of the missile. This has to be considered in advanced design simulations. Especially for experimental studies this could make it necessary to introduce a hot model technique in order to get correct results (Ref. 129).
- Simulation of heat loads for IR windows and radomes (Refs. 18, 45 and 130).
- Simulation of heat loads and structural stability of fins, surfaces and structures.
- Consideration of the behaviour of different materials under heat loads (Ref. 131).
- Active cooling of radomes and structures (Refs. 132 and 133): A lengthy research program has produced some practicable solutions for this difficult problem already (Fig. 47). The aerodynamic interaction of the cooling flow - for example chemically reacting $\text{NO}_2/\text{N}_2\text{O}_4$ - with the boundary layer flow has to be simulated. A multi-port ejection seems favourable in comparison to a single slot ejection because of the more homogeneous mixing in the case referenced (Fig. 48).
- Passive cooling is executed by ablating materials (Ref. 131). The process of ablation can be sublimation (as teflon) or some kind of carboniza-

tion or other heat-consuming chemical reactions. The thermodynamic parameters of the materials considered for the design have to be known, the ablation process has to be simulated and the effect of the cooling on the heat balance has to be modelled.

- Simulation of heating and cooling of surfaces, structures and components due to aerothermodynamic or internal heat sources and sinks. Radiation, convection and conduction effects in the interior of the missile have to be included.

2.4.4 AEROELASTICS AND STRUCTURAL MECHANICS

Different to the impression one could get by reading the headline a project aerodynamicist certainly will not take over the responsibilities of the specialists in structural mechanics. But similar to other subjects mentioned he has, on one hand, to know thoroughly the problems he could run into during the design process and, on the other hand, must be able to give fast qualitative answers during a study or predesign on problems where aerodynamic effects are coupled with other aeromechanical ones. For structural mechanics several interactions can appear; aeroelastic ones are an outstanding example. Aeroelastic effects may change the aerodynamic characteristics of the missile and will influence in that way the manoeuvrability (Fig. 49) and the overall flight performance (Ref. 134). Right in early design phases control people ask about missile eigenfrequencies. They often have approximately the same values as the frequencies of the control parameters and can cause then unfavourable interferences (Ref. 135). Major work packages to be treated are

- Calculation of aerodynamic moments and load distributions for complex surfaces - like cylindrical or otherwise curved shells (Ref. 136) - and for complex structural configurations to simulate the mechanical reactions or the structural stability. In many of the more ambitious cases the aerodynamic values will be unsteady ones (Ref. 137).
- Estimation of the static and dynamic bending of bodies (Refs. 138 and 139) and of wings. For missiles the bending motion of the body usually is of higher significance since the wing spans are small in most cases. The flutter of the wings is of higher relevance for airplanes which is the reason that most approaches for aeroelastic methods have investigated this aspect. Eigenfrequencies and eigenforms of the vibrational modes have to be estimated. In a strict sense one would have to simulate aeroelastic effects in an integrated aerodynamical/light mechanical/aeroelastic form since there will be a coupling

between all those parts (Ref. 140). For example, there will be an aeroelastic response to a fast flight manoeuvre (e.g. for a vertical launch and fast turn to horizontal flight). This and the changed geometry influence the aerodynamic characteristics of the missile and lead to different aeroelastic response and flight paths. In practical cases this global simulation is replaced by a quasi-steady approach which gives sufficient estimations under normal conditions.

- The vibration of shells or other surfaces (Ref. 136) and their interaction with the aerodynamic boundary layer flow can be the cause for aeroacoustic effects or for later structural damage.
- Mechanical stress on surfaces can be introduced by aerothermodynamic effects or by dust and rain impact.
- Sufficient data of structural characteristics have to be available for the materials used in missile design.
- The reaction of flexible structures like membranes, parachutes, gliders or thin retarder or control surfaces to steady or unsteady aerodynamic loads have to be simulated.

2.4.5 FLIGHT MECHANICS AND INTEGRATED SIMULATION

In the standard working procedure during the design process aerodynamics and flight mechanics represent separated packages. This is true according to the fact that in most cases the time-sequence of different flight and flow conditions around the missile can be interpreted as a sequence of quasi-steady states and, therefore, may be separated from each other. Nevertheless, a very close cooperation of both specialists is necessary even in this case, since a flight mechanical simulation is the only way to test if the missile configuration designed by the aerodynamicist shows a sufficient agreement with the demanded flight performance of the system. In advanced design phases the inclusion of the control laws into the flight simulation is needed for this prove. For all these simulations flight mechanics codes incorporate the aerodynamic characteristics by a more or less elaborate (steady) aeromodel, from which the parameters for the actual flight conditions are derived by interpolation or analytically.

In a few cases of unsteady aerodynamic or aeroelastic behaviour or of intensive coupling between flight mechanics and other acromechanical subjects like thermodynamics or signature determination it will be necessary to execute a combined simulation. In this case for each integration step

of the flight mechanical (eventually controlled) simulation the new aerodynamical or other relevant parameters are determined. Here, one has to differentiate between cases where a real interaction between the two subjects exists or where only some parameters are time-dependent and have thus to be simulated along certain trajectories.

The following situations seem to claim for a coupled simulation

- Store separation: Many investigations have been executed on this subject (Refs. 141 and 142, and Refs. quoted there). There are two major aspects of store separation. Airplane aerodynamicists mainly account for the safety of the carrier after separation. Missile aerodynamicists are interested in the initial errors introduced by the inhomogeneous flow field and have to assure for the appropriate flight performance in spite of the deviations and additional stresses caused by the separation.
- Ejection of submunition: This is similar to the store separation problem but the reaction on the dispenser and the interaction with other submunitions has to be taken into account.
- For the proper simulation of the parachute/load system not only the flight mechanical degrees of freedom have to be included but also the aeroelastic deformation of the canopy and the severe aerodynamic interactions.
- Very fast manoeuvres like vertical launch at high speeds with fast turn to horizontal flight or end game manoeuvres may lead to situations where the process cannot be considered to be quasi-steady any more but where an unsteady simulation has to be executed.
- Optimization of propulsion performance during the flight, for example for double impulse propulsion (DIP systems).
- Simulation of the aeroelastic behaviour of the missile or of components during the flight.
- Simulation of aerothermal heating and of ablation along the flight path.
- Determination of IR, radar and other signature cross-sections of missiles during the flight and in dependence of a fixed or also moving observer.

In other cases a very close cooperation of acromechanical design specialists with flight simulation people is necessary and mutual understanding of the basic problems on each side is essential:

- New digital control methods need a much higher precision of the aerodynamic model. Transonic flow regimes, although passed very quickly, unsteady conditions or areas close to zero angle of attack, yaw and other small effects have to be described rather exact to be able to design complex control systems.
- The same is true to control an unstable missile.
- The verification of experimental or numerical design data, mainly for aerodynamics, can be improved by deriving these data from free-flight measurements (Ref. 143). A parameter identification procedure using an optimization method has to be used. Many of the airplane flight testing techniques can be used except that for missiles the data acquisition and transmission is still insufficient in many cases.

2.4.6 AEROACOUSTICS

For civil applications aeroacoustic aspects have been playing an important role for a long time and are getting increasing importance because noise can be very troublesome. Therefore, quite high effort is made not only for ventilators, cars and trains to reduce the aerodynamically induced noise, but large programs exist also for helicopters and for airplanes to reduce this type of noise together with the other, non-aeroacoustic, components. For helicopters the main source of noise are the blades moving with transonic speeds at the tip, and for airplanes engines and jet flow are responsible for most of the aerodynamic noise. However, not the noise annoying the population is of interest in missile design but the acoustic signature. Especially for helicopters, both the detection and the camouflage aspect have been investigated intensively (Ref. 144). For airplanes and missiles there used to be only a limited need to take this type of signature into account, mainly because of their high speed. This is changing now. Long range missiles with terrain-following features could be detected early by acoustic sensors at a forward position and could be attacked if their speed is not high enough. So both aspects mentioned before are arising here again. Drones have a low speed usually and are therefore also detectable in the acoustic regime. Another problem in this case is the aerodynamic noise produced by a flying vehicle equipped with acoustic sensors.

Even the aerodynamic sound of a glider could cause errors in the detections. Structural stress on a missile can be produced by acoustic effects as for example in the case of store carriage close to an engine. A recent survey of the problems is given in Ref. 145.

Major tasks that have to be investigated in the field of aeroacoustics within the context of missile design are

- generation of aeroacoustical noise by the fluctuations of turbulent boundary layers or of unsteady separated vortical flow
- simulation of the propagation of sound in dependence of the environmental conditions
- active control of noise generation by silencers
- passive control of noise emission or propagation by constructive measures or by the use of appropriate materials.

2.4.7 SIGNATURES IN THE IR / VISIBLE / UV

Nations engaged in the development or defense of strategic or tactical ballistic missiles have been interested for a long time to get information about the radiation emitted from those systems. SDI and other initiatives intensified the research in this field. According to the changing scenarios the interest in such information is even growing and many additional TBM launch sites for possible terrorist attacks are considered now.

For a TBM the highest detectability is given in the boost phase when the hot plume emits radiation of almost all wavelengths. During the re-entry phase the surface of the TBM is heated by aerothermodynamic effects and consequently emits a solid body radiation with a maximum in the IR or even the visible range according to its temperature. A general survey of rocket radiation is given by Ref. 146.

Conventional missiles have been detected in most cases by the visible smoke produced during their boost phase. Observations of the smoke give clear evidence of the missile trajectory, speed, distance and launch site. With the development of 'smokeless' fuels and with an increased probability for night and adverse weather strikes this type of signature is no longer sufficiently large for target detection and observation. Therefore, the observation of heated surface radiation (mainly for long range missiles of high velocity or for drones with minimal signature demands) and of plume signatures (during propulsion phases of long range missiles) is of high interest. For missiles with a short flight time the signature aspects seem to be much less important because of the resulting extremely short reaction times for defense. Another aspect of optical features of the plume is its possible interference with the guidance system of the missile. The laser beams of laser beam riders or that of guidance and control systems using laser data links can be disturbed, attenuated or absorbed by the plume. Summarizing these main tasks the following subjects have to be investigated:

- Emission of the missile surface according to Planck's law for black or nearly black body radiation. The temperature distribution along

the surface may be influenced by aerodynamic heating or by heat producing components. Especially nozzles or engines are high energy radiators. The spectrum emitted by the solid surfaces is continuous.

- Minimization of this radiation by measures in missile airframe and propulsion unit. The design of missile afterbody shapes and of exhaust nozzles can be tailored to reduce the radiation of hot areas. An appropriate selection of materials for the surface can support this.

- Emission of jets and plumes: This radiation consists of discrete spectral lines which arise from transitions between vibration-rotation states for the IR and electronic states for the visible and UV regimes. The most important spectral ranges for plume detection at the moment are the middle infrared region of 3-5 μm and the solar blind ultraviolet spectral region below 300 nm.

As mentioned before, the hot combustion products of a missile propulsion system appear in an highly turbulent plume as they expand through the nozzle into the afterbody flow. These products consist of hot gases from the combustion process (mainly carbon and hydrogen oxides), of activated and deactivated molecules promoted by chemical reactions, of accelerated particles of incompletely burnt solid fuel, of mist or drops of incompletely burnt liquid fuel, soot, metal oxide condensates (e.g. Al_2O_3 , MgO , ZrO_2 , ZrC or B_2O_3), or other solid constituents. The parameters of the plume are modelled by aerodynamic tools as described before. The radiation can originate from chemical reactions during the burning process inducing excitations in electronic or molecular vibrational and rotational states, from chemiluminescence, fluorescence or exothermal reactions producing radiation or it can originate from thermal emission in the afterburning phase introduced by secondary chemical reactions or by afterburning of solid or liquid fuel constituents with atmospheric or plume components heated by shock waves and mixed by aerodynamic processes. The solid particles, additionally, can execute catalytic effects on chemical reactions or on the emission. They emit radiation according to their temperature and they will scatter any radiation passing the plume.

All possible spectral regimes for optical emission have been investigated intensively. Examples are, for the IR Refs. 147 and 148, for the visible Ref. 149, and for the UV Ref. 148. A typical infrared emission spectrum is shown in Fig. 50.

- Modelling of the rocket exhaust smoke and its visibility (Refs. 96 and 150 - 152).

- Selection of appropriate fuels for a missile to be designed (Ref. 153).

- Reflection of radiation at missile surfaces

- Simulation of background radiation to determine the contrast between the missile and the optical environment.

- Transmission of radiation (of missile or plume signature or of a laser beam) through the atmosphere. Influences consist of atmospheric turbulence causing fluctuations of the refraction index of the air because of temperature differences, and of scattering and absorption by molecules, aerosols, dust, mist, haze, rain, or snow (Ref. 154).

- Determination of the trajectory and observer position dependence of the signature. Since this has to be done with small time steps for a complete flight or at least for a phase of it, the (plume) radiation model used in missile design has to be fast and cheap enough to allow this. That is not an easy task, since the simulation of the aerodynamically, chemically and optically very complex and highly interacting processes must be simplified considerably without neglecting the most important effects for each project case.

- Numerical simulation of the transmission of a laser beam through a missile exhaust plume.

2.4.8 RADAR AND MW SIGNATURES

Missiles, especially long range ones, are threatened more and more by defensive measures. These depend on early and sure detection. Airplane designers have been used to that for a long time and have worked out concepts for 'stealthy' aircraft with low signatures. Since radar is the signature regime of highest applicability with respect to environmental conditions, radar signature is the one that is usually reduced in the first step. The same becomes true now for missiles and there is an increasing number of design concepts for 'stealthy' missiles. The difference of the progress in both areas can be seen from the fact that it is quite a challenge to reach a radar cross-section for a missile comparably low to that of a stealth bomber. One important value for radar detectability is the radar cross section (RCS). This is usually not the geometrical cross-section seen from a certain aspect angle but rather a value proportional to the reflected electromagnetic energy. Because of the physical characteristics of electromagnetic waves the radar beam is not simply reflected by a surface like a beam of light in a mirror but the radar receiver rather sees a limited number of discrete centers of dispersion.

These are mainly surface areas normal to the beam, surfaces with internal angles that reflect the beam several times backwards to the receiver, or areas where electromagnetic energy is scattered into the direction of the incoming wave by diffraction effects at discontinuities of the surface like corners, edges, inlets, gaps or slots.

The other essential value for radar detectability is the detection range. Since it is proportional to the fourth power of the RCS, the cross-section of a missile has to be reduced by orders of magnitude to reduce the detection range considerably.

To reach a missile design with a minimal radar cross-section one has to apply the general rules derived for airplanes. There are two basic approaches to RCS reduction, namely to design a shape with a minimal backscatter, and to use suitable coating materials and layers for energy absorption and cancellation (Refs. 155 and 156).

The RCS aspects mentioned until now are equivalent to the signature of the missile surface in the optical regime. As it was the case for optical signatures, there is also a radar and microwave emission of the plume and the possibility of radar beam attenuation by it (Ref. 157). Microwave radar (the term is extended usually to the range of 3 GHz to 120 GHz) is used for missile location, tracking and guidance. For successful operation the communication links must be free of serious distortion. By passing the plume, attenuation or unwanted modulation can occur because of interactions between the radar or microwave beam and the free electrons within the hot, turbulent exhaust gases. On the other hand, the scattering of the incident wave and the emission of radiation of the proper wave lengths from sources within the plume offer the opportunity to detect TBMs or missiles during propulsion phase.

The specialist in aeromechanics designing a missile certainly will not become a specialist in radar or MW aspects. But the simultaneously very strong interaction of missile shape with aerodynamics and signature, especially radar and MW signatures, make it necessary that the designer at least is able to make a reasonable guess for the RCS value reached by his modified shape (Figs. 51-53). Only by a close cooperation of both disciplines a simultaneous optimization for a good aerodynamic performance and for a very low signature can be reached.

The main tasks for this work are

- Estimation of radar cross-sections of complete missiles. Detailed numerical and experimental studies of the missile and optimization of components will have to be executed by specialists. Since the numerical tools in this field have similar features to the aerodynamic CFD methods, these specialists might well be included in a modern aerodynamics/aeromechanics team.

- Optimization of the overall missile geometry and of critical components like intakes for air-breathing missiles in close connection of aerodynamical and RCS aspects.

- Estimation of aerodynamic and aeroclastic problems of radar coatings and absorbers.

- Simulation of the radar cross-section and of the observed signal during the flight in dependence of the different trajectory positions and aspect angles and of the position of the radar emitter and receiver.

2.5 NEW TOOLS OF MISSILE AEROMECHANICS

Similar to the advances of different technologies that help to reach new system requirements there are new tools that have been developed or have grown up during the last years which will support design aerodynamicists to meet the increased demands within this field. The innovations took place in the numerical simulations, promoted by advances in computer hardware and software, and in experimental studies represented by test facilities and installations and by measurement and evaluation techniques.

2.5.1 DATA PROCESSING

No discussion is necessary about the improvements of computer performance and about the decreasing prices for a given computer power over the last years (Refs. 159 and 160). It seems that this trend will continue for a while. The availability of rather powerful workstations at a moderate price opened the possibility to use those installations for most of the daily work in design aeromechanics at even increased requirements in their performance. Therefore, nowadays supercomputers are mainly used for numerical simulations with advanced CFD programs and for large size problems. The vector machines that were predominant for several years are being replaced now by parallel architectures which - if this technique can be transferred to a degree of simplicity in handling that makes it attractive also for the aerodynamicist not specialized in numerics - can make the decentralized and cheap work station even more attractive and would allow the use of numerical methods already during earlier design phases where it cannot be afforded today.

Another important advance on this area during the last years are the new possibilities of post-processing. Different graphic tools including the use of colours allow to get new insights into

results of numerical simulations. Fundamental physical processes may be studied in that way by using appropriate simulation methods for numerical experiments where parameters that are not accessible for measurements can be changed easily and independently from others. For time-dependent or unsteady processes animation tools can be used which help the imagination which often gets into trouble with 3D and time-dependent pictures. For project use in missile design it can be very helpful to see in a preliminary simulation on the screen not only the constructive or aerodynamic consequences of a change in design parameters but also the new flight performance. All this can be of great help as mentioned, but it urgently asks for appropriate interpreters, since nothing is earned with purely producing nice coloured pictures. It seems that this is a widespread problem and that good interpreters are very rare compared with numerical specialists.

An additional problem arising within this context is the question of commercial software. The answer to it certainly depends on the philosophy of the different industries and of their man-power to produce own software. But it seems that some general statements can be made. An increasing spectrum of commercial software is offered in fields where a high number of customers are to be expected. In these cases the quality and the handling, the transferability to different machines, the compatibility with earlier versions and with other programs, the maintenance and the training are usually adequate. This is true for example for postprocessing tools, for subroutine libraries, for CAD / CAE packages and for several finite element (FE) programs. It is difficult for fluid dynamic program systems to reach this standard, since the number of users with very high demands in precision and flow conditions - as in the aerospace industry - is limited. Therefore, these codes are optimized very often for subsonic flow around complicated structures which are created by combined CAD codes or have to execute simulations for special applications in a narrow field, mostly for classical mechanical engineering problems. The benefit of these programs for missile design usually is limited to the solution of special problems. For the wide variety of tasks in missile design aeromechanics as outlined before, we have to use codes that are easily adaptable to novel project needs and to experiences gained during the design process. This only seems practicable for self-developed programs, not for 'black box' codes.

2.5.2 NUMERICAL METHODS OF AERODYNAMICS

According to the increasing computer power the use of computational methods has been extended

largely in the last years. Since there is a wide variety of such methods that have grown up over a long time, starting with very simple ones at the time of the first computers up to the most recent ones, and since the term 'numerical' or 'CFD' method is vague and dependent on time and situation, a short overview is given on all major approaches used in missile design at the moment. Some advantages and disadvantages of empirical/semi-empirical, 'numerical' and experimental prediction methods are presented in Fig. 54. The consequence that has to be drawn by the design aerodynamicist from these arguments is, that he needs a tool box with all essential methods and that he has to choose them adequately according to his problems, to the demands in precision and to the effort that can be made. In most cases the more simple and universal tools will be used probably, but each tool can be of high importance in some cases.

'Numerical' methods are essential to compute unconventional configurations like airbreathing missiles, to determine load distributions for structure calculations, local flow field properties (e.g. velocity profiles at an inlet entry section or shear stresses for aeroacoustic methods), temperature distributions, and to provide the designer with fundamental information on the physical effects taking place in complex flow fields (e.g. lateral jet flow interacting with the missile surface and the external flow field). The different methods mentioned within this context are arranged according to their degree of linearization or physical approximation.

A general survey on more advanced computational methods is given in Refs. 159-162.

Empirical methods

Whenever it is possible, a designer will base the preliminary design on an existing data base for similar configurations and will use interpolation, possibly combined with some theoretical considerations. But if the design requirements lead to a configuration that is quite different from the ones in existing data bases one has necessarily to turn to other methods.

Semi-empirical methods

These tools constitute the every day tools for design engineers. They only need a very small amount of computer time and, since they are interactive and very easy to be used, they are well suited to calculate sets of different configurations for systematic design studies. Most of the codes are based on the component build-up technique (Refs. 163 and 205) which computes the single components like body, wing, and tail separately by different simple methods (slender body, shock expansion, linearized potential) or from an experi-

mentally or numerically determined data base and considers the interactions between the components by introducing interference factors.

According to the different experiences in different companies and institutions a large number of such prediction codes exists (Ref. 164). Most of them can compute conventional missiles with circular body and two series of cruciform fins. Only a few can handle unconventional configurations (elliptic or square cross-section fuselages, or airbreathing missiles), Ref. 165.

For the cases where good data bases exist and where the theoretical methods can be applied, very good predictions are possible. In addition to the standard coefficients like normal force, moment, center of pressure and drag (Fig. 55) also damping coefficients (Fig. 56) can be predicted with a precision that is sufficient for design purposes. Using additional experimental data or theoretical methods one can even include very high angles of attack (Figs. 73 and 74) or other specific features.

According to the approach used, difficulties will arise in the prediction quality for configurations far outside the data bases and for coefficients that are small in comparison with interaction effects. Such problems may appear, consequently, for control effectiveness, hinge moments, induced rolling moments and others.

Therefore, continuous improvements of semi-empirical methods are necessary parallel to the increasing experience.

Major fields for this work should be

- a data base for bodies and surfaces at high angles of attack and development of methods to improve vortical interaction modelling
- development of methods to determine the interactions of lifting surfaces with arbitrarily shaped bodies
- modelling of the effects of airframe inlets on stability, control and others.

A survey of new semi-empirical approaches will be given in another lecture of this series.

Linearized potential methods

The most commonly used methods to solve the linearized potential equation are the surface singularity techniques. For the analysis of subcritical flows these so called panel methods are very effective tools for engineering purposes. A variety of different codes has been developed (e.g. Refs. 166-168), all of which are able to calculate very complex configurations (Fig. 57). High order methods can simulate geometries of high curvature with less numerical effort, but often they are less stable numerically than low order ones. The extension of panel techniques to supersonic flows is somewhat difficult because reflections of Mach waves in the interior of bodies

and discontinuities of singularity distributions across the panels have to be handled. In addition, it is not possible to treat detached shocks adequately. Therefore, only a few supersonic panel programs have been developed.

Where applicable, panel methods can predict global and local aerodynamic parameters with good accuracy and at a reasonable price. However, they are based on linearized equations and are, therefore, limited to very small angles of attack. Since this is a very severe restriction for missiles, some panel methods have been extended to include nonlinearities due to vortical effects or to nonlinear compressibility associated with shock waves.

More details on this subject are presented in Refs. 169-171. A few examples are shown in Figs. 26, 39, 40, 91, 92, and 112.

Linearized potential theory also has been used for unsteady approaches (Refs. 120, 122, and 123).

Full potential methods

Two approaches to the nonlinear equations are made. The field panel methods (Ref. 172) solve the integral equations iteratively. They can use a grid that is similar to that for the linearized theory. Similar to the panel methods vortex models can be introduced and unsteady approaches have been made. Field panel methods even proceed into the domain of Euler codes for high subsonic Mach numbers where supersonic velocities may occur locally.

Full potential methods (Ref. 173) are finite difference schemes, need a finer grid, are more sensitive numerically and less flexible for extension in vortex modelling.

Both approaches have been used to a greater extent for airplane wing investigations than in missile design.

Euler methods

The Euler equations represent the full set of conservation equations for continuous media when viscosity is omitted. They allow 'weak' solutions and can, therefore, model physical discontinuities like shock waves. Vortex generation is not described by this method except for cases where rotation is introduced indirectly by, for example a Kutta condition, a curved shock or some numerical dissipation caused by a coarse grid. The most direct way is to introduce a local Kutta condition to make the surface velocity vectors parallel to a given separation plane ('forced separation technique'). On the other hand, the transport of any vorticity within the field - no means how it was created - is considered by the equations but no diffusion terms are included and, again, it will take place only indirectly (e.g. by numerical dissipation).

Due to the progress in computing Euler methods are feasible today for later phases of missile design. Fast Euler codes (e.g. space marching) are used even in preliminary design phases. Still, a major effort is needed in comparison to the surface element methods to solve the large number of equations resulting from the 3D spacial grid elements that are necessary. Also grid generation itself still requires an high effort, especially for unconventional configurations and if a large variety of different shapes has to be considered.

On one hand steady flow conditions can be simulated by solving the steady Euler equations. For supersonic flow they are hyperbolic in space and a space-marching technique can be used. On the other hand the unsteady Euler equations have to be solved. All flow variables in the field are advanced in time until a steady state is reached. This procedure can be used for any speed range, but if the flow is purely supersonic a pseudo-unsteady marching procedure may be introduced (Ref. 174). It consists in a plane by plane time iteration using only the upstream information for each step. For second order accuracy this means taking into account two upstream planes. Convergence is reached quickly if one starts the time-iteration of each plane with the results of the preceding one. Only three consecutive planes have to be stored simultaneously in that way which considerably helps saving computer time and space. To demonstrate the capabilities of Euler codes to compute very complex geometries some examples for missile project design are given.

The following codes have been used:

- FLU3C (Ref. 175) is an explicit monodomain code based on upwind schemes. It is used with a space-marching procedure for supersonic flow.
- FLU3M (Refs. 176 and 177) is an explicit or implicit multi-domain code also based on upwind schemes. For a two species flow the explicit Roe solver is used. The code is applicable to transonic and supersonic flow. A space-marching procedure is available.
- SESAME (Ref. 178) is a multi-domain code based on a centered Jameson-Schmidt numerical scheme with implicit residual smoothing of Lerat. Scheme stability is provided by addition of artificial second and fourth order viscosity terms. This code is suited mainly for subsonic flows.
- EUFLEX (Refs. 179 and 180) is an explicit or implicit multiblock code based on a cell centered FVM scheme with residual smoothing. Several modifications of this code exist for different applications, including viscous extensions.

Fig. 58 shows the surface pressure distribution (FLU3C) of a conventional missile, and in

particular the body area influenced by the lifting surfaces. A similar result for a more complicated shape (ASTER 15 - anti-missile ground/surface-to-air missile) can be seen in Fig. 59. For the different configurations tested (different booster dimensions with different chord length, span and apex position of the tail) good agreement with experimental data was achieved. Fig. 60 presents the isobars on the surface of ASTER and in a cross-sectional plane where one can observe the vortical structures produced by the tip edges of the long wings. The comparison in Fig. 61 of experimental and FLU3C pressure data on the wing shows good agreement. Fig. 62 is an example for the unconventional shape of a ramjet missile (ANS - anti-navire supersonique). It shows the mesh and the surface pressure distribution. The following examples were calculated by using multiblock grids in order to refine the mesh in critical regions. In Fig. 63 the Mach number contours for a cross-sectional plane of a rolling anti-tank missile equipped with a direct thrust vector control system are shown. Four blocks with a total of 220000 cells were used in the SESAME calculation which permits to take into account the spinning effect by including the inertial and Euler terms into the Euler equations. Downstream interactions between jets and fins are predicted fairly well, while lower precision is observed on the body where viscous effects dominate. The interaction of a supersonic lateral jet with the external flow results in a very complicated flow-field. Euler calculations are unable to simulate the separation upstream of the jet and all of the many viscous effects involved within this problem, but can provide an useful insight into the complex flow phenomena. FLU3M calculations have been executed for the ASTER missile with one lateral jet located at the lower vertical wing and the other one at the horizontal wing. The mesh consisted of 24 blocks with 550000 cells totally. Fig. 64 presents the Mach number contours in a transversal plane behind the exits of the lateral jets. Good results are obtained for the normal and side forces and for the induced center of pressure.

Boundary layer methods

Boundary layer codes are a fast tool to simulate viscous flow effects close to the surface, but away from separation areas. A survey on methods appropriate for missile design is given in Ref. 181. A very useful tool for general geometries is the second-order boundary layer theory (Refs. 182, applications in Refs. 171 and 180). In this approach it is supposed that the curvature of the geometry is not very small compared with the boundary layer thickness, which is assumed in classical theories. Consequently, pressure gradients within the boundary layer due to centrifugal forces caused by surface curvature are taken into account. The boundary layer flow is matched

satisfactorily with the external inviscid flow which is not the case for classical approaches. For turbulence a Baldwin-Lomax model is used in Ref. 182. Another approach is the 3C3D code by CERT/ONERA. In this method the momentum and the energy boundary layer equations are integrated along local streamlines. This means that the integration always proceeds in the same direction independent of the crossflow direction.

The inviscid solution for the boundary layer calculation can be obtained by a panel or an Euler code. To improve the speed of the combined procedure a good coupling process has to be established. This is true to an even higher extent when a zonal method consisting of a combined Euler/boundary-layer/Navier-Stokes calculation shall be used (Ref. 183).

As an example for a coupled FLU3C/3C3D calculation Fig. 65 shows the mesh, the inviscid streamlines at the wall and the friction lines for ASTER 15. For the inviscid streamlines one can distinguish the lines starting at the leading edge of the wings. They correspond with a region where the boundary layer starts its development again.

A restart procedure has been included in the boundary layer code in order to deal with such sudden changes in geometry.

In the same manner, lines arriving at the trailing edges of the control panels and of the fins are abandoned for downstream computation. The skin friction lines show open three-dimensional separations, mainly due to secondary shocks attached to lifting surfaces.

Navier-Stokes methods

Because of the high effort necessary, Navier-Stokes methods are - even more than Euler codes - a tool that is used only rarely in missile design at the moment. But for certain cases it will be the only tool that is applicable and one has to put up with the expenses. Sometimes even a 2D calculation will be of some use (Fig. 83), although most missile problems are 3D in nature.

Navier-Stokes equations should be capable to describe a wide class of flow phenomena around a missile. Predicted quantities include pressure discontinuities, flow separation, vorticity fluctuations, shear stresses due to viscosity effects, temperature distributions at high velocities with heated and radiating wall, mixing flows and other effects where viscosity is a major feature. Due to the limitations imposed by present computers and due to incomplete understanding of turbulence, the full set of Navier-Stokes equations has to be simplified in order to make them applicable to technical problems.

One first approximation is the time-averaging of rapidly fluctuating parameters. This leads to the Reynolds-Averaged Navier-Stokes equations (RANS) which require some kind of a turbulence model to complete the set of equations for the

solution. This approximation has to be used for the most complex flows including large scale separations. Turbulence modelling is one of the big problems for practical work and is still an important research subject.

A further approximation neglects the viscosity terms in the streamwise direction. It is called Thin-Layer Navier-Stokes (TLNS) approach. Finally, if one neglects unsteady terms and streamwise viscous diffusion, one obtains the Parabolized Navier-Stokes (PNS) equations. They are applicable only for supersonic flow. Fig. 66 shows the Mach number contours on ASTER for a fully turbulent flow computation using the TLNS code FLU3PNS (Ref. 185) with a Baldwin-Lomax turbulence model with a Degani-Schiff modification for vortical flows. In the example one can observe the separation along body and wings.

Further details on Navier-Stokes methods are given in another lecture of this series.

Boltzmann methods

The full Navier-Stokes equations can be derived from the Boltzmann equations. They consider the flow to consist of discrete molecules behaving in accordance to the statistical gas theory rather than describing the continuum. The use of this direct simulation method for molecular flows is completely utopical at the moment for standard project purposes. Research work on this field is done for very rarefied flows (e.g. re-entry studies) and around simple geometries (Ref. 162).

Chaos theory

This method, too, is far from being used to solve practical problems. But, since it considers physical processes that lead to 'chaotic' structures starting from neighbouring initial conditions, it could in a long term help to understand and to model turbulent effects (Ref. 186 and 187).

2.5.3 EXPERIMENTAL METHODS

The major motive for experimental studies - which in missile aerodynamics mostly consist of wind-tunnel tests plus specific experiments according to other areas of aeromechanics - still is the validation of the aerodynamic model of the missile in advance of the first flight tests. The wind-tunnel measurements are always necessary, but they are relatively expensive because of the costs for design, construction and manufacturing of the model, and because of the high wind-tunnel costs including energy, personnel and measurement installations. Therefore, one has to reduce the effort and the extent of the measurements as much as possible. Extended numerical studies can help to cut the number of configurational varia-

tions and to optimize the test program. In the case of final validation measurements often a large quantity of data has to be acquired, like forces and moments, pressure distributions, all flow-field parameters, surface and structural temperatures, signatures, emission and transmission information and other aeromechanical parameters. Such a campaign may be divided into several parts to allow for adaptations in the wind-tunnel model or in the experimental set-up. This requires a good on-line data evaluation and aerodynamicists who can decide with high reliability about the quality of the data, the information covered by them and about on-line changes in the measurement program.

Another purpose of an experiment can be to set up a physical model for complicated flow conditions or to decide between different geometrical shapes in early design phases. For this task one needs test facilities that can be used without high effort and without too many restrictions in experimental set-ups. The typical results in this case are usually visualizations and qualitative data. Only in rare cases there is a severe demand for high precision at this time. This is mainly a task for research and for the validation process of codes.

The wind-tunnel facilities and testing techniques have been improved continuously over the last decade (Ref. 188), although the investments were not distributed equally to the installations, of course. Larger cross-sections, more realistic Reynolds numbers, better flow quality, lower noise level, higher Mach numbers, and more realistic pressures and temperatures were the major tasks in improvements. Especially high effort has been made in hypersonic testing (Refs. 189 and 190) because of the existence of several ambitious space programs in different nations. Some of these improvements are very useful for missile aerodynamics. But just in the hypersonic regime we have quite different flow parameters for missiles compared with space vehicles. The velocities of realistic missiles or projectiles extend to only about $Ma=10$ but at sea-level conditions. This makes it very difficult to find a wind-tunnel that is appropriate for realistic hypersonic missile tests. Also the correlation of wind-tunnel parameters with free-flight conditions is very complicated or even questionable in this regime. Not much effort has to be expected to solve these problems, not only because missile tests represent only a marginal part of the wind-tunnel budget, but because - at least in Europe - wind-tunnel institutions have been submitted to severe restrictions due to the sharp governmental and industrial budget cuts in aerospace and military developments. The shut-down of facilities has to be expected and a single-sourcing of certain installations seems to be strived for within the next years in Europe.

There have been important advances in model support and model manipulation, decreasing the overall time needed for measurements and allowing for time-dependent programmes (Refs. 191 and 192). Supported by the advances in computer power and in postprocessing software, on-line analysis of data is usual now. This allows to select optimal missile configurations and to modify measurement programs in an appropriate way. Similarly, the data handling, data reduction and final analysis has been improved considerably. The new capabilities of data processing also offer the chance to carry out several experimental tasks simultaneously, as for example a 6-component measurement of the complete missile, a 3-component measurement of the control surfaces, the measurement of distortion and swirl at the intakes and the measurement of the amount of air passing a model with open intakes. An important information are the values of the reliability of the wind-tunnel data and of the tolerance of the measured data.

There have been considerable advances of measurement techniques over the last years, made possible partly because of general technological improvements and - especially for measurements of hypersonic flow parameters like local temperatures, thermal fluxes and concentrations of different species - because of the space programs (Refs. 193-198). Only a few of the new techniques can be mentioned here. One general tendency is to execute measurements and visualization in very short time and to incorporate a quantitative evaluation into the visualization procedure. Another trend is that for 2D or even 3D non-intrusive investigations of the flow characteristics (Ref. 199). Some of the most interesting developments on this wide field are piezo arrays for pressure measurements, particle image velocimetry (PIV), coherent anti-Stokes Raman scattering (CARS) or laser Raman scattering, and laser fluorescence measurements for flow parameter investigations. These are urgently needed by CFD specialists to validate their codes. A method that is of good use in hypersonics is the liquid crystal technique (Refs. 200-202 and Fig. 67). Of very high interest is the new optical pressure measurement system (OPMS), Fig. 68, that produces quantitative results by a modern postprocessing and that could be combined with the infrared thermography (Ref. 204) for comprehensive investigations in the hypersonic regime without needing an expensive and geometrically large instrumentation of the model.

The need for free-flight measurements and for validation of the numerical and experimental aerodynamic characteristics by reducing and analyzing these data has to be emphasized again. In spite of general improvements in the telemetry techniques and in electronic data acquisition

devices it is still a major problem to get reliable results from test flights.

3. GENERAL PROBLEMS AND APPROACHES OF THE AEROMECHANICAL DESIGN OF MISSILES

3.1 METHODICS OF AEROMECHANICAL DESIGN

Repeatedly, missile aerodynamicists have reflected their role in the missile design procedure (Refs. 1 and 2). The reason for this may be the fact that missile aerodynamics does not play a similarly prominent role in the design procedure as airplane aerodynamics in the corresponding one, although missile aerodynamics is not a smaller challenge.

The iterative design cycle as it used to be in former years (Fig. 69) is still valid for conventional missiles. In this case different special work packages can be separated within a system concept that coordinates them. The interactions of aerodynamics with adjacent subjects is shown in Fig. 70. For advanced types of missiles these interactions are much more intensive and much more involved (Fig. 71).

But still, there is a design cycle - or better a helix, since it is an iterative process where aerodynamic information are summed up while the work packages proceed from first qualitative approximations to a well-established aerodynamic model based on experiments and numerical investigations. This is produced by the fact that the tactical demands and the airframe design and the corresponding internal components are being defined in more detail progressively with increasing development and state of knowledge of the different specialists involved.

Although many other demands often seem to dominate the aerodynamic ones on a first glance, the flight performance is a major task and this is dominated by the aerodynamic design. Therefore, the aerodynamicist not only suggests an optimized shape - perhaps only a relatively 'optimal' one because of important other demands - but he also has to answer continuously questions on penalties for deviations from this design. Except for special applications, mainly at low subsonic flight, the missile will end up in having a rather 'aerodynamic' shape. This is the main reason why the aerodynamicist has to integrate other aeromechanical topics that will influence the airframe shape into his design process.

3.2 SPECIAL ASPECTS OF AEROMECHANICAL DESIGN OF MISSILES

In addition to the general survey of special subjects that have to be covered in the aeromechanical design of missiles as given before, some remarks are made here on several specific design problems and tools.

3.2.1 CLASSICAL MISSILE AERODYNAMICS

This point is mentioned more for completeness since there are several good textbooks (Refs. 205-207), lectures (Refs. 1 and 208) and reviews on this subject (Refs. 2, 3, 158, and 209). Major tasks in this field are the aerodynamic performance, mainly in lift and drag (Refs. 85 and 210), and the static stability (Refs. 211 and 212) and controllability.

For practical design work the component build-up technique is still used (Refs. 163 and 205). As the name indicates, the aerodynamic characteristics of the airframe components as body (Ref. 213) and wings (Refs. 214 and 215) are summed up in isolation. Then the values describing the interference effects between the different components are summed up by using the component loads and the more or less general interference factors. In this way the overall loads for an air frame are built-up after and after. Although this concept is mathematically valid only for small interference effects and for a linear dependence of the aerodynamic characteristics from the flow parameters, the method is open for extensions to describe other problems. By defining hybrid 'interference factors' from pure experience, even unconventional aerodynamic effects in special project cases can be covered. The characteristics of the different components or, in some cases, of a set of strongly interfering components can be evaluated by appropriate methods (first guess, semi-empirical calculation, CFD, experiment) and can in that way be improved continuously during the design process according to the helical advance in this procedure. The second lecture of this series will present a more extended review on this subject.

3.2.2 VERY HIGH ANGLES OF ATTACK

It has always been a significant feature of missiles that very high angles of attack can be reached during certain flight phases like vertical launch (Fig. 72) or fast manoeuvres during the end game (Ref. 4). A large number of studies have been executed in this field for that reason (Refs. 216-218). A special lecture is given on this subject within this series.

For angles of attack of about 10° a breakdown of the flow around the wings can occur already (Ref. 219). This $C_{L_{max}}$ characteristics leads to a non-linearity in the global characteristics, too (Figs. 73 and 74). This feature can be covered within a component build-up method in a semi-empirical manner (Ref. 220): The nonlinear aerodynamic characteristics of the body alone is obtained in a conventional way, for example with a potential method with some vortex modelling. If this model takes into account the asymmetric vortex separation on the body between about 30° and 60° the characteristics are valid up to about 60° (Ref. 221). Now we need the characteristics of the wing. They can originate from a systematic experimental investigation (Ref. 222) or from a semi-empirical approach which combines a potential and boundary-layer calculation with a criterion for full separation and a vortex model. These two components are then summed up with the conventional interference method (Ref. 223) and result in an improved numerical description of the characteristics (Figs. 73 and 74) which is sufficient for most project needs. The problem not solved for this angle of attack regime are the severe and irregular side forces introduced by the asymmetric vortex separation (Refs. 224 and 225). But it seems that they are relevant only for subsonic speeds. The model mentioned above (Ref. 220) could cover that feature, but a sufficient empirical data base for the vortex simulation is needed.

In some cases one has to regard unsteady simulations for manoeuvres in this incidence range (Ref. 226), since hysteresis effects may appear during unsteady separation.

3.2.3 MISSILES OF UNCONVENTIONAL SHAPE

Several recent examples for project designs with unconventional shapes are presented in this chapter. Two classes of unconventional shapes are distinguished, circular bodies with intakes of different form, and missiles with non-circular cross sections.

CIRCULAR BODIES WITH INTAKES

Major recent projects concerned the two classes of ramjet or ramrocket missiles and of turbojet missiles. For missiles with intakes the number, shape and position of the air intakes has to be chosen by taking into account the following aspects (Refs. 227 and 228):

- internal performance as thrust and specific impulse

- external aerodynamic characteristics as drag and lift-to-drag ratio
- operational constraints like overall dimensions (because of store carriage) and signatures (RCS and IRS)
- type of the autopilot (bank-to-turn or skid-to-turn control).

Some recent examples are shown in Fig. 75.

- Missiles with a single intake: Nose intakes (e.g. SEA DART, TALOS) have high pressure recoveries but are poorly integrated. Annular intakes (e.g. SA4, GANEF) are better in integration but show the poorest performance of all intakes. Chin intakes (e.g. ASALM, SLAT) are well suited for bank-to-turn flight control and for long range missions. They use the windward upstream part of the missile nose as a supersonic compression ramp. Ventral intakes are an excellent solution for intake design. They are quite compact and their performance is good. Different types of ventral intakes are shown in Fig. 76. Top mounted intakes are an optimal solution with respect to RCS, since this intake will be hidden for a ground based radar by the body. Because it is situated at the leeward side it is limited in incidence.

- Missiles with two lateral intakes (e.g. ASMP, ALRAAM): This configuration is well adapted to bank-to-turn control. The intakes can be located diametrically opposite or be inclined towards the bottom. The first is better in supplying the chamber and in the increment of the normal force. The latter one shows a better internal performance.
- Missiles with four intakes (e.g. ANS, SA6): This configuration is well suited for skid-to-turn control. However, at high angles of attack the intakes on the leeward side will reach their operation limit. Also, the lift-to-drag ratio of these configurations is not optimal. Two lateral intakes are sufficient to induce additional lift, the other ones mainly induce drag.

Independently from their position with respect to the missile all intakes could have different shapes - axisymmetric, half-axisymmetric, rectangular with classical or with inverted shape, and many others.

The selection of the longitudinal location will be made in a compromise between the flowfield around the fuselage, the length of the diffuser, the resulting center of pressure and the attachment points on the fuselage while the normal force is only slightly modified usually.

External aerodynamics of intakes

A survey of these characteristics is given in Refs. 229 and 230.

Airbreathing configurations may be classified into two families:

- configurations with nose, chin or annular intakes. Only the drag of the fuselage is influenced by them.
- configurations with lateral intakes. Lift, stability and drag are modified in this case.

The lift is usually increased by lateral intakes. Its span mainly influences the lift, the length of the intake nacelle changes the center of pressure, the type of the intake can change lift and stability. The roll position of the intakes is also important for the characteristics.

The drag of the air intake may constitute a considerable amount of the overall drag of the missile. For a configuration with four axisymmetric air intakes at Mach 2 at sea level the intake drag can represent 38% of the total drag - 9% for the pressure drag of the inlets, 15% for the pressure drag of the fairing boattails and 14% for the friction drag. To optimize the drag in a special case one has to consider the thrust/drag balance.

To obtain an high performance of the air intakes one has to guarantee for an optimal flow field around the fuselage. To constitute this one has to avoid low energy areas (boundary layers, vortices). Low velocity areas are favourable. The flow captured by the air intakes must be homogeneous and must have a total pressure level compatible with the optimal performance conditions of the engine. A difficult problem is caused by the nose vortices on the lee side of the fuselage at angles of attack larger than 5° . These vortices are responsible for high total pressure losses in the air intakes. Longitudinal strakes upstream of the air intakes can modify the natural development of the boundary layer around the fuselage at incidence and give a chance to enforce in that way a vortex separation apart from the intake.

Internal aerodynamics of intakes

The main aerodynamic features to be determined are

- mass flow ratios in the duct and in the internal boundary layer bleed
- total pressure recovery
- pre-entry drag and cowl drag

all three for large ranges of Mach number, angle of attack and altitude, and

- characteristic curves (for total pressure recovery versus mass flow ratio) in order to assess the maximal total pressure recovery
- pressure and temperature distributions along the walls of the air intake to produce information needed for the structural design.

These features depend on complex physical phenomena as boundary layers, shock-shock and shock-boundary layer interactions, turbulence, corner flow, flows in boundary layer bleeds.

Due to this complexity, air intake studies are usually splitted into two phases. During the first one the isolated air intake is evaluated using an average external flowfield consisting of local Mach number, local total pressure, local angles of attack and sideslip and so on. In the second (development) phase this preliminary design is improved by taking into account the realistic and complete flowfield entering the air intake. A special lecture will present more details on these problems.

MISSILES WITH NON-CIRCULAR CROSS SECTIONS

Two classes of missiles are concerned within this chapter

- subsonic modular stand-off missiles with square or rectangular cross sections
- supersonic or hypersonic air-breathing missiles with elliptical or triangular cross sections.

A typical subsonic modular stand-off missile has been presented in Fig. 11. The layout shows a square cross-section body with the wing mounted at the upper side to allow unrestricted ejection of the submunitions. The sharp corners of the body induce flow separation and the resulting vortex sheets produce a nonlinear lift characteristics. In that way a square body provides a much higher normal force than a circular body of the same cross-sectional area. When the body is rolled the separated vortices are changed to asymmetrical shape and will induce lateral forces and moments.

Typical supersonic/hypersonic air-breathing missiles (Refs. 29, 231, and 232) are presented in Fig. 77.

Their objectives are

- optimal integration of the intakes with respect to the fuselage flowfield
- low drag
- high lift-to-drag ratio
- low RCS value
- good integrability for store carriage.

Of the different possible shapes as waveriders, elliptical or triangular cross sections Fig. 77 shows two types:

- waveriders that are designed for minimum drag (streamlines on the leeward side are not deflected) and for maximum lift behaviour (the bow shock wave coincides with the leading edges)
- lenticular shapes are designed for high lift-to-drag ratios at constant cross section and for high lift at incidence (the sharp leading edges generate vortex separation).

3.2.4 GRID WINGS

Grid wings are an example for unconventional shape of a missile component, in this case of a stabilizing and possibly deflecting fin. This constructive solution seems to be of such favourable behaviour that most of the modern Russian high velocity missiles use it (Ref. 24).

There are different shapes adapted to different applications (Fig. 78). Thorough investigations have been made for a long time to determine the constructive and even production aspects of these wings as well as the aerodynamic characteristics and their thermodynamic features including internal and external cooling (Ref. 233). The fins can be all moveable and in this way become a control surface.

The grid wing can be considered as to be derived from biplanes, multi-planes or profile cascades. Its lift characteristics is linear up to values of about 25° . The increase in drag seems not to be prohibitive and can be optimized by a proper design of the internal grid density. A standard vortex-lattice method has been used to derive theoretical results for subsonic flow and angles of attack up to 18° (Ref. 234). Comparisons with experimental values showed a good agreement (Fig. 79). Another study was executed using a supersonic panel method (Ref. 235) to investigate the Mach number and grid density dependence for supersonic speeds up to about Mach 5. Ref. 233 shows C_x and C_z characteristics up to 90° at supersonic Mach numbers (Fig. 80).

3.2.5 HYPERSONIC AERODYNAMICS

Designing an hypersonic missile is quite a challenge since there are many demands that seem to collide with general physics. At least we are often at the limit of what can be made at this time. Compared with the design of space vehicles (Ref. 236) hypersonic missiles will be of lower speed but also at lower altitudes which not simply compensates the other effect but leads to consi-

derably different features. In addition to that, the typical demands on missile design are another reason for the different approach that has to be made.

Nevertheless, fundamental insights, tools and facilities may be transferred from space vehicle research and design (Ref. 237). Hypersonic aerodynamics is very closely connected with aerothermodynamics. Most of the practical problems that have to be solved arise from that field. Pure aerodynamics for the hypersonic speed range is mainly influenced by thermal effects in the way that hot surfaces lead to different boundary layer effects, that temperature distributions and heat transport have to be included in the energy equations and that changes in the constituents of the flow ('real gas effects') also influence the energy equation.

Nevertheless, it seems that the global forces and moments at high Mach numbers can be derived relatively well from semi-empirical methods. The problem of these tools mainly is the lack of good validation data since the correlation of wind-tunnel results with free-flight conditions is problematic, especially for the drag. Other simple design methods are Newton methods for high altitude and high Mach number conditions and shock expansion theory applicable only at lower Mach numbers. For first estimations they are a good help. An interesting goal is to have a simple engineering code for hypersonic missile optimization including some thermodynamic features (Ref. 238).

For a later development phase or if detailed questions have to be answered, numerical codes have to be used (Ref. 239). A first step could be the use of an Euler method. A time-efficient space marching code can be used if for each space step cross-section the Mach number normal to the plane is greater than one. Otherwise, a time stepping procedure must be used. A semi-empirical real gas model may be implemented into the Euler codes. Results for missile applications up to Mach 8 (Ref. 180) do not show a considerable deviation from ideal gas values of force and moment characteristics. The Euler codes may be coupled with a higher-order boundary-layer code adapted to the hypersonic flow regime by taking into account the appropriate entropy layer.

Other methods are the viscous-shock-layer approximation which takes into account that the bow shock is almost parallel to the missile surface in the front part and which in that way comes to a procedure much cheaper than higher codes, and the different approximations to the Navier-Stokes equations. But at the present time it will be not affordable in money and time in most cases to use such a code as a design tool.

3.2.6 LATERAL JET CONTROL

As mentioned before, there are several hardware realizations for lateral jet control. In this chapter mainly the pyrotechnical method is considered. This does not influence severely the generality of the statements since flight performance and aerodynamic effects of different types are quite similar.

Limitation of moment control and advantages of pyrotechnical force control

The conventional control of missiles consists in responding to a lateral acceleration command and in controlling some deflectable control surfaces which create a moment in that way. This moment introduces an angular movement of the missile resulting in a change of incidence which in turn creates an aerodynamic lift force ensuring the desired manoeuvre.

There are two disadvantages of this classical control method:

- There will be a time delay between the steering command and the time when the response is acting on the missile, because of a number of different intermediate physical and technical steps. The angular movement required to create the lateral acceleration has to be introduced; it is governed by the aerodynamic parameters (missile moment of inertia, aerodynamic damping moment). This applies to any type of moment control, independent of aerodynamic or jet control.
- The forces acting on an aerodynamic control surface are proportional to the dynamic pressure, i.e. to the density of the air and to the velocity of the missile, and will, therefore, have low effectiveness at launch (low speed) and at high altitudes (low density).

The use of a lateral propulsive unit close to the center of gravity of the missile overrides partly these advantages, thus enabling

- a considerable reduction of the response time and, as a result, a reduction in the passing distance for targets for which short reaction times are demanded, as for example for fast manoeuvring targets
- manoeuvres of the missile at very low speed and at high altitudes.

However, pyrotechnical force control has certain constraints:

- Used as the only control of a missile its operational domain is limited by its powder consumption. In particular, using a gas generator connec-

ted to the nozzles with a distributor, the powder consumption is independent from the manoeuvre, even at zero command.

- The missile cannot be controlled after the full consumption of the powder.
- The missile has to be designed in a way that it will obtain an almost fixed center of gravity during the use of this control system.
- The aerodynamic design of the missile has to take into account the interaction effects caused by the jets.

Taking into account all these advantages and disadvantages one can say that the purely pyrotechnical force control technology is highly suitable for anti-tank and for very short range missiles, or for missiles that will use this system only for a short time, for example during the final guidance phase (thus limiting the operation time) and in addition to an associated aerodynamic control system (thus limiting the required power level).

Two types of systems are used at the moment:

A first possibility is to provide the missile with a set of small multiple side thrusters arranged peripherally close to the center of gravity. The axis of each side thruster must be inclined so that the force produced by it will cross the center of gravity. The component of the side force normal to the missile axis is used as control force and its axial component is used to maintain the speed. As it is difficult in practice to increase the number of side thrusters, this type of control is used when the flight time and the demands on the manoeuvrability are low, e.g. anti-tank DRAGON.

Another possibility which allows for higher manoeuvrability is to use a continuous gas generator linked with jet interceptors or with an exhaust distributor towards the nozzles. Two nozzles are needed for an autorotating missile (anti-tank ERYX), and three or four for a stabilized missile in rotation. Additionally, as for the side-thruster control, the nozzles can be inclined backwards to maintain the speed.

Additional systems as liquid fuel devices are considered in present design studies.

Aerodynamic interactions due to a lateral jet

The transverse ejection of a lateral jet into an external flow causes an highly complex flow field (Fig. 81) leading to a set of interactions of two types (Fig. 82) - local and downstream interactions.

The local interactions (Figs. 83 and 84) are related to the jet obstacle effect which, at supersonic speeds, produces a detached shock upstream of

the nozzle exit and a separation of the boundary layer forming a shock that generates a zone of overpressure. Immediately downstream of the nozzle exit the external flow deflected by the jet produces a depression zone. The induced pressure distribution around the body close to the nozzle exit position leads - for a nozzle situated close to the center of pressure and for a fuselage without wings in this region - to a small interaction force usually of opposite direction to the thrust force and to a slight nose-up pitching moment. This unfavourable interaction means a jet effectiveness ratio lower than one. Suitable parameter combinations have to be found in such a case to handle this problem.

The downstream interactions (Fig. 85) are due to the highly vortical character of the flow downstream of the jet. Far from the nozzle exit the jet wake takes the form of two counter-rotating vortices resulting from the curvature of the jet itself and from its rounding by the external flow. The velocity induced by these vortices on lifting or control surfaces located downstream usually will lead to a loss in lift and moment.

The resulting effects of the lateral jet interactions are

- an interaction force which has to be added to the lateral thrust force and which can affect the efficiency of this thrust
- 'disturbing' moments in pitch and roll for which negative effects on the controllability of the missile have to be avoided.

In designing a missile that has to be controlled by lateral jets it is, therefore, necessary

- to optimize the shape of the missile and the parameters of the lateral thrust system with respect to the aerodynamic implications of these two preceding effects
- to achieve a complete model of the resulting control forces and moments (thrust plus interference) which is required in the control studies.

The design for a practical case will proceed iteratively: First the missile will be designed with respect to aerodynamic and other criteria. The flight dynamical simulation - usually including guidance and control - defines the demands on the control system, on forces, moments, response and operation time. These data, together with the parameters for lateral jet modules, are the basis for the aerodynamic design of the lateral jet system. This has to consider the efficiency of the system including the interference effects. The resulting new aerodynamic model has to be validated by flight simulations, and so on.

To keep the costs low for this design cycle one needs rather efficient design tools. This is not the case for extended experimental studies and for advanced numerical codes which will be suitable only in later design phases. Several simpler methods exist that can simulate the local interactions of the lateral jet with the flow. But practice has shown that they are valid only for a limited number of parameter variations. Therefore, more basic information are needed on lateral jet effects. Systematic wind-tunnel studies should help to clarify the influence of the different parameters and to develop better design tools describing the local interactions. For the downstream interactions one can use standard potential methods with vortex tracking models at Mach numbers up to about 5. This should be sufficient for early phases, while in later ones also CFD codes and extended measurements are needed.

3.2.7 AEROTHERMODYNAMICS

As described before, this subject is the most critical one for hypersonic missile design. But also for lower speeds aerodynamic heating will be of interest in some cases. In addition, the thermodynamic simulation of structural and component temperature characteristics can be a work package in a design process. The results of all these investigations will, among other areas, influence the selection of materials appropriate for the different demands. The aerothermodynamical (and structural) coefficients for the materials in question are, on the other hand, input data for the simulation (Ref. 241).

According to the different particular work packages within this field there are several approaches and tools that have to be used. The appropriate simulation of the aerodynamic flow (velocity, boundary layer, shock interactions, heated surface, real gas or catalytic effects etc.) is the first part. This has been discussed already. In a second step the heat transfer into the wall has to be modelled including the radiation energy flows to and from the surface (Fig. 86). The third step is to calculate the heat flow within the skin by conduction and with regard to the convection and radiation at its boundaries. Another task is to simulate the temperature characteristics of internal components due to external (environment, radiation, aerothermodynamics) or internal (heat sources like electrical devices) heating.

An overview of aerodynamic heating approaches for design purposes is given in Ref. 242. Specific engineering methods are described by Refs. 243-245. A simple but fast and very efficient early design code (Ref. 246) has been used to calculate temperature distributions along the body and the

fin surface of an hypersonic projectile over a flight trajectory (Fig. 84):

The pressure distribution is provided by a second order shock expansion method. The heat transfer from the boundary layer is calculated for different body geometries (Refs. 247 and 248) by assuming a 'cold' isolated wall. The recovery enthalpy is modelled by semi-empirical coefficients based on boundary layer parameters like the Prandtl number. It is proportional to the temperature gradient between the boundary layer and the wall. The determination of the heat transfer rates is based on the Reference Enthalpy Method (Ref. 249). In a third step the time-dependent temperatures within the wall are determined. The 'cold-wall' heat transfer rates have to be transferred to 'hot-wall' rates which are material and time dependent. These rates are modelled by heat rate balance equations. The heat transfer within the wall is considered to be one-dimensional for relatively thin walls where conduction in axial direction may be neglected (Ref. 250). In other cases - as for examples in wings - a two-dimensional approximation (Ref. 251) has to be used. The mathematical heat balance model considers the shell to be subdivided into several structural layers. Each one is described by its properties (density, thermal conductivity, specific heat and - for the outer and inner surface - emissivity) and defines a balance equation. The resulting matrix equation is solved and gives the desired temperatures.

For more advanced design phases more effort can be put into these calculations. In this case a combined Euler and boundary-layer calculation seems to be appropriate for the determination of the aerodynamic parameters in many cases. For the simulation of the wall temperatures a similar approach as above or more refined 3D methods could be used.

The reaction of the surface temperature to active cooling is mainly a problem of construction and of aerodynamics. No severe changes in the procedures mentioned above are necessary except, that one has to consider the modified boundary layer temperature and, perhaps a different heat transfer rate. Passive cooling by ablative effects is more complicated. There are not only changes in the surface structure - like roughness - which can cause severe aerodynamic effects, but also the chemical processes taking place in the ablating material can change the thermodynamic behaviour of the wall. For sublimating materials like teflon this still can be modelled quite well by the above method (Fig. 88). For carbonization or similar processes this method has to be modified considerably.

The unsteady as well as the equilibrium temperatures of internal components or structures can be approximated in a rather simple design approach

by a node model, where each nodal point represents a unit of the complete system distinct from the others by its thermal coefficients and where each connection between different points can represent heat transfer by conduction, convection or radiation. In this way a complicated structure can be described by a system of a few nodes leading to a corresponding set of coupled linear differential equations in time that can be solved for the unsteady temperatures rather fast if the different interaction coefficients (conductivities, and so on) for the connections are given. For more detailed investigations one of the standard finite element programs should be used.

3.2.8 AEROELASTICS

In contrast to airplanes not the flutter of the wings is the major problem for missile design usually, but the bending motion of the body, especially if light-weight materials are used and if manoeuvres at high speeds are executed, leading to very large normal accelerations. A first guess for the static bending deformation and for the eigenfrequencies has to be made in early design phases. An unfavourable interference of these frequencies with the frequencies of the control parameters must be avoided in this phase already.

For a more detailed approach in later design phases standard codes for structural mechanics or dynamics have to be applied. But for fast guesses the body may be approximated by shaft theory (Ref. 252): For typical flight conditions the aerodynamic normal force distribution and the centrifugal force distribution according to the mass distribution and the normal acceleration are calculated. If the bending deformation is relatively small the law of Hooke is valid, as well as the hypothesis of Bernoulli that only bending moments will appear in this system. For given distributions of cross-sectional areas and of the elastic constants one can solve the fourth order differential equation by finite difference schemes. The boundary conditions have to be chosen for a system being free at both ends. To calculate the eigenvibrations and the eigenfrequencies one can easily define an eigenvalue problem in matrix form which is solved by a Martin - Wilkinson method. An example is given in Figs. 89 and 90. The corresponding eigenfrequencies are 42 Hz, 147 Hz and 272 Hz for the first, second and third eigenvibration, respectively.

3.2.9 AEROMECHANICAL SIMULATION

A combined flight mechanical simulation has to be executed for aeroelastics, aerothermodynamics, some questions in signature simulation, for unsteady aerodynamics and other time-dependent

processes. In the present chapter only store separation with mutual interference of aerodynamic characteristics and the trajectory is considered.

In a fast design approach a store separation problem can be solved by setting up a simple vortex and jet flow model and use an equivalent angle of attack method. In this way one can, for example, give a quick qualitative answer to the question for the flight behaviour of the missile when the trajectory has to cross the wake of the airplane. In most cases of such early design work the coupling of aerodynamics and flight mechanics is done indirectly by executing an aerodynamic parameter study of the missile in a disturbed flow field and subsequently simulating the trajectory with this modified aerodynamic model. Very detailed investigations using advanced aerodynamic tools can be carried out in this way. A reasonable method for design purposes is to use a panel program extended by a viscous vortex modelling (Ref. 253). First, the flow around the carrier airplane has to be simulated with and without the store (Fig. 91), then the behaviour of the aerodynamic coefficients in dependence of the dispenser position relative to the disturbed flow can be determined (Fig. 92). The separation trajectory is calculated subsequently (Fig. 93).

In cases like that of Fig. 93, where not only the flight path crosses the downwash area but where a change in geometry takes place (the wing is unfolded during the first 1.5 seconds) a combined aerodynamical and flight mechanical simulation should be executed. Using the method described this is already very time-consuming and expensive but at least affordable for short flight periods. For higher CFD codes a combined simulation like that usually will not be possible during a design process. If it is necessary to use such codes the separated approach as described above will be favoured.

3.2.10 AEROACOUSTICS

Aeroacoustic effects always have been used to locate artillery positions and microphones are the common sensors for submarine detection. In recent years advances have been made to use the emitted noise spectrum for location and identification of covered helicopters. On the other hand, there are intensive studies going on to reduce helicopter and airplane (propulsion engine) noise. For missiles similar aspects can be of interest. To simulate aeroacoustic noise for design purposes one usually starts with the FW-H equation of Ffowcs Williams - Hawkins (Refs. 254 and 255) which originates from Lighthill (Refs. 256 and 257). This equation describes the generation and expansion of noise emitted from monopole,

dipole or quadrupole sources. Octopoles are neglected in this approximation. The FW-H equation is valid for rigid bodies that are impermeable for sound or energy. CFD methods can be used to determine the different source terms. The dipole and monopole sources can be derived from changes of the flow velocities and of the aerodynamic pressures (viscous and inviscid), respectively. The quadrupole terms have to be determined from the shear stress tensor of the flow. The solution procedure of the FW-H equation allows subsequently to simulate the pressure distribution around the noise emitting body induced by the propagation of the sound.

An alternative method by Moehring et al. (Ref. 258) is found in several references (e.g. Ref. 259). It is based on the idea of a sound emitting vortex field. Formally this theory is solved in a similar way as the FW-H approach. Again, pressure and velocity characteristics of the flow have to be determined in a first step. A special aspect of this procedure is that the quadrupole term is written as a tensor function of the vortex distribution.

A very recent method uses a stochastic approach (Ref. 260). Again, mean and turbulent aerodynamic quantities of the flow have to be determined in a first step by CFD methods.

3.2.11 RADAR CROSS SECTION (RCS)

The survival of a missile - which is closely linked to its penetrativity - is very much related to the detection range by a defensive radar. Since this distance is proportional to the fourth root of the radar cross section (RCS), one can easily understand that a very remarkable reduction of a RCS is necessary to increase its survivability by a significant amount. Such spectacular reductions of the RCS have been achieved in the past mainly for airplanes. Fig. 94 compares the RCS of the B-52, the B-1B and the US Air Force Stealth Bomber.

The following paragraphs will present a few methods to reduce the RCS of a missile. As mentioned before, there are two basic approaches to reduce the RCS:

- to optimize the shape of the airframe in order to minimize backscatter (Fig. 95)
 - to coat the airframe in order to absorb the incoming energy instead of reflecting it.
- Both approaches have to be used coherently in missile design to achieve the low-observability margin required over the appropriate frequency range.

The aerodynamicist is mainly involved in the design of the missile shape. He must define the airframe geometry taking into account constraints

like the following ones which may be related indirectly with the selection of the materials:

- suppress specular points (direct reflections at the surfaces into the direction of possible observers)
- avoid surface irregularities
- avoid straight leading edges, especially those parallel to polarization directions of probable radar signals
- avoid visible links between different materials.

These constraints impose special demands on the missile designers.

Demands for the design of the outer shape are

- design smooth profiles for the lifting surfaces and for the fuselage
- smoothen the link between body and fins
- use an elliptical fuselage
- sweep and curve the leading edges.

Typical demands for air intakes are

- subsonic intakes have to be integrated into the fuselage
- the interior design of the duct has to take into account an eventual coating with absorbing materials
- if a coating of the wall is intended the duct has to be shaped in a way to maximize the number of reflections
- use a top mounted intake to hide it from a ground based radar
- the lips of the intake have to be shaped appropriately.

There is a great advantage of positioning surfaces in a direction where the radar wave hits them almost tangentially and not in normal directions to edges.

To illustrate this some very simple considerations are made (Ref. 155):

When the diameter of a sphere is remarkably larger than the radar wavelength then its RCS is approximately the same as the cross section at any aspect angle. In Figs. 96 and 97 the radar signal reflected by the sphere is compared with that of a square plate of the same cross section for different aspect angles. Consider a wavelength of about one fifth of the length of the plate - regarding the note in Ref. 155 that it concerns a 10λ square - which could be for example a 20 cm square fin for a 7.5 GHz radar.

At normal incidence angle the reflection from the square plate will be 300 times the one from the sphere. If one rotates now the plate about one edge, the RCS decreases and becomes equal to that of the sphere at an aspect angle of 35° off the normal direction. When the angle is increased further the reflection drops for another factor of 3.

If one rotates now the plate about a diagonal line relative to the incident wave the RCS decrease of a factor of 300 is reached at 6° off the normal direction already and is divided by another factor of 300 when the plate reaches a shallow angle to the incoming radar, which amounts to a total change in RCS of factor 90000 between maximum and minimum.

Taking this into account, it seems easy to reduce the RCS of wings and of control fins by positioning them in a way that their edges are never aligned with the incident wave. However, multiple reflections will complicate the situation.

For example, energy aimed into a cavity bounces back for all types of cavity shapes (Fig. 98). If one can attenuate the signal with each bounce by an absorbing material a multibounce design - for an intake, for example - will show considerable advantage provided that it can be realized without sacrificing the aerodynamic performance of the intake.

The methods used for the simulation of the RCS are surveyed in Ref. 261. A simple design method - comparable to the semi-empirical component build-up method of aerodynamics - is the 'canonical shape method'. A major problem inherent in it is the modelling of the interference effects, since for electromagnetic fields one has to consider phases and rather severe interactions. Another approach is the 'wire grid method' (Ref. 262). This is applicable for antennas and for structures consisting of wires. Therefore, it is usually not of interest for missile design. The 'continuous surface model' by patches (Ref. 261) is an alternative approach to the modelling of complex 3D structures. It is mainly used for smooth surfaces. Mostly the patches are chosen to be triangular or rectangular panels. As in the wire grid method the electric or the magnetic field integral equations may be used for the calculation. A considerable amount of computer time is necessary already for realistic examples. A further approach is the 'physical optics theory' (Refs. 261 and 263 - 265). It is based on the diffraction theory of Kirchhoff who described the diffraction phenomena of light by approximating the boundary conditions at the surface of the scattering object with the aid of optical principles. The method has been extended to nonperfect conductivity and double reflections for complicated structures. An even higher amount of computer time is needed in those cases, but still the size of the panels can be chosen only to describe the body appropriately, it has not to be correlated to the wavelength. This means that the same grid as used in aerodynamic panel calculations can be used for RCS simulations in most cases. This makes the method very attractive and shows that panel and physical optics calculations can be executed in the same phase of

the missile design cycle. An example for a physical optics result for a typical missile shape is given in Fig. 99.

The most advanced method - and, because of the large number of 3D grid elements that are needed, the most expensive one - are the 'Maxwell methods' (Refs. 266 and 267). They are comparable with the Navier-Stokes approaches, but are even more expensive since the 3D meshes used there have to have a small fraction of the radar wavelength in size. These methods solve the time-dependent curl equation of Maxwell numerically. They describe the propagation of an electromagnetic wave into a space containing an arbitrary-shaped dielectric or conducting body. By time-stepping or by repeatedly implementing a finite-difference analogon to the curl equations at each cell of the corresponding space grid, the incident wave is tracked when propagating to the structure and interacting with it by penetration and diffraction. The final result is completed when each cell has reached a steady state.

3.2.12 OPTICAL SIGNATURES

Conventional detection of missiles by the smoke signature in the visible range has been described above; applicable design tools exist (Refs. 149-151).

Most optical signature investigations deal with the IR signature since it is the one within the optical regime that is the most independent from environmental conditions, although still a lot of problems arise from them. Anyway, for a short description it is enough to consider IR, because all other optical frequencies show in principle the same features.

The signature depends on the temperature distribution on the airframe surface and within the propulsive jet and plume, on the emissivities and on the apparent surfaces.

For subsonic missiles hot parts are mainly located at the rear, i.e. the visible inner parts of the engine or nozzle and the core of the plume. Also air intakes may emit radiation or may allow a look into the hot internal structure. The signature may be minimized in these cases

- by shielding the hot parts, mainly the jet pipe or nozzle
- by mixing fresh air into the hot flux behind the base to decrease its temperature significantly
- by the use of flattened nozzle exit sections which reduce the length of the plume core and enhance its chance to be masked by the airframe at low aspect and elevation angles
- by the use of a top-mounted air intake which cannot be seen from a ground-based sensor.

For supersonic missiles the whole airframe has to

be added to these radiative sources due to aerodynamic heating. For this aspect the optimization can be done by

- finding an optimum between a few small hot spots and a cooler but larger surface
- cooling the airframe
- designing a shape that deflects solar and background radiation
- using stealthy IR paintings that are consistent with RCS requirements.

According to the statements above the first step to simulate optical signatures in a design phase is to model the temperature distribution over the missile during the mission. In a very fast approach one can simply use Planck's equation (possibly for certain spectral windows) to get a radiation intensity for a given observer (Fig. 100).

Plumes take much more effort even for a first guess, except one can use some of the existing data sheets (e.g. Ref. 146). For a rather smokeless plume an optical depth model similar to that used for stellar atmospheres can be used approximately (Fig. 101). A small fraction of particles will change the temperature-dependent absorption coefficient. A semi-empirical plume model is appropriate for this method.

More accurate simulations of the IR signature - mostly executed for possibly hostile TBMs, since they are not accessible for measurements - need a very detailed modelling of the flow parameters to calculate the vibration-rotation and electronic spectra of all constituents of the plume. Each single line or at least each band envelope has to be considered. This method is very expensive, not only because of the effort to execute the radiation calculation with such a high resolution but also because each particular calculation like the acrothermodynamic and the plume simulation has to be executed for many time steps of the complete mission and within the given scenario (Fig. 102). For all models the background radiation and the transmission through the atmosphere to the observer has to be simulated. Several standard environmental and transmission codes can be used for that purpose. In the case of a detailed study for a re-entry vehicle one gets a set of spectral distributions depending on the environment and the location of the observer (Fig. 103). A more detailed discussion of this subject will be given in a separate lecture of this series.

3.3 EXAMPLES OF MODERN MISSILE DESIGN

To illustrate some of the different subjects discussed in this lecture three recent examples for missile design are presented. Of course, they do not include all the problems that can arise in

practical work but one can guess from them the possible contexts of some of the special tasks.

3.3.1 HIGH VELOCITY MISSILE

Since no results of a detailed study on hypersonic missiles are available for publication to the authors at the moment, the TLVS (Taktisches Luft-Verteidigungs-System) missile is presented as an example for an high velocity missile. A design study has been finished recently.

The main design demand was an high hit probability for the possible targets (helicopters, airplanes, missiles, TBMs) which, in consequence, leads to the secondary demands of fast reaction at launch (\rightarrow vertical launch, Fig. 104) and of very high manoeuvrability.

The missile will be equipped with a double impulse propulsion (DIP) system and with an active radar sensor. The component most relevant for aerodynamic design is the lateral jet control located close to the center of gravity and using four liquid fuel propulsion units. This system helps to increase the performance in the end game by shortening the reaction time of the control system.

Since the maximum velocity is only about Mach 4.5, hypersonic effects are not yet of very high importance. Nevertheless, aerodynamic heating along the trajectory had to be checked. First guesses for the aeroelastic behaviour were of importance because of the fast manoeuvres at high lateral accelerations and of the rather high L/D ratio with a relatively lightweight structure.

Not every detail of the lateral jet control system was investigated during the study. But the hardware development has made considerable advances - it will deliver 6000 N of lateral thrust - and the studies concerning aerodynamic interaction effects have proved the applicability of the system. Though, as has been mentioned before, the location of the lateral jet exhausts at the surface of a cylinder is not optimal for the efficiency (for many points on the trajectory the jet effectiveness ratio is smaller than one) and some further improvements are certainly possible.

Most of the aerodynamic effort that has been made during the design study was to find an optimal airframe design for the missile. Manoeuvrability, range, modularity and flexibility were major aspects. Some of the considerations are presented. To reach high lateral accelerations the missile has to be trimmed up to high angles of attack. Since this is necessary for any roll position of the missile, a purely axisymmetric body without

lifting or control surfaces would be optimal. But, on the other hand, it is very difficult to stabilize and to control a pure body. For a missile with wings and fins the aerodynamic characteristics (e.g. normal force and pitching moment) are dependent on the roll angle (Fig. 105). One can see that the influence of the fins can be negligible in some cases while this is not the case for the wings. Therefore, a much higher effort is necessary to include this roll dependence into the control system.

Another disadvantage of a winged configuration is that it can be trimmed only up to smaller angles of attack than a wingless missile. Fig. 106 shows a mission diagram for a missile. For a given velocity and altitude one can read from it the trim conditions needed for different demands to lateral acceleration and for the actual center of gravity. This is located usually at about 50% to 60% of the body length and will change to more forward positions while the fuel is being consumed. The angle of attack that can be trimmed is reduced then and with it the maximal normal acceleration. One can see from Fig. 106 that the winged configuration has an aerodynamically better performance - the lift is twice that of a wingless missile at the same incidence - but the maximal angle where it can be trimmed is much smaller. One can also see that for normal accelerations of less than 10g the drag of the wingless configuration is smaller than the other one. Therefore, the winged missile will have a higher drag for most of the mission except for a few extreme manoeuvres. To achieve a similar range to trim the winged missile one would have to consider a variable wing geometry which would introduce constructive difficulties for missions of this type. The disadvantage of the wingless configuration is its lower performance which means a slower reaction to control commands. This has been improved by using the lateral jet device.

3.3.2 DISPENSERS

In contrast to the above example which presented a very conventional geometry, the airframe shape of dispensers usually is rather unconventional, often with variable components. In addition to that, one has to solve the aerodynamic problems of aircraft carriage and store separation, of high manoeuvrability at very low altitudes, submunition ejection and multi-body interference, possibly with retarders or gliders. The usually high subsonic speed will be increased in the future to low supersonic ones and, therefore, includes in both cases the transonic speed regime where difficulties arise, especially for such geometries.

A family of dispensers is presented here.

DWS (Dispenser Weapon System) was developed for JAS39 Gripen but is adaptable to most other combat aircraft. It is an unpowered stand-off missile with a range of up to about 10 km dependent on the speed at launch and with a cruise altitude of 200m to 30m. It is in production already.

The dispenser may be adapted to different submunition loads. The submunition is delivered by forced sideward ejection lot after lot in controllable intervals (Fig. 107).

Since the span was limited, a planar wing was selected to attain the manoeuvrability required in the pitch plane. In consequence, there are primarily bank-to-turn manoeuvres and high angles of attack (up to 20°) and small angles of sideslip occur. The aircraft carrier causes a large nose down pitching moment which means that the angle of attack range had to be extended down to 20°. To increase the manoeuvrability the guidance and control have been decided to work in three axes (pitch, yaw and roll). A body with a flat rectangular section with a height/width ratio of about 0.5 cannot be controlled by a conventional tail arrangement with elevator and rudder. Therefore, a cruciform tail configuration was chosen and had to be adapted to the rectangular body. There is a small boat tail with 30°/45° fin arrangement including fixed fin sockets for actuator installation. The nose is symmetrical with a nearly elliptical cross section.

KEPD / CASOM (Kinetic Energy Projectile Dispenser) and TADS (Target Adaptive Dispenser System) are advanced members of this dispenser family. The stand-off capability is up to a long range due to turbojet propulsion. Launch and forget features at all weather conditions are included. The long range at moderate (high subsonic) velocities make stealth features necessary. In addition, terrain following manoeuvres are executed at low altitude (Fig. 109).

There are different warheads for the modular concepts: KEPD can alternatively carry a penetrator shot by a Davis gun or submunitions. TADS shall carry self-targeting submunitions that will be ejected almost vertically by a short burning rocket motor. An IR seeker with an image processor is integrated into the nose section (Fig. 108).

The development phase is being started if enough customers will be found. The configurational design shows again a body with almost rectangular cross section, a bifurcated or chin inlet, asymmetric cruciform tail configuration and variable geometry of the exposed part of the wing. To minimize the IR signature, exhaust duct covers will be used, the radar cross section is optimized by adapting the shape in accordance to aerodynamic needs (Fig. 108) and can be improved by coatings.

The similar design of the dispenser family makes the design and development much more effective. Relatively large data bases have been built up after and after, so that many modifications can be easily interpolated from existing information. Major aerodynamic work packages included wind-tunnel tests with air flow through the model to investigate inlet effectiveness (distortion and swirl), and to execute 6-component measurements for the global model and for different built-up configurations and 3-component measurements for the control fins. Store separation tests were added. Pressure and load distributions had to be calculated for different versions by a panel method which incorporated empirical data for high angles of attack from wind tunnel tests. Interference effects on the dispenser passing the jet plume or the downwash of the wing during uprise manoeuvres had to be considered. A semi-empirical approximation and a panel method including advanced vortex modelling have been used for this simulation.

Special aerodynamic features of dispensers, especially those of this family are

- the non-axisymmetric body causes a distinct body lift and severe vortical flow
- the wing design (aspect ratio, sweep angle, profile) has to consider the high lift characteristics of the body: at about $\alpha=20^\circ$
 $C_{Z_{wing}}=C_{Z_{body}}=50\%$
- the pitching moment stability should be as little as possible to improve the manoeuvrability
- guidance and control requirements demand a very high accuracy in aerodynamic modelling to handle the nonlinear pitching moment characteristics caused by body and wing vortical downwash interference effects on the fins
- there are only small angles of sideslip due to bank-to-turn manoeuvres, except for the store separation phase
- the small yaw and roll stabilities due to influences of the rectangular body, to the high wing arrangement and to the control fin configuration reduce the requirements for roll control
- vortices separated from body edges show severe influence on the effectiveness of the propulsion inlet, especially for the bifurcated side inlets
- the variable wing has to meet the required pitching moment stability in folded (at release) and unfolded (during free flight) position.

3.3.3 FIBER OPTIC GUIDED MISSILE

A good example of this type of missiles is POLYPHEM which is currently in a first development phase. It covers all typical features mentioned before. Its range is about 2 km to

30 km; launch elevation is about 60° to make launches possible from a covered position. The missile is guided from the firing position by the use of a TV or IR camera with a real-time transmission of data in both directions (Fig. 110). By using optical fibre these signals cannot be disturbed. The use of a turbojet engine with adjustable power setting opens a wide range of manoeuvres. Due to the current technological state of image processing the flight velocity has to stay below about 250 m/s.

The overall system design (Fig. 111) is to a great extent conventional. The body is axisymmetric and, apart from the external cable channel cylindrical. There is a large cruciform wing (possibly folded before launch) and rear tail control. The profile of the wing is symmetrical. The missile is roll-positioned in its x-position, subsequently cartesian control and skid-to-turn flight mode is utilized. The span of the wing was derived from the limitations for maximum angle of attack and from the requirement of maximum lateral acceleration. The design and the location of the wing and the fins took into account the vortical downwash and the interference effects of the jet exhausts with rudder effectiveness (Fig. 112). Key components of the missile are the turbojet engine, the fibre optical guidance system incorporating up to 100 km optical fibre on a bobbin in the missile afterbody, and the image processing for target acquisition and distinction.

The aerodynamic design has been executed in three major cycles. The numerical design allowed first simulations of the performance. Preliminary wind tunnel tests with an inexpensive model, tested in a low-cost facility, improved the mathematical aerodynamic model for advanced simulations. Large-scale wind tunnel tests (full scale model including cold gas exhaust simulations) finally established the aerodynamic model which is used now for flight simulations and for guidance and control design. The internal aerodynamics of the intake was tested on a separate inlet model.

The normal force and pitching moment characteristics are almost linear over the full angle of attack range up to 16° . At higher incidence asymmetric separation occurs on the wings inducing a severe rolling moment. The missile possesses static longitudinal stability over the whole flight. The x roll position chosen is highly favourable with respect to maximum trim lift coefficient since flow separation is postponed to higher angles of attack.

Recently, a design study was started to extend the range of POLYPHEM considerably for sea-defense missions. In addition to sea-skimming manoeuvres the missile needs a stealth design in

this case. A first design for a low RCS version a monowing design utilizing coordinated bank-to-turn flight mode, is shown in Fig. 113. To optimize the aerodynamic design, the signature and flight performance one has to include all these aspects in the simulations. Substantial decrease in RCS compared with conventional designs is necessary to decrease the detection range considerably. Not the overall values for the RCS are important but only those at aspect angles in coincidence with the target or other defence installations (e.g. AWACS) during the full trajectory of the (sea-weaving) missile. Aerodynamic aspects like flight performance, drag or intake efficiency must not be neglected in the early design phase.

REFERENCES

(internal reports usually are not distributable)

1. Brebner, G.G. "A Brief Review of Air Flight Weapons", in "Missile Aerodynamics", AGARD LS 98, March 1979, Paper 1.
2. Knoche, H.-G. "Trends in Missile Development and their Corresponding Requirements with Respect to Aerodynamics", in "Missile Aerodynamics", AGARD CP 336, September 1982, Paper 1.
3. Nielsen, J.N. "The Present Status and the Future of Missile Aerodynamics", in "Stability and Control of Tactical Missile Systems", AGARD CP 451, May 1988, Paper K-1.
4. Lacau, R.G. and Robert, M. "Some Trends in Missile Aerodynamics", in "Missile Aerodynamics", AGARD CP 493, April 1990, Paper 1.
5. Shank, E.B., Thein, B.K., Campbell, D.C., and Wargovich, M.J. "A Comparison of Various Less Lethal Projectiles. Final Report", Army Land Warfare Laboratory, Aberdeen Proving Ground, Maryland, LWL-TR-74-79, June 1974.
6. Egner, E.O., Williams, L.W. "Standard Scenarios for the Less-Lethal Weapons Evaluation Modcl. Final Report", U.S. Army Human Engineering Laboratory, Aberdeen Proving Ground, Maryland, HEL-TM-20-75, August 1975.
7. Sullivan, M.L. "The National and International Implications of U.S. Army Military Police Operations. Study Project", U.S. Army War College, Carlisle Barracks, Pennsylvania, April 1992.
8. Feierlein, J. "Schonende Einsatzverfahren (Benign Intervention Technologies)", Dasa-Bericht Nr. TN-VAS-A-94-0001, February 1994.
9. Fair, H.D. "Hypervelocity Hyperkinetic Energy Weapons", Military Technology, October 1990, pp. 39-55.
10. Crispin, B. "Introduction and Overview", in "Ramjet and Ramrocket Propulsion Systems for Missiles", AGARD LS 136, September 1984, Paper 1.
11. Bendot, J.G., Heins, A.E. Jr., and Piercy, T.G. "Ramjet Air Induction System Design for Tactical Missile Application", in "Ramjet and Ramrocket Propulsion Systems for Missiles", AGARD LS 136, September 1984, Paper 2.
12. Besser, H.-L. "Solid Propellant Ramrockets", in "Ramjet and Ramrocket Propulsion Systems for Missiles", AGARD LS 136, September 1984, Paper 7.
13. Billig, F.S. "Ramjets with Supersonic Combustion", in "Ramjet and Ramrocket Propulsion Systems for Missiles", AGARD LS 136, September 1984, Paper 8.
14. Zarlingo, F.C. "Overview of Propulsion Concepts for Tactical Missiles", in "Missile Aerodynamics", AGARD CP 493, April 1990, Paper 22.
15. Cronvich, L.L. "Aerodynamic Considerations for Autopilot Design", in Hensch, M.J. and Nielsen, J.N. (Eds.) "Tactical Missile Aerodynamics", Progress in Astronautics and Aeronautics, Volume 104, Washington, D.C., American Institute of Aeronautics and Astronautics, 1986, ISBN 0 930403 13 4, pp.3-42.
16. Gate, M.S. and Randall, R.S. "Alternative Polar Homing Strategies", in "Stability and Control of Tactical Missile Systems", AGARD CP 451, May 1988, Paper 12.
17. Gazzina, A. "How to Control Unstable Missile Airframes: Methodology and Limitations", in "Stability and Control of Tactical Missile Systems", AGARD CP 451, May 1988, Paper 13.
18. Hingst, U.G. "Laminar / Turbulent Flow Transition Effects on High-Speed Missile Domes", in "Missile Aerodynamics", AGARD CP 493, April 1990, Paper 27.
19. Bryson, A.E. Jr. "Dryden Lecture: New Concepts in Control Theory 1959-1984", AIAA 22nd Aerospace Sciences Meeting, January 1984, AIAA-84-0161.
20. "Missile Interceptor Guidance System Technology", AGARD LS 173, October 1990.
21. Trümper, M. "Potential Applications of Fuzzy Logic for Control and Surveillance of Space Vehicles", DGLR Jahrbuch 1992 I, pp.415-422.

22. Brebner, G.G. "The Control of Guided Weapons", in "Missile Aerodynamics", AGARD LS 98, March 1979, Paper 7.
23. Rutledge, W.H., Polansky, G.F., and Clark, E.L. "Aerodynamic Design and Performance of a Bent-Axis Geometry Vehicle", J.Spacecraft, Vol.25, 4, July 1988, pp.257-262.
24. Raupach, I. "Neue Russische Lenk Waffen. Wendig und weitreichend", Flug Revue, February 1994, pp.50-51.
25. Haug, T., Ostertag, R., and Schäfer, W. "Fiber Reinforced Ceramics for Aerospace Applications", in Brandt, J., Hornfeld, H., and Neitzel, M. (Eds.) "Advanced Materials and Structures from Research to Application", SAMPE European Chapter, 1992, pp.163-173.
26. DeMeis, R. "Ring Wing Aids Missile Maneuverability", Aerospace America, November 1993, pp.42-43.
27. Dickmann, H.E. "Grundlagen zur Theorie ringförmiger Tragflügel (frei umstroemte Düsen)", Ing.-Arch., Vol.11, 1940, pp.36-52.
28. Weissinger, J. "Zur Aerodynamik des Ringflügels in inkompressibler Strömung", Z.f.Flugwiss., Vol.4, 3/4, March 1956, pp.141-150.
29. Schindel, L.H. "Waveriders", in Hensch, M.J. and Nielsen, J.N. (Eds.) "Tactical Missile Aerodynamics", Progress in Astronautics and Aeronautics, Volume 104, Washington, D.C., American Institute of Aeronautics and Astronautics, 1986, ISBN 0 930403 13 4, pp.198-242.
30. O'Neill, M.K.L. and Lewis, M.J. "Optimized Scramjet Integration on a Waverider", J.Aircraft, Vol.29, 6, November 1992, pp.1114-1121.
31. O'Neill, M.K.L. and Lewis, M.J. "Design Tradeoffs on Scramjet Engine Integrated Hypersonic Waverider Vehicles", J.Aircraft, Vol.30, 6, November 1993, pp.943-952.
32. He, X. and Emanuel, G. "Nonslender Waveriders", J.Aircraft, Vol.31, 1, January 1994, pp. 125-131.
33. Meyers, T.D. "Integral Boost, Heat Protection, Port Covers and Transition", in "Ramjet and Ramrocket Propulsion Systems for Missiles", AGARD LS 136, September 1984, Paper 4.
34. Haines, A.B. "Prospects for Exploiting Favourable and Minimising Adverse Aerodynamic Interference in External Store Installations", in "Subsonic/Transonic Configuration Aerodynamics", AGARD CP 285, May 1980, Paper 5.
35. Jackson, C.M. Jr. and Sawyer, W.C. "Bodies with Noncircular Cross Sections and Bank-to-Turn Missiles", in Hensch, M.J. and Nielsen, J.N. (Eds.) "Tactical Missile Aerodynamics", Progress in Astronautics and Aeronautics, Volume 104, Washington, D.C., American Institute of Aeronautics and Astronautics, 1986, ISBN 0 930403 13 4, pp.168-197.
36. Peterson, C.W. "Fallschirme höchster Bremsleistung", Spektrum der Wissenschaft, July 1990, pp.98-105.
37. Weinacht, P. and Sturek, W.B. "Navier-Stokes Predictions of Static and Dynamic Aerodynamic Derivatives for High L/D Finned Projectiles", in "Missile Aerodynamics", AGARD CP 493, April 1990, Paper 20.
38. Herring, P.G.C. "The Aerodynamic Characteristics of Long Rod Projectiles", in "Missile Aerodynamics", AGARD CP 493, April 1990, Paper 19.
39. Kilian, F.-P., Kirsche, H., and Fiegler, H. "Guidance and Control Technology for Electromagnetic Launched Air Defense Projectiles", in "4th European Symposium on Electro magnetic Launch Technology", 1993.
40. Danberg, J.E., Sigal, A., and Celmins, I. "Aerodynamic Characteristics of a Family of Cone-Cylinder-Flare Projectiles", J.Spacecraft, Vol.27, 4, July 1990, pp.355-360.
41. Mikhail, A.G. "Drag Correlation and Predictions of Surface Groove Drag for Kinetic Energy Projectiles", J.Spacecraft, Vol.26, 5, September 1989, pp.308-313.
42. Krishna, R.C., Graham, J.M.R., and Hillier, R. "Numerical Modelling of Sabot Aerodynamics", in "Missile Aerodynamics", AGARD CP 493, April 1990, Paper 21.
43. Bornstein, J., Celmins, I., Plostins, P., and Schmidt, E. "Launch Dynamics of Fin-

- Stabilized Projectiles", *J. of Spacecraft and Rockets*, Vol.29,2, March 1992, pp.166-172.
44. Beal, C. and Sweetman, B. "Beyond Sidewinder. Trends in Air-to-Air Missile Development", *International Defense Review*, January 1994, pp.39-43.
 45. Schäfer, W., Schröder, H.W., and Spelz, U. "Composite Radomes for High Mach Numbers", in "5th European Electromagnetic Windows Conference", September 1989, pp.50-57.
 46. Houghton, J.S. "Retarders for Stores and Submunitions", in "Weapons Aerodynamics", The Royal Aeronautical Society, December 1988, Paper 10.
 47. Schilling, H., Friedrichs, R., and Christ, D. "Experimental Aerodynamics for Hot Gas Jet Reaction Control System", in "Missile Aerodynamics", AGARD CP 493, April 1990, Paper 26.
 48. Smith, R.J. "Aerodynamic Interactions between Submunitions and Dispensers", in "Weapons Aerodynamics", The Royal Aeronautical Society, December 1988, Paper 9.
 49. Cottrell, C.J., Martinez, A., and Chapman, G.T. "Study of Multibody Aerodynamic Interference at Transonic Mach Numbers", *AIAA J.*, Vol.26, 5, May 1988, pp.553-560.
 50. Nikolitsch, D. "Aerodynamische Interferenzen mehrerer Flugkörper", MBB-Bericht Nr. UA-1178-90, March 1990.
 51. Wohlfahrt, M. "Die Auftriebsverteilung von flexiblen Segeln längs der Spannweite", *ZAMP*, Vol.67, July 1987, pp.281-291.
 52. Nickel, K.L.E. "A Theory of Sail-Wings", *Z.Flugwiss. Weltraumforsch.*, Vol. 11, November 1987, pp.321-328.
 53. Jackson, P.S. and Christie, G.W. "Numerical Analysis of Three-Dimensional Elastic Membrane Wings", *AIAA J.*, Vol.25, 5, May 1987, pp.676-682.
 54. Lee, C.K. "Modelling of Parachute Opening: An Experimental Investigation", *J.Aircraft* Vol.26, 5, May 1989, pp.444-451.
 55. Shpund, Z. and Levin, D. "Static and Dynamic Coefficients of a Cross-Type Parachute", *J.Aircraft*, Vol.31, 1, January 1994, pp. 132-137.
 56. Sugimoto, T. "Wing Design for Hang-gliders Having Minimum Induced Drag", *J.Aircraft*, Vol.29, 4, July 1992, pp.730-731.
 57. Wood, M.E. and Partington, R. "Retarded Store Interference", in "Missile Aerodynamics", AGARD CP 493, April 1990, Paper 12.
 58. Schmidt, R.-A. "Treffverhalten von Fallschirmsystemen II", MBB-Bericht Nr. UA-1023-89-2, January 1990.
 59. Doherr, K.-F. and Schilling, H. "Nine-Degree-of-Freedom Simulation of Rotating Parachute Systems", *J.Aircraft*, Vol.29, 5, September 1992, pp.774-781.
 60. von Hoessle, W. "Lichtwellenleiter als neue Technologie fuer Lenkflugkörper", in "Technologie der Systemkomponenten der Lenkflugkörper", Carl-Cranz-Seminar LR 3.06, 1992, Paper 10.
 61. Pai, P.F. and Nayfeh, A.H. "Fully Nonlinear Model of Cables", *AIAA J.*, Vol.30, 12, December 1992, pp.2993-2996.
 62. Sigal, A. "Aerodynamic Effects of Body Roughness", *J.Spacecraft and Rockets*, Vol.30, 3, May 1993, pp.298-303.
 63. Settles, G.S. and Dolling, D.S. "Swept Shock Wave / Boundary-Layer Interactions", in Hensch, M.J. and Nielsen, J.N. (Eds.) "Tactical Missile Aerodynamics", *Progress in Astronautics and Aeronautics*, Volume 104, Washington, D.C., American Institute of Aeronautics and Astronautics, 1986, ISBN 0 930403 13 4, pp.297-379.
 64. Corby, N. and Berry, J.B. "A Wind Tunnel Rig for the Measurement of Magnus Force and Moment on Spinning Models", in "Missile Aerodynamics", AGARD CP 493, April 1990, Paper 13.
 65. Ericsson, L.E. and Reding, J.P. "Asymmetric Vortex Shedding from Bodies of Revolution", in Hensch, M.J. and Nielsen, J.N. (Eds.) "Tactical Missile Aerodynamics", *Progress in Astronautics and Aeronautics*, Volume 104, Washington, D.C., American Institute of Aeronautics and Astronautics, 1986, ISBN 0 930403 13 4, pp.243-296.
 66. Delery, J.M. "Physics of Vortical Flows", *J.Aircraft* Vol.29, 5, September 1992, pp.856-876.

67. Richards, C.J. "Supersonic Air Intakes for Missiles", in "Weapons Aerodynamics", The Royal Aeronautical Society, December 1988, Paper 5.
68. Goldsmith, E.L. "Some Aspects of Engine and Airframe Integration for Ramjet and Ramrocket Powered Missiles", in "Ramjet and Ramrocket Propulsion Systems for Missiles", AGARD LS 136, September 1984, Paper 3.
69. Thomas, A.N. Jr. "Inlets", in Hensch, M.J. and Nielsen, J.N. (Eds.) "Tactical Missile Aerodynamics", Progress in Astronautics and Aeronautics, Volume 104, Washington, D.C., American Institute of Aeronautics and Astronautics, 1986, ISBN 0 930403 13 4, pp.129-167.
70. Braden, I.A. and Pierpont, P.K. "Pressure and Force Characteristics at Transonic Speeds of a Submerged Divergent-Walled Inlet on a Body of Revolution", NACA RM L53C13, 1953.
71. Bos, H.J. "Optimum Supersonic Wings with Subsonic Leading Edges", J.Aircraft, Vol.23, 4, April 1986, pp.326-332.
72. Pittman, J.L. "Supersonic Airfoil Optimization", J.Aircraft, Vol.24, 12, December 1987, pp.873-879.
73. Gupta, S.C. "OPSGER: Computer Code for Multiconstraint Wing Optimization", J.Aircraft, Vol.25, 6, June 1988, pp.572-574.
74. Siladic, M. and Carcy, G.F. "Extension of Inverse Design Techniques for Multicomponent Airfoils", AIAA J., Vol.26, 6, June 1988, pp.745-747.
75. Bangui, F. "Probleme inverse pour un profil d'aile", MBB-Bericht, AS524, March 1989.
76. Selig, M.S. and Maughmer, M.D. "A Multi-Point Inverse Airfoil Design Method Based on Conformal Mapping", in "29th Aerospace Sciences Meeting", January 1991, AIAA-91-0069.
77. Dulikravich, G.S. "Aerodynamic Shape Design and Optimization: Status and Trends", J.Aircraft, Vol.29, 6, November 1992, pp.1020-1026.
78. Selig, M.S. and Maughmer, M.D. "Generalized Multipoint Inverse Airfoil Design", AIAA J., Vol.30, 11, November 1992, pp.2618-2625.
79. Chen, J.L. and Tsai, W.C. "Shape Optimization by Using Simulated Biological Growth Approaches", AIAA J., Vol.31, 11, November 1993, pp.2143-2147.
80. "Optimum Design Methods in Aerodynamics", AGARD-FDP-VKI Special Course, April 1994.
81. Burbank, P.B. "A Method for Calculating the Contour of Bodies of Revolution with a Prescribed Pressure Gradient at Supersonic Speed with Experimental Verification", NACA TN 3555, March 1956.
82. Sahu, J. and Nietubicz, C.J. "Three-Dimensional Flow Calculations for a Projectile with Standard and Dome Bases", J. Spacecraft and Rockets, Vol.31, 1, January 1994, pp. 106-112.
83. Delery, J. and Siricix, M. "Ecoulements de Culot", in "Missile Aerodynamics", AGARD LS 98, March 1979, Paper 6.
84. Tanner, M. "Steady Base Flows", Prog. Aerospace Sci., Vol.21, 1984, pp.81-157.
85. Krieger, R.J. and Vukelich, S.R. "Tactical Missile Drag", in Hensch, M.J. and Nielsen, J.N. (Eds.) "Tactical Missile Aerodynamics", Progress in Astronautics and Aeronautics, Volume 104, Washington, D.C., American Institute of Aeronautics and Astronautics, 1986, ISBN 0 930403 13 4, pp.383-420.
86. Delcry, J. and Lacau, R.G. "Prediction of Base-Flows", in "Missile Aerodynamics", AGARD-FDP-VKI Special Course, May 1987.
87. Delery, J. and Wagner, B. "Results of GARTEUR Action Group AG09 on 'Flow Past Missile Afterbodies'", in "Missile Aerodynamics", AGARD CP 493, April 1990, Paper 25.
88. "GARTEUR Action Group 09 Final Report 'Flow Past Missile Afterbodies'", GARTEUR TP No.061, November 1991.
89. Danberg, J.E. and Nietubicz, C.J. "Predicted Flight Performance of Base-Bleed Projectiles", J.Spacecraft and Rockets, Vol.29, 3, May 1992, pp.366-372.
90. Sahu, J., Nietubicz, C.J., and Steger, J.L. "Navier-Stokes Computations of Projectile Base Flow with and without Mass Injection", AIAA J., Vol.23, 9, September 1985, pp.1348-1355.

91. Andersson, K., Gunners, N.E., and Hellgren, R. " 'Swedish Base Bleed' Increasing the Range of Artillery Projectiles through Base Flow", in "Propellants and Explosives I", Weinheim, Verlag Chemie GmbH, 1985, pp.69-73.
92. Romer, R. "Reichweitensteigerung bei Artilleriegeschossen", Wehrtechnik, October 1976, pp.54-58.
93. "Deutsche Artillerie heute - morgen", Wehrtechnik, February 1984, pp.74-87.
94. Fu, J.-K. and Liang, S.-M. "Drag Reduction for Turbulent Flow over a Projectile: Part I", J. Spacecraft and Rockets, Vol.31, 1, January 1994, pp.85-92.
95. Liang, S.-M. and Fu, J.-K. "Drag Reduction for Turbulent Flow over a Projectile: Part II", J. Spacecraft and Rockets, Vol.31, 1, January 1994, pp. 93-98.
96. Dash, S.M., Wolf, D.E., Beddini, R.A., and Pergament, H.S. "Analysis of Two-Phase Flow Processes in Rocket Exhaust Plumes", J.Spacecraft, Vol.22, 3, May 1985, pp.367-380.
97. Wuest, W. "Contamination Study for Meteosat-LO3 Due to Retro Rocket Firing. Part I: Status Review on Fundamentals of Gas Particle Plume Flow", DFVLR-AVA Bericht Nr. IB 222-81 A 07, 1981.
98. Dash, S.M. "Analysis of Exhaust Plumes and Their Interaction with Missile Airframes", in Hensch, M.J. and Nielsen, J.N. (Eds.) "Tactical Missile Aerodynamics", Progress in Astronautics and Aeronautics, Volume 104, Washington, D.C., American Institute of Aeronautics and Astronautics, 1986, ISBN 0 930403 13 4, pp.778-851.
99. Sommerfeld, M. "Expansion of a Gas/Particle Mixture in Supersonic Free Jet Flow", Z.Flugwiss.Weltraumforsch., Vol.11, 2, March 1987, pp.87-96.
100. Datta, N., and Das, S.K. "Turbulent mixing of an axially symmetrical jet of dusty fluid", Z.Flugwiss.Weltraumforsch., Vol.12, 1988, pp.368-372.
101. Dash, S.M., Sinha, N., and York, B.J. "Computational Models with Advanced Thermochemistry for the Analysis of Missile / Plume Flowfield Interactions", in "Missile Aerodynamics", AGARD CP 493, April 1990, Paper 31.
102. Kessel, P.A. "Secondary Smoke", in "Rocket Motor Plume Technology", AGARD LS 188, June 1993, Paper 3.
103. Dash, S.M. "Rocket Motor Plume Flowfields: Phenomenology and Simulation", in "Rocket Motor Plume Technology", AGARD LS 188, June 1993, Paper 4.
104. Schlünder, E.U. "Über die Ausbreitung turbulenter Freistrahlen", Z.Flugwiss., Vol.19, 3, March 1971, pp.108-113.
105. Abramovich, G.N. "The Theory of Turbulent Jets", Cambridge, Massachusetts, M.I.T., 1963.
106. Waxweiler, E. "Semi-empirisches Verfahren zur Berechnung der Isotachen und Isothermen eines freien turbulenten Treibstrahls", Dasa-Bericht Nr. TN-VAS41-93-0015, 1993.
107. Danielson, A.O. and Dillinger, R.B. "Investigations of Thrust Vector Control for High-Alpha Pitchover", in "Stability and Control of Tactical Missile Systems", AGARD CP 451, May 1988, Paper 21.
108. Waidmann, W. "Numerische und experimentelle Untersuchungen zur Schubvektorsteuerung durch Sekundäinjektion", DLR-Bericht Nr. DLR-FB 91-31, July 1991.
109. Leinfelder, H. "Thermo-Fluidodynamische Steuerungen von Flugkörpern", MBB-Bericht Nr. UA-1083/87, December 1987.
110. Spaid, F.W. and Cassel, L.A. "Aerodynamic Interference Induced by Reaction Controls", AGARDograph No.173, 1973.
111. Hancock, G.J. "A Review of the Aerodynamics of a Jet in a Cross Flow", Aeronautical J., May 1987, pp.201-213.
112. Naumann, K.W. and Srulijes, J. "Die Flugbahnsteuerung mittels seitlich austretender Strahlen. Literaturübersicht", ISL-Bericht Nr.R 117/85, 1985.
113. "Computational and Experimental Assessment of Jets in Cross Flow", AGARD, 72nd FDP Meeting and Symposium, April 1993.
114. Watman, H. and Meyer, R.C. "A Review of Lateral Jet - Supersonic Stream Interactions with Reference to Reaction Control Applications", Grumman Aircraft

- Engineering Corporation, Report No. ADR 01-07-63.2, 1963.
115. Schlichting, H. and Truckenbrodt, E. "Aerodynamics of the Airplane", New York, Mc Graw-Hill International Book Company, 1979.
 116. Fuchs, H. "Prediction of Dynamic Derivatives", in "Stability and Control of Tactical Missile Systems", AGARD CP 451, May 1988, Paper 6.
 117. "Dynamic Stability Parameters", AGARD CP 235, May 1978.
 118. Schneider, C.P. "Analytical Determination of Dynamic Stability Parameters", in "Dynamic Stability Parameters", AGARD LS 114, March 1981, Paper 12.
 119. Schneider, C.P. "Application to Missile Dynamics", in "Dynamic Stability Parameters", AGARD LS 114, March 1981, Paper 18.
 120. Hennig, P. and Hartner, E. "Instationäre Beiwerte von Flugkörpern, Teil V: Derivative der Längsstabilität von Flügel-Rumpf-Anordnungen in Unter- und Überschallströmung", MBB-Bericht Nr. UA-830-84, March 1985.
 121. "Unsteady Aerodynamics - Fundamentals and Applications to Aircraft Dynamics", AGARD CP 386, May 1985.
 122. Hennig, P. "Beschleunigte Bewegungen von Flugkörpern I", MBB-Bericht Nr. UA-994/86, July 1986.
 123. Hennig, P. "Beschleunigte Bewegungen von Flugkörpern II", MBB-Bericht Nr. UA-0994-88, July 1988.
 124. "Theoretical and Experimental Methods in Hypersonic Flows", AGARD CP 514, April 1993.
 125. Richards, B.E. "Kinetic Heating of High Speed Missiles", in "Missile Aerodynamics", AGARD LS 98, March 1979, Paper 9.
 126. Hirschel, E.H. "Heat Loads as Key Problem of Hypersonic Flight", Z.Flugwiss. Weltraumforsch. Vol.16, 1992, pp.349-356.
 127. Wada, Y., Ogawa, S., and Kubota, H. "Thermo-Chemical Models for Hypersonic Flows", Computers Fluids, Vol.22, 2/3, 1993, pp.179-187.
 128. Mabey, D.G. "Heat Transfer Effects on Aerodynamics and Implications for Wind-Tunnel Tests", J.Aircraft, Vol.29, 2, March 1992, pp.224-230.
 129. Hirschel, E.H. "Hot Experimental Technique: a New Requirement of Aerothermodynamics", in "New Trends in Instrumentation for Hypersonic Research", NATO Advanced Research Workshop, April 1992.
 130. Halbig, H. "Radome für Hochgeschwindigkeitsflugkörper - Anforderungen und geeignete Werkstoffe", MBB-Bericht Nr. TN- AS522-92-002, January 1992.
 131. Thornton, E.A. "Thermal Structures: Four Decades of Progress", J.Aircraft, Vol 29, 3, May 1992, pp.485-498.
 132. O'Connor, J.P. and Haji-Sheikh, A. "Numerical Study of Film Cooling in Supersonic Flow", AIAA J., Vol.30, 10, pp.2426-2433.
 133. Hodge, R.A., Raghuraman, P., and Murray, A.L. "Window Cooling Technology Program", J.of Spacecraft and Rockets, Vol.30, 4, July 1993, pp.466-476.
 134. Waszak, M.R. and Schmidt, D.K. "Flight Dynamics of Aeroelastic Vehicles", J.Aircraft, Vol.25, 6, June 1988, pp.563-571.
 135. Swaim, R.L. "Aeroelastic Interactions with Flight Control (A Survey Paper)", AIAA-83-2219, 1983.
 136. Singh, A.V. "Random Vibration of Cylindrical Shells", AIAA J., Vol.25, 12, December 1987, pp.1641-1643.
 137. Wu, M.-S., Garcia-Fogeda, P., and Liu, D.D. "Potential Flow Over Bodies of Revolution in Unsteady Motion", AIAA J., Vol.27, 6, June 1989, pp.725-733.
 138. Garcia-Fogeda, P. and Liu, D.D. "Analysis of Unsteady Aerodynamics for Elastic Bodies in Supersonic Flow", J.Aircraft, Vol.24, 12, December 1987, pp.833-840.
 139. Garcia-Fogeda, P. and Liu, D.D. "Supersonic Aeroelastic Applications of Harmonic Potential Panel Method to Oscillating Flexible Bodies", J.Spacecraft, Vol.25, 4, July 1988, pp.271-277.
 140. Ericsson, L.E. "Aeroelasticity, Including Dynamic Effects of Separated Flow", in

- "Dynamic Stability Parameters", AGARD LS 114, March 1981, Paper 13.
141. Mathews, C.B. "Store Separation", in "Missile Aerodynamics", AGARD LS 98, March 1979, Paper 8.
 142. Deslandes, R. "Marginal Release Disturbances on Advanced Missiles", in "Stability and Control of Tactical Missile Systems", AGARD CP 451, May 1988, Paper 24.
 143. Hamel, P.G. "Determination of Aircraft Dynamic Stability and Control Parameters from Flight Testing", in "Dynamic Stability Parameters", AGARD LS 114, March 1981, Paper 10.
 144. Lee, S. "Reduction of Blade-Vortex Interaction Noise Through Porous Leading Edge", AIAA J. Vol.32, 3, March 1994, pp.480-488.
 145. Hardin, J.C. and Hussaini, M.Y. (Eds.) "Computational Aeroacoustics", New York, Springer-Verlag, Inc., 1993, ISBN 0 387 94074 X.
 146. Eerkens, J.W. "Rocket Radiation Handbook. Volume I: Rocket Radiation Phenomenology and Theory. Volume II: Model Equations for Photon Emission Rates and Absorption Cross-Sections", Airesearch Manufacturing Company, Torrance, Calif., Report No. FTD-CW-01-01-74, 1974.
 147. Nelson, H.F. and Tucker, E.O. "Boron Slurry-Fueled Jet Engine Exhaust Plume Infrared Signatures", J.Spacecraft, Vol.23, 5, September 1986, pp.527-533.
 148. Dirscherl, R. "Plume Radiation", in "Rocket Motor Plume Technology", AGARD LS 188, June 1993, Paper 6.
 149. Miller, E. "Prediction of the Visible Signature of Solid Rocket Plumes", J.Spacecraft, Vol.27, 1, January 1990, pp.82-84.
 150. Victor, A.C. and Breil, S.H. "A Simple Method for Predicting Rocket Exhaust Smoke Visibility", J.Spacecraft, Vol.14, 9, September 1977, pp.526-533.
 151. Victor, A.C. "Effects of Multiple Scattering on Rocket Exhaust Plume Smoke Visibility", J.Spacecraft, Vol.26, 4, July 1989, pp.274-278.
 152. Chastenet, J.C. "Plume Primary Smoke", in "Rocket Motor Plume Technology", AGARD LS 188, June 1993, Paper 1E.
 153. Smith, P.K. "Propulsion", in "Rocket Motor Plume Technology", AGARD LS 188, June 1993, Paper 2.
 154. Altmann, K. "Untersuchung der atmosphärischen Einflüsse auf ein Nd-Laser-Leitstrahlverfahren", MBB-Bericht Nr. TN-AE33-16/85, 1985.
 155. Brown, A.C. "Fundamentals of Low Radar Cross-Sectional Aircraft Design", J.Aircraft, Vol.30, 3, May 1993, pp.289-290.
 156. Knott, E.F., Shaeffer, J.F., and Tuley, M.T. "Radar Cross Section. Its Prediction, Measurement and Reduction", Norwood, Mass., ARTECH House, Inc., 1985 (ISBN 0 89006 174 2).
 157. Lawrence, R. "Microwave Properties and Systems Overview", in "Rocket Motor Plume Technology", AGARD LS 188, June 1993, Paper 5.
 158. Cronvich, L.L. and Liepmann, H.P. "Advanced Missile Technology", NASA Contractor Report 3187, 1979.159. Chapman, D.R. "Computational Aerodynamics Development and Outlook", AIAA J., Vol.17, 12, December 1979, pp.1293-1313.
 160. Hancock, G.J. "Aerodynamics - the Role of the Computer", Aeronautical J., Vol.89, August 1985, pp.269-279.
 161. "Focus'92 Computational Fluid Dynamics Part I", Aerospace America, January 1992.162. "Focus'92 Computational Fluid Dynamics Part II", Aerospace America, February 1992.
 163. Hensch, M.J. and Nielsen, J.N. "The Equivalent Angle-of-Attack Concept for Engineering Analysis", in Hensch, M.J. and Nielsen, J.N. (Eds.) "Tactical Missile Aerodynamics", Progress in Astronautics and Aeronautics, Volume 104, Washington, D.C., American Institute of Aeronautics and Astronautics, 1986, ISBN 0 930403 13 4, pp.482-518.
 164. Lacau, R.G. "A Survey of Missile Aerodynamics", NEAR Conference on Missile Aerodynamics. Monterey, 1988.

165. Champigny, P., Baudin, D., and Gonidec, P. "Prevision des coefficients aerodynamiques de missiles munis de prises d'air", AGARD CP 493, 1990.
166. Hoeijmakers, H.W.W. "A Panel Method for the Prediction of Aerodynamic Characteristics of Complex Configurations in Linearized Subsonic and Supersonic Flow", AGARD CP 336, 1982.
167. Fornasier, L. "Linearized Potential Flow Analysis of Complex Aircraft Configurations by HISSS, a Higher-Order Panel Method", AIAA Paper 85-0281, 1985.
168. Nikolitsch, D. "Leistungssteigerung im Manöverflug, Teil 1", MBB-Bericht Nr. UA-1082/87, November 1987.
169. Dillenius, M.F.E. and Allen, J.M. "Paneling Methods with Vorticity Effects and Corrections for Nonlinear Compressibility", in Hemsch, M.J. and Nielsen, J.N. (Eds.) "Tactical Missile Aerodynamics", Progress in Astronautics and Aeronautics, Volume 104, Washington, D.C., American Institute of Aeronautics and Astronautics, 1986, ISBN 0 930403 13 4, pp.572-631.
170. Mendenhall, M.R. and Perkins, S.C. Jr. "Vortex Cloud Model for Body Vortex Shedding and Tracking", in Hemsch, M.J. and Nielsen, J.N. (Eds.) "Tactical Missile Aerodynamics", Progress in Astronautics and Aeronautics, Volume 104, Washington, D.C., American Institute of Aeronautics and Astronautics, 1986, ISBN 0 930403 13 4, pp.519-571.
171. Nikolitsch, D. "Leistungssteigerung im Manöverflug, Teil 2", MBB-Bericht Nr. UA-1082/89, October 1989.
172. Lu, S. and Voss, R. "TDLM - A Transonic Doublet Lattice Method for 3D Potential Unsteady Transonic Flow Calculation", DLR-Bericht Nr. DLR-FB 92-25, 1992.
173. Pittman, J.L., Miller, D.S., and Siclari, M.J. "Supersonic Full Potential Method Applied to Missile Bodies", in Hemsch, M.J. and Nielsen, J.N. (Eds.) "Tactical Missile Aerodynamics", Progress in Astronautics and Aeronautics, Volume 104, Washington, D.C., American Institute of Aeronautics and Astronautics, 1986, ISBN 0 930403 13 4, pp.632-668.
174. Wardlaw, A.B. Jr., Solomon, J.M., and Baltakis, F.P. "Euler Space Marching Methods Applied to Missiles", in Hemsch, M.J. and Nielsen, J.N. (Eds.) "Tactical Missile Aerodynamics", Progress in Astronautics and Aeronautics, Volume 104, Washington, D.C., American Institute of Aeronautics and Astronautics, 1986, ISBN 0 930403 13 4, pp.669-722.
175. Borrel, M., Montagne, J.L., Diet, J., Guillen, P., and Lordon, J. "Upwind Scheme for Computing Supersonic Flows around a Tactical Missile", La Recherche Aerospaciale no. 1988-2, 1988.
176. Guillen, P. and Dormieux, M. "Design of a 3D Multidomain Euler Code", Computational Mechanics Institute, Supercomputing in Fluid Flows, Boston, 1989.
177. Dormieux, M., Guillen, P., and Abgrall, R. "Numerical Simulation of Transverse Jet Flows by a Non Reactive Two Species Multidomain Euler Flow Solver", AIAA Paper 90-0126, 1990.
178. Couaillier, V. "Multigrid Method for Solving Euler and Navier-Stokes Equations in Two and Three Dimensions", 8th GAMM Conference on Numerical Methods in Fluid Dynamics, 1989.
179. Eberle, A. "3D Euler Calculations Using Characteristic Flux Extrapolation", AIAA-Paper 85-0119, 1985.
180. Huber, I. "Hyperschall-FK-Aerodynamik, Teil II", MBB-Bericht Nr. UA-1035-89-II, September 1989.
181. Cebeci, T. "Three-Dimensional Boundary Layers on Missiles", in Hemsch, M.J. and Nielsen, J.N. (Eds.) "Tactical Missile Aerodynamics", Progress in Astronautics and Aeronautics, Volume 104, Washington, D.C., American Institute of Aeronautics and Astronautics, 1986, ISBN 0 930403 13 4, pp.723-777.
182. Monnoyer de Galland, F. "Calculation of Three-Dimensional Attached Viscous Flow on General Configurations Using Second Order Boundary-Layer Theory", Z. Flugwiss. Weltraumforsch., Vol.14, 2, March 1990, pp.95-108.
183. Schmatz, M.A., Monnoyer, F., and Wanie, K.M. "Numerical Simulation of Transonic Wing Flows Using a Zonal Euler/Boundary-Layer/Navier-Stokes Approach", 16th ICAS Congress, August 1988, Paper 88.4.6.3.

184. Gaible, F., Cariou, R., and Houdeville, R. "Numerical Simulation of Three Dimensional Supersonic Flows Euler and Boundary Layer Solvers", AIAA Paper 93-0531, 1993.
185. Chaput, E., Dubois, F., Lemaire, D., Moulcs, G., and Vaudescal, J.L. "FLU3PNS: A Three Dimensional Thin Layer and Parabolized Navier-Stokes Solver Using the MUSCL Upwind Scheme", AIAA Paper 91-0728, 1991.
186. Gouldin, F.C. "Interpretation of Jet Mixing Using Fractals" AIAA J., Vol.26, 11, November 1988, pp.1405-1407.
187. "Non Linear Dynamics and Chaos", AGARD LS 191, June 1993.
188. "Wind Tunnel and Testing Techniques", AGARD CP 348, September 1983.
189. Modarress, D. and Azzazy, M. "Modern Experimental Techniques for High-Speed Flow Measurements", J.Aircraft, Vol.26, 10, October 1989, pp.889-899.
190. Scaggs, N.E. "Future Requirements for Hypersonic Aerodynamic and Aerothermodynamic Facilities", in "AIAA 17th Acroospace Ground Testing Conference", AIAA 92-3903, July 1992.
191. Sawyer, W.C., Stallings, R.L. Jr., Wilcox, F.J. Jr., Blair, A.B., Monta, W.J., and Plentovich, E.B. "New Test Techniques to Evaluate Near Field Effects for Supersonic Store Carriage and Separation", in "Stability and Control of Tactical Missile Systems", AGARD CP 451, May 1988, Paper 16.
192. Allen, J.M., Shaw, D.S., and Sawyer, W.C. "Remote Control Missile Model Test", in "Stability and Control of Tactical Missile Systems", AGARD CP 451, May 1988, Paper 17.
193. Dankert, C., Cattolica, R., and Sellers, W. "Local Measurement of Temperatures and Concentrations: A Review for Hypersonic Flows", in "Theoretical and Experimental Methods in Hypersonic Flows", AGARD CP 514, April 1993, Paper 12B.
194. Miller, C.G. "Pressure and Force Measurements on Models Set in Hypersonic Flows: A Review", in "Theoretical and Experimental Methods in Hypersonic Flows", AGARD CP 514, April 1993, Paper 13.
195. Boutier, A., Yanta, W.J., and Smcets, G. "Velocity Measurements in Hyper sonic Flows: A Review", in "Theoretical and Experimental Methods in Hypersonic Flows", AGARD CP 514, April 1993, Paper 14.
196. Troliger, J., Eitelberg, G., and Rapuc, M. "Flow Visualization and Spectroscopy in Hypersonic Flows: New Trend", in "Theoretical and Experimental Methods in Hypersonic Flows", AGARD CP 514, April 1993, Paper 15.
197. Wendt, J.F., Balageas, D., and Neumann, R.D. "Thermal Flux Measurements in Hypersonic Flows - A Review", in "Theoretical and Experimental Methods in Hypersonic Flows", AGARD CP 514, April 1993, Paper 16.
198. Hillier, R., Kirk, D.C., Sell, M., and Soltani, S. "Studies of Hypersonic Viscous Flows", in "Theoretical and Experimental Methods in Hypersonic Flows", AGARD CP 514, April 1993, Paper 32.
199. Bütetfisch, K.-A., Dick, P., and Ewald, B. (Eds.) "2D-Meßtechnik", DGLR-Workshop, October 1988, DGLR Bericht 88-04.
200. Schoeler, H. and Banerji, A. "Visualization of Separation Effects on Blunt Cones at High Mach Numbers", DFVLR-AVA Bericht Nr. IB 222-84 A 38, 1984.
201. Schoeler, H. "Thermal Imaging on Missiles in Hypersonic Flow", in "Missile Aerodynamics", AGARD CP 493, April 1990, Paper 29.
202. Reda, D.C. and Aeschliman, D.P. "Liquid Crystal Coatings for Surface Shear-Stress Visualization in Hypersonic Flows", J.Spacecraft and Rockets Vol.29, 2, March 1992, pp.155-158.
203. Engler, R.H., Hartmann, K., Troyanovski, I., and Vollan, A. "Description and Assessment of a New Optical Pressure Measurement System (OPMS) Demonstrated in the High Speed Wind Tunnel of DLR in Goettingen", DLR-Bericht Nr. DLR-FB 92-24, 1992.
204. Henckels, A. "Einsatz der Infrarot-Thermographic in der Hyperschall-Aerothermodynamik", DLR-Bericht Nr. IB - 39113 - 93A15, 1993.

205. Nielsen, J.N. "Missile Aerodynamics", Mountain View, Calif., 1960 (reprint 1988), ISBN 0 9620629 0 1.
206. Chin, S.S. "Missile Configuration Design", New York, McGraw-Hill Book Company, Inc., 1961.
207. Hensch, M.J. and Nielsen, J.N. (Eds.) "Tactical Missile Aerodynamics", Progress in Astronautics and Aeronautics, Volume 104, Washington, D.C., American Institute of Aeronautics and Astronautics, 1986, ISBN 0 930403 13 4.
208. Brebner, G.G. "General Missile Aerodynamics", in "Missile Aerodynamics", AGARD LS 98, March 1979, Paper 2.
209. Ericsson, L.E. "Prediction of Tactical Missile Dynamics", in "Stability and Control of Tactical Missile Systems", AGARD CP-451, May 1988, Paper 7.
210. Hoerner, S.F. "Fluid-Dynamic Drag", Midland Park, N.J., S.F.Hoerner, 1965.
211. Champigny, P. "Prevision de la Stabilité Aerodynamique des Missiles", in "Stability and Control of Tactical Missile Systems", AGARD CP 451, May 1988, Paper 1.
212. Fornasier, L. and D'Espinay, P. "Prediction of Stability Derivatives for Missiles Using the HISS Panel Code", in "Stability and Control of Tactical Missile Systems", AGARD CP 451, May 1988, Paper 3.
213. Esch, H. "Bodies", in "Missile Aerodynamics", AGARD LS 98, March 1979, Paper 4.
214. Stahl, W.H. "Aerodynamics of Low Aspect Ratio Wings", in "Missile Aerodynamics", AGARD LS 98, March 1979, Paper 3.
215. Stallings, R.L. Jr. "Low Aspect Ratio Wings at High Angles of Attack", in Hensch, M.J. and Nielsen, J.N. (Eds.) "Tactical Missile Aerodynamics", Progress in Astronautics and Aeronautics, Volume 104, Washington, D.C., American Institute of Aeronautics and Astronautics, 1986, ISBN 0 930403 13 4, pp.89-128.
216. Wardlaw, A.B. Jr. "High-Angle-of Attack Missile Aerodynamics", in "Missile Aerodynamics", AGARD LS 98, March 1979, Paper 5.
217. "High Angle-of-Attack Aerodynamics", AGARD LS 121, March 1982.
218. Nelson, R.C. "The Role of Flow Visualization in the Study of High-Angle-of-Attack Aerodynamics", in Hensch, M.J. and Nielsen, J.N. (Eds.) "Tactical Missile Aerodynamics", Progress in Astronautics and Aeronautics, Volume 104, Washington, D.C., American Institute of Aeronautics and Astronautics, 1986, ISBN 0 930403 13 4, pp.43-88.
219. Hartmann, K., Kanagarajan, V., and Nikolitsch, D. "Body Wing Tail Interference Studies at High Angles of Attack and Variable Reynolds Number", in "16th ICAS Congress", August 1988.
220. Hartmann, K., and Nikolitsch, D. "Systematic Investigations of Wing-Body-Tail Interference at High Angles of Attack", in "Missile Aerodynamics", AGARD CP 493, April 1990, Paper 14.
221. Nikolitsch, D. "Normal Force and Pitching Moment Coefficient of Bodies and Wing-Body Combinations at Very High Angles of Attack", in "AIAA 16th Aerospace Sciences Meeting", January 1978, AIAA Paper 78-63.
222. Esch, H. "Normalkraft- und Kippmomentenmessung an schlanken Flugkörperflügeln im unteren Transschallbereich bei großen Anstellwinkeln", DFVLR Bericht Nr. IB 391-82-A-02, 1982.
223. Nikolitsch, D. "Calculation of Pressure Distributions, Forces and Moments of Cruciform Wing-Body Combinations up to High Angles of Attack", in "AIAA 19th Aerospace Sciences Meeting", January 1981, AIAA Paper 81-0398.
224. Ericsson, L.E. and Reding, J.P. "Review of Vortex-Induced Asymmetric Loads - Part I", Z.Flugwiss.Weltraumforsch., Vol.5, 3, June 1981, pp.162-174.
225. Ericsson, L.E. and Reding, J.P. "Review of Vortex-Induced Asymmetric Loads - Part II", Z.Flugwiss.Weltraumforsch., Vol.5, 6, December 1981, pp.349-366.
226. Schiff, L.B., Tobak, M., and Malcolm, G.N. "Mathematical Modeling of the Aerodynamics of High-Angle-of-Attack Maneuvers", AIAA-80-1583, 1980.
227. Laruelle, G. "Supersonic Missile Air Intakes: Design and Development Criteria", La Recherche Aerospaciale no. 1987-6, 1987.

228. Laruelle, G. "Missile Intakes", in "Intake Aerodynamics", VKI Lecture Series, 1988-04.
229. Hayes, C. "Aerodynamic Characteristics of a Series of Twin-Inlet Air-Breathing Missile Configurations", "I: Axisymmetric Inlets at Supersonic Speeds", NASA TM 84558; "II: Two-Dimensional Inlets at Super sonic Speed", NASA TM 85559.
230. Champigny, P. "Problemes lies a l'aerodynamique externe des missiles aerobies", in "Missile Aerodynamics", AGARD CP 336, September 1982, Paper 29.
231. Rasmussen, M.L., Jischke, M.C., and Daniel, D.C. "Aerodynamics of Cone-Derived Waverider Missile Configurations", in "Missile Aerodynamics", AGARD CP 336, September 1982, Paper 20.
232. Schindel, L.H. "High Lift/ Drag Ratio Hypersonic Missiles", in "Missile Aerodynamics", AGARD CP 336, September 1982, Paper 23.
233. Bjelozerkovskij, S.M. (Ed.) "Reshetchatye Kryl'ya" (= Grid Fins), Moskow, Maschinostroenie, 1985.
234. Brooks, R.A. and Burkhalter, J.E. "Experimental and Analytical Analysis of Grid Fin Configurations", J.Aircraft, Vol.26, 9, September 1989, pp.885-887.
235. Deininger, W. and Nikolitsch, D. "Acrodynamische Untersuchung von Gitterflügeln", MBB-Bericht Nr. TN-AS52-06/89, 1989.
236. "5th International Aerospace Planes and Hypersonics Technologies Conference", AIAA / DGLR, November 1993, Papers AIAA-93-5000 through 5152.
237. Anderson, J.D. "A Survey of Modern Research in Hypersonic Aerodynamics", AIAA 17th Fluid Dynamics, Plasma Dynamics, and Lasers Conference, AIAA Paper 84-1578, June 1984.
238. Thompson, R.A. and Riley, C. "Engineering Code for Hypersonic Vehicle Optimization", J. Spacecraft and Rockets, Vol.31, 1, January 1994, pp.150-152.
239. Hirschel, E.H. "Berechnung von Hyperschallströmungen - Ansätze, Möglichkeiten, Empfehlungen", MBB Bericht Nr. LKE122-AERO-MT-724, 1985.
240. Endmann, P., Hennig, P., and Nikolitsch, D. "Aerodynamische Wirkungen von Querschubströmungen an Flugkörpern. Übersichtsbericht", DASA-Bericht Nr. TN-VAS 41-94-0005, August 1994.
241. Tenney, D.R., Lisagor, W.B., and Dixon, S.C. "Materials and Structures for Hypersonic Vehicles", J.Aircraft, Vol.26, 11, November 1989, pp.953-970.
242. Neumann, R.D. and Hayes, J.R. "Introduction to Aerodynamic Heating Analysis of Supersonic Missiles", in Hensch, M.J. and Nielsen, J.N. (Eds.) "Tactical Missile Aerodynamics", Progress in Astronautics and Aeronautics, Volume 104, Washington, D.C., American Institute of Aeronautics and Astronautics, 1986, ISBN 0 930403 13 4, pp.421-481.
243. Mathauer, H. "Aerodynamic Heating of Missiles", in "Missile Aerodynamics", AGARD CP 336, September 1982, Paper 21.
244. Wurster, K.E., Zoby, E.V., and Thompson, R.A. "Flowfield and Vehicle Parameter Influence on Results of Engineering Aerothermal Methods", J.Spacecraft, Vol.28, 1, January 1991, pp.16-22.
245. Riley, C.J. and DeJarnette, F.R. "Engineering Aerodynamic Heating Method for Hypersonic Flow", J.Spacecraft and Rockets Vol.29, 3, May 1992, pp.327-334.
246. Huber, I. "Überblick über ein acrothermodynamisches Auslegungsverfahren an Hand verschiedener Demonstrationsbeispiele" Dasa-Bericht Nr. TN-VAS 41- 93-0005, 1993.
247. Wing, L.D. "Aerodynamic Heating for Wedge/Wedge or Cone/Cone at Angles of Attack from Zero to Approximately 40°", Fairchild Hiller Corporation Report No. ER-116, 1968.
248. Wing, L.D. "Tangent Ogive Nose Aerodynamic Heating Program: NQLDW019", Goddard Space Flight Center, Report No. X-742-71-161, April 1971.
249. Eckert, E.R.G. and Tewfik, O.E. "Use of Reference Enthalpy in Specifying the Laminar Heat Transfer Distribution Around Blunt Bodies in Dissociated Air", J. of the Aerospace Sciences, Vol.27, 6, June 1960, pp.464.

250. Wing, L.D. "10-Element One-Dimensional Structural Heating Programs", Goddard Space Flight Center, Report No. X-721-69-454, 1969.
251. Wing, L.D. "A 28-Element Two-Dimensional Structural Heating Program N2LDW018)", Goddard Space Flight Center, Report No. X-721-70-221, June 1970.
252. Waxweiler, E. "Verfahren zur Bestimmung von Biegelinie, Biegemoment, Scherbeanspruchung und Eigenschwingungen von schlanken Flugkörpern", MBB-Bericht Nr. TN-VAS41-92-0040, 1992.
253. Nikolitsch, D. and Waxweiler, E. "Einfluß beliebiger Windfelder auf Flugkörper und aeromechanische Abgangssimulation", DASA-Bericht Nr. TN-VAS41-92-0050, 1992.
254. Ffowcs Williams, J.E. "The Noise from Turbulence Convected at High Speed", Philosophical Transactions of the Royal Society, Vol.A 255, 1963, pp.469-503.
255. Ffowcs Williams, J.E. and Hawkings, D.L. "Sound Generation by Turbulence and Surfaces in Arbitrary Motion", Philosophical Transactions of the Royal Society, Vol.A 264, 1969, pp.321-342.
256. Lighthill, M.J. "On Sound Generated Aerodynamically. I. General Theory", Proceedings of the Royal Society, Vol. A 211, 1952, pp.564-587.
257. Lighthill, M.J. "On Sound Generated Aerodynamically. II. Turbulence as a Source of Sound", Proceedings of the Royal Society, Vol.A 222, 1954, pp.1-32.
258. Moehring, W. "On Vortex Sound at Low Mach Number", J.Fluid Mech., Vol.85, 4, 1978, pp.685-691.
259. Bridges, J. and Hussain, F. "Direct Evaluation of Aeroacoustic Theory in a Jet", J.Fluid Mech., Vol.240, 1992, pp.469-501.
260. Bechara, W., Bailly, C., Lafon, P., and Candel, S.M. "Stochastic Approach to Noise Modeling for Free Turbulent Flows", AIAA J., Vol.32, 3, March 1994, pp.455-463.
261. Stein, V. "The Solution of Scattering and Radiation Problems for Complex Configurations Based on 3-D Grid and Patch Models", in "Application of Mesh Generation to Complex 3D Configurations", AGARD CP 464, May 1989, Paper 22.
262. Stein, V. "Numerical Modeling: Integral Equation Method", in "Theoretical Aspects of Target Classification", AGARD LS 152, 1987, Paper 10.
263. Stein, V. "Physical Optics Method: Prediction of Radar Signatures", in "Theoretical Aspects of Target Classification", AGARD LS 152, 1987, Paper 5.
264. Schropp "Entwicklung eines Programmes zur Berechnung von Radarquerschnitten nach der Physical Optics Methode", MBB-Bericht Nr. TN-AK32-33/88, November 1988.
265. Schropp "Berechnung der Radarquerschnittsflächen von zwei Flugkörpern", MBB-Bericht Nr. TN-AK32-34/88, November 1988.
266. Umashankar, K. and Taflovic, A. "A Novel Method to Analyze Electromagnetic Scattering of Complex Objects", IEEE Trans. Electromagnetic Compatibility, Vol. EMC-24, 4, November 1982, pp.397-405.
267. Grashof, J. "Finite-Volume Method for the Time-Dependent Maxwell Equations and Prediction of the Scattering from Perfectly Conducting Bodies", in "Numerical Field Calculation in Electrical Engineering", 3rd International IGTE Symposium, 1988.
268. Hennig, P. "Berechnung von IR-Strahlungsspektren aerothermisch erhitzter Flugkörper längs ihrer Flugbahn", MBB-Bericht Nr. UA-1020/86, 1986.

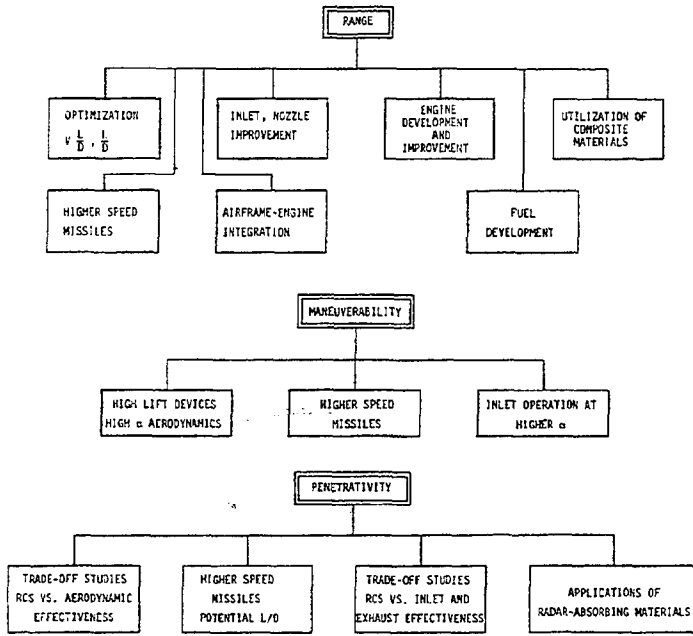


Fig. 1: Technology improvement areas related to range, manoeuvrability, and penetrativity (Ref. 2).

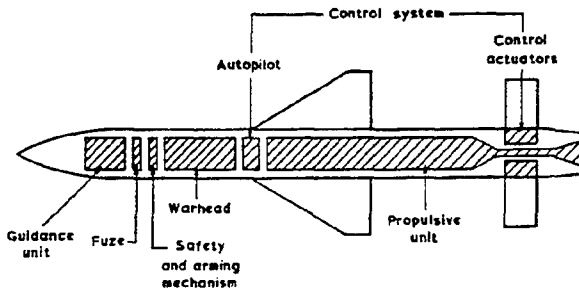


Fig. 2: Layout of a typical guided weapon (Ref. 1).

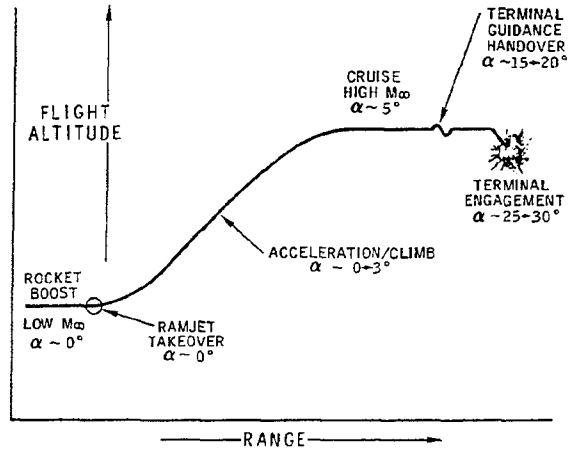


Fig. 4: Advanced air-to-air missile flight profile (Ref. 11).

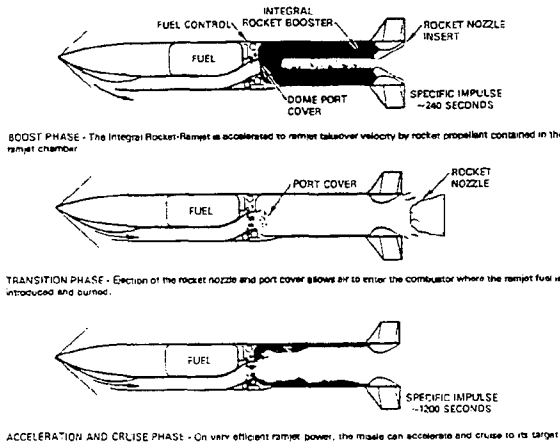


Fig. 3: How the integral rocket-ramjet works (Ref. 11).

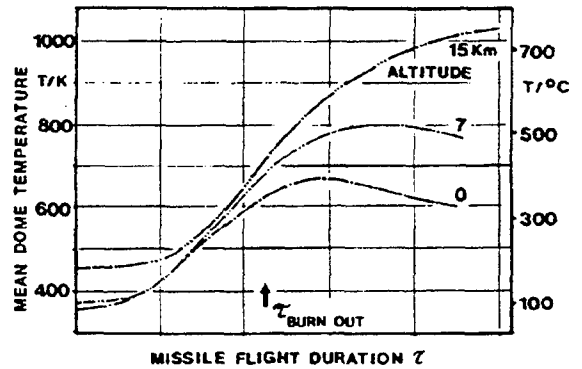


Fig. 5: Mean dome temperatures versus flight time and altitude (Ref. 18).

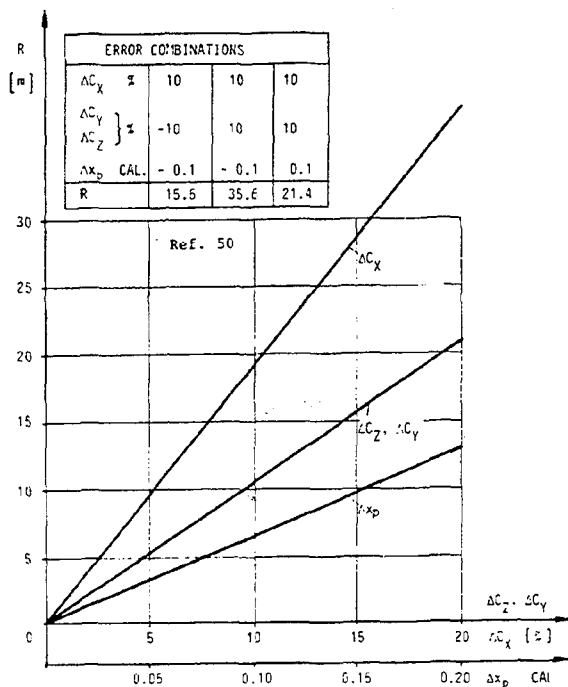


Fig. 6: Miss distance R of a missile with observer as a function of the errors of the aerodynamic coefficients (Ref. 2).

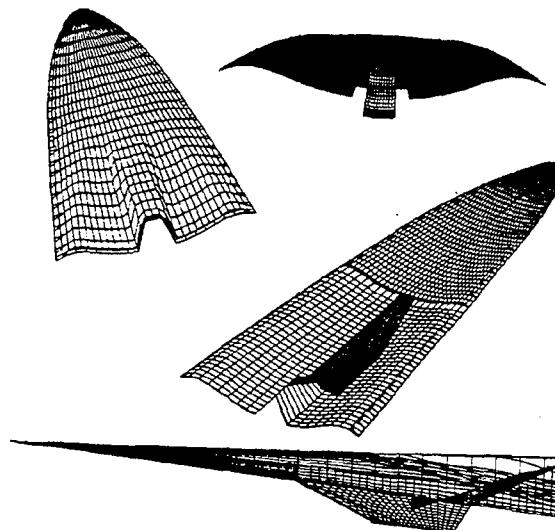


Fig. 8: Mach 8 baseline cruise scramjet integrated waverider. Top left: top view of the vehicle. Top right: view from tail. Center: undersurface with engine ramp, cowl and nozzle. Bottom: side view (from Ref. 31).

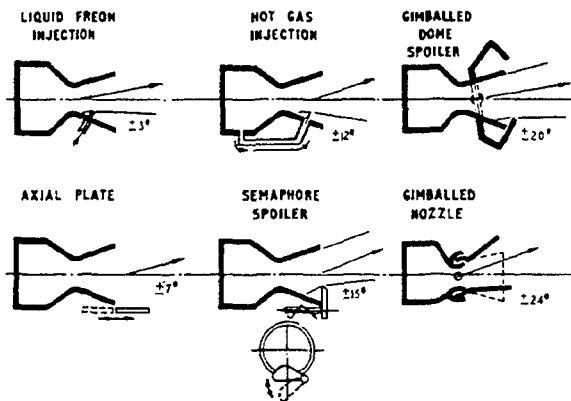


Fig. 7: Some thrust vector control systems (Ref. 22).

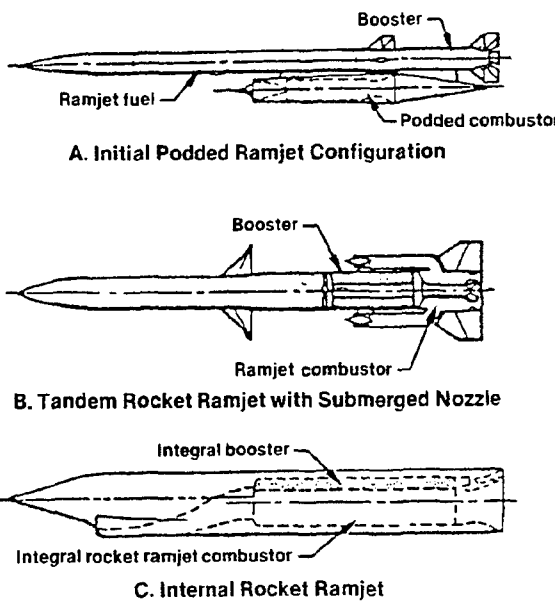


Fig. 9: Evolution of integral rocket ramjet configuration (Ref. 33).

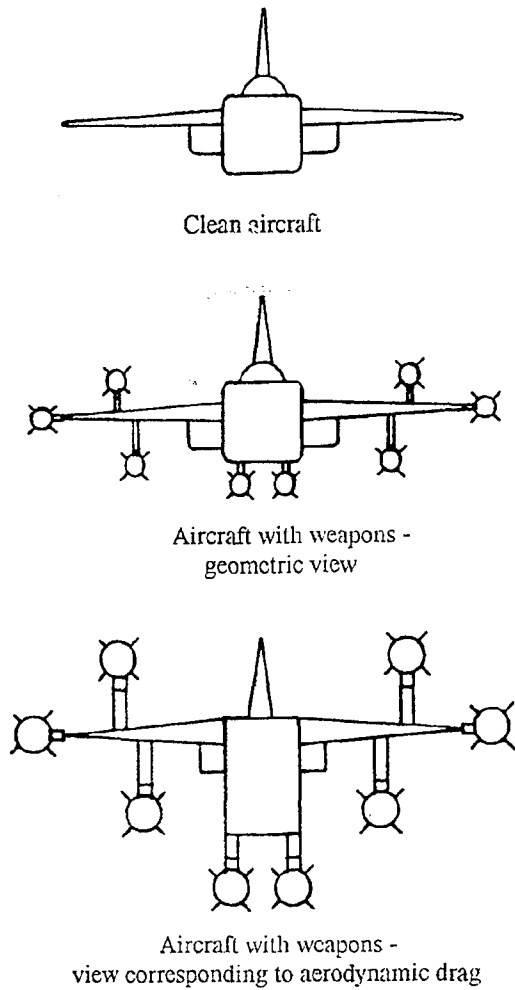


Fig. 10: Drag of not integrated stores (Ref. 34).

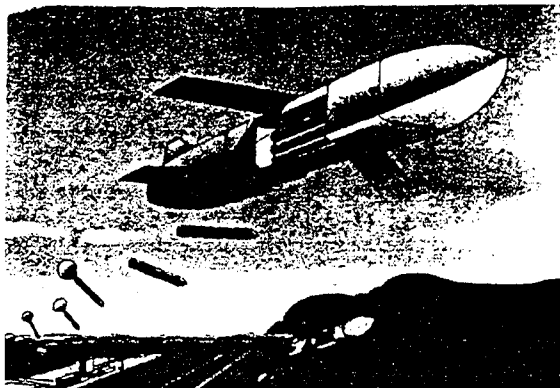


Fig. 11: APACHE Modular stand-off-missile (Ref. 4).

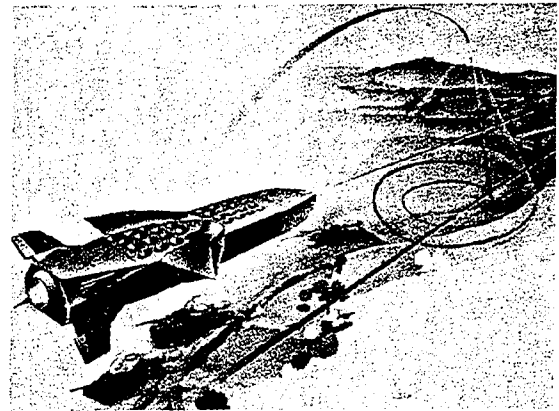


Fig. 12: TADS (Target Adaptive Dispenser System).

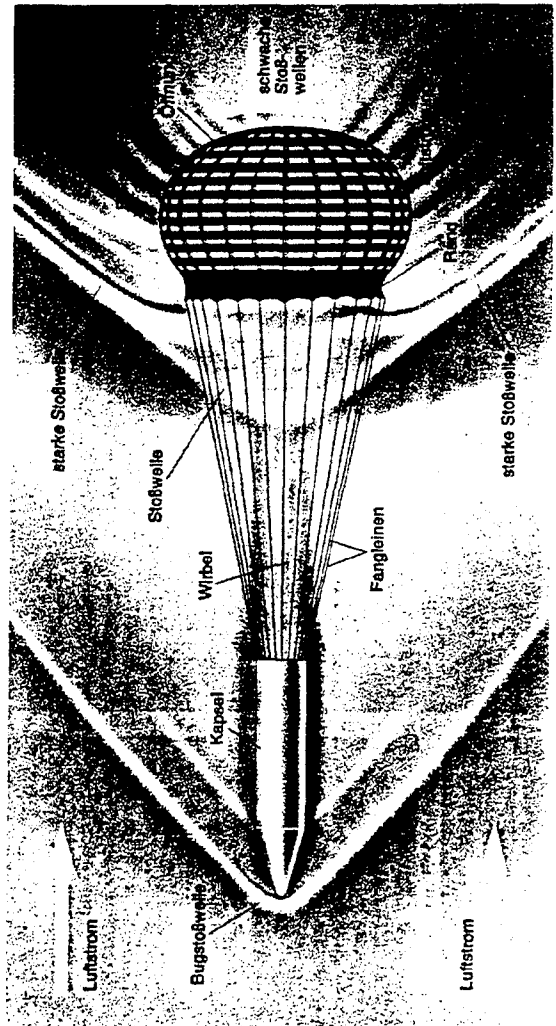
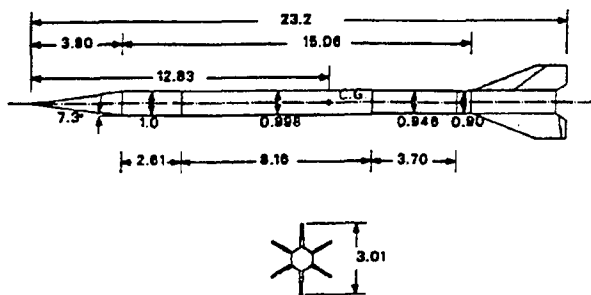


Fig. 13: Ribbon parachute at supersonic speed (Ref. 36).



ALL DIMENSIONS IN CALIBERS (ONE CALIBER = 27.05 mm)

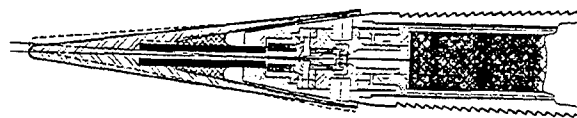
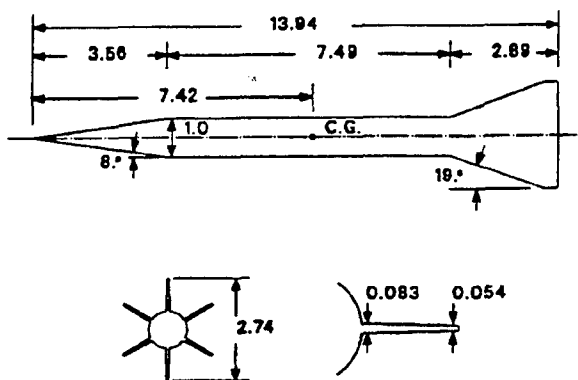


Fig. 16: Bended nose control device (moved by hot gas or electro-/piezo-mechanically) (Ref. 39).



ALL DIMENSIONS IN CALIBERS (ONE CALIBER = 35.2 mm)

Fig. 14: Schematic sketches of hypersonic projectiles M829 (above) and M735 (below) from Ref. 37.

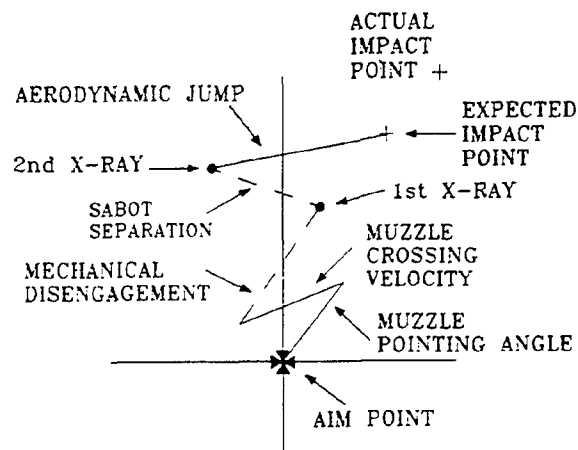


Fig. 17: Vector diagram indicating the closure analysis with sources of disturbance to the projectile trajectory (Ref. 43).

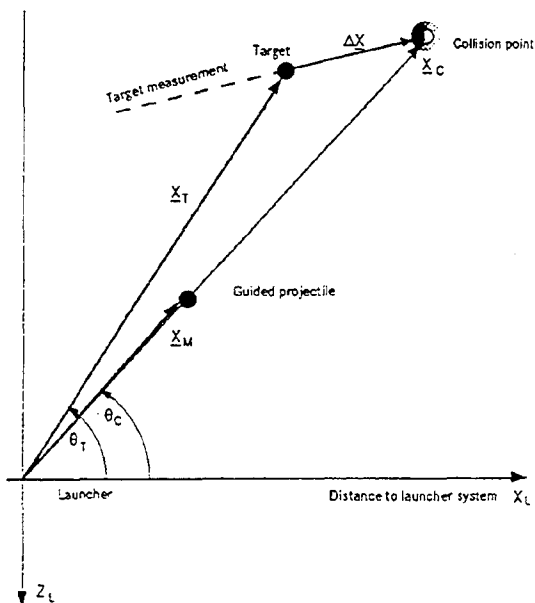


Fig. 15: Principle of collision point oriented line-of-sight guidance (Ref. 39).

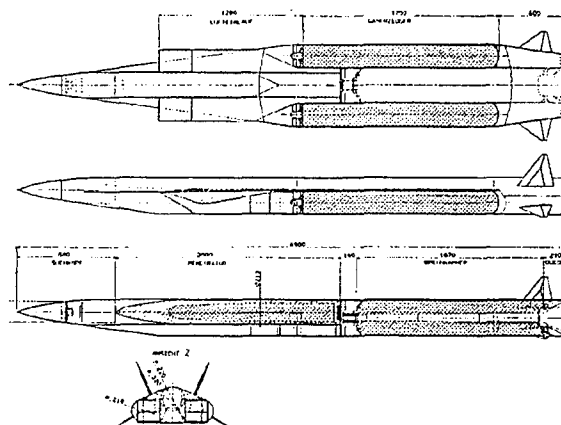


Fig. 18: Sketch of a potential high velocity missile with integrated intakes.

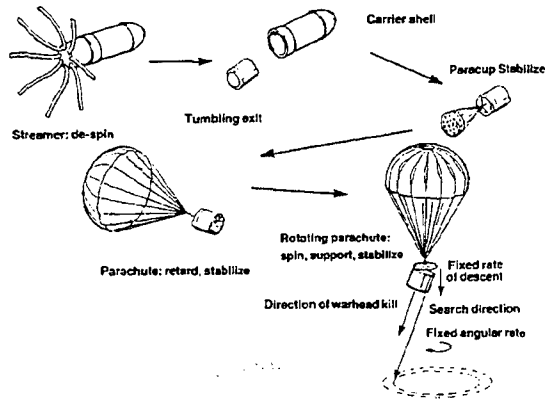


Fig. 19: Retarder applications (Ref. 46).

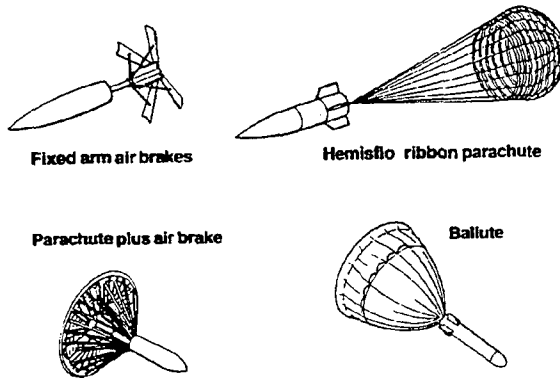


Fig. 20: Retarded Bombs (Ref. 46).

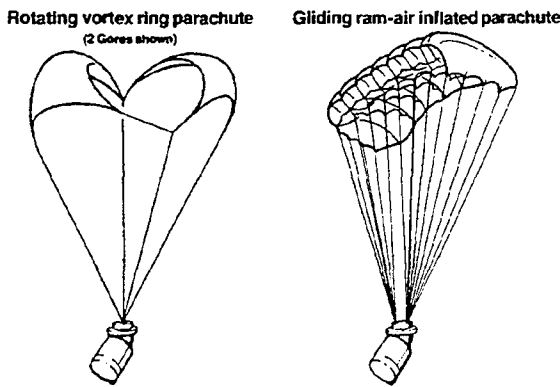


Fig. 21: Rotating and gliding parachutes (Ref. 46).

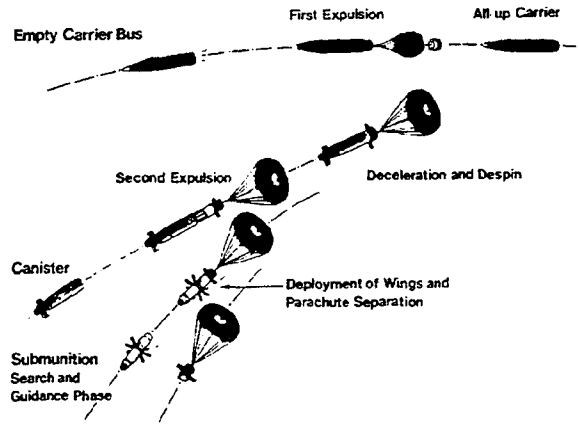


Fig. 22: Overall function of the guided terminal phase of a brilliant ammunition concept (Ref. 47).

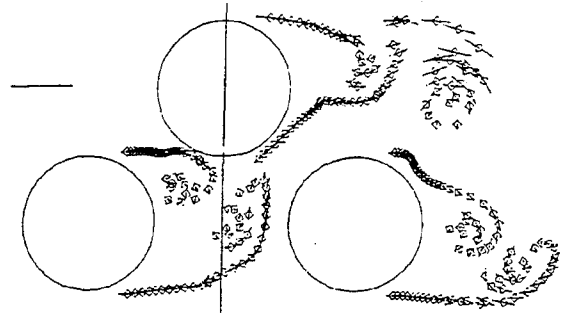


Fig. 23: Dynamics of clouds of finite viscous vortex areas for interacting circular bodies in normal flow (Ref. 50).

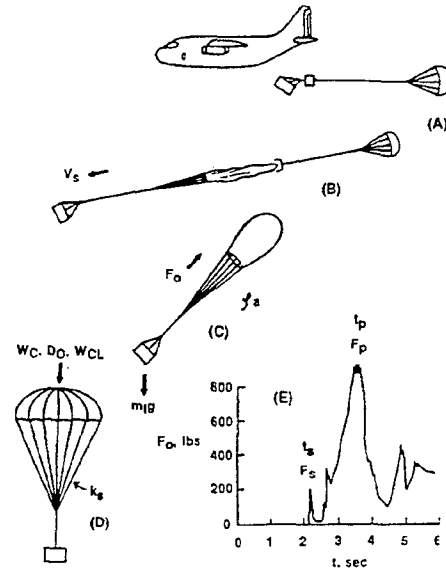


Fig. 24: Schematic sketch of an air-drop operation (A-D) and typical history of parachute opening force (E) (Ref. 54).

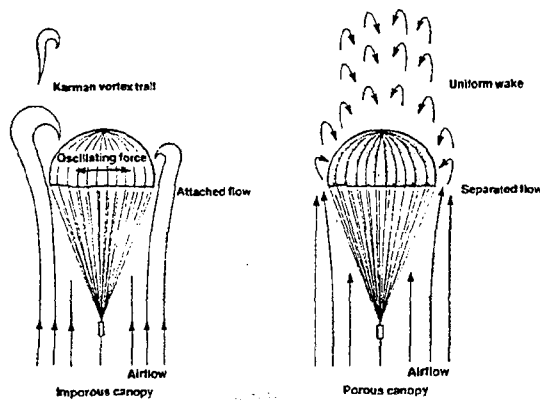


Fig. 25: Porosity effect on canopy stability (Ref. 46).

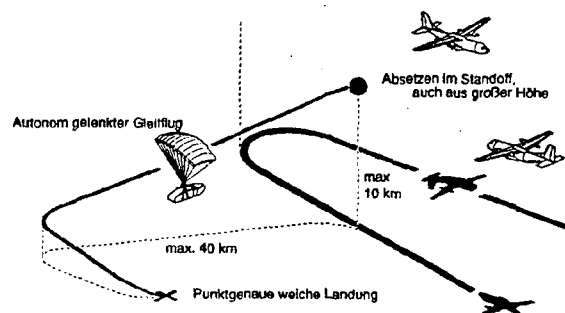


Fig. 28: Delivery concept for a supply glider (Ref. 8).

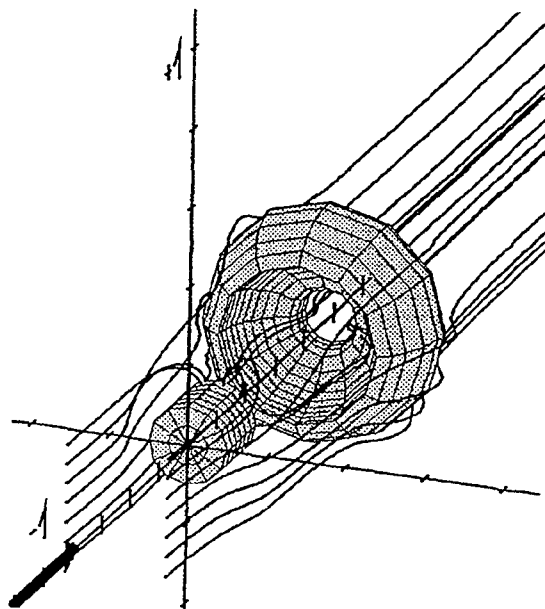


Fig. 26: Load/parachute configuration with interaction of vortical flow separated from both parts (Ref. 58).

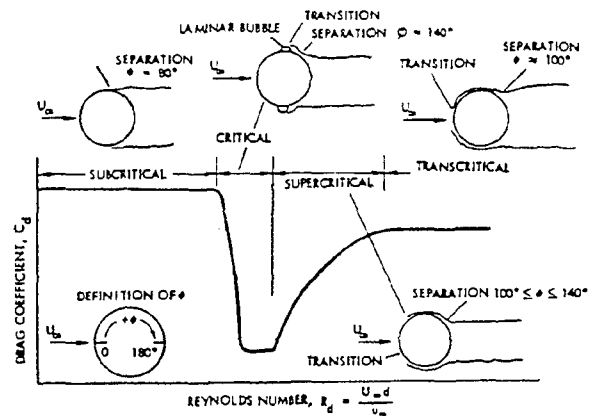


Fig. 29: Separation effects for a body with circular cross section (Ref. 65).

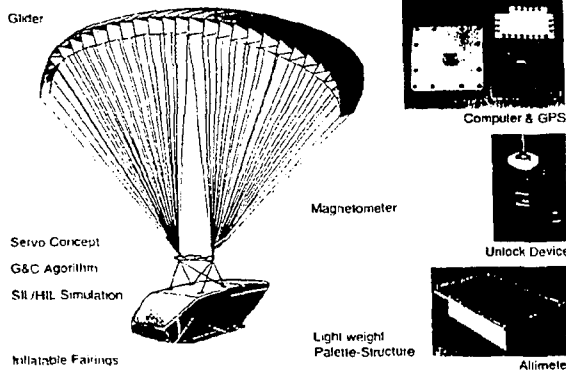


Fig. 27: Components of a supply glider.

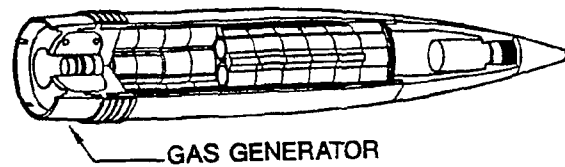


Fig. 30: Schematic sketch of M864 gas generator (Ref. 89).

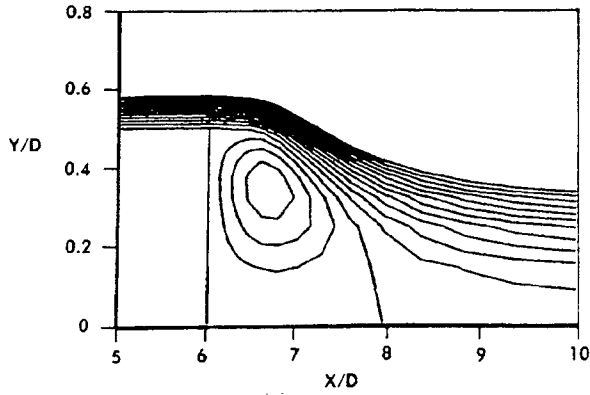


Fig. 31: Stream function contours without base bleed ($I=0$), $Ma=0.9$ (Ref. 90).

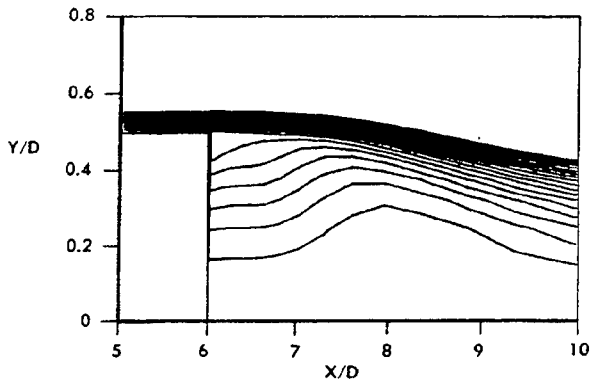


Fig. 32: Stream function contours with base bleed ($I=0.13$), $Ma=0.9$ (Ref. 90).

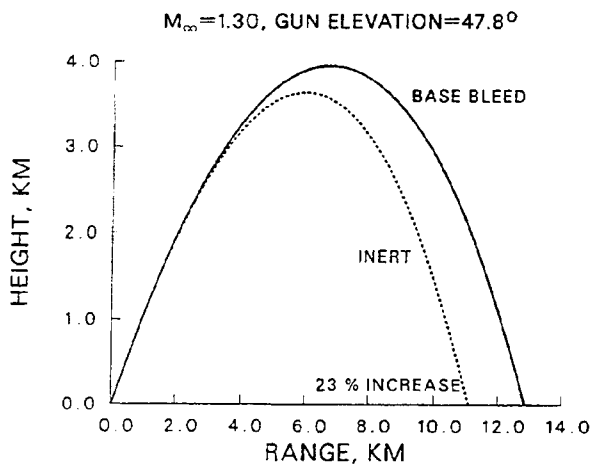


Fig. 33: Predicted M864-L trajectories with and without base bleed (Ref. 89).

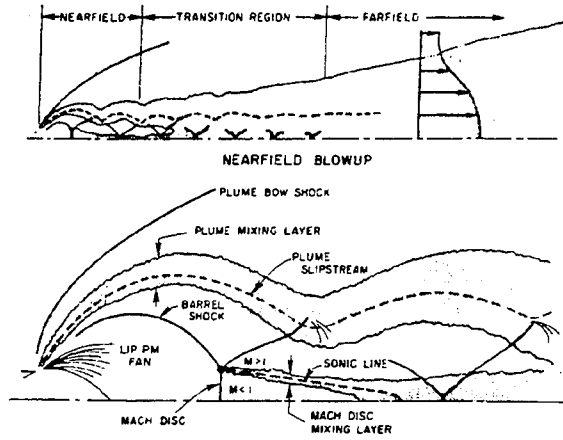


Fig. 34: Schematic sketch of a rocket exhaust plume flowfield (Ref. 96).

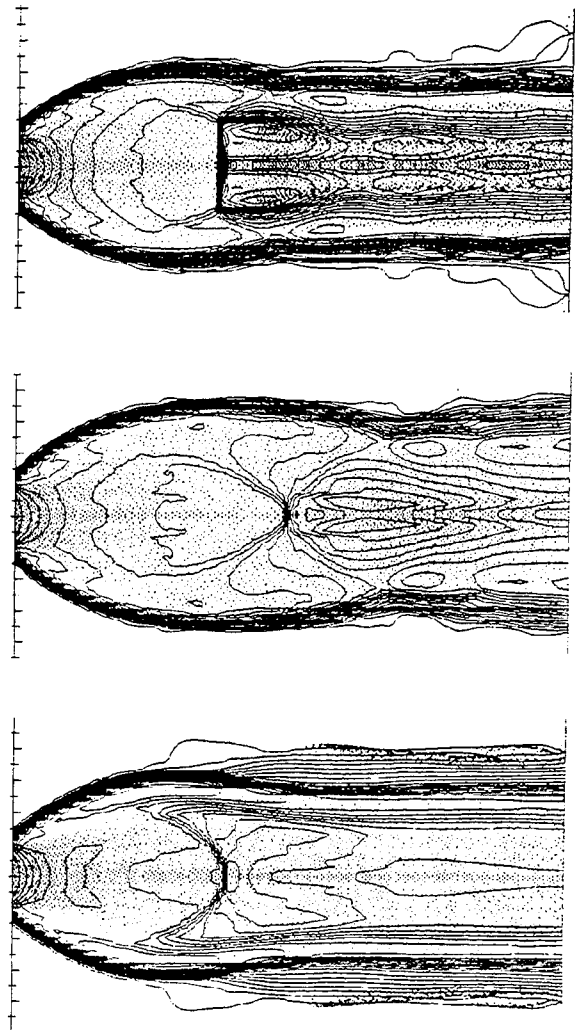


Fig. 35: Free jet structure for different particle parameters, gas velocity contour lines and particles (dots), (Ref. 99).

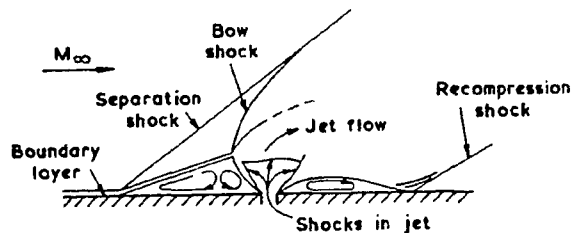


Fig. 36: Typical flow pattern of two-dimensional sonic or supersonic jet in supersonic flow (Ref. 110).

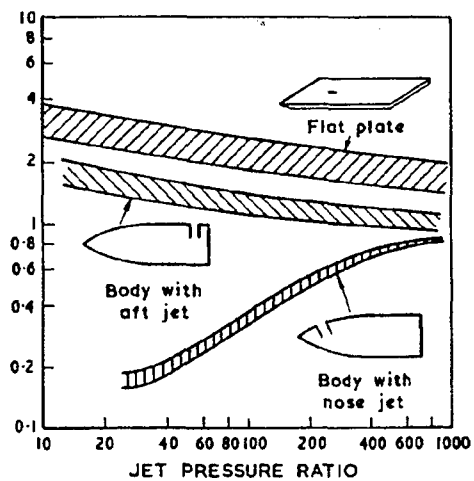


Fig. 37: Jet effectiveness ratio for sonic lateral jets in a supersonic stream, $2.4 < Ma < 4.5$ (Ref. 114).

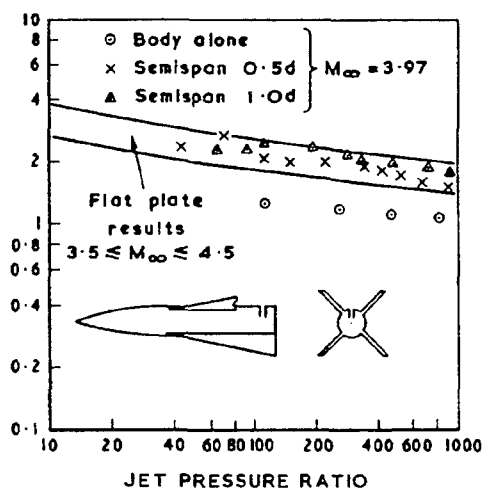


Fig. 38: Effect of adjacent surfaces on the jet effectiveness ratio (Ref. 114).

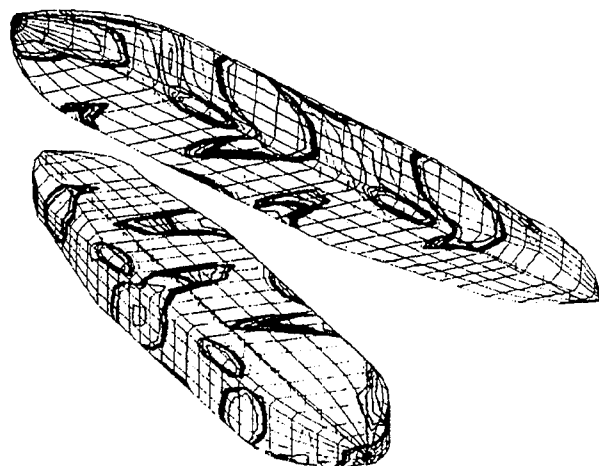


Fig. 39: Pressure distribution induced on a body in axial flow disturbed by a lateral sinusoidal gust.

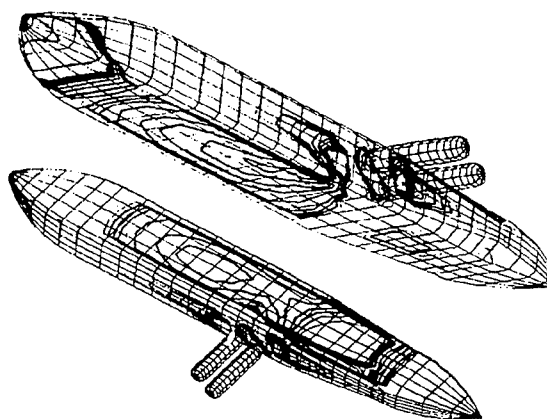


Fig. 40: Interference effects between dispenser and two submunition bodies directly after the ejection; pressure distribution at $Ma=0.546$, $\alpha=5^\circ$, panel method.

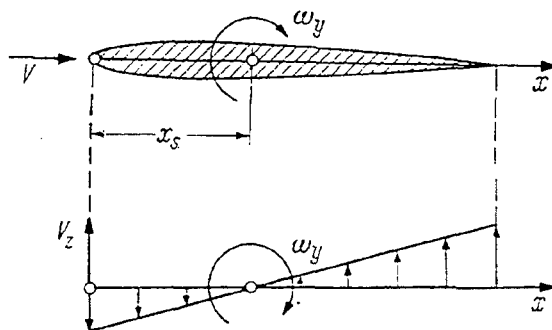


Fig. 41: Distribution of the additional flow on a wing induced by the pitching motion (Ref. 115).

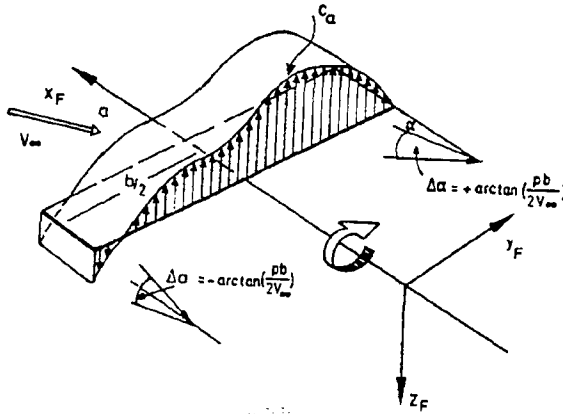


Fig. 42: Roll-rate induced wing lift distribution C_a (Ref. 116).

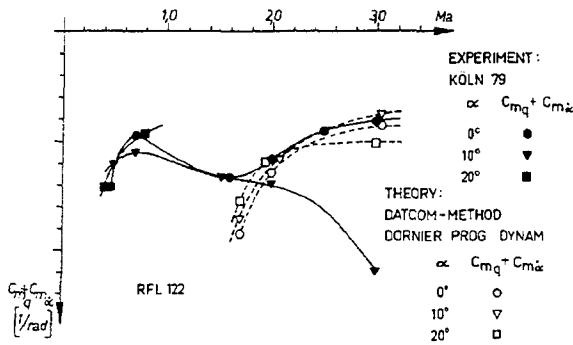


Fig. 43: Pitching moment results $C_{mq} + C_{m\dot{\alpha}}$ of a wing-body-tail configuration with free oscillation tests at the DFVLR Cologne (Ref. 116).

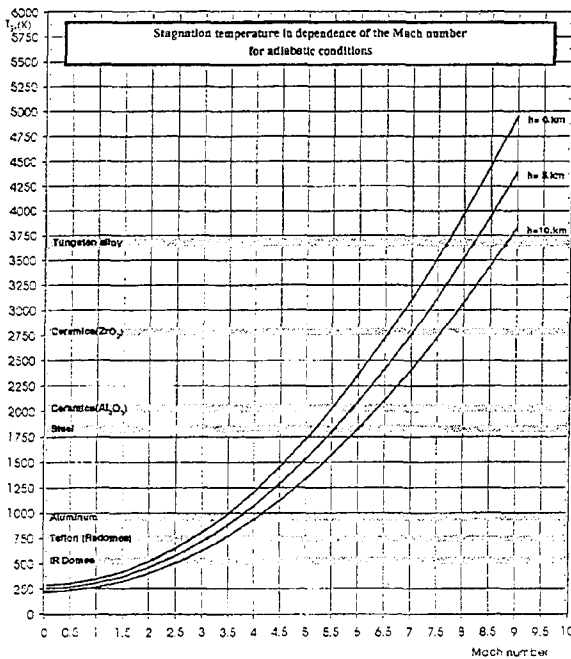


Fig. 44: Stagnation temperature in dependence of Mach number and altitude.

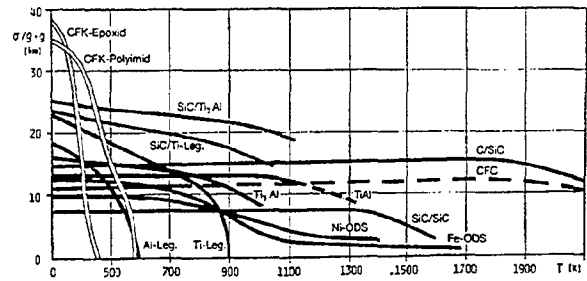


Fig. 45: Materials and the temperature dependence of their specific tensile strengths (Ref. 126).

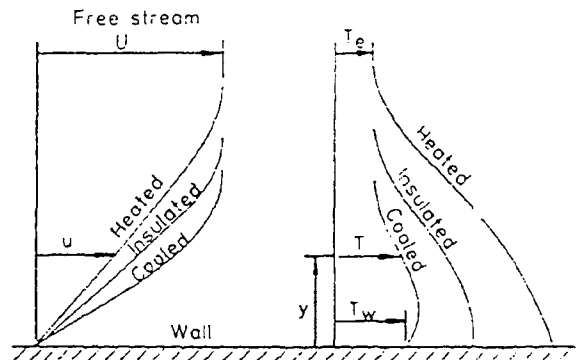


Fig. 46: Schematic sketch of velocity and temperature boundary layer in a compressible viscous flow (Ref. 128).

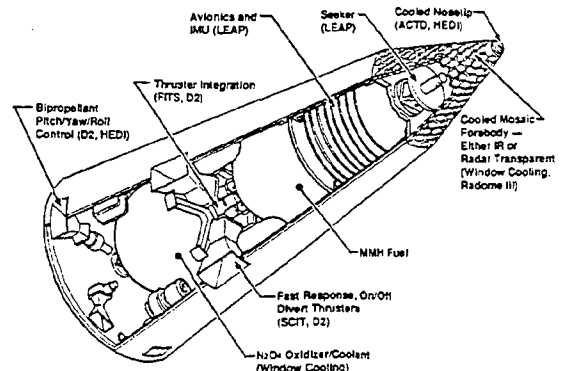


Fig. 47: Hypersonic interceptor with a mosaic window (Ref. 133).

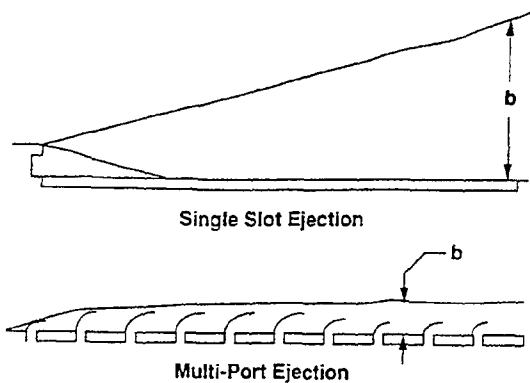


Fig. 48: Single slot and mosaic mixing thickness (Ref. 133).

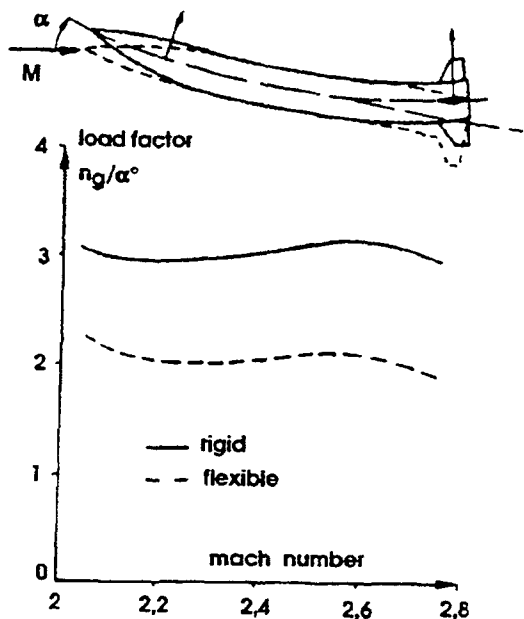


Fig. 49: Effect of missile flexibility on the manoeuvrability (Ref. 4).

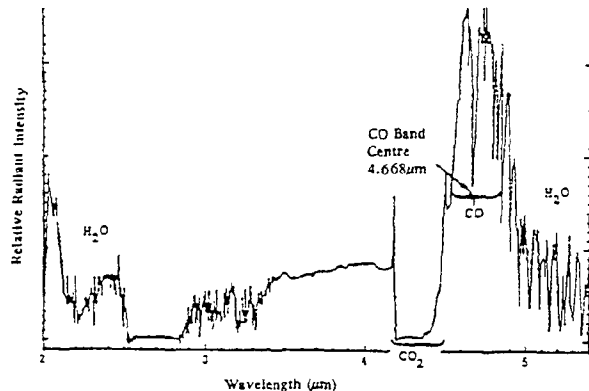


Fig. 50: Typical infrared emission of a missile plume (Ref. 148).

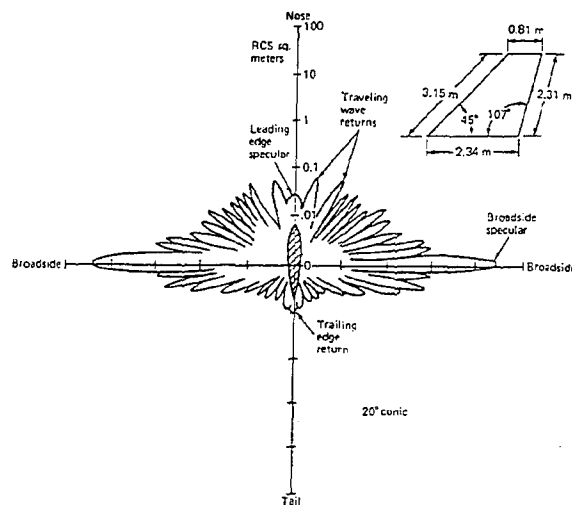


Fig. 51: RCS characteristics of a vertical tail (Ref. 158).

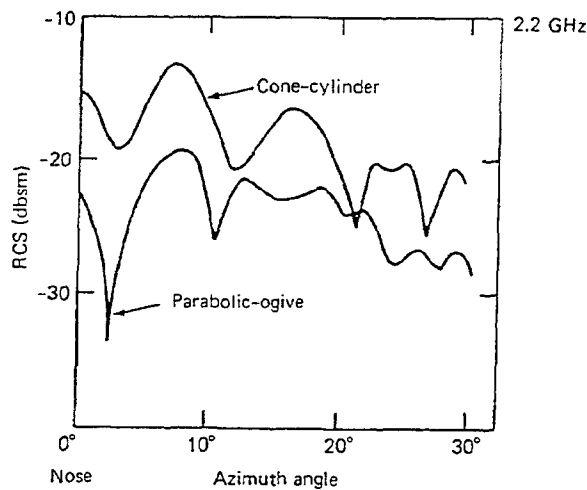


Fig. 52: RCS characteristics of different forebody shapes (Ref. 158).

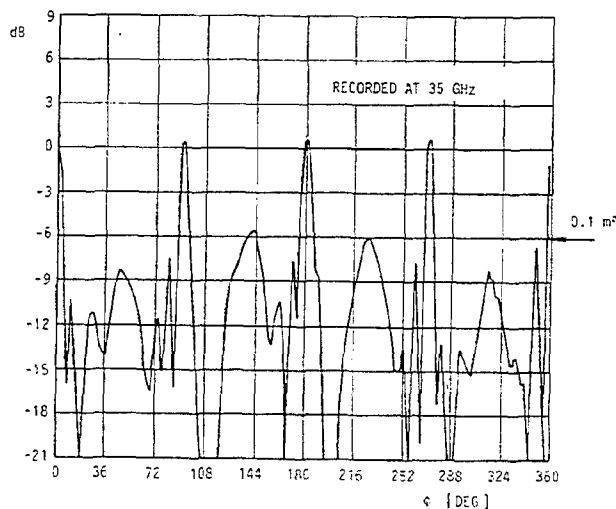


Fig. 53: Radar cross section of a cruciform configuration versus roll angle (Ref. 158).

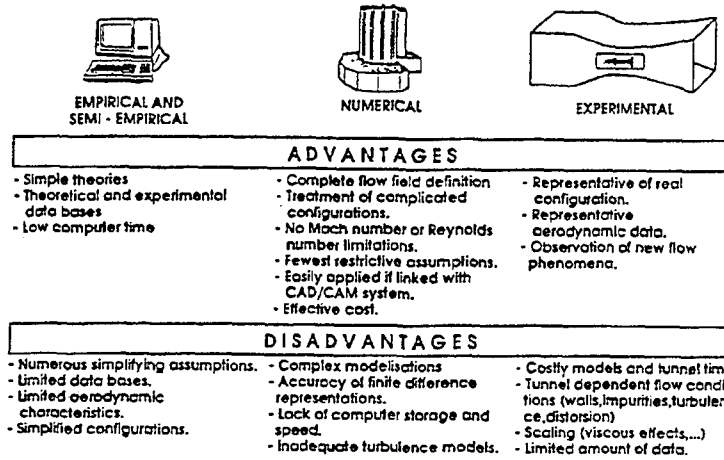


Fig. 54: Comparison of different tools for aerodynamic predictions.

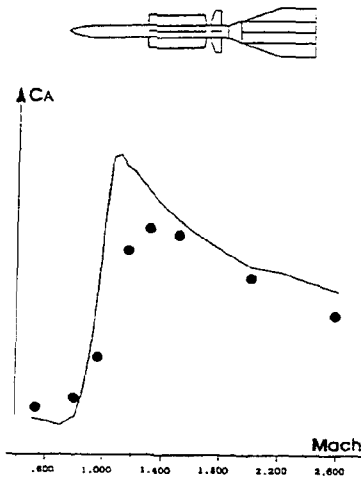


Fig. 55: Drag prediction for a complex missile.

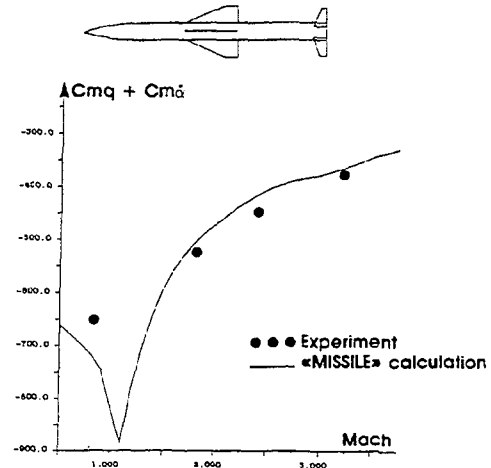


Fig. 56: Prediction of pitch damping coefficient.

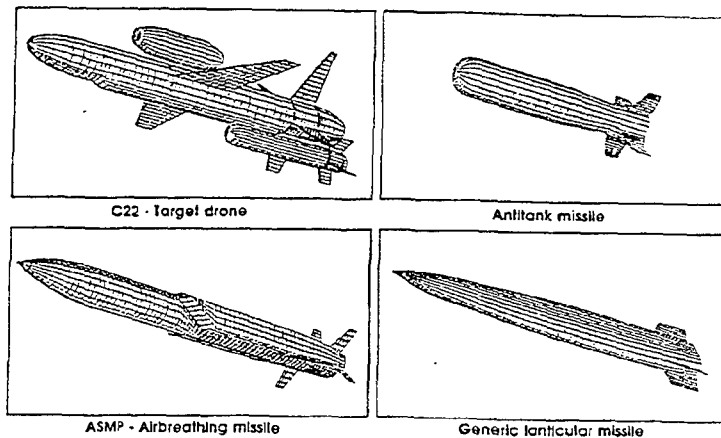


Fig. 57: Panelling for complex configurations.

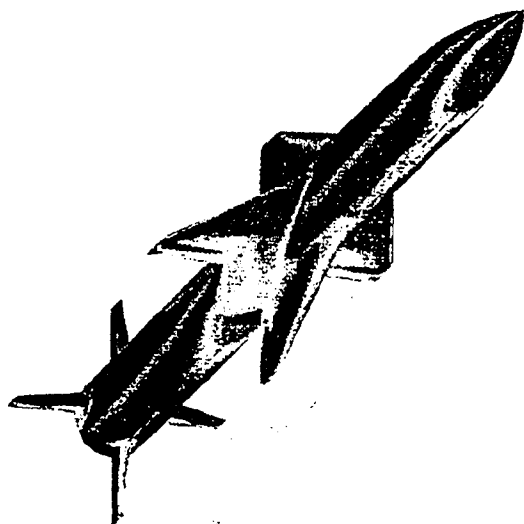


Fig. 58: Surface pressure distribution on a wing-body-tail configuration at $Ma=2$, $\alpha=20^\circ$; Euler solution with FLU3C.

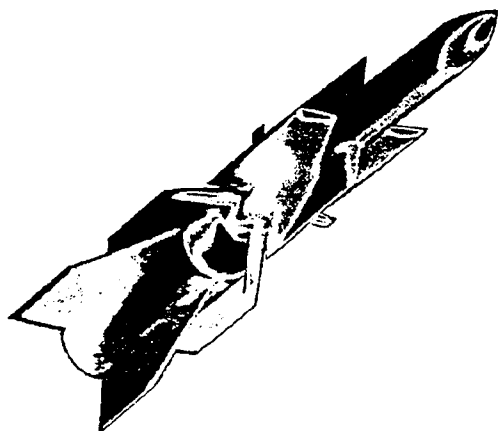


Fig. 59: Surface pressure distribution on ASTER 15; Euler solution with FLU3C.

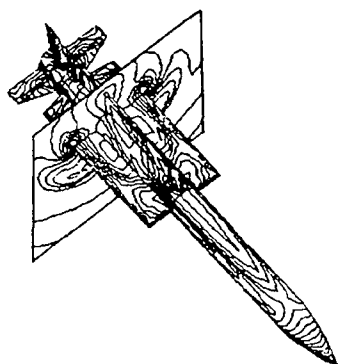


Fig. 60: Isobars for ASTER at $Ma=2.5$, $\alpha=10^\circ$; Euler solution with FLU3C.

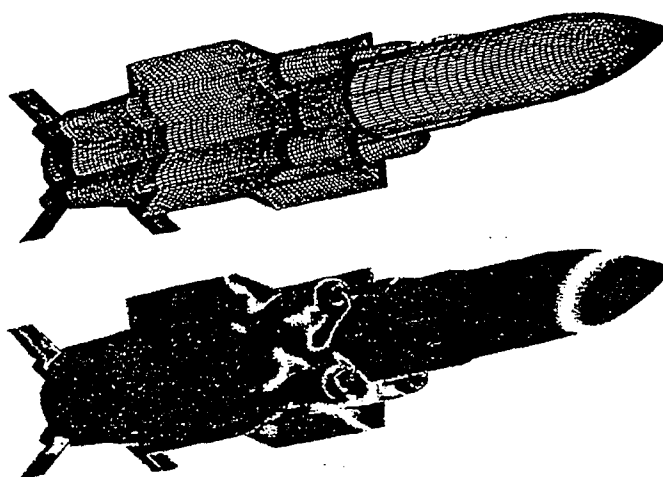


Fig. 62: Mesh and surface pressure distribution for ANS missile at $Ma=2$, $\alpha=4^\circ$; Euler solution with FLU3C.

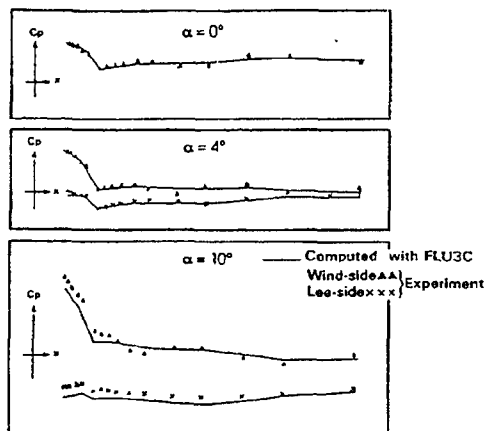
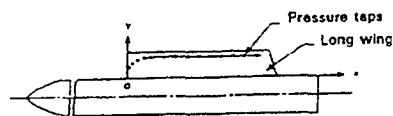


Fig. 61: Comparison of experimental and Euler FLU3C surface pressures on a long wing (ASTER) at $Ma=2.5$.

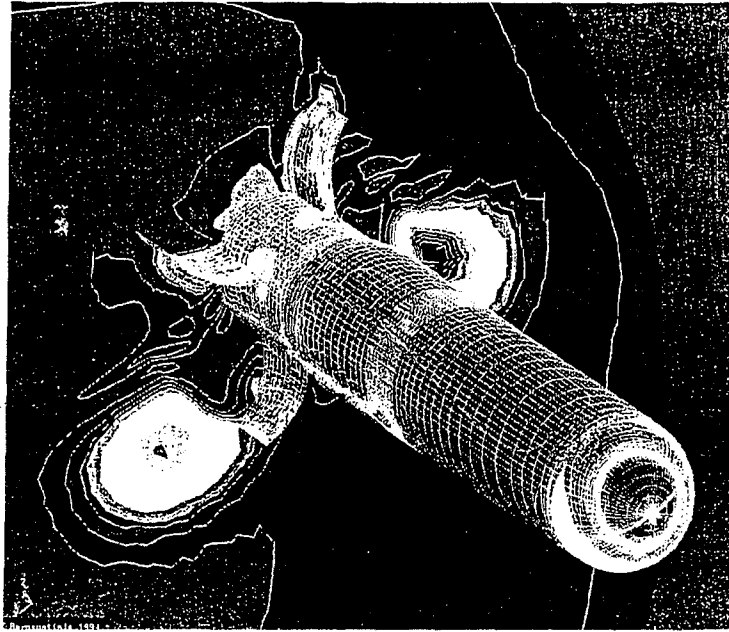


Fig. 63: Mach number distribution for a spinning anti-tank missile with lateral jets at $Ma=0.3$, $\alpha=0^\circ$; Euler solution with SESAME.

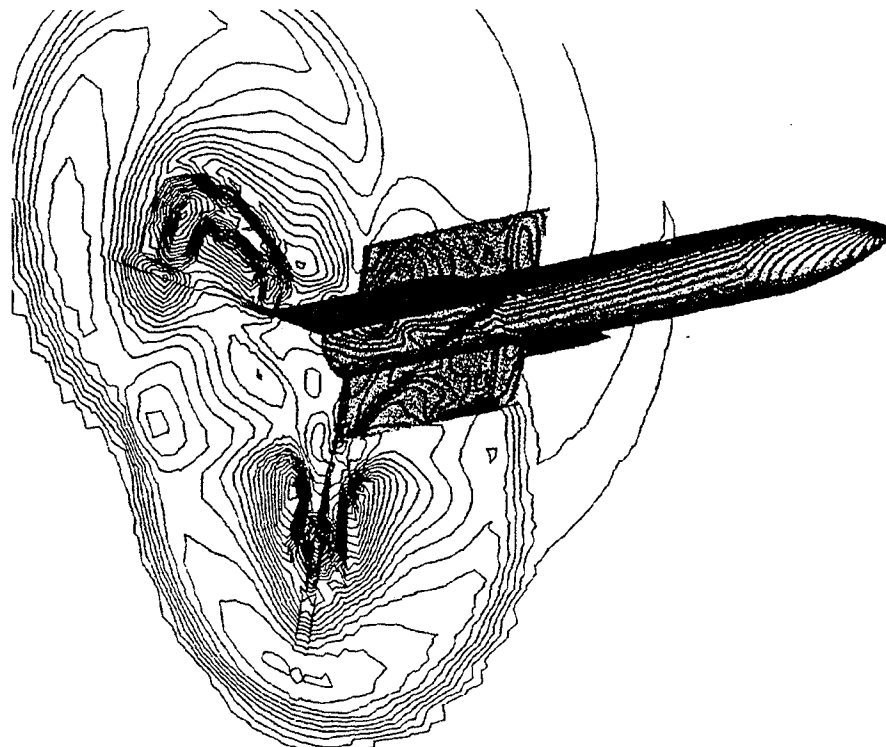


Fig. 64: ASTER with two lateral jets; Mach number contours in a transverse plane downstream the injection at $Ma=3$, $\alpha=10^\circ$; Euler solution with FLU3M.

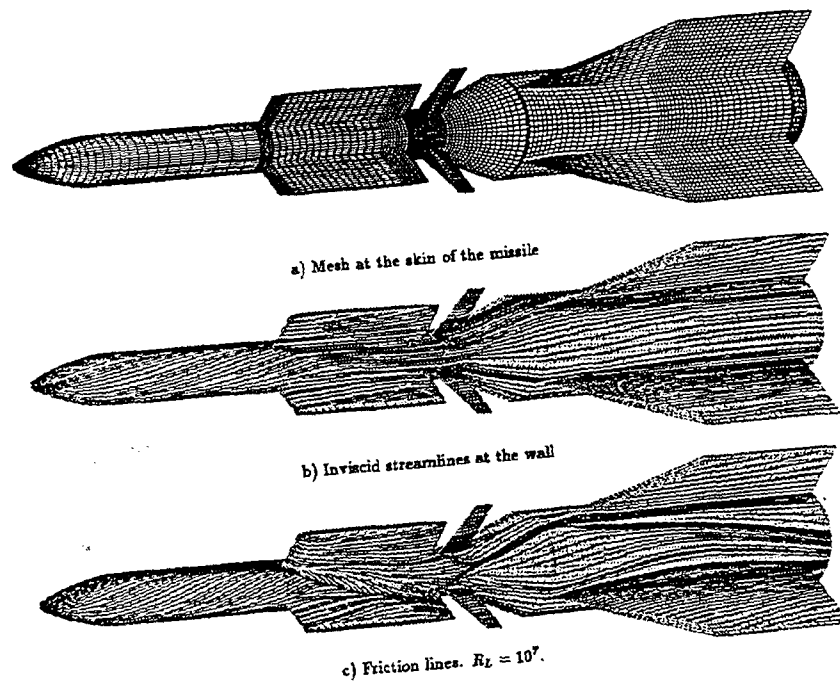


Fig. 65: Euler and boundary layer solutions for ASTER 15 at $Ma=4.5$, $\alpha=5^\circ$ (Ref. 184).

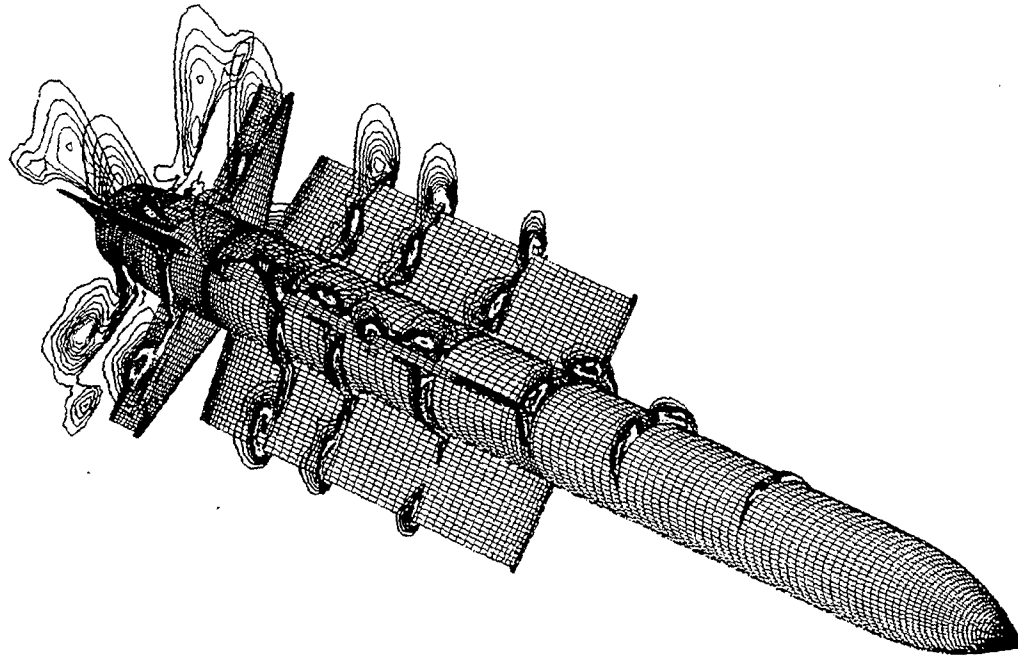


Fig. 66: Mach number contours of ASTER at $Ma=3$, $\alpha=10^\circ$, $Re_D=8.6 \cdot 10^5$; TLNS solution.

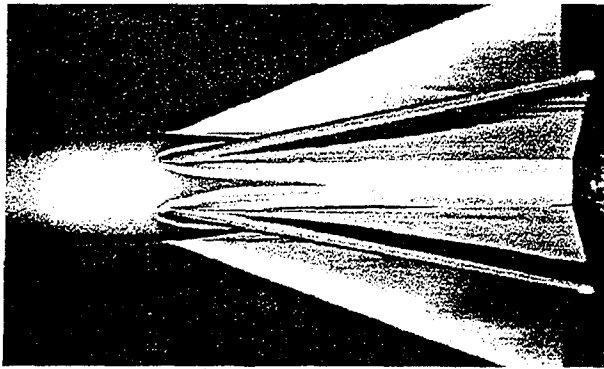


Fig. 67: Afterbody and fins of a KE projectile (pressure side) with liquid crystals at $Ma=3$, $\alpha=4^\circ$ (Ref. 201).

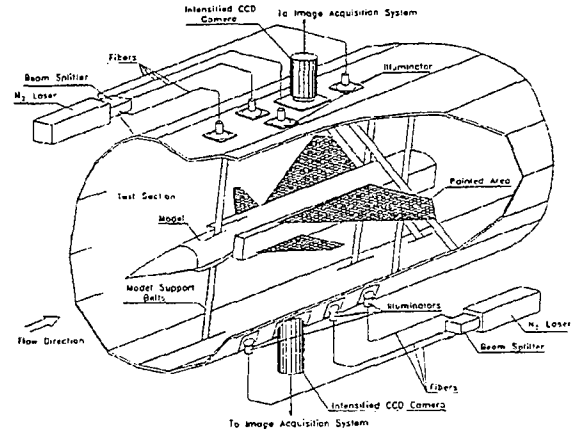


Fig. 68: Sketch of a general layout of OPMS in a wind tunnel (Ref. 203).

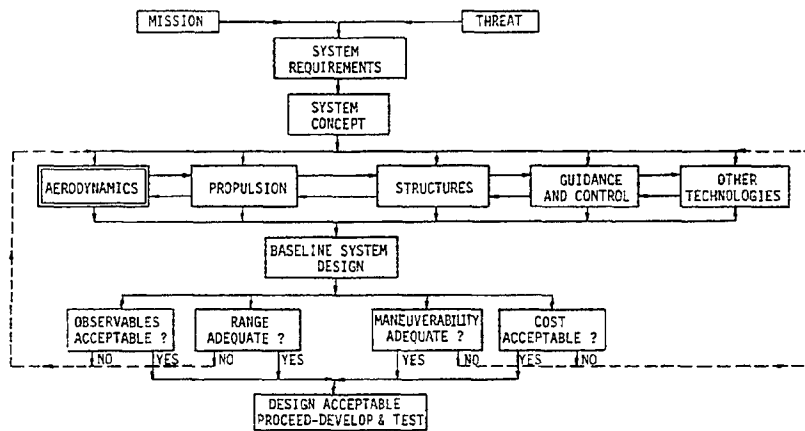


Fig. 69: Sketch of the iterative design cycle for missiles (Ref. 2).

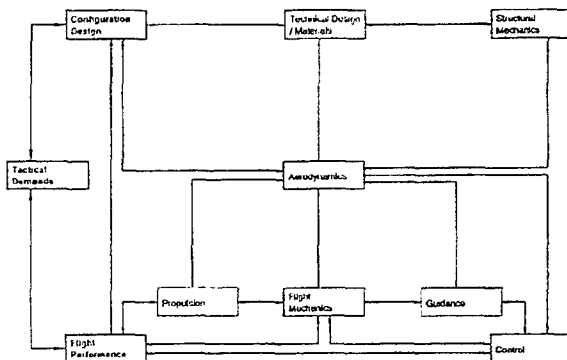


Fig. 70: Sketch of interactions of technology areas in the design of conventional missiles.

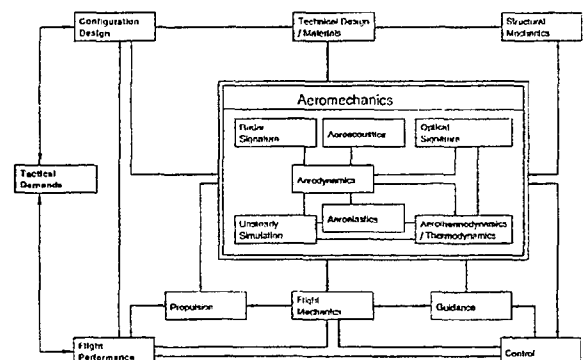


Fig. 71: Sketch of interactions of technology areas in the design of modern missiles.

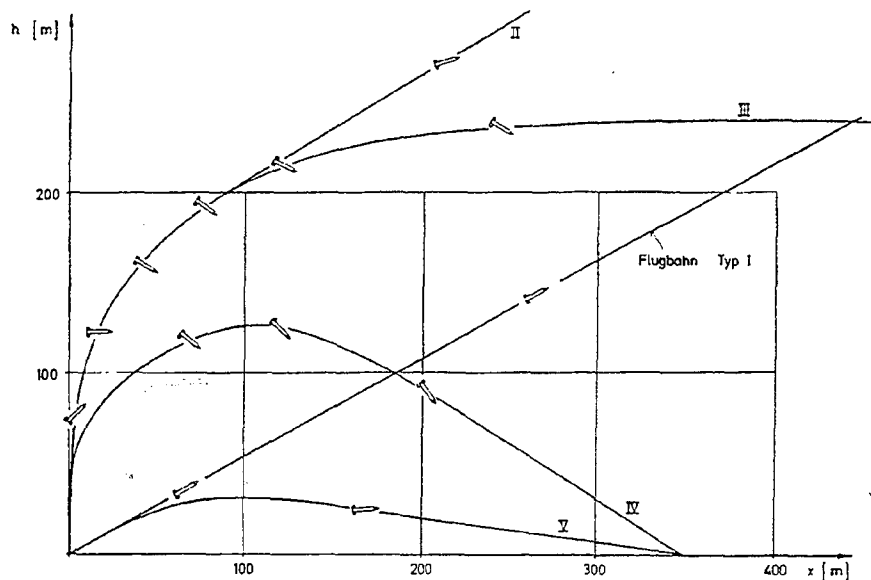


Fig. 72: Typical trajectories of missiles with vertical or nearly vertical launch.

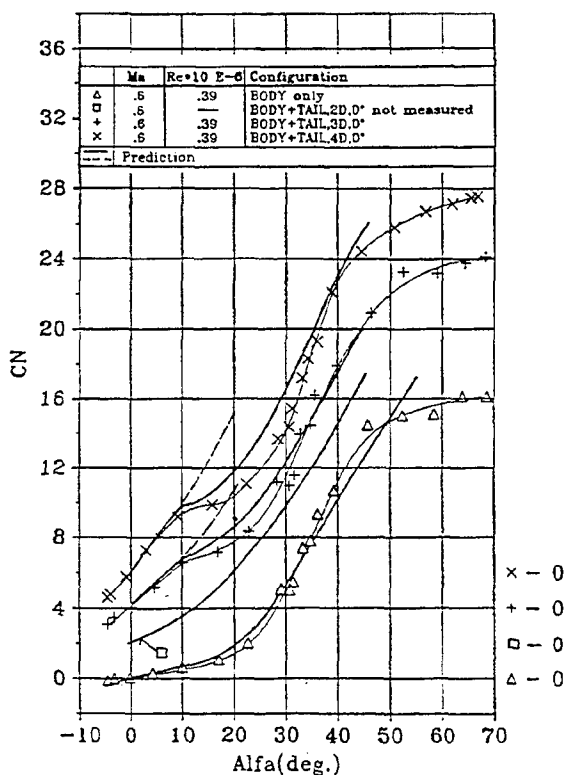


Fig. 73: Normal force coefficient versus angle of attack. All lifting surfaces in + position. Calculations with (—) and without (---) corrections beyond α_{crit} (Ref. 220).

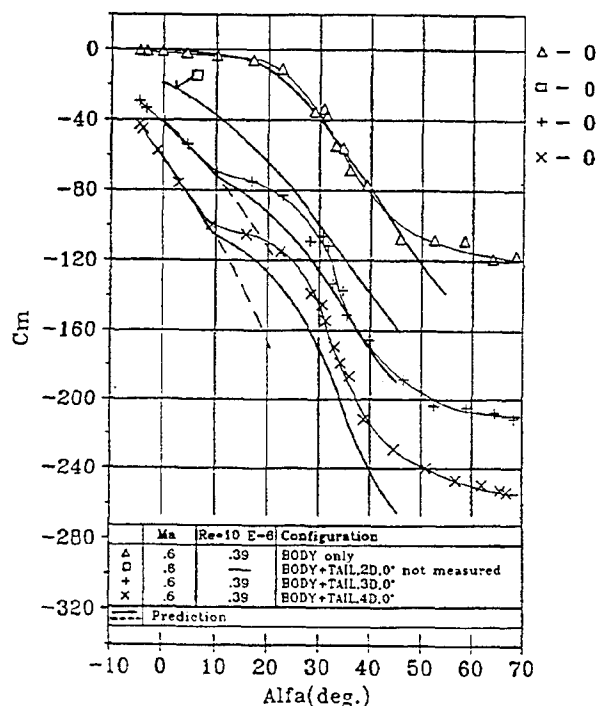


Fig. 74: Pitching moment coefficient versus angle of attack. All lifting surfaces in + position. Calculations with (—) and without (---) corrections beyond α_{crit} (Ref. 220).

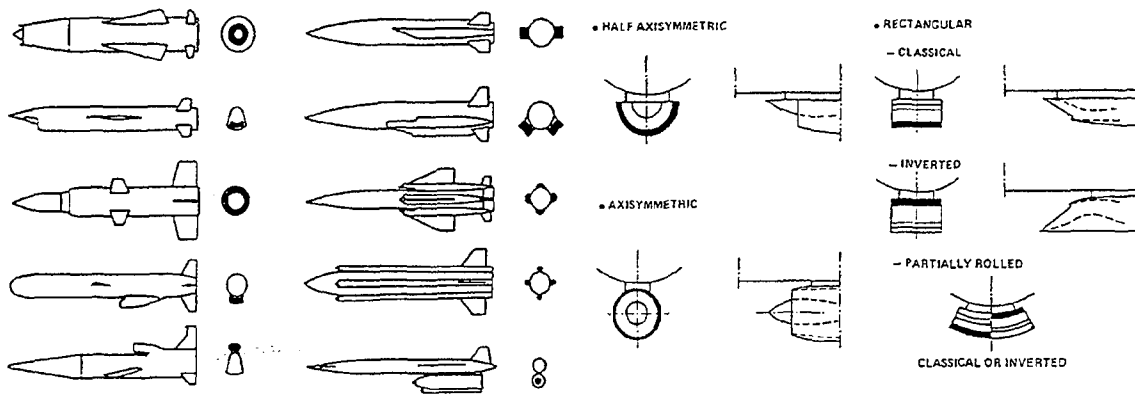


Fig. 75: Sketch of missiles with different types of intake positions (Ref. 4).

Fig. 76: Sketch of different types of ventral intakes (Ref. 4).

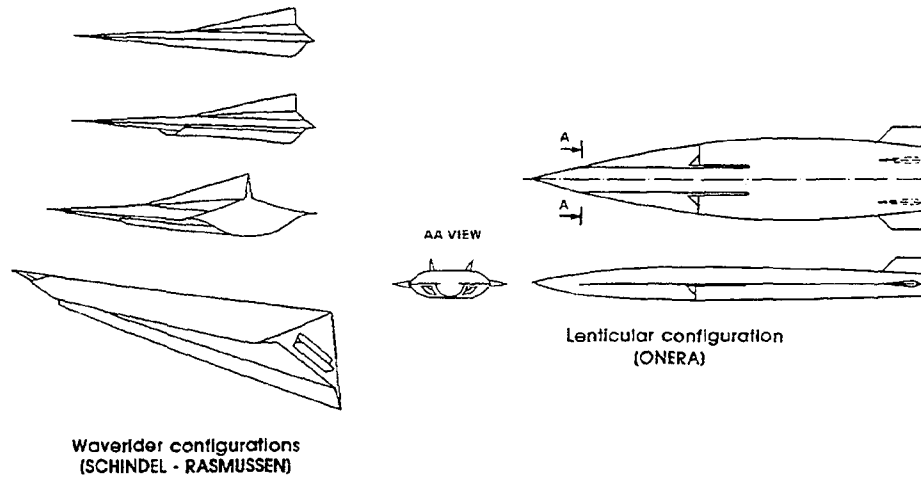


Fig. 77: Configurations with non-circular cross-section: Waverider (Refs. 29, 231 and 232) and lenticular (ONERA) configurations.

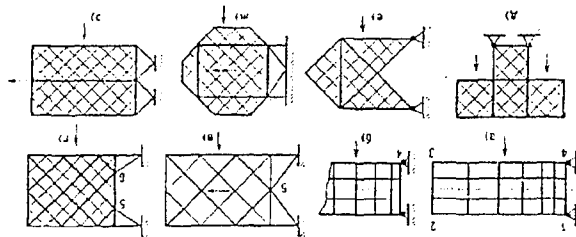


Fig. 78: Sketches of different types of grid wings (Ref. 233).

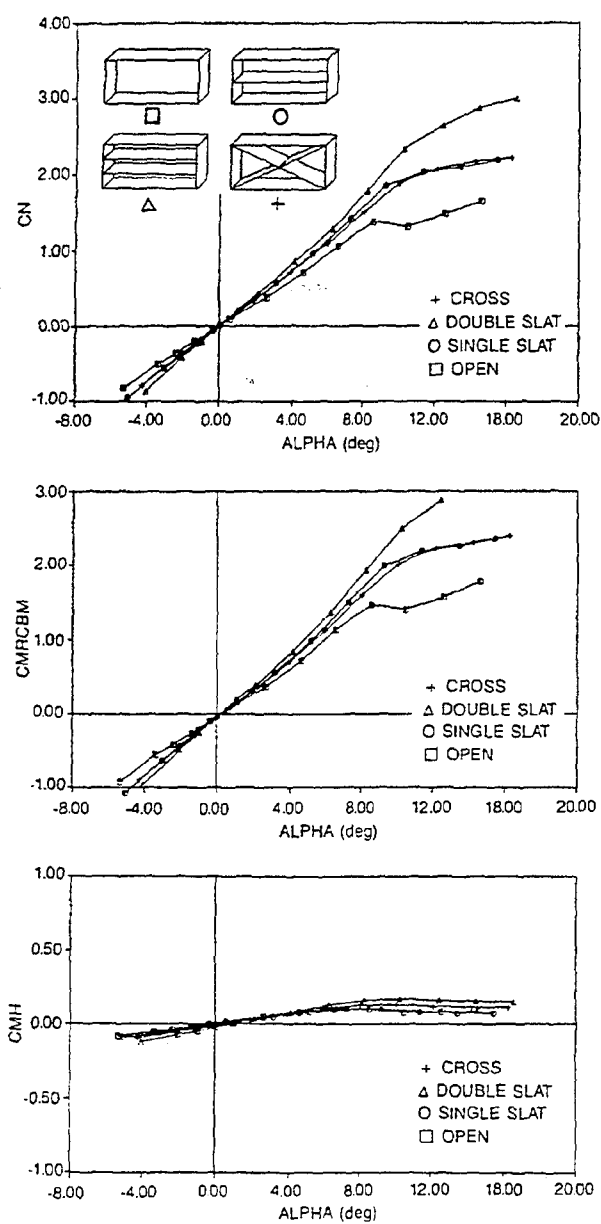


Fig. 79: Grid-fin aerodynamic coefficients versus angle of attack for the four 7.62x15.24-cm fins (CN = normal force, CMRCBM = chordwise bending moment at root, and CMH = hinge moment) (Ref. 234).

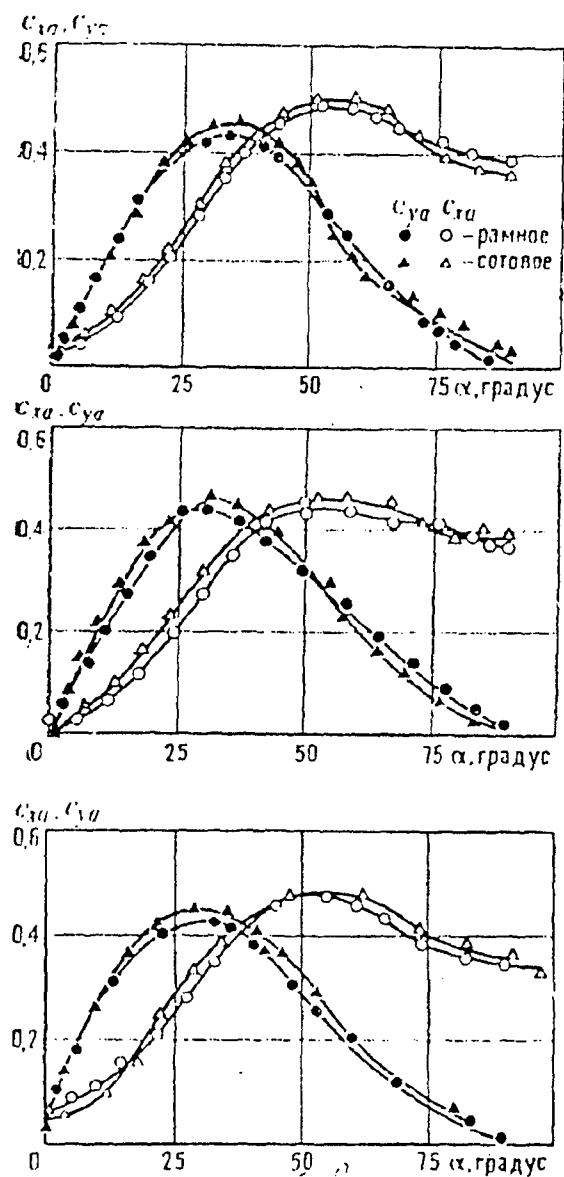


Fig. 80: Experimental C_Z and C_X characteristics versus angle of attack of two grid wings (frame and comb) at Mach numbers 1.85, 2.5, and 3.5 (Ref. 233).

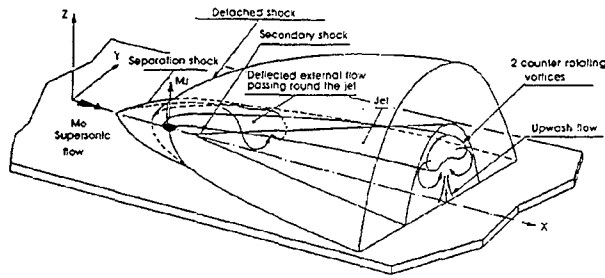


Fig. 81: 3D sketch of a lateral jet in an external supersonic flowfield (Ref. 4).



Fig. 82: Schlieren visualization of lateral jet control: Local and downstream interactions of jet and external flow (Ref. 4).

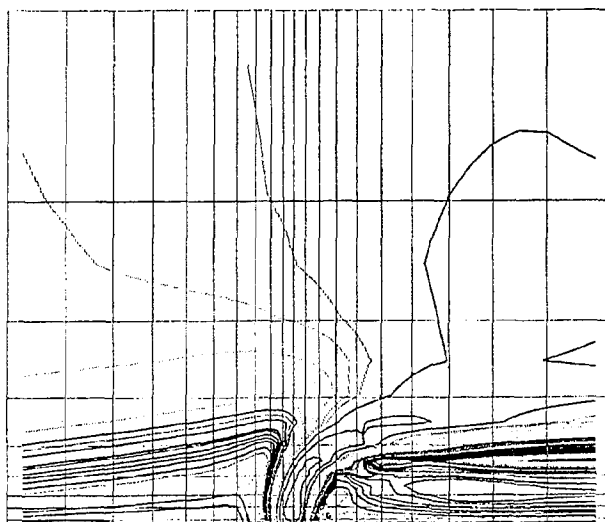


Fig. 83: Lateral jet in an external subsonic flow; local interactions (Ref. 240).

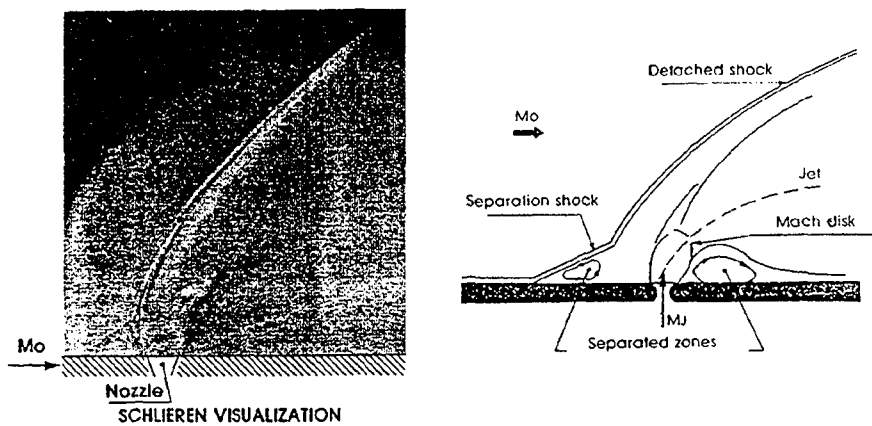


Fig. 84: Lateral jet in an external supersonic flow; local interactions (Ref. 4).

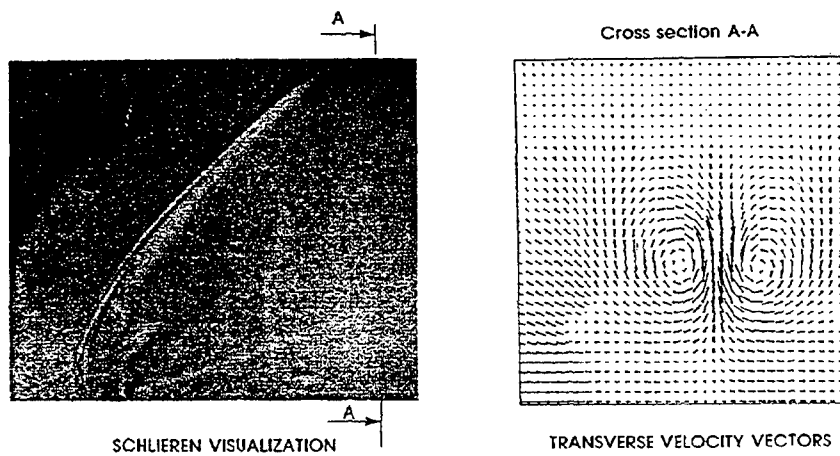


Fig. 85: Lateral jet in an external supersonic flow; downstream interactions (Ref. 4).

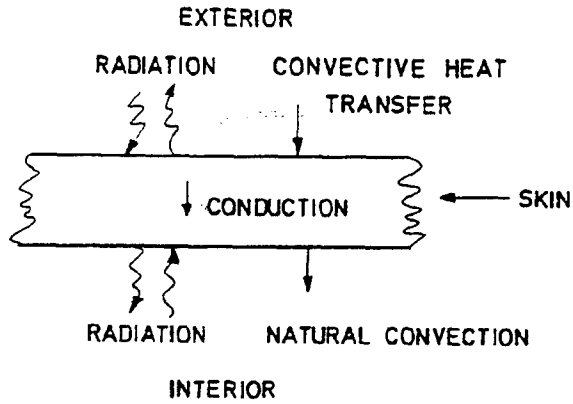


Fig. 86: Sketch of the contributions to the skin heat transfer (Ref. 125).

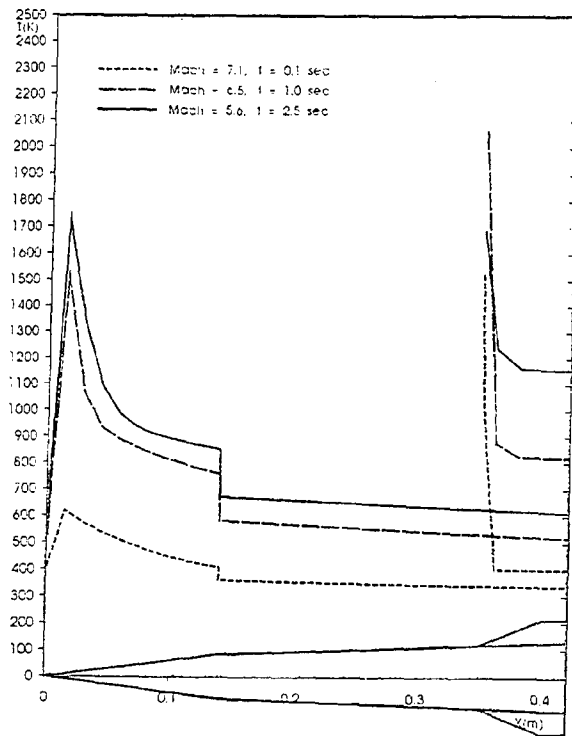


Fig. 87: Surface temperature for an hypersonic projectile along its trajectory (Ref. 246).

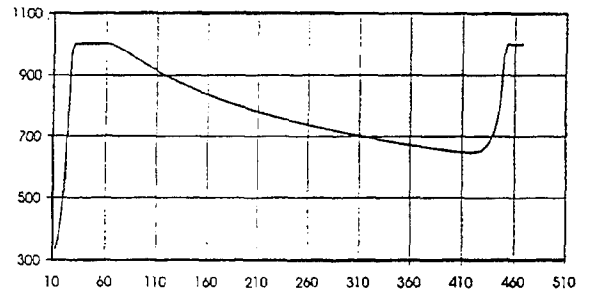
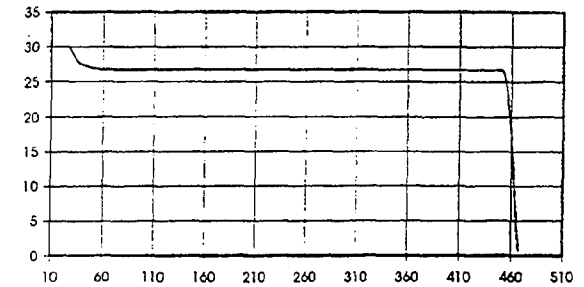
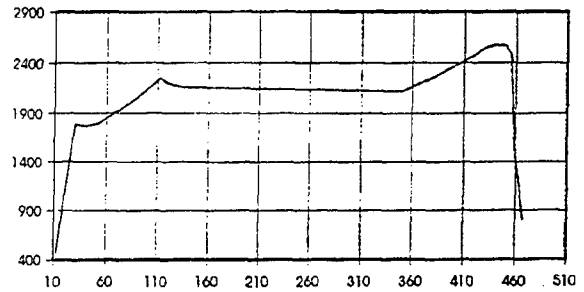
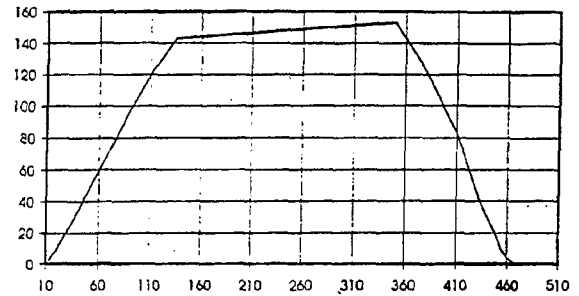
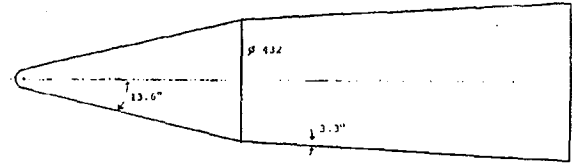


Fig. 88: Re-entry vehicle with sublimating surface material: Geometry, altitude, velocity, thickness of the ablative coating, surface temperature (Ref. 246).

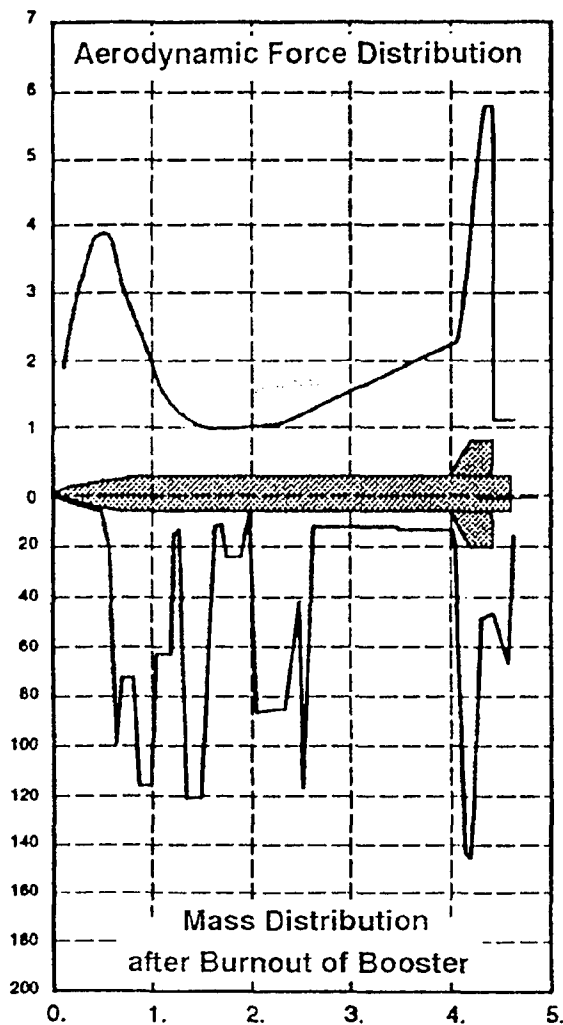


Fig. 89: Load distribution on a missile body for lateral acceleration.

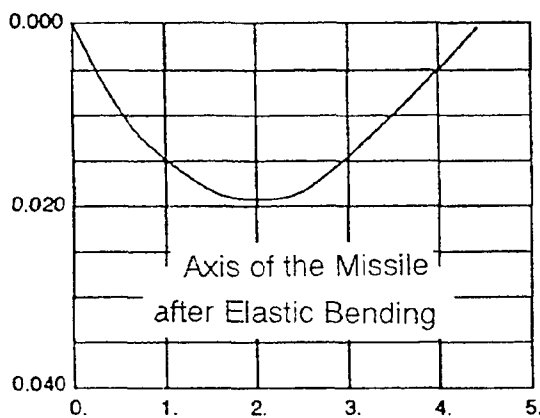


Fig. 90: Static deformation of the missile body.

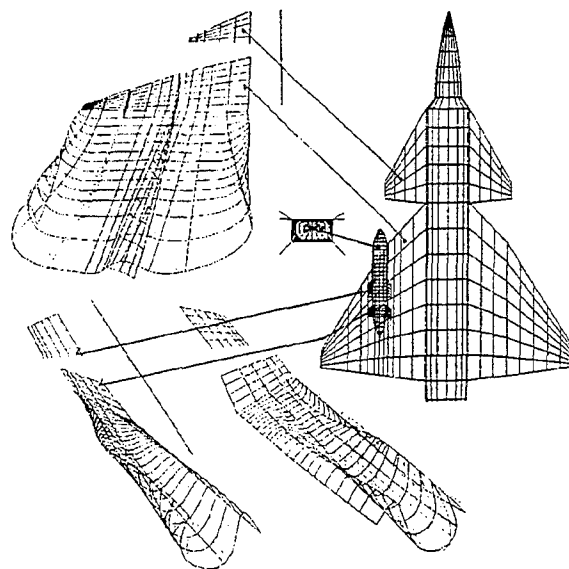


Fig. 91: Simulation of a dispenser (DWS) carried under the wing of an airplane (Viggen).

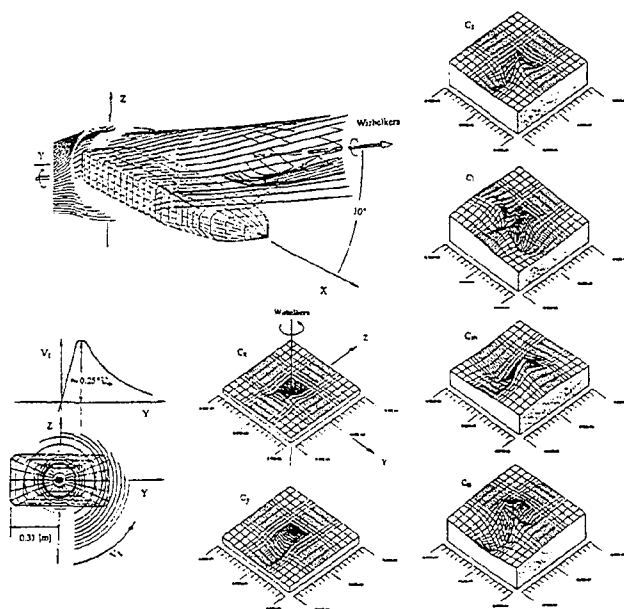


Fig. 92: Dispenser in a vortical flowfield of comparable diameter to the cross section. Aerodynamic coefficients C_x , C_y , C_z , C_l , C_m , C_n are shown in dependence of y and z coordinates (Ref. 253).

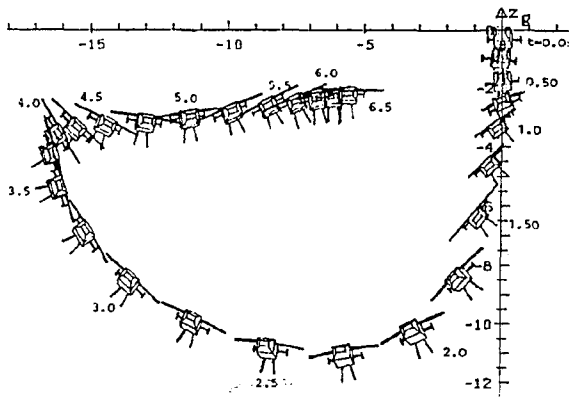


Fig. 93: Separation trajectory in y-z plane of a dispenser with movable wings for $t=0.0$ to 6.5 sec.

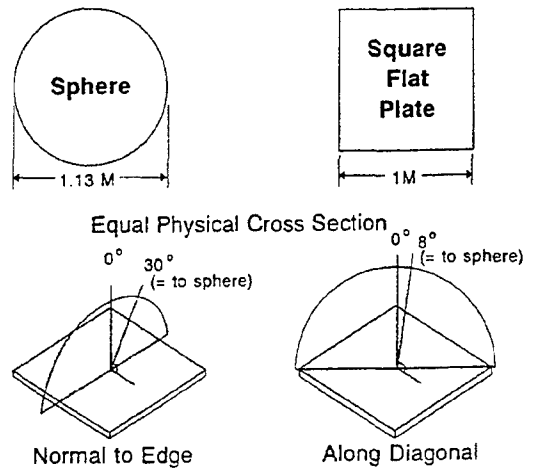


Fig. 96: RCS of a square plate in comparison to a sphere (Ref. 155).

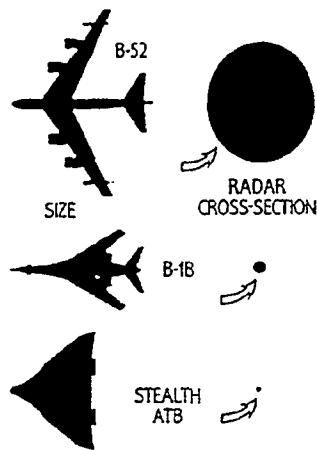


Fig. 94: Radar cross sections of three US aircraft (Ref. 4).

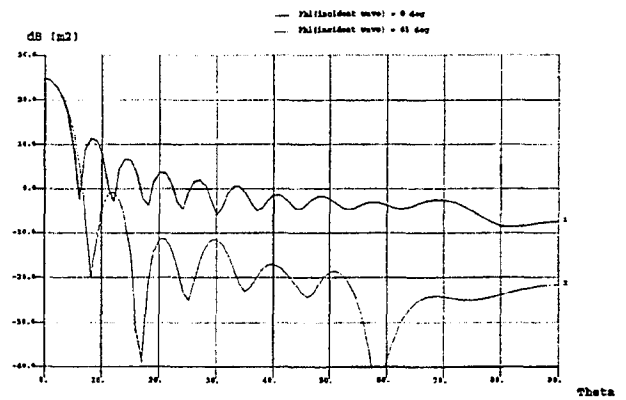


Fig. 97: RCS of a plate with dimension $5\lambda \times 5\lambda$, $\phi\phi$ -polarization.

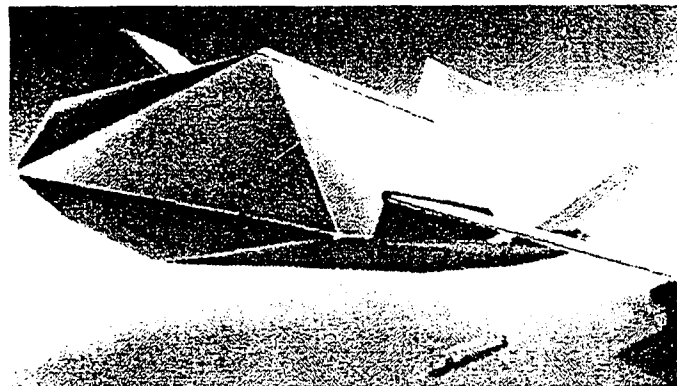


Fig. 95: Low Observable Configuration, Texas Instruments concept (artist's view).

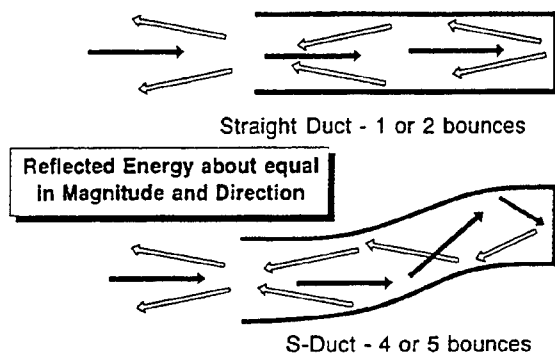


Fig. 98: Energy return from ducts (Ref. 155).

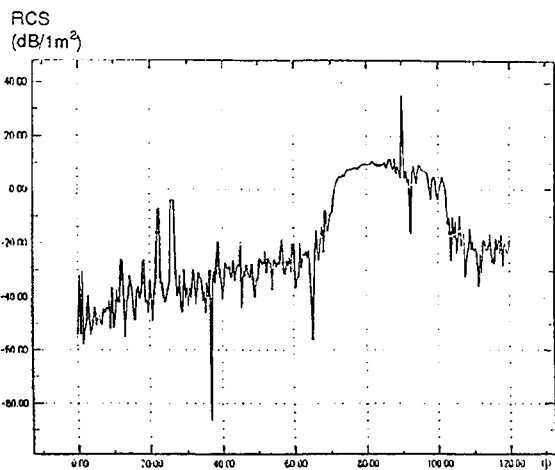
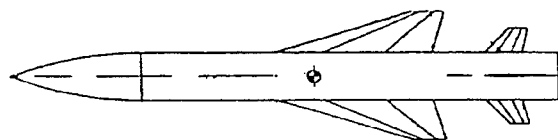


Fig. 99: RCS of a typical missile configuration at 10 GHz, aspect angle $\theta = 0^\circ$ (Ref. 265).

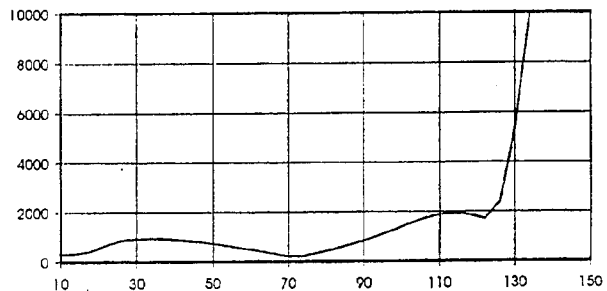
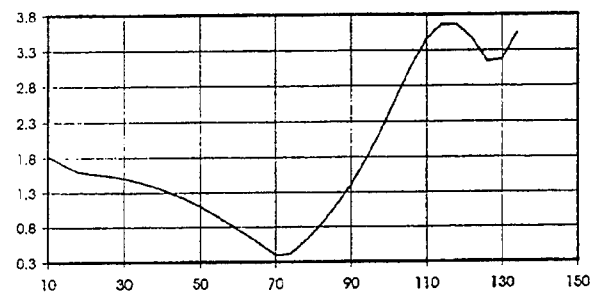
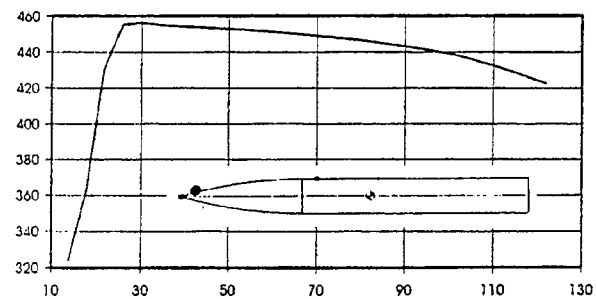
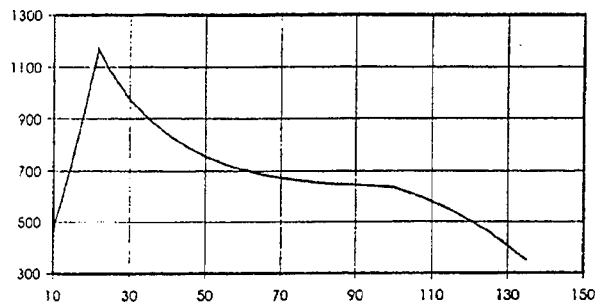


Fig. 100: Optical signature of a generic missile along its trajectory; velocity, representative temperature, visible surface, radiation intensity (Ref. 246).

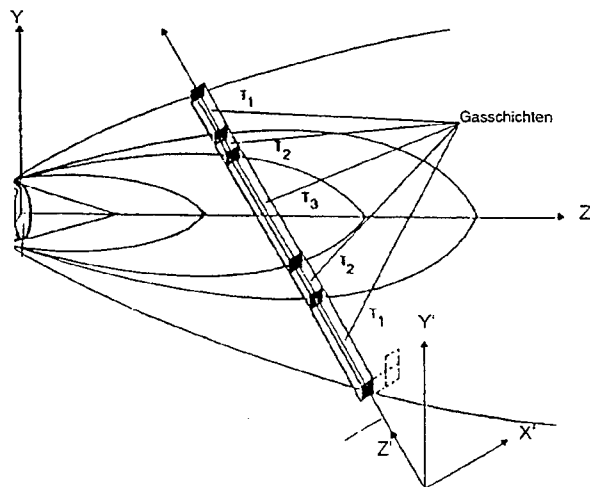


Fig. 101: Sketch of the optical depth method for a smokeless plume.

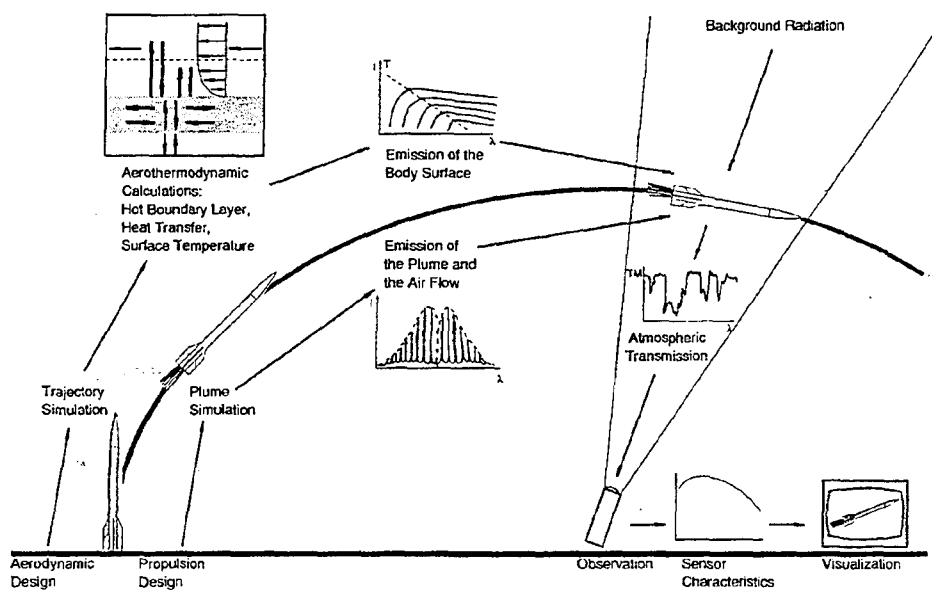


Fig. 102: Sketch of the full scenario for the signature simulation of a TBM.

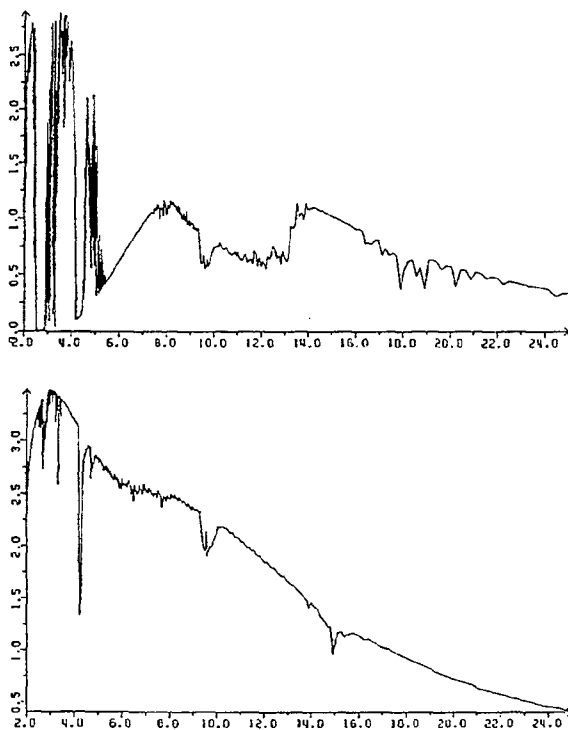


Fig. 103: Spectral signature of a re-entry vehicle (without plume) at 36 km altitude for an observer at 0 km altitude, 36 km distance, 180° aspect angle (above), and for an observer at 40 km altitude, 37 km distance and 180° aspect angle (Ref. 268).

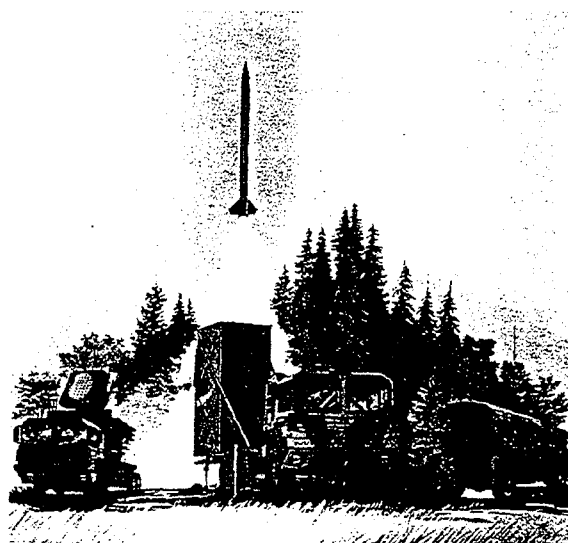


Fig. 104: TLVS missile at vertical launch.

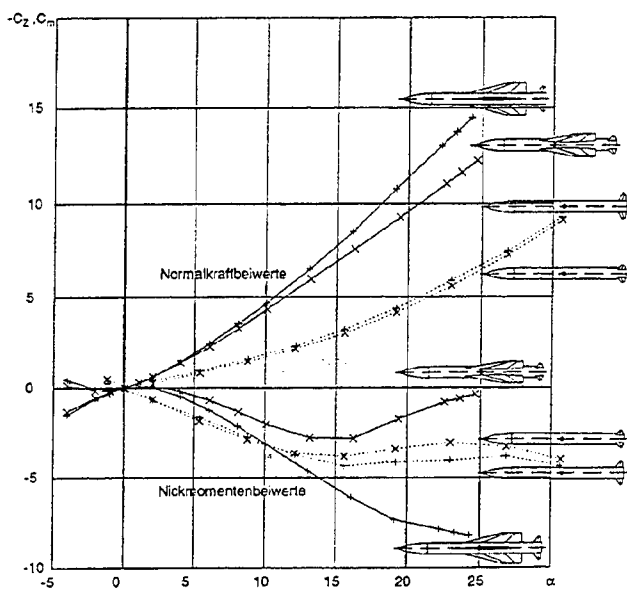


Fig. 105: Normal forces and pitching moments for missiles with and without wings for + and x roll positions at $Ma=1.5$; semiempirical method.

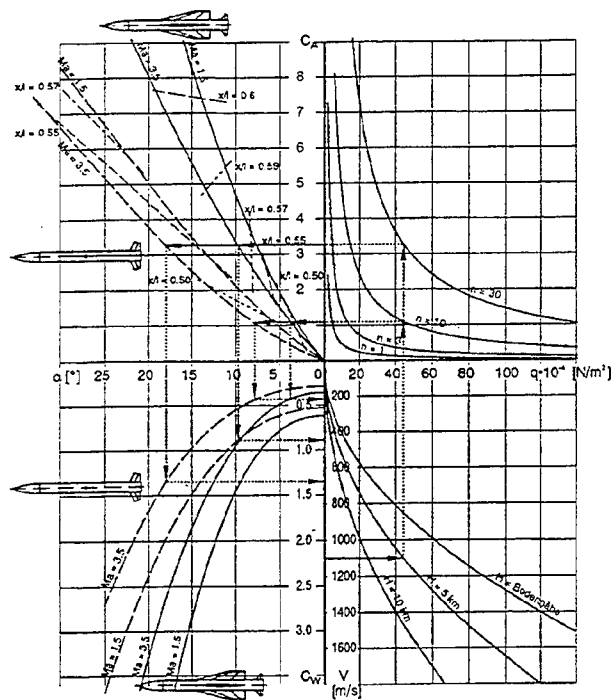


Fig. 106: Mission diagram for a missile with and without wings.

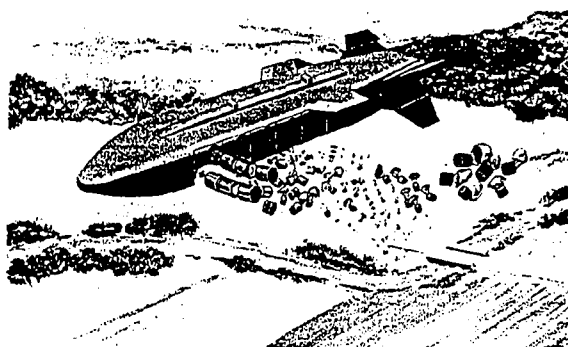


Fig. 107: DWS 39, ejection of submunition.

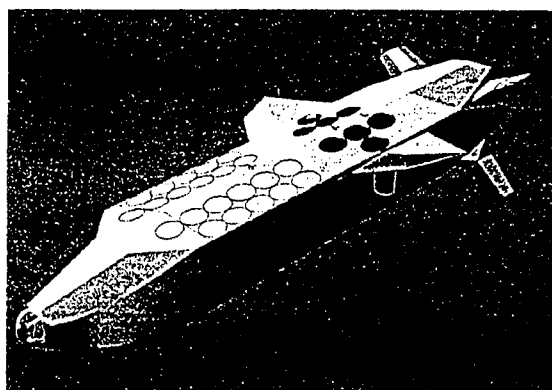


Fig. 108: TADS model with low RCS shape.

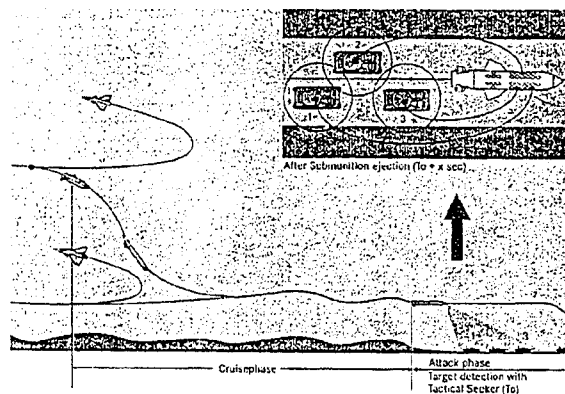


Fig. 109: Flight profile for TADS in cruise and attack phase.

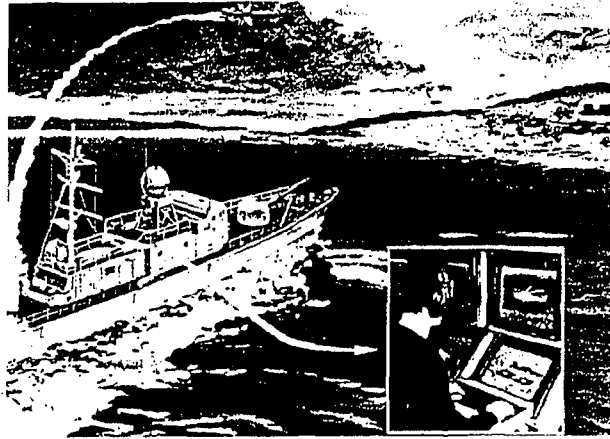


Fig. 110: POLYPHEM for ship to coast mission; vertical launch and remote control by image processing.

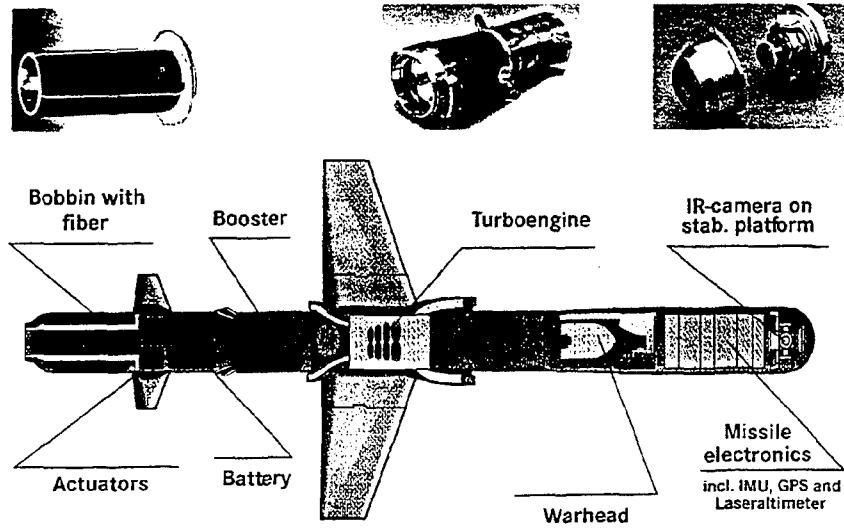


Fig. 111: Main components and key-technologies for POLYPHEM.

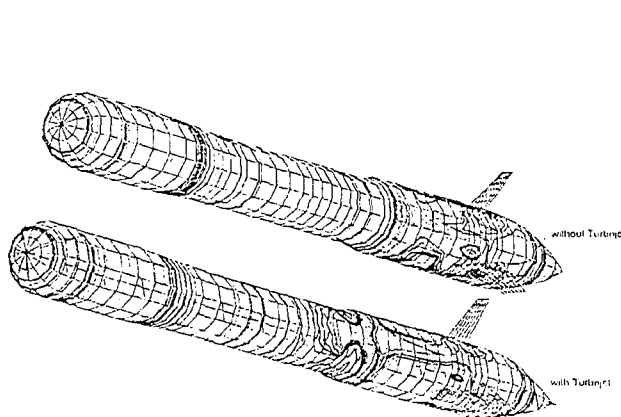


Fig. 112: Tangential velocity distribution on the surface of POLYPHEM with and without turbojet and for deflected fins; panel calculation including a viscous jet model.

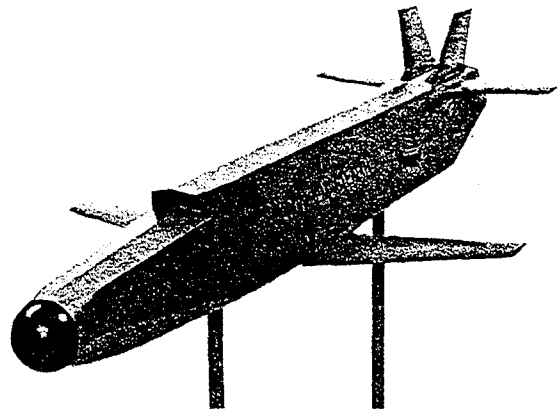


Fig. 113: Model of a stealth design for a long range sea-skimming POLYPHEM.

**ENGINEERING CODES FOR AEROPREDICTION:
STATE-OF-THE-ART AND NEW METHODS**

Frank G. Moore
Weapons Systems Department
Naval Surface Warfare Center
Dahlgren Division (Code G04)
Dahlgren Virginia 22448-5000
U.S.A

1.0 ABSTRACT

This paper discusses the pros and cons of numerical, semiempirical and empirical aeroprediction codes. It then summarizes many of the more popular approximate analytical methods used in state-of-the-art (SOTA) semiempirical aeroprediction codes. It also summarizes some recent new nonlinear semiempirical methods that allow more accurate calculation of static aerodynamics on complete missile configurations to higher angles of attack. Results of static aerodynamic calculations on complete missile configurations compared to wind tunnel data are shown for several configurations at various flight conditions. Calculations show the new nonlinear methods being far superior to some of the former linear technology when used at angles of attack greater than about 15 degrees.

2.0 SYMBOLS AND DEFINITIONS

A_p	Planform area of the body or wing in the crossflow plane (ft ²)	C_m	Spanwise pitching moment of wing airfoil section
A_{ref}	Reference area (maximum cross-sectional area of body if a body is present or planform area of wing if wing-alone) (ft ²)	$C_{Mq} + C_{M\dot{\alpha}}$	Pitch damping moment coefficient derivative
A_w	Planform area of wing in crossflow plane (ft ²)	C_N	Normal Force Coefficient $(\frac{NormalForce}{\frac{1}{2}\rho_{\infty}V_{\infty}^2 A_{ref}})$
a	Speed of sound (ft/sec)	C_n	Spanwise normal force of wing airfoil section
AR	Aspect ratio = b^2/A_w	C_{N_B}	Body alone normal force coefficient
b	Wing span (not including body) (ft)	$C_{N_{B(V)}}$	Negative afterbody normal-force coefficient due to canard or wing shed vortices
C_A, C_{AB}, C_{AF}	Total, base, and skin friction axial force coefficients respectively	$C_{N_{B(W)}}$	Additional normal-force coefficient on body due to presence of wing
C_D	Drag Coefficient = $\frac{Drag}{\frac{1}{2}\rho_{\infty}V_{\infty}^2 A_{ref}}$	$\Delta C_{N_{B(W)}}$	Additional normal-force coefficient on body due to a control deflection of the wing
C_{Dc}	Crossflow drag coefficient	C_{N_L}	Linear component of normal-force coefficient
$C_{f\infty}$	Mean skin friction coefficient based on freestream Reynolds number $(R_c)_{\infty}$	$C_{N_{NL}}$	Nonlinear component of normal-force coefficient
C_M	Pitching moment coefficient (based on reference area and body diameter if body present or mean aerodynamic chord if wing alone)	$C_{N_{T(V)}}$	Negative normal-force coefficient component on tail due to wing or canard shed vortex
		$C_{N_{W(B)}}$	Normal-force coefficient of wing in presence of body
		$\Delta C_{N_{W(B)}}$	Additional normal-force coefficient of wing in presence of body due to a wing deflection
		$C_{N_{\alpha}}$	Normal-force coefficient derivative
		C_p	Pressure Coefficient $(\frac{p-p_{\infty}}{\frac{1}{2}\rho_{\infty}V_{\infty}^2})$
		C_{P_B}	Base pressure coefficient

$(C_{PB})_{NF,\alpha}$	Base pressure coefficient with no fins present and at angle of attack		wing to wing-alone normal-force coefficient derivative at $\delta = 0$ deg
$(C_{PB})_{\alpha,\delta,t/c,x/c}$	Base pressure coefficient with fins present of some t/c , x/c , δ , and body at some α	$K_{W(B)}$	Ratio of normal-force coefficient derivative of wing in presence of body to that of wing alone at $\delta = 0$ deg
C_{P_0}	Stagnation pressure coefficient		
c_r	Root chord (ft)	$k_{B(W)}$	Ratio of additional body normal-force coefficient derivative due to presence of wing at a control deflection to that of the wing alone at $\alpha = 0$
c_t	Tip chord (ft)		
d	Body diameter (ft)		
d_{ref}	Reference body diameter (ft)	$k_{W(B)}$	Ratio of wing normal-force coefficient derivative in presence of body due to a control deflection to that of wing alone at $\alpha \neq 0$ deg
e	Internal energy (ft^2/sec^2)		
F	Dimensionless empirical factor used in tail normal-force coefficient term due to canard or wing shed vortices to approximate nonlinear effects due to a control deflection	$[k_{W(B)}]_{SB}$	Value of $k_{W(B)}$ calculated by slender-body theory at $\alpha = 0$
		$\Delta K_{B(W)}, \Delta K_{W(B)}$	Nonlinear corrections to $K_{B(W)}$ and $K_{W(B)}$ due to angle of attack
F_1, F_2, F_3	Symbols defining parameters used in base drag empirical model	l	Length (ft)
f_w, f_t	Lateral location of wing or tail vortex (measured in feet from body center line)	l_N	Nose length (can be in calibers or feet)
		LT	Linear Theory
H	Heat transfer coefficient based on wall local temperature ($ft-lb)/(ft^2-sec-^{\circ}R$)	M	Mach number = V/a
H_0	Total enthalpy (ft^2/sec^2)	M_N	Normal Mach number to body axis = $M \sin \alpha$
H_i	Heat transfer coefficient based on wall local specific enthalpy [$slug/(ft^2-sec)$]	N_i, N_t	Transformation factors used in Eckert reference enthalpy to approximate three-dimensional effects for laminar and turbulent flow ($= 3$ and 2 , respectively)
h	Specific enthalpy (ft^2/sec^2)	p	Pressure (lb/ft^2) or roll rate (rad/sec)
h_{aw}	Adiabatic wall specific enthalpy (ft^2/sec^2)	p_c	Pressure of a cone of given half angle (lb/ft^2)
h_e	Specific enthalpy at outer edge of boundary layer (ft^2/sec^2)	P_r	Prandtl number
h_T	Height of wing or canard shed vortex at tail center of pressure (ft)	\dot{q}	Pitch Rate (rad/sec)
h_w	Specific enthalpy at wall (ft^2/sec^2)	\dot{q}_w	Heat transfer rate ($ft-lb)/(ft^2-sec)$ at wall
h^*	Reference value of specific enthalpy (ft^2/sec^2)	$\dot{q}_{w,l}, \dot{q}_{w,t}$	Heat transfer rate at wall for laminar or turbulent flow, respectively
i	Tail interference factor	R	Gas constant [for air $R = 1716 ft-lb/(slug-^{\circ}R)$]
k_1	Empirical factor defined in wing-alone nonlinear normal-force coefficient term	Re	Reynolds Number = $\frac{\rho V l}{\mu}$
$K_{B(W)}$	Ratio of additional body normal-force coefficient derivative due to presence of		

$(Re)_c$	Critical Reynolds number where flow transitions from laminar to turbulent flow	α	Angle of attack (degrees)
Re_D	Reynolds number based on diameter of wing leading edge bluntness	$\dot{\alpha}$	Rate of change of angle of attack (deg/sec)
r	Radius of body (ft)	α_c	Angle of attack where wing-body interference factor starts decreasing from its slender-body theory value (degrees)
r_n	Radius of nose tip (ft)	α_D	Angle of attack where the wing-body interference factor reaches a minimum (degrees)
r_w, r_t	Radius of body at wing or tail locations	α_w, α_T	Local angle of attack of wing or tail ($\alpha + \delta_w$ or $\alpha + \delta_T$, respectively, in degrees)
r/s	Ratio of body radius to wing or tail semispan plus the body radius	β	$\sqrt{M^2-1}$ or $\sqrt{1-M^2}$ depending on whether flow is supersonic or subsonic. Also, Mach angle, $\beta = \sin^{-1}(1/M)$
S	Entropy (ft-lb)/(slug - °Rankine)	δ	Control deflection (degrees)
s	Distance along body surface in SOSET (also wing or tail semispan plus the body radius in wing-body lift methodology)	δ_{eq}	Angle between a tangent to the body surface at a given point and the velocity vector (degrees)
SB	Slender-body theory	δ_w, δ_T	Deflection of wing or tail surfaces (degrees), positive leading edge up
T	Temperature (°R or °K)	Φ	Velocity potential
T_{aw}, T_o, T_w	Adiabatic wall, total, and wall temperature, respectively	ϕ	Circumferential position around body where $\phi = 0$ is leeward plane (degrees)
t/c_r	Tail thickness to its root chord	λ	Taper ratio of a lifting surface = c_t/c_r
t/d	Tail thickness to body diameter	Ψ_1, ζ_1	First order axial and crossflow solutions of velocity potential equation
u, v, w	Perturbation velocity components, (ft/sec)	Ψ_2	Second order particular solution to full potential equation
V	Velocity (ft/sec)	η	Parameter used in SOSET and also used in viscous crossflow theory for nonlinear body normal force (in this context, it is the normal force of a circular cylinder of given length-to-diameter ratio to that of a cylinder of infinite length)
V_e	Velocity at edge of boundary layer (ft/sec)	η_n	Value of η in viscous crossflow theory for $M_N = 0$
V_p	Velocity parallel to leading edge of wing (ft/sec)	μ_o, μ^*	Viscosity coefficient at stagnation or reference conditions, respectively (slug/ft-sec)
x	Distance along the axis of symmetry measured positive aft of nose tip (feet or calibers)	ρ, ρ_o, ρ^*	Density of air at local, stagnation, or reference conditions, respectively (slugs/ft ³)
x/c	Parameter used in base drag methodology to represent the number of chord lengths from the base (measured positive upstream of base)	γ	Specific heat ratio
x_{cp}	Center of pressure (in feet or calibers from some reference point that can be specified)		
x_L, x_T	Laminar and turbulent flow lengths on body (ft)		
y_{cp}	Spanwise center of pressure of wing semispan		
Z	Compressibility factor		

θ	Local body slope at a given point (degrees)	including material requirements and selection, structural member thicknesses required to withstand the loads, and as inputs for heat transfer or ablation analysis (Table 3-1). Generally, an interactive design process occurs between the aerodynamicist, the structural designer, and the flight dynamicist to arrive at a configuration that meets some set of desired launcher constraints and performance requirements given a warhead and possibly a guidance system as well.
θ_c	Cone half angle	
Λ	Leading edge sweep angle of wing or tail (degrees)	Prior to 1971, the tactical weapons aerodynamicist could do one of three things to obtain aerodynamics. The individual could perform flight tests of a full-scale configuration; or design, build, and test a wind tunnel model over the flight range of interest; or finally, utilize existing handbooks, wind tunnel data reports, and theoretical analysis to estimate empirically the aerodynamics of a given configuration.
∞	Free-stream conditions	
2-D	Two dimensional	The first two approaches were often more costly, time consuming, and accurate than needed in the preliminary design stages, whereas the latter approach was more time consuming than desired but also had no general accuracy assessment.
3-D	Three dimensional	
3DTWT	3-D thin wing theory	A fourth alternative (which did not exist prior to 1971), to compute aerodynamics on a complete configuration over the Mach number and angle of attack range of interest, is to have a general computer program to perform such a task. There are three alternative theoretical approaches to develop such a code (see Table 3-2). The first of these is solution of the full Navier Stokes equations. The only assumptions associated with this set of equations is continuum flow (that is the flowfield region is not sparsely populated with air molecules such as at altitudes greater than about 200 to 250 thousand ft) and the turbulence model selected. A second theoretical alternative is to assume the viscous flow region lies in a thin layer near the body and thus solution of the Navier Stokes equations can be reduced to that of an inviscid flowfield plus a thin boundary layer near the surface. This, combined with empirical estimates of base drag and other protuberance aerodynamics, gives a complete set of aerodynamics for the configuration of interest. A third theoretical alternative is to assume the body perturbs the flowfield only slightly and then to make appropriate approximations to the Euler and Boundary Layer Equations. These approximate theories are then combined with other theoretical approaches and empirical data for the complete aerodynamics code.
AP81	Aeroprediction 1981	
AP93	Aeroprediction 1993	
APC	Aeroprediction code	
BD	Base Drag	
BL	Boundary Layer	
FNS	Full Navier-Stokes	
GSET	Generalized shock-expansion theory	
IMNT	Improved modified Newtonian theory	
MNT	Modified Newtonian theory	
NASA/LRL	National Aeronautics and Space Administration/Langley Research Center	
NS	Navier-Stokes	
NSWCDD	Naval Surface Warfare Center, Dahlgren Division	
PNS	Parabolized Navier-Stokes	
SE	Shock expansion	
SOSET	Second-order shock-expansion theory	
SOTA	State of the art	
TAT	Turn-Around Time	
TLNS	Thin Layer Navier-Stokes	

3.0 INTRODUCTION AND BACKGROUND

3.1 Uses for Aerodynamics

Aerodynamics are required throughout the design process of any flight vehicle. These aerodynamics are used for flight performance estimates including range, maneuverability, miss distance, and stability analysis. In addition, they are used for structural analysis

There are several uses that can drive the type of theory chosen for the aeroprediction code. These are listed in Table 3-3. For example, if missile synthesis is being performed where a very large number of configurations are investigated to conduct top level trade studies involving engine types, warhead types, material requirements, etc. as a function of range, maneuverability, or response time, then it is desirable to have an easy to use, robust, and computationally fast

TABLE 3-1. WHAT AERODYNAMICS ARE USED FOR

Flight Dynamics	Structures
<ul style="list-style-type: none"> o Range Computation o Engagement of Target and Miss Distance o Maneuverability Estimates o Any Trajectory Analysis (3 DOF, 5 DOF, 6 DOF)* 	<ul style="list-style-type: none"> o Loads (Pressure) o Aeroheating (Inputs to Heat Transfer Codes) o Ablation Analysis Inputs

*DOF = Degree of Freedom

TABLE 3-2. HOW WE GET AERODYNAMICS

<ol style="list-style-type: none"> 1. Wind Tunnel, Free Flight Data, Ballistic Range 2. Empirical Estimates: Wind Tunnel Reports, Handbooks, Experience, etc. 3. Aeroprediction Codes <ol style="list-style-type: none"> A. Navier Stokes -- Continuum Flow B. Euler Equations + Boundary Layer -- inviscid outer layer + thin viscous layer near surface + some empirical techniques C. Approximations to Euler and Boundary Layer Equations + Empirical Techniques

TABLE 3-3. AERODYNAMIC CODE REQUIREMENTS AND USES IN VARIOUS MISSILE DESIGN STAGES

Design Stage	Aero Code Design Requirements	Trade Studies (Typical)	Aerodynamics Uses
Missile Synthesis	Robustness Ease to Use Minimal Input Parameters Extremely Fast Computationally 25 Percent Accuracy	Engine Types Warhead Types Material Requirements Typical Weights Guidance Types Airframe Control Type	Range Maneuverability Response Time
Missile Preliminary Design	Blend of Robustness, Ease of Use, and Accuracy Fast Computationally 10 percent Accuracy	Structural Layout (Material, Thickness, etc.) Aero Shape vs. Engineering and Guidance Size Hot vs. Cold Structure	Range Maneuverability Miss Distance (3 DOF) Structural Design
Detailed Design and Problem Solving (or Analysis Codes)	Accuracy (<5 percent) Computationally Affordable User Friendliness and Robustness Still Important	Detailed Structural Design Including Material Selection Investigating Critical Problem Areas	Range Maneuverability Miss Distance (6 DOF) Structural Design

code. At the same time, accuracy may be sacrificed to achieve these goals.

After a missile synthesis of a large number of concepts has been conducted, generally several of these concepts are taken a step further in the design process. Here, structural layouts, packaging of all components, and better definition of weights are typical requirements that allow improved estimates of range, maneuverability, and preliminary miss distance. This means that the aerodynamic code requirements need a blend of robustness, ease of use, and accuracy while still being computationally cost effective. Accuracies in aerodynamics of 10 percent or so are generally expected.

Finally, one or two configurations are selected for more detailed performance estimates. This means accuracy in the aerodynamics estimates of better than 5 percent in most cases. Each of the three design levels discussed require different levels of accuracy, computational speed, and robustness and, therefore, aid in the choice of the level of theoretical complexity needed to meet the requirements.

To meet the theoretical aerodynamics computer code needs, the Navy began developing such a code in 1971 based on the 3C approach of Table 3-2. This code falls into the second category of Table 3-3. Since the first version of the NSWCDD Aeroprediction code was released, there have been four versions produced since that time.

Each of these versions attempted to meet the requirements as seen by the tactical weapons community. The first version was for general-shaped bodies alone.¹ It was the first such weapons code known that combined a good mix of accuracy in aerodynamic computations, ease of use, and computational time. It is believed that this mix led to the code's initial popularity and requests for additional capability. In 1974,^{2,3} the code was extended to allow up to two sets of lifting surfaces in the computational process. In 1977,^{4,5} dynamic aerodynamic derivatives were added to the code's capability. In 1981, the code extended the Mach number range up to eight and added high angle-of-attack capability for a narrow range of configurations.^{6,7} Finally, the last version of the code extended the Mach number range higher to include real gas effects, added new nonlinear lift methodology for wings and interference effects, and developed an improved base drag methodology.^{8,9}

This paper will serve several purposes. First, a review of the state-of-the-art (SOTA) aerodynamic prediction codes will be given. Second, a review of some of the more useful approximate theoretical methods will be made. These methods are conventional and have been in use for many years. Third, a more detailed review of new nonlinear aerodynamic methods introduced over the past 3 years into the fifth version of the

Aeroprediction Code (AP93) will be given. Finally, a comparison of static aerodynamics using experiment, AP93 and the older version of the Aeroprediction Code (AP81) will be made on several complete missile configurations.

3.2 Types of Aeroprediction Codes

Aeroprediction Codes will be defined and broken down into three classes. These classes are empirical, semiempirical, and numerical codes. The empirical codes are analogous to the codes used in Missile Synthesis in Table 3-3. The semiempirical and some numerical codes are used primarily in the missile preliminary design stage of Table 3-3. Finally, the numerical codes are the only ones with the accuracy and capability to do the detailed design application as shown in Table 3-3.

In terms of a definition, empirical codes typically calculate aerodynamics by a series of simple formulas that have been approximated based on data fits. Typically, these codes can be implemented on a hand calculator in many cases and are the most simplistic and least accurate of the code classes.

The semiempirical codes typically attempt to calculate a force or moment using approximations to the exact equations of motion. When this approach fails (such as at higher angles of attack), empirical estimates or methods are used. This blend of approximate theories and empirical estimates is why this class of codes is termed semiempirical. The semiempirical codes, in contrast to the empirical codes, generally will calculate pressure distribution on the body and lifting surfaces. It is this blend of theory with the empirical estimates that allows the semiempirical codes to improve accuracy over the empirical codes.

The third class of codes is called numerical. These codes will define a grid around the configuration that is composed of points in two or three dimensions. Numerical techniques are then employed to solve the equations of motion at all grid points in the flow field that is bounded by the body and shock or body and outer boundary of the flow if the Mach number is subsonic. Numerical Codes are generally based on the linearized or full potential equations of motion, the full Euler equations or the full or reduced level of Navier Stokes equations. If the potential or Euler equations are used, other methods (such as boundary layer equations) must be used for skin friction. Also, empirical estimates are used for base drag. Hence, even though these codes are numerical, in most cases to get complete forces and moments on a configuration, the use of some empirical data will be necessary. Also, if the potential equations are solved in a numerical form, the accuracy is similar to the semiempirical codes. The only difference between the two is that the semiempirical codes seek pressure distributions on the body and wings without solving the entire flowfield. This saves a tremendous amount of computational time.

A final point worthy of discussion are the assumptions inherent in each level of theory. These assumptions are given as a function of the theoretical approach in Table 3-4. Upon examination of Table 3-4, the level of code sophistication, computational time, overall cost and accuracy goes down in going from the top to the bottom of the table.

One way to try to compare the level of sophistication versus accuracy, and the cost of the various codes, is through the examination of the total cost to obtain a set of aerodynamics. To do this, Table 3-5, which compares the educational, computer, and computational time requirements of the various Aeroprediction Codes in use at NSWCDD has been prepared. Referring to Table 3-5, the level of sophistication increases in going from top to bottom of the table. For example, the MAIR Code is close to an empirical code but it does have some theory included so that it would be in the class of semiempirical codes. The Missile III, Aeroprediction versions 81 and 93, HABP, and Missile DATCOM, are all semiempirical codes. NANC and BODHEAT are primarily numerical codes based on approximations to the Euler and Boundary Layer equations. SWINT/ZEUS, CFL3DE and GASP, of course, are all numerical codes. The Aeroprediction 81/93, SWINT/ZEUS, MAIR, NANC, and BODHEAT were all developed at NSWCDD. The Missile III was developed by Nielsen Engineering and Research (NEAR), HABP and Missile DATCOM by McDonnell Douglas of St. Louis, and the Navier Stokes Codes were developed jointly by NASA/LRC and VPI.

Included in Table 3-5 is the time required to learn how to use the code, the set-up time for a typical geometry, and the computer time for the one case referenced to the same computer (CDC 865). Also shown are other criteria including typical educational level of the user as well as the size of the computer required. To get the total cost of using a code, it is necessary to add the manpower set-up time to the computer cost and prorate the training time over some nominal expected usage. Experience has shown that most project and program managers are willing to pay the costs of SWINT/ZEUS type codes and any above that in Table 3-5. However, the cost and requirements of the full Navier Stokes codes must come down substantially before they will be used on a routine basis for design. This means much additional research as well as advancements in computer speed are still needed in this area.

To illustrate this point, a particular example was chosen for cost comparisons. The example is to develop a set of trim aerodynamics on a typical missile configuration to be used as an input to a three-degree-of-freedom (3 DOF) flight simulation model. This example is quite typical of what an empirical or semiempirical code would be used for. By definition, trim is that combination of angles of attack (α 's) and control deflections (δ 's) that give zero pitching moment about the vehicle center of gravity. To determine the (α , δ)

map as a function of Mach number, one must compute the static aerodynamics over enough α , δ , M conditions so the flight envelope will be covered. Also, it will be assumed that the missile is a surface launched, tail control, cruciform fin configuration which has a Mach range of 0 to 4, angle of attack range of 0 to 30°, control deflection of 0 to 20°, and altitude 0 to 80,000 feet. These conditions are reasonable for many of the worlds missiles. To cover the flight envelope, 7 Mach numbers, 5 α 's and 5 δ 's are assumed. This gives a total of $7 \times 5 \times 5 = 175$ cases. Furthermore, skin friction varies with attitude so 5 altitudes will be chosen, giving a total of 180 cases for which aerodynamics are to be computed on a single configuration.

Before costs of each computer code can be made for this particular example, some assumptions must be made. These assumptions are given in Table 3-6. These assumptions are based on NSWCDD experience in using the various aeroprediction codes. The cost to perform the set of trim aerodynamics calculations using these codes is shown in Figure 3-1. It should be noted that the cost assumes that Parabolized Navier Stokes and Euler plus boundary layer are used at subsonic axial Mach number conditions although the codes in use at NSWCDD are steady hyperbolic marching solutions and will not function where the axial Mach number decreases to one. To go to unsteady computation would require costs to be multiplied by a factor of at least 10. Hence, the PNS and Euler plus B.L. costs are based on steady flow of supersonic Mach numbers. For a combination of steady and unsteady computations, the cost of these codes would probably be about five times greater than those shown in Figure 3-1.

There are several points worthy of note in analyzing Figure 3-1. First, for practical routine computations, Full Navier Stokes and Thin Layer Navier Stokes are beyond the cost most program managers are willing to pay. Secondly, they are even beyond the wind tunnel cost to obtain comparable aerodynamics. Thirdly, steady PNS, steady Euler plus boundary layer, and semiempirical (Aeroprediction) are all within most allowable aerodynamics budgets. Going to unsteady computations for subsonic axial Mach numbers makes the cost requirements much higher and may not be affordable and robust to cover the entire flight regime.

A second way of comparing aerodynamic computations is the total time it takes to get the complete set of computations performed. These results are estimated, again based on NSWCDD experience, and shown in Figure 3-2. Again, the same caveat, with respect to the PNS and Euler Codes, applies here as to Figure 3-1. For most development programs, the semiempirical codes obviously have the most desirable turn-around-time (TAT). The Euler and PNS are marginal and experimental and Navier-Stokes (N-S) and Thin Layer Navier-Stokes (TLNS) generally unacceptable except as long lead items. The combination of cost, accuracy, and complexity of the various means of computing

TABLE 3-4. ASSUMPTIONS OF FLOW FIELD EQUATIONS

- | | |
|----|---|
| 1. | Full Navier Stokes (high angle of attack) |
| | A. Continuum Flow |
| | B. Turbulence Model |
| 2. | Thin Layer Navier Stokes (moderate separation) |
| | A. Neglect Streamwise and Circumferential Gradients of Stress Terms |
| | B. Turbulence Model |
| | C. Continuum Flow |
| 3. | Parabolized Navier Stokes (small separation) |
| | A. Steady State |
| | B. Neglects Streamwise Viscous Gradient |
| | C. Approximate Streamwise Pressure Gradient in Subsonic Portion of Flow Near Surface |
| | D. Turbulence Model |
| | E. Continuum Flow |
| 4. | Euler Equations + Boundary Layer (small separation) |
| | A. Viscous Region Confined to Thin Region Near Body Surface |
| | B. Large Reynold's Number |
| | C. Neglect Streamwise Gradients of Stress Terms |
| | D. Neglect Normal Pressure Gradient |
| | E. Turbulence Model |
| | F. Continuum Flow |
| 5. | Euler Equations |
| | A. Neglect all Viscous Terms |
| | B. Continuum Flow |
| 6. | Full Potential Equations |
| | A. Neglect all Viscous Terms |
| | B. Flow is Isentropic (no shock waves) |
| | C. Continuum Flow |
| 7. | Linearized Potential Equations |
| | A. Neglect all Viscous Terms |
| | B. Flow is Isentropic (no shock waves) |
| | C. Body Creates Small Disturbances in Flowfield |
| | D. Continuum Flow |
| 8. | Theoretical Approximations |
| | A. Certain Other Simplifications to Euler, Potential Equations, or Boundary Layer Equations |
| | B. Continuum Flow |
| 9. | Empirical Data Base |
| | A. Data Base Covers Vehicles and Flight Regime of Interest |
| | B. Enough Data is Available to do Good Interpolations |

TABLE 3-5. EDUCATIONAL AND TIME REQUIREMENTS FOR
AEROPREDICTION CODES IN USE AT NSWCDD

Code	Typical User Educational Level	Typical Time Required to Learn to Use Code	Set-Up Time	Computational Time for 1 Case (Same Computer)	Computer Required
1. MAIR	Coop, B.S., M.S., Ph.D	< 1 wk	< 1 day	< 1 second	P. C.
2. Missile III	Coop, B.S., M.S., Ph.D	≈ 1 wk	< 1 day	< 1 second	P. C.
3. Aeroprediction 81 and 93	Coop, B.S., M.S., Ph.D	≈ 1 wk	< 1 day	< 1 second	P. C.
4. HABP	B.S., M.S., Ph.D.	≈ 2 wk	< 1 wk	< 1 second	Micro Vax
5. Missile DATCOM	B.S., M.S., Ph.D.	≈ 2 wk	< 1 wk	< 1 second	Micro Vax
6. NANC	M.S., Ph.D.	≈ 3 wk	< 2 wks	10 seconds	Vax CDC Super Mini
7. BODHEAT	M.S., Ph.D.	≈ 3 wk	< 1 wk	10 seconds	Vax CDC Super Mini
8. SWINT/ZEUS	M.S., Ph.D.	≈ 1 month	< 1 month	1-3 minutes	Vax CDC Super Mini
9. N.S. (CFL3DE, GASP)	Ph.D., some M.S.	≈ months-yrs	≈ months	≈ hrs-days	Cray or Super Mini

TABLE 3-6. ASSUMPTIONS IN COST ESTIMATES TO COMPUTE SET OF TRIM
AERODYNAMICS WITH VARIOUS AEROPREDICTION CODES

Estimated Costs	Cray II Computer at \$500/HR	
	Engineer Time = 110K/work year	
	Engineer is assumed to know how to use codes so no training time is involved	
	Need enough resolution in grid size to predict skin friction drag	
	Wind Tunnel (W/T) includes models and test cost	
CODE	SET UP TIME	COMPUTER TIME
FNS	5 Weeks	20 Hours
TLNS	5 Weeks	17 Hours
PNS	2-5 Weeks	12 Minutes
EULER + BL + B.D.	2 Weeks	1.5 Minutes
AEROPREDICTION	0.5 Day	1.0 Seconds

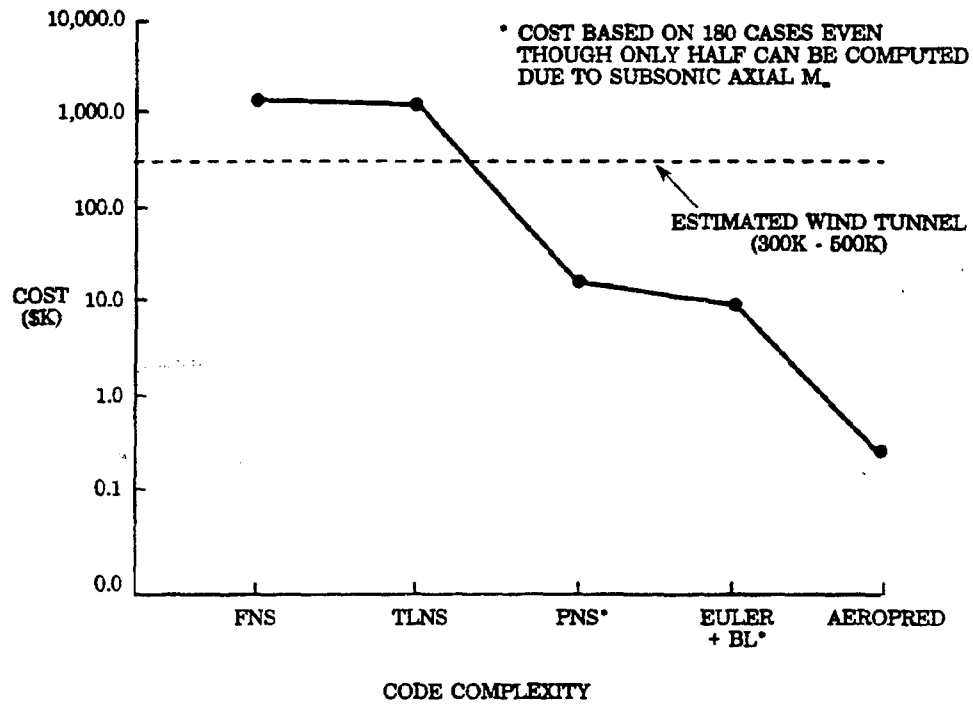


FIGURE 3-1. ESTIMATED COST TO OBTAIN SET OF TRIM AERODYNAMICS

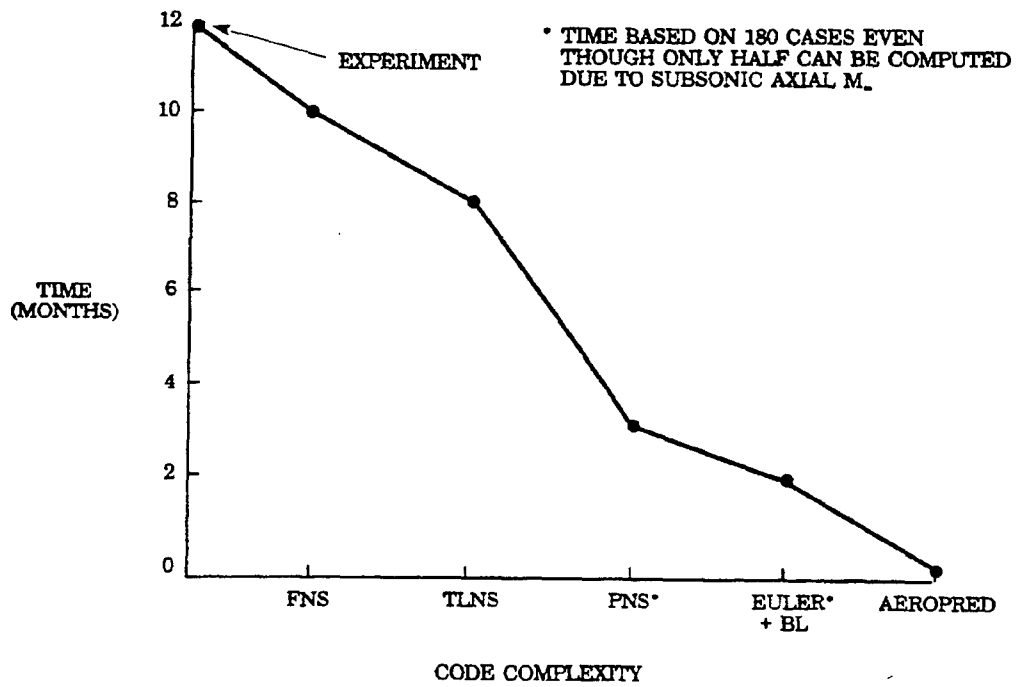


FIGURE 3-2. ESTIMATED TIME TO GENERATE SET OF TRIM AERODYNAMICS

aerodynamics has led most agencies to a mix of the various approaches. The most used codes still remain the semiempirical codes with Euler plus Boundary Layer becoming more and more prevalent as the robustness and ease of use improves. Navier Stokes and Thin Layer Navier Stokes are used for specialized problems or a few validation cases of other codes; much work is still needed to improve user friendliness for this class of codes. Wind tunnel data still remains the most reliable but time consuming method to obtain Aerodynamics.

3.3 Codes in Use

Lacau¹⁰ listed many of the codes in use today for calculating aerodynamics. He categorized them as empirical or semiempirical, full potential, linearized potential, Euler, Full Navier Stokes, and Parabolized Navier Stokes. Reference 11 added several of the more recent codes to this list. Due to space limitations of this paper, these lists will not be shown. Interested readers are referred to references 10 and 11 for more details of these codes.

This completes the discussion on the state-of-the-art in aerodynamic codes and the various means to obtain aerodynamics. The bulk of the remainder of this paper will be directed at the semiempirical code known as NSWC Aeroprediction as given in Table 3-5. To that extent, the next section will briefly cover many of the more popular approximate theoretical techniques used by many of the semiempirical codes in references 10 and 11. This will be followed by the new technology developed for the latest version of the Aeroprediction Code (AP93). Finally, a comparison with experiment of the AP93 and AP81 will be given for several missile configurations.

4.0 CONVENTIONAL APPROXIMATE AERODYNAMIC METHODS

This section of the paper will review some of the more important approximate aerodynamic methods that have proved quite useful in the development of semiempirical codes. Time and space will not permit derivation of the methods from first principles. However, appropriate references will be given for the interested reader. The approach taken here, in the presentation of the material, will be to mention the assumptions inherent in each method, relevant equations, and possibly show an example or two as may be warranted.

4.1 Hybrid Theory of Van Dyke (HTVD)¹²

The Hybrid Theory of Van Dyke¹² combines a second-order axial solution to the potential equation with a first-order crossflow solution first espoused by Tsien.¹³ The advantage of this method is that it gives second-order accuracy in the axial direction where first-order accuracy is generally unacceptable for drag computations. On the other hand, first-order accuracy in the crossflow plane is typically acceptable for normal force and center of pressure computations. The fundamental reason for this is that perturbations in the

flow, due to the presence of a body, have more impact in the axial as opposed to the normal force direction. Hence, to get axial force accuracy compatible with a goal of ± 10 percent requires second-order methods, whereas ± 10 percent accuracy on C_N can be obtained with first-order methods in many cases.

As already mentioned, the Hybrid theory comes from the potential equation of fluid mechanics. It is limited to supersonic flow (we have used this method down to $M_\infty = 1.2$) where the assumption of isentropic flow (shock waves are weak) can be made. This typically limits the upper Mach number range to about $M_\infty = 2.0$ to 3.0, depending on the body shape. Also, the slope of the body surface must be less than the Mach Angle. The Tsien solution, or crossflow part of the solution, comes from the linearized perturbation equation. On the other hand, the second-order solution to the axial flow is found by obtaining a particular solution to a reduced version of the full potential equation. This is the key to the accuracy improvement afforded by Van Dyke solution in that some of the nonlinearity inherent in the axial flow problem is brought into the solution by this process. The beauty of the Van Dyke method is that this particular second-order solution is given entirely in terms of the first-order solution. That is, one simply solves the first-order perturbation solution for the axial flow and then solves an algebraic equation for the second-order solution where the boundary condition at the body is satisfied.

In equation form, the general first-order perturbation problem is:¹²

$$\Phi_{rr} + \Phi_r/r + \Phi_{\theta\theta}/r^2 - (M_\infty^2 - 1)\Phi_{xx} = 0 \quad (1)$$

with boundary conditions that do not allow any upstream disturbances:

$$\Phi(0, r, \phi) = \Phi_x(0, r, \phi) = 0 \quad (1a)$$

and that require the flow to be tangent to the body surface:

$$\Phi_r(x, r_b, \phi) + \sin \alpha \cos \phi = \frac{dr}{dx} [\cos \alpha + \Phi_x(x, r_b, \phi)] \quad (1b)$$

The subscripts in Equation (1) indicate partial derivatives. The solution to Equation (1) is satisfied identically by:

$$\Phi(x, r, \phi) = \Psi_1(x, r) \cos \alpha + \zeta_1(x, r) \sin \alpha \cos \phi \quad (2)$$

The first term of Equation (2) is the first-order axial solution, and the second term is the first-order crossflow solution. Since the equation is linear, these two solutions can be found independently, and then added together. The axial solution, $\Psi_1(x, r)$, for a general body is found by placing a series of sources and

sinks along the x axis and satisfying the boundary conditions at each point. The crossflow solution, $\zeta_i(x, y)$, is found by placing a series of doublets along the axis, again satisfying the boundary conditions.

The particular second-order solution that Van Dyke found for the reduced full potential equation is

$$\Psi_2 = M_\infty^2 \left[\Psi_{1x} (\Psi_1 + Nr\Psi_{1r}) - \left(\frac{r}{4}\right) \Psi_{1r}^3 \right] \quad (3)$$

$$\text{where } N = \left(\frac{\gamma + 1}{2}\right) \frac{M_\infty^2}{\beta^2}$$

Second-order axial velocity components Ψ_{2x} and Ψ_{2r} are also defined in terms solely of the first-order solution $\Psi_1(x, r)$.

Once the second-order axial perturbation velocity components Ψ_{2x} , Ψ_{2r} are computed, along with the first-order crossflow components ζ_{1x} and ζ_{1r} , the total perturbation velocities are then:

$$\frac{u}{V_\infty} = (\cos\alpha) (1 + \Psi_{2x}) + (\sin\alpha \cos\phi) \zeta_{1x} \quad (4a)$$

$$\frac{v}{V_\infty} = \cos\alpha (\Psi_{2r}) + (\sin\alpha \cos\phi) (1 + \zeta_{1r}) \quad (4b)$$

$$\frac{w}{V_\infty} = -(\sin\alpha \sin\phi) \left(1 + \frac{\zeta_{1r}}{r}\right) \quad (4c)$$

The pressure coefficient at each body station is then:

$$C_p(x, \phi) = -\frac{2}{\gamma M_\infty^2} \left\{ \left[1 + \frac{\gamma - 1}{2} M_\infty^2 \left(1 - \frac{u^2 + v^2 + w^2}{V_\infty^2} \right) \right]^{\frac{\gamma}{\gamma - 1}} - 1 \right\} \quad (5)$$

Finally the force coefficients are:

$$C_A = \frac{2}{\pi r_r^2} \int_0^l \int_0^\pi C_p(x, \phi) \frac{r dr}{dx} d\phi dx \quad (6)$$

$$C_N = -\frac{2}{\pi r_r^2} \int_0^l \int_0^\pi C_p(x, \phi) \cos(\phi) r d\phi dx \quad (7)$$

$$C_M = \frac{1}{\pi r_r^3} \int_0^l \int_0^\pi C_p(x, \phi) \cos(\phi) x r d\phi dx \quad (8)$$

and the center of pressure in calibers from the nose is

$$X_{C_p} = -C_M/C_N \quad (9)$$

It should be pointed out that in the actual numerical integration of Equations (6), (7), and (8) the integration must be carried out in segments of the body between each discontinuity due to the discontinuous pressure distribution.

Also, the hybrid theory of Van Dyke is limited to pointed bodies of revolution. Bluntness will be considered later.

4.2 Second-Order-Shock-Expansion Theory (SOSET)¹⁴

First-order Expansion Theory was first proposed by Eggers et al. for bodies of revolution flying at high supersonic speeds.¹⁵ Basically, the Shock-expansion Theory computes the flow parameters at the leading edge of a two-dimensional (2-D) surface with the oblique shock wave relations and with the solution for a cone at the tip of a three-dimensional (3-D) body. Standard Prandtl-Meyer Expansion (PME) is then applied along the surface behind the leading edge or tip solution to get the complete pressure distribution over the body surface. Referring to Figure 4-1, this theory inherently assumes that the expansion waves created by the change in curvature around the body are entirely absorbed by the shock and do not reflect back to the body surface. Since the theory assumes constant pressure along one of the conical tangent elements of the surface, fairly slender surfaces must be assumed or many points along the surface assumed to obtain a fairly accurate pressure distribution. Another way of stating this is to minimize the strength of the disturbance created by Mach waves emanating from the expansion corner and intersecting the shock, the degree of turn should be small.

Syverson (et al.) extended the generalized Shock-expansion Theory on pointed bodies and sharp airfoils to what he called a second-order theory.¹⁴ He defined the pressure along a conical frustum by

$$p = p_c - (p_c - p_2)e^{-\eta} \quad (10)$$

instead of a constant on each segment as was the case in the generalized theory. Here p_c is the pressure on a cone with the given cone half angle equal to the slope of the conical segment with respect to the axis of symmetry. p_2 is the pressure just aft of a conical segment which is calculated from a Prandtl Meyer Expansion (PME) of the flow around a corner (as shown in Figure 4-2, going from points 1 and 3 to points 2 or 4, for example).

Also

$$\eta = \frac{\left(\frac{\partial p}{\partial s}\right)_2 (s - s_2)}{p_c - p_2} \quad (10a)$$

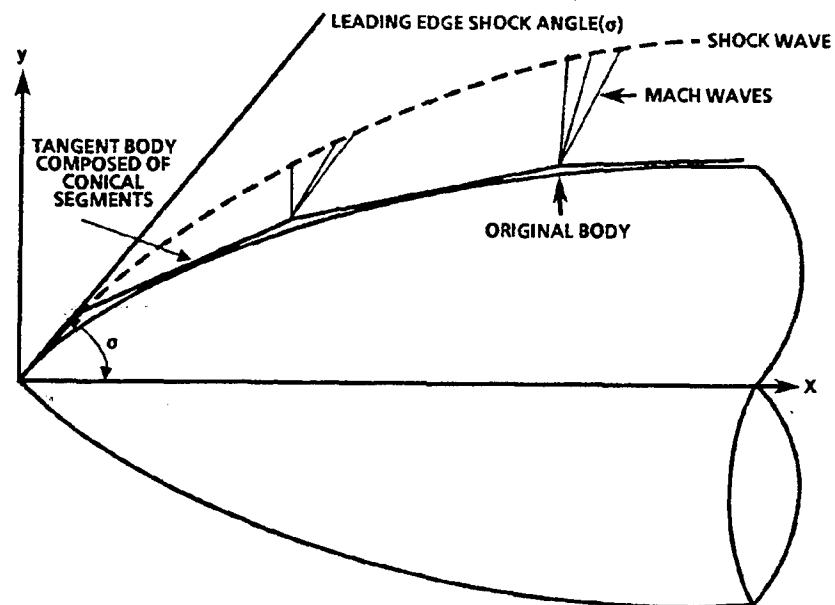


FIGURE 4-1. APPROXIMATION OF TRUE BODY BY ONE COMPOSED OF STRAIGHT LINE SEGMENTS TANGENT TO SURFACE

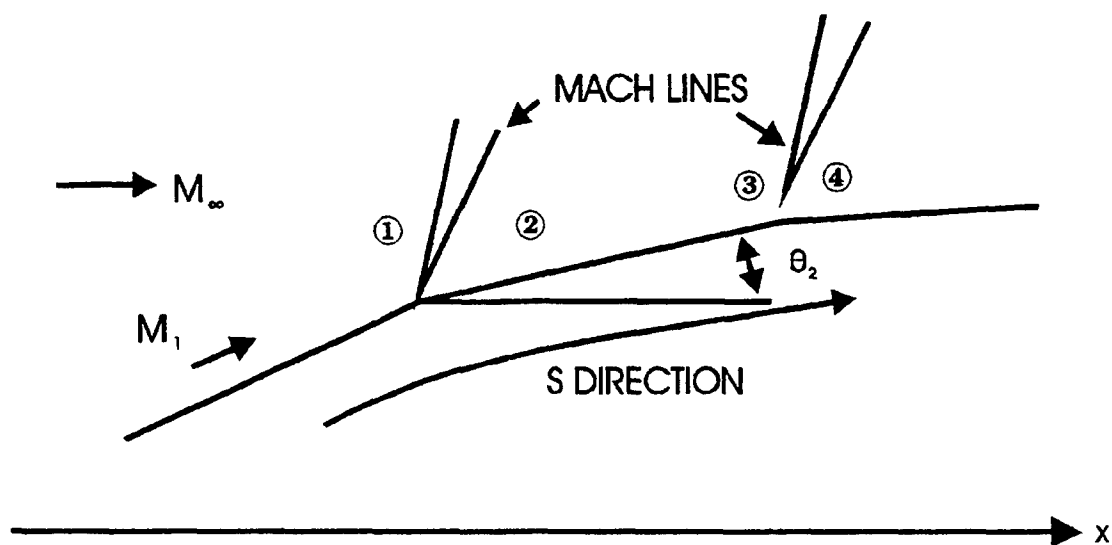


FIGURE 4-2. FLOW ABOUT A FRUSTRUM ELEMENT

Thus, examining p from Equation (10), it can be seen, for example, on the frustrum element in Figure 4-2 that the pressure varies from the pressure of the generalized theory at point 2 to that of a cone of angle θ_2 and Mach number M_2 as s gets large. Syvertson and Dennis approximated the pressure gradient as¹⁴

$$\left(\frac{\partial p}{\partial s}\right)_2 = \frac{B_2}{r} \left(\frac{\Omega_1}{\Omega_2} \sin \theta_2 - \sin \theta_1\right) + \frac{B_2}{B_1} \frac{\Omega_1}{\Omega_2} \left(\frac{\partial p}{\partial s}\right)_1 \quad (11)$$

where

$$B_{1,2} = \frac{\gamma p_{1,2} M_{1,2}^2}{2(M_{1,2}^2 - 1)}$$

$$\Omega_{1,2} = \frac{1}{M_{1,2}} \left[\frac{1 + \frac{\gamma-1}{2} M_{1,2}^2}{\frac{\gamma+1}{2}} \right]^{\frac{\gamma+1}{2(\gamma-1)}}$$

Finally, for negative angles such as would occur on a boattailed configuration, p_e was replaced by p_∞ . No discussion was given for blunt bodies. It should be noted that if η of Equation (10) becomes negative, the SOSET reverts to the generalized or first-order Shock-expansion Theory. This is because Equation (10) will not give the correct asymptotic cone solution for negative values of η .

Experience has shown that SOSET gives very good pressure distributions for low to moderate angles of attack and at $M_\infty \geq 2$. As Mach numbers decrease below about 2.5, the SOSET becomes increasingly inaccurate until about $M_\infty = 1.5$, where the accuracy is generally unacceptable. This applicable Mach number range is very complimentary to the Hybrid Theory of Van Dyke where the accuracy is best between $1.2 \leq M_\infty \leq 2.5$.

4.3 Modified Newtonian Theory (MNT)¹⁶

Newtonian Impact Theory assumes that, in the limit of high Mach number, the shock lies on the body. This means that the disturbed flow field lies in an infinitely-thin layer between the shock and body. Applying the laws of conservation of mass and momentum across the shock yields the result that density behind the shock approaches infinite values and the ratio of specific heats approaches unity. The pressure coefficient on the surface becomes¹⁶

$$C_p = 2 \sin^2 \delta_{eq} \quad (12)$$

where δ_{eq} is the angle between the velocity vector and a tangent to the body at the point in question (see Figure 4-3). δ_{eq} is defined by:

$$\sin(\delta_{eq}) = \sin \vartheta \sin \alpha - \sin \alpha \cos \vartheta \cos \theta \quad (13)$$

Lees¹⁶ noted that a much more accurate prediction of pressure on the blunt-nose body could be obtained by replacing the constant "2" in Equation (12) with the stagnation pressure coefficient C_{p_0} . C_{p_0} can be calculated from:

$$C_{p_0} = \frac{2}{\gamma M_\infty^2} \quad (14)$$

$$\left\{ \left[\frac{(\gamma + 1)M_\infty^2}{2} \right]^{\frac{\gamma}{\gamma-1}} \left[\frac{\gamma + 1}{2\gamma M_\infty^2 - (\gamma - 1)} \right]^{\frac{1}{\gamma-1}} - 1 \right\}$$

MNT is thus defined by:

$$C_p = C_{p_0} \sin^2 \delta_{eq} \quad (15)$$

Equation (15) allows the calculation of the pressure coefficient all along the blunt surface of a missile nose or wing leading edge for a perfect gas where C_{p_0} is given by Equation (14) and $\sin \delta_{eq}$ from Equation (13).

Experience has shown that the MNT gives very acceptable estimates of pressure coefficient on the blunt portion of a nose or leading edge, even at Mach numbers where the assumptions of Newtonian Impact Theory are violated.

4.4 Hybrid Theory of Van Dyke Combined With Modified Newtonian Theory (HTVD/MNT)¹

As noted in the discussion on the Hybrid Theory, it is limited to conditions where the body slope is less than the local Mach angle. This means it is not applicable in the nose region of a blunt missile. On the other hand, MNT gives very acceptable estimates of pressure coefficients in the nose region, even for low supersonic Mach numbers where the assumptions, inherent in the Newtonian Impact Theory, are violated. Moore was the first to recognize the possibility of combining these two theories. The key to the successful combination was in the starting solution. At low supersonic Mach numbers, the pressure overexpands on a blunt nose tip as it proceeds around the blunt portion from the stagnation point to the given portion of the nose. In order to capture this overexpansion, Moore found that it was necessary to start the HTVD near its maximum acceptable slope and allow the pressure to expand around the surface.¹ Simultaneously, the MNT was started at the stagnation point and allowed to expand until the pressure coefficients of the MNT and the HTVD were equal. This was defined as the Match point. Upstream of the Match point, MNT was used in the force and moment calculations, whereas downstream, HTVD was used. Figure 4-4 is an illustration of the boundaries of perturbation and Newtonian theories. Figure 4-5 illustrates the capability of this theory to accurately predict pressure coefficients

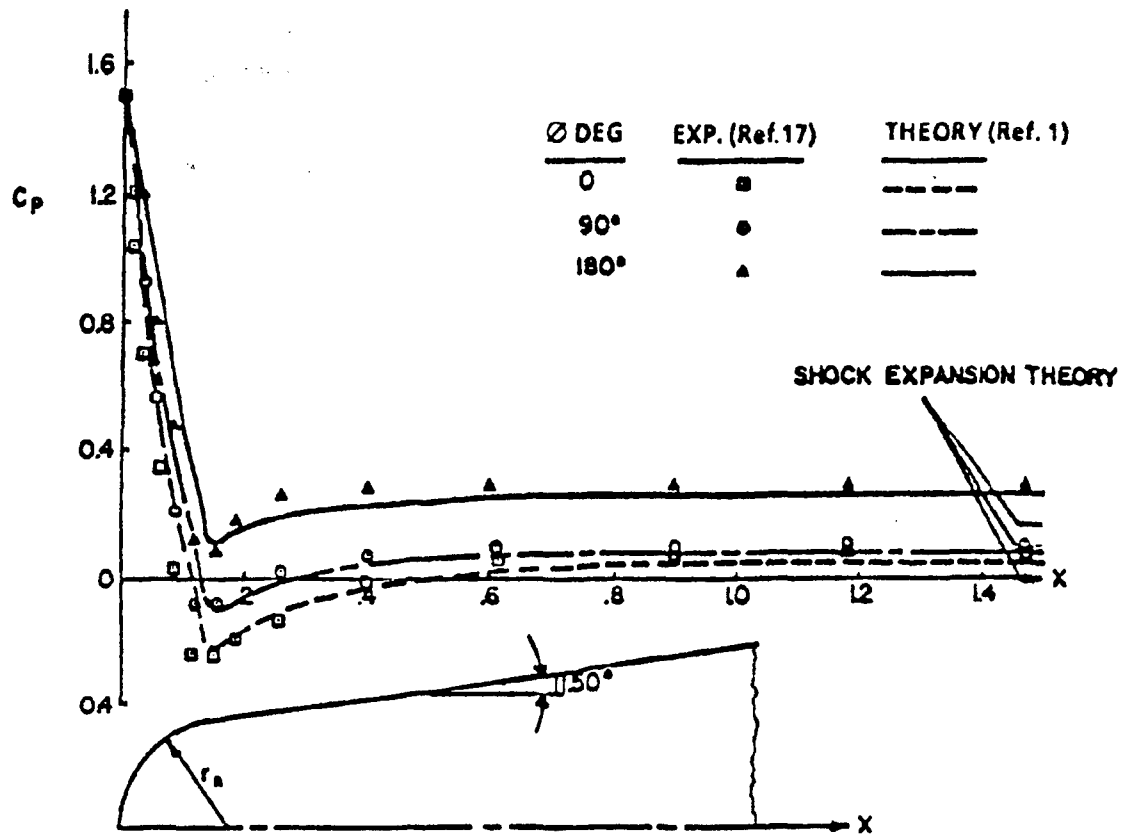


FIGURE 4-5. COMPARISON OF THEORY AND EXPERIMENT FOR BLUNTED CONE

$$\frac{r_n}{r_B} = 0.35, M_\infty = 1.5, \alpha = 8^\circ, \theta_c = 11.5^\circ$$

on a 35 percent blunt cone of 11.5° half angle at $\alpha = 8^\circ$ and at $M_\infty = 1.5$. Note the excellent agreement of the combined theory all along the surface at $M_\infty = 1.5$. Particularly impressive is its ability to capture the overexpansion region around $x = 0.1$ to $x = 0.4$. Also, note that SOSET gives fairly poor estimates at $M_\infty = 1.5$. On the other hand, at $M_\infty = 2.96$ (while the results are not shown), the HTVD/MNT is no better (and maybe slightly worse) than the SOSET/MNT, which will be discussed next.

To the author's knowledge, the HTVD/MNT remains the only accurate engineering method to estimate low supersonic Mach number aerodynamics for blunt and sharp tip bodies of revolution. Attempts were made to extend the SOSET/MNT down to the low supersonic Mach number range, but without success.

4.5 Second-Order-Shock-Expansion Theory Combined with Modified Newtonian Theory (SOSET/MNT)^{17,18}

Jackson et al.¹⁷ combined SOSET with MNT to treat blunt-nosed configurations with or without flares. Jackson et al.,¹⁷ like Syvertson and Dennis,¹⁴ assumed that the lifting properties could be predicted by assuming that the original body is made up of several equivalent bodies of revolution represented by the various meridians (see Figure 4-6). They assumed the match point between the MNT and second-order shock pressure prediction to be the angle that corresponds to shock detachment on a wedge with the given freestream Mach number.

De Jarnette et al.¹⁸ made significant improvements to the work of Jackson et al.¹⁷ and Syvertson.¹⁴ These new improvements included the following:

1. An exact (as opposed to an approximate) expression for the pressure gradient downstream of a corner.
2. A new expression for pointed-cone pressures at angle of attack which improves the initial pressure prediction over that of tangent cone theory.
3. A new technique for calculating pressures on bodies at incidence.

The pressure computations at angle of attack, showed improvement over the method of Jackson.¹⁷ De Jarnette, et al.¹⁸ derived a new expression for pointed-cone pressure at $\alpha > 0$ by combining Slender Body Theory, Newtonian Theory, and an approximate expression for $C_{p_{\alpha=0}}$ to give:

$$C_p(\alpha, \theta, e, M) = C_{p_{\alpha=0}} + \Delta C_p \quad (16a)$$

where

$$\Delta C_p = -\sin 2\alpha \sin 2\theta \cos \Phi + \sin^2 \alpha \cos^2 \theta \quad (16b)$$

$$\left[\left(2 - \frac{1}{\beta} \right) (1 - \tan^2 \theta) - \left(2 + \frac{2}{\beta} \right) \sin^2 \Phi \right]$$

$$C_{p_{\alpha=0}} = \sin^2 \theta_c \quad (16c)$$

$$\left[1 + \frac{(\gamma + 1)K^2 + 2}{(\gamma - 1)K^2 + 2} \ln \left(\frac{\gamma + 1}{2} + \frac{1}{K^2} \right) \right]$$

and

$$K^2 = (M_\infty^2 - 1) \sin^2 \theta_c$$

Note also, that while Equation (16) was strictly defined for pointed cone pressures at angle of attack, it could also be used in a Tangent cone sense to obtain pressures at any point on a body surface. De Jarnette actually used loading functions to obtain body alone lift properties, however.¹⁸

Figure 4-7 presents results of De Jarnette et al.¹⁸ compared to experiment. The case chosen is the same configuration of Figure 4-5, except here, the method of De Jarnette et al.¹⁸ is used versus Jackson et al.¹⁷ in Figure 4-5. It is seen that the theory of De Jarnette et al.¹⁸ does show good results for pressure prediction and therefore forces and moments as well.

4.6 Allen-Perkins Viscous Crossflow Theory¹⁹

A fairly simple, yet quite powerful, method for computing body-alone nonlinear aerodynamics was introduced by Allen-Perkins.¹⁹ Allen reasoned that the total force on an inclined body of revolution is equal to the potential term discussed previously plus a cross flow term. This term is based on the drag force experienced by an element of a circular cylinder of the same diameter in a stream moving at the cross component of the stream velocity, $V_\infty \sin \alpha$. This crossflow term is primarily created by the viscous effects of the fluid as it flows around the body, often separating and creating a nonlinear normal force coefficient. In equation form, the so called viscous crossflow theory is:

$$C_{N_{NL}} = \eta C_{d_c} \left(\frac{A_p}{A_{ref}} \right) \sin^2 \alpha \quad (17)$$

Here η is the drag proportionality factor or crossflow drag of a cylinder of finite length to one of infinite length. C_{d_c} is the crossflow drag coefficient. Also, the crossflow theory assumes the center of pressure of the nonlinear term is at the centroid of the planform area. Generally, the total center of pressure is a weighted average of the linear and nonlinear components of normal force. That is

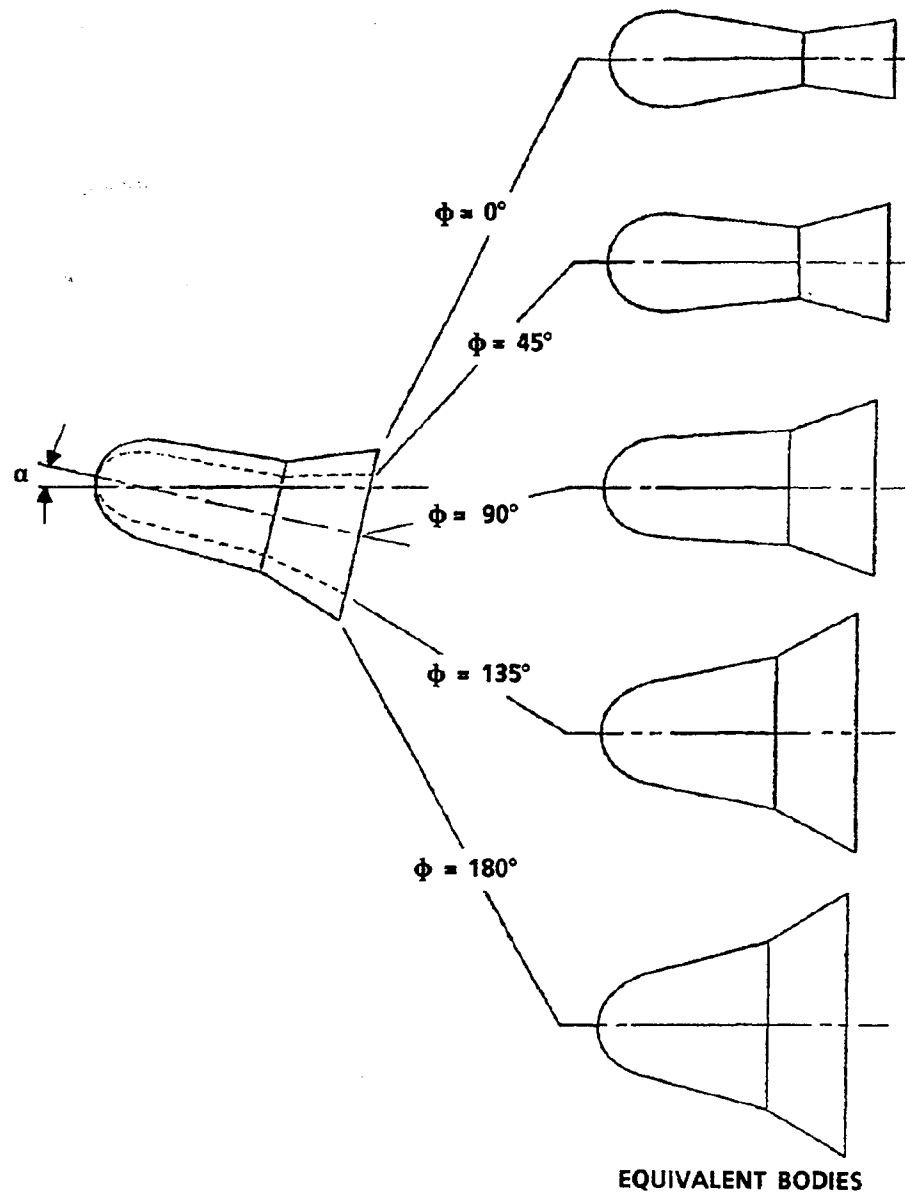


FIGURE 4-6. TYPICAL EQUIVALENT BODY SHAPES USED FOR COMPUTING LIFTING PROPERTIES WITH SECOND-ORDER SHOCK EXPANSION THEORY

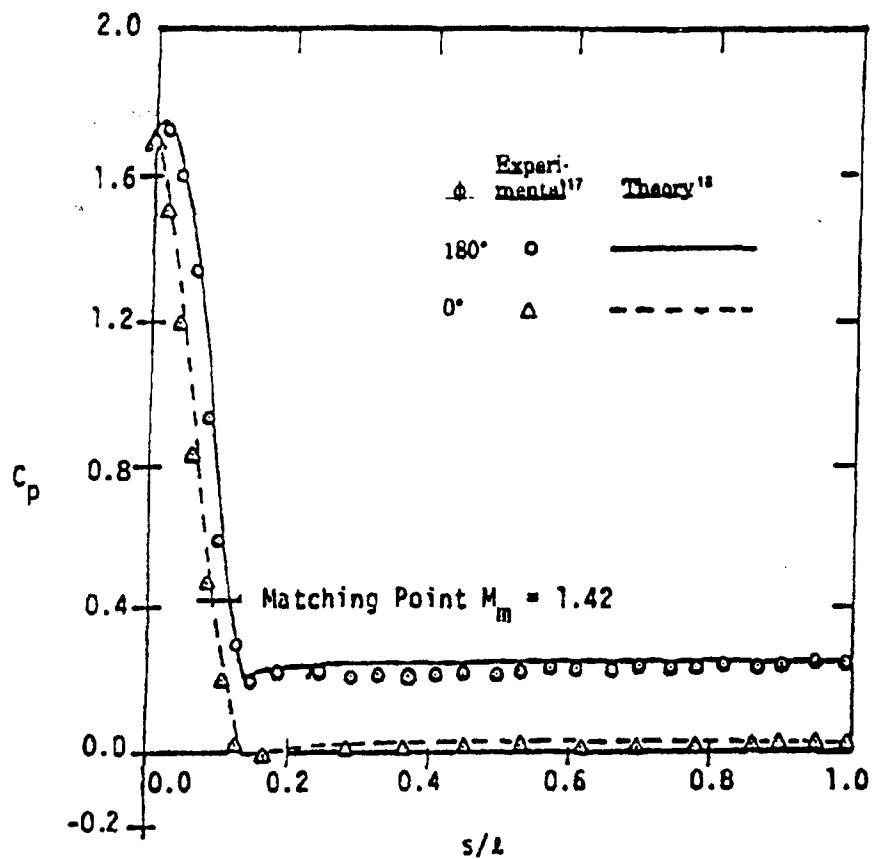


FIGURE 4-7. PRESSURE DISTRIBUTION ON A BLUNTED NOSE

$$\frac{r_n}{r_B} = 0.35, M_\infty = 2.96, \alpha = 8^\circ, \theta_c = 11.5^\circ$$

$$X_{cp} = \frac{(X_{cp})_{NL} C_{N_{NL}} + (X_{cp})_L C_{N_L}}{C_{N_{NL}} + C_{N_L}} \quad (18)$$

The pitching moment about a given point X_0 is then

$$C_M = -C_N(X_{cp} - X_0) \quad (19)$$

The original work of Allen did not include compressibility effects in η but Reynolds number effects were shown in C_{d_c} at low crossflow Mach numbers.

4.7 Van Driest II Method For Skin Friction Drag²⁰

Another powerful, yet simple, method for performing aerodynamic computations, is the Van Driest II method for computing skin-friction drag. This method, as derived, is based on two dimensional turbulent boundary layer flow. Strictly speaking, it is only applicable to regions of flow on the lifting surfaces where the flow is turbulent, two dimensional, and the viscous region is primarily confined to a thin layer near the surface (boundary layer). In practice, however, it has been applied to two and three dimensional surfaces with success.

The turbulent mean skin-friction coefficient according to Van Driest²⁰ is:

$$\frac{0.242 (\sin^{-1} C_1 + \sin^{-1} C_2)}{A(C_{f_w})^{1/2} (T_w/T_\infty)^{1/2}} = \quad (20a)$$

$$\log_{10}(R_{e_w} C_{f_w}) - \left(\frac{1+2n}{2} \right) \log_{10}(T_w/T_\infty)$$

where

$$C_1 = \frac{2A^2 - B}{(B^2 + 4A^2)^{1/2}} \quad ; \quad C_2 = \frac{B}{(B^2 + 4A^2)^{1/2}}$$

and

$$A = \left[\frac{(\gamma-1)M_\infty^2}{2 \frac{T_w}{T_\infty}} \right]^{1/2} \quad ; \quad B = \frac{1+(\gamma-1)/2M_\infty^2}{T_w/T_\infty} - 1$$

The variable n of Equation (20a) is the power in the power viscosity law:

$$\frac{\mu}{\mu_\infty} = \left(\frac{T_w}{T_\infty} \right)^n \quad (20b)$$

The freestream Reynolds number and adiabatic wall temperature are given by:

$$R_{e_\infty} = \frac{\rho_\infty V_\infty \ell}{\mu_\infty} \quad (21)$$

$$\frac{T_w}{T_\infty} = 1 + 0.9 \frac{\gamma-1}{2} M_\infty^2 \quad (22)$$

Equations (20) through (22) allow the calculation of the mean turbulent skin-friction over the entire body or wing area. The skin-friction axial force coefficient on each component is then:

$$C_{A_f} = C_{f_w} \frac{A_{wet}}{A_{ref}} \quad (23)$$

where A_{wet} is the surface area of the component in question.

For most flows, a portion of the flow is laminar. An approximation to the mean skin-friction coefficient for laminar flow can be obtained from reference 20:

$$C_{f_l} = \frac{1.328}{\sqrt{R_e}} \quad (24)$$

Here the Reynolds number is based on the distance where transition occurs rather than the reference length, as was the case for Equation (21).

The point where transition occurs is dependent on many factors. Experience has shown, for flight vehicles, a transition Reynolds number of 1×10^6 for the body and 0.5×10^6 for the wings gives acceptable numbers. For wind tunnel models without a trip, a transition Reynolds number of 3 to 5 million is more reasonable due to a smooth surface. If a boundary layer trip is used, the entire configuration component should have turbulent flow.

4.8 Lifting Surface Theory²¹

Lifting Surface Theory refers to the solution of the flow over a three dimensional wing where the distribution of pressure is allowed to vary in both the spanwise and chordwise direction. The fundamental equation is the three dimensional perturbation equation, here written in rectangular coordinates, as:

$$(1-M_\infty^2) \Phi_{xx} + \Phi_{yy} + \Phi_{zz} = 0 \quad (25)$$

The Flow tangency boundary condition requires:

$$\left. \begin{aligned} \Phi_z &= \frac{\partial z_u}{\partial x} \text{ at } z = 0^+ \\ \Phi_z &= \frac{\partial z_l}{\partial x} \text{ at } z = 0^- \end{aligned} \right\} \text{ for } (x,y) \text{ on } S \quad (25a)$$

If the wing thickness is neglected and we limit ourselves to missiles, then wing chamber can also be neglected. Then the boundary conditions in Equation (25a) become:

$$\Phi_z = -\alpha \quad (25b)$$

for both the upper and lower surfaces.

In addition to this boundary condition, the Kutta condition (which requires the velocity on the upper and lower surfaces at the trailing edge to be equal) is also imposed for subsonic flow.

The assumptions involved in the Lifting Surface Theory, as applied to most missile configurations, are therefore small perturbations in the flow due to the presence of the wing and the thickness and chamber effects are zero or small compared to angle of attack effects.

Equation (25) may be simplified somewhat by using the Prandtl-Glauert rule (72) to relate the compressible subsonic normal force or pitching moment to the incompressible case. That is:

$$(C_N)_{M_{AR,\alpha}} = \frac{(C_N)_{0,AR,\alpha}}{\sqrt{1 - M_\infty^2}} \quad (26)$$

$$(C_M)_{M_{AR,\alpha}} = \frac{(C_M)_{0,AR,\alpha}}{\sqrt{1 - M_\infty^2}}$$

Using the above relations, the normal force and pitching moment on a given wing at any subsonic Mach number may be found by calculating the aerodynamics of the same wing at zero Mach number.

For $M_\infty = 0$, Equation (25) reduces to Laplace's equation

$$\nabla^2 \Phi = 0 \quad (27)$$

with boundary condition (25b).

There are many methods to solve Equation (27). The one used here is that of Chadwick et al.,²¹ which closely follows Ashley et al.²² The velocity potential Φ is given by:

$$\Phi(x,y,z) = -\frac{1}{8\pi} \iint_S \frac{\Delta C_p(x_1,y_1)}{(y-y_1)^2+z^2} \left[1 + \frac{x-x_1}{\sqrt{(x-x_1)^2+(y-y_1)^2+z^2}} \right] dx_1 dy_1 \quad (28)$$

Here, x_1, y_1 are coordinates of an element of the lifting surface that has a differential pressure coefficient of ΔC_p between the lower and upper surfaces at this point (x_1, y_1) . It is required to determine the pressure loading over the entire surface. Following Chadwick,²¹ Equation (28) is first differentiated with respect to z and the limit as $z \rightarrow 0$ taken. The result is then equated to the boundary condition, Equation (25b) to obtain: The cross on the y_1 integral indicates a singularity at $y = y_1$, in which case Mangler's principal-value technique²² can be applied. The details of the solution of the integral Equation (29) for $\Delta C_p(x,y)$ will not be

$$\alpha(x_1,y_1) = \frac{1}{8\pi} \iint \frac{\Delta C_p(x_1,y_1)}{(y-y_1)^2} \left[1 + \frac{x-x_1}{\sqrt{(x-x_1)^2+(y-y_1)^2}} \right] dx_1 dy_1 \quad (29)$$

repeated here as they are given in detail in many references (see for example, Chadwick²¹). Worthy of note, however, is the fact that Equation (29) is an integral equation for which the wing loading ΔC_p is to be found as a linear function of angle of attack. This wing loading is first approximated by a series expansion with a set of unknown coefficients of number equal to the number of surface elements on the wing planform. That allows each ΔC_p to be influenced by all other elements of the wing. The unknown coefficients in each ΔC_p series are found by solution of an inverse matrix. $\Delta C_p(x,y)$ is then calculated.

Once the span loading $\Delta C_p(x,y)$ is known over the entire wing surface, the normal force at a given spanwise location is:

$$c_n = \frac{1}{c} \int_{x_{LE}}^{x_{TE}} \Delta C_p dx \quad (30)$$

The total normal force for the entire wing is:

$$C_N = \frac{2}{S_{ref}} \int_0^{b/2} cc_n dy \quad (31)$$

The pitching moment of a given airfoil section, about the point where the wing leading edge intersects the body, is then (positive leading edge up):

$$c_m = -\frac{1}{c l_{ref}} \int_{x_{LE}}^{x_{TE}} x \Delta C_p dx \quad (32)$$

The total pitching moment becomes:

$$C_M = \frac{2}{S_{ref}} \int_0^{b/2} cc_m dy \quad (33)$$

If it is desired to calculate the pitching moment about some other reference point, then

$$C_{M_o} = C_M + C_N \frac{x_o}{l_{ref}} \quad (34)$$

where x_o is the distance from the reference point to the juncture of the wing leading edge with the body. The center of pressure of an airfoil section is:

$$x_{CP} = -\frac{c_m}{c_n} \quad (35)$$

or of the entire wing

$$x_{CP} = -\frac{C_M}{C_N} \quad (36)$$

Finally, the spanwise center of pressure of a wing semispan is:

$$y_{CP} = \frac{\int_0^{b/2} cc_n y dy}{\int_0^{b/2} cc_n dy} \quad (37)$$

Equations (30), (31), (32), (33), and (37) can be solved by numerical quadrature, such as Simpson's rule, with special attention given to the leading edge singularity.

It should also be mentioned that if one is interested in dynamic derivatives,²³ these aerodynamics can be obtained by a modification to the boundary condition, Equation (25a). That is, for rolling and pitching motions, the angle of attack in Equation (25a) is replaced by:

$$\alpha(x,y) = \alpha_o + \frac{py}{V_\infty} + \frac{q(x-x_{ref})}{V_\infty} \quad (38)$$

Equation (27) is a linear partial differential equation so that solutions can be combined together in a linear fashion. This means, for roll damping, simply set $\alpha_o = q = 0$ and the boundary condition is

$$\alpha(x,y) = \frac{py}{V_\infty} \quad (38a)$$

Likewise, for pitch damping, $\alpha_o = p = 0$ and

$$\alpha(x,y) = \frac{q(x-x_{ref})}{V_\infty} \quad (38b)$$

4.9 Three Dimensional Thin Wing Theory²²

Three Dimensional Thin Wing Theory (TDTWT) is quite similar to lifting surface theory (LST) in the sense the same perturbation Equation (25) is used. The only difference is that TDTWT is normally used to represent the supersonic flow solutions of Equation (25) versus LST for the subsonic solutions. Since, for supersonic flow, solutions to Equation (25) are hyperbolic versus elliptic for the subsonic case, they generally are easier to obtain. This is because no upstream influence is felt by a disturbance at a given point on the wing surface. In contrast, the subsonic solutions required a matrix inversion at each wing element to determine the unknown coefficients used to determine the pressure differential from lower to upper surfaces. On the other

hand, the assumptions of TDTWT are the same as for LST. They both assume small perturbations in an isentropic flow. The isentropic flow assumption means no shock waves are allowed.

In contrast to the body solutions generated by Van Dyke, adequate wing solutions can be obtained at higher Mach numbers. This is because of the low slopes present on most wing planforms (thickness is generally very small), the wing frontal area is generally less than 10 percent of the body frontal area, and in the region of leading edge bluntness, where perturbation theory is invalid, modified Newtonian Theory is used for wave drag calculation.

The most general boundary conditions for Equation (25) in supersonic flow are the flow tangency condition specified by

$$\frac{w(x,y)}{V_\infty} = \Phi_z = \frac{\partial F}{\partial X} = \quad (39)$$

$$\left(\frac{dz}{dx}\right)_{x,y} + \alpha + \frac{py}{V_\infty} + \frac{q(x-x_{ref})}{V_\infty} + \dot{\alpha}t$$

and the perturbation velocities must vanish upstream from the point where the disturbance originates. Mathematically, this can be stated in the form

$$u(o^-,y,z) = v(o^-,y,z) = w(o^-,y,z) = 0 \quad (40)$$

Since Equation (25) is linear, individual solutions can be added together. This allows individual treatment of the Equation (39) boundary condition for drag, lift, roll and pitch damping computations. For wave drag calculations, only the first term of Equation (39) is retained and the other terms are set to zero. For lift calculations, the angle of attack α is retained and the other terms set to zero. For roll damping, the third term of Equation (29) is retained and the other terms set to zero. For pitching rate, the q term of Equation (39) is retained and the other terms set to zero. Finally, for a constant vertical acceleration, the last term is retained and the other four terms set to zero. Pitch damping moment, $C_{M_q} + C_{M_{\dot{\alpha}}}$, normally refers to the sum of the terms due to a constant pitch rate and constant vertical acceleration.

The solution to Equation (25), using the first term of Equation (39) as the boundary condition, will give the axial force coefficient of a sharp wing. If the leading edge is blunt, MNT is used in conjunction with perturbation theory. The general solution to Equation (25) is:²²

$$\Phi(x, y, 0) = -\frac{w(x, y)}{\pi} \int \int_R \frac{dx_1 dy_1}{\sqrt{(x-x_1)^2 - \beta^2(y-y_1)^2}} \quad (41)$$

The pressure coefficient at any point on the wing surface is

$$C_p = -2\Phi_x(x, y, 0) \quad (42)$$

The perturbation velocity Φ_x , at a given point p , is dependent on the location of the point with respect to the line of sources and sinks which generates the wing leading edge or other discontinuity and whether this point is in a subsonic or supersonic flow region. For example, referring to Figure 4-8A, if point P is at P_1 , and the wing generator is a subsonic source or sink line (SOSL), then

$$\Phi_x = -\frac{2w(x_{p1}, y_{p1})}{\pi\beta\sqrt{\eta^2-1}} \cosh^{-1} \sqrt{\frac{\eta^2-1}{\sigma^2-1}} \quad (43)$$

where w is determined from the boundary condition and is (for the airfoil section at $y = y_{p1}$):

$$w(x_{p1}, y_{p1}) = \left. \frac{dz}{dx} \right|_{x=x_{p1}}$$

In Equation (43), the definitions

$$\eta = \frac{k}{\beta}$$

$$k = \tan \Lambda \quad (43a)$$

$$\sigma = \frac{ky_p}{x_p}$$

have been used. If $P = P_2$, the induced velocity at P_2 due to a given SOSL is:

$$\Phi_x = -\frac{2w(x_{p2}, y_{p2})}{\pi\beta\sqrt{\eta^2-1}} \cosh^{-1} \sqrt{\frac{\eta^2-\sigma^2}{1-\sigma^2}} \quad (44)$$

At the wing tip, there is an additional disturbance within the Mach line emanating from the tip leading edge (Figure 4-8B). The induced velocity in this region, $P = P_3$ is:

$$\Phi_x = -\frac{w(x_{p3}, y_{p3})}{\pi\beta\sqrt{\eta^2-1}} \cosh^{-1} \left[\frac{\eta^2+|\sigma|}{\eta(|\sigma|+1)} \right] \quad (45)$$

The absolute value of σ is taken because σ is actually negative for the point P_3 . The induced velocity at any point, say $P = P_4$, outside of the Mach lines emanating from the beginning of the SOSL is zero since this point is out of the zone of influence.

If the wing generator is supersonic, the Mach lines from point 0 in Figure 4-9A lie behind the SOSL. If in Figure 4-9A, $P = P_1$, then the induced velocity at P_1 due to the disturbance caused by the SOSL is:²⁴

$$\Phi_x = -\frac{w(x_{p1}, y_{p1})}{\beta\sqrt{1-\eta^2}} \quad (46)$$

If $P = P_2$, the induced velocity is

$$\Phi_x = -\frac{w(x_{p2}, y_{p2})}{\pi\beta\sqrt{1-\sigma^2}} \left[\pi - 2\sin^{-1} \sqrt{\frac{\eta^2-\sigma^2}{1-\sigma^2}} \right] \quad (47)$$

Referring to Figure 4-9B, the additional induced velocity inside the area bounded by the tip and the Mach line emanating from the tip ($P = P_3$) is:

$$\Phi_x = -\frac{w(x_{p3}, y_{p3})}{\pi\beta\sqrt{1-\eta^2}} \cos^{-1} \left[\frac{|\sigma|+\eta^2}{\eta(1+|\sigma|)} \right] \quad (48)$$

Again, if $P = P_4$, the point is out of the zone of influence of the SOSL and thus the induced velocity is zero.

The induced velocity at a given point on any wing geometry can now be computed by the proper superposition of the triangular SOSL shown in Figures 4-8 and 4-9. This is because of the linear nature of the governing flow-field Equation (1). As an example of how the above superposition principle works, consider the wing shown in Figure 4-10. For simplicity, the slopes χ_1 and χ_2 are constant. The wing AHJD can be represented by the superposition of five SOSL. The first has the planform AEH and source intensity:

$$w(x_p, y_p) = V_\infty \chi_1 \quad (49)$$

where χ_1 is the slope of the segment AB. The second has the planform BIF and intensity

$$w(x_p, y_p) = (\chi_2 - \chi_1) V_\infty \quad (50)$$

and the third has the planform DJG and intensity

$$w(x_p, y_p) = -\chi_2 V_\infty \quad (51)$$

The other two SOSL represent the tip effects. They are the planforms HJL and IJL and have source intensities of opposite signs than those representing the wing.

The above procedure can be applied to a wing of general planform. The only difference is that for each point in question, the slope is not constant as was the case in the simplified example. Then for some general point located on the wing surface, the total induced velocity due to all sources and sinks is found by applying one of the Equations (43) through (48) for each SOSL. The particular equation applied depends upon the location of the point relative to the SOSL and

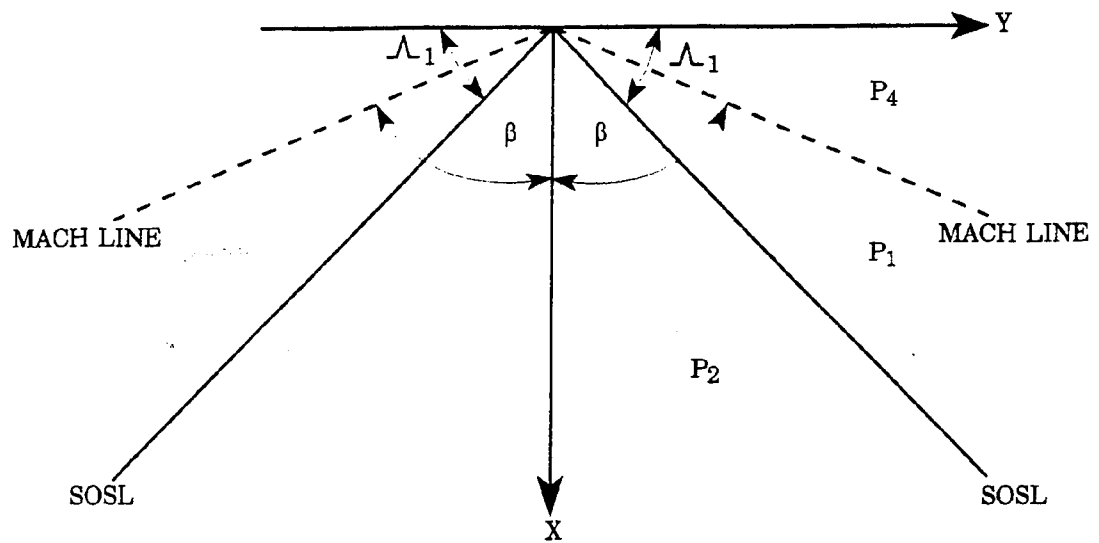


FIGURE 4-8A. TRIANGULAR SURFACE SYMMETRIC ABOUT X AXIS FOR SUBSONIC SOSL

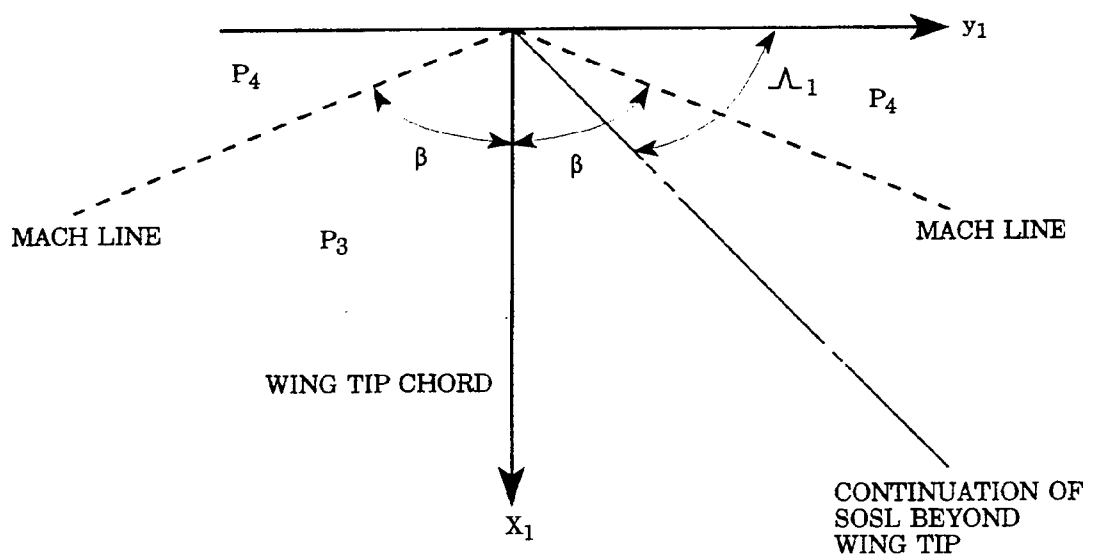


FIGURE 4-8B. WING TIP EFFECTS FOR SUBSONIC SOSL

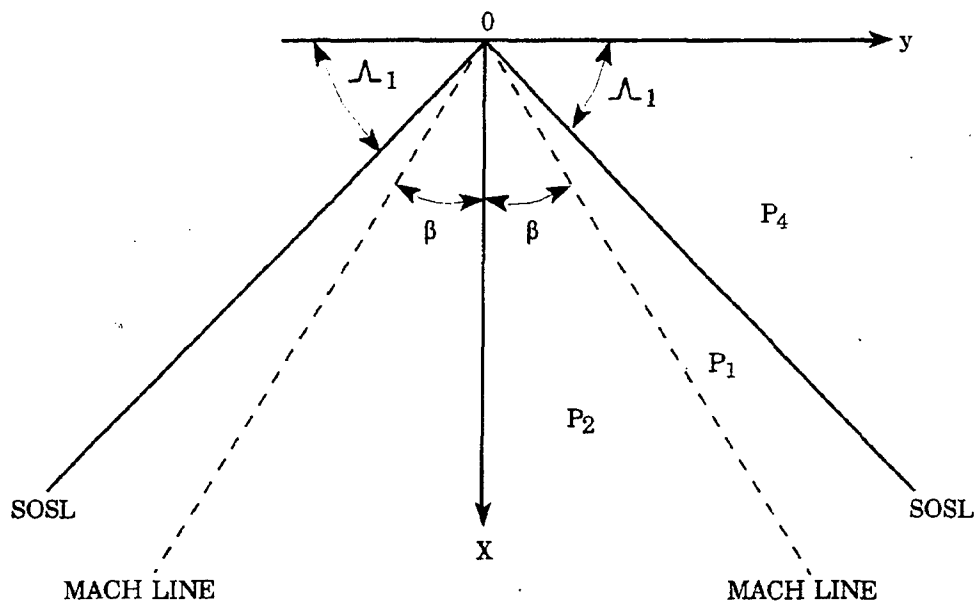


FIGURE 4-9A. TRIANGULAR SURFACE SYMMETRIC ABOUT X AXIS FOR SUPERSONIC SOSL

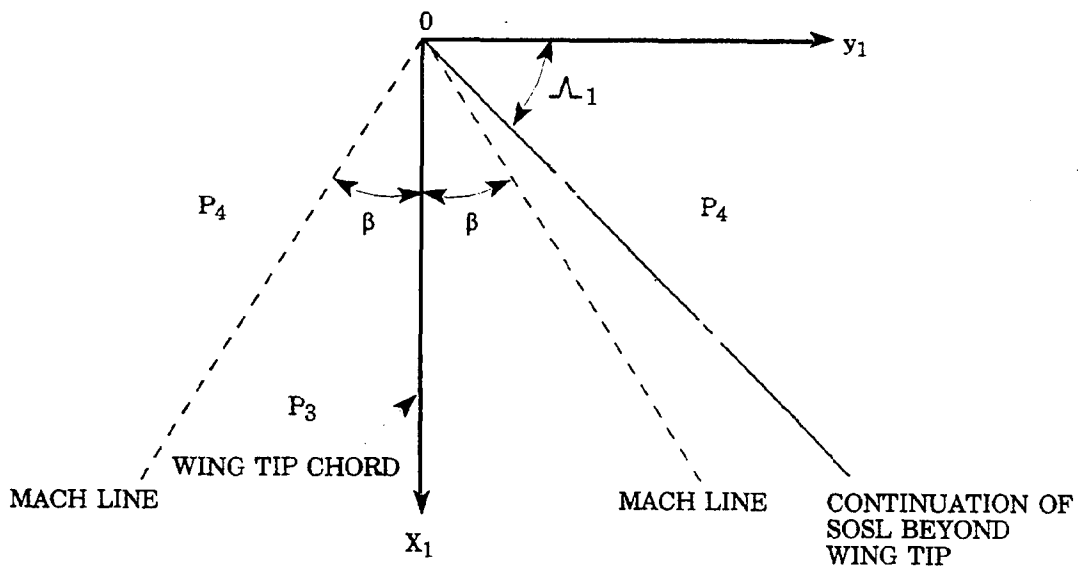


FIGURE 4-9B. WING TIP EFFECTS FOR SUPERSONIC SOSL

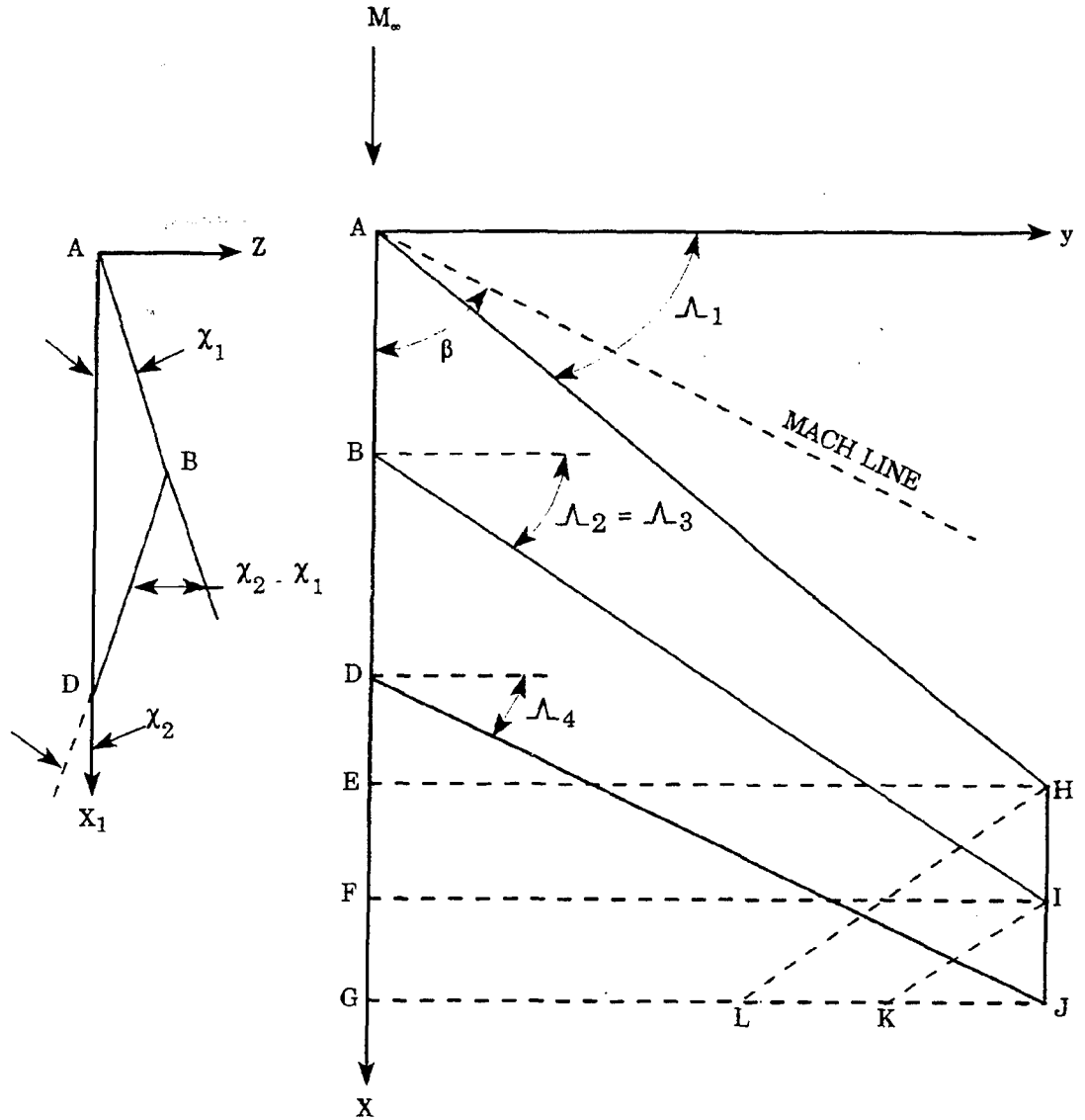


FIGURE 4-10. LINEAR SUPERPOSITION OF TRIANGULAR SOURCE AND SINK DISTRIBUTIONS

the Mach line as discussed earlier. These individual contributions are then summed to get the total induced velocity. Knowing the total induced velocity at a point allows one to calculate the pressure coefficient at the given point by Equation (42).

The pressure coefficient can be calculated at a given number of spanwise and chordwise locations. The drag of a given airfoil section at the spanwise station $y = y_A$ is then

$$c_d = \frac{2}{c(y_A)} \int_0^c (y_A) C_p(x, y_A) w(x, y_A) dx \quad (52)$$

The total drag for one fin of semispan $b/2$ is then:

$$C_D = \frac{1}{S_w} \int_0^{b/2} c_d c(y) dy \quad (53)$$

where $S_w = b/2(c_i + c_o)$. For cruciform fins, the total drag coefficient is:

$$C_D = \frac{4}{S_w} \int_0^{b/2} c_d c(y) dy \quad (54)$$

If it is desired to base the drag coefficient on the body cross-sectional area, the Equation (54) must be multiplied by the factor S_w/S_{ref} .

Equations (52) and (54) can be integrated by numerical quadrature if the generators of the wing surface are supersonic. If the generators are subsonic, linear theory indicates the pressure coefficients go to infinity at the wing generators. Physically, this cannot be true which means that for a subsonic SOSL, linear theory is not valid at the SOSL. The reason is that the velocity perturbations in the vicinity of the discontinuities are no longer small, violating one of the assumptions in linear theory. However, the velocity perturbations are small a slight distance from the SOSL so that linear theory can be applied. Numerical experiments indicated a distance of five thousandths of the chord length from the SOSL is sufficient and the value of pressure calculated at this point can be assumed to exist up to the SOSL.

The analysis using TDTWT has been illustrated for the axial force computation using the first term of the boundary condition of Equation (39). A very similar process is used for the lift, roll and pitch damping computations. The reader is referred to references 2 and 4 for the practical application of the theories for these force or moment components. Time will not permit the many applications of TDTWT.

4.10 Slender Body and Linear Theory For Interference Lift Computation²⁵

The method almost universally used for including interference between the various missile components into approximate aeroprediction codes is that due to Pitts, et al.²⁵ There are three primary types of interference lift (note that lift and normal force are used

interchangeably here) to be concerned with. These are the effects on the wing due to the presence of the body, the effect on the body due to the presence of a wing, and finally, the effect on an aft lifting surface due to wing or body shed vortices. Wing to wing or shock wave interference will not be discussed at present.

To better understand the interference lift components, it is instructive to examine the total normal force of a configuration as defined by Pitts et al.²⁵ This is given by

$$C_N = C_{N_B} + [(K_{W(B)} + K_{B(W)})\alpha + (k_{W(B)} + k_{B(W)})\delta_w](C_{N_\alpha})_W \quad (55)$$

$$+ [(K_{T(B)} + K_{B(T)})\alpha + (k_{T(B)} + k_{B(T)})\delta_T](C_{N_\alpha})_T + C_{N_{TV}} + C_{N_{BV}}$$

The first term in Equation 55 is the normal force of the body alone including the linear and nonlinear components; the second term is the contribution of the wing (or canard) including interference effects and control deflection; the third term is the contribution of the tail including interference effects and control deflection; and the last term is the negative downwash effect on the tail or body due to wing shed or body shed vortices. The K 's represent the interference of the configuration with respect to angle of attack, and the k 's represent the interference with respect to control deflection. Each of these interference factors is estimated by slender body or linear theory.²⁵ As such, they are independent of angle of attack.

The various interference factors, as defined by slender body theory (SBT), are:²⁵

$$K_{W(B)} = 2/\pi \left\{ \frac{(1+r^4/s^4) \left[\frac{1}{2} \tan^{-1} \frac{1}{2}(s/r-r/s) + \pi/4 \right]}{(1-r/s)^2} \right. \quad (56)$$

$$\left. - \frac{r^2/s^2 [(s/r-r/s) + 2 \tan^{-1}(r/s)]}{(1-r/s)^2} \right\}$$

$$K_{B(W)} = (1+r/s)^2 - K_{W(B)} \quad (57)$$

$$k_{W(B)} = \frac{1}{\pi^2} \left\{ \frac{\pi^2 (s/r+1)^2}{4 (s/r)^2} + \frac{\pi [(s/r)^2+1]^2}{(s/r)^2 (s/r-1)^2} \sin^{-1} \right.$$

$$\left. \left[\frac{(s/r)^2-1}{(s/r)^2+1} \right] - \frac{2\pi (s/r+1)}{s/r(s/r-1)} + \frac{[(s/r)^2+1]^2}{(s/r)^2 (s/r-1)^2} \right. \quad (58)$$

$$\left. \left(\sin^{-1} \left[\frac{(s/r)^2-1}{(s/r)^2+1} \right] \right)^2 - \frac{4(s/r+1)}{s/r(s/r+1)} \sin^{-1} \right.$$

$$\left. \left[\frac{(s/r)^2-1}{(s/r)^2+1} \right] + \frac{8}{(s/r-1)^2} \log \left[\frac{(s/r)^2+1}{2s/r} \right] \right\}$$

$$k_{B(W)} = K_{W(B)} - k_{W(B)} \quad (59)$$

Figure 4-11 plots the interference lift factors given by Equations (56) through (59) as a function of the body radius to wing semispan plus body radius ratio (r/s).

As the Mach number increases supersonically, SBT gives values of $K_{B(W)}$ which are too high if the wing is near the missile rear. This is because much of the carryover lift onto the body is actually lost to the wake of the vehicle. Figure 4-12 illustrates this for the no afterbody, infinite afterbody, and short afterbody cases. Linear theory formulations are available for the infinite and no afterbody cases to replace Equation (57) if the parameter

$$\beta AR(1+\lambda)[1/(m\beta)+1]>4 \quad (60)$$

Moore² then linearly interpolated between the infinite and no afterbody cases as a function of the area covered by the Mach lines to obtain $K_{B(W)}$ for the short afterbody case.

Strictly speaking, the methodology discussed here is limited to slender bodies with triangular planforms of low aspect ratio. Experience has shown, that if the correct value of wing-alone lift is computed, the interference factors can give very reasonable results for wings which do not have triangular planforms or even have low aspect ratio. Moore² showed how an engineering estimate of interference lift could be obtained, even for planforms such as that shown in Figure 4-13A. The actual SBT configuration is that shown in Figure 4-13B. Since most of the interference lift occurs near the wing body juncture, reference 2 used approximations given by Equation (61)

$$\begin{aligned} [K_{B(W)}]_{II} &= [K_{B(W)}]_I G \\ [K_{W(B)}]_{II} &= 1 + ([K_{W(B)}]_I - 1)G \\ [k_{W(B)}]_{II} &= 1 + ([k_{W(B)}]_I - 1)G \\ [k_{B(W)}]_{II} &= ([k_{W(B)}]_I - [k_{W(B)}]_I)G \end{aligned} \quad (61)$$

to estimate the interference factors of the wing in Figure 4-13A. G in Equation (61) is the ratio of the root chord of the wing for which the interference factor is desired to that of the wing that slender body theory assumes. That is

$$G = \frac{(c_r)_{II}}{(c_r)_I}$$

The last two terms of Equation (55) are also interference terms. $C_{N_{TW}}$ is the lift on the tail caused by the vortices shed by the wing or canard upstream. $C_{N_{B(W)}}$ is the negative lift on the afterbody due to wing

shed vortices. These terms are also calculated analytically and are given by:

$$C_{N_{TW}} = \frac{(C_{N_s})_W (C_{N_s})_T [K_{W(B)} \sin \alpha + k_{W(B)} \sin \delta_w] i(s_T - r_w) A_W}{2\pi (AR)_T (f_w - r_w) A_{ref}} \quad (62)$$

$$C_{N_{B(W)}} = \frac{-4\Gamma}{A_W V_\infty} \left[\frac{f_w^2 - r_w^2}{f_w} - f_T + \frac{r_T^2}{\sqrt{f_T^2 + h_T^2}} \right] \quad (63)$$

Here i is the tail interference factor given by Pitts et al.²⁵ and Γ is the strength of the wing shed vortex.

4.11 Empirical Methods^{2,4,6}

It is fair to wonder why approximate aeroprediction codes are defined as semiempirical with all the theoretical methods discussed so far. The truth is, that while these methods allow the individual component forces and moments to be calculated fairly rigorously at a given Mach number or angle of attack, there are still many conditions where the analytical methods presented previously are either not applicable or the difficulty in applying them is not worth the effort. In those cases, empirical methods are generally used. The combination of theoretical and empirical techniques in a code is thus why they are called semiempirical codes. A few examples where empirical methods are used are transonic aerodynamics, body alone subsonic aerodynamics, and base drag of the body and lifting surfaces. There are actually analytical methods available for transonic aerodynamic computations. However, most of the methods are inconsistent from a computational standpoint with the approximate codes. What is done in many cases, is to use the sophisticated analytical tools^{2,4,6} to estimate the transonic aerodynamics, as a function of key geometric parameters, then to include these into an engineering code in a table lookup fashion. Obviously, for a vehicle that spends a large portion of its time in the transonic flow region, $0.8 < M_\infty < 1.2$, it would be justifiable to use a more sophisticated estimation process.

The base drag empirical method will be discussed in more detail in the next section of the report, which deals with some of the newer nonlinear methods developed in the past three years.

5.0 NEW APPROXIMATE AERODYNAMIC METHODS

This part of the paper will deal with many of the new aerodynamic prediction methods developed over the past 3 years. These methods include extension of the SOSET to include real gas effects (including two new nonlinear angle-of-attack pressure predictors), an improved version of the Modified Newtonian Theory (IMNT), and improvements to the Allen and Perkins viscous crossflow theory; also included are a new nonlinear wing-alone method, new nonlinear wing body and body wing interference methods due to angle of attack, a new nonlinear wing body interference method due to control deflection, a method for treating

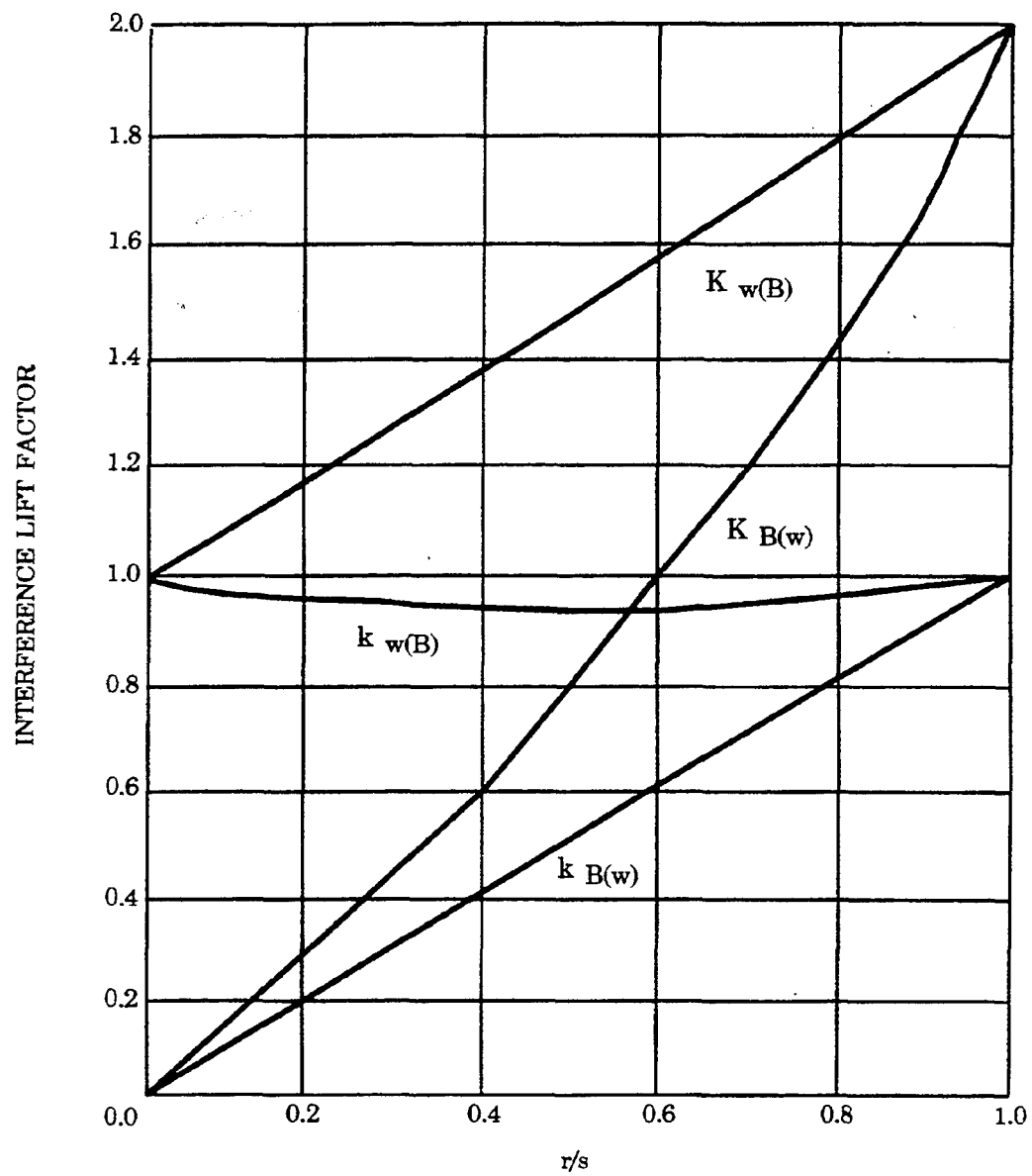


FIGURE 4-11. SLENDER BODY THEORY INTERFERENCE LIFT FACTORS

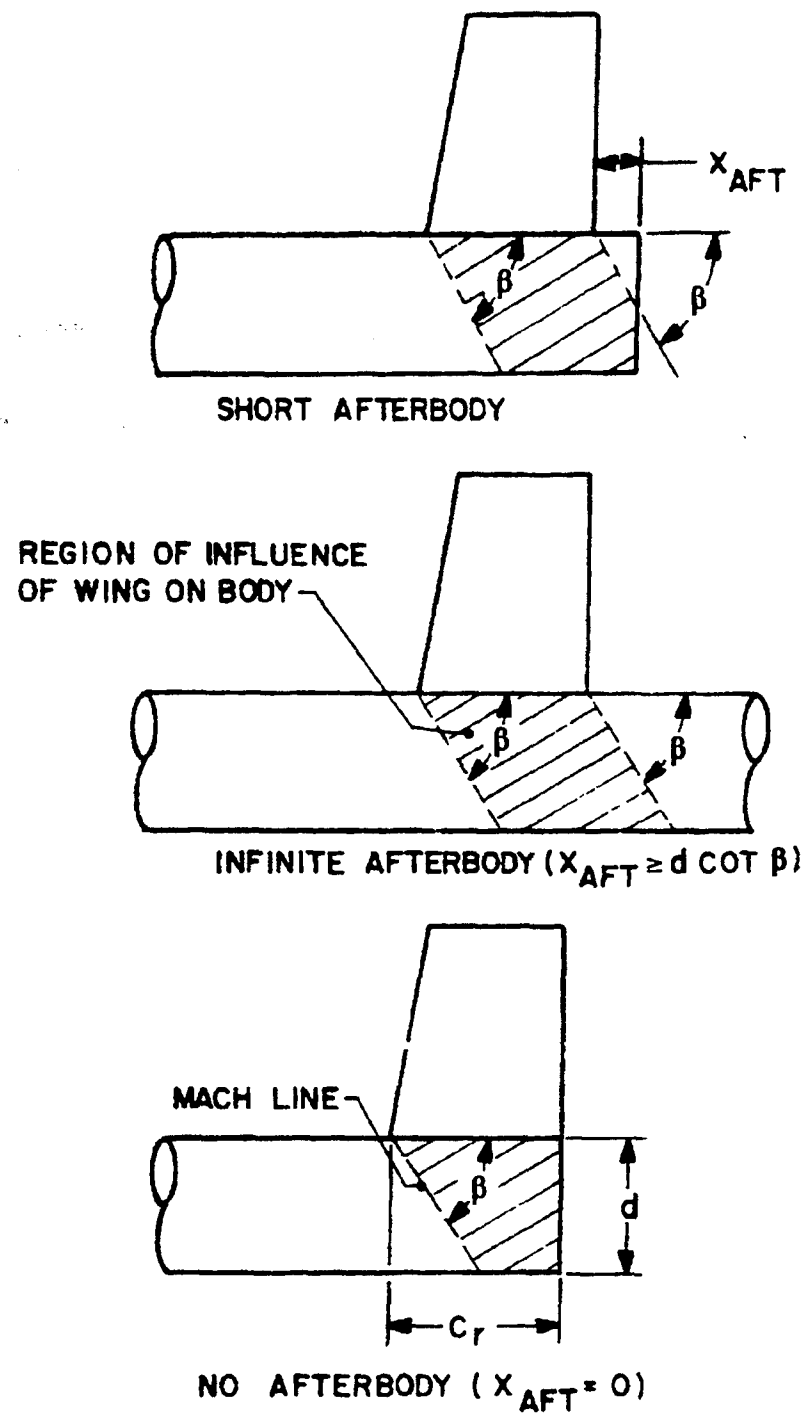


FIGURE 4-12. DETERMINATION OF $K_{B(N)}$ FOR HIGH-ASPECT-RATIO RANGE AT SUPERSONIC SPEEDS

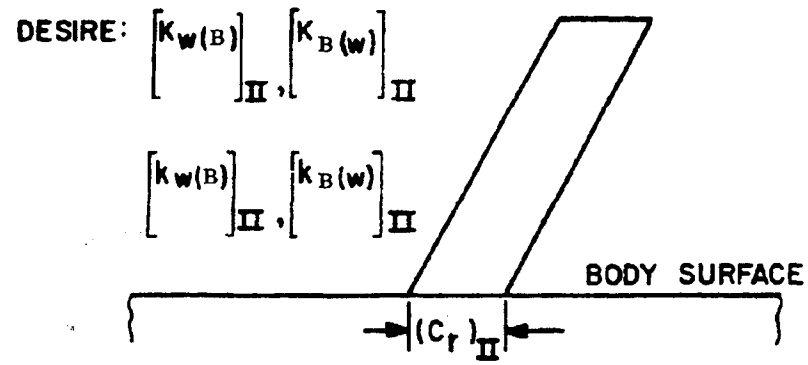


FIGURE 4-13A. WING FOR WHICH INTERFERENCE LIFT IS DESIRED

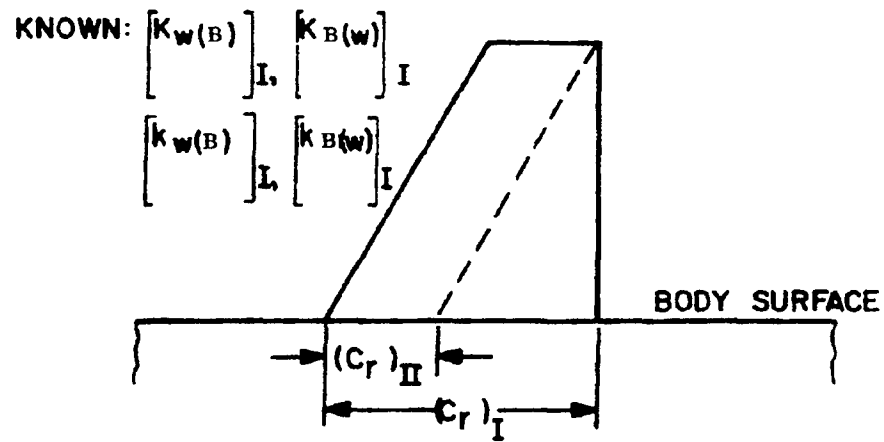


FIGURE 4-13B. ASSUMED SLENDER BODY REPRESENTATION

nonlinear wing tail interference, and an improved base drag prediction model.

These new methods and improvements were directed at three weak areas in the NSWCCD Aeroprediction Code of 1981 (AP81): (1) limited Mach number and inability to compute temperatures at the surface for aeroheating calculations, (2) lack of nonlinear lift capability except for the body alone, and (3) base drag methodology that was not robust enough in terms of including fin effects.

5.1 SOSET Extended to Real Gases^{26, 27}

The main reason the fourth version⁷ of the aeroprediction code was limited to Mach number 8 was that, above $M_\infty = 6$ real gas effects start becoming important but, can still be neglected at $M_\infty = 8$. However, as Mach number increases substantially above $M_\infty = 6$, the need to include real gas effects into the aeroprediction code increases if one is interested in inviscid surface temperatures. If one is only interested in forces and moments, real gas effects have a slight effect on the pitching moment, but only second-order effects on axial and normal force.²⁸ However, one of the key issues in high-speed vehicles is aerodynamic heating, material selection, and insulation. Any excess weight can have a strong adverse impact on vehicle performance. Thus, a simple yet accurate method of estimating vehicle surface temperature (inviscid) for use in heat transfer analysis is needed.

Figure 5-1²⁶ is an illustration of the importance of real gas effects. It plots the static temperature behind a normal shock for both perfect and real gases at an altitude of 170,000 ft. At this altitude, the speed of sound is approximately 1100 ft/sec and the freestream air temperature is approximately 283°K. The normal shock would occur in the vicinity immediately ahead of the blunted portion of a seeker or the missile nose. Note that the temperatures of interest to tactical weapons aerodynamicists can be very high, for high Mach number conditions assuming a perfect gas. Also shown on the figure are the real gas results.²⁹ Note, in particular, the plot of T_R/T_p , the ratio of the real gas to perfect gas temperature. For Mach numbers of 6 or less, this ratio is unity or near unity. This is the reason that aerodynamic computations below $M_\infty = 6$ could neglect real gas effects with little error. However, as M_∞ goes above $M_\infty = 6$, the error in temperature using the perfect gas assumption becomes increasingly large. This is of particular importance to materials and structures engineers designing the system to withstand these temperatures. Also shown in Figure 5-1 is the melting point of typical structural materials used in present-day missile design. The actual-use temperature is less than the melting-point temperature. For missiles that fly at any appreciable time above the maximum-use temperature of a given material, some form of active cooling or insulation would be required. This means additional dead weight and, hence, less performance for the missile. It is therefore obvious that a reasonably accurate estimate of temperature is essential for the design of the seeker and the structure of the weapon. To meet the need for a fairly accurate method of predicting surface temperature, SOSET was extended to include real gas effects. In so doing, new approximate methods were developed for angle of attack pressure

prediction and an improved version of MNT was derived. These new methods will be briefly described.

SOSET and MNT for perfect gases were discussed in 2.1 and 2.3, respectively. Refer to 2.1 for the SOSET methodology and to Moore, et al.^{26, 27} for the extension to real gases. It is noted that to extend SOSET to real gases requires several things: (1) a cone solution for real gases (p_c); (2) a Prandtl-Meyer Expansion (PME) for real gases (p_2); (3) a derivation of a new pressure derivative $(\partial p/\partial s)_2$, where the perfect-gas assumption has not been made; and (4) a way to compute temperature given values of pressure.²⁶ After the real-gas pressure derivative $(\partial p/\partial s)_2$ was derived and checked, it was found that $(\partial p/\partial s)_2$ became negative for many cases, causing one to choose between the Generalized Shock Expansion Theory (GSET where $\eta = 0$) and the tangent cone theory ($\eta = \infty$). In comparisons of the pressure prediction to full Euler computations, it was found that a better way to implement the shock expansion theory for $M \geq 6$ was to redefine Equation (10) as

$$p = p_c - (p_c - p_2) \eta_1 \quad (64)$$

with η_1 being an input parameter chosen by the user. It was found that a value of $\eta_1 = 0$ gave slightly better pressure predictions for slightly blunt configurations, whereas a value of $\eta_1 = 1$ gave better accuracy where bluntness was large. Thus, final implementation of SOSET in AP93 is Equation (64), with η_1 as an input, p_c the real-gas tangent cone pressure, and p_2 the real-gas value of pressure computed from a Prandtl-Meyer expansion.

To compute inviscid temperatures (and other properties) along the surface of a pointed or blunt body, the constancy of entropy along the surface for perfect, frozen, or equilibrium chemically reacting flows is used. Knowing the value of entropy and pressure from the pointed cone solution²⁹ or the normal shock solution for a blunt body,³⁰ one can then use the thermofit equations of Tannehill and Mugge³¹ and Srinivasen, et al.,³² to determine other properties, i.e.,

$$\left. \begin{aligned} T &= T(p, S) \\ \rho &= \rho(p, S) \\ a &= a(p, S) \\ e &= e(p, S) \end{aligned} \right\} \quad (65)$$

The remaining properties at the body surface can be found from standard thermodynamic relationships, i.e.,

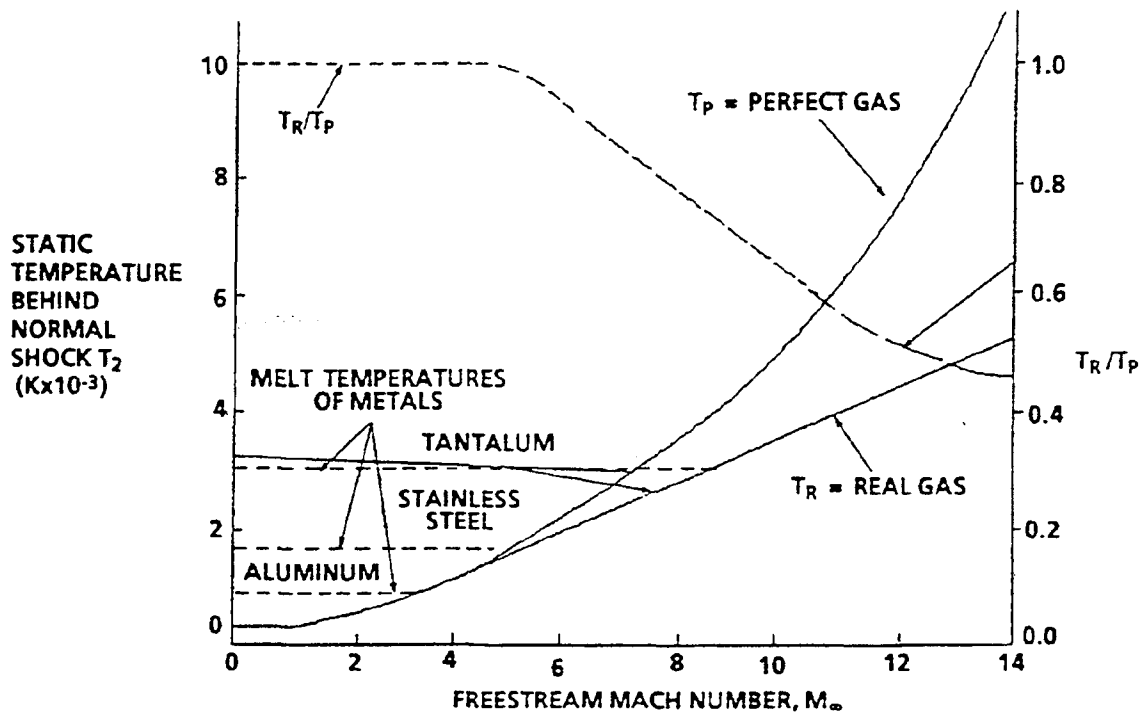


FIGURE 5-1. TEMPERATURE BEHIND A NORMAL SHOCK AS A FUNCTION OF FREESTREAM MACH NUMBER ($H = 170\text{kft}$)

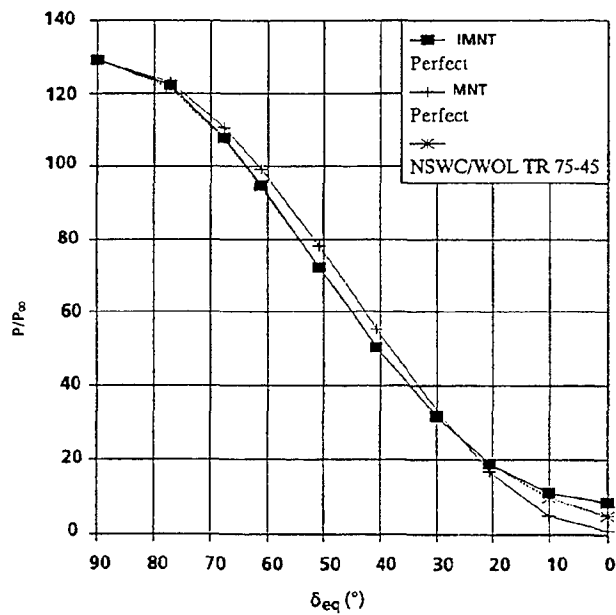


FIGURE 5-2. SURFACE PRESSURE DISTRIBUTION OVER A HEMISPHERICAL FOREBODY AT $M_\infty = 10$

$$\left. \begin{aligned}
 h &= e + p/\rho \\
 H_0 &= \left(\frac{\gamma_\infty R}{\gamma_\infty - 1} \right) T_{0_\infty} = \text{constant} \\
 V &= \sqrt{2(H_0 - h)} \\
 M &= V/a \\
 \gamma &= \frac{a^2 \rho}{p} \\
 Z &= \frac{p}{\rho RT}
 \end{aligned} \right\} \quad (66)$$

In the process of computing surface properties, three new pressure prediction methods were derived. The first of these was to give an improved pressure coefficient prediction on the blunt nose of a missile configuration over that provided by the MNT. If the pressure coefficient of MNT is defined as

$$(C_p)_{MNT} = C_{p_0} \sin^2 \delta_{eq} \quad (67)$$

then the nose pressure on the blunt nose part of a missile is given by

$$C_p = (C_p)_{MNT} - \Delta C_p \quad (68)$$

ΔC_p of equation (68) is defined by

$$\Delta C_p = k \cos^m (\delta_{eq}) [\cos \delta_{eq} - \cos(\delta_{eq})_m] \quad (69)$$

where $(\delta_{eq})_m = 25.95$ deg, $m = 2.78$, and

$$k = 2.416 C_{p_0} + 4.606 \left[0.1507 C_{p_0}^2 + \frac{1.124}{M_\infty^2} C_{p_0} \right]^{1/2}$$

Figure 5-2 shows the results of the Improved Modified Newtonian theory (IMNT) of Equations (68) and (69), compared to Equation (67) alone, and a full numerical solution of the Euler equations³³ for a hemispherical forebody at $M_\infty = 10$. The IMNT gives up to 7 percent improvement in pressure compared to the MNT. Even past the match point ($\delta_{eq} < 25.95$ deg), the IMNT gives good agreement with the numerical solution down to δ_{eq} values of 10 deg. This level of accuracy in pressure prediction will also translate into more accurate drag computations, particular on bodies with large bluntness.

The other two pressure prediction formulas have to do with calculating the pressure on a point behind the blunt nose portion of the body but at an angle of attack. These are

$$\begin{aligned}
 C_p(\alpha, \phi) &= C_{p_{\alpha=0}} - (2\alpha) \sin(2\theta) \cos(\phi) + \\
 &\quad (F \cos^2 \theta) \alpha^2 + \\
 &\quad (4/3 \sin(2\theta) \cos(\phi)) \alpha^3
 \end{aligned} \quad (70)$$

where

$$F = \left(2 - \frac{1}{\beta} \right) (1 - \tan^2 \theta_c) - \left(2 + \frac{2}{\beta} \right) \sin^2 \phi$$

and

$$C_p(\alpha, \phi) = C_{p_{\alpha=0}} - \frac{(2\alpha) \sin(2\theta) \cos(\phi)}{3} \quad (71)$$

Equation (70) is used for pointed body configurations, as well as for blunt body configurations in the windward plane area ($60^\circ < \phi \leq 180^\circ$). Equation (71) is used in the leeward plane ($\phi \leq 60^\circ$) for configurations with blunt noses. In Equation (70), $(C_p)_{\alpha=0}$ is the pressure coefficient at $\alpha = 0$, which comes from Equation (64). Figure 5-3 is an example of the application of Equation (70) to a cone along with the associated inviscid surface temperatures. The approximate results are close to the exact cone solution.³⁴

Figure 5-4 presents the comparison of the present methodology for predicting inviscid surface temperatures on a 20-percent blunt cone at $\alpha = 10$ deg and $M_\infty = 15$. These results are compared to a full numerical solution of the Euler equations (ZEUS)³⁵ for both perfect and real gases. The real-gas temperatures are substantially lower than the perfect-gas results and also agree with the full Euler solution except in the vicinity of the overexpansion region past the blunt tip. Figure 5-4 uses most of the theory developed for the approximate methodology in Equations (64) through (71), along with the assumptions used in computing temperature.

5.2 Aeroheating³⁶

The AP93 methodology computes boundary layer heating information in the form of a heat transfer rate, \dot{q}_w ; a heat transfer coefficient, H ; and a recovery temperature (adiabatic wall temperature), T_{aw} , at each computational point.³⁶ These variables are related as shown in Equation (72).

$$H = \frac{\dot{q}_w}{T_{aw} - T_w} \quad (72)$$

T_w is the wall temperature. For high-temperature flows, the heat transfer coefficient is often expressed in terms of enthalpies.

$$H_i = \frac{\dot{q}_w}{h_{aw} - h_w} \quad (73)$$

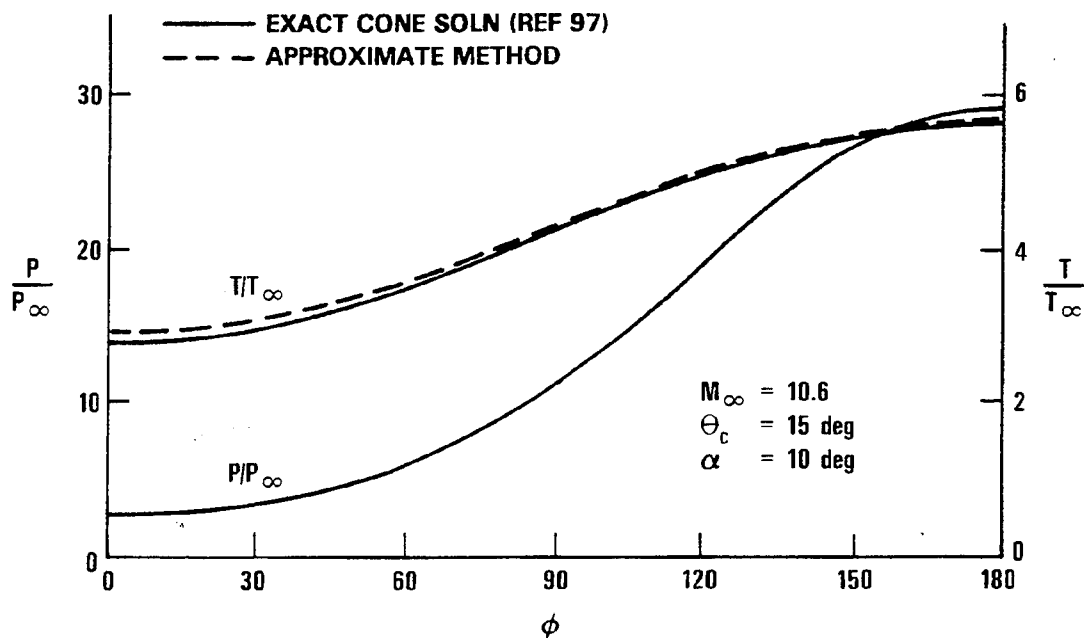


FIGURE 5-3. PERFECT-GAS COMPARISON OF EXACT AND APPROXIMATE CONE SOLUTIONS

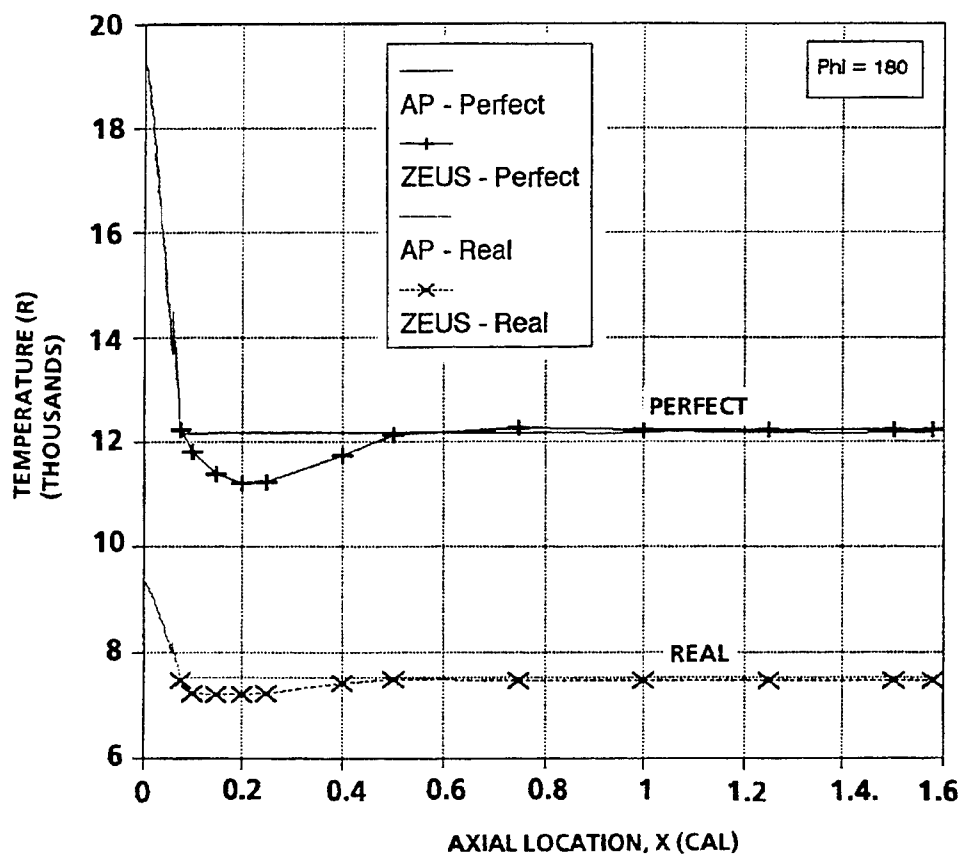


FIGURE 5-4. COMPARISON OF APPROXIMATE AND EXACT TEMPERATURE IN WINDWARD PLANE OF A 20 PERCENT BLUNT CONE ($M_\infty = 15$, $\alpha = 10$ DEG)

At temperatures above about 1500°R, Equation (73) is the more rigorously correct of the two. The heat transfer is normalized as shown in Equations (72) and (73) because the coefficients H and H_1 remain fairly constant over a wide range of wall temperatures, even though the actual heat transfer rate, \dot{q}_w , may vary significantly. Thus, since T_{aw} and h_{aw} are not functions of wall temperature, once a heating computation is performed for a given Mach number/altitude combination, it need not be repeated simply because of changes in wall conditions. This weak coupling greatly simplifies the problem of tracking the time-dependent thermal response of a surface exposed to boundary layer heating. The aerodynamic solution may be obtained first with a code such as AP93, and the results stored in tabular form as functions of Mach number, altitude, and angle of attack. This information can then be accessed by an independent algorithm to compute the time-varying heat transfer rates and the resulting integrated surface temperature history along any given trajectory that lies within the limits of the data matrix.

The only departure from the use of true inviscid surface conditions as boundary layer edge properties occurs in the case of blunt bodies. The curvature of the detached bow shocks associated with these configurations creates an entropy layer near the body surface. The inviscid solution would give a uniform boundary layer edge entropy over the entire body equal to that behind a normal shock at the free-stream Mach number, since this is the entropy along the inviscid streamline that wets the body surface. In reality, because of the finite thickness of the boundary layer, the true edge entropy is that which exists at some point in the entropy layer located at a distance above the surface equal to the local boundary layer thickness. This entropy value is determined by an iterative mass balance technique.³⁶

Once appropriate boundary layer edge conditions are determined, a series of specialized analytical relations are used to determine the aerodynamic heating at various locations. At the nose tip stagnation point, a simplified version of the Fay-Riddell formula³⁷ gives

$$\dot{q}_w = 0.763Pr^{-0.6} \sqrt{\rho_0 \mu_0} \sqrt{\frac{dV_e}{dx} (h_{aw} - h_w)} \quad (74)$$

The stagnation point velocity gradient, dV_e/dx , is determined from the Newtonian theory, assuming a spherical nose tip. At the nose tip, the flow will always be laminar.

If control surfaces are present, the viscous heating along their leading edge stagnation lines is determined by the Beckwith and Gallagher swept-cylinder relations³⁸ modified to include real-gas effects.³⁹ For the laminar case,

$$\dot{q}_{w,l} = 0.57Pr^{-0.6} \sqrt{\rho_0 \mu_0} \sqrt{\frac{dV_e}{dx} (h_{aw} - h_w) (\cos\Lambda)^{1.1}} \quad (75)$$

where Λ is the leading edge sweep angle and dV_e/dx is the stagnation line velocity gradient derived from Newtonian theory, assuming, a cylindrical leading edge. For turbulent flow,

$$\dot{q}_{w,t} = 1.04Pr^{-0.6} \frac{(\rho^* \mu^*)^{0.8}}{(\mu_0)^{0.6}} (V_p \sin\Lambda)^{0.6} \left(\frac{du_e}{dx} \right)^{0.2} (h_{aw} - h_w) \quad (76)$$

where V_p is the flow velocity parallel to the leading edge stagnation line and the (*) superscript denotes evaluation at a reference enthalpy given by⁴⁰

$$h^* = 0.5(h_w + h_e) + 0.22(h_{aw} - h_e) \quad (77)$$

The (e) subscript denotes evaluation at the boundary layer edge. The laminar or turbulent status of the flow is determined by comparison of the Reynolds number, based on the leading edge diameter, to user-specified upper and lower limits. If Re_D is below the lower limit, laminar values are used. If Re_D is above the upper limit, fully turbulent flow is assumed. For intermediate values of Re_D , a linear combination of laminar and turbulent values is computed.

For points on the body, the Eckert reference enthalpy flat plate formulation is used.⁴¹ For laminar flow,

$$\dot{q}_{w,l} = 0.332(Pr^*)^{-0.667} \frac{\rho^* V_e}{\sqrt{\frac{Re^*}{N_t}}} \quad (78)$$

and for the turbulent case,

$$\dot{q}_{w,t} = 0.185(Pr^*)^{-0.667} \frac{\rho^* V_e}{\left[\ln \frac{Re^*}{N_t} \right]^{2.584}} \quad (79)$$

N_t and N_l are transformation factors that allow for the approximation of three-dimensional (3-D) effects. They are equal to three and two, respectively. The laminar or turbulent flow character, is determined as before by comparing the local Reynolds number, based on boundary layer running length, to user-specified upper and lower limits.

Heating rates on the surfaces of wings, fins, or canards are determined by using Equations (78) and (79) but in this case, N_t and N_l are both equal to one because of the two-dimensional (2-D) nature of the flow. The degree of turbulence is determined in the same manner as for the body.

An example of the new aeroheating method is given in Figure 5-5. Figure 5-5 shows the heat transfer rate on a 15 degree half angle cone with a nose radius of 1.1 inches as a function of distance along the axis of symmetry. Conditions considered are $M_\infty = 10.6$ and angle of attack 10 degrees. Comparisons are made with a more complicated approximate technique⁴² that uses streamline tracking combined with the axisymmetric

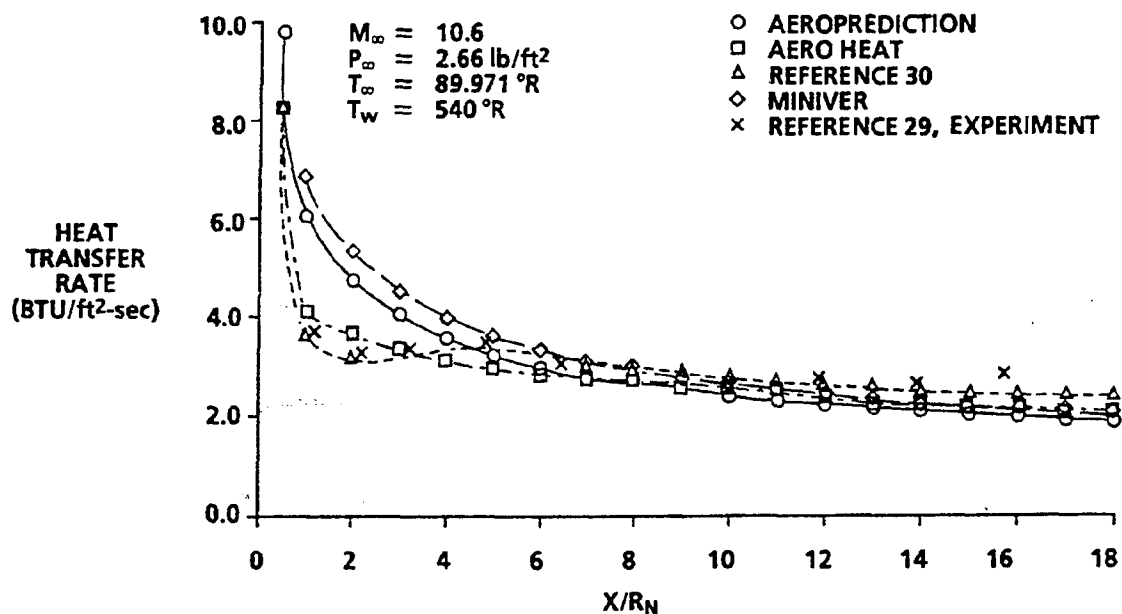


FIGURE 5-5. WINDWARD PLANE HEAT TRANSFER RATES FOR 1.1-IN. NOSE RADIUS, 15-DEG HALF-ANGLE CONE AT $\alpha = 10$ DEG

TABLE 5-1. CONFIGURATION INDEX

Config	Fins Off	t/c				x/c		δ			$(M_{\infty} = 2.0)$	$(M_{\infty} \geq 2.5)$
		0.05	0.10	0.15	0	1.0	2.0	0	10	20		
1	X										Sweep	Sweep
2				X	X				X		0,5,10	0
3				X	X				X		0,5,10	0
4				X	X					X	0,5,10	0
5			X		X				X		0,5,10	0
6			X		X				X		0,5,10	0
7			X		X					X	0,5,10	0
8		X			X				X		0,5,10	0
9		X			X				X		0,5,10	0
10		X			X					X	0,5,10	0
11		X				X		X			0,5,10	0
12			X			X		X			0,5,10	0
13				X		X		X			0,5,10	0
14				X			X	X			0,5,10	0
15			X				X	X			0,5,10	0
16		X					X	X			0,5,10	No data

analog to model 3-D effects. Experimental data are also shown⁴⁵ along with the results from the MINIVER³⁹ code used in a tangent cone mode. AP 93 and MINIVER tend to under predict the data by about 10 - 15 percent, a performance that is credible considering the simplified nature of the solution. Note that the AP 93 gives improved results over MINIVER in the vicinity of the stagnation region due to the more accurate calculation of entropy at the edge of the boundary layer and more accurate real gas properties.

5.3 Base Drag^{44,45}

The AP81 estimated base drag using a composite of empirical data for the body alone. Also, an approximation was made for the effect of angle-of-attack, fin location, and fin thickness effects as a function of Mach number based on a limited amount of data. As a result, a request was made to the National Aeronautics and Space Administration, Langley Research Center (NASA/LRC) to perform additional wind tunnel tests, where additional base pressure measurements could be taken to try and quantify the effects mentioned, plus those due to control deflection.

Wilcox was the chief engineer for the tests that were conducted and reported.^{44,45} Eighty-nine base pressure taps were placed around a 7.2 caliber, 5-inch diameter body with a side mounted sting. These taps were placed every 22.5 deg in circumferential location and at several radii from the body centroid toward the outer edge. The configuration matrix of data taken is shown in Table 5-1. The base pressure measured at each of the 89 orifice locations was then averaged over its incremental base area to get the average base pressure at each condition, of Table 5-1. Based on these average base pressure measurements at each test condition, changes in base pressure, and hence, base drag because of a particular physical model change, or flight condition change could be readily computed by simply subtracting the two data points.

Using the process described, along with a wind tunnel data base not available when AP81 was developed,⁴⁶ a new empirical estimate of base pressure coefficient

C_{P_B} was derived. This new estimate is shown in Figure 5-6 and compared to the AP81 value of C_{P_B} . The two curves are similar, with the AP93 slightly higher than AP81 for $M_\infty \leq 1.5$ and slightly lower than AP81 for $M_\infty \geq 3.0$. Body-alone angle-of-attack effects on base pressure are then estimated by

$$(C_{P_B})_{NF,\alpha} = (C_{P_B})_{NF,\alpha=0} [1 + 0.01F_1] \quad (80)$$

Here, $(C_{P_B})_{NF,\alpha=0}$ comes from Figure 5-6 and F_1 , the increase due to angle of attack from Figure 5-7. Boattail and power-on effects on base drag are estimated as present in AP81.

At this point, it is worth noting that, while the databases of Moore, et al., and Butler, et al., helped to improve the estimate of base pressure as a function of Mach number and angle of attack for the body alone,^{44,45,46} additional data are still needed for $\alpha \leq 15$ deg at all Mach numbers. This need is indicated by the dotted lines in Figure 5-7, which are extrapolations from data available for $\alpha \geq 15$ deg and engineering judgement. This same statement will also be even more true for fin effects due to control deflection and angle of attack, as will be discussed in the following paragraphs.

The total body base pressure coefficient for fins located flush with the base is

$$(C_{P_B})_{\alpha,\delta,t/c,x/c=0} = [1 + 0.01F_2] (C_{P_B})_{NF,\alpha=0} + 0.01F_3(t/d) \quad (81)$$

where $(C_{P_B})_{NF,\alpha=0}$, F_2 , and F_3 come from the AP93 curve of Figures 5-6, 5-8, and 5-9, respectively.

In Figure 5-8, no data were taken for $M_\infty < 2$,^{44,45} and none could be found in the literature. Hence, the data for $M_\infty = 2$ are assumed to apply for $M_\infty < 2$ as well. While this is a big assumption, it is believed to be better than neglecting the base pressure effect due to control deflection and angle of attack, which other engineering aerodynamics codes do. It is also worth noting that Figure 5-9 indicates what is intuitively obvious: for small control deflections and angles of attack, fin thickness effects are important in base pressure estimation, whereas for large values of α and δ , the additional change in C_{P_B} due to fin thickness is minimal.

The final parameter to define the effect on base pressure is fin location relative to the body base. This is done through Equation (82), where

$$(C_{P_B})_{\alpha,\delta,t/c,x/c} = (C_{P_B})_{NF,\alpha} + 0.01(\Delta C_{P_B})_{\alpha,\delta,t/c,x/c} \quad (82)$$

Here $(C_{P_B})_{NF,\alpha}$ is the body-alone base pressure coefficient at a given angle of attack given by Equation (80) and $(\Delta C_{P_B})_{\alpha,\delta,t/c,x/c}$ is the total change due to the presence of fins at a given α , δ , t/c , and x/c . An example of $(\Delta C_{P_B})_{\alpha,\delta,t/c,x/c}$ is given in Figure 5-10 for $M_\infty = 2.0$ and $|\alpha + \delta| = 10$ deg. Moore, et al., showed other curves for this parameter.⁴⁴ Figure 5-10 shows that the change in base pressure due to all variables present varies from that at $x/c = 0$, where the fins dominate to that of the body alone where the fins have no effect ($x/c \approx 2.5$).

5.4 Improved Method For Body Alone Normal Force and Center of Pressure^{47,48}

The normal-force coefficient of the body alone is estimated by⁴⁷

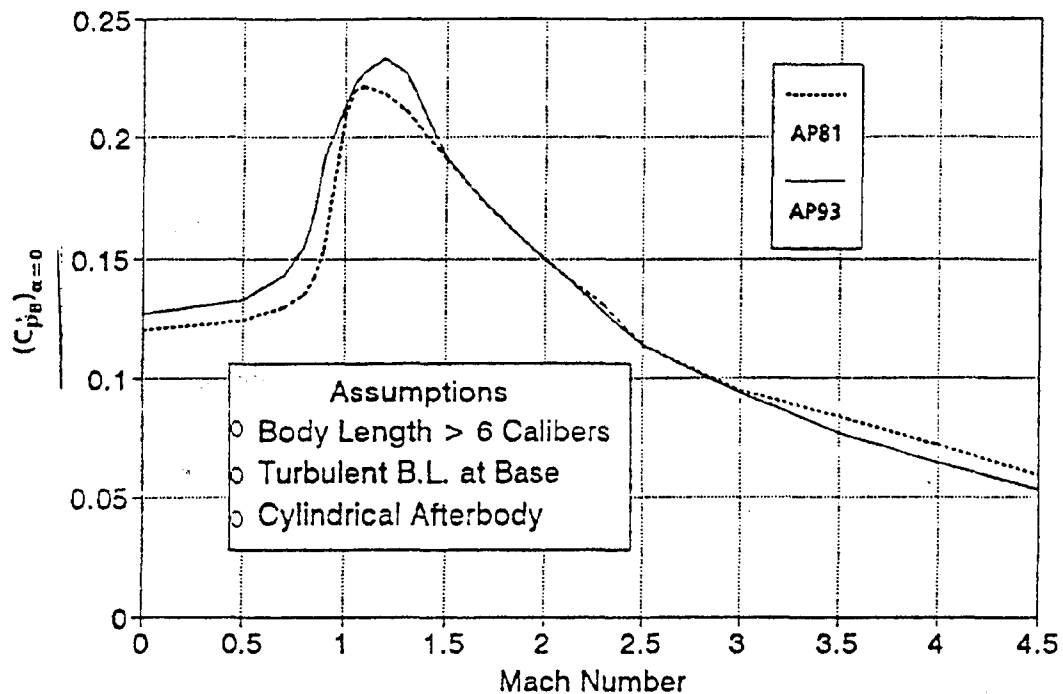


FIGURE 5-6. MEAN BODY-ALONE BASE PRESSURE COEFFICIENT USED IN AP81 AND AP93

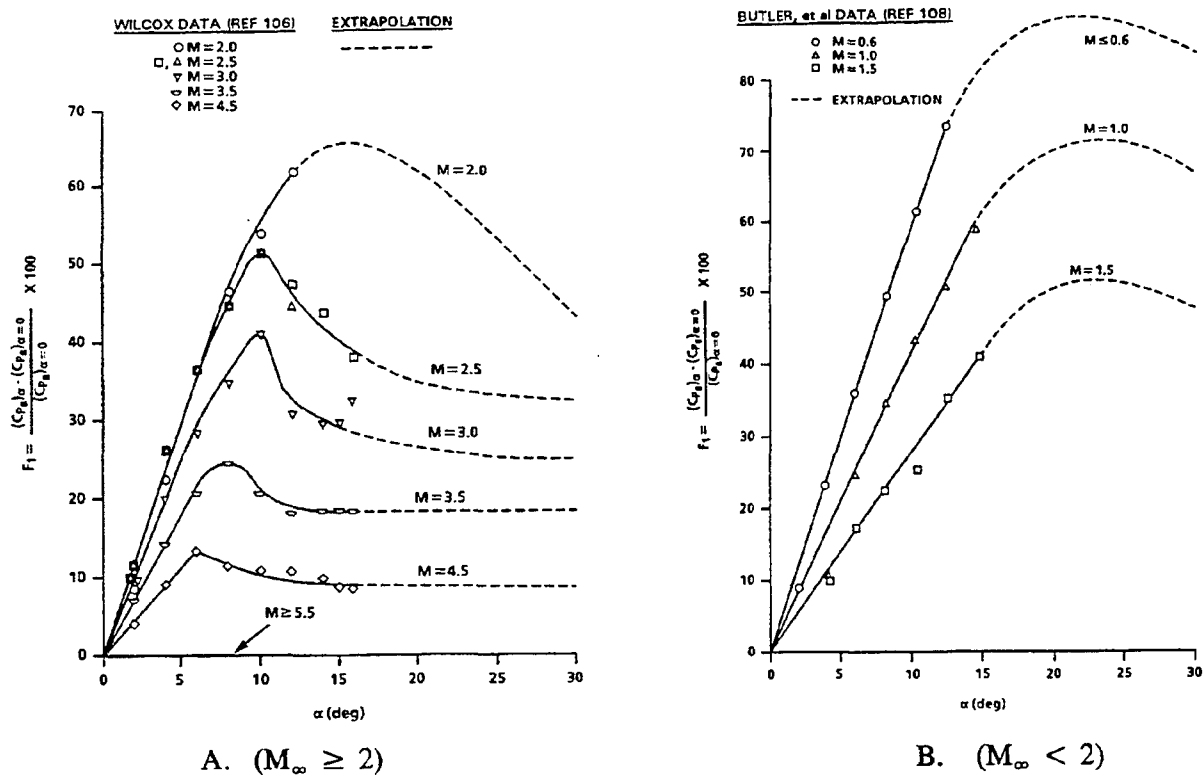


FIGURE 5-7. PERCENT CHANGE IN BODY-ALONE BASE PRESSURE COEFFICIENT DUE TO ANGLE OF ATTACK

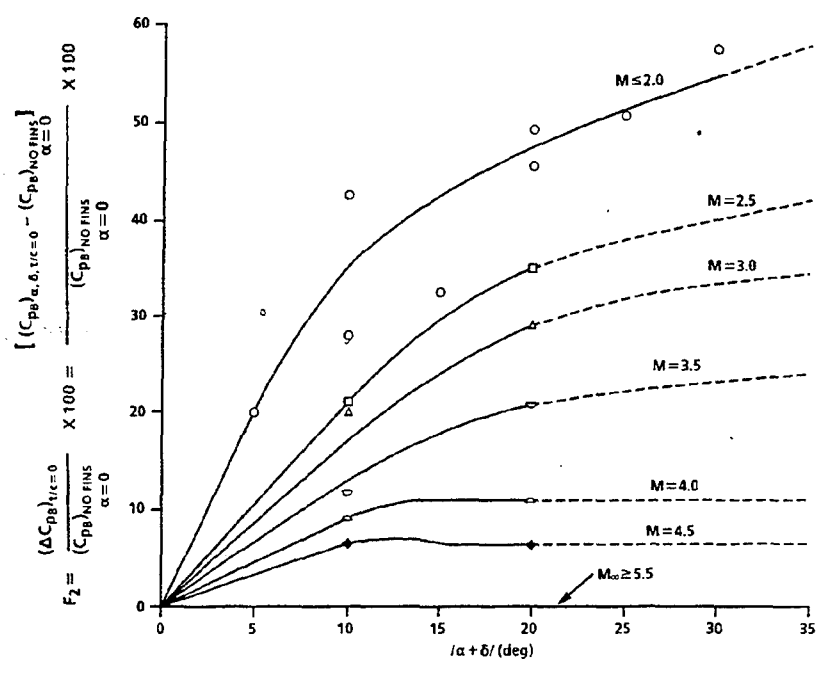


FIGURE 5-8. PERCENT CHANGE IN BASE PRESSURE COEFFICIENT DUE TO COMBINED EFFECTS OF ANGLE OF ATTACK AND CONTROL DEFLECTION ($t/c \approx 0$)

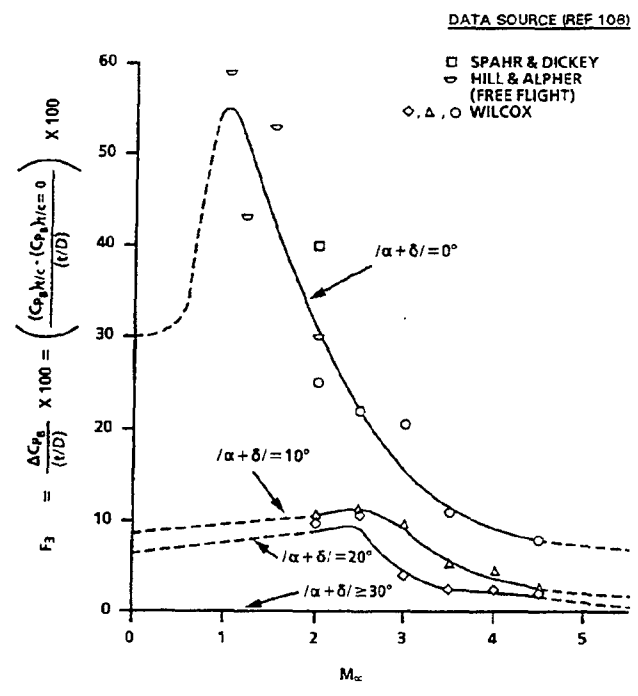


FIGURE 5-9. ADDITIONAL PERCENT CHANGE IN BASE PRESSURE COEFFICIENT DUE TO FIN THICKNESS AT VARIOUS VALUES OF $|\alpha + \delta|$

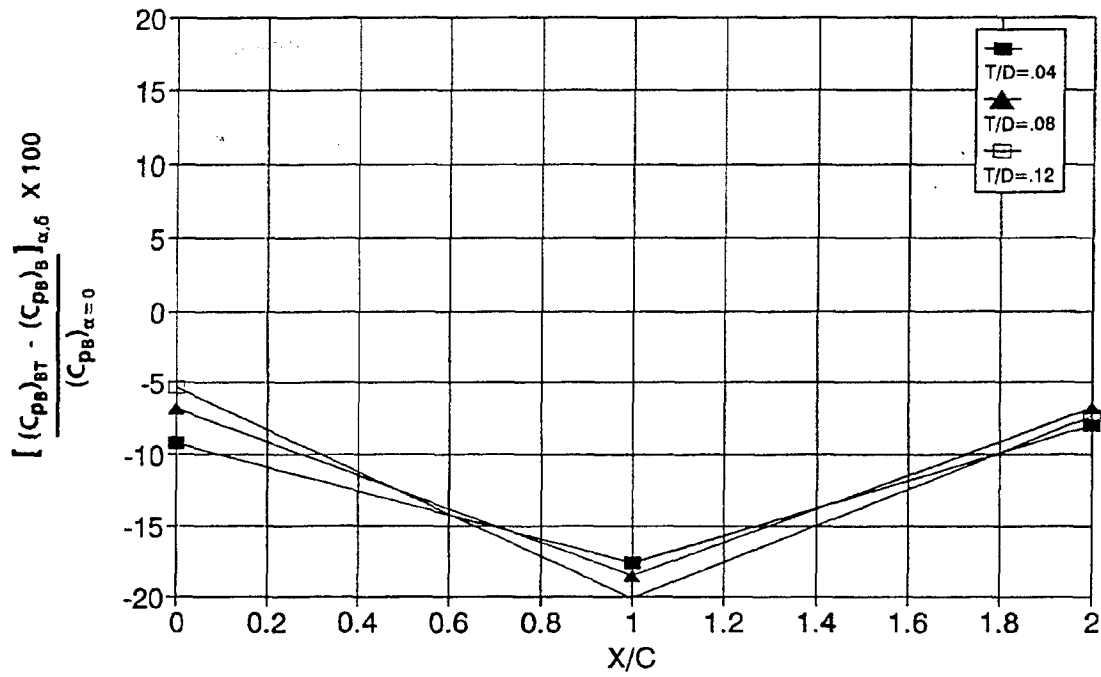


FIGURE 5-10. PERCENT CHANGE IN BASE PRESSURE COEFFICIENT DUE TO FIN LOCATION
 $|\alpha + \delta| = 10 \text{ DEG}, M_\infty = 2.0$

$$C_N = C_{N_L} + C_{N_{NL}} \quad (83)$$

where C_{N_L} is the linear term and $C_{N_{NL}}$ the nonlinear term. The linear term is predicted in AP81 by either SOSET, second-order Van Dyke combined with MNT, or empirical depending on the Mach number range.^{1, 6} The nonlinear term is estimated by the Allen-Perkins viscous crossflow theory.¹⁹ No changes were made in the linear term of Equation (83) in AP93 from AP81. Three changes in the nonlinear term of Equation (83) were made for the AP93.

The nonlinear term of Equation (83) is¹⁹

$$C_{N_{NL}} = \eta C_{d_c} \sin^2 \alpha \frac{A_p}{A_{ref}} \quad (84)$$

The first change from AP81 is in the value of η . AP81 used an incompressible value of η with no account of compressibility effects, although compressibility effects have been clearly shown.⁴⁹ The compressibility effect is shown in Figure 5-11A along with the line drawn to represent the data. This line is defined as

$$\eta = \begin{cases} \left(\frac{1-\eta_0}{1.8} \right) M_N + \eta_0 & \text{for } M_N \leq 1.8 \\ 1 & \text{for } M_N > 1.8 \end{cases} \quad (85)$$

where η_0 is the incompressible value of η ($M_N = 0$) used in AP81.¹

The second change is in the value of the crossflow drag coefficient used. This value was changed to allow the effect of transition on the body surface to affect the value chosen. This affects the value of C_{d_c} for M_N values of 0.5 and less. Also, the value of C_{d_c} is slightly lower for $0.6 \leq M_N \leq 2.2$ than that used in AP81. This is based on the large NASA Tri-Service Data Base.⁵⁰ The new value of C_{d_c} used in AP93 is given in Figure 5-11B. If the flow on the body is a combination of laminar and turbulent (the case for most conditions), a value somewhere in between the two values on the Figure 5-11B curve for $M_N \leq 0.5$ will be computed. If X_L defines the length of laminar flow on the body and X_T is the total length, then for $M_N \leq 0.5$,

$$C_{d_c} = 1.2 - \left(\frac{X_L}{X_T} \right) 0.8 \quad (86)$$

Thus, if $X_L = 0$ so flow over the body is fully turbulent, a value of $C_{d_c} = 1.2$ will be computed, whereas a value of 0.4 will be picked if the flow is fully laminar.

The third change made in AP93 was in the center-of-pressure location. AP81 used a weighted average of the normal force center of pressure of the linear term and nonlinear term, where the nonlinear term X_{cp} was at the centroid of the planform area in the crossflow plane and the X_{cp} of the linear term was computed theoretically or empirically. Both of these values were held constant as angle of attack increased, the only change being from the changing values of the normal-force terms of Equation (83). In numerical experiments using the NASA Tri-Service Missile Data Base, it was found that the assumption of a constant value of center of pressure with angle of attack was not completely correct. It is suspected that as angle of attack increases, the center of pressure of the linear term of Equation (83) changes and can no longer be assumed to be constant. An empirical way to represent this change with Mach number is given in Figure 5-11C. This change is effective for $\alpha \geq 10$ deg. Between $\alpha = 0$ and 10 deg, the correction is implemented in a linear fashion between zero at $\alpha = 0$ to its full value at $\alpha = 10$ deg.

Figure 5-12 is an example of the normal-force and center-of-pressure comparisons of the AP81, AP93, and experimental data. The data are for a 12.33-caliber tangent-ogive cylinder configuration with a 3.0-caliber nose.⁵⁰ The improvements made in AP93 give significantly better results on both C_N and X_{cp} as a function of angle of attack.

5.5 Wing-Alone Nonlinear Normal Force and Center of Pressure

One of the major reasons the AP81 gave poor results at $\alpha > 10$ deg for many missile configurations was the failure to include nonlinearities in wing lift. Using NASA and ONR Data Bases^{51,52} a semiempirical method was developed for the nonlinear wing-alone normal-force term analogous to the body-alone Equations (83) and (84).^{47,48} The nonlinear term of wing-alone lift, therefore, can be defined as

$$C_{N_{NL}} = f(M_N, AR, \lambda) \left(\frac{A_p}{A_{ref}} \right) \sin^2 \alpha \quad (87)$$

Here, $f(M_N, AR, \lambda)$ is analogous to the ηC_{d_c} of the body alone in Equation (84). Since the total wing-alone normal force is known for a given AR , M_∞ , λ , and α ,^{51,52} and the linear value of lift is known from the 3-D thin-wing theory or lifting surface theory from AP81; the nonlinear normal force of the wing alone is

$$C_{N_{NL}}(M_N, AR, \lambda) = C_N(M_N, AR, \lambda) - C_{N_L}(M_N, AR, \lambda) \quad (88)$$

Using the data of References 51 and 52, Equation (88) values were generated and a parameter k_1 defined as

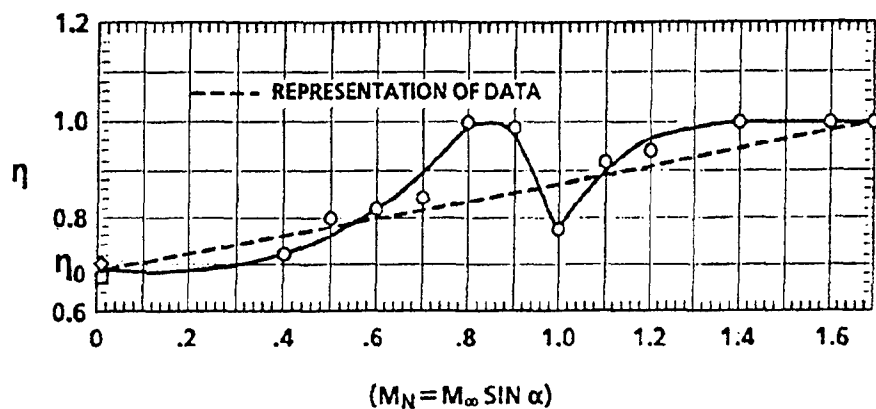


FIGURE 5-11A. COMPRESSIBILITY EFFECTS ON CROSSFLOW DRAG PROPORTIONALITY FACTOR

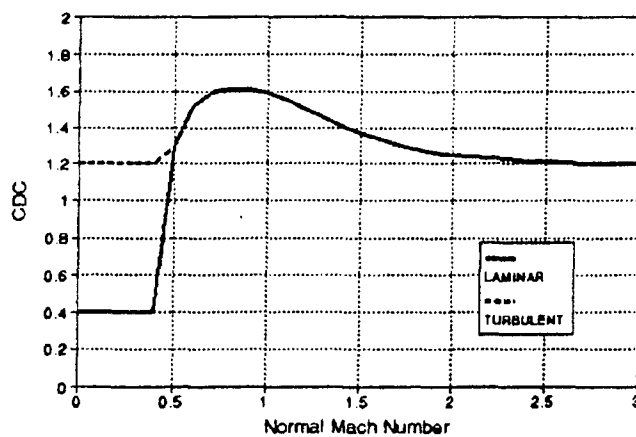


FIGURE 5-11B. CROSSFLOW DRAG COEFFICIENT FOR AN OGIVE-CYLINDER CONFIGURATION

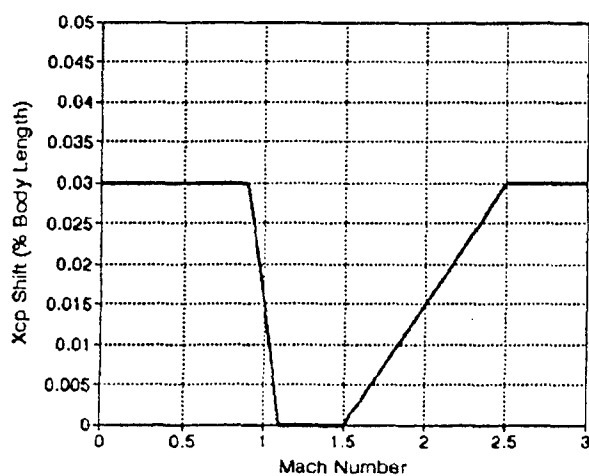


FIGURE 5-11C. CENTER-OF-PRESSURE SHIFT IN BODY-ALONE NORMAL FORCE FOR $\alpha \geq 10$ DEG

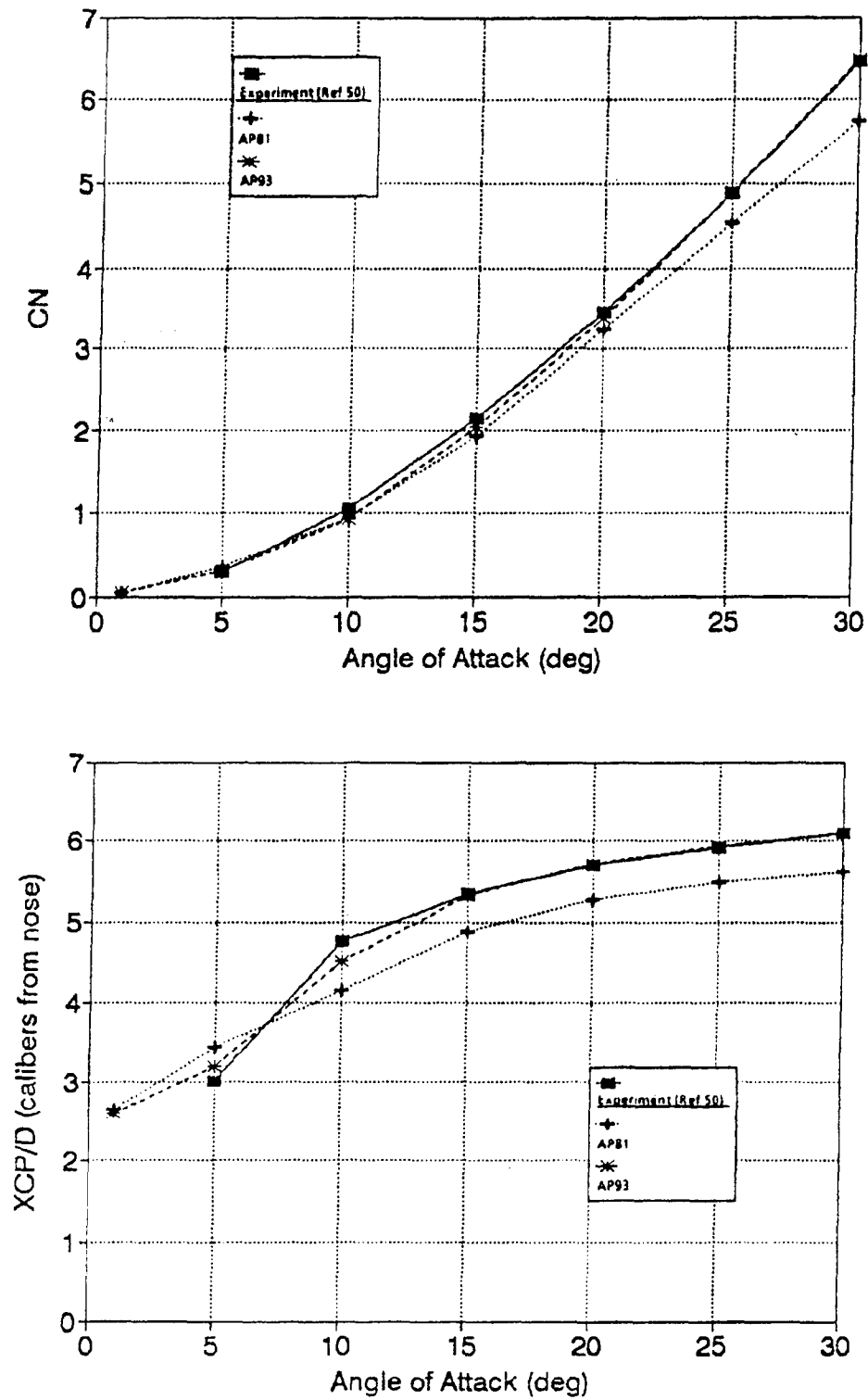


FIGURE 5-12. BODY-ALONE NORMAL-FORCE COEFFICIENT AND CENTER OF PRESSURE ($M_\infty = 3.5$)

$$k_1 = \frac{C_{N_{NL}}(M_{\infty}, AR, \lambda)}{\sin^2 \alpha} \quad (89)$$

was generated. Tables of k_1 for both high and low Mach numbers are given in Tables 5-2 and 5-3. The total wing-alone normal force in AP93 is therefore

$$C_{N_w} = C_{N_L} + k_1 \sin^2 \alpha \frac{A_w}{A_{ref}} \quad (90)$$

The second term of Equation (90) was neglected in AP81.

The center of pressure of the wing-alone lift was assumed to vary quadratically between its linear theory value at $\alpha = 0$ to the centroid of the planform area (adjusted for thickness effects) at $\alpha = 60$ deg.

Defining the center of pressure of the wing-alone linear term as A and the center of pressure of the nonlinear term as B (both in percent of mean geometric chord), then the center of pressure of the wing lift is

$$(X_{cp})_w = A + \frac{1}{36} |\alpha_w| [B - A] + \frac{1}{5400} \alpha_w^2 [A - B] \quad (91)$$

α_w is the total angle of attack in degrees on the wing. Figure 5-13 gives an example of the AP93 methodology compared to AP81 and experimental data. This particular case shows significant improvement in wing-alone normal force of the AP93 versus AP81 when compared to the experiment. However, no improvement in center of pressure is obtained because $\lambda = 0$ and the centroid of Planform area is the same as experimental data suggest.

5.6 Wing-Body and Body-Wing Nonlinear

Interference Factors Due to Angle of Attack^{47,48}

The total configuration normal-force coefficient at a given angle of attack, control deflection and Mach number is given by Equation (55) repeated here for convenience:

$$C_N = C_{N_e} + [(K_{W(B)} + K_{B(W)})\alpha + (k_{W(B)} + k_{B(W)})\delta_w](C_{N_e})_w \quad (55)$$

$$+ [(K_{T(B)} + K_{B(T)})\alpha + (k_{T(B)} + k_{B(T)})\delta_T](C_{N_e})_T + C_{N_{TV}} + C_{N_{BV}}$$

Moore, et al., found that the wing-body interference factor $K_{W(B)}$ had the qualitative behavior as shown in Figure 5-14.⁴⁷ At low angles of attack, slender-body theory appeared to be a good estimate of $K_{W(B)}$. This estimate was adjusted slightly for $M_{\infty} \leq 1.5$ by an amount $\Delta K_{W(B)}$. At some angle of attack defined as α_c , $K_{W(B)}$ seemed to decrease in a nearly linear fashion. The rate of this decrease was a function of Mach number: the higher the Mach number, the larger the rate of decrease. At some point defined as α_D , the $K_{W(B)}$ appeared to reach a minimum and remain about

constant. As a result of this analysis, a mathematical model was derived to define $K_{W(B)}$ in terms of its slender-body theory value $[K_{W(B)}]_{SB}$ and an empirical correction derived from several databases.^{50, 51, 52} This model given in Figure 5-14 is

$$K_{W(B)} = [K_{W(B)}]_{SB} + [\Delta K_{W(B)}]_{\alpha=0} \left(\frac{r/s}{0.5} \right) \text{ for } \alpha \leq \alpha_c$$

$$K_{W(B)} = [K_{W(B)}]_{SB} + \left\{ [\Delta K_{W(B)}]_{\alpha=0} + \frac{dK_{W(B)}}{d\alpha} (\alpha - \alpha_c) \right\} \left(\frac{r/s}{0.5} \right) \text{ for } \alpha_c \leq \alpha \leq \alpha_D$$

$$K_{W(B)} = [K_{W(B)}]_{SB} + \left\{ [\Delta K_{W(B)}]_{\alpha=0} + \frac{dK_{W(B)}}{d\alpha} (\alpha_D - \alpha_c) \right\} \left(\frac{r/s}{0.5} \right) \text{ for } \alpha > \alpha_D \quad (92)$$

The empirical corrections to $K_{W(B)}$ are also in a form that can be defined mathematically as opposed to a table lookup procedure. These equations for

$$[\Delta K_{W(B)}]_{\alpha=0}, \frac{dK_{W(B)}}{d\alpha}, \alpha_c, \alpha_D$$

are as follows:

$$[\Delta K_{W(B)}]_{\alpha=0}$$

$$[\Delta K_{W(B)}]_{\alpha=0} = 0.22 \quad \text{for } M_{\infty} \leq 1.0$$

$$[\Delta K_{W(B)}]_{\alpha=0} = -0.44[M_{\infty} - 1.5] \quad \text{for } 1.0 < M_{\infty} \leq 1.5$$

$$[\Delta K_{W(B)}]_{\alpha=0} = 0 \quad \text{for } M_{\infty} > 1.5$$

$$\frac{d[K_{W(B)}]}{d\alpha}$$

$$\frac{d[K_{W(B)}]}{d\alpha} = -(0.00283M_{\infty} + 0.025)$$

(94)

TABLE 5-2. VALUES OF k_1 FOR LOW MACH NUMBERAR \leq 0.5; $M_\infty < 4.0$

λ/M_∞	0.0	0.5	1.0	1.5	2.0	2.5	3.0	3.5	4.0	4.5
0.0	1.55	1.57	1.60	1.60	1.51	1.25	0.92	0.56	0.29	0.16
0.5	2.84	2.90	2.82	2.30	1.35	1.00	0.80	0.64	0.47	0.33
1.0	2.37	2.45	2.43	2.31	1.50	1.05	0.90	0.75	0.61	0.48

AR \leq 1.0; $M_\infty < 3.5$

λ/M_∞	0.0	0.5	1.0	1.5	2.0	2.5	3.0	3.5	4.0	4.5
0.0	1.32	1.48	1.46	0.99	0.40	0.22	0.12	0.09	0.09	0.11
0.5	2.44	2.45	1.85	0.70	0.31	0.19	0.20	0.26	0.36	0.43
1.0	1.20	1.22	1.10	0.50	0.45	0.50	0.65	0.78	0.88	0.94

AR \leq 2.0; $M_\infty < 3.5$

λ/M_∞	0.0	0.5	1.0	1.5	2.0	2.5	3.0	3.5	4.0	4.5
0.0	-1.80	-1.84	-1.95	-1.50	-0.20	0.00	0.10	0.20	0.25	0.30
0.5	-1.80	-1.84	-1.95	-1.50	-0.20	0.30	0.41	0.60	0.72	0.80
1.0	-1.45	-1.47	-1.35	-0.70	0.20	0.60	0.83	0.98	1.09	1.15

TABLE 5-3. VALUES OF k_1 FOR HIGH MACH NUMBERAR \leq 0.5; $M_\infty < 4.0$

$\lambda/M_\infty \sin^\alpha$	0.0	0.5	1.0	1.5	2.0	2.5	3.0	3.5	4.0	4.5	5.0	5.5	6.0
0.0	-1.60	-0.98	0.23	0.55	0.71	0.82	0.89	0.92	0.95	0.95	0.95	0.95	0.95
0.5	-0.87	-0.24	0.33	0.60	0.73	0.82	0.89	0.92	0.95	0.95	0.95	0.95	0.95
1.0	-0.31	0.09	0.46	0.68	0.78	0.87	0.91	0.93	0.95	0.95	0.95	0.95	0.95

AR \leq 1.0; $M_\infty < 3.5$

$\lambda/M_\infty \sin^\alpha$	0.0	0.5	1.0	1.5	2.0	2.5	3.0	3.5	4.0	4.5	5.0	5.5	6.0
0.0	-0.39	-0.39	-0.29	0.06	0.29	0.48	0.60	0.69	0.75	0.81	0.86	0.91	0.94
0.5	0.14	0.17	0.29	0.46	0.63	0.76	0.85	0.90	0.92	0.95	0.95	0.95	0.95
1.0	0.30	0.50	0.86	0.93	0.94	0.95	0.95	0.95	0.95	0.95	0.95	0.95	0.95

AR \leq 2.0; $M_\infty < 3.5$

$\lambda/M_\infty \sin^\alpha$	0.0	0.5	1.0	1.5	2.0	2.5	3.0	3.5	4.0	4.5	5.0	5.5	6.0
0.0	-0.25	-0.05	0.20	0.50	0.80	0.95	0.95	0.95	0.95	0.95	0.95	0.95	0.95
0.5	0.02	0.29	0.80	0.98	0.98	0.97	0.97	0.96	0.95	0.95	0.95	0.95	0.95
1.0	0.66	1.02	1.14	1.18	1.15	1.09	1.02	0.96	0.95	0.95	0.95	0.95	0.95

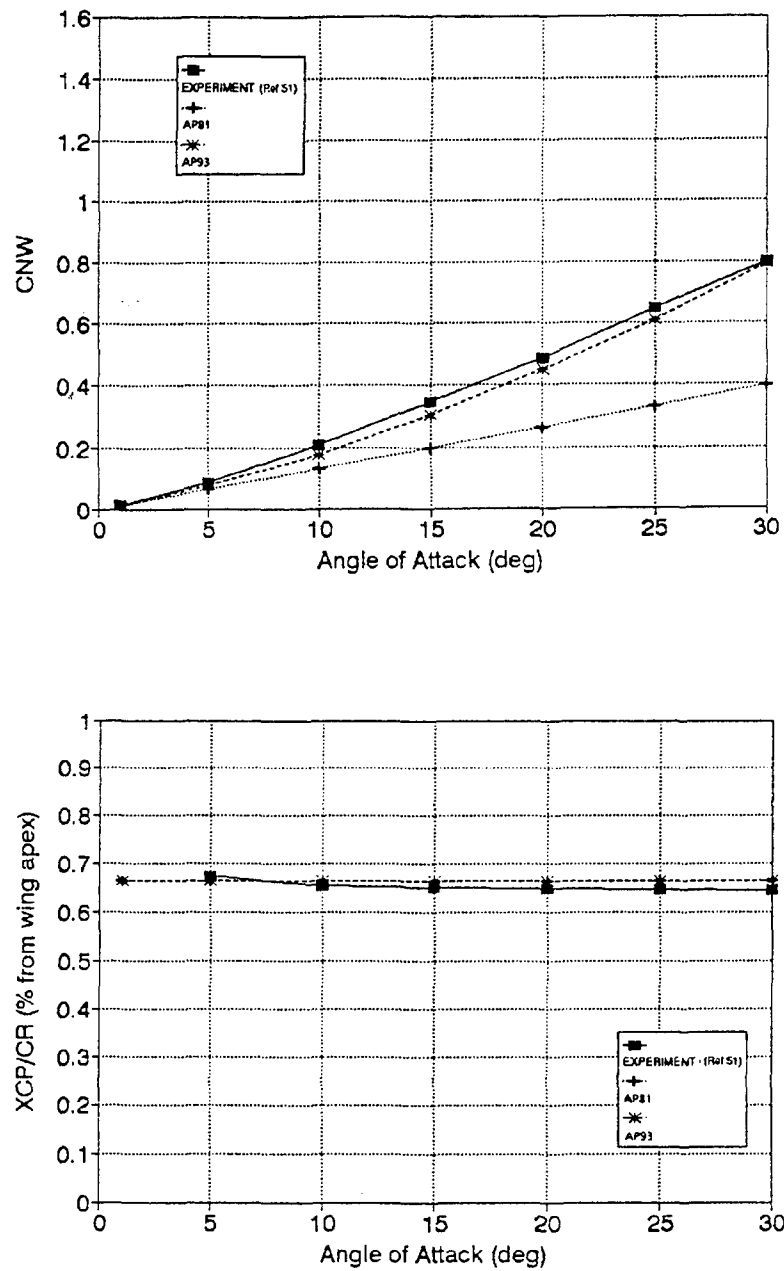
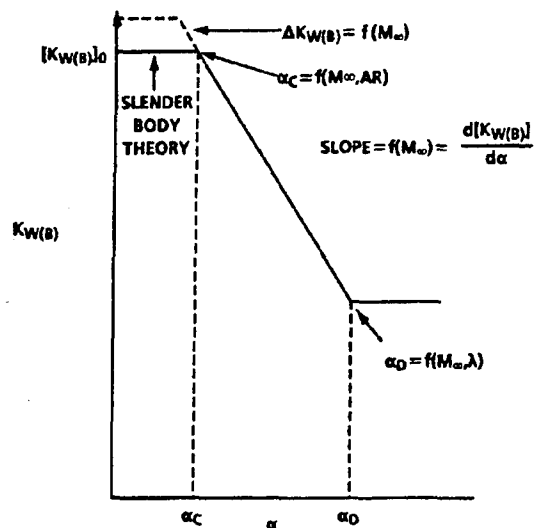


FIGURE 5-13. WING-ALONE NORMAL-FORCE COEFFICIENT AND CENTER OF PRESSURE
(AR = 0.5, $\Lambda = 0.0$, $M_\infty = 1.6$)



GENERAL EQUATION:

$$K_{W(B)} = [K_{W(B)}]_{SB} + [\Delta K_{W(B)}]_{\alpha=0} \frac{r/s}{0.5} \text{ for } \alpha \leq \alpha_c$$

$$K_{W(B)} = [K_{W(B)}]_{SB} + [\Delta K_{W(B)}]_{\alpha=0} \frac{r/s}{0.5} + \left(\frac{dK_{W(B)}}{d\alpha} \right) \frac{(\alpha - \alpha_c)(r/s)}{0.5} \text{ for } \alpha_c \leq \alpha \leq \alpha_D$$

$$K_{W(B)} = [K_{W(B)}]_{SB} + \left\{ [\Delta K_{W(B)}]_{\alpha=0} + \frac{dK_{W(B)}}{d\alpha} (\alpha_D - \alpha_c) \right\} \left(\frac{r/s}{0.5} \right) \text{ for } \alpha > \alpha_D$$

FIGURE 5-14. QUALITATIVE BEHAVIOR OF WING-BODY INTERFERENCE FACTORS AS A FUNCTION OF ANGLE OF ATTACK

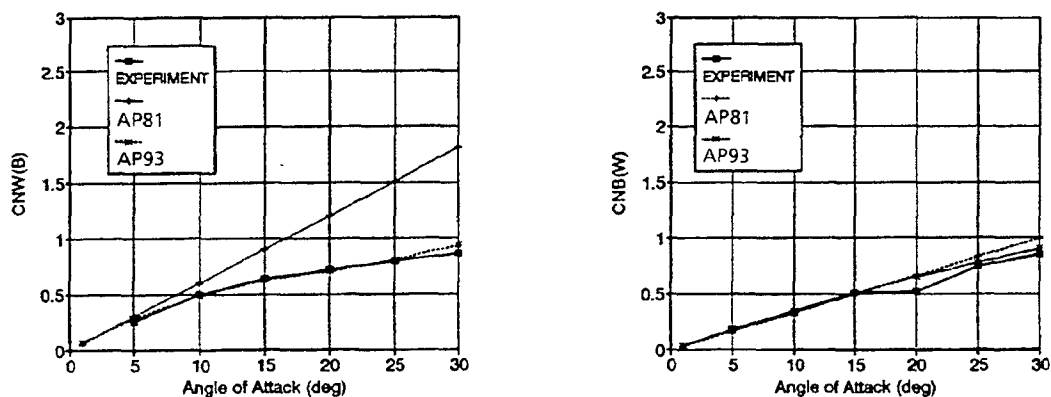


FIGURE 5-15. WING-BODY AND BODY-WING INTERFERENCE AS A FUNCTION OF α (AR = 2.0, $\lambda = 0$, $M_\infty = 1.2$)

$$\alpha_c$$

$$M_\infty < 2.0$$

$$\alpha_c = 12.5 - 1.06M_\infty - 2.59M_\infty^2 \quad \text{for } AR \leq 0.5$$

$$\alpha_c = 12.5 - 6.25M_\infty \quad \text{for } AR = 1.0$$

$$\alpha_c = 4.5 + 2.25M_\infty - 2.25M_\infty^2 \quad \text{for } AR \geq 2.0$$

$$M_\infty > 2.0$$

$$\alpha_c = 0$$

$$\alpha_D$$

$$\alpha_D = 33.3 - 8.19M_\infty + 0.82M_\infty^2 \quad \text{for } \lambda = 0$$

$$\alpha_D = 25.3 - 6.62M_\infty + 0.66M_\infty^2 \quad \text{for } \lambda = 1.0$$

$$\alpha_D = [\alpha_D]_{\lambda=1.0} + \lambda[(\alpha_D)_{\lambda=0} - (\alpha_D)_{\lambda=1.0}] \quad \text{for } 0 < \lambda < 1.0$$

The semiempirical model for $K_{B(W)}$ was also defined in terms of its slender body or linear theory value, plus a correction due to nonlinearities associated with angle of attack. The mathematical model for $K_{B(W)}$ was defined as¹⁰⁹

$$K_{B(W)} = [K_{B(W)}]_{LT}^{SB} + \frac{r/s}{0.5} \left\{ [\Delta K_{B(W)}]_{\alpha=0} + \frac{d[K_{B(W)}]}{d\alpha} |\alpha| \right\} \quad (97)$$

Unfortunately, a mathematical model for $[\Delta K_{B(W)}]_{\alpha=0}$ and $d[K_{B(W)}]/d\alpha$ was difficult to define because of the variability of the constants as a function of the parameters of interest. As a result, a three-parameter table lookup for these two parameters is used in AP93 based on the data in Table 5-4. The parameters in the table lookup include M_∞ , λ , and AR. Linear interpolation is used.

Examining cases where r/s is small, it was found that at high angles of attack, the wing-alone solution was not recovered properly through the process, Equations (92) and (97). To remedy this situation, the AP93 nonlinear interference factors were blended into those predicted by slender-body or linear theory as r/s became small. The specific equations used to do this are

For $r/s \geq 0.25$

$$K_{W(B)} = [K_{W(B)}]_{AP93} \quad (98a)$$

$$K_{B(W)} = [K_{B(W)}]_{AP93}$$

For $0.05 < r/s < 0.25$

$$K_{W(B)} = [K_{W(B)}]_{SBT} - ([K_{W(B)}]_{SBT} - [K_{W(B)}]_{AP93})(r/s - 0.05)/0.2$$

$$K_{B(W)} = [K_{B(W)}]_{LT}^{SBT} - ([K_{B(W)}]_{LT}^{SBT} - [K_{B(W)}]_{AP93})(r/s - 0.05)/0.2$$

For $r/s \leq 0.05$

$$K_{W(B)} = [K_{W(B)}]_{SBT}; \quad K_{B(W)} = [K_{B(W)}]_{LT}^{SBT} \quad (98c)$$

In essence, the model represented by Equations (98a) through (98c) uses the nonlinear interference factors for r/s values greater than 0.25; they use a blend of slender-body or linear theory and the nonlinear values of interference factors for r/s values between 0.05 and 0.25. They also use the slender-body or linear theory values for r/s values less than 0.05. Hence, when the body vanishes ($r/s = 0$), the wing-alone solution will be automatically recovered in a smoother and more accurate way.

Figure 5-15 is an example of the normal force on the wing in the presence of the body and the normal force on the body in the presence of the wing using AP93 theory, the AP81 theory, and compared to experimental data. Note that

$$C_{N_{W(B)}} = C_{N_W} K_{W(B)}$$

$$C_{N_{B(W)}} = C_{N_B} K_{B(W)} \quad (99)$$

Hence, Figure 5-15 is actually a representation of the normal-force coefficient on the wing and additional normal force on the body due to the wing. Thus, Equation (99) is a representation of the accuracy of not only $K_{W(B)}$ and $K_{B(W)}$, but C_{N_W} in conjunction with the interference factors. This is a more true indication of the accuracy of the code because there are actually two of the component force terms that make up Equation (39). As seen in Figure 5-15, the AP93 methodology is superior to the AP81 theory as angle of attack increases.

The center of pressure of the new value of normal force of the wing in the presence of the body estimated by Equation (92) is assumed to remain at the values of the wing-alone solution of AP93 given by Equation (91). The center of pressure of the additional lift on the body due to the presence of the wing is estimated using the AP81 method, which is either slender-body or linearized theory. These values are modified for short afterbodies.²

TABLE 5-4. DATA FOR BODY-WING NONLINEAR SEMIEMPIRICAL INTERFERENCE MODEL

		Data for $[\Delta K_{B(W)}]_{\alpha=0}$								
		Mach Number								
Aspect Ratio	Taper Ratio	≤ 0.6	0.8	1.2	1.5	2.0	2.5	3.0	3.5	≥ 4.5
≤ 0.25	0, 0.5, 1.0	-0.1	-0.1	0.5	0.6	0.7	0.8	0.7	0.5	0.3
0.5	0.5	-0.28	-0.1	0.13	0.11	0.05	-0.02	-0.06	0	0
1.0	0.5	-0.26	-0.2	0.15	0.21	0.15	0	0	0	0
≥ 2.0	0.5	-0.13	-0.04	0.12	0.43	-0.16	0	0.37	-0.08	-0.16
0.5	0	-0.3	-0.06	0.26	0.28	0.17	0.12	0.14	0	0
≥ 2.0	0	-0.2	-0.1	0.12	0.52	0.12	0.15	0.22	-0.06	-0.22
0.5	1.0	-0.16	0.08	0.26	0.14	-0.12	0	-0.05	-0.10	0
≥ 2.0	1.0	-0.2	-0.1	0.12	0.45	-0.02	0.11	0.28	-0.17	-0.3
		Data for $d[K_{B(W)}]/d\alpha$								
		Mach Number								
Aspect Ratio	Taper Ratio	≤ 0.6	0.8	1.2	1.5	2.0	2.5	3.0	3.5	≥ 4.5
≤ 0.25	0, 0.5 1.0	0.018	0.013	-0.010	-0.023	-0.013	-0.022	-0.031	-0.025	-0.031
0.5	0.5	0.019	0.010	-0.008	-0.010	-0.013	-0.013	-0.013	-0.012	-0.012
1.0	0.5	0.013	0.010	-0.007	-0.013	-0.020	-0.017	-0.012	-0.012	-0.012
≥ 2.0	0.5	0.010	0.011	0	-0.013	-0.010	-0.017	-0.040	-0.012	-0.012
0.5	0	0.033	0.022	0	-0.007	-0.010	-0.008	-0.014	-0.012	-0.012
≥ 2.0	0	0.010	0.010	-0.007	-0.020	-0.011	-0.020	-0.023	-0.012	-0.012
0.5	1.0	0.019	0	-0.019	-0.010	-0.007	-0.013	-0.014	-0.012	-0.012
≥ 2.0	1.0	0.010	0.01	-0.007	-0.017	0	-0.017	-0.026	-0.012	-0.012

In exercising the AP93 on missile configurations in the transonic speed regime ($0.6 \leq M \leq 2.0$), it was found that some of the nonlinear lift associated with small aspect ratio fins ($AR \leq 1.4$) was lost due to shock-wave formation. An empirical approach in the AP81 accounted for a certain amount of linear lift loss. This appeared to be satisfactory for the larger aspect ratio fins, where the nonlinear normal-force term with angle of attack was negative. However, when the fins have a positive nonlinear normal force due to angle of attack, some of this force appears to be lost with shock waves. This loss was estimated empirically as a function of Mach number and angle of attack for a wing that had an area-to-body reference area of about one. These data for ΔC_N losses due to compressibility effects are given in Table 5-5. A two parameter linear interpolation is made from Table 5-5 for a given M_∞ and α to compute ΔC_N . ΔC_N is further degraded for taper ratio for values of $\lambda < 0.5$. The specific equations for ΔC_N are

$$\begin{aligned} \Delta C_{N_{B(W)}} &= -(\Delta C_N) \frac{A_w}{A_{ref}} \quad \text{for } \lambda \geq 0.5 \\ \Delta C_{N_{B(W)}} &= -(\Delta C_N) \left(\frac{A_w}{A_{ref}} \right) \left(\frac{\lambda}{0.5} \right) \quad \text{for } 0.1 \leq \lambda \leq 0.5 \quad (100) \\ \Delta C_{N_{B(W)}} &= -0.2 \Delta C_N \left(\frac{A_w}{A_{ref}} \right) \quad \text{for } \lambda \leq 0.1 \end{aligned}$$

5.7 Nonlinear Wing-Body Interference Factor Due to Control Deflection⁸

Initially, it was planned to use slender-body theory for the interference factors $k_{W(B)}$ and $k_{B(W)}$, as currently done in AP81. This plan was based on results comparing computations (using Equations (55) where all the nonlinearities are included) with experimental data at $\delta = 0$ for both body-tail and wing-body-tail or dorsal-body-tail configurations.⁴⁷ These comparisons were good and seemed to indicate that new technology was superior to existing engineering approaches.

However, when results were examined for configurations that had control deflections on either the aft or forward lifting surface, they were found to be not as good as desired. This led to the conclusion that nonlinear interference factors, due to control deflection, were also required to improve the performance of AP93 when compared to experimental data.

The approach taken was to use the AP93 with the nonlinearities of wing-alone, wing-body, and body-wing interference effects due to angle of attack included, use the slender-body estimates of $k_{W(B)}$ and $k_{B(W)}$ for control deflection, and derive empirical modifications to $k_{W(B)}$ based on numerical experiments compared to actual missile data. Because $k_{W(B)}$ appears in the vortex lift on the tail due to canard or wing shed vortices, the numerical experiments were conducted with canard body-tail configurations.

Referring to Equation (55), the vortex normal-force coefficient on the tail is²⁵

$$C_{N_{\pi T}} = \frac{(C_{N_a})_W (C_{N_c})_T [K_{W(B)} \sin \alpha + F k_{W(B)} \sin \delta_w] i (s_T - r_T) A_w}{2\pi (AR)_T (f_w - r_w) A_{ref}} \quad (101)$$

Equation (101) has a factor F that multiplies the term due to control deflection in the wing-tail vortex lift. This factor is needed in addition to the nonlinearity for $k_{W(B)}$, partly because the negative afterbody lift due to control deflection is not presently modeled in either AP81 or AP93. This term is defined by Equation (63).

The main reason this term was not included in the AP81 code was that it required an estimate of f_T , which is the position of the canard shed vortex at the tail. Also, Nielsen, et al., indicated that this term was generally much smaller than that computed by Equation (101).⁵² To account for this term, a vortex tracking algorithm or an empirical correction to the term in Equation (101) is needed. For angles of attack much greater than 25 or 30 deg, a vortex tracking algorithm may be needed. However, up to α of about 30 deg, a nonlinear model of interference effects resulting from control deflection was developed by defining $k_{W(B)}$ as a function of angle of attack and Mach number and F as a function of Mach number and angle of attack.

Using the work of Nielsen, et al., McKinney, and Smith, et al., for low Mach number,^{52, 53, 54} a semiempirical nonlinear model for $k_{W(B)}$ and the parameter F were derived from numerical experiments. The mathematical model for $k_{W(B)}$ is based on slender-body theory similar to $k_{W(B)}$ and $k_{B(W)}$ and modified for angle of attack or control deflection. In general, it was found that

$$\begin{aligned} k_{W(B)} &= C_1(M) [k_{W(B)}]_{SB} + C_2(|\alpha_w|, M_\infty) \\ F &= C_3(M, |\alpha_w|) \end{aligned} \quad (102)$$

More specifically, $k_{W(B)}$, C_1 , C_2 , and F are defined in Figure 5-16 for Mach numbers where data are available. For Mach numbers less than 0.8 and greater than 4.6, the equations derived for those conditions have been used. The current method for using the empirical estimate for $k_{W(B)}$ from Figure 5-16 is to linearly interpolate between Mach numbers for a given value of α , δ , and M_∞ .

The model in Figure 5-16 has a lot of similarities to the nonlinear $K_{W(B)}$ model already discussed: at low angle of attack, slender-body theory gives a reasonable estimate of $k_{W(B)}$. However, as angle of attack increases, $k_{W(B)}$ decreases up to low supersonic Mach numbers. For higher supersonic Mach numbers, $k_{W(B)}$ actually increases at higher angles of attack, presumably due to compressibility effects. Also, for low angles of

<u>M ≤ 8</u>
If $ \alpha_w \leq 24.0 \rightarrow k_{w(B)} = 1.4[k_{w(B)}]_{SB}$ If $ \alpha_w > 24.0 \rightarrow k_{w(B)} = 1.4 [.000794 \alpha_w ^2 - .0933 \alpha_w + 2.71]$ F = 1.1
<u>M = 1.1</u>
If $ \alpha_w \leq 15.0 \rightarrow k_{w(B)} = 1.3[k_{w(B)}]_{SB}$ If $ \alpha_w > 15.0 \rightarrow k_{w(B)} = 1.3 [.00087 \alpha_w ^2 - .0825 \alpha_w + 1.98]$ F = 1.1
<u>M = 1.5</u>
If $ \alpha_w \leq 10.0 \rightarrow k_{w(B)} = .9[k_{w(B)}]_{SB}$ If $ \alpha_w > 10.0 \rightarrow k_{w(B)} = .9[k_{w(B)}]_{SB} - .015[\alpha_w - 10.0]$ If $ \alpha_w \leq 20.0 \rightarrow F = .8$ If $ \alpha_w > 20.0 \rightarrow F = .8 + .10[\alpha_w - 20.0]$
<u>M = 2.0</u>
If $ \alpha_w \leq 10.0 \rightarrow k_{w(B)} = .9[k_{w(B)}]_{SB}$ If $ \alpha_w > 10.0 \rightarrow k_{w(B)} = .9[k_{w(B)}]_{SB} - .005[\alpha_w - 10.0]$ If $ \alpha_w \leq 20.0 \rightarrow F = .8$ If $ \alpha_w > 20.0 \rightarrow F = .8 + .17[\alpha_w - 20.0]$
<u>M = 2.3</u>
If $ \alpha_w \leq 20.0 \rightarrow k_{w(B)} = .9[k_{w(B)}]_{SB}$ If $ \alpha_w > 20.0 \rightarrow k_{w(B)} = .9[k_{w(B)}]_{SB} - .005[\alpha_w - 20.0]$ If $ \alpha_w \leq 30.0 \rightarrow F = .9$ If $ \alpha_w > 30.0 \rightarrow F = .9 + .15[\alpha_w - 30.0]$
<u>M = 2.87</u>
If $ \alpha_w \leq 20.0 \rightarrow k_{w(B)} = .9[k_{w(B)}]_{SB}$ If $ \alpha_w > 20.0 \rightarrow k_{w(B)} = .9[k_{w(B)}]_{SB} - .005[\alpha_w - 20.0]$ If $ \alpha_w \leq 30.0 \rightarrow F = .9$ If $ \alpha_w > 30.0 \rightarrow F = .9 + .17[\alpha_w - 30.0]$
<u>M = 3.95</u>
$k_{w(B)} = .8[k_{w(B)}]_{SB}$ If $ \alpha_w \leq 40.0 \rightarrow F = 0.9$ If $ \alpha_w > 40.0 \rightarrow F = 0.9 + .4[\alpha_w - 40.0]$
<u>M ≥ 4.6</u>
If $ \alpha_w \leq 20.0 \rightarrow k_{w(B)} = 0.75[k_{w(B)}]_{SB}$ If $ \alpha_w > 20.0 \rightarrow k_{w(B)} = 0.75[k_{w(B)}]_{SB} + .01[\alpha_w - 20.0]$ If $ \alpha_w \leq 35.0 \rightarrow F = .9$ If $ \alpha_w > 35.0 \rightarrow F = .9 + .3[\alpha_w - 35.0]$
where $\alpha_w = \alpha + \delta$

FIGURE 5-16. NONLINEAR WING-BODY INTERFERENCE MODEL DUE TO CONTROL DEFLECTION

TABLE 5-5. LOSS OF WING NONLINEAR NORMAL FORCE DUE TO SHOCK-WAVE EFFECTS IN TRANSONIC FLOW

M_∞	$ \alpha + \delta , \text{deg}$									
	0	5	10	15	20	25	30	35	≥ 40	
≤ 0.4	0.0000	0.0000	0.0000	0.0000	0.0000	0.0000	0.0000	0.0000	0.0000	0.0000
0.6	0.0000	0.0000	0.0000	0.0000	-0.0220	-0.2060	-0.6890	-0.9500	-1.300	
0.8	0.0000	0.0000	0.0000	0.0000	-0.0531	-0.2200	-0.7100	-1.010	-1.400	
1.2	0.0000	0.0000	-0.0093	-0.0293	-0.1651	-0.04167	-0.7629	-1.070	-1.500	
1.5	0.0000	0.0000	-0.0653	-0.1111	-0.1556	-0.4444	-0.7000	-1.070	-1.500	
2.0	0.0000	0.0000	-0.0076	-0.0376	-0.1502	-0.1142	-0.0951	-0.0700	-0.0500	
≥ 2.5	0.0000	0.0000	0.0000	0.000	0.0000	0.0000	0.0000	0.0000	0.0000	

TABLE 6-1. AP93 METHODS FOR BODY-ALONE AERODYNAMICS

Component/Mach Number Region	Subsonic $M_\infty < 0.8$	Transonic $0.8 \leq M_\infty < 1.2$	Low Supersonic $1.2 \leq M_\infty \leq 2.4$	High Supersonic $2.4 < M_\infty \leq 6.0$	Hypersonic $M_\infty > 6.0$
Nose Wave Drag	-	Semiempirical based on Euler Solutions	Second-Order Van Dyke plus MNT	SOSET plus IMNT	SOSET plus IMNT Modified for Real Gases
Boattail or Flare Wave Drag	-	Wu and Aoyoma	Second-Order Van Dyke	SOSET	SOSET for Real Gases
Skin Friction Drag	Van Driest II				
Base Drag	Improved Empirical Method				
Aeroheating Information	-	-	-	-	SOSET plus IMNT for Real Gases
Inviscid Lift and Pitching Moment	Empirical	Semiempirical based on Euler Solutions	Tsien First-Order Crossflow	SOSET	SOSET for Real Gases
Viscous Lift and Pitch Moment	Improved Allen and Perkins Crossflow				

attack, a value of F near one is found for the vortex lift model, indicating again reasonable accuracy of the theory in reference 25. However, as angle of attack is increased, F increases above one for many Mach numbers. That is, Equation (101) gives values of $C_{N_{TV}}$ too small due to control deflection of a forward surface. As already mentioned, this is most probably due to the neglect of the effect on the afterbody Equation (63), which accounts for a greater percentage of the afterbody effect compared to the Equation (101) results, as angle of attack increases.

6.0 SUMMARY OF METHODS IN 1993 VERSION OF NSWCDD AEROPREDICTION CODE (AP93) AND COMPARISON WITH EXPERIMENT^{8, 47}

The methods used for computing forces and moments in the AP93 are summarized in Tables 6-1, 6-2, and 6-3. Note that the code can now be useful for computing aerothermal information as well as forces and moments. This means the code now has five uses:

- a. Providing inputs to flight dynamics models that estimate range or miss distance
- b. Assessing static stability of various missile configurations
- c. Assessing various design parameters in terms of optimizing the configuration
- d. Assessing structural integrity using the loads portion of the code
- e. Assessing aerothermal aspects of a design using heat transfer coefficients at high Mach numbers.

As seen in Tables 6-1, 6-2, and 6-3, there are many methods that go into the overall makeup of a component build up code, such as the APC. The past 20 years have shown that this type of code can be quite useful when used in preliminary or conceptual design studies to provide down selection on many configuration alternatives in a fairly accurate and cost-effective manner. Most of the methods listed in the tables have been briefly summarized in sections of the report.

Several different complete missile configurations have been considered in the validation of the AP93 code compared to experimental data.^{8, 47} A sample of several of the flight conditions on a few of the configurations considered will be given here. Also, there will be comparisons with AP81 or other SOTA aeroprediction codes when such results are available in the literature. Funds were not available to do a thorough comparison.

The first case for comparison of the AP93 and AP81 is the configuration shown in Figure 6-1A. The body

shown has a three-caliber tangent ogive nose with total length of 12.33 calibers with aspect ratio 2.0 tails and 0.1 dorsals. Mach numbers of 4.5 and 10 are considered and comparisons are made with ZEUS code. Results of these comparisons in terms of normal force coefficient and center of pressure as a function of angle of attack are shown in Figure 6-1B. Center of pressure results show the AP93 within two percent of the body length compared to the ZEUS computations at all angles of attack considered. On the other hand, the AP81 center of pressure results differ by as much as 8 percent of body length from the ZEUS code. Examining normal force coefficient comparisons, it is seen that at Mach 4.5 AP93 is within 5 percent of ZEUS code, whereas AP81 results are low as much as 30 percent due to omission of nonlinear wing-alone and interference lift. At $M = 10$, the normal force of AP93 is within 13 percent of the ZEUS code, whereas AP81 results are off by as much as 40 percent.

The second configuration, Figure 6-2A, is taken from Howard and Dunn.⁵⁵ The dorsals have an aspect ratio of 0.12 and tail surfaces have an aspect ratio of 4. The aeroprediction code will not handle the configuration as shown at the top of Figure 6-2A. Experience has shown it necessary to keep the lifting surface area, centroid of area, span, taper ratio, and aspect ratio the same in the configuration modification process. This means the tip and root chord of the dorsal and tail surfaces had to be adjusted with these constraints in mind. The new adjusted configuration is shown at the bottom of Figure 6-2A. Hence, this configuration has all parameters outside the empirical data base for use in the AP93 including Mach number, aspect ratio, body configuration, and r/s .

Howard and Dunn showed only normal force coefficient results for the body-tail and body-dorsal-tail configurations at $M = 0.1$.⁵⁵ Results of the AP81, AP93, and Missile DATCOM are shown in Figure 6-2B compared to experiment for both the body-tail and body-dorsal-tail configurations. For the wing-body case, the AP93, and Missile DATCOM produce almost identical results; both show higher C_N values than experiment, particularly at low angles of attack. It is not clear why this discrepancy exists. The AP81 results, which have the older values of C_{dc} and no nonlinear wing lift, show even higher results than either the AP93 or Missile DATCOM.

The body-dorsal-tail configuration results of Figure 6-2B show that the AP93 is clearly superior to both the AP81 and Missile DATCOM. Normal force errors of the AP93 are less than 5 percent at all conditions, whereas errors of the AP81 and Missile DATCOM are as high as 40 and 50 percent, respectively. The fundamental reason for the AP93 success is the nonlinear wing-alone normal force and interference factor methodology. At $\alpha = 30^\circ$, the body-dorsal and dorsal-body contributes about $\frac{2}{3}$ of the total configuration normal force.

TABLE 6-2. AP93 METHODS FOR WING-ALONE AND INTERFERENCE AERODYNAMICS

Component/Mach Number Region	Subsonic $M_\infty < 0.8$	Transonic $0.8 \leq M_\infty < 1.2$	Low Supersonic $1.2 \leq M_\infty \leq 2.4$	High Supersonic $2.4 < M_\infty \leq 6.0$	Hypersonic $M_\infty > 6.0$
Wave Drag	-	Empirical	Linear Theory plus MNT	Shock Expansion (SE) plus MNT Along Strips	SE plus MNT for Real Gases Along Strips
Skin Friction Drag	Van Driest II				
Trailing Edge Separation Drag	Empirical				
Body Base Pressure Caused by Tail Fins	Improved Empirical				
Inviscid Lift and Pitching Moment ·Linear ·Nonlinear	Lifting Surface Theory Empirical	Empirical Empirical	3DTWT Empirical	3DTWT or SE Empirical	3DTWT or SE Empirical
Wing-Body, Body-Wing Interference ·Linear ·Nonlinear	Slender-Body Theory or Linear Theory Modified for Short Afterbodies Empirical				
Wing-Body Interference due to δ ·Linear ·Nonlinear	Slender-Body Theory Empirical				
Wing Tail Interference	Line Vortex Theory with Empirical Modifications for $k_{w(B)}$ Term and Nonlinearities				
Aeroheating	None Present				SE plus MNT for Real Gases

TABLE 6-3. AP93 METHODS FOR DYNAMIC DERIVATIVES

Component/Mach Number Region	Subsonic $M_\infty < 0.8$	Transonic $0.8 \leq M_\infty < 1.2$	Low Supersonic $1.2 \leq M_\infty \leq 2.4$	High Supersonic $2.4 < M_\infty \leq 6.0$	Hypersonic $M_\infty > 6.0$
Body Alone	Empirical				
Wing and Interference Roll Damping Moment	Lifting Surface Theory	Empirical	Linear Thin Wing Theory	Linear Thin Wing Theory or Strip Theory	
Wing Magnus Moment	Assumed Zero				
Wing and Interference Pitch Damping Moment	Lifting Surface Theory	Empirical	Linear Thin Wing Theory	Linear Thin Wing Theory or Strip Theory	

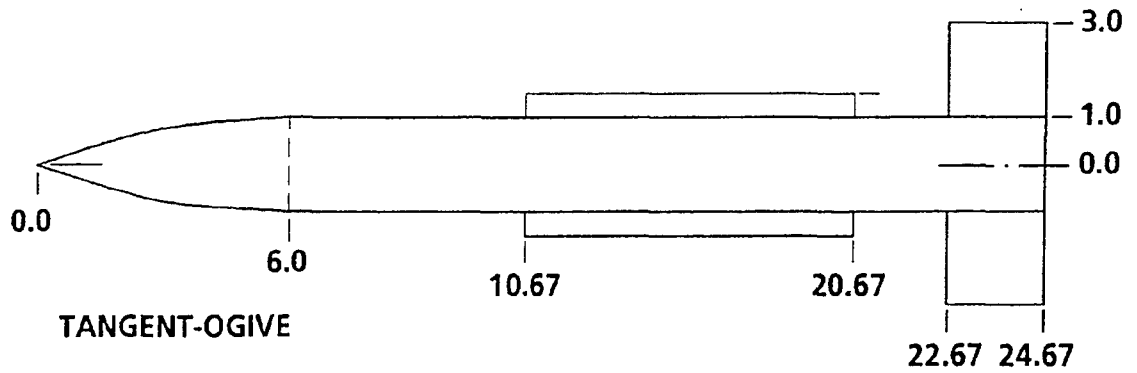


FIGURE 6-1A. BODY-DORSAL-TAIL CONFIGURATION USED FOR COMPARING ZEUS, IAP, AND OAP COMPUTATIONS

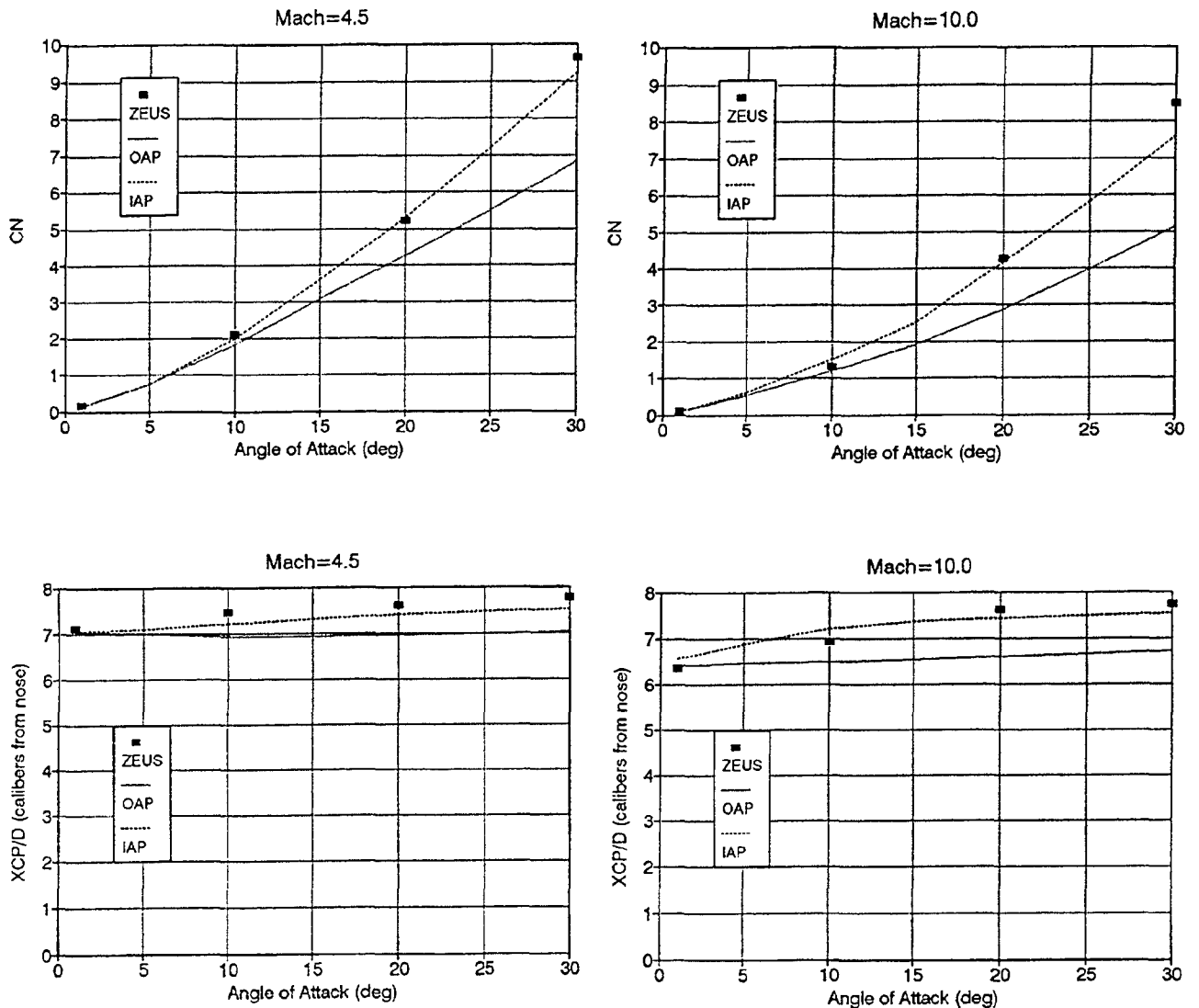
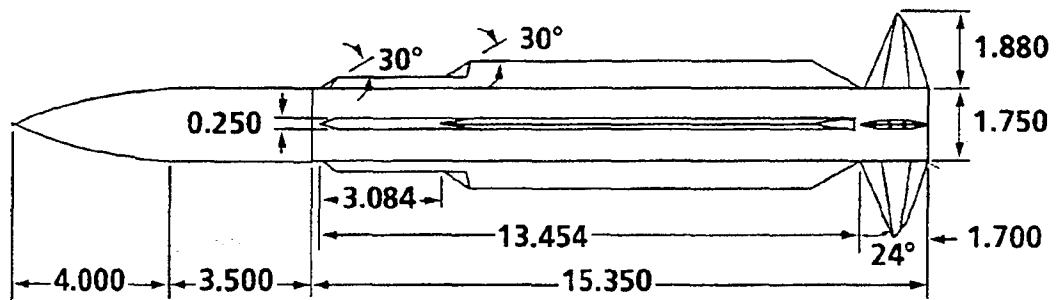
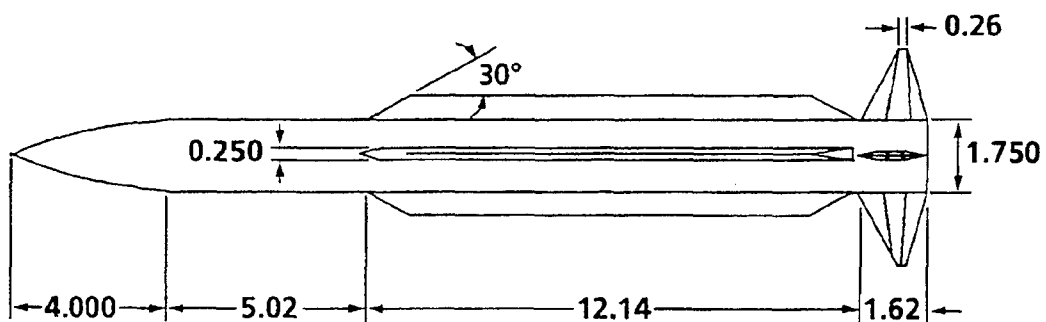


FIGURE 6-1B. COMPARISON OF PRESENT NORMAL FORCE COEFFICIENT AND CENTER OF PRESSURE COMPUTATIONS WITH THE ZEUS CODE FOR THE DORSAL-BODY-TAIL CONFIGURATION OF FIGURE 6-2A.



**CONFIGURATION TESTED IN WIND TUNNEL (FROM
REFERENCE 29 WHERE DIMENSIONS ARE IN INCHES)**



MODIFIED CONFIGURATION USED IN AEROPREDICTION COMPUTATIONS

PARAMETERS FOR BOTH MODELS

$(AR)_T = 4.0$	$b_t = 3.76$ in.	$\lambda_T = .16$	$(\Lambda_{LE})_T = 24^\circ$	$A_T = 3.54$ in. ²
$(AR)_D = .12$	$b_D = 1.32$ in.	$\lambda_D = .77$	$(\Lambda_{LE})_D = 60^\circ$	$A_D = 14.2$ in. ²

FIGURE 6-2A. CONFIGURATION USED FOR COMPARISON WITH MISSILE DATCOM AND EXPERIMENT

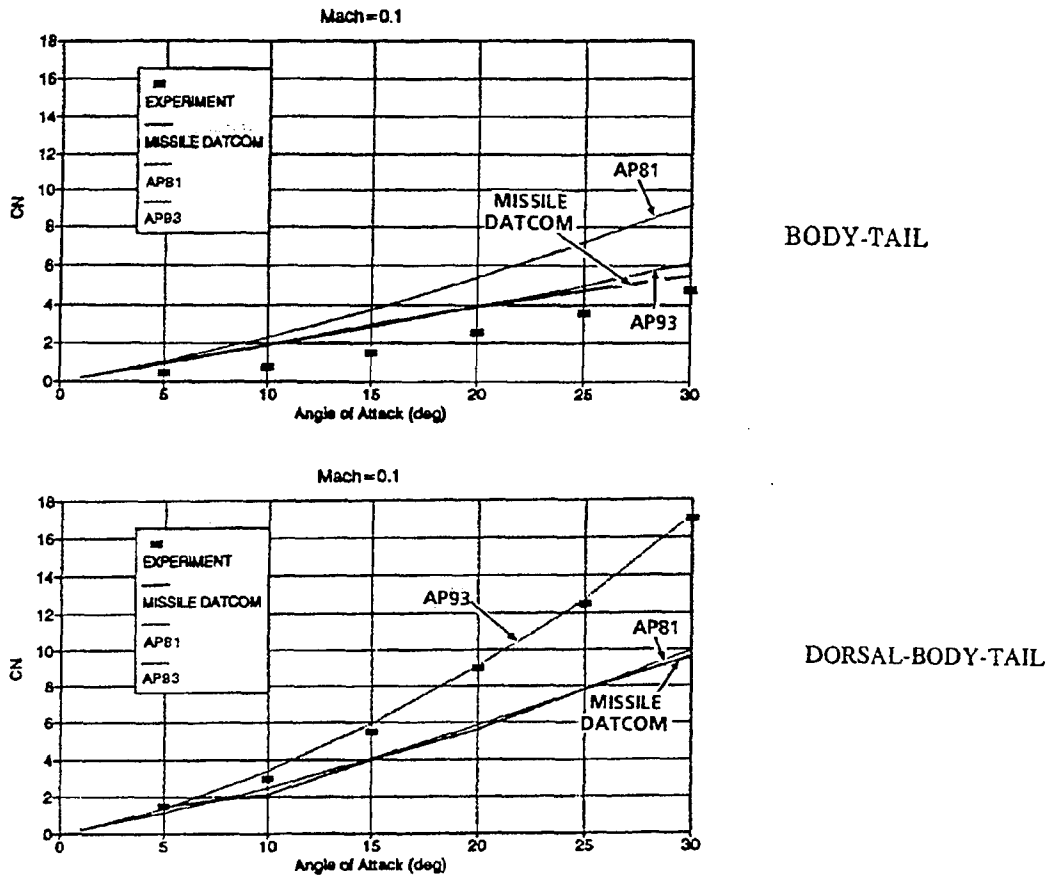


FIGURE 6-2B. COMPARISON OF PRESENT NORMAL FORCE COEFFICIENT WITH THAT PREDICTED BY MISSILE DATCOM AND EXPERIMENT FOR CONFIGURATION OF FIGURE 6-2A

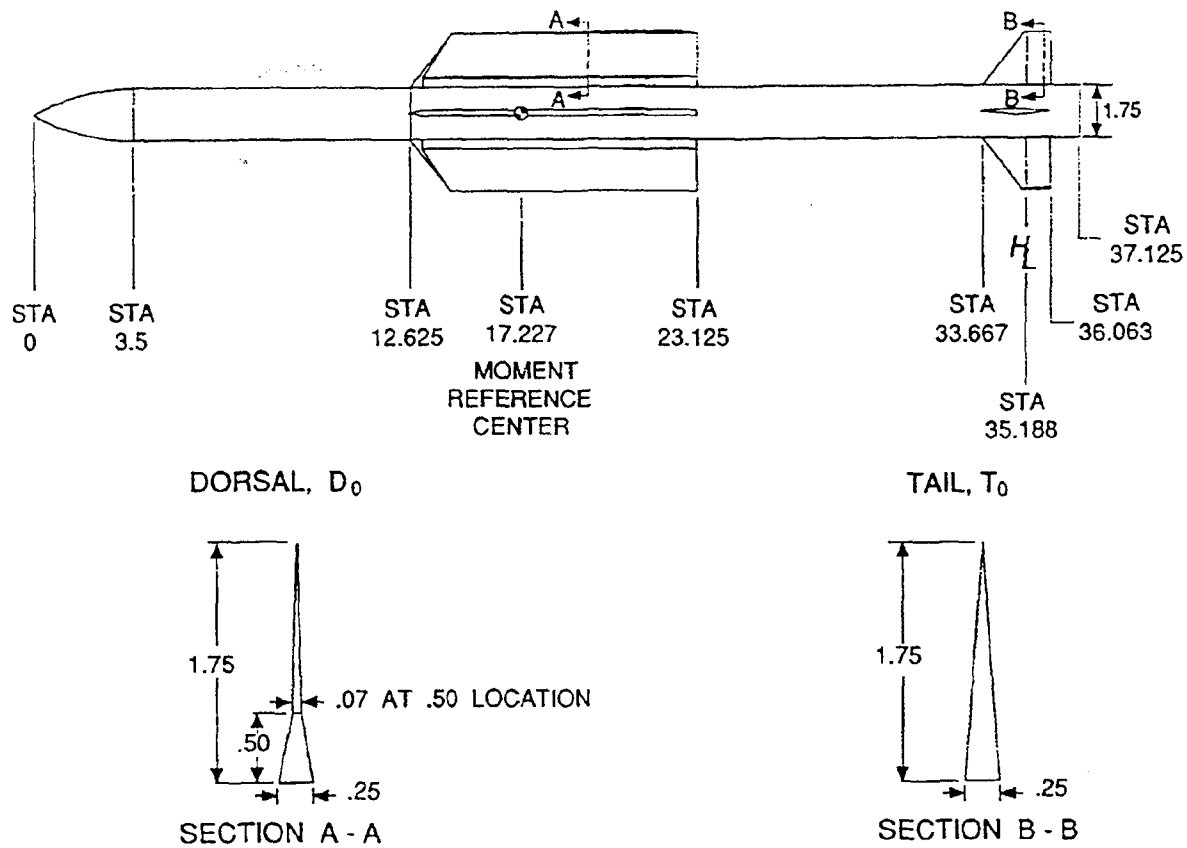


FIGURE 6-3A. DORSAL-BODY-TAIL CONFIGURATION USED FOR COMPARING MISSILE 3, AP93, AND AP81 COMPUTATIONS

The third configuration for validation of the new semiempirical methodology is shown in Figure 6-3A. This configuration also differs substantially from the geometry characteristics from which the new semiempirical methodology was derived. The body is 21.2 versus 12.33 calibers long with a 2-caliber Von Karman versus a 3-caliber tangent-ogive nose. The dorsals and tail surfaces have aspect ratios of 0.36 and 2.14, respectively, both at the outer edge of the data base.

Wind tunnel data exist for both the body-tail and body-dorsal-tail configuration for Mach numbers of 2.3 to 4.6 and at several roll orientations.⁵⁶ Comparisons are made at $\phi = 0^\circ$ roll and at Mach numbers of 2.3 and 4.6 for both the body-tail and body-dorsal-tail configurations. Results of these comparisons are shown in Figure 6-3B for the body-tail and Figure 6-3C for the body-dorsal-tail. The AP93 results are within the expected accuracy bounds on normal force, center of pressure, and pitching moment. While AP81 results are not shown for clarity, significant improvements in normal force for both body-tail and body-dorsal-tail configurations occur with less significant improvements in center of pressure. As noted in the comparisons, the AP93 is slightly superior to Missile 3⁵⁷ for most pitching moments and the two codes (AP93 and Missile 3) are about equal in normal force prediction.

A fourth case considered is the canard-body-tail case shown in Figure 6-4A.⁵⁸ The configuration is somewhat of an extreme case for the body-alone aerodynamics because it is a hundred percent blunt and is about 22.3 calibers long. The configuration tested in the wind tunnel has hangers attached to the body for aircraft carry and launch. However, tests were conducted with and without the hangers, and the results showed that C_N and C_M were unchanged but C_A was increased with the hangers present. The AP93 and AP81 theoretical computations are compared to the corrected data of Groves and Fournier,⁵⁸ where the hangers have been omitted. Results are given in Figures 6-4B through 6-4I for Mach numbers of 0.8, 2.86, and 4.63 and at canard deflections of 0, 10, and 20 deg. Examining Figures 6-4B through 6-4I, it is shown that AP93 gives good agreement with experimental data under almost all conditions. Significant improvements of the AP93 over the AP81 are seen at the lower Mach numbers and at the higher Mach number, higher angle-of-attack conditions.

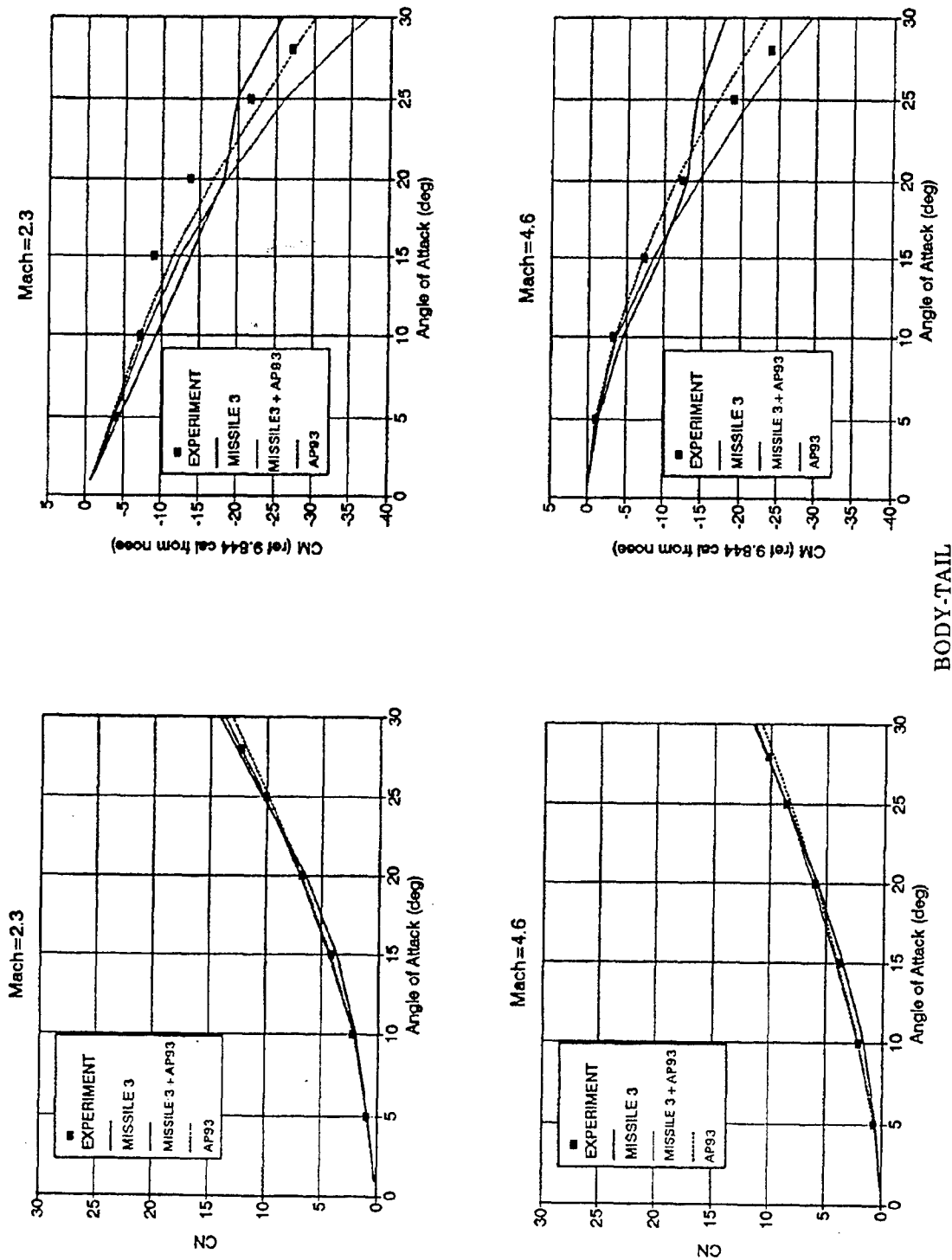
In analyzing why this improvement occurs at those conditions, it is noted that the aspect ratio of the tail surfaces of the configuration of Figure 6-4A is about 0.87 and that of the canard is about 1.7. Examining Tables 6-2 and 6-3, the nonlinearity in wing-alone lift is small for Mach numbers greater than about 1.5. As normal Mach number increases, $[M_\infty \sin(\alpha + \delta)]$ and Mach numbers exceed about 3.5 to 4.0, nonlinearity due to compressibility becomes important. As long as the aerodynamics are fairly linear, the AP81 gives good

results up to moderate angles of attack. However, when nonlinearities are present, the AP93 shows significant improvement. This improvement is the greatest on the Figure 6-4A configuration at low Mach number because the nonlinear normal-force term on the canards is negative, whereas that of the tails is positive. The combination produces a strong couple in terms of the pitching moment as evidenced by Figures 6-4A through 6-4I. A good nonlinear capability, such as that present in the AP93, is absolutely essential to get accurate stability and control information for these cases. Just examining Figure 6-4B, the center of pressure of the AP81 at $\alpha = 20$ deg differs from the experimental data by -9.4 percent of the body length versus 1.3 percent for the AP93.

A fifth case considered in the validation of the AP93 code is a configuration representative of the SPARROW missile tested at NASA/LRC.^{53, 59} The configuration tested and reported by Monta is shown in Figure 6-5A.⁵⁹ The configuration tested by McKinney is just like the one tested by Monta, except it had wiring tunnels and wave guides present.⁵³ These appendages add to the normal force and pitching moment, but were not accounted for in the analytical computations that are presented in Figure 6-5. The Monta configuration did not have these appendages present and was the main set of data used for the nonlinear empirical model validation. These results are distinguished in Figure 6-5 by the fact that the cases that had wave guides present are indicated.

Results of the AP81 and AP93, compared to the experiment for the configuration of Figure 6-5A, are shown in Figure 6-5B through 6-5G. Results are presented in terms of C_N and C_M versus angle of attack for various control deflections and Mach numbers. The nonlinear models with and without control deflection show the AP93 code agreeing much closer to the data at all Mach numbers than the linearized approaches of AP81. On the other hand, the fact that the body-alone normal force of AP81 had the nonlinearities included makes the comparisons to experimental data better than it would be otherwise.

In examining Figure 6-5B, it is seen that both C_N and C_M of AP93 agree with the experiment at $\delta = 0$ and $\delta = 10$ deg for $M_\infty = 1.5$ whereas, C_N and C_M of the AP81 are both considerably in error as angle of attack increases above 5 to 10 deg. For $M_\infty = 2.35$ (Figure 6-5C), both C_N and C_M of AP 93 at $\delta = 0$ and 20 deg agree with the data. Again, AP81 yields considerable error at $\alpha \geq 10$ deg, although the error is decreasing with increasing Mach number. For $M_\infty = 3.95$ (Figure 6-5C), AP81 gives acceptable results for C_N and C_M up to $\alpha = 15$ to 20 deg and at both $\delta = 0$ or 20 deg. The comparison with data gets worse above $\alpha = 20$ deg, whereas AP93 comparisons show good agreement at all values of α and δ . The same statements basically hold true for the $M_\infty = 4.6$ comparisons (Figure 6-5C).



BODY-TAIL

FIGURE 6-3B. COMPARISON OF PRESENT NORMAL FORCE COEFFICIENT AND PITCHING MOMENT COEFFICIENTS WITH MISSILE 3 ON THE CONFIGURATION OF FIGURE 6-3A (BODY-TAIL PORTION OF)

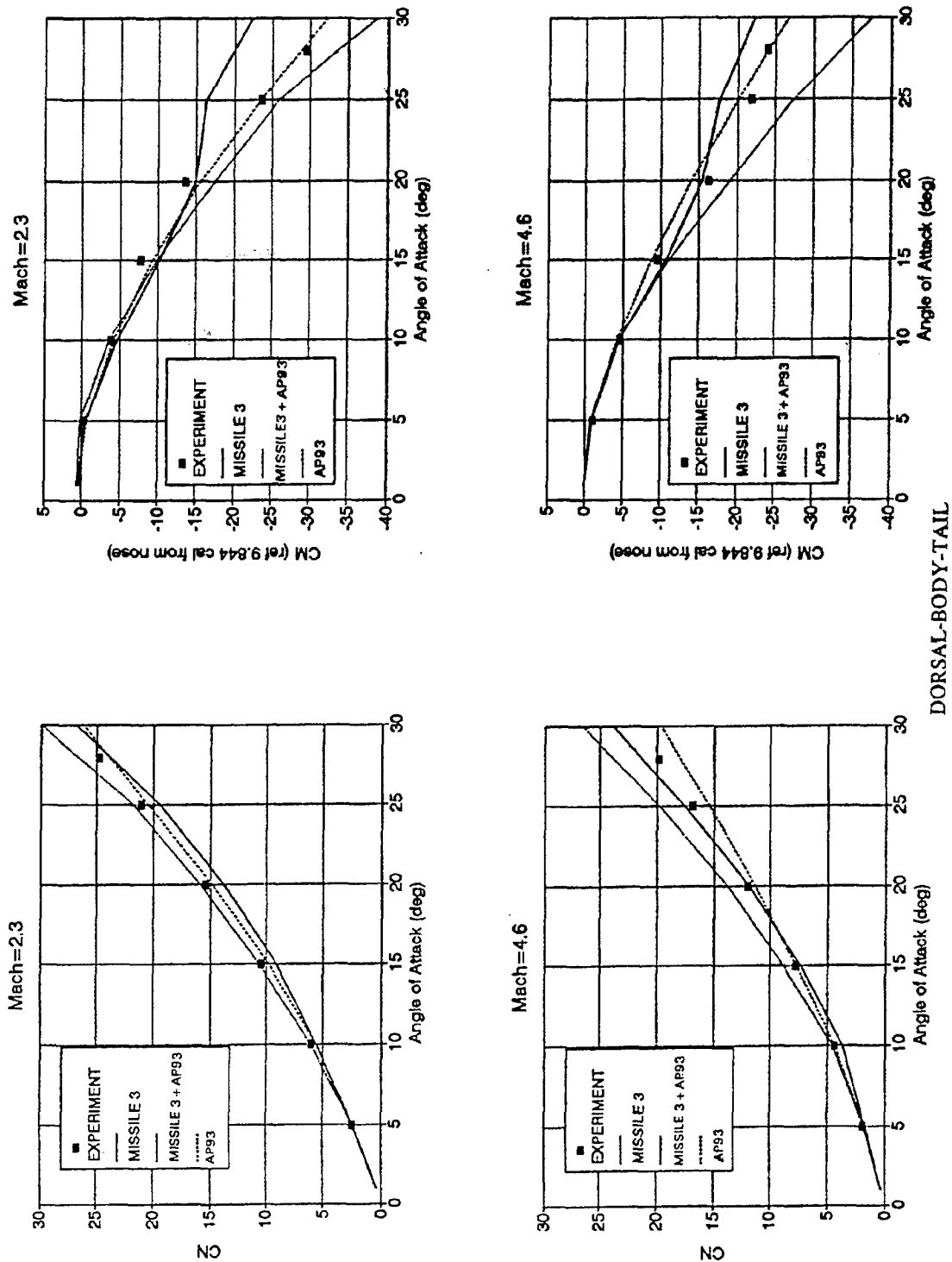


FIGURE 6-3C. COMPARISON OF PRESENT NORMAL FORCE COEFFICIENT AND PITCHING MOMENT COEFFICIENTS WITH MISSILE 3 ON CONFIGURATION OF 6-3A

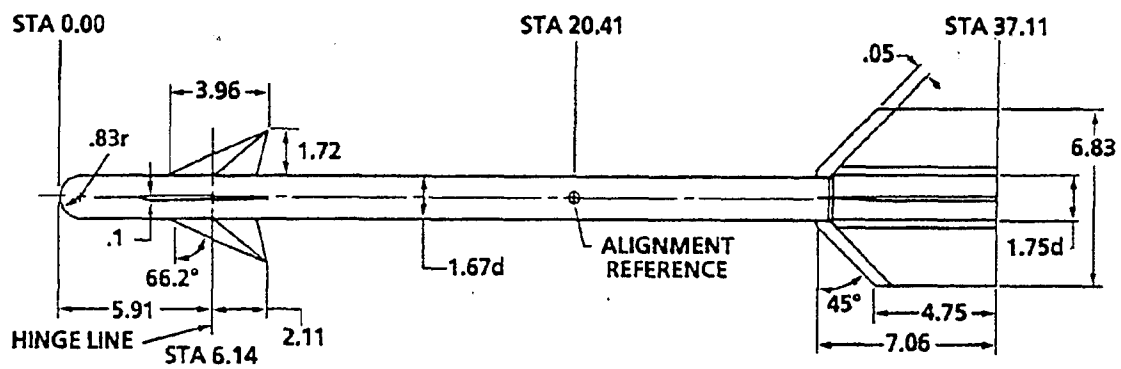


FIGURE 6-4A. CANARD-BODY-TAIL CONFIGURATION USED IN VALIDATION PROCESS⁵⁸

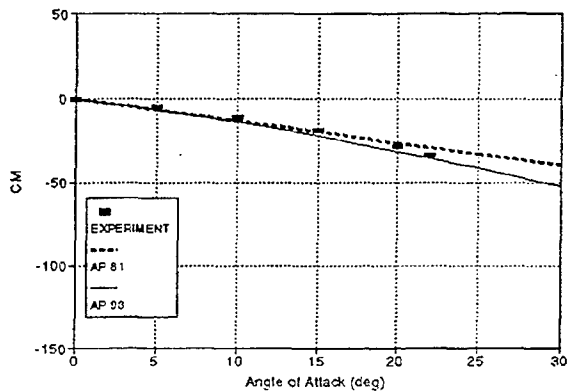
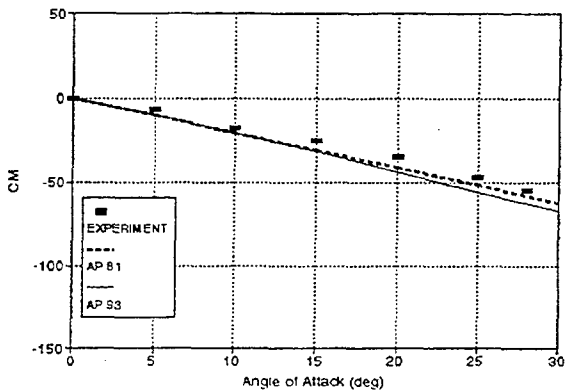
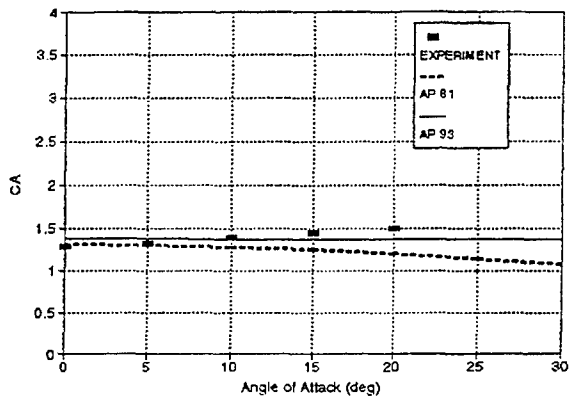
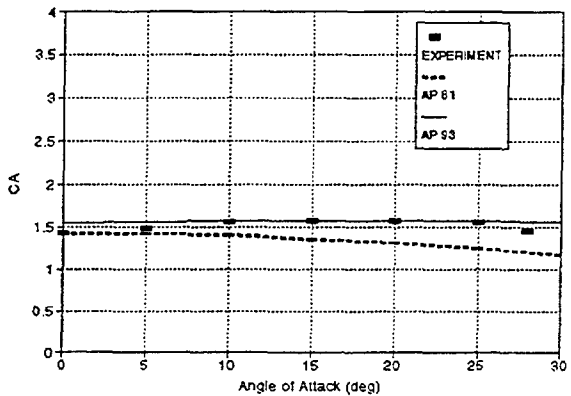
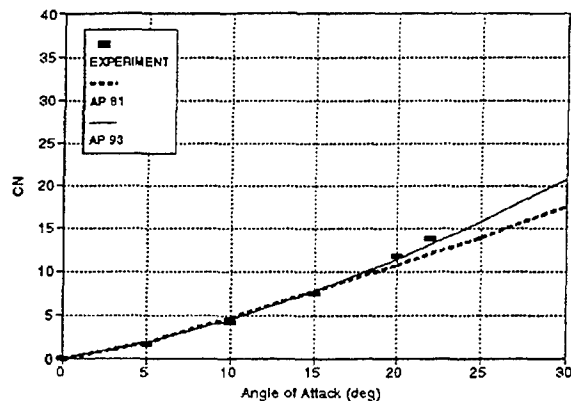
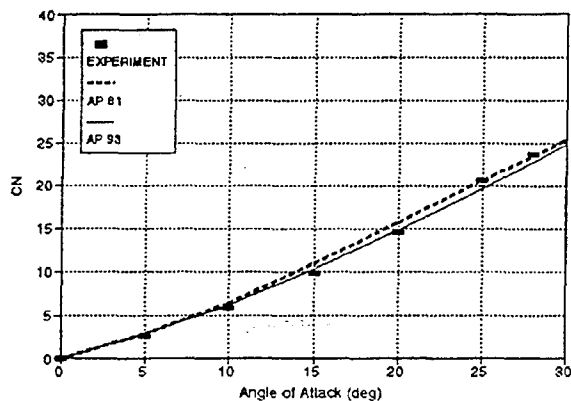


FIGURE 6-4B. NORMAL- AND AXIAL-FORCE AND PITCHING MOMENT COEFFICIENTS FOR CONFIGURATION OF FIGURE 6-4A ($M_\infty = 2.86, \delta = 0^\circ$)

FIGURE 6-4C. NORMAL- AND AXIAL-FORCE AND PITCHING MOMENT COEFFICIENTS FOR CONFIGURATION OF FIGURE 6-4A ($M_\infty = 4.63, \delta = 0^\circ$)

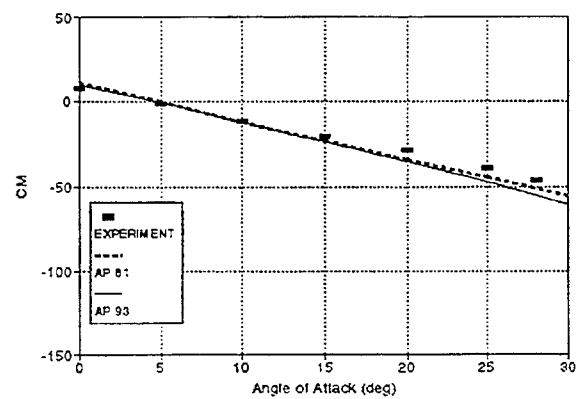
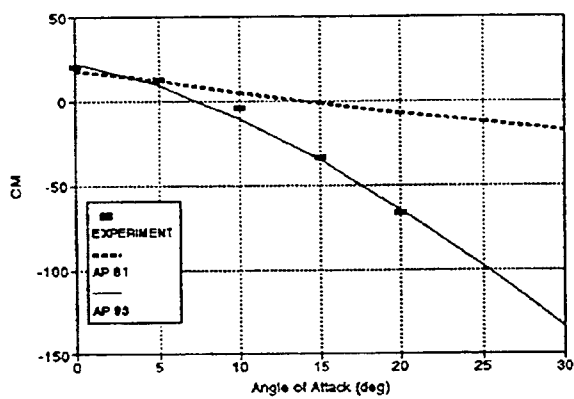
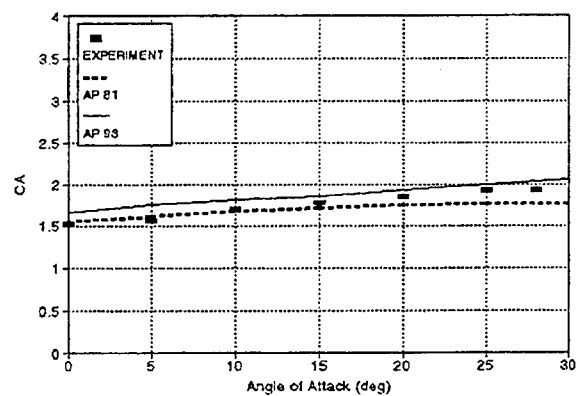
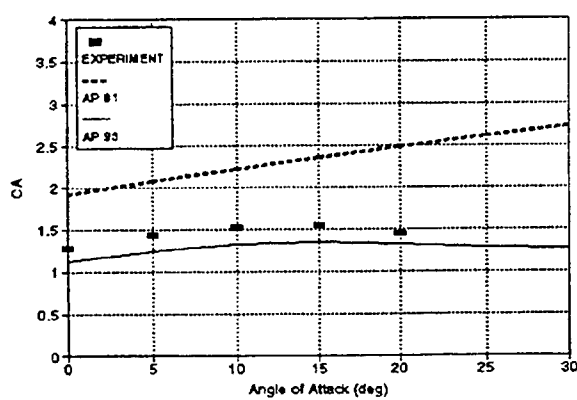
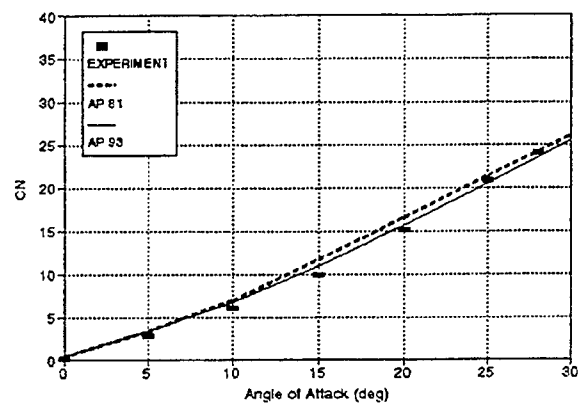
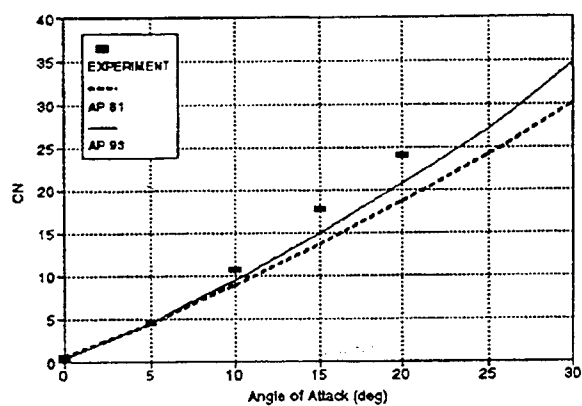


FIGURE 6-4D. NORMAL- AND AXIAL-FORCE AND PITCHING MOMENT COEFFICIENTS FOR CONFIGURATION OF FIGURE 6-4A
($M_\infty = 0.8$, $\delta = 10^\circ$)

FIGURE 6-4E. NORMAL- AND AXIAL-FORCE AND PITCHING MOMENT COEFFICIENTS FOR CONFIGURATION OF FIGURE 6-4A
($M_\infty = 2.86$, $\delta = 10^\circ$)

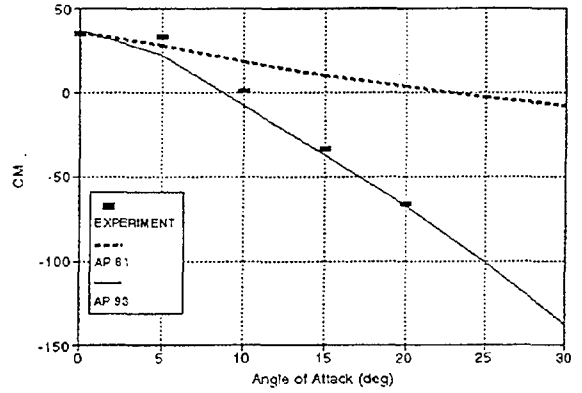
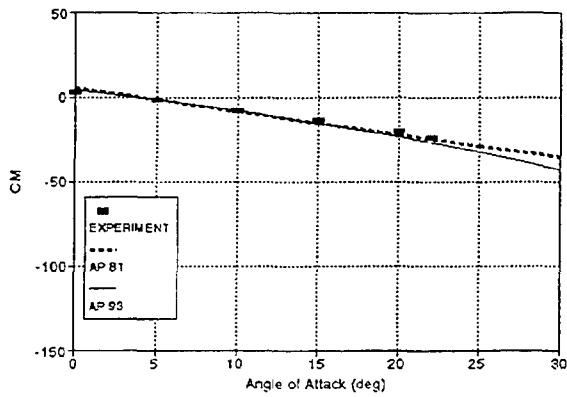
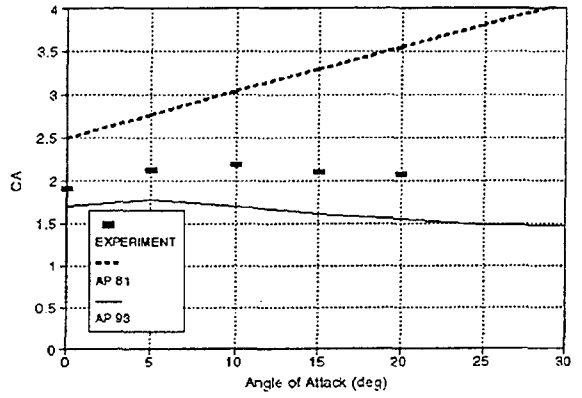
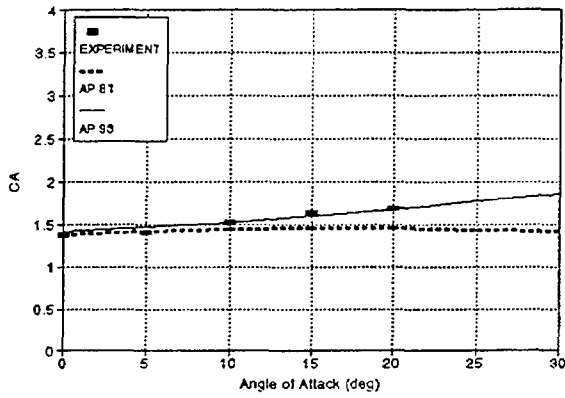
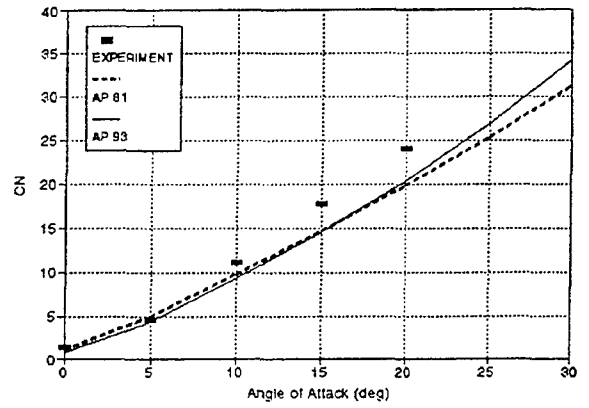
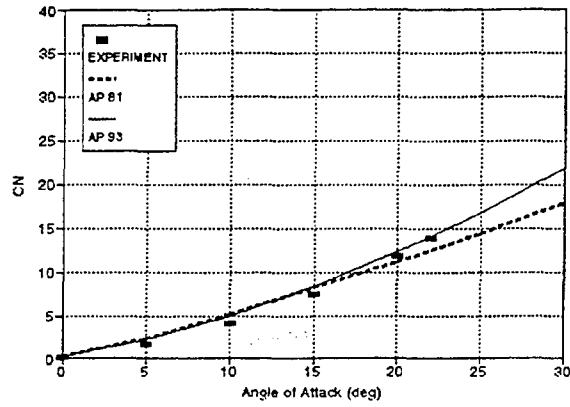


FIGURE 6-4F. NORMAL- AND AXIAL-FORCE AND PITCHING MOMENT COEFFICIENTS FOR CONFIGURATION OF FIGURE 6-4A ($M_\infty = 4.63, \delta = 10^\circ$)

FIGURE 6-4G. NORMAL- AND AXIAL-FORCE AND PITCHING MOMENT COEFFICIENTS FOR CONFIGURATION OF FIGURE 6-4A ($M_\infty = 0.8, \delta = 20^\circ$)

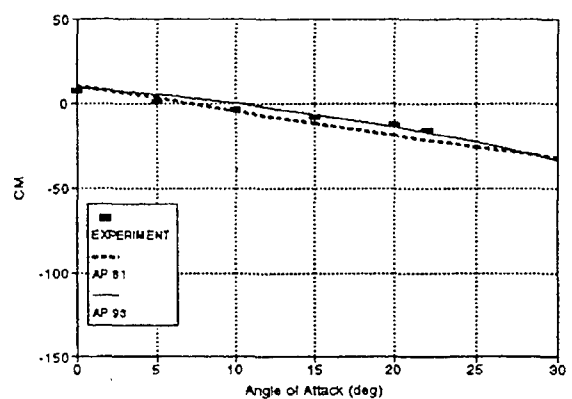
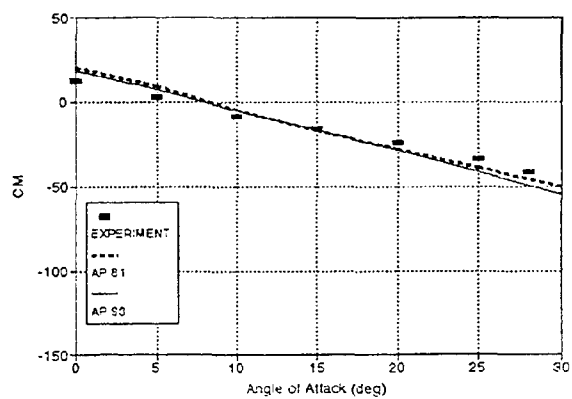
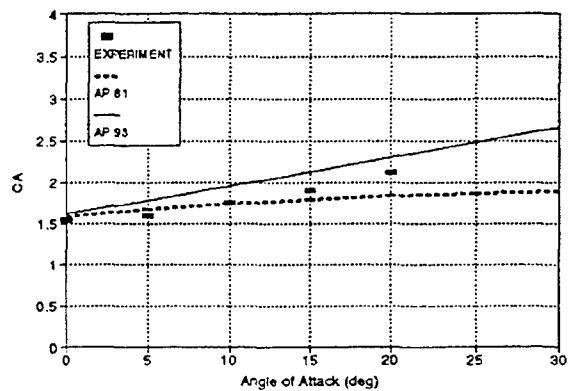
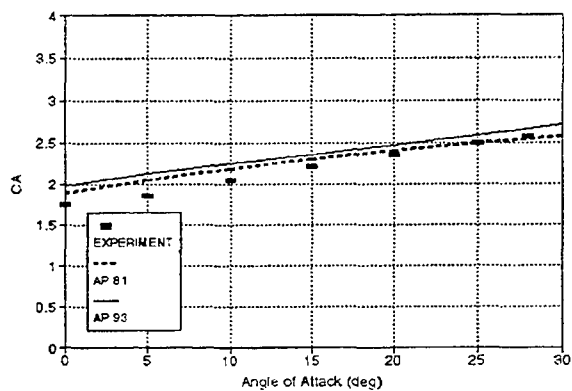
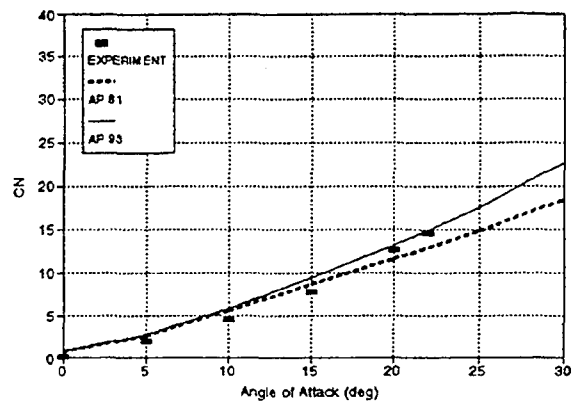
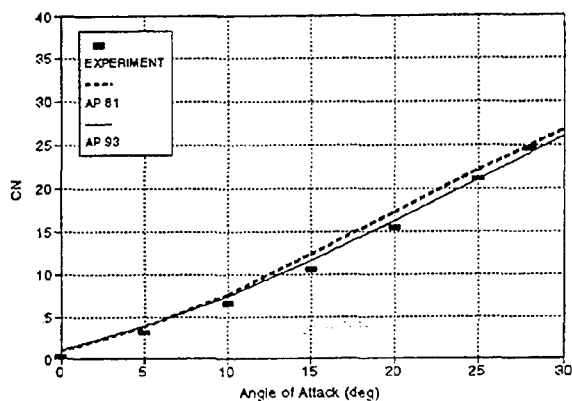


FIGURE 6-4H. NORMAL- AND AXIAL-FORCE AND PITCHING MOMENT COEFFICIENTS FOR CONFIGURATION OF FIGURE 6-4A
($M_\infty = 2.86$, $\delta = 20^\circ$)

FIGURE 6-4I. NORMAL- AND AXIAL-FORCE AND PITCHING MOMENT COEFFICIENTS FOR CONFIGURATION OF FIGURE 6-4A
($M_\infty = 4.63$, $\delta = 20^\circ$)

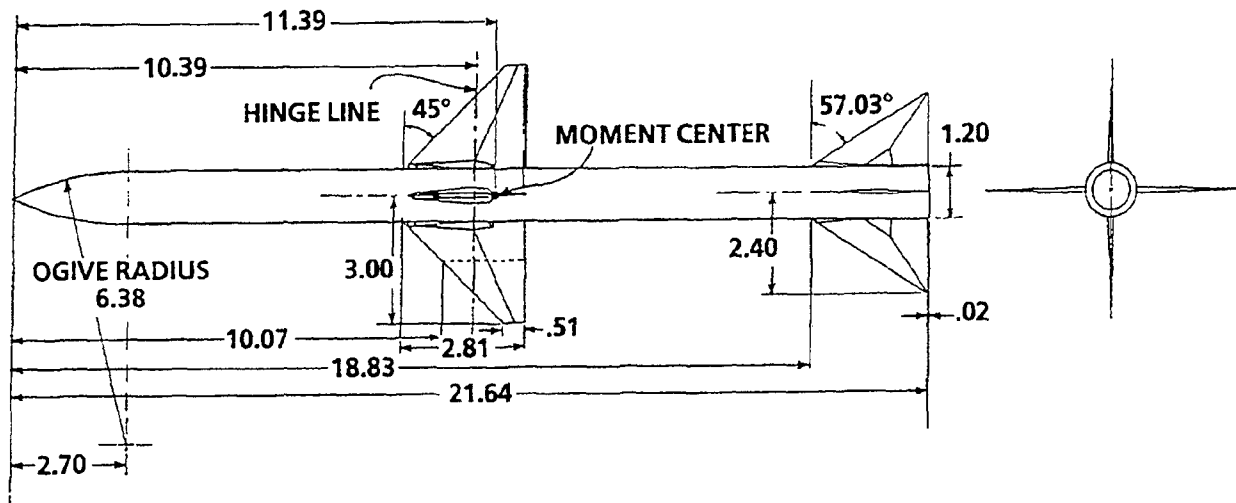
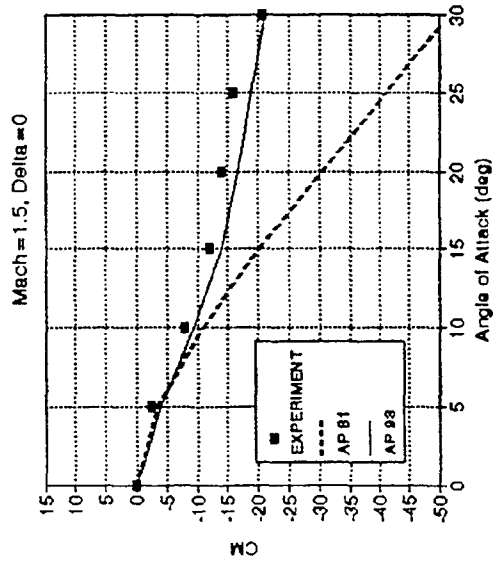
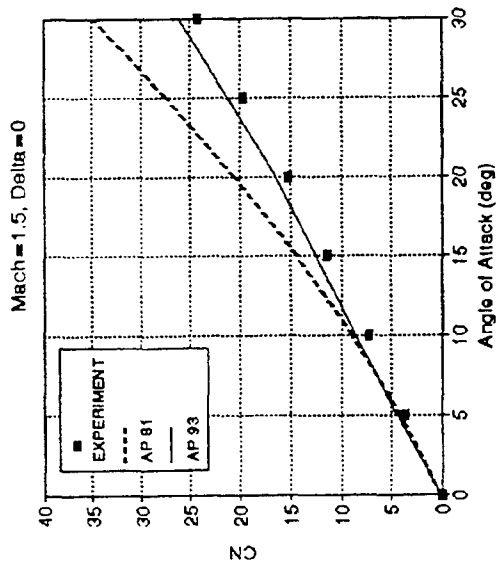
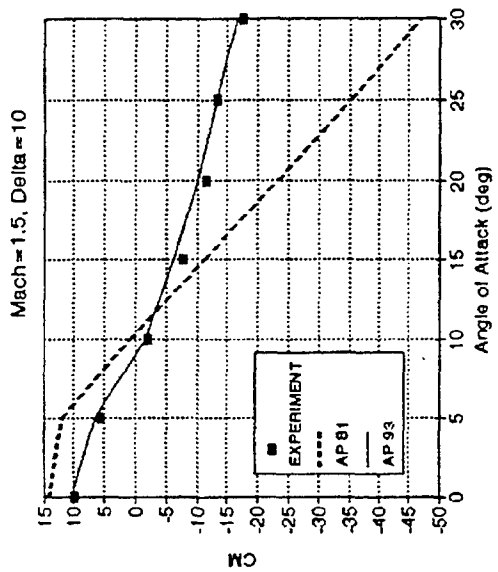
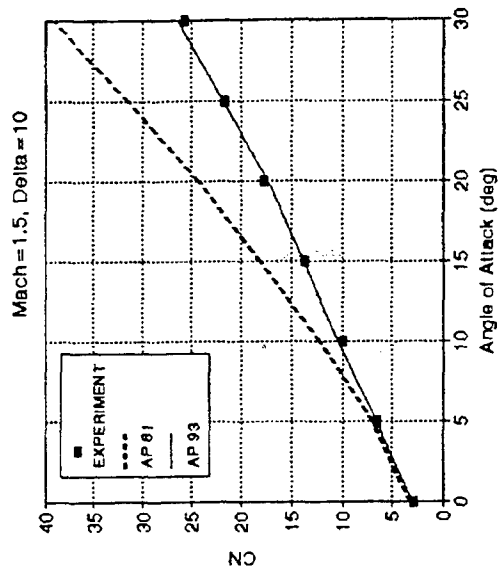
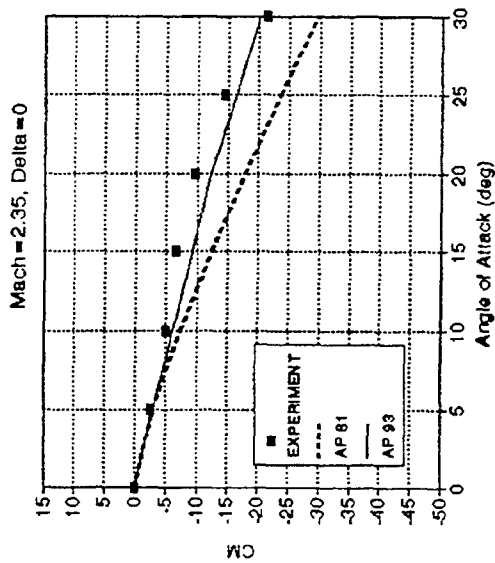
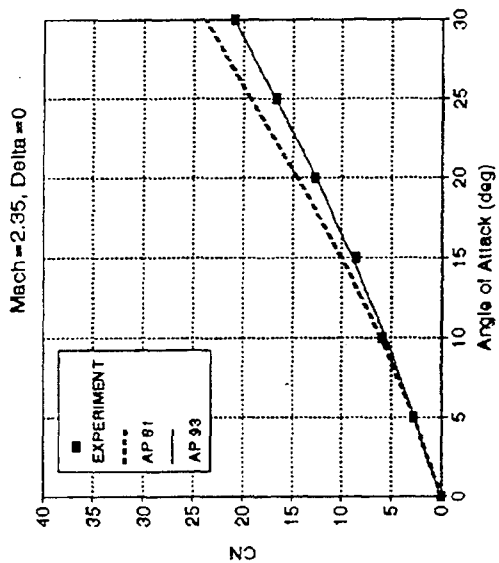
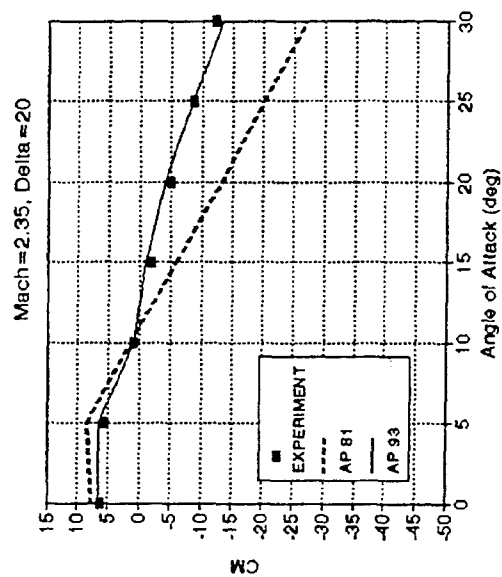
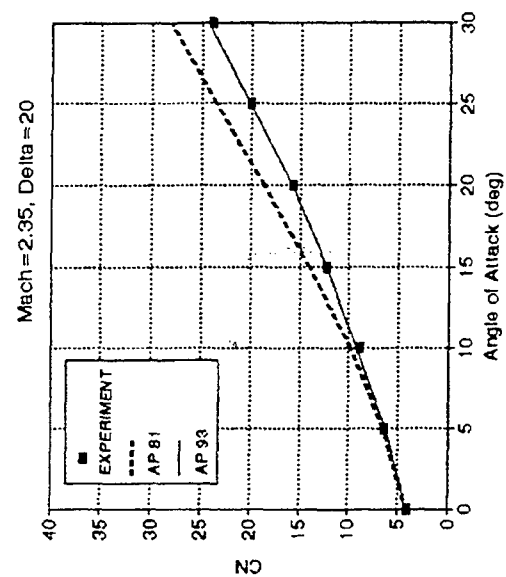


FIGURE 6-5A. AIR-TO-AIR MISSILE CONFIGURATION USED IN VALIDATION PROCESS^{42,43}



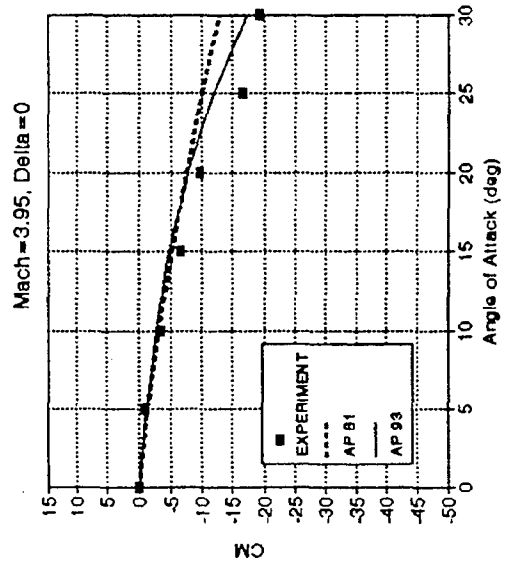
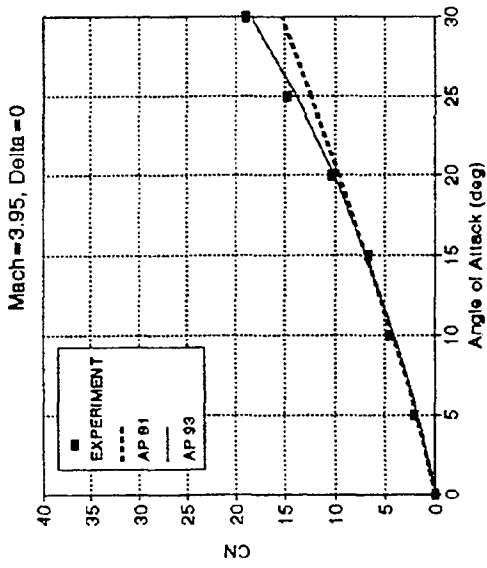
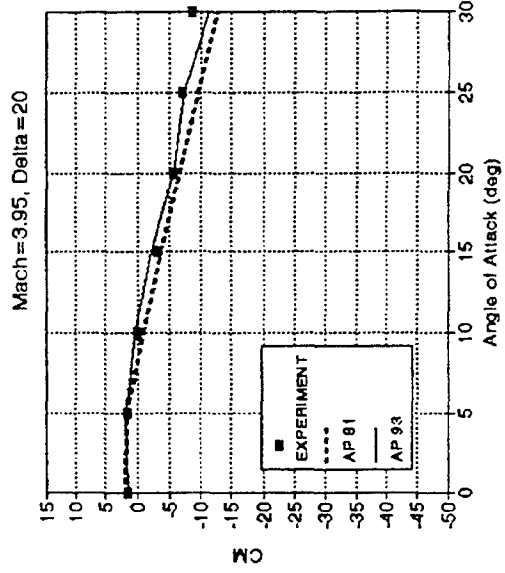
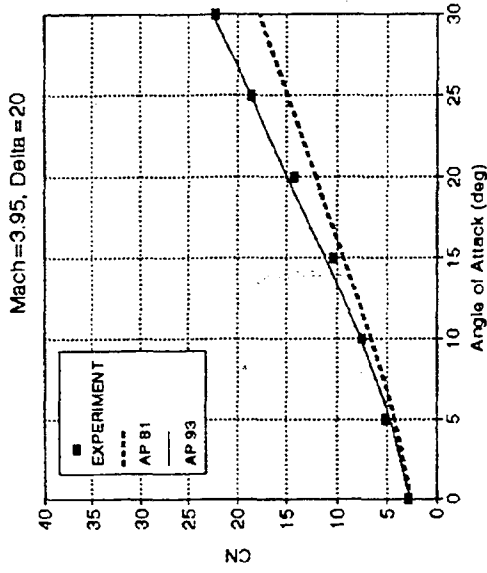
NO WAVE GUIDES

FIGURE 6-5B. NORMAL-FORCE AND PITCHING MOMENT COEFFICIENTS FOR CONFIGURATION OF FIGURE 6-5A FOR VARIOUS MACH NUMBERS AND CONTROL DEFLECTIONS



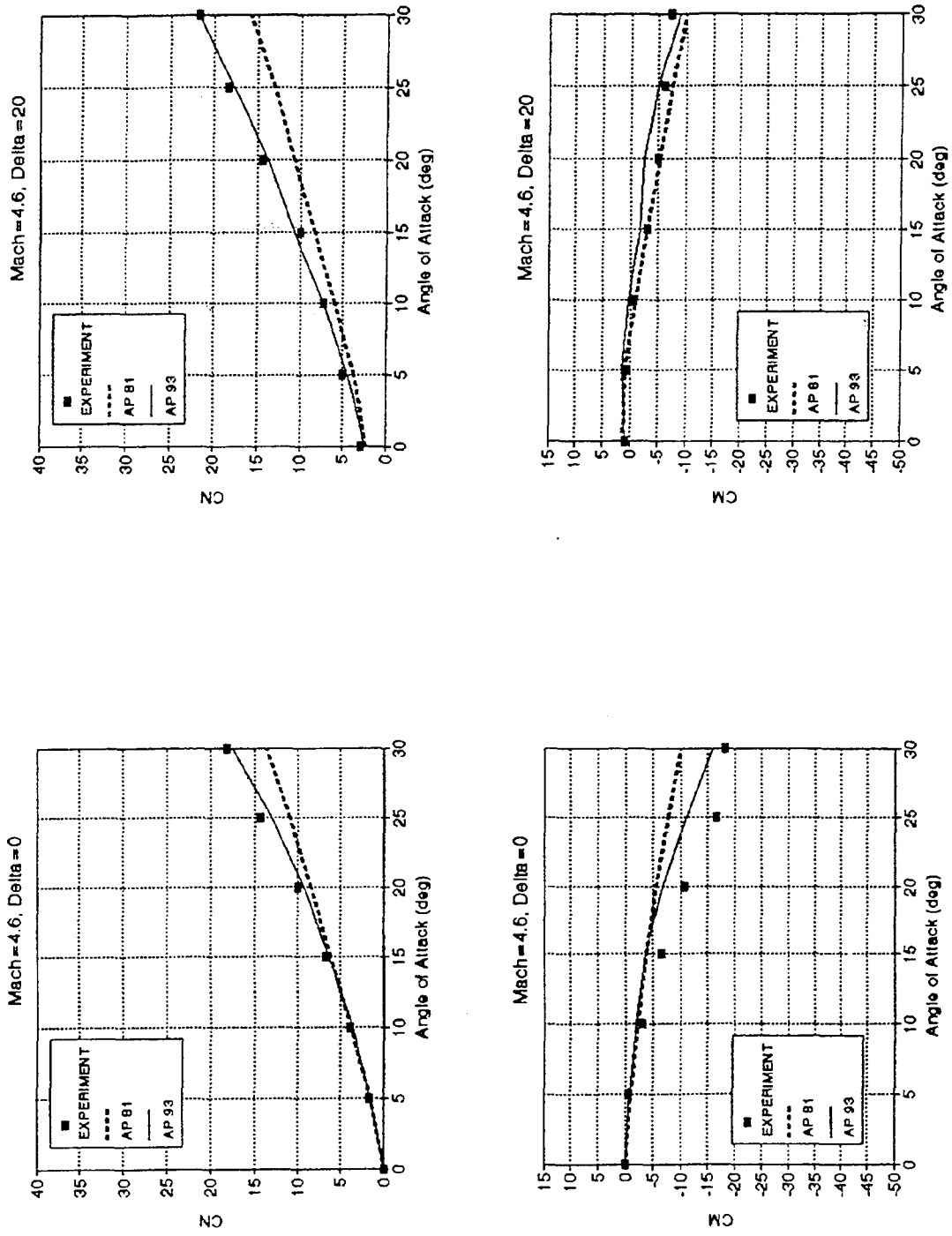
NO WAVE GUIDES

FIGURE 6-5C. NORMAL-FORCE AND PITCHING MOMENT COEFFICIENTS FOR CONFIGURATION OF FIGURE 6-5A FOR VARIOUS MACH NUMBERS AND CONTROL DEFLECTIONS (CONTINUED)



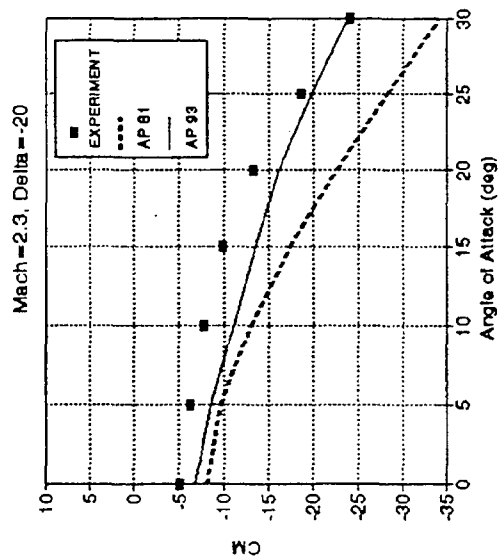
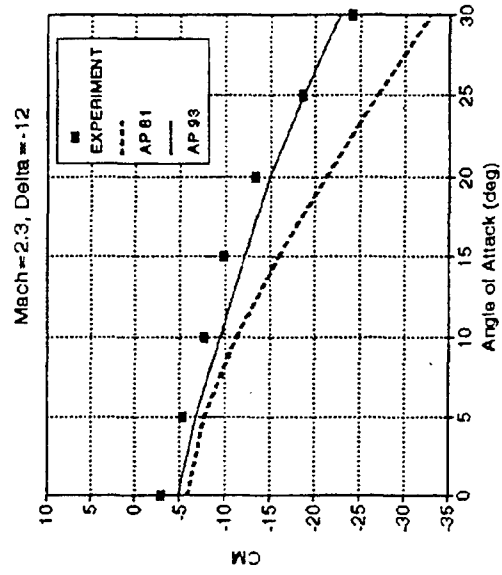
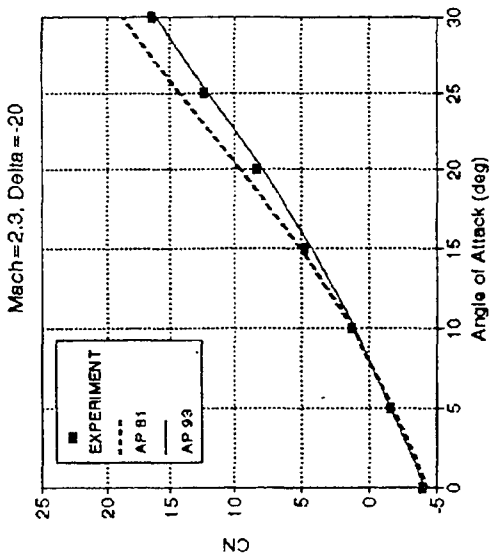
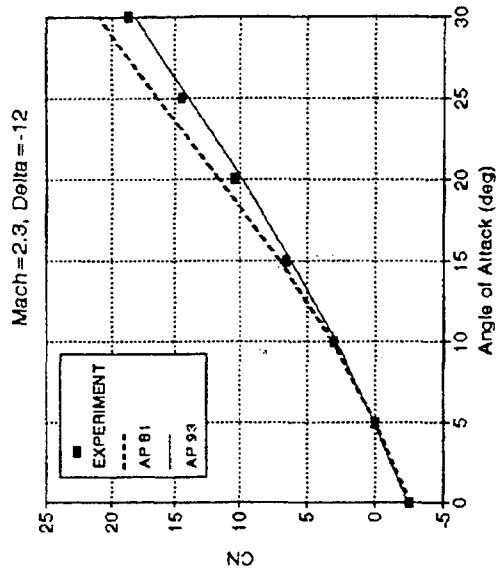
NO WAVE GUIDES

FIGURE 6-5D. NORMAL-FORCE AND PITCHING MOMENT COEFFICIENTS FOR CONFIGURATION OF FIGURE 6-5A FOR VARIOUS MACH NUMBERS AND CONTROL DEFLECTIONS (CONTINUED)



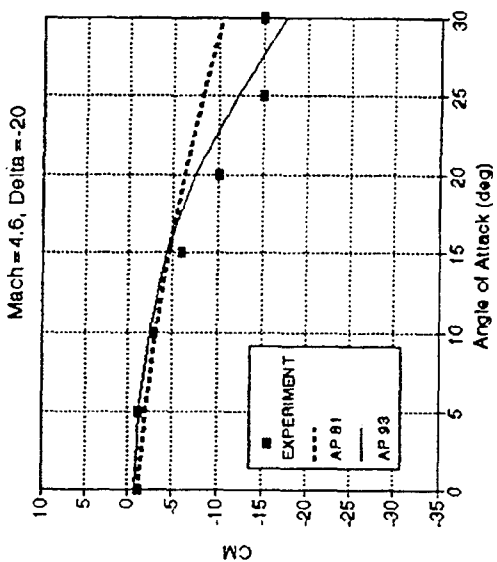
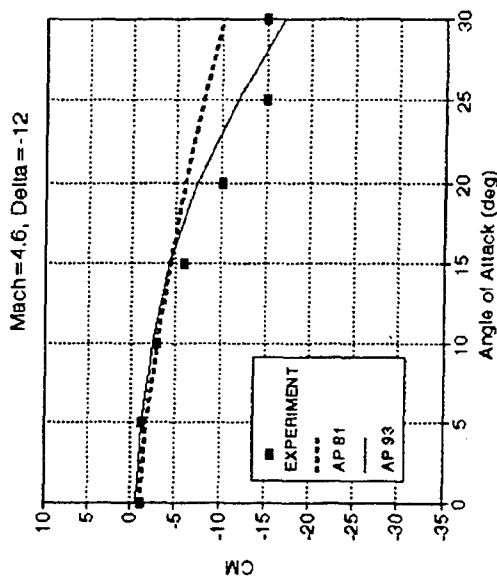
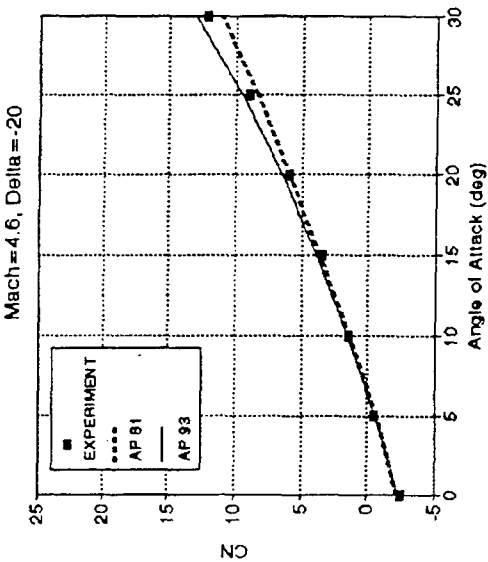
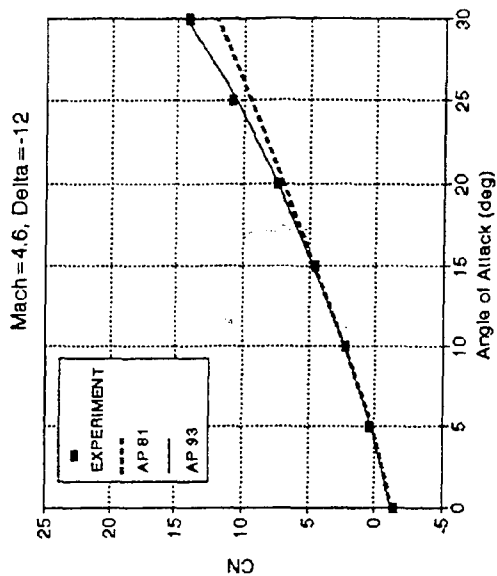
NO WAVE GUIDES

FIGURE 6-5E. NORMAL-FORCE AND PITCHING MOMENT COEFFICIENTS FOR CONFIGURATION OF FIGURE 6-5A FOR VARIOUS MACH NUMBERS AND CONTROL DEFLECTIONS (CONTINUED)



WITH WAVE GUIDES

FIGURE 6-5F. NORMAL-FORCE AND PITCHING MOMENT COEFFICIENTS FOR CONFIGURATION OF FIGURE 6-5A FOR VARIOUS MACH NUMBERS AND CONTROL DEFLECTIONS (CONTINUED)



WITH WAVE GUIDES

FIGURE 6-5G. NORMAL-FORCE AND PITCHING MOMENT COEFFICIENTS FOR CONFIGURATION OF FIGURE 6-5A FOR VARIOUS MACH NUMBERS AND CONTROL DEFLECTIONS (CONTINUED)

Figures 6-5F and 6-5G show the comparisons of AP81 and AP93 to the McKinney data,⁵³ which is the same configuration as that of Figure 6-5A, except that wave guides and wiring tunnels were attached to the wind tunnel model. As already mentioned, no account was taken for these appendages in the analytical computations. Note that AP93 agrees much more with the data than AP81 for both $M_\infty = 2.3$ and 4.6 at all values of δ . In comparing the wind tunnel data for the cases with and without appendages, it can be seen that the appendages add only a few percent to the aerodynamics.

A sixth and final case used in the validation and development of the nonlinear aerodynamics model is shown in Figure 6-6A. Note that in Figure 6-6A, two configurations were actually tested, one that had a full-tail surface and a second that had a partial cutout removed.⁵⁴ The AP93 will not handle the partial-wing configuration as it stands, so an engineering model of this wing must be created. Experience has shown that the lifting surface area, aspect ratio, span, leading edge sweep angle, and centroid of the presented area, must be held constant. The chord is varied so as to meet these constraints. Hence, the configuration that represents the partial-wing results is the body canard of Figure 6-6A, plus the AP93 representation of the partial tail shown in the lower right of Figure 6-6A.

Figures 6-6B through 6-6D present comparisons of AP93 with wind tunnel test data. Data were only available at $M_\infty = 0.2$; however, this complements the previous data set for the SPARROW missile in the sense that no subsonic data were available for that case. Full-tail and partial-tail results are denoted on the figure. Some results were available from Reference 54 for the Missile Datcom.⁶⁰ These results are also shown where available.

As seen in the figure, the AP93 gives improved results for pitching moment and normal force for most conditions, compared to the Missile Datcom. While center of pressure is not shown, the AP93 computations are generally within the goal of ± 4 percent of the body length. For example, at $\alpha = 30$ deg, $\delta = -20$ deg, x_{cp} for the data, AP93 and Missile Datcom are 5.39, 4.91, and 3.75 calibers, respectively, with respect to the moment reference point. This represents errors of 2.1 and 7.3 percent of the body length, respectively, for the AP93 and Missile Datcom codes.

Many other cases have also been considered in the validation of the new AP93 code.^{8, 47} In general, it has been found that, on average, the AP93 code has reduced the normal force and center of pressure errors of the AP81 code by half, and reduced the axial force errors by about twenty-five percent. There are cases where AP81 actually does better than AP93. However, these are quite rare, and in averaging several hundred data points for various configurations, at various Mach numbers and, at 5° increments in angle of attack from

0 to 30° , the reduction in errors of AP93 over AP81 is significant. While no equivalent systematic comparison with other SOTA codes has been made, the AP93 was superior to other engineering codes at most conditions where comparisons were made.

7.0 ACKNOWLEDGEMENTS

Numerous investigators have assisted the author in the aeroprediction work at NSWCDD over the past 23 years. Many of them are listed in the references. These individuals include W. McKerley, Gil Graff, R. Swanson, L. Devan, L. Mason, J. Sun, M. Armistead, S. Rowles, T. Hymer, and R. McInville at NSWCDD. Also, contributions have been made by F. De Jarnette at N.C. State, Frank Baltakis of Advanced Technology Associates, Nielsen Engineering and Research, and Lockheed Missiles and Spacecraft. Appreciation is expressed to each of these individuals or organizations for their roles.

Those who had the foresight to sponsor the work are not referenced and are also acknowledged. W. Pasiuk of the Naval Sea Systems Command was the first individual to sponsor the work. He was joined by the Naval Air Systems Command, B. Volz and D. Hutchins in 1977. A small amount of support was also given by the U.S. Army Missile Command, R. Deep; and the Air Force Armament Lab, D. Daniel. Currently, the work is being supported by the Office of Naval Research, D. Siegel, through the Surface Launched Weapons Technology Program at NSWCDD (R. Staton) and the Air Launched Weapons Technology Program at the Naval Weapons Center, (T. Loftus). Other funding has also been obtained from the NSWCDD Independent Research Program.

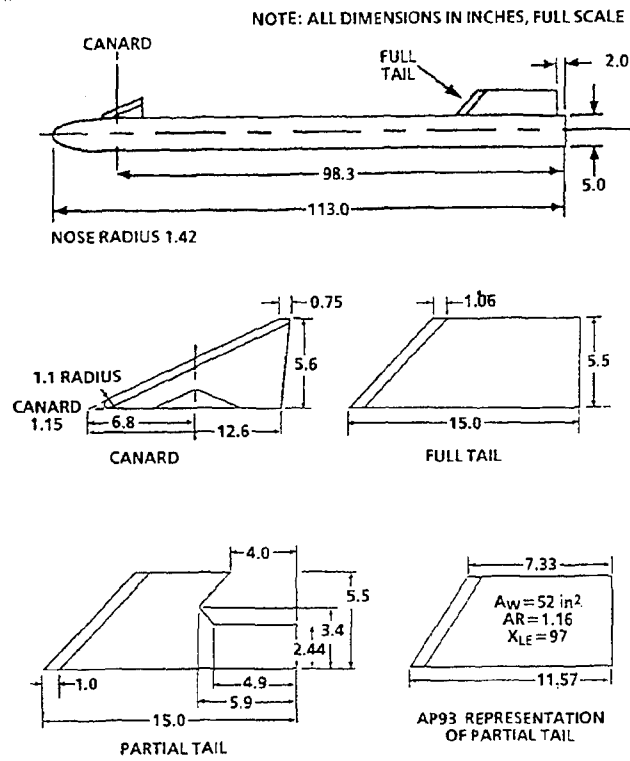


FIGURE 6-6A. CANARD-CONTROLLED MISSILE CONFIGURATION WITH FULL-TAIL, PARTIAL-TAIL, AND AP93 REPRESENTATION OF PARTIAL TAIL FOR USE IN VALIDATION PROCESS⁵⁴

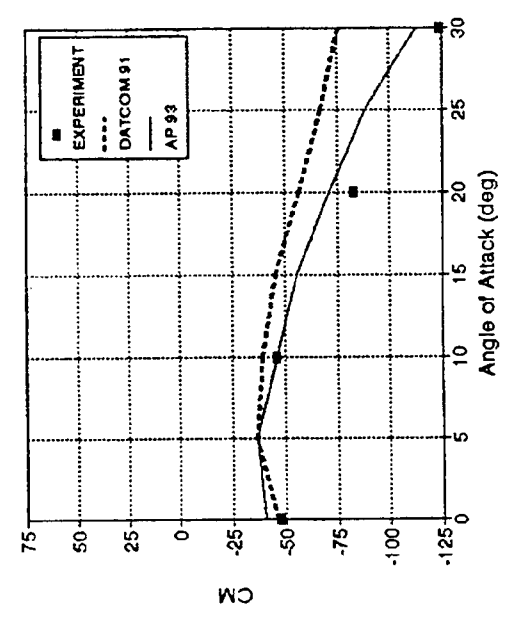
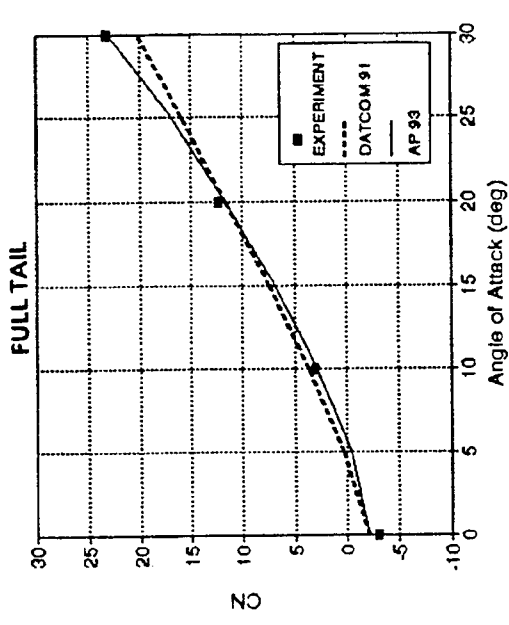
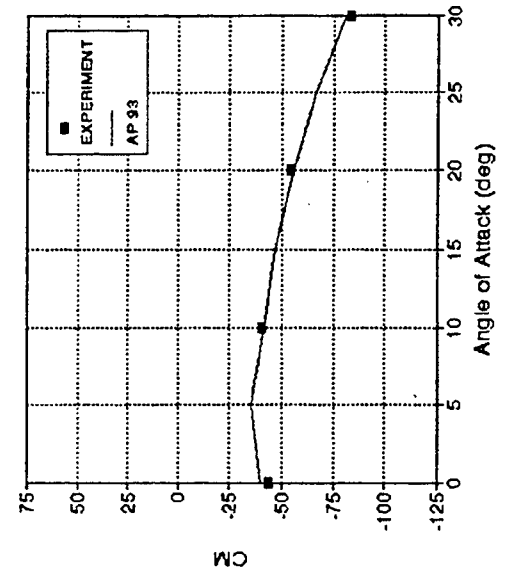
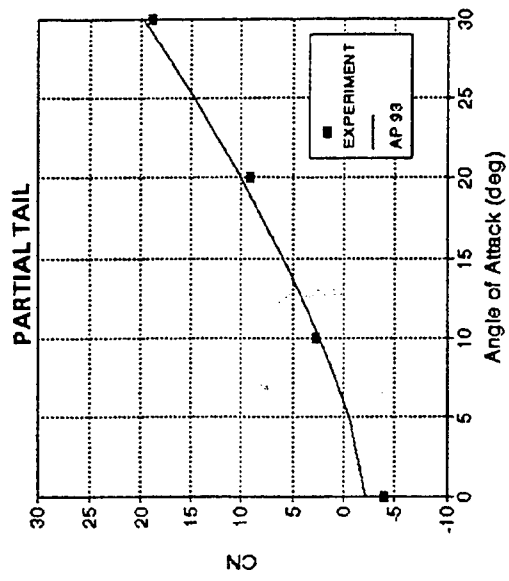


FIGURE 6-6B. COMPARISON OF AP93 TO WIND TUNNEL DATA AND MISSILE DATCOM FOR NORMAL-FORCE AND PITCHING MOMENT COEFFICIENTS OF FIGURE 6-6A CONFIGURATION ($M_\infty = 0.2, \delta_c = -20^\circ$)

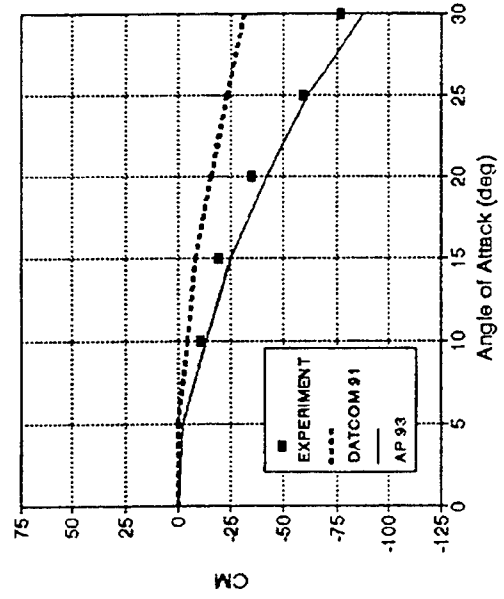
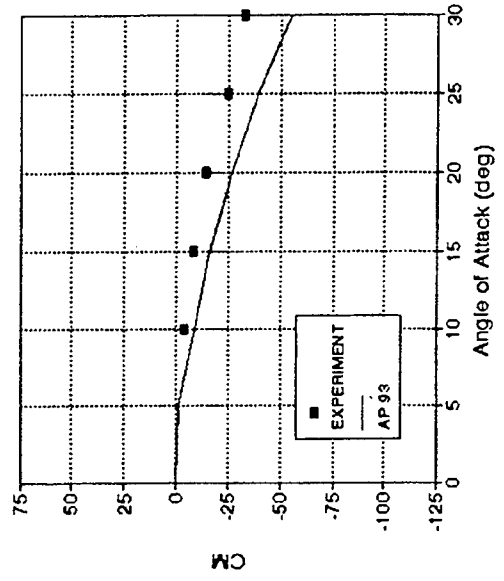
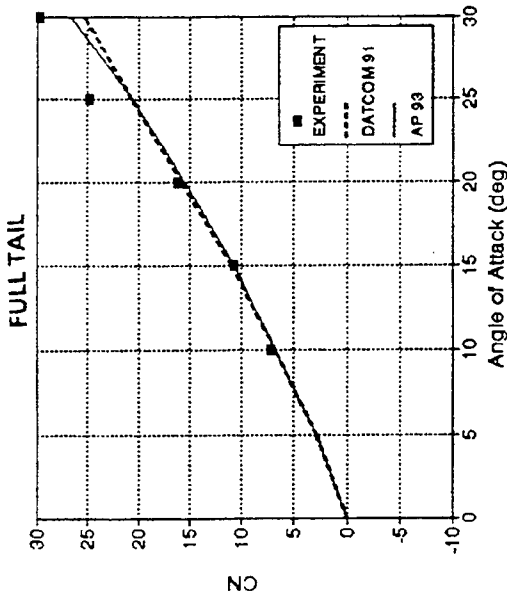
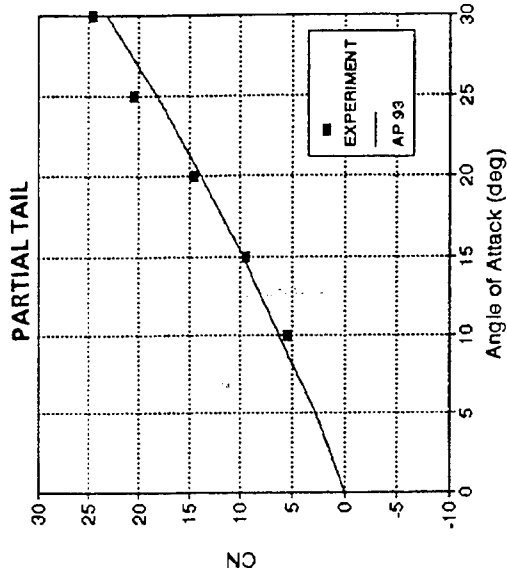


FIGURE 6-6C. COMPARISON OF AP93 TO WIND TUNNEL DATA AND MISSILE DATCOM FOR NORMAL-FORCE AND PITCHING MOMENT COEFFICIENTS OF FIGURE 6-6A CONFIGURATION ($M_\infty = 0.2, \delta_c = 0^\circ$)

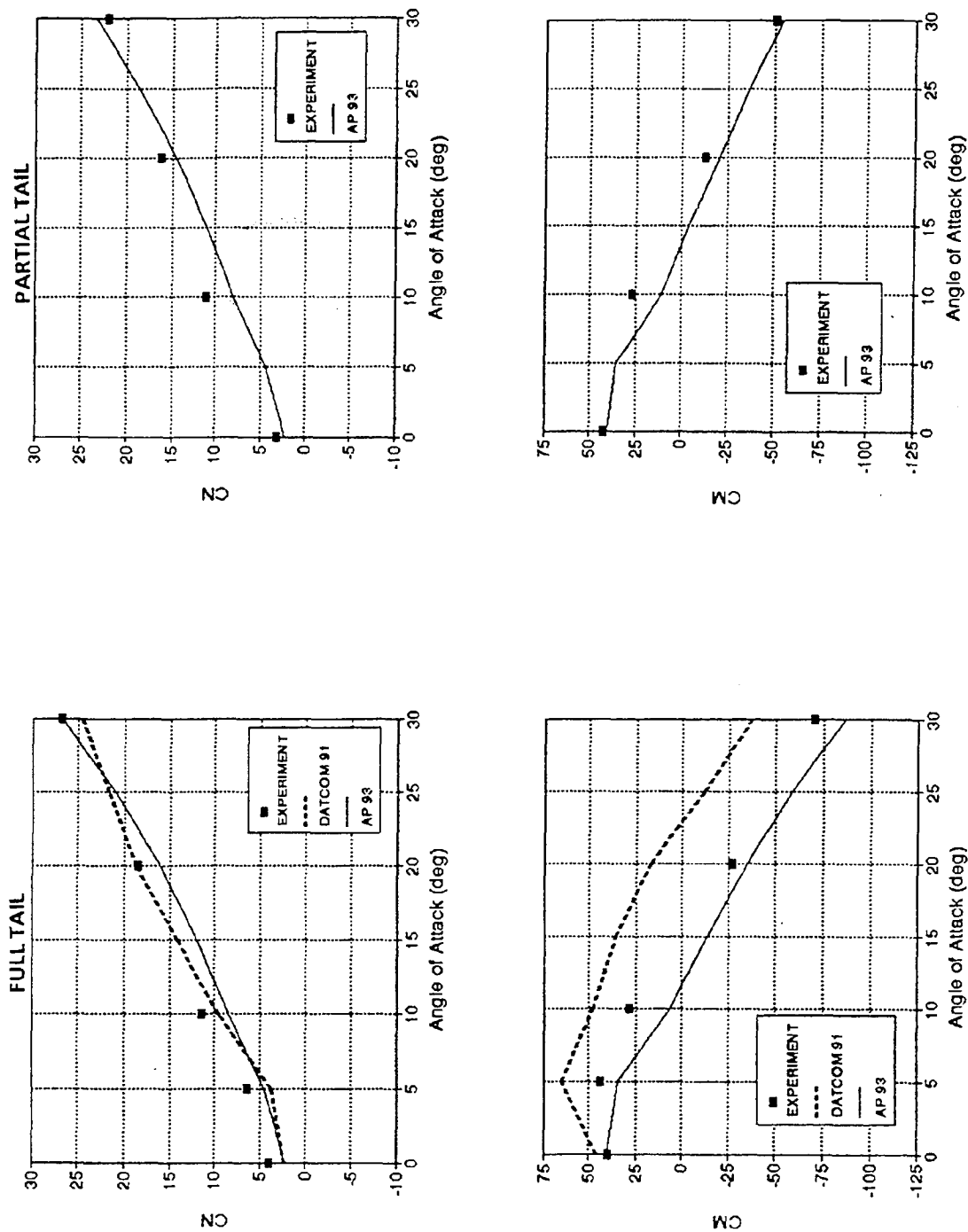


FIGURE 6-6D. COMPARISON OF AP93 TO WIND TUNNEL DATA AND MISSILE DATCOM FOR NORMAL-FORCE AND PITCHING MOMENT COEFFICIENTS OF FIGURE 6-6A CONFIGURATION ($M_\infty = 0.2, \delta_c = 20^\circ$)

8.0 REFERENCES

1. Moore, F. G., *Body Alone Aerodynamics of Guided and Unguided Projectiles at Subsonic, Transonic, and Supersonic Mach Numbers*, NWL TR-2796, Nov 1972, NWL, Dahlgren, VA.
2. Moore, F. G., *Aerodynamics of Guided and Unguided Weapons: Part I-Theory and Application*, NWL TR-3018, Dec 1973, NWL, Dahlgren, VA.
3. Moore, F. G. and McKerley, W. C., *Aerodynamics of Guided and Unguided Weapons: Part II-Computer Program and User Guide*, NWL TR-3036, Jan 1974, NWL, Dahlgren.
4. Moore, F. G. and Swanson, R. C., *Aerodynamics of Tactical Weapons to Mach Number 3 and Angle of Attack 15 Degrees: Part I-Theory and Application*, NSWC DL TR-3584, Feb 1977, NSWC DL, Dahlgren VA.
5. Swanson, R. C. and Moore, F. G., *Aerodynamics of Tactical Weapons to Mach Number 3 and Angle of Attack 15 Degrees: Part II-Computer Program and Usage*, NSWC DL TR-3600, Mar 1977, NSWC DL, Dahlgren VA.
6. Devan, L., *Aerodynamics of Tactical Weapons to Mach Number 8 and Angle of Attack 180°: Part I, Theory and Application*, NSWC TR 80-346, Oct 1980, NSWC, Dahlgren, VA.
7. Devan, L. and Mason, L., *Aerodynamics of Tactical Weapons to Mach Number 8 and Angle of Attack 180°: Part II, Computer Program and Users Guide*, NSWC TR 81-358, Sep 1981, NSWC, Dahlgren, VA.
8. Moore, F. G.; Hymer, T. C.; and McInville, R. M.; *Improved Aeroprediction Code: Part I-Summary of New Methods and Comparison with Experiment*, NSWCDD/TR-93/91, May 1993, NSWCDD, Dahlgren, VA.
9. Moore, F. G.; McInville, R. M.; and Hymer, T. C.; *Improved Aeroprediction Code: Part II-Computer Program Users Guide and Listing*, NSWCDD, Dahlgren, VA, Aug 1993.
10. Lacau, R. G.; "A Survey of Missile Aerodynamics," *proceedings of NEAR Conference on Missile Aerodynamics*, NEAR, Inc., Mountain View, CA, Oct 1988, paper 1.
11. Moore, F. G., *State of the Art Engineering Aeroprediction Methods with Emphasis on New Semiempirical techniques for Predicting Nonlinear Aerodynamics on Complete Missile Configurations*, NSWCDD/TR-93-551, Nov 1991, NSWCDD, Dahlgren, VA.
12. Van Dyke, M. D., *First and Second-Order Theory of Supersonic Flow Past Bodies of Revolution*, *Journal of Aeronautical Sciences*, Vol.18, No. 3, Mar 1951, pp.161-179.
13. Tsien, H. S., *Supersonic Flow Over an Inclined Body of Revolution*, *Journal of Aeronautical Sciences*, Vol. 5, No. 12, Oct 1938, pp. 480-483.
14. Syvertson, C. A. and Dennis, D. H., *A Second-Order Shock-Expansion Method Applicable to Bodies of Revolution Near Zero Lift*, NACA TR 1323, 1957.
15. Eggers, A. J.; Syvertson, C. A.; and Kraus, S.; *A Study of Inviscid Flow about Airfoils at High Supersonic Speeds*, NACA Report 1123, 1953.
16. Leis, L., "Hypersonic Flow," *Inst. Aero. Science*, preprint No. 554, 1955.
17. Jackson, C. M., Jr.; Sawyer, W. C.; Smith, R. S., *A Method for Determining Surface Pressures on Blunt Bodies of Revolution at Small Angles of Attack in Supersonic Flow*, NASA TN D-4865, Nov 1968.
18. De Jarnette, F. R.; Ford, C. P.; and Young, D. E., *A New Method for Calculating Surface Pressures on Bodies at an Angle of Attack in Supersonic Flow*, AIAA Paper No. 79-1552, AIAA 12th Fluid and Plasma Dynamics Conference, Williamsburg, VA, Jul 1974.
19. Allen, J. H. and Purkins, E. W., *Characteristics of Flow over Inclined Bodies of Revolution*, NACA RM A 50L07, Mar, 1951.
20. Van Driest, E. R., "Turbulent Boundary Layers in Compressible Fluids," *Journal of Aeronautical Sciences*, Vol. 18, No. 3, 1951, pp. 145-160, 216.
21. Chadwick, W. R., "External Loads Using Nonplanar Lifting Surface Theory," *Journal of Aircraft*, Vol.11, No. 3, Mar, 1974, pp. 181-188.
22. Ashley, Holt, Landahl, Martin; *Aerodynamics of Wings and Bodies*, Addison-Wesley Publishing Company, Inc., Reading, Ms., 1965, Chapter 7.
23. Purvis, J. W., *Lifting Surface Theory Calculations of Aerodynamic Wing-Tail Load Distributions During Subsonic Maneuvers*, NWL TR-2787, Aug 1972 NSWCDD, Dahlgren, VA.

24. Margolis, K.; *Supersonic Wave Drag of Sweptback Tapered Wings at Zero Lift*, NACA TN 1448, 1947.
25. Pitts, W. C.; Nielson, J. N.; and Kaatari, G. E.; *Lift and Center of Pressure of Wing-Body-Tail Combinations at Subsonic, Transonic, and Supersonic Speeds*, NACA TR 1307, 1957.
26. Moore, F. G.; Armistead, M. A.; Rowles, S. H.; and De Jarnette, F. R.; *Second-Order Shock-Expansion Theory Extended to Include Real Gas Effects*, NAVSWC TR-90-683, Feb 1992, NSWCDD, Dahlgren, VA.
27. Moore, F. G.; Armistead, M. J.; Rowles, S. H.; and De Jarnette, F. R.; "New Approximate Method for Calculating Real Gas Effects on Missile Configurations," *Journal of Spacecraft and Rockets*, Vol. 30, No.1, Jan-Feb, 1993.
28. Park, C., and Leon, S., *Calculation of Real-Gas Effects on Blunt-Body Trim Angles*, AIAA paper no 89- 0685, Aerospace Sciences meeting, Reno, NV., Jan 1989.
29. Hudgins, Henry E., Jr., *Supersonic Flow About Right Circular Cones at Zero Yaw in Air at Chemical Equilibrium, Part I-Correlation of Flow Properties*, TM 1493, Picatinny Arsenal, PA, Aug 1965.
30. Wittliff, C. E. and Curtis, J. T., *Normal Shock Wave Parameters in Equilibrium Air*, Cornell Aero Lab Report, CAL-III, Nov 1961.
31. Tannehill, J. C. and Mugge, P. H., *Improved Curve Fits for the Thermodynamic Properties of Equilibrium Air Suitable for Numerical Computation using Time-Dependent Shock-Capturing Methods*, NASA CR-2470, 1974.
32. Srinivasan, S.; Tannehill, J.; and Wielmuenster, K., *Simplified Curve Fits for the Thermodynamic Properties of Equilibrium Air*, Report ISSU-ERI-AMES 86401, Jun 1986, Engineering Research Institute, Iowa State Univ., Ames, IA.
33. Morrison, A. M.; Solomon, J. M.; Ciment, M.; and Ferguson, R. E., *Handbook of Inviscid Sphere-Cone Flow Fields and Pressure Distributions: Volume I*, NSWC/WOL/TR 75-45, Dec 1975, White Oak, MD.
34. Jones, D. J., *Numerical Solutions of the Flow Field for Conical Bodies in a Supersonic Stream*, National Research Council of Canada, Report LR-507, Jul 1968, Otlawa, ON, Canada.
35. Wardlaw, A. B.; Davis, S., *A Second-Order-Gudonov Method for Supersonic Tactical Missiles*, NSWC TR-86-506, 1986, NSWC, Dahlgren, VA.
36. McInville, R. and Moore, F. G., *Incorporation of Boundary Layer Heating Predictive Methodology into the NAVSWC Aeroprediction Code*, NSWCDD/TR-93/29, Apr 1993, NSWCDD, Dahlgren, VA.
37. Anderson, J. D., *Hypersonic and High Temperature Gasdynamics*, McGraw-Hill Book Co., New York, NY, 1989.
38. Beckwith, I. E. and Gallagher, J. J., *Local Heat Transfer and Recovery Temperatures on a Yawed Cylinder at Mach Numbers of 4.15 and High Reynolds Numbers*, NASA Technical Report R-104, 1961.
39. Hender, D. R., *A Miniature Version of the JA70 Aerodynamic Heating Computer Program, H800 (MINIVER)*, McDonnell-Douglas Astronautics Co., Report MCD G0462, Jun 1970, St. Louis, MO.
40. Eckert, E. R. G., *Engineering Relations for Heat Transfer and Friction in High-Velocity Laminar and Turbulent Boundary Layer Flow over Surfaces with Constant Pressure and Temperature*, Transactions of the ASME, Vol. 78, No. 6, Aug 1956.
41. Eckert, E. R. G., *Survey of Boundary Layer Heat Transfer at High Velocities and High Temperatures*, WADC Technical Report 59-624, Apr 1960.
42. Riley, C. J. and De Jarnette, F. R., "Engineering Aerodynamic Heating Method for Hypersonic Flow," *Journal of Spacecraft and Rockets*, Vol. 29, No. 3, May-Jun 1992.
43. Cleary, J. W., *Effects of Angle of Attack and Bluntness on Laminar Heating Rate Distribution of a 15° Cone at a Mach Number of 10.6*, NASA TN D-5450, 1969.
44. Moore, F. G.; Wilcox, F.; and Hymer, T., *Improved Empirical Model for Base Drag Prediction on Missile Configurations Based on New Wind Tunnel Data*, NSWCDD/TR-92/509, Oct 1992, NSWCDD, Dahlgren, VA.
45. Moore, F. G.; Wilcox, F.; and Hymer, T., *Base Drag Prediction on Missile Configurations*, AIAA Paper, No. 93-3629, to be presented at Atmospheric Flight Mechanics Conference, Aug 1993, Monterey, CA.

46. Butler, C.; Sears, E.; and Pellas, S., *Aerodynamic Characteristics of 2-, 3-, and 4-caliber Tangent-Ogive Cylinders with Nose Bluntness Ratios of 0.00, 0.25, 0.50, and 0.75 at Mach Numbers from 0.6 to 4.0*, AFATL-TR-77-8, Jan 1977.
47. Moore, F. G.; Hymer, T.; and Devan, L., *New Methods for Predicting Nonlinear Lift, Center of Pressure, and Pitching Moment on Missile Configurations*, NSWCDD/ TR-92/217, Jul 1992, NSWCDD, Dahlgren, VA.
48. Moore, F. G.; Devan, L.; and Hymer, T., *A New Semiempirical Method for Computing Nonlinear Angle-of-Attack Aerodynamics on Wing-Body-Tail Configurations*, AIAA Paper, No. 93-0038, 31st Aerospace Sciences Meeting, Jan 1993.
49. Jorgensen, L. H., *Prediction of Static Aerodynamic Characteristics for Slender Bodies Alone and with Lifting Surfaces to Very High Angles of Attack*, NASA TR R-474, Sep 1977.
50. NASA Langley Research Center Tri-Service Missile Data Base, transmitted from NASA/LRC Jerry M. Allen to NAVSWC, 5 Nov 1991 (formal documentation in process).
51. Stallings, R. L., Jr. and Lamb, M., *Wing-Alone Aerodynamic Characteristics for High Angles of Attack at Supersonic Speeds*, NASA Technical Paper 1889, Jul 1981.
52. Nielsen, J. N.; Hensch, M. J.; and Smith, C. A., *A Preliminary Method for Calculating the Aerodynamic Characteristics of Cruciform Missiles to High Angles of Attack Including Effects of Roll Angle and Control Deflections*, ONR Report CR 215-226-4F, Nov 1977, ONR, Arlington, VA.
53. McKinney, R. L., *Longitudinal Stability and Control Characteristics of an Air-to-Air Missile Configuration at Mach Numbers of 2.3 and 4.6 and Angles of Attack from -45° to 90°*, NASA TM X-846, 1972.
54. Smith, E. H.; Hebbard, S. K.; and Platzler, M., *Aerodynamic Characteristics of a Canard-Controlled Missile at High Angles of Attack*, AIAA Paper, No. 93-0763, Presented at 31st Aerospace Sciences Meeting, Reno, NV, 11-14 Jan 1993.
55. Howard, R. M. and Dunn, A., "Missile Loads at High Angles of Attack," *Journal of Spacecraft and Rockets*, Vol. 28, No. 1, Jan-Feb, 1991.
56. Bible, J. E. and Hardy, S. R., *Wind Tunnel Test Data of the High Performance Point Defense Missile HPPDM obtained in the NASA Langley Unitary Plan Wind Tunnel*, NAVSWC TR 90-475, in publication.
57. Lesieutre, D. J.; Mendenhall, M. R.; and Nazario, S. M., *Prediction of the Aerodynamic Characteristics of Cruciform Missiles Including Effects of Roll Angle and Control Deflection*, NEAR-TR-360, 1986, NEAR, Inc., Mountain View, CA.
58. Graves, E. and Fournier, R., *Stability and Control Characteristics at Mach Numbers from 0.2 to 4.63 of a Cruciform Air-to-Air Missile with Triangular Canard Controls and a Trapezoidal Wing*, NASA-TM-X-3070, Nov 1974.
59. Monta, W. J., *Supersonic Aerodynamic Characteristics of a Sparrow III Type Missile Model with Wing Controls and Comparison with Existing Tail-Control Results*, NASA TP 1078, Nov 1977.
60. Vukelich, S. R. and Jenkins, J. E., *Missile DATCOM: Aerodynamic Prediction on Conventional Missiles Using Component Build-Up Techniques*, AIAA Paper No 84-0388, 1984.

LATERAL JET CONTROL FOR TACTICAL MISSILES

P. CHAMPIGNY

Office National d'Etudes et de Recherches Aéropatiales (ONERA)
29, Avenue de la Division Leclerc - 92320 CHATILLON (FRANCE)

R.G. LACAU

AEROSPATIALE - MISSILES
Annexe Les Gâtines - 91370 VERRIERES-LE-BUISSON (FRANCE)

1. INTRODUCTION

Control systems of some missiles currently under development show a noticeable evolution when compared with those of previous generations. They comply with the evolution of the increasingly rapid, agile, stealthy and hardened threat, and with the reorientation of its conditions of use.

In this intricate context, standard aerodynamic pilot can be insufficient, particularly due to poor response time and decreasing effectiveness at low dynamic pressure.

Consequently it can prove necessary to replace standard aerodynamic control system or, as the case may be, to associate it with pyrotechnical devices which have high performance characteristics due to their rapidity of action and whose effectiveness is independent of flight conditions. Missiles equipped with such systems are conferred agility and accuracy which cannot be obtained otherwise. In addition, they show new possibilities of use such as the capability of firing in confined space or vertically.

The aim of this paper is to give a survey of lateral jets as control system of tactical missiles. The paper is divided into four parts.

The first part gives a brief analysis of new control requirements pertaining to tactical missiles, presents the advantages of lateral jet control and describes two types of applications for missiles designed and developed by AEROSPATIALE-MISSILES. The first example relates to the ground/surface-to-air missile ASTER which has anti-missile capability, the second example concerns the anti-tank missile ERYX.

The second part presents in detail the phenomenological aspects of lateral jets and the influence of various flow parameters and missile geometry on control system performance.

The third part describes some wind-tunnel testing problems.

The fourth and last part is dedicated to computation for valuation and understanding of the aerodynamic interactions.

2. EVOLUTION OF REQUIREMENTS IN THE TACTICAL MISSILE CONTROL DOMAIN

Requirements relative to control system performance of modern tactical missiles are increasingly strict. A brief analysis of some aspects of the anti-tank warfare and the air defence warfare permits to precise these requirements and their origins.

In the anti-tank warfare domain, the growing urbanization of industrial countries and the increase of the guerilla warfare threat is leading to the search for a man portable weapon, capable of confined space firing and high accuracy at short range firing level. Obviously, missile launch will have to be performed at very low speed so as to protect the gunner during confined space firings.

Consequently, the missile control system capable of such a mission will have to be effective at low speed (confined space firing), be provided with a good manoeuvring capability (effectiveness against moving targets) and with a very short response time (particularly, short-range accuracy).

The analysis of air defense combat reinforces these trends. Thus, future air-to-air missiles will have to be lightweight. Indeed, this type of missiles will have to be carried by the same aircraft in sufficient numbers so as to counter saturating attacks. Consequently, these missiles will have to be fitted with a lightweight warhead and, in return, be very accurate even at high altitude and low firing range (dogfight).

Thus the control system of these missiles will have to combine extremely short response time with a high manoeuvring capability which can be set into operation in extreme dynamic pressure conditions (low speed, high altitude).

Within the framework of ground/surface to air warfare, it is necessary to take into consideration, besides the saturating attack threat, risks of late unmasking of stealthy targets. Such targets, taking advantage of terrain camouflage, can, in addition, be supported by countermeasures designed to delay their detection. A procedure such as vertical firing is an adequate response allowing all-directional defense within a minimum period of time, and permitting, thanks to trajectory shaping, a diving trajectory sheltered from protection jammers. The missile control system will have to control this trajectory from zero velocity, in particular in the case of a launch from a moving platform (ship for example).

Furthermore, the targets of a ground-to-air missile can also be missiles. Given the velocity and the manoeuvring capability of such targets, anti-missile missiles will also have to be capable of a very short response time (some tenths of milliseconds as a maximum) and a very high manoeuvring capability so as to destroy their target with a conventional warhead.

In short, for many reasons, control systems of future tactical missiles must, at various degrees, according to the type of interception, be provided with the following capabilities:

- a very short response time (of approximately a tenth of milliseconds in the extreme case of anti-missile warfare);
- high manoeuvrability, perhaps in the order of 50 g or more for certain applications;
- significant effectiveness at very low speed level and high altitude, i.e. at low dynamic pressure.

3. STANDARD AERODYNAMIC CONTROL LIMITATIONS

To execute a lateral acceleration order, standard aerodynamic control generates a moment through fins. This moment transmits an angular movement to the missile, which generates an aerodynamic angle of attack and, as a result, an aerodynamic lift allowing to make the required manoeuvre.

Figure 3.1 shows this process in the case of a standard missile fitted with tail control surfaces.

Schematically, the aerodynamic control takes from the missile kinetic energy the energy necessary for modifying the trajectory curvature. Consequently, the

system is relatively light and quite easy to set into operation. However, it has the following main limitations:

- limitation in response time due to the delay between the order and execution, a delay linked to the parameters which rule the angular movement necessary for generating lateral acceleration (missile inertial moment, aerodynamic damping moment,....) independently of the type of fins used. Typically, the time constant of an aerodynamic pilot can range, as a function of altitude, from one tenth to some tenths of second,
- limitation in manoeuvrability when the dynamic pressure (ρV^2) is low, i.e. when the missile velocity is low (at launch for instance) or when the altitude is high.

As a result, aerodynamic control systems do not comply with requirements as listed §2. Consequently, when the mission concerns difficult targets or unusual condition of use, such system will have to be completed, or to be replaced, by an other system such as pyrotechnical devices.

4. PYROTECHNICAL SYSTEM CONTROL

Moments and forces necessary for missile control can be generated, partially or totally, using pyrotechnical devices such as thrusters or thrust deflectors. It is obvious that forces generated by such devices are not affected by missile velocity or air density. In addition, it is possible to generate or deflect such forces with extremely low delays ranging from some milliseconds to about ten milliseconds, according to the size and the type of the system used. Consequently, these systems can perfectly replace aerodynamic system control, or can be complementary.

They can be used either as "moment generators" or "force generators". Combined modes can be of interest as well as associations with a standard aerodynamic pilot in order to benefit from advantages specific to each of them.

4.1. Pyrotechnical moment control

In this type of control, the pyrotechnical system generates a force whose point of application is far from the center of gravity. Consequently, this type of control is similar to standard aerodynamic control but, as a major advantage, is effective even at low dynamic pressure.

The new US surface-to-air missile ERINT (figure 4.1) is an example of missile using such a control system, with a battery of 180 thrusters located in the forepart of the body.

4.2. Direct thrust vector control: PIF (french acronym for Pilotage en Force) [1,2]

Direct thrust vector control consists in directly generating lateral acceleration thanks to a propulsion force applied to the missile center of gravity.

Among systems which can be planned for this type of control, let us quote missiles equipped with a thruster battery (figure 4.2) or with a gas generator associated with a switching unit (figure 4.3).

In the first case, typically adapted to a rolling missile, thrusters are ignited when the propulsion force they generate has the required roll orientation. The response time is equal to the thruster ignition time (some ms) increased by the time necessary for obtaining the required orientation (as a function of rotation velocity and number of non-consummed thrusters).

In the second case, gases are supplied by two semi-boosters whose simultaneous combustion ensures gravity center invariancy. A switching unit directs gases to nozzles located in one of the two diametrically opposed directions. In this case, the force establishment response time is reduced to the switching unit response time, for example, ten milliseconds.

It can be noted that, in the two above cases, it is advisable to slightly direct the propulsion jets rearwise which will contribute to sustain the missile velocity.

Advantages of direct thrust vector control (PIF)

Applications of direct thrust vector control used as the only control means are limited to missile whose flight time is short, due to problems of propellant consumption and, consequently, of gas generator weight and dimensions. As a result, it is in principle well suited to anti-tank or very short range surface-to-air missions.

4.3. PIF-PAF control (PAF: french acronym for Pilotage Aérodynamique Fort) [1,2]

The advantage of PIF control is displayed when PAF control has reached its limits (response time, manoeuvrability with low-dynamic pressure). If these two types of control are combined, we benefit from their respective advantages.

Advantages of PIF-PAF control

The main upgradings conferred by this type of control are the following:

- high manoeuvrability, since the missile benefits from the PIF in addition to the aerodynamic load factor. We can particularly appreciate the advantage of this characteristic at high altitude, associated with that of a rapid response for the interception of some types of

ballistic missiles (in the endoatmospheric domain); the very high relative velocity upon interception, combined with short homing ranges, requires rapidity and manoeuvrability capabilities which can be provided by the PIF-PAF control system;

- homing stability advantage thanks to load factor obtained with very limited pitch movement;
- finally and, above all, an extremely short response time allowing to obtain missdistances compatible with the hard kill of attackers making high penetrating manoeuvres.

5. LATERAL JET CONTROL APPLICATIONS

5.1. Surface-to-air weapon system ASTER

The principle of PIF-PAF control is applied to the surface-to-air missile ASTER which will be assigned difficult missions such as the interception of rapid missiles (Mach > 2) manoeuvring under high load factor in intense countermeasure conditions. In addition, the threat can be omnidirectional (figure 5.1).

This missile is based on a two-stage design which includes (figure 5.2):

- a terminal dart, called ASTER which is light and highly agile owing to the PIF-PAF control system,
- a jettisonable booster whose acceleration level and operating time depend on the assigned mission.

It is fired vertically so as to ensure omnidirectional coverage with an extremely short response time. During the accelerated phase, the trajectory is shaped so as to enable the missile to meet short-range requirements. At the beginning of the acceleration phase, shaping is controlled by thrust deflection (acting as a moment control system).

During the terminal phase, an active seeker homes the missile towards the target. In the late homing phase, the PIF system assists an highly manoeuvring aerodynamic pilot. Thanks to this association, all types of targets can be intercepted.

The PIF control is performed using a device fitted with 4 nozzles which are set two by two in diametrically opposite directions in two orthogonal planes (the missile is roll-stabilized). A clever switching unit command allows to obtain the required orientation of the lateral propulsion force.

A tricky problem is the interaction between lateral jets and missile aerodynamics which will be described in detail in chapter 6.

5.2. Anti-tank weapon system ERYX

ERYX is a short range anti-tank weapon system (50 to 600 meter-range) which complies with strict requirements:

- high terminal effectiveness;
- high hit probability, at any distances, of "pop up" and moving targets;
- confined space firing;
- one-man portable missile and shoulder-firing capability;
- low cost, compatible with large-scale distribution.

There is no standard solution to the problem raised. Indeed, confined space firing implies, for the gunner's safety, a launch at very low speed. However and in an antinomic way, accurate guidance against targets moving at short range requires, from launch phase, a high manoeuvring capability and a very low response time of the missile.

Such requirements are not compatible with the use of a standard aerodynamic control system. In order to solve this problem AEROSPATIALE has designed the ERYX missile which is fitted with a direct thrust vector control system (PIF system).

The missile layout is shown in figure 5.3. We will notice the original layout of the missile which is fitted with a booster housed in the front section, a PIF device at the center of gravity and a powerful warhead in the rear section.

This layout is favorable to control effectiveness and to warhead effectiveness whose stand off is thus optimized.

A tricky problem is the interaction between lateral jets and missile aerodynamics which will be described in detail in §6.

The missile is ejected from its launching tube at approximately 18 m/s. This low speed allows confined space firing and is totally safe for the gunner as shown on figure 5.4.

6. DESCRIPTION OF THE AERODYNAMIC INTERFERENCE

6.1. Background

The flowfield associated with the interaction of a sonic or supersonic gaseous jet with a transverse external flow is very complex.

Literature on the subject is very abundant. In particular synthesis works of SPAID and CASSEL [3] and MARGASON [4] can be mentioned.

Description of the aerodynamic interference will be presented, based largely on results of ONERA experiments, jets from flat-plate or from bodies of revolution. These experiments include flow visualization, static pressure distribution, flowfield survey and induced force results.

Some of the important features of the flowfield created by a jet interacting with an external crossflow are illustrated in figure 6.1.

We can distinguish two types of interaction:

- the local interactions, in the neighbourhood of the nozzle; they are due to the fact that the jet plume presents an obstacle to the external flow, and it causes modifications of the pressure distributions over the surface around the jet exit,
- the downstream interactions, in the far wake; they come from the vortex structure of the jet wake, which can have significant effects when lifting surfaces are located downstream of jet controls.

6.2. Local interactions

6.2.1. Jets in supersonic external flow

6.2.1.1. General description

The interaction between an axisymmetric underexpanded jet and flow over a body from which the jet exhausts is illustrated in figure 6.2. For these ONERA experiments, the jet exhausts from a supersonic nozzle, canted downstream, and the boundary layer approaching the jet is turbulent.

As shown in figure 6.2, the jet plume presents as an obstacle to the external flow, which causes, in supersonic flow, a strong shock and a separation of the boundary layer upstream of the jet. As a result of high pressure levels downstream of the shock, the jet is turned in the direction of the axial flow (figure 6.3). The shock structure is highly three dimensional, bounded by a 3D mixing layer as it can be seen from the oilflow visualization (figure 6.2). Downstream, the mixing layer surrounds the plume and reattaches to the body with a secondary shock whose trace is evident in the oilflow pattern.

In the jet, near the nozzle exit, another shock structure appears; this shock, referred to as the Mach disk, is commonly encountered in highly underexpanded axisymmetric jets exhausting into still air. Here, as the jet plume is transverse to a supersonic external flow, the Mach disk is also turned in the downstream direction.

From recent ONERA experiments, JACQUIN [5] underlined that strong instabilities expand in the jet mixing layer. This can be seen from the schlieren

photograph in figure 6.4, obtained with very short "time exposure". We can see that these turbulent structures appear mainly in the region upstream and above the jet. This is related to a benefit effect of the jet curvature for the development of centrifugal instabilities. Consequently, acoustic waves can be observed between the jet and the bow shock, whose shape is not so smooth as one could expect. It seems that these waves come from the region just upstream of the nozzle exit. The comparison between the two photographs of the figure 6.4, show that for a warm jet, the acoustic waves are more intense, which is in accordance with the fact that in this case the convective velocities in the jet mixing layer are much higher.

6.2.1.2. Bow shock

In the analysis of jet-induced aerodynamic interference, most of the shock shape predictions are made using the analogy with the detached shock of a blunt body [6] (figure 6.5).

Nevertheless, it is very difficult with such models to take into account all the flow parameters.

From schlieren visualizations made for different flow conditions (fig. 6.6) we observe that the distance between the bow shock and the nozzle exit increases when the jet pressure increases, when the external Mach number decreases or when the jet exit Mach number decreases.

In the same way, the separated zone just ahead of the bow shock grows when the jet pressure increases.

6.2.1.3. Mach disk location

As mentioned in [8], the knowledge of the position of the Mach disk is very important for the prediction of the jet trajectory. This position is generally determined from schlieren visualisations, and from such measurements BILLIG [7] has proposed correlations for the Mach disk location. As shown in figure 6.7, these correlations agree quite well with ONERA experiments.

6.2.1.4. Pressure distributions

A typical induced pressure distribution near the jet is shown in figure 6.8. Here the supersonic jet exhausts from a flat plate into a Mach 2 external flow. Upstream of the nozzle exit, the jet bow shock and separation shock induce high pressures. Downstream, we first observe a low pressure region which corresponds to a separated (recirculation) zone under the jet; then the pressure increases up to an overpressure, due to a reattachment shock.

A jet pressure ratio effect is presented in figure 6.9. When the pressure ratio increases, the obstruction

produced by the jet increases, and consequently the different zones, of high pressure and low pressure, are larger, whereas the pressure levels are quite similar, except for the lowest pressure ratio, for which the jet is overexpanded rather than underexpanded.

The influence of the jet exit Mach number is shown in figure 6.10, for flow conditions corresponding to the same jet momentum flux (or approximatively the same thrust). The sonic jet, which is highly underexpanded, produces relatively larger disturbances than the supersonic jets.

Figure 6.11 presents results obtained at different external Mach numbers. This effect is more difficult to analyse because it depends on the various possible choices for the flow parameters. For a constant momentum flux ratio ($p_j \gamma M_j^2 / p_o \gamma M_o^2$) we observe that when the Mach number M_o decreases, first the bow shock moves upstream, and secondly that the pressure levels are more important (lower pressure in the recirculation zone, higher pressure in front of the jet).

The effect of inclining the thrust axis of a circular jet relative to the external flow direction is shown in figure 6.12. For these experiments, the jet was canted downstream, and as expected the result is that the disturbances are much lower, in particular for the upstream boundary layer separation. An inverse effect will be encountered for a jet canted upstream.

A similar effect is observed for a rectangular cross-sectional shape of the nozzle in comparison to a circular one (figure 6.13). This can be explained by the fact that for the same exit area, a rectangular nozzle, with a streamwise orientation, is less large, and so the jet obstruction and the disturbances are lower.

For practical application, the gas exhausting from the nozzle comes from the combustion of propellants, while ambient temperature air is commonly used in wind-tunnel test as the jet gas. The main difference between the two gases is that the hot jet has much higher velocities. Figure 6.14 shows a comparison between cold and hot jets, for which the nozzle exit pressure and the nozzle thrust were the same. The induced pressure distributions indicate a forward shift of the separation and bow shock, but only a slight effect on the downstream disturbances.

Most of the jet interaction data available in the literature are obtained from experiments with flat plate. For missile applications, the jet issues from a body of revolution, which is often at non-zero incidence, that is to say that the external flow is non-uniform. Moreover, an effect of the local radius of curvature of the surface near the nozzle could be expected.

The results presented figure 6.15 show that in both

cases the flowfield structure is very similar, in particular for the pressure distribution. Only a slight effect of the body incidence is discernible.

6.2.2. Jets in subsonic external flow

6.2.2.1. General description

In a subsonic crossflow, the general behavior of the flow structure is similar to that in supersonic crossflow, except that there is no bow shock and no separated shock ahead of the nozzle exit. However, for underexpanded jets, internal shock (Mach disk) are always present (figure 6.16).

For subsonic Mach numbers, the dynamic pressure of the external flow is much smaller; as a result, the jet is less turned in the direction of the axial flow than it was in supersonic crossflow, and its penetration is better.

Moreover, for a very low speed external flow, the only mechanism responsible for the deflection of the jet is the entrainment associated with the turbulence in the mixing layer.

6.2.2.2. Pressure distributions

Induced pressure distributions near a supersonic jet exhausting from a body of revolution into a Mach 0.5 external flow are shown in figure 6.17.

We observe the same tendencies as before:

- a region of high pressure, upstream, due to the jet obstruction;
- a region of low pressure downstream;
- higher disturbances when the jet pressure ratio increases.

An effect of the external Mach number is presented in figure 6.18 for a fixe jet pressure ratio. When the Mach number decreases, the dynamic pressure of the external flow is smaller and smaller, and consequently jet entrainment effect is higher and higher.

Therefore, the overpressure level, upstream of the jet decreases, and when the external flow velocity is very low ($M_o < 0.3$) the entrainment effect tends to induce negative pressure coefficients all around the nozzle exit.

Downstream, the pressures are always very low, in particular at $M_o = 0.1$ for which low levels are encountered far downstream.

6.3. Downstream interactions

6.3.1. Description

From visualisations and flowfield surveys, the structure of the wake associated with a crossflow jet can be

sketched as shown in fig. 6.19.

All along its turning process, the jet itself disappears quickly, and the main identifiable structure in the far wake is a set of contrarotating vortices. Nevertheless we can also distinguish secondary vortices close to the wall; this horseshoe vortex is due to the adverse pressure gradient just ahead of the jet, which causes the boundary layer to roll up.

An example of flow-field measurements obtained at ONERA [5] is presented in figure 6.20. The data were obtained for a Mach 2 underexpanded hot jet ($T_{ij}/T_{io} = 3$) in a Mach 2 crossflow, and for a momentum flux ratio $\rho_j V_j^2 / \rho_o V_o^2$ of 10.

Vector plots of the in-plane velocities, total temperature contours, vorticity contours, turbulence level contours, and total pressure contours are presented for different cross-section downstream of the nozzle exit.

From these measurements, the different distinguishable features of a jet exhausting into a crossflow are underlined:

- figure 6.20b shows large upwash velocities in the symmetry plane, in particular for the most upstream cross-section; these are due to the combined effect of the jet entrainment and vortices; this figure also shows that, downstream, the flowfield is dominated by a vortex pair,
- although there is not a clearly defined boundary between the jet and the freestream, the temperature contours (figure 6.20c) show the kidney shape of the jet, which is evidence of the presence of lateral vortices, which transport mainstream fluid into the jet,
- these main vortices are clearly identified by the vorticity contours in figure 6.20d; a horseshoe vortex can also be seen, close to the wall ($x/D_j = 10$); the main vortices seems to come from the jet itself, although a third vortex system is also apparent in the jet, just above the previous one at $x/D_j = 5$; these last vortices could be the vestiges of the free jet ring vortices which evolve from the boundary layer of the nozzle; the origin of this vortex system will be discussed deeply in section 6.3.2,
- the turbulence levels $(u'^2 + v'^2 + w'^2)^{1/2} / V_o$, measured using laser velocimeter, are very high in the vicinity of the main vortices (fig. 6.20e) and much higher than for classical shear layer; they are the reflect of a strong mixing between the jet and the mainstream,
- the characteristics of the jet decay, which can be seen from the temperature measurements (fig. 6.20c), are again clearly visible from the total

pressure contours in figure 6.20f ; under the jet, a low pressure region is also visible, between the two main vortices,

- from these measurements, different trajectories can be characterised (figure 6.21):
 - . the jet trajectory, which corresponds to the location of the maximum of total pressure or total temperature;
 - . the vortices trajectory, which corresponds to the maximum of vorticity.

When a jet exhausts from a body of revolution at zero incidence, the wake structure is very similar to the one from a flat plate (figure 6.22). For a positive incidence, the jet being located on the windward side of the body, we observe that the jet trajectory is closer to the body and the body vortices on the leeward side are slightly affected. For a negative incidence, these body vortices are virtually cancelled and only the jet vortices are visible, but altered, in comparison to those at zero incidence.

For missile applications, the main problem associated with jet control is that the vortex structure of the jet can have significant effects on lifting surfaces located downstream of the nozzle.

An example of such interactions is presented in figure 6.23 for panel forces measured with or without the presence of a jet. As it can be seen, the induced lift is negative; this is due to the velocities induced by the vortices on the wing, but also to the low dynamic pressure encountered in the jet wake.

For a windward location of the nozzle, we can also note that the interactions increase when the body incidence increases, because the jet plume is swept across the body.

Moreover, during a manoeuvre, if the jet is not located in the pitch plane, large rolling moment can be induced on the missile, as shown in figure 6.24.

6.3.2 - Origin of the vortices

The origin of the main vortices has been the subject of many investigations for the last years, but an improved understanding has not been well established.

On the basis of the analogy with the flow structure on a solid circular cylinder in crossflow, some authors suggest that the vortices come from the recirculation zone behind the jet.

In fact, from a recent analysis, JACQUIN [8] suggests that these vortices are an extension of the free jet ring vortices which evolve from the nozzle exit (figure 6.25), and this assumption is corroborated by computational investigations using Navier-Stokes codes

(see for example [9]).

This physical scheme is based on the fact that it exists two possible sources of vorticity in the flow (figure 6.26):

- vertical vorticity (ω_z) produced by the crossflow which shears the jet fluid along the lateral edges;
- transverse vorticity (ω_x) coming from the boundary layer in the nozzle.

For the first mechanism, the vortex strength Γ_z is a function of the crossflow velocity and size of the nozzle, and the contribution of Γ_z to the main vortices (Γ_x) requires a reorientation of the vortex lines (vortex tilting). Within this process, the vortex strength is independent of the jet velocity, whereas experimental results show that the strength of the main vortices increases when the jet momentum flux increases.

For the second mechanism, JACQUIN [8] demonstrates that the vortex strength is a function of R^2 (jet momentum flux ratio: $R^2 = p_j \gamma M_j^2 / p_o \gamma M_o^2$), which is in agreement with experiments (figure 6.27).

Finally, it seems that the first mechanism is not sufficient to explain the presence of the main vortices, and that the second mechanism is the most important.

6.3.3 - Vortex strength and location

A lot of velocity measurements have been made for a jet in a subsonic crossflow, which give a good description of the vorticity properties.

An example of such data, from FEARN and WESTON [22] is presented in figure 6.28. As it can be seen, the vortices gradually weaken each other by the diffusion of vorticity across the symmetry plane.

Similar results have been obtained from ONERA tests for a jet issuing from a flat plate in a supersonic external flow. The vortex characteristics are presented in figures 6.29 to 6.32, in non-dimensional form for the maximum vorticity ($\omega_{max}/(U_o/d_j)$), lateral spacing (d_j/d_j) and vortex penetration (h/d_j).

Figure 6.29 shows that the vorticity decreases all along the jet trajectory, as it did in the FEARN and WESTON experiments for incompressible flow. In the same way the lateral spacing increases, which corresponds to an increase of the vortex diffusion.

We have seen previously that the vortex strength (circulation Γ) increases with R^2 (momentum flux ratio). For the maximum vorticity in the core of the vortices, it seems from figure 6.30 that this vorticity is quite independent of R^2 , except for the lowest ratio.

In this last figure, an effect of the external Mach number is also presented. As expected, when M_o

increases the vortex penetration (h) decreases, and we can note that the vorticity decreases also.

Another factor that affects the vorticity properties is the nozzle exit shape and jet deflection angle. The data presented in figure 6.31 show that for a rectangular jet, with a streamwise orientation, the vorticity is greater than for the circular jet; the lateral spacing and penetration of the vortices are also higher. The other important feature of this figure is that inclining the nozzle downstream increases the vorticity.

The jet temperature effect has been investigated recently by JACQUIN [5]. There is only a slight increase of the vorticity (figure 6.32) while the jet temperature increases from 300 to 900 K, at a fixed momentum flux ratio $R^2 = 10$.

When a jet exhausts from a body of revolution, which corresponds to a more practical application, we have already seen that the induced pressure distributions were very similar with those on a flat plate. For the vorticity properties, the results presented in figure 6.33 show again a great similarity in the vortex strength and position.

7. JET INTERACTION PERFORMANCE

7.1. Definitions

In predicting jet interaction performance, the principal subject of analysis is usually the aerodynamic forces induced by the jet. For simple configurations such as a flat plate or a body of revolution, they can be obtained by integration of the induced pressure distributions. For a complete missile configuration, in addition, we must take in account the forces induced on the wing and (or) the control surfaces, and the overall induce forces (and moments) are generally obtained by direct force measurements (see § 8).

Another common terminology used by most in discussing jet interaction performance is amplification factor. Two amplification factors are defined as:

$$K_F = (F_i + F_j)/F_j \quad \text{Force amplification factor}$$

$$K_M = (M_i + M_j)/M_j \quad \text{Moment amplification factor}$$

where :

- F_i Interaction force
- F_j Nozzle delivered thrust = $F_v - p_o A_j$
- F_v Nozzle vacuum thrust
- p_o Freestream static pressure
- A_j Nozzle exit area
- M_i Interaction moment
- M_j $F_j l_j$
- l_j Moment arm of nozzle thrust

For mid-body thrusters, a special definition is required for the moment amplification factor, since the thrust acts through, or near the centre of gravity (centre of moment) :

$$K_M = 1 + M_i/F_j D$$

D body diameter

7.2. General features

An example of induce forces obtained from ONERA experiments [10] is shown in figure 7.1 for a generic missile configuration. The supersonic jet was exhausting from a location near the centre of gravity, and the external Mach number was 2.0.

Under these conditions, the interaction force always act in opposition to the jet thrust, whereas the induced pitching moment is positive (nose-up for a jet located on the windward side of the body).

Consequently, the force amplification factor K_F is less than 1 (figure 7.2), that is to say the interference is unfavourable. On the contrary, the moment amplification factor K_M is greater than 1.

Some insight into this behavior can be gained by re-examining the results presented chapter 6.

As it can be seen from the pressure distribution on the body, figure 6.15, the high pressure region upstream of the nozzle gives a favourable interaction, but the region of low pressure, downstream, is relatively larger, so that the overall force induced on the body alone is negative, and the induced moment is positive.

This behavior is quite different of that of a jet exhausting from a flat plate in supersonic flow, for which the force amplification factor is greater than 1 (figure 7.3). This is due to the high pressure regions lying to either side of the nozzle (figure 7.4), which are, for a body, wrapped around it, so that the contribution of these regions to the normal force is greatly diminished relatively to a flat plate situation.

In the same way, for aft mounted jets, the region of low pressure can be largely reduced and as a result the interaction force is generally positive and the force amplification factor greater than 1.

From figure 7.1, we can also observe that the interaction force increases with increasing jet pressure, but at a smaller rate, so that the force amplification factor increases (figure 7.2).

For the body + tail configuration, due to the negative lift induced on the tail surfaces by the jet wake (figure 6.23), the interaction force and moment are larger. Moreover, when the body angle of attack increases, the jet wake gets closer to the tail and the interference

force is even more unfavourable.

7.3. Effect of the nozzle geometry

For a gas generator which operates at a fixed mass flow, the maximum nozzle thrust is generally obtained with a highly supersonic exit Mach number, and as the nozzle throat area is fixed, the nozzle exit area will be large. Under these conditions, the data in figure 7.5 show that the interaction normal force and corresponding amplification factor are independent of the nozzle exit Mach number for the range investigated here ($M_j = 2.5$ to 3.5).

On the other hand, for a given exit Mach number, when the nozzle dimensions increase, the interaction force increases also, so that the amplification factor is nearly constant (figure 7.6). This indicates that the interaction force is proportional to jet momentum, or nozzle thrust. We can also note that this is true for both configurations, body alone or with a tail, in other words for both the local interactions and the downstream interactions.

An effect of the nozzle cant angle is presented in figure 7.7. The results obtained show that when the nozzle is canted downstream, the interaction forces on a body + tail configuration are approximately the same, but as the normal thrust (perpendicular to the body axis) is lower, the amplification factor decreases. On the contrary, a forward cant angle will certainly give an increase of the amplification factor, but this nozzle design produces also an axial component of the thrust equivalent to a drag for the missile.

The influence of the shape of the nozzle exit is also presented in figure 7.7. As seen previously, for a slendered rectangular nozzle (length > width) the interactions are lower than those for a circular nozzle and this leads here to a less unfavourable interference. For aft mounted jets, a large slot nozzle will be preferred, because the larger the nozzle is, the larger the blocking of the upstream flowfield is, and the larger the favourable interaction forces will be ($K_F > 1$).

7.4. Influence of the external flow (Mach number, incidence)

We have seen previously that in subsonic flow, when the external Mach number decreases the blockage effect of the jet plume decreases and so the overpressure levels upstream of the nozzle (figure 6.18). Consequently the negative normal force induced on the body increases.

In supersonic flow, when the Mach number increases, changes are mainly observed in the recirculation region where the pressure coefficient increases (figure 6.11). As a result the induced normal force will be less and less unfavourable.

For the forces induced on the tail surfaces by the jet wake, we generally observe that they decrease when the external Mach number increases (from the subsonic to the supersonic regime).

These trends give a smooth variation of the overall induced normal force, as presented in figure 7.8, which decreases when M_o increases.

In term of force amplification factor, which takes in account the dynamic pressure ratio between the jet and the external flow, the situation is quite different (figure 7.9). For very low Mach numbers, the dynamic pressure tends to zero, so the K_F coefficient tends to 1. Then, when the Mach number increases, the force amplification factor K_F decreases, reaches a minimum for about Mach 2 and then increases for the highest Mach numbers, K_F being always smaller than 1.

Figure 7.10 presents the moment amplification factor for a missile which uses forward jet as a moment control. The trends are very similar to those observed previously for the force amplification factor, that is to say that for the Mach number range considered (Mach > 2) the moment amplification factor increases with M_o . Here we can note that values greater than 1 are obtained for the highest Mach numbers.

The sensitivity of jet interaction to missile incidence is presented in figure 7.11. It can be seen that the force amplification factor is lower when the jet exhausts on the windward side (positive incidence for the case presented here). This is mainly caused by the downstream interactions on the tail control surfaces which are much higher when the incidence increases, the jet plume being swept across the afterbody.

On the contrary, for negative incidence (jet on leeward side), the jet plume moves away from the tail surfaces and the downstream interactions decreases. Moreover, the local dynamic pressure of the external flow decreases and the local interactions around the nozzle are more favourable. These two effects make a large increase in the force amplification factor K_F .

7.5. Effect of jet gas

Most of the wind-tunnel tests conducted for jet interaction studies are made using cold air as a jet gas, whereas in free flight it is a hot gas coming generally from the combustion of propellants.

The effect of jet gas properties on the aerodynamic interference has been the subject of several investigations [3] but the conclusions of these studies are not very clear, some data showing no discernible effect of jet temperature or molecular weight, while others indicate quite large effects. This is probably due to the scaling parameters which are considered for the comparisons.

An example of results obtained at ONERA is presented in figure 7.12 for a body-tail configuration at Mach 2.0. The data are relative to three different gases: cold air, a combustion gas, and cold helium. For these experiments, the nozzles from which the gas exhausts, had the same exit diameter (geometric similarity) but different throat diameters, so that the jet momentum fluxes were the same for the three gases at a give pressure ratio (p_j/p_o).

The choice of the third gas was dictated by the fact that this gas has a very low molecular weight and so a high constant R . Therefore, even for cold helium, the jet velocities are much higher than for air, and close to those encountered with a combustion gas.

From figure 7.12, it can be seen that at zero incidence the aerodynamic interference are lower for the combustion gas than for air, but very similar to those measured with helium. These results point out that even if the momentum flux ratio is the most important jet interaction scaling parameter, the effect of jet velocity is not negligible.

Nevertheless, for 11° of incidence, the trends are totally different: the largest interference are obtained with the combustion gas and the use of helium doesn't give better results than air. It seems that, in this case for which the downstream interactions are preponderant, another simulation parameter has to be taken in account.

7.6. Influence of wing location

It has been seen (§ 6.3) that the downstream interactions on tail surfaces are very important, and that they reduce the force amplification factor. These interactions depend on the size and roll position of the wings, but also of their distance from the jet as shown in figure 7.13.

From the most aft position, when the wings get closer to the jet, we observe first an increase of the interaction (amplification factor K_F smaller) due to stronger vortices in the jet wake; then, when the distance between the wing and the jet becomes relatively small, the interference are favourable rather than not (large increase in K_F) due to the interaction of the bow shock with the wing (figure 6.2).

8. WIND-TUNNEL TESTING

8.1. Simulation of jet interaction flowfield

The problem encountered here concerns the formulation of similarity parameters for the jet interaction flowfield since it is generally not possible in wind-tunnel to make test at full scale with the same flow conditions as in flight.

Aerodynamic simulation requirements (dynamic and thermal), in the absence of jet flow are well-known:

- geometric similarity;
- same Mach number, Reynolds number, Prandtl number, specific heat ratio and wall temperature.

If the jet flow was considered to be independent of the external flow, these requirements ought to be applied simply to both flows, but for combined flowfield, additional terms relative to diffusion must be taken in account.

These requirements are highly restricting, but important simplifications are usually permissible in wind-tunnel tests.

For the external flow, which is generally air in wind-tunnel, and which can be considered as a perfect gas for most applications, duplication of M_o and Re_L is only necessary.

For the jet flow, it is essential to simulate two phenomena:

- its expansion from the nozzle exit (jet boundary, Mach disk,...);
- its mixing with the external flow.

For the first point, this leads to duplicate γ_j , M_j and p_j/p_o . For the second point, the main parameter to take in account is V_j/V_o , since the free shear layer is turbulent at Reynolds numbers of practical interest.

Nevertheless, for measurements in wind-tunnel, it is not very easy to use hot gas thrusters similar to those used on flight vehicles, and the simulation gas is generally cold air.

In this case, it seems from experimental results, that the best scaling parameters are jet pressure ratio p_j/p_o and jet momentum flux ratio $\rho_j V_j^2 / \rho_o V_o^2$.

As seen previously, the use of a low molecular weight gas (helium for example) can improve the simulation, because the jet velocity is higher ($\approx 3 V_{j,air}$) for the same jet momentum flux. In comparison to helium at ambient temperature, for air the resulting total temperature would be 2000K.

8.2. Flow surveys

Most of the experimental investigations devoted to flowfield analysis are made with jets issuing from a flat plate rather than from a body of revolution. The main reason is that the measurements are easier to do, and easier to analyse, and we have seen previously that the main phenomena are very similar in both cases.

Figure 8.1 shows such an experimental set up in the ONERA S5Ch wind-tunnel, which is very simple, the jet being issued from the wall of the wind-tunnel.

Surface flow phenomena can be studied by means of:

- static pressure measurements,
- oil flow visualisations.

An example of oil flow visualisation obtained at ONERA is presented in figure 8.2. The technique used here consists of a fluorescent viscous coating illuminated by a U.V. light [11]. The advantages of this technique is that the oil film is very thin (lower interaction), and that more details can be observed than with current technique.

For flowfield analysis, different kind of measurements can be made using:

- pitot probe,
- 3, 5 or 7 holes probe,
- thermocouple,
- vapor-screen visualisation,
- laser doppler velocimeter,
- spontaneous Raman scattering.

The last two techniques, which are not very usual, present the advantages of being non-intrusive, and of giving detailed informations for mixing flows.

We have seen previously some LDV results relative to turbulence levels (figure 6.20e). An other example of results is shown in figure 8.3 which illustrates some difficulties inherent in the seeding process of two different flows (bias seeding). We can observe large differences according to whether the particles come from the external flow, from the jet, or from both.

An example of density measurements using spontaneous Raman scattering is given in reference [12]. This technique is based on vibrational frequencies of molecules, stimulated by a laser beam and the light intensity scattered is proportional to the molecular concentration in the probe volume. Moreover, if different gases are used for the external flow and the jet, partial densities measurements can be made. Figure 8.4 shows a result where the different discontinuities (shocks, expansions) are clearly visible, as the presence of the jet. On the assumption that the main flow and the jet are expanding isentropically outside the shocks, the static pressure in the flow can be calculated also (figure 8.5).

8.3. Force measurements

This technique is the most commonly used for the determination of the overall interference on realistic configurations. The measurements are made with a strain gauge balance installed inside the model.

There are two possibilities for the model arrangement:

- either to measure all the forces: nozzle thrust and aerodynamic forces,
- or to measure only the induced aerodynamic forces, the gas supply system being dissociate from the weighted part of the model.

This second possibility is generally preferred because it gives the best accuracy for the determination of the jet interference. This can be explained by the fact that the nozzle thrust is generally one order of magnitude greater than the induced aerodynamic forces, and a small uncertainty on this thrust would affect greatly the results in the first case. Moreover, the disturbing reactions and deformations induced by the gas supply are not taken in account.

However the model arrangement need to be more complex, with a very rigid sting, and a special balance.

A sketch of test set-up used at ONERA is given in figure 8.6. The sting, hollow, supplies the nozzle with air (or any other gas, such as helium). According to the size of the model, the balance can be installed nearby the gas supply, or can be annular, around the sting.

With that model, it is also possible to use hot gas thruster, with small propellant charge. During such tests, the problem encountered is an oscillation of the model when the charge is ignited (figure 8.7). Nevertheless, if the model is well designed, the oscillations are rapidly damped, and a steady state is reached in less than 0.5 s, allowing a good estimation of the induced force and moment.

Figure 8.8 shows a photograph of a generic missile in the ONERA S3MA supersonic wind-tunnel. On this photograph, the gas supply system is clearly visible aft the sting.

8.4. Unsteady measurements

Different unsteady phenomena encountered with jet controls can have significant effects on the control system performance.

The first one concerns the starting process of the jet which governs the response time of the control system. Classical unsteady measurements (force, pressure) can be made, but it can be interesting to have some more details about this starting process. For this purpose a special test set-up has been developed at ONERA-IMFL, which allows simultaneous pressure measurements and ultra-high-speed shadowgraph visualisations.

Figure 8.9 shows a series of photographs obtained at 20 μ s intervals. The starting process of the jet is well displayed as well as the jet wake expansion which rate is approximatively equal to the external flow speed.

An example of unsteady force measurements is shown in figure 8.10 for the ASTER missile at full scale in the ONERA S2MA wind-tunnel [13].

This missile is fitted with four nozzles which are supplied by a hot gas generator through a switching unit (see figure 4.3).

The objectives of this test were to measure the aerodynamic performance, and more precisely to evaluate the response time of the jet control system.

The combination of the overall forces measured with an internal balance, and the inertial forces measured with accelerometers give the net aerodynamic forces. As it can be seen on figure 8.10, the induced lift response is in a good agreement with the nozzle thrust response.

The second unsteady phenomenon concerns spinning missile, for which a delay may exist between the thruster ignition and the developpement of the jet interference.

In order to study such effects, a special test set-up has been developed by ONERA (figure 8.11). The external part of the model and the jet control system are driven in rotation separately (but at the same rate), so that only the aerodynamic forces are measured (not the jet thrust), as previously. The model is equipped with a main balance (4 components), non rotating, a rollmeter, and several accelerometers.

9. COMPUTATION.

In the past, interaction studies between pyrotechnical lateral jets and missile aerodynamics were mainly based on long and expensive experimental tests. Nowadays, thanks to progress in data processing technology and numerical computation methods, it is possible to predict these complex interactions and therefore to reduce the aerodynamic design cycle.

This chapter presents some calculations made around fundamental, generic and industrial configurations in supersonic and subsonic flows. They are mainly Euler calculations which, from an engineering point of view, give usefull results.

9.1. Supersonic configurations

For these configurations we use two Euler codes developed by ONERA, in collaboration with AEROSPATIALE:

- FLU3C [14] based on a mono-domain grid strategy
- FLU3M [15] based on a multiblock grid strategy with a two species perfect gas modelisation.

Both codes solve the unsteady equations. To compute steady flows, flow variables are advanced in time until an asymptotic limit is reached. This procedure is valid for any speed range. We use it for the subsonic pocket between the bow shock and the nozzle exit. Outside this region, where the flow is fully supersonic, a pseudo-marching procedure is used in which the steady solution is obtained in a plane using an upwind scheme and driving the time derivatives to zero, then proceeding to the next plane, in the flow direction.

9.1.1. Fundamental configurations [17]

The aim of these calculations is to establish Euler capability to predict the structure of the flow.

9.1.1.1. Flat plate

Figure 9.1 presents the wind-tunnel model with the different types of measurements: schlieren, pressure taps along the X axis (passing through the center of the nozzle exit), probing in a transverse plane located 17.5 D_e (exit diameter) downstream the nozzle.

The test facility used is the ONERA S5Ch wind-tunnel in Chalais-Meudon.

As the configuration has a symmetric vertical plane, calculations were performed only on one half domain ($y > 0$). The computer code used is the Euler code FLU3C and the grid has about 700,000 points with 200 points in the exit nozzle section which is rectangular as for the model. This very fine grid has been used to be sure of capturing the phenomena which could be obtained by an Euler simulation.

The freestream and jet conditions used are the following:

- freestream Mach number 2,
- cold air for the jet with the nozzle axis normal to the plate, exit Mach number 2.5 and total pressure ratio 14.3.

Figures 9.2 to 9.6 show that Euler calculations predict the main features of the flow: detached shock, secondary shock, Mach disk, overpressure and low pressure regions in the vicinity of the nozzle and, vortices downstream. However, Euler calculation overestimate the total pressure and the height of the vortices and, of course, do not predict the boundary layer separation upstream the nozzle exit.

9.1.1.2. Fuselage

Figure 9.7 presents the fuselage and a view of the model in the ONERA S2MA wind-tunnel. This

fuselage is a cylindrical body of diameter D equal to 0.1 m, with a parabolic ogive of length $3D$. The jet issues from an axisymmetric nozzle inclined rearward at an angle of 60 degrees from the missile axis and located $8.5 D$ from the nose. Ten 5 hole probes are distributed on a rake, which can rotate around the body. Experimental data acquisition were obtained with this device in 3 planes respectively located $10 D$, $12 D$ and $15 D$ downstream the nose. These probings were realised with a large number of freestream and jet conditions.

Calculation has been performed on one half domain (symmetric configuration), with the Euler code FLU3C and with a grid of about 190,000 points with 153 points in the nozzle exit section.

The freestream and jet conditions used are the following :

- freestream Mach number 2 and incidence 0° ,
- cold air for the jet, nozzle exit Mach number 2.5 and total pressure ratio 28.

As for the flat plate, Euler calculations predict the main features of the flow: detached shock, secondary shock, overpressure and low pressure regions in the vicinity of the nozzle and vortices downstream. Figure 9.8 presents an example of the cross-flow velocity in a transverse plane located $6.5 D$ downstream the nozzle. We observe that calculations are close to experimental results, especially jet penetration height is much better predicted than for the flat plate.

9.1.2. Generic configuration: wing-body [17]

The configuration concerns an ogive-cylinder fuselage equipped with four cruciform wings in "+" or "x" attitude (figure 9.9).

The tests, made in the ONERA S3MA wind-tunnel in Modane, consisted in measuring panel forces on each wing with and without lateral jet interactions.

Calculations have been performed on one half domain (symmetric configuration) with the Euler code FLU3C and with a grid of about 380,000 points.

The freestream and jet conditions used are the following :

- freestream Mach number 2
- cold air for the jet with an nozzle exit Mach number 2.5 and a total pressure ratio 14.

Figures 9.10 and 9.11 show variation of the normal force coefficient as a fonction of the incidence respectively for a horizontal wing (+ configuration) and a leeward wing (x configuration). The computation provides a good representation of the changes in the

normal force coefficient C_N as a fonction of incidence, and in particular the differences at a given incidence between values with and without jet.

9.1.3. Industrial configuration: ASTER missile.

The ASTER missile (see § 5.1) is a cruciform missile with four low aspect ratio wings and four control surfaces. The thrust vector control is achieved by means of jets emerging from the tip edge of the wings.

The configuration has been calculated in a "+" position with one lateral jet emerging from the leeward wing (figure 9.12). For this configuration, two series of wind-tunnel tests have been carried out: one with cold air, and the other with powder gas jet.

9.1.3.1. Cold air jet interactions [17]

Calculations have been performed on one half domain (symmetric configuration) with the Euler code FLU3C and with a grid of 300,000 points.

The freestream Mach number is 2 and the incidence is 12° .

Figure 9.13 shows the pressure distributions on the missile with and without lateral jet. The jet interactions are clearly visible, in particular the favorable over pressure on the wings due to the detached shock.

For the case with jet, figure 9.14 shows the pressure distribution on the surface of the ASTER and the pressure contours in a traverse plane located just downstream the nozzle. This figure shows the complexity of the flow and the obvious usefulness of these computations for the understanding of complex physical phenomena.

Figure 9.15 illustrates the effect of altitude on the shape and position of the primary shock. We observe good agreement between computations and experiments.

Lastly, figure 9.16 presents the relative errors on the overall aerodynamic coefficients. These results are also fully satisfactory: about 5% for C_N and less than 0.25 D for the stability.

9.1.3.2. Powder gas jet effects [16, 18]

Tests carried out for ASTER missile with cold air jet and powder gas jet, are linked by similarity criteria (conservation of nozzle thrust, exhaust section area and expansion ratio). These criteria have been chosen to keep interactions as identical as possible between the two jets (especially for jet penetration height) in order to reduce powder gas jet tests and replace them by cold jet tests. Nevertheless small variations on the aerodynamic coefficients are observed between these

tests.

To predict these variations, we have simulated the powder gas jet as a perfect gas with the same specific heat ratio and the same molecular weight. In other words, we have simulated these variations by a jet total temperature and a jet species effect. For this purpose, the flow is modelised as a mixture of two inviscid non-reactive perfect gas. This model is of course not able to simulate all physical phenomena: turbulent mixing layer between the jet and the external flow, reactive flow, etc. However, it will be shown that this modelisation can be sufficient to predict these effects.

Four calculations have been performed with the multidomain and two-species Euler code FLU3M. They correspond to the following cases:

- without jet (available experimental data),
- with cold air jet (available experimental data),
- with hot air jet (no experimental data),
- with perfect gas modeling the powder gas jet (available experimental data for powder gas jet).

Cold air jet and hot air jet nozzle exit conditions differ only by the total temperature. The freestream Mach number is 1.6 and the incidence 8 degrees.

The mesh we use is made of 8 domains and about 400,000 points (see figure 9.17). This grid is much more refined and regular than the one used in the previous paragraph.

Figure 9.18 shows a view of the wall pressure computed with the cold air jet and with the perfect gas modelling the powder gas jet. We observe only very small differences.

The integrated pressure differences between these two cases (powder gas and cold air) show an effect as experiments do, that is to say, a slight increase in the normal force and a slight move of the center of pressure downstream. We also observe that the effects of total temperature and species have the same weight.

In conclusion we can say that an Euler two-species gas model with a total temperature effect is able to simulate lateral powder gas jet interactions and to give much better results than the one-species gas model, even with total temperature effect.

9.2. Subsonic configurations

9.2.1. Fundamental configuration: fuselage [18]

This fuselage is the same as the one presented in § 9.1.1.2.

The aim of these calculations is to establish Euler and Navier-Stokes codes ability to predict aerodynamic interactions. The Euler calculations were made with

SESAME code developed by ONERA [19, 20]. A grid of 122x41x34 points was used. The Navier-Stokes calculations were performed by SAIC with PARCH3D code [21]. The turbulent viscosity was obtained from the two-equations $k-\epsilon$ turbulence model. The grid used has 151x71x31 points.

The freestream and jet conditions are the following:

	Freestream	Jet (air)
Mach number	0.8	2.5
Total pressure	0.95 bar	22 bar
Incidence	0°	60°
Total temperature	293 K	293 K

Comparisons of calculations with experimental data are displayed in a cross-section located 12D downstream from the nose (3.5 D from the nozzle).

Figure 9.19 shows axial component of the vorticity vector contours in the transverse plane. The two contra-rotating vortices in the jet wake are well simulated and their location is in a good agreement with experimental results. However, Euler and Navier-Stokes calculations overestimate the vorticity by around 50%. Another pair of vortices appears in the experimental data very close to the body. These vortices are only detected by the Navier-Stokes calculation.

Figure 9.20 shows Mach number contours in the same section. We observe from this figure that calculations are qualitatively close to experimental results, as far as the jet cross-section structure and size arc similar. Mach number maximum value in this section is well predicted by both calculations, with a difference to experimental results lower than 10%. This maximum location is nearly the same for experimental data and Navier-Stokes calculation. Euler calculation locates this maximum about 0.5D closer to the missile body than experimental results.

Total pressure contours are also well predicted. In particular the extrema are well predicted by the Navier-Stokes calculation, with the proper locations.

In all cases, we note that the shape of the jet cross-section is rounder and more expanded for the Euler calculation than for the Navier-Stokes one.

In a general way, it appears that a better agreement with experiment is obtained through Navier-Stokes calculation. However, Euler calculation is quite able to predict the flow structure and to give good results.

9.2.2. Generic configuration: wing-body

The test-case considered is a body of revolution with a cruciform tail in "x" attitude. The jet issues from the body at mid-length, and 2D upstream of the panels.

The freestream and jet conditions are:

- freestream Mach number 0.8,
- cold air for the jet with a nozzle exit Mach number 2.5 and a total pressure ratio 25.

Calculations have been performed on the complete configuration with the Euler code FLU3M, and with a grid of about 450,000 points (figure 9.21).

The mesh is fine enough in the vicinity of the nozzle to ensure a good convergence of the calculations.

Figure 9.22 shows total pressure contours in a crossflow plane just ahead of the tail panels. In comparison to experiments, we can see that the jet penetration and the shape of the wake are well predicted as well as the maximum of total pressure (in the jet).

Forces induced on the panels have also been calculated and are compared to experimental results in figure 9.23. Although the vorticity properties in the jet wake are not well predicted by this inviscid flow simulation, the induced forces are in good agreement with experiment.

9.2.3. Industrial configuration: anti-tank missile [18]

This configuration is similar to the ERYX's one presented in § 5.2.. Two nozzles are located at the center of gravity. Each nozzle axis is inclined rearward so that thrust axial component contributes to accelerate the missile. Jets deflectors located at the nozzle exit section ensure missile steering. Missile spin rate permits to control the flight with these two nozzles.

All calculations were made at zero incidence and with a freestream Mach number equal to 0.3. Jet conditions at the nozzle exit section were defined with a preliminary 3D Navier-Stokes calculation of the flow into the nozzle with the deflector. The nozzle exit section was simulated by a rectangular hole on the missile body, and jet conditions were imposed in this section for the external calculations around the body.

Calculations were performed using the Euler code SESAME, which permits to take into account the missile spinning effects by including inertial and Coriolis terms in Euler equations.

In this respect, three calculations were made:

- missile with jets and without spinning effect,
- missile without jet and with spinning effect,
- missile with jets and with spinning effect.

Figure 9.24 shows the grid used for all calculations. Because of wings curvature and spinning effect, symmetry was not employed, and a grid of about 220,000 points was generated.

Mach number contours in a transverse plane are shown in figure 9.25 for calculations performed with jets. Jet wake is visible in each half plane, and located close to the wings. Without any spinning effect, the jet wake is approximately symmetrical to the other one, some differences appearing due to wings curvature. When spinning effect is included in calculation, jet wake structure does not change, but its location is modified; the jets turn around missile axis, and angular deviation obtained depends on the flow direction at the nozzle exit section compared to rotated external flow direction.

Figure 9.26 shows local normal force on the wings due to external flow for the three calculations. Without spinning effect, interactions due to lateral jets create a depression, particularly on upper wings n° 3 and 4, which was confirmed by wind-tunnel results. With spinning effect and without jets, a normal force appears on each wing which induces a rolling moment tending to slow down the missile spin rate. With spinning effect and with jets, forces on the wings induce yawing and pitching moments.

These phenomena are clearly non linear because forces on the wings for the missile with spinning effect and jets are different from those obtained by simply adding forces for the missile with spinning effect alone and for the missile with jets alone.

10. CONCLUSIONS

The use of lateral thrusters to control missiles in subsonic or supersonic flight is very attractive, and enables fast response manoeuvre.

Nevertheless, this type of control system leads to complex aerodynamic interactions which are not easily foreseeable.

For many years, predictions of jet interference have been relied on experiments. A lot of experimental data have been obtained, including static pressure distribution, flowfield survey, flow visualization and induced forces. They allow a good knowledge of jet interactions, although the origin of wake vortices is not clearly well established.

Over the last years, major progress have been achieved in the field of CFD methods, due to improvements in numerical algorithms, grid generation, physical modelling, as well as more powerful supercomputers. With such methods, good predictions of jet interference can now be obtained, even with Euler codes which give good results for jet wake effect. For local interactions, which are mainly dependent of viscous effects, improvements in numerical simulations are still necessary to produce quantitatively efficient results at a reasonable cost.

REFERENCES

- [1] G. SELINCE. "Un Nouveau Concept de Pilotage des Missiles. Application aux Sol-Air". AGARD LS n° 135, 1984.
- [2] B. LAZURE. "Pif-Paf Control of Tactical Missiles". AGARD n° 14, 1988.
- [3] F.W. SPAID, L.A. CASSEL. "Aerodynamic interference induced by reaction controls". AGARDograph n° 173, 1973.
- [4] R.J. MARGASON. "Fifty years of jet in crossflow research". AGARD 72nd FDP meeting. Paper n° 1. 1993.
- [5] R. GAILLARD, P. GEFFROY, L. JACQUIN, G. LOSFELD. "Etude expérimentale sur les interactions entre un jet supersonique chauffé transversal et un écoulement supersonique externe". AGARD 72nd FDP meeting, Paper n° 39, 1993.
- [6] H.T. HSIA. "Equivalence of secondary injection to a blunt body in supersonic flow". AIAA Journal, Vol. 4, n° 10, 1966.
- [7] F.S. BILLIG, R.C. ORTH, L. LASKY. "A unified analysis of gaseous jet penetration". AIAA Journal, Vol. 9, n° 6, 1971.
- [8] L. JACQUIN. "Phenomenological description and simplified modelling of the vortex wake issuing from a jet in a crossflow". La Recherche Aérospatiale, 1994.
- [9] R.I. SYKES, W.S. LEWELLEN, S.F. PARKER. "On the vorticity dynamics of a turbulent jet in a crossflow". Journal of Fluid Mechanics, 1986.
- [10] M. LEPLAT, P. CHAMPIGNY, M. ROBERT. "Interactions aérodynamiques de jets transversaux sur missiles". AGARD CP 431, 1987.
- [11] R. GAILLARD, G. LOSFELD, F. MICHELI. "Description des moyens de mesure et de visualisation de la soufflerie S5Ch de l'ONERA". 15th International Congress on Instrumentation in Aerospace Simulation Facilities. ISL, 1993.
- [12] L. BOBIN. "Experimental investigation of a jet in a crossflow by spontaneous Raman scattering". 15th International Congress on Instrumentation in Aerospace Simulation Facilities. ISL, 1993.
- [13] J.P. DREVET, M. ROBERT. "Mesure des efforts instantanés sur une maquette soumise à des variations rapides de commande". AGARD CP 429, 1988.
- [14] M. BORREL, J.L. MONTAGNE, J. DIET, Ph. GUILLEN, J. LORDON. "Méthode de Calcul d'Écoulements autour de Missiles Tactiques à l'aide d'un Schéma Décentré". La Recherche Aérospatiale, 1988-2.
- [15] Ph. GUILLEN, M. DORMIEUX. "Design of a 3D Multidomain Euler Code". Computational Mechanics Institute, Supercomputing in Fluid Flow, Boston, 1989.
- [16] M. DORMIEUX, Ph. GUILLEN, R. ABGRALL. "Numerical Simulation of Transverse Jet Flows by a Non Reactive Two Species Multidomain Euler Flow Solver". AIAA paper n° 90-0126, Reno.
- [17] M. DORMIEUX, C. MAHE. "Calculs Tridimensionnels de l'Interaction d'un Jet Latéral avec un Écoulement Supersonique Externe". AGARD-CP n° 437, 1988.
- [18] M. DORMIEUX, R. MARSAA-POEY. "Numerical Assessment of Aerodynamic Interactions on Missiles with Transverse Jets Control". AGARD-CP-534, 1993.
- [19] A.M. VUILLOT. "Multidomain 3D Euler Solver for Flows in Turbomachines". Proceedings of the 9th. ISABE Symposium, 1989.
- [20] V. COUAILLER. "Multigrid Method for Solving Euler and Navier-Stokes Equations in Two and Three Dimensions". 8th. GAMM Conf. on Numerical Method in Fluid Dynamics, 1989.
- [21] S.M. DASH, B.J. YORK, N. SINHA, R.A. LEE, A. HOSANGADI, and D.C. KENZAKOVSKI. "Recent Developments in the Simulation of Steady and Transient Transverse Jet Interactions for Missile, Rotorcraft, and Propulsive Applications". AGARD-CP-534, 1993.
- [22] R. FEARN, R.P. WESTON. "Vorticity associated with a jet in a crossflow". AIAA Journal n° 2, 1974.

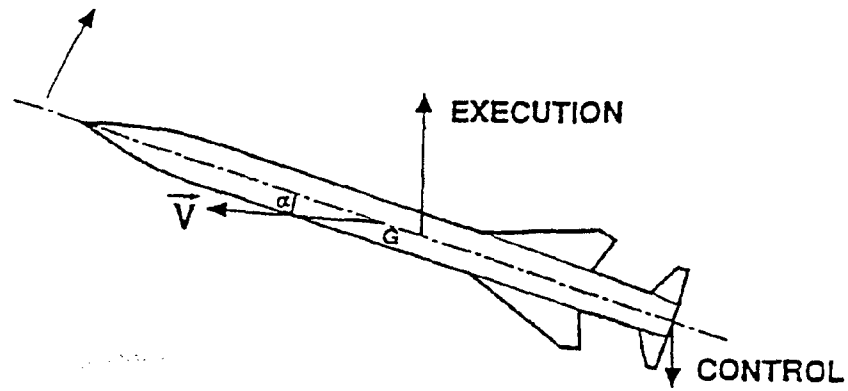


Fig. 3.1 - STANDARD AERODYNAMIC CONTROL

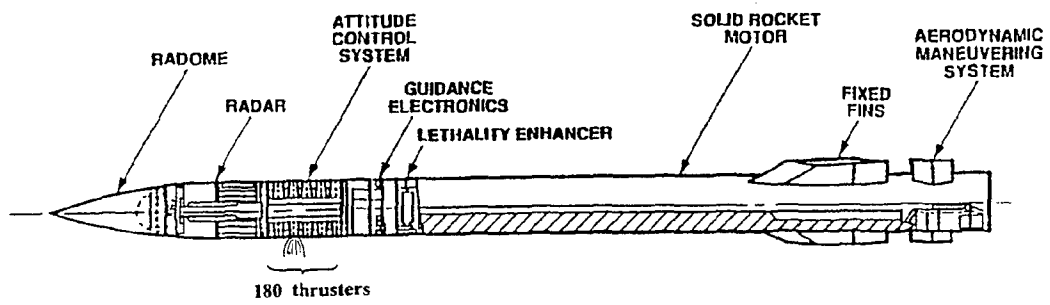


Fig. 4.1 - MOMENT CONTROL USING THRUSTERS - ERINT MISSILE



Fig. 4.2 - DIRECT THRUST VECTOR CONTROL USING THRUSTERS

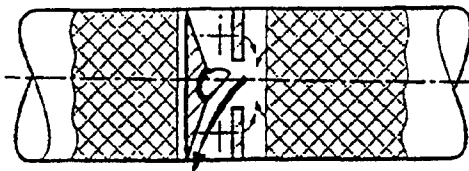


Fig. 4.3 - GAS GENERATOR AND SWITCHING UNIT

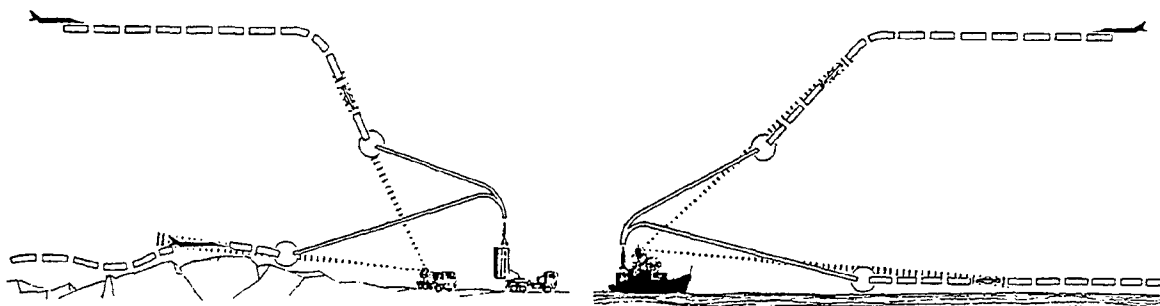


Fig. 5.1 - SURFACE-TO-AIR ANTIMISSILE SYSTEM-ASTER

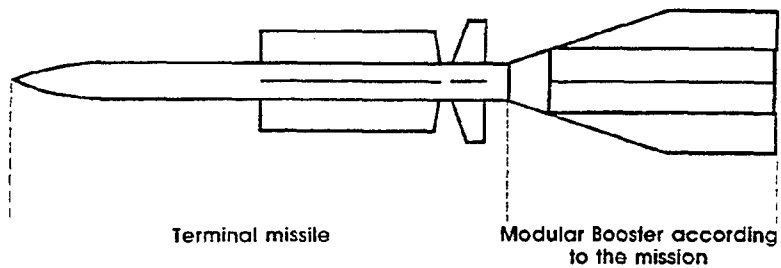


Fig. 5.2 - ASTER CONFIGURATION

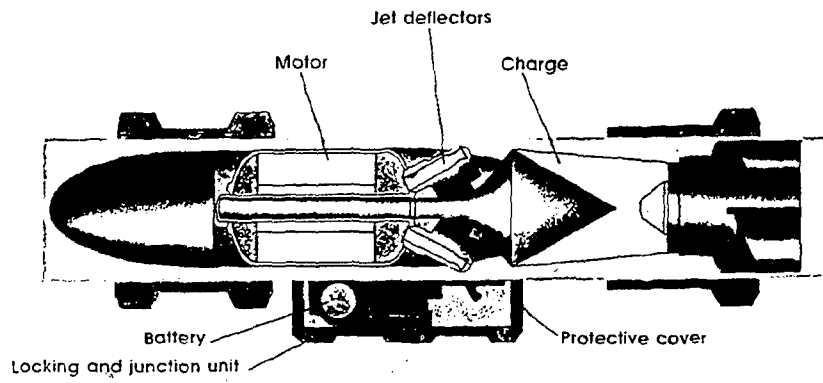


Fig. 5.3 - ERYX - SHORT RANGE ANTITANK MISSILE

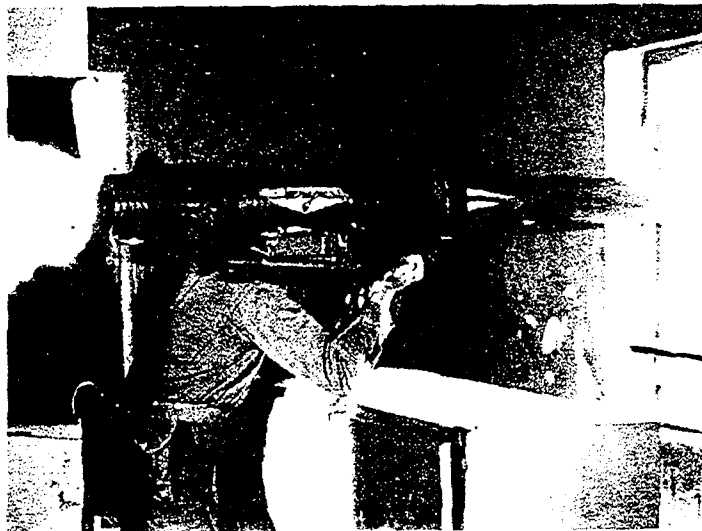


Fig. 5.4 - ERYX - FIRING FROM CONFINED SPACE

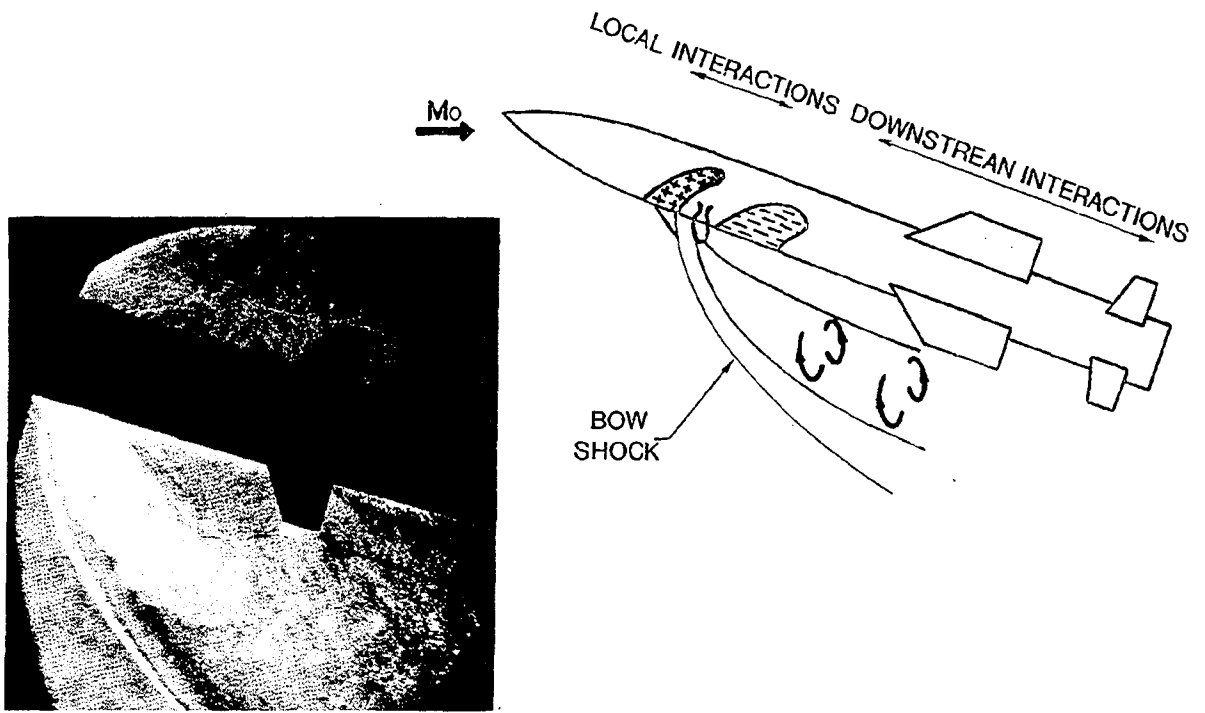


Fig. 6.1 - SKETCH OF JET INTERACTION

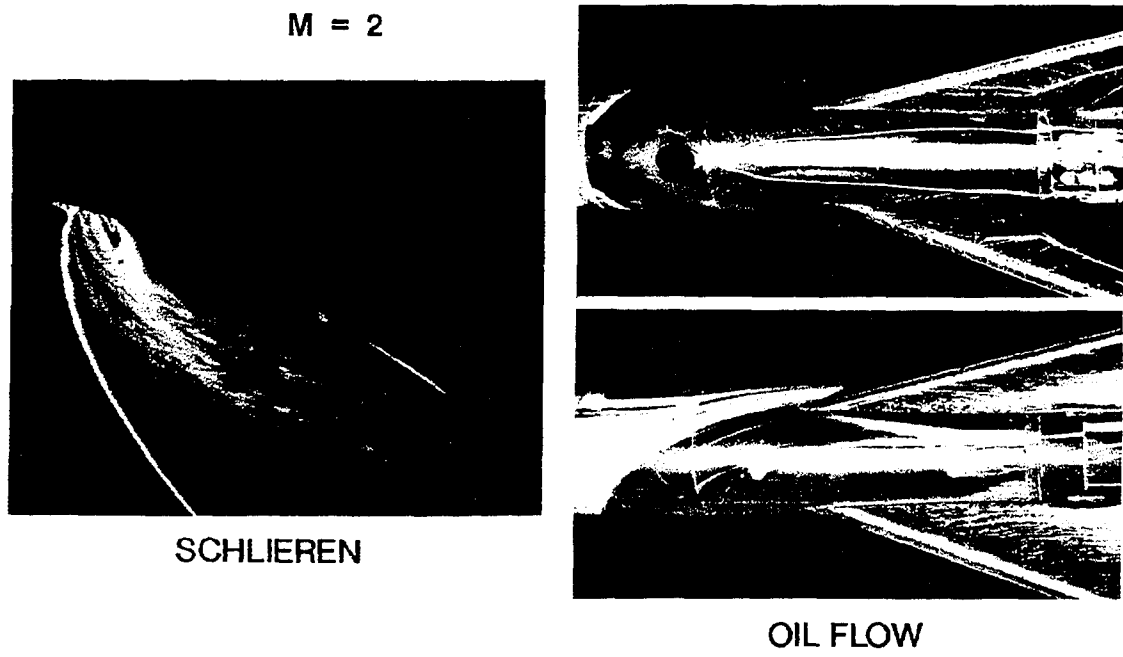
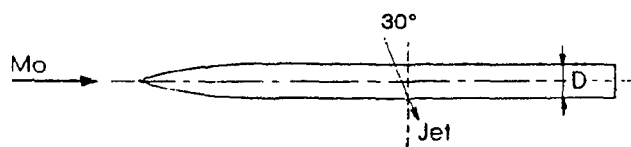


Fig. 6.2 - VISUALIZATIONS OF JET INTERACTION



$P_j/P_o = 6.45$

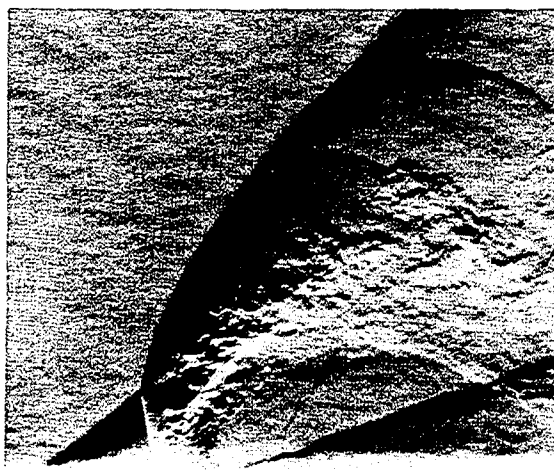


$P_j/P_o = 12.9$

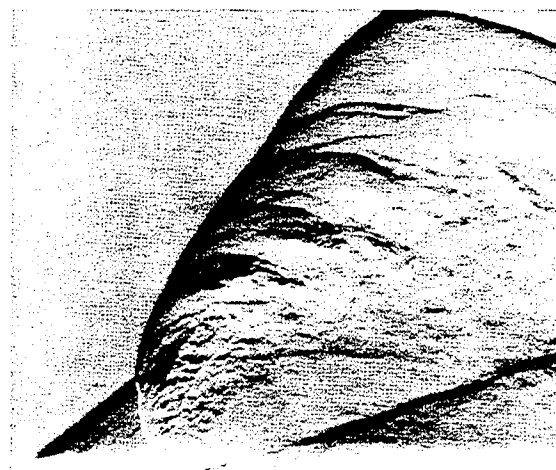
$Mo = 2.0$

Fig. 6.3 - SCHLIEREN VISUALIZATIONS OF THE SHOCK STRUCTURE

$Mo = 2.0$ $P_j/P_o = 10$

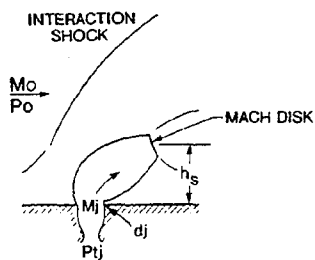


cold jet



hot jet

Fig. 6.4 - SCHLIEREN VISUALIZATIONS WITH SHORT TIME EXPOSURE



BILLIG [7]

$$\frac{h}{d_j} \text{ or } \frac{h'}{d_j} = f \left(M_o, \frac{P_{tj}}{P_o}, \frac{\delta_j}{\delta_o} \right)$$

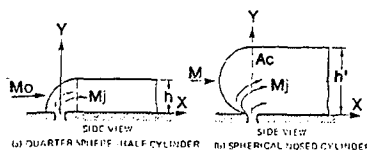


Fig. 6.5 - ANALOGY BETWEEN A BLUNT BODY AND A JET IN A CROSSFLOW

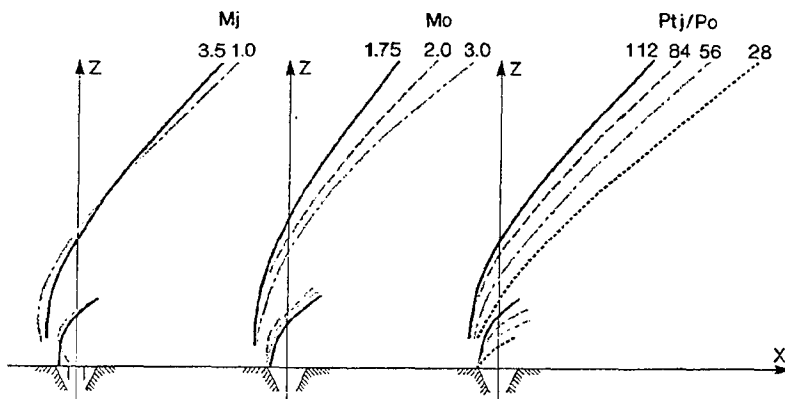


Fig. 6.6 - BOW SHOCK SHAPE - ONERA EXPERIMENTS

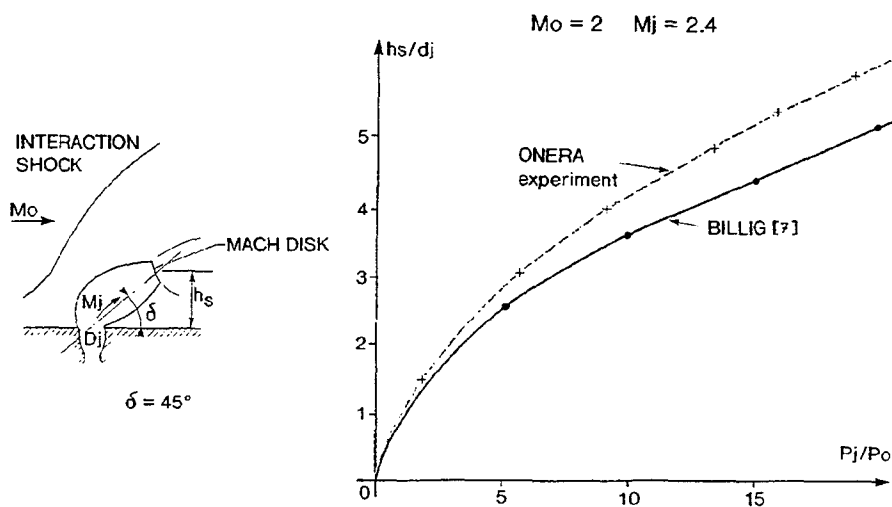


Fig. 6.7 - MACH DISK LOCATION FOR A JET IN CROSSFLOW

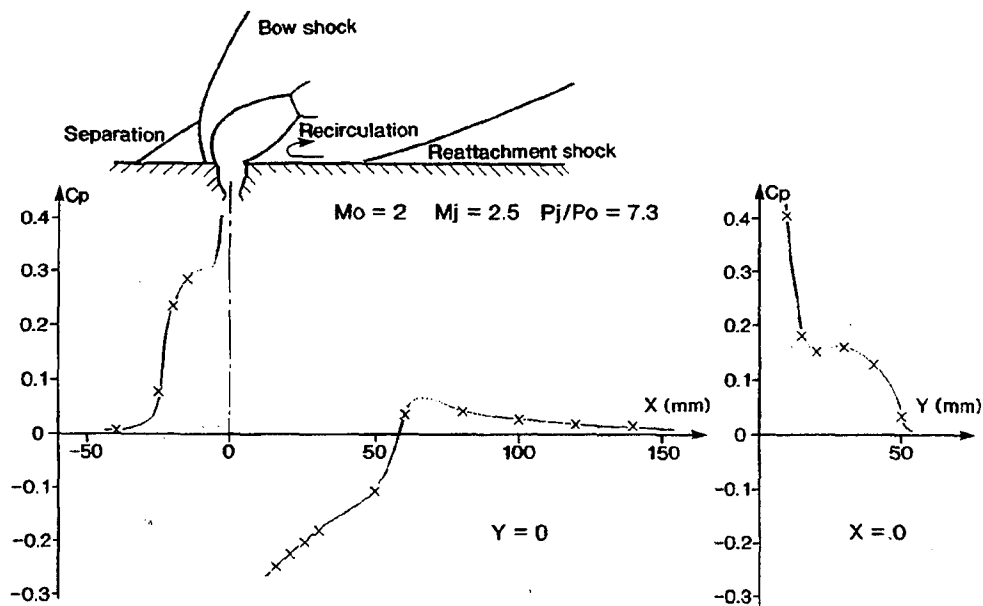


Fig. 6.8 - TYPICAL PRESSURE DISTRIBUTION IN SUPERSONIC CROSSFLOW

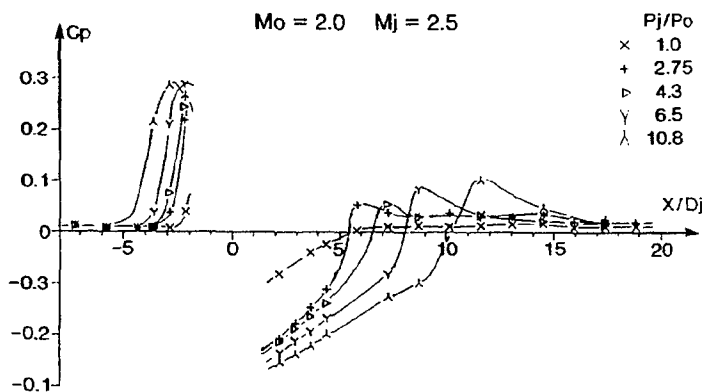


Fig. 6.9 - EFFECT OF JET PRESSURE RATIO ON PRESSURE DISTRIBUTION

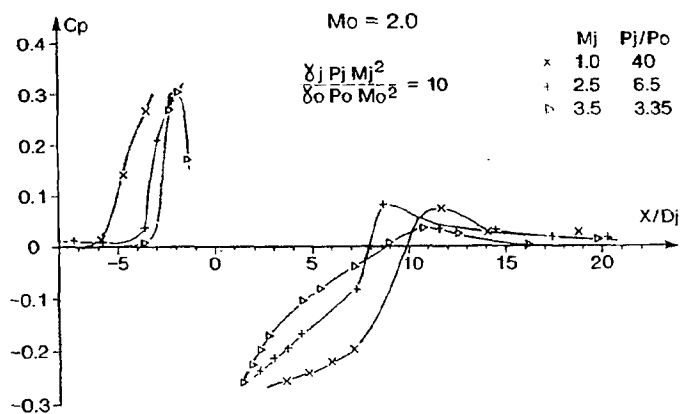


Fig. 6.10 - EFFECT OF JET EXIT MACH NUMBER ON PRESSURE DISTRIBUTION

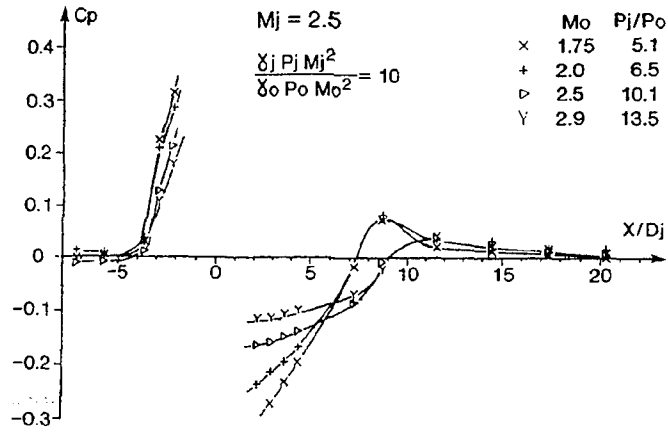


Fig. 6.11 - EFFECT OF FREESTREAM MACH NUMBER ON PRESSURE DISTRIBUTION

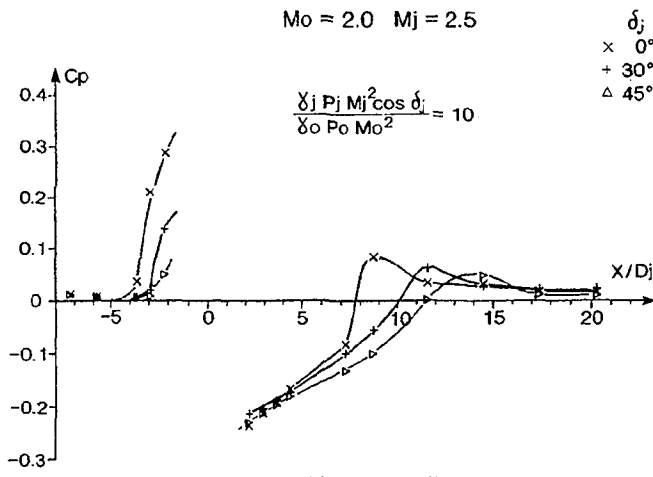


Fig. 6.12 - EFFECT OF JET CANT ANGLE ON PRESSURE DISTRIBUTION

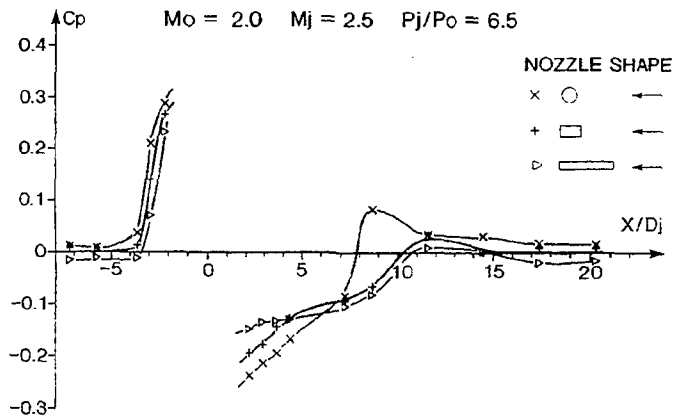


Fig. 6.13 - EFFECT OF NOZZLE SHAPE ON PRESSURE DISTRIBUTION

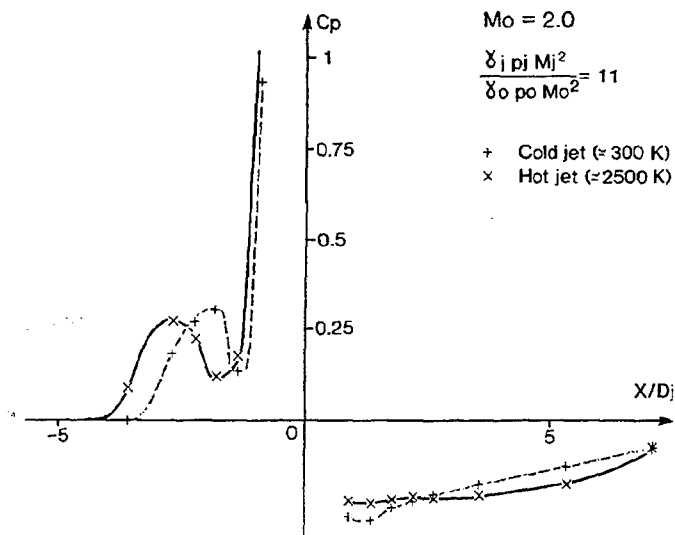


Fig. 6.14 - EFFECT OF JET TEMPERATURE ON PRESSURE DISTRIBUTION

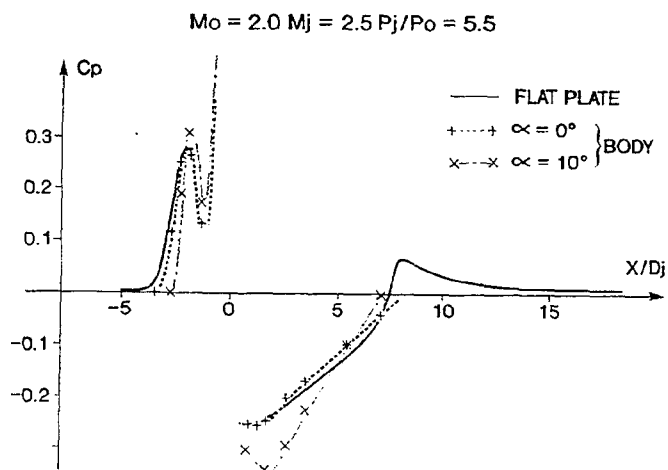
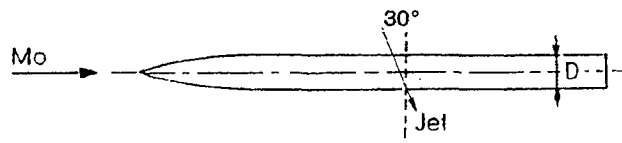


Fig. 6.15 - COMPARISON BETWEEN A JET FROM A FLAT PLATE AND A JET FROM A BODY OF REVOLUTION



$Mo = 0.8 - P_j/P_o = 2$

$$\frac{\delta P_j M_j^2}{\delta P_o Mo^2} = 20$$

$Mo = 2.0 - P_j/P_o = 12.5$

Fig. 6.16 - EFFECT OF FREESTREAM MACH NUMBER ON JET TRAJECTORY

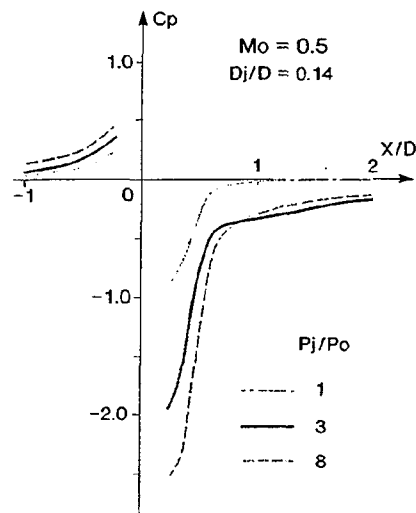


Fig. 6.17 - TYPICAL PRESSURE DISTRIBUTION IN SUBSONIC CROSSFLOW

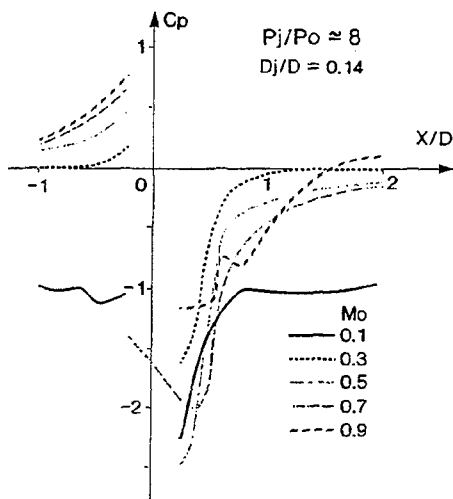
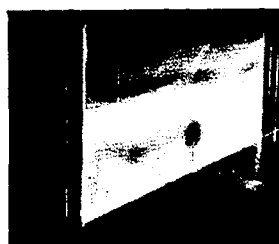


Fig. 6.18 - EFFECT OF FREESTREAM MACH NUMBER ON PRESSURE DISTRIBUTION



VAPOUR-SCREEN PHOTOGRAPH
 $Mo = 2.0$ $X/D_j = 7$

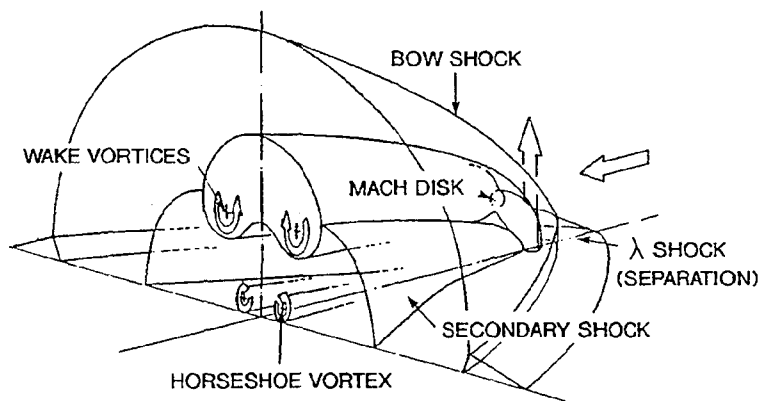


Fig. 6.19 - SKETCH OF FLOW STRUCTURE

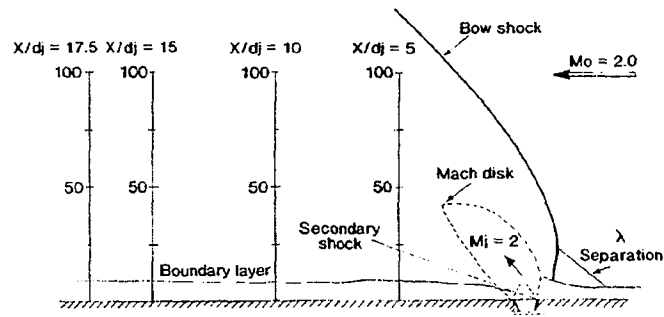
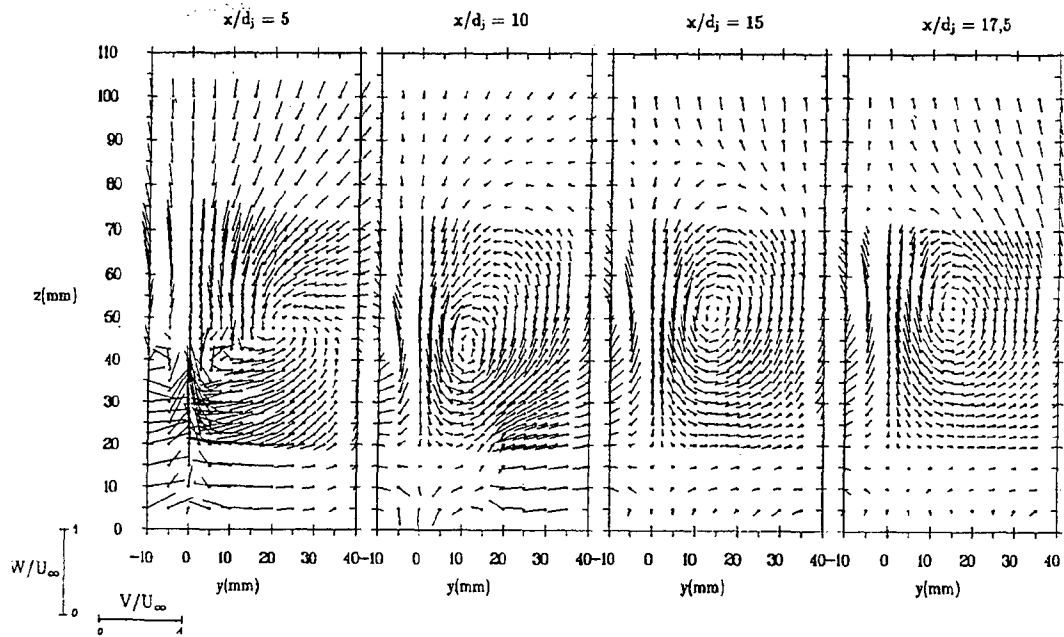
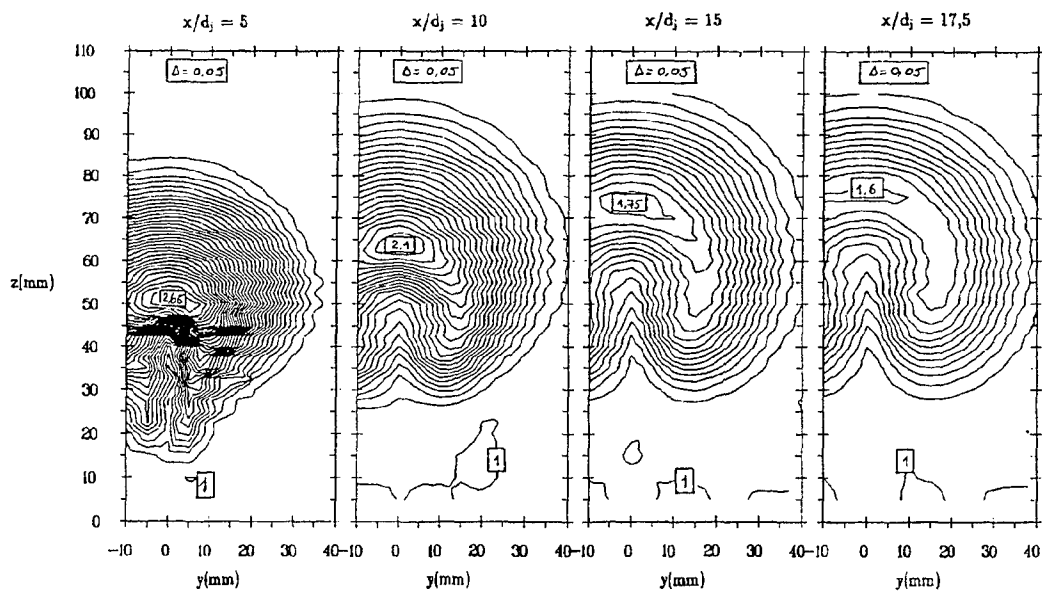


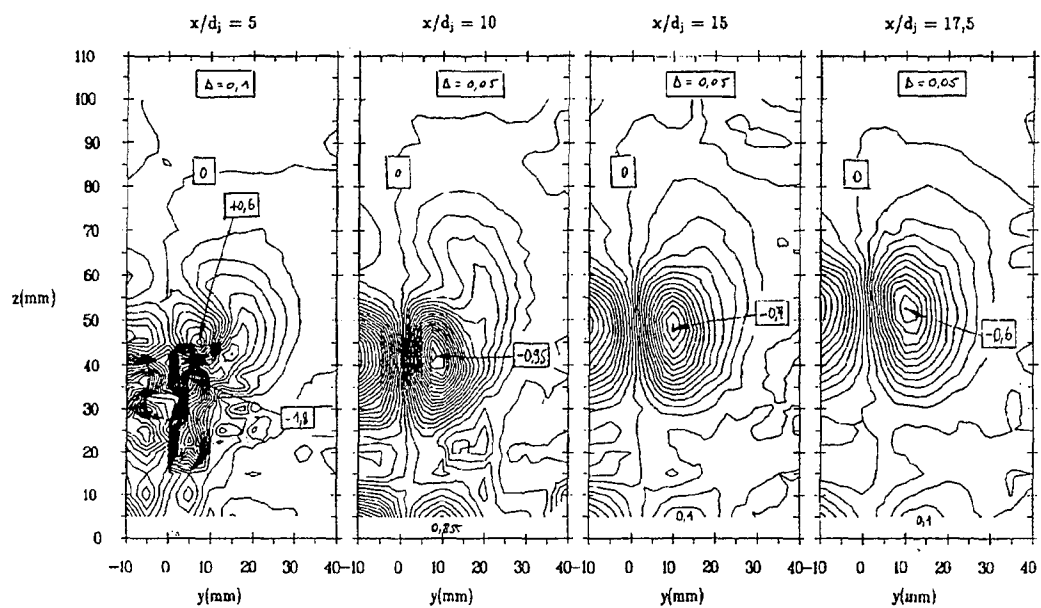
Fig. 6.20 - FLOWFIELD MEASUREMENTS FOR A JET FROM A PLAT a) Description
 ($P_j/P_o = 10$)



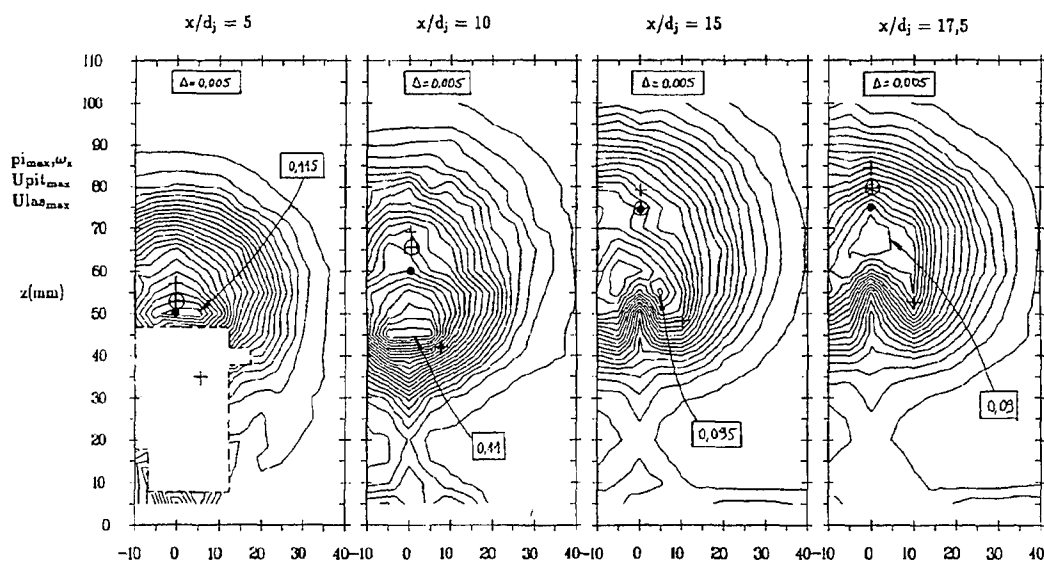
b) Crossflow velocity vectors



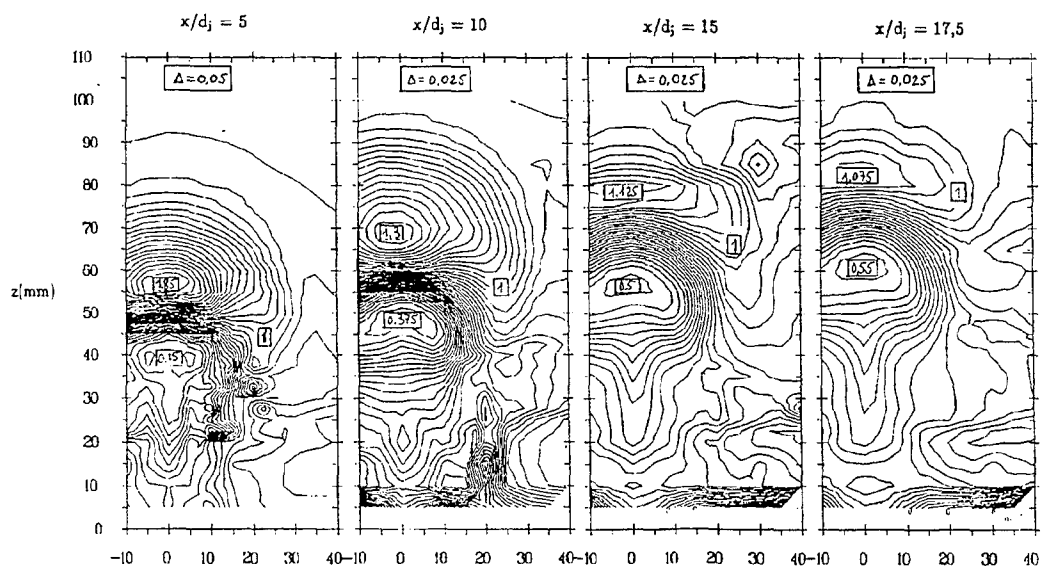
c) Total temperature contours (T_i/T_o)



d) Vorticity contours ($\omega_x \cdot d_j / U_0$)



e) Turbulence contours ($(u'^2 + v'^2 + w'^2) / U_0^2$)



f) Total pressure contours (P_t / P_{t0})

$Mo = 2.0 \quad Mj = 2.0 \quad R^2 = 10$

- * ωx
- o Pi
- + Ti
- x ρU_0^2
- max
- min

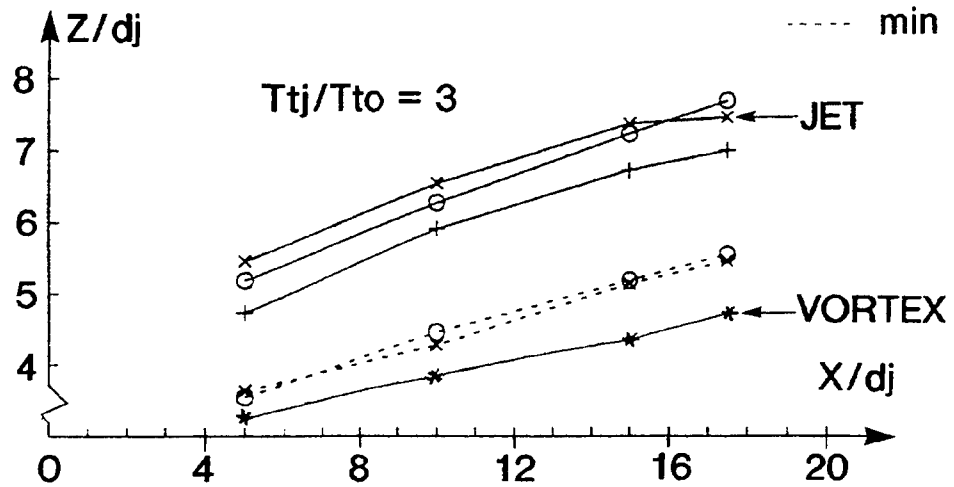


Fig. 6.21 - JET AND VORTICES TRAJECTORIES

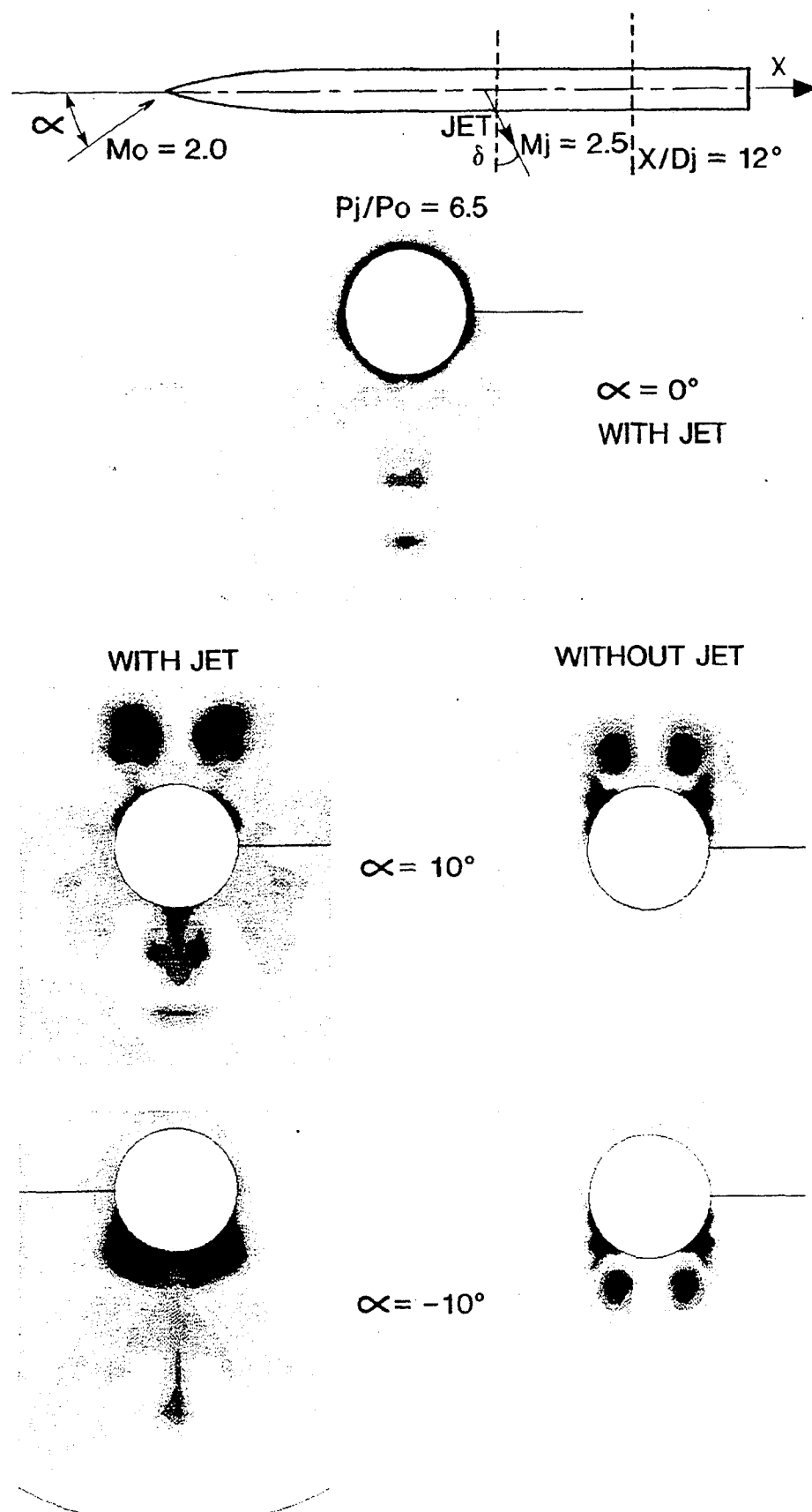


Fig. 6.22 - FLOWFIELD STRUCTURE FOR A JET FROM A BODY OF REVOLUTION - TOTAL PRESSURE CONTOURS

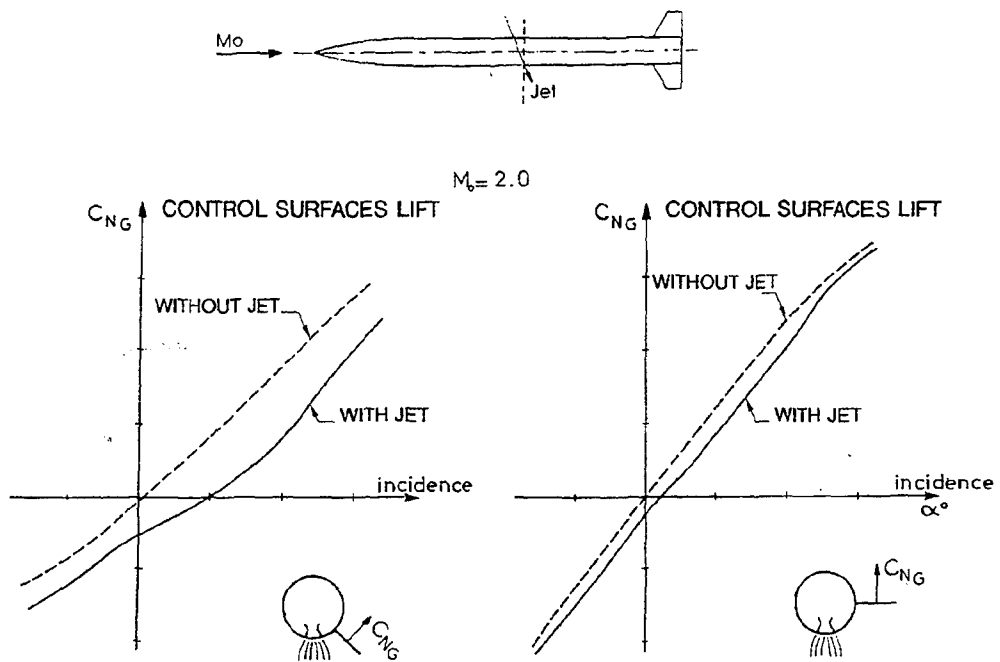


Fig. 6.23 - INDUCED LIFT ON CONTROL SURFACES

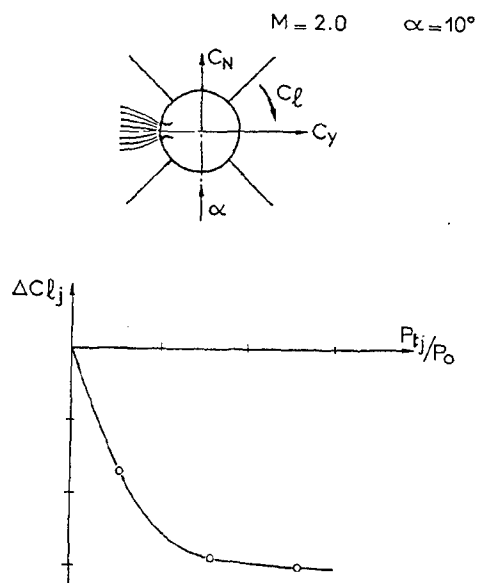


Fig. 6.24 - ROLLING MOMENT INDUCED BY A TRANSVERSE JET ON A MISSILE CONFIGURATION

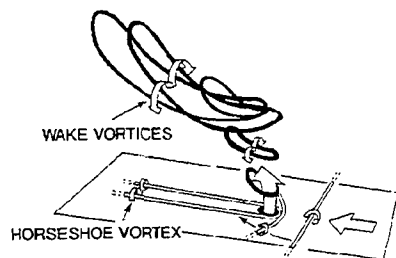


Fig. 6.25 - MECHANISM FOR THE VORTEX FORMATION

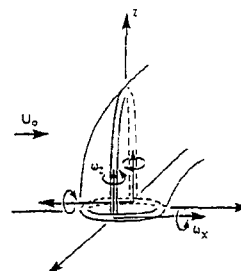


Fig. 6.26 - SOURCE OF VORTICITY

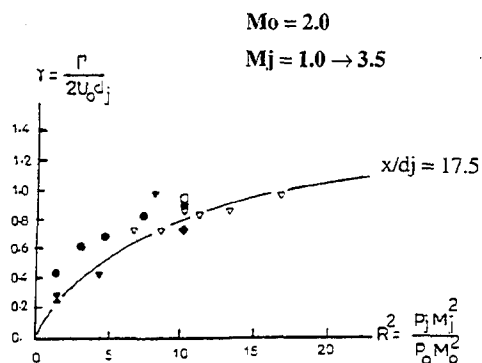


Fig. 6.27 - VORTEX STRENGTH (ONERA EXPERIMENTS)

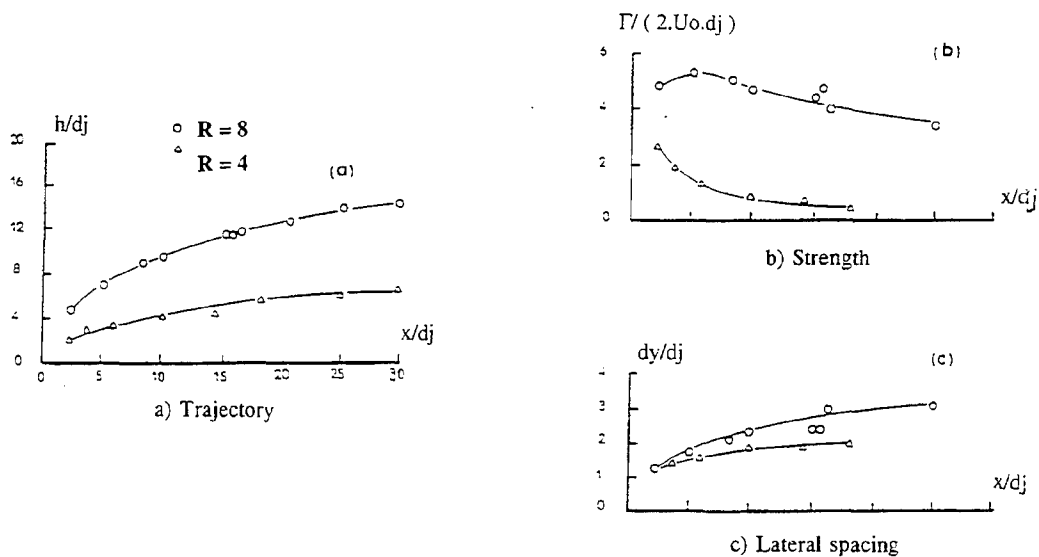


Fig. 6.28 - VORTICITY PROPERTIES IN LOW SPEED FLOW FROM FEARN AND WESTON [22]

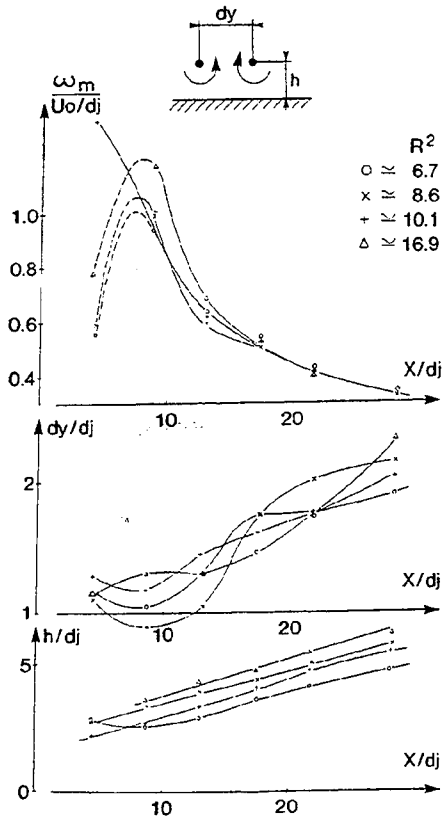


Fig. 6.29 - VORTICITY PROPERTIES IN SUPERSONIC CROSSFLOW ($M_o = 2.0$, $M_j = 2.5$) - EFFECT OF JET MOMENTUM FLUX RATIO

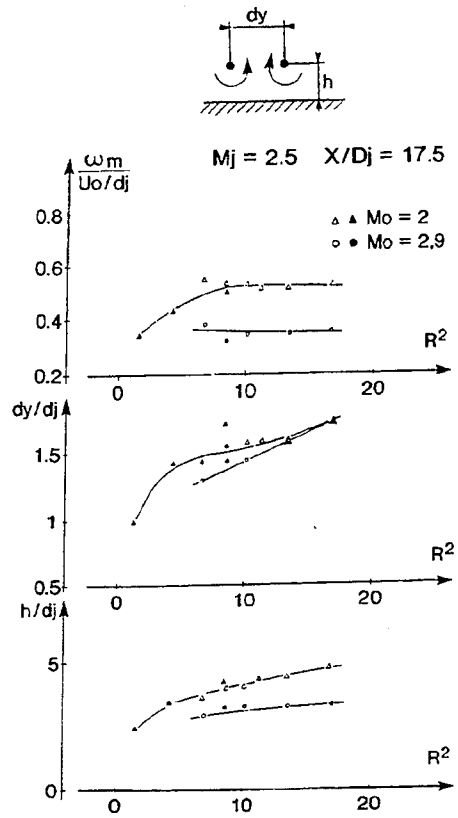


Fig. 6.30 - VORTICITY PROPERTIES - EFFECT OF M_o , ($M_j = 2.5$, $X/D_j = 17.5$)

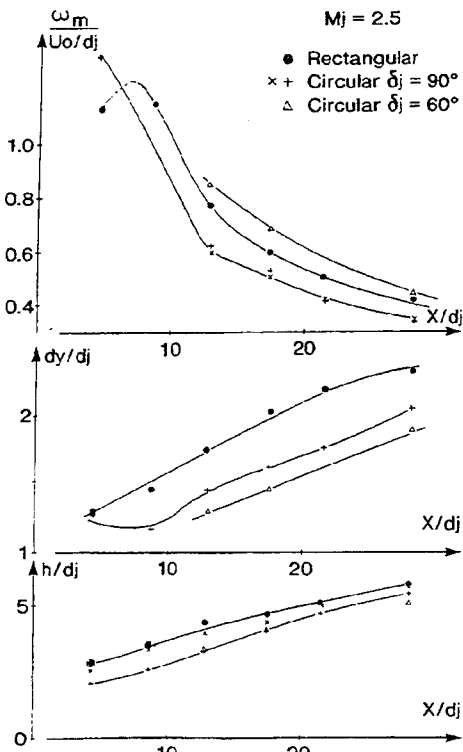


Fig. 6.31 - VORTICITY PROPERTIES - EFFECT OF NOZZLE SHAPE ($M_o = 2.0$, $R^2 = 10$)

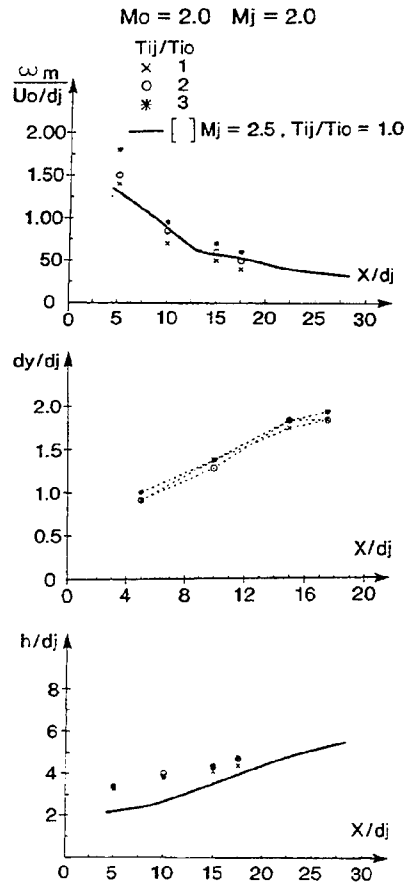


Fig. 6.32 - VORTICITY PROPERTIES - EFFECT OF JET TEMPERATURE ($M_o = 2.0$, $R^2 = 10$)

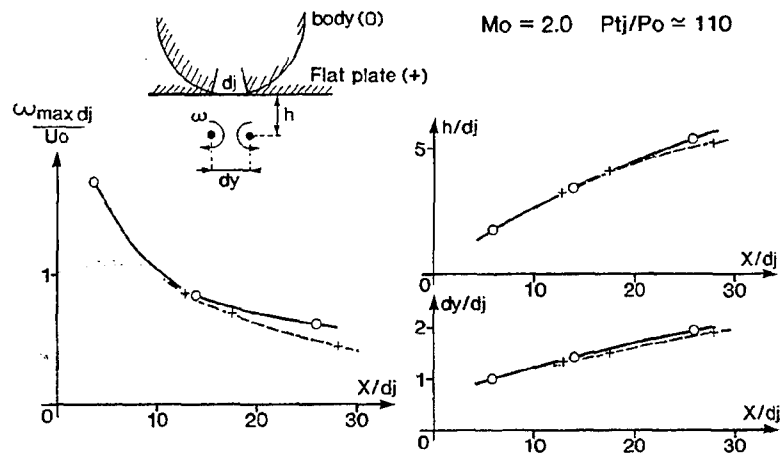


Fig. 6.33 - VORTICITY PROPERTIES - JET FROM A FLAT PLATE OR FROM A BODY OF REVOLUTION AT $\alpha = 0$

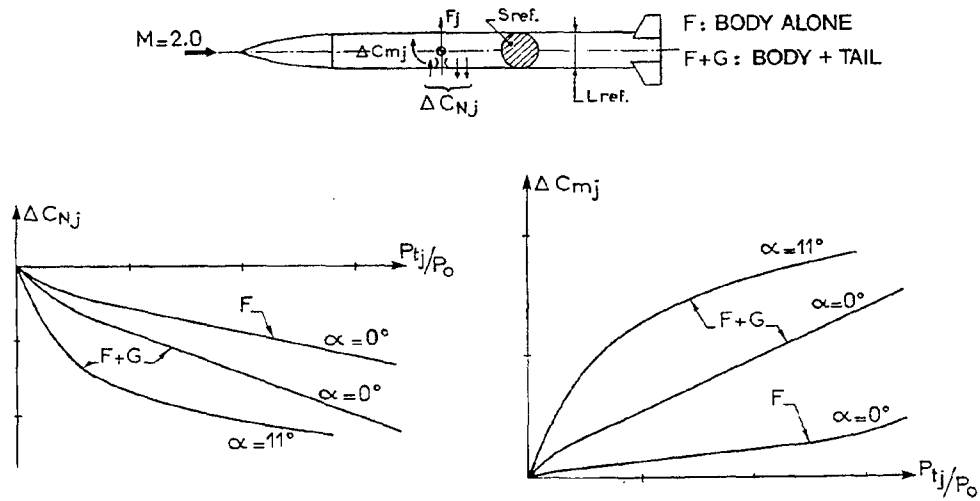


Fig. 7.1 - TYPICAL INTERACTION FORCE AND MOMENT ON A MISSILE CONFIGURATION

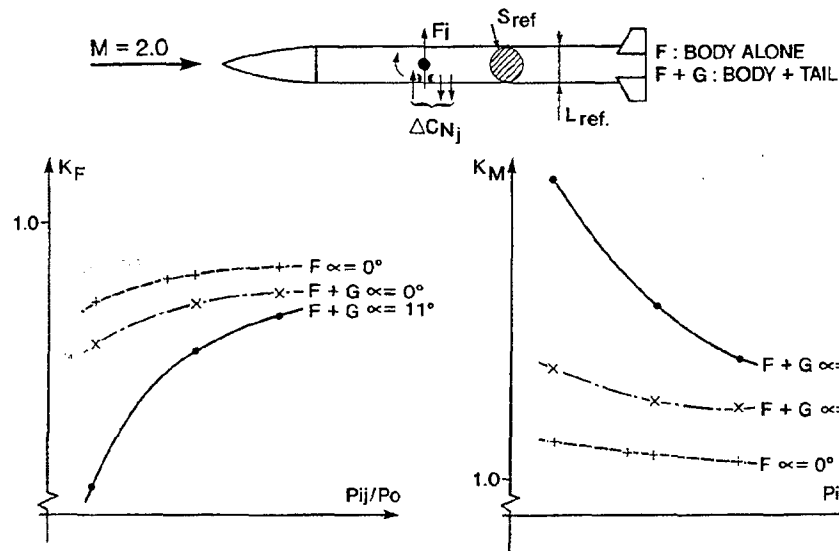


Fig. 7.2 - TYPICAL AMPLIFICATION FACTOR FOR A MISSILE CONFIGURATION

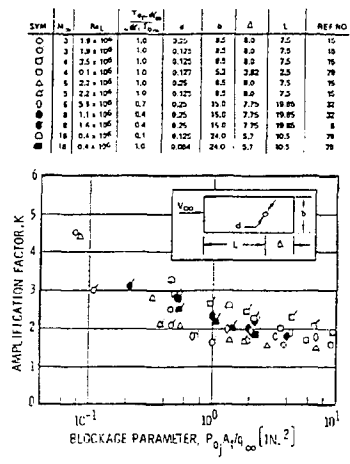


Fig. 7.3 - SUMMARY OF AMPLIFICATION FACTOR DATA FOR JETS EXHAUSTING FROM A FLAT PLATE

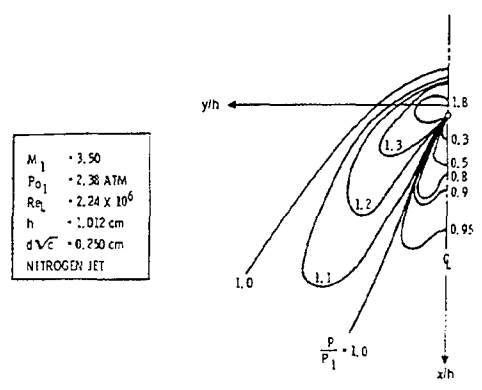


Fig. 7.4 - TYPICAL INTERFERENCE PRESSURE CONTOURS FOR CIRCULAR JET AND TURBULENT BOUNDARY LAYER

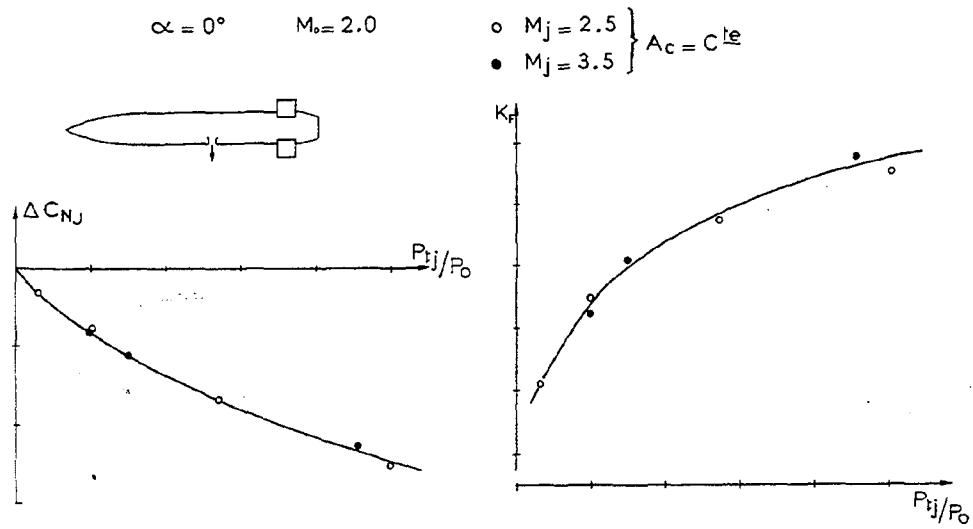


Fig. 7.5 - EFFECT OF JET EXIT MACH NUMBER ON INTERACTION FORCE

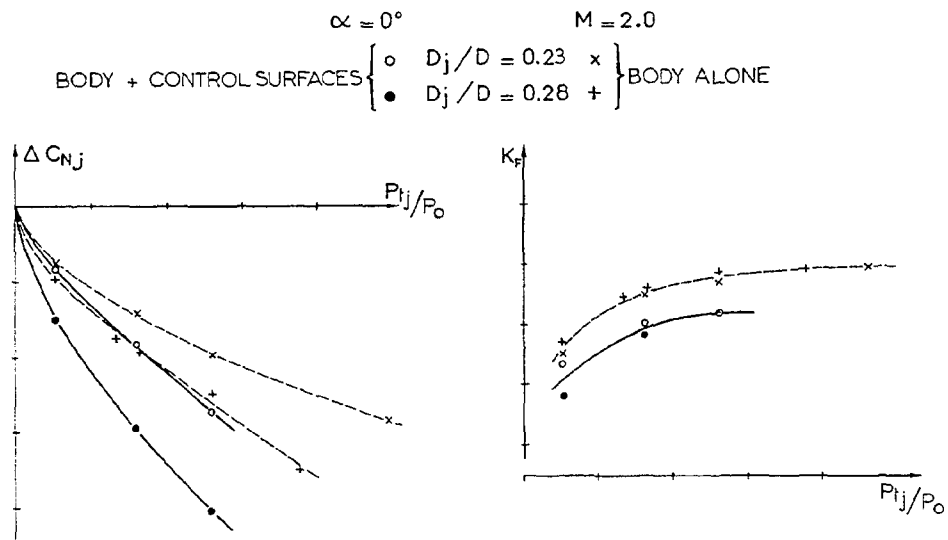


Fig. 7.6 - EFFECT OF JET EXIT AREA ON INTERACTION FORCE

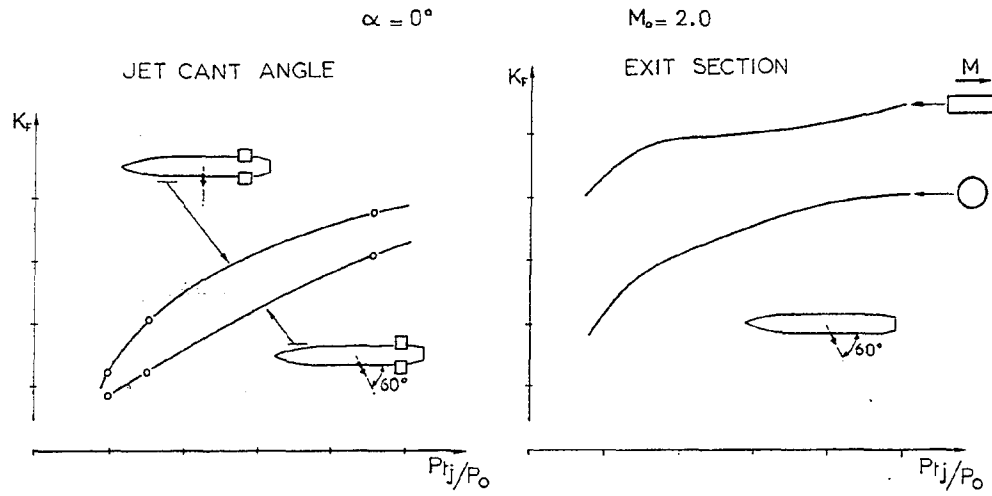


Fig. 7.7 - EFFECT OF NOZZLE GEOMETRY ON FORCE AMPLIFICATION FACTOR

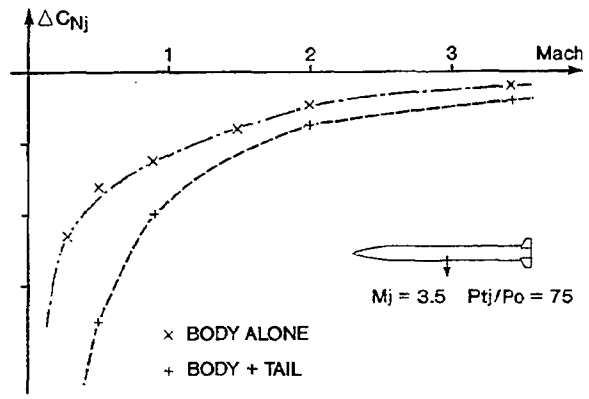


Fig. 7.8 - EFFECT OF FREESTREAM MACH NUMBER ON INTERACTION FORCE

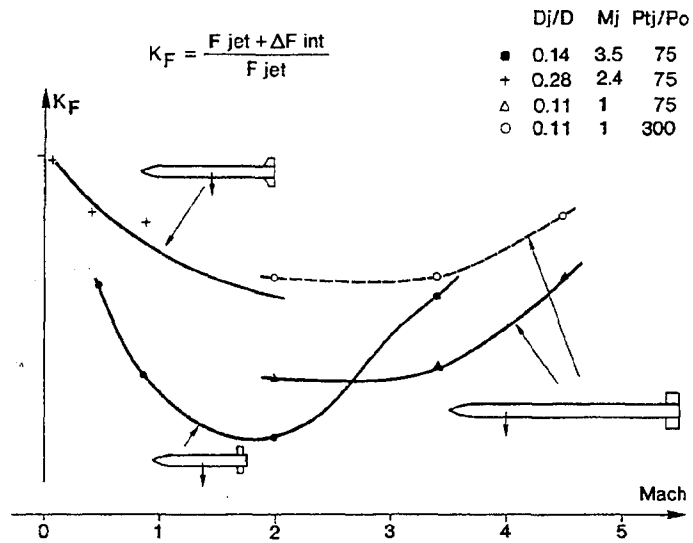


Fig. 7.9 - EFFECT OF FREESTREAM MACH NUMBER ON FORCE AMPLIFICATION FACTOR

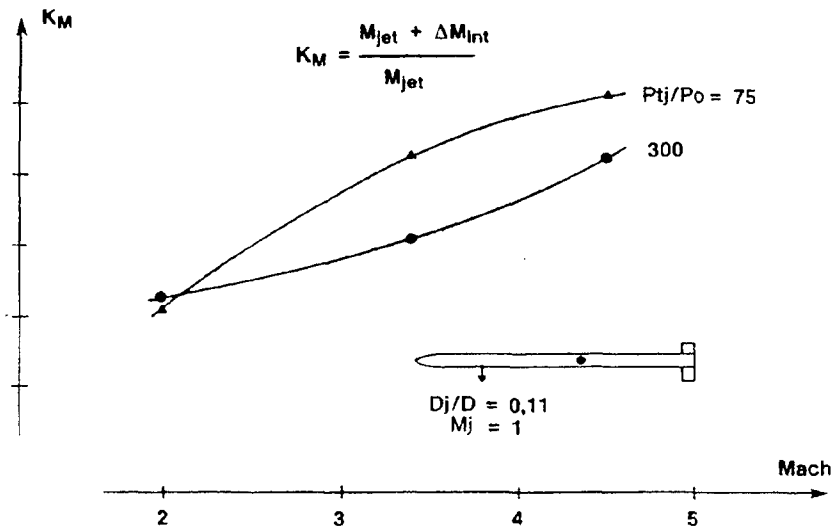


Fig. 7.10 - EFFECT OF FREESTREAM MACH NUMBER ON MOMENT AMPLIFICATION FACTOR

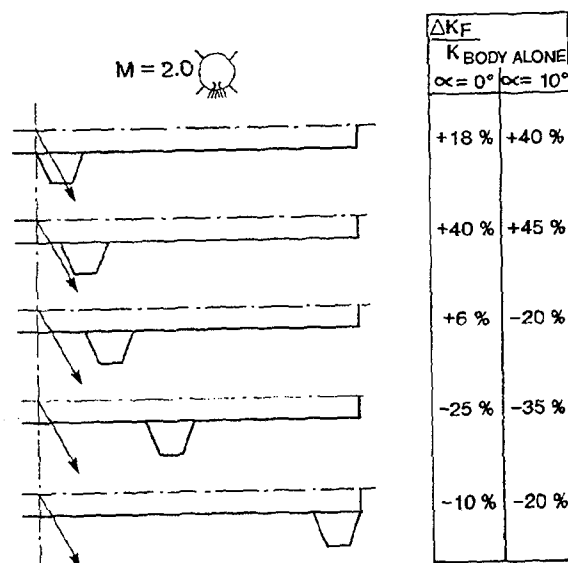


Fig. 7.13 - EFFECT OF WING LOCATION ON FORCE AMPLIFICATION FACTOR

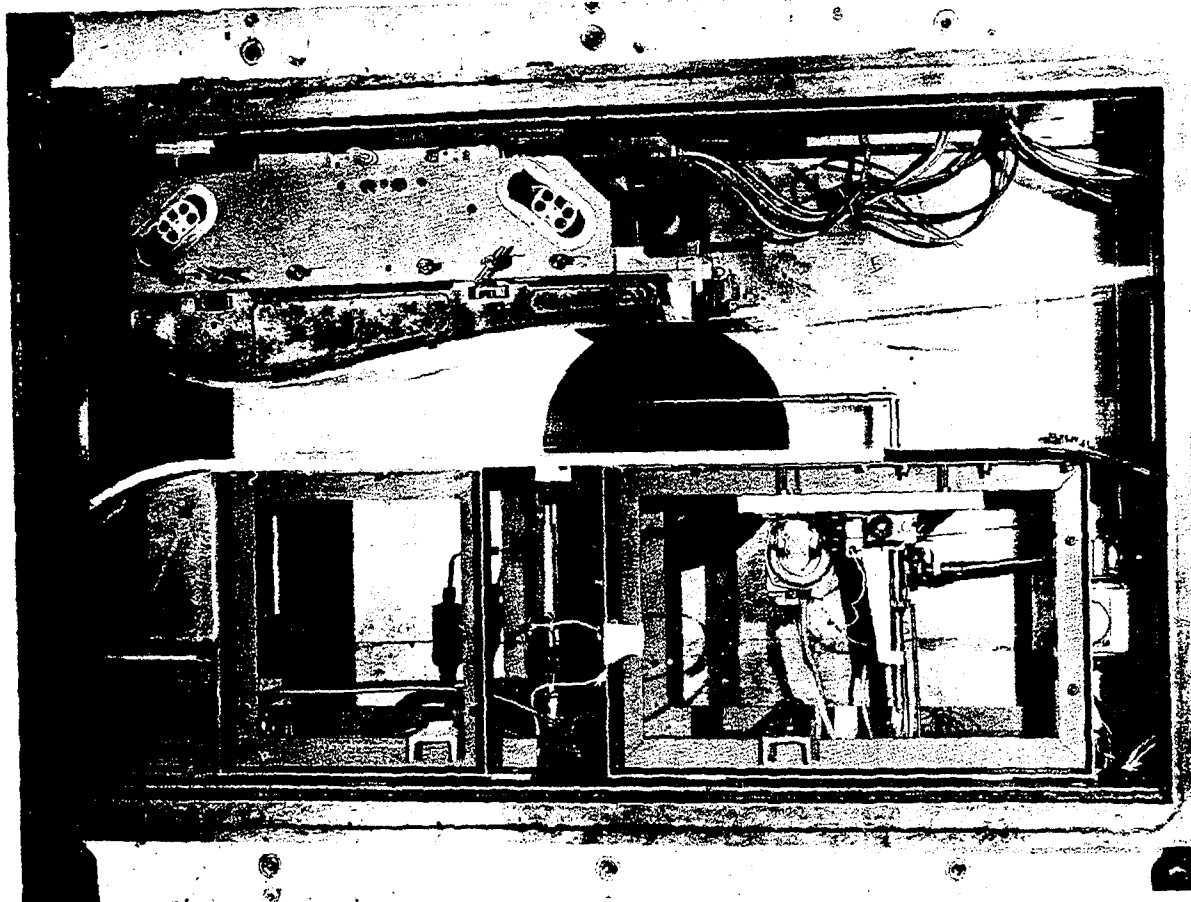


Fig. 8.1 - EXPERIMENTAL SET UP IN ONERA S5CH WIND-TUNNEL

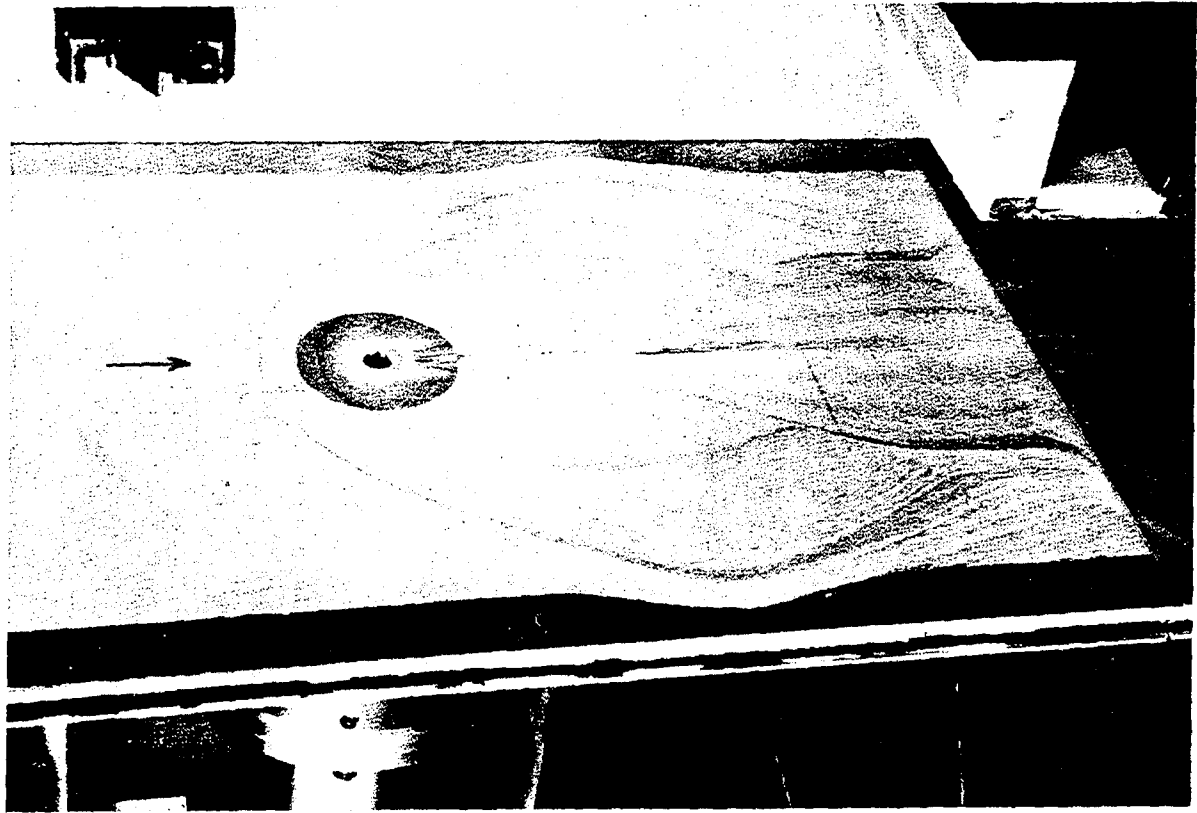


Fig. 8.2 - OIL FLOW VISUALIZATION - FLUORESCENT VISCOUS COATING

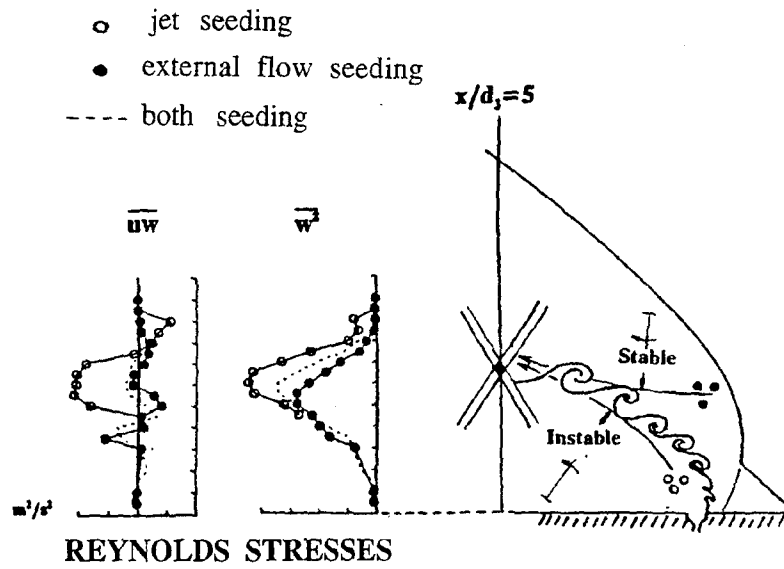


Fig. 8.3 - L.D.V. MEASUREMENTS - BIAS SEEDING

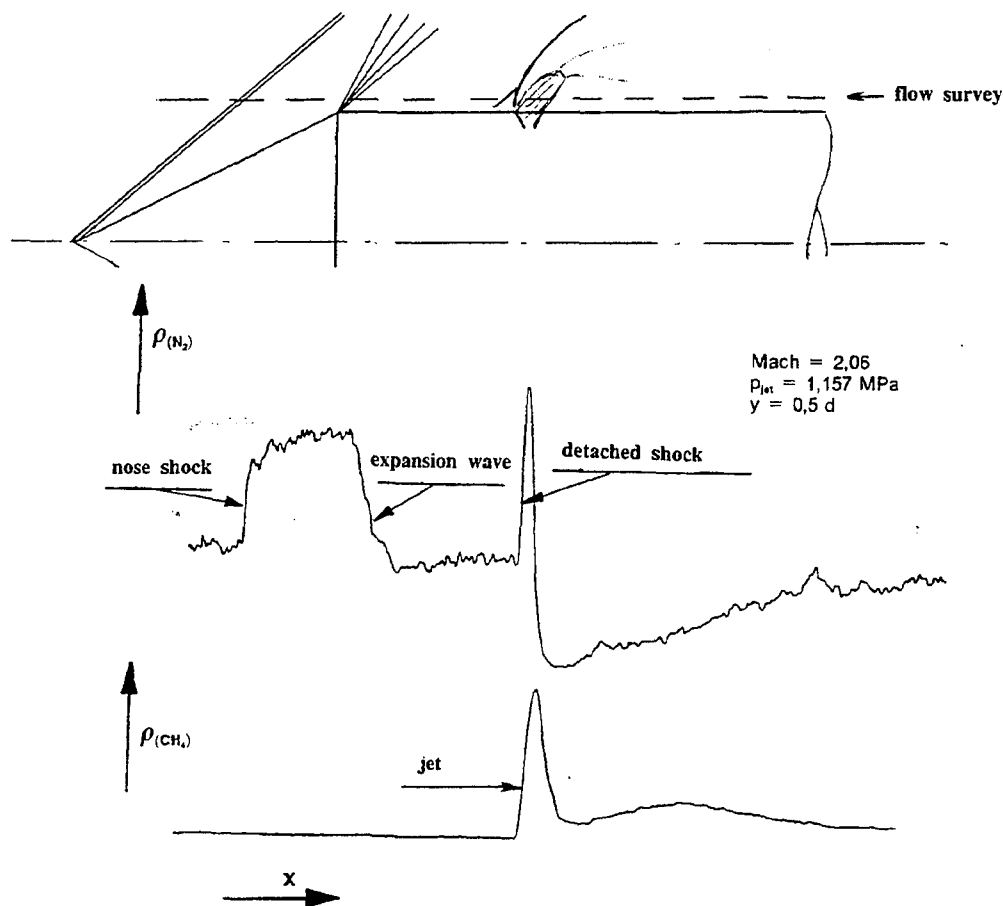


Fig. 8.4 - SPONTANEOUS RAMAN SCATTERING
PARTIAL DENSITIES OF NITROGEN
AND METHANE

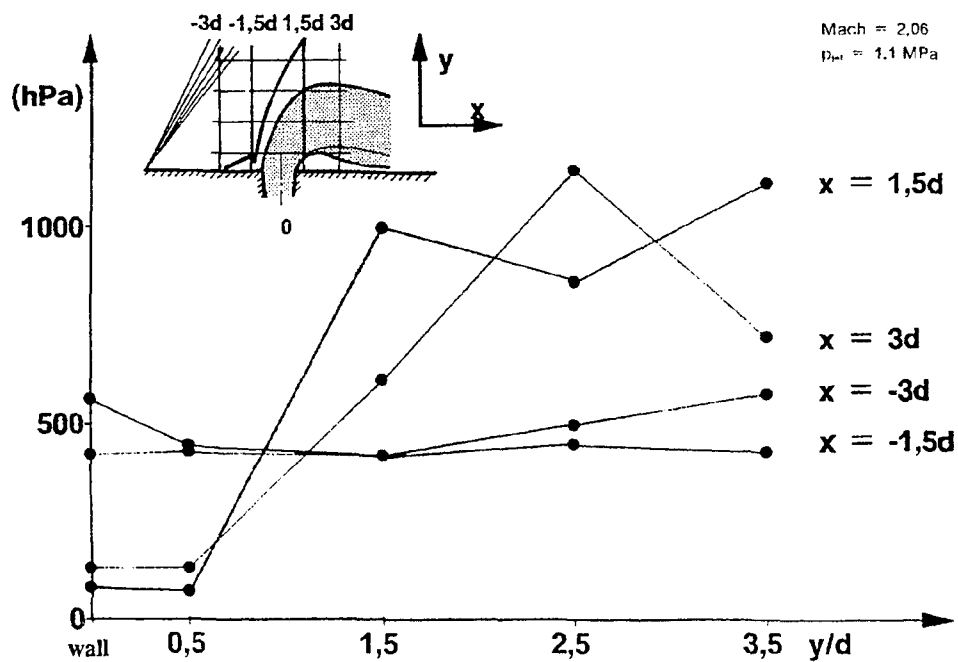


Fig. 8.5 - SPONTANEOUS RAMAN SCATTERING
PRESSURE PROFILES IN TRANSVERSE
DIRECTION

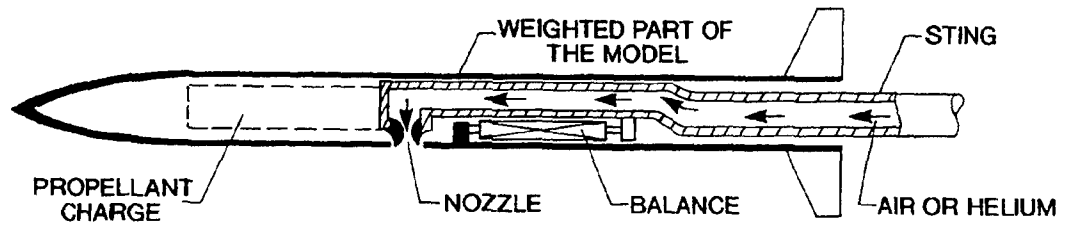


Fig. 8.6 - TEST SET UP FOR FORCE MEASUREMENTS

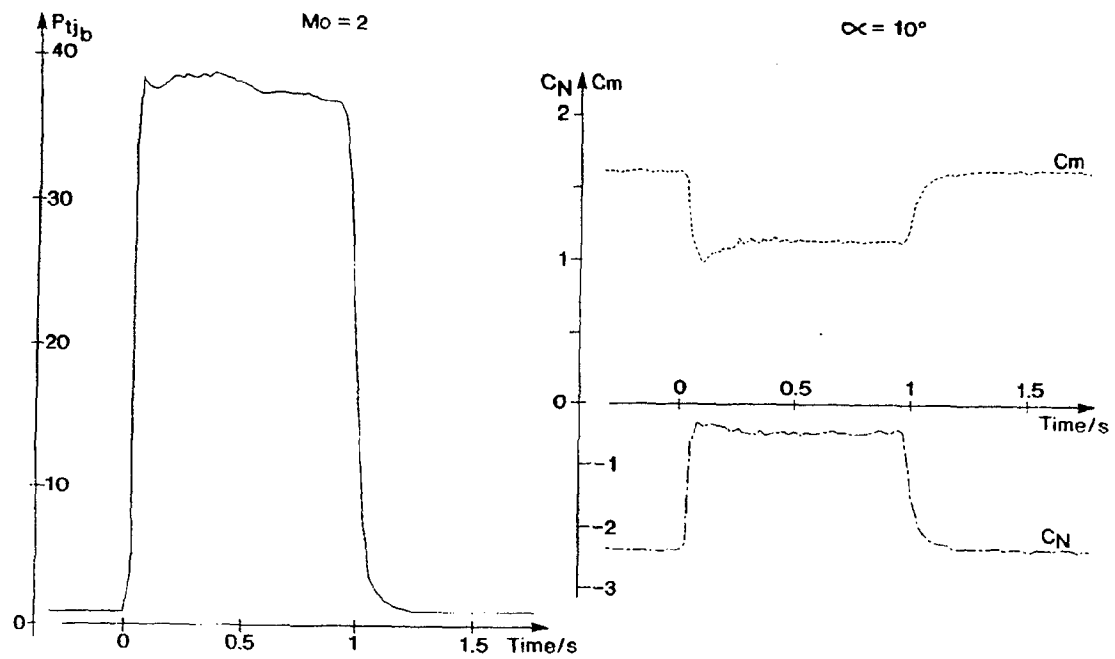


Fig. 8.7 - FORCE MEASUREMENTS USING THRUSTER

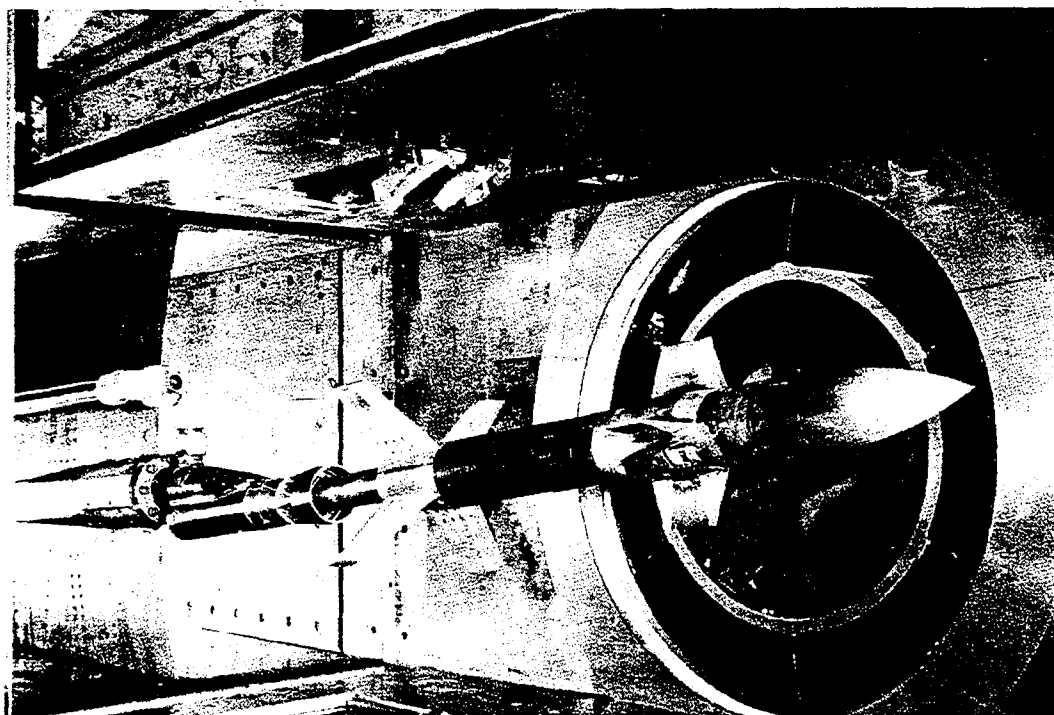


Fig. 8.8 - TYPICAL TEST MODEL IN ONERA S3MA WIND-TUNNEL

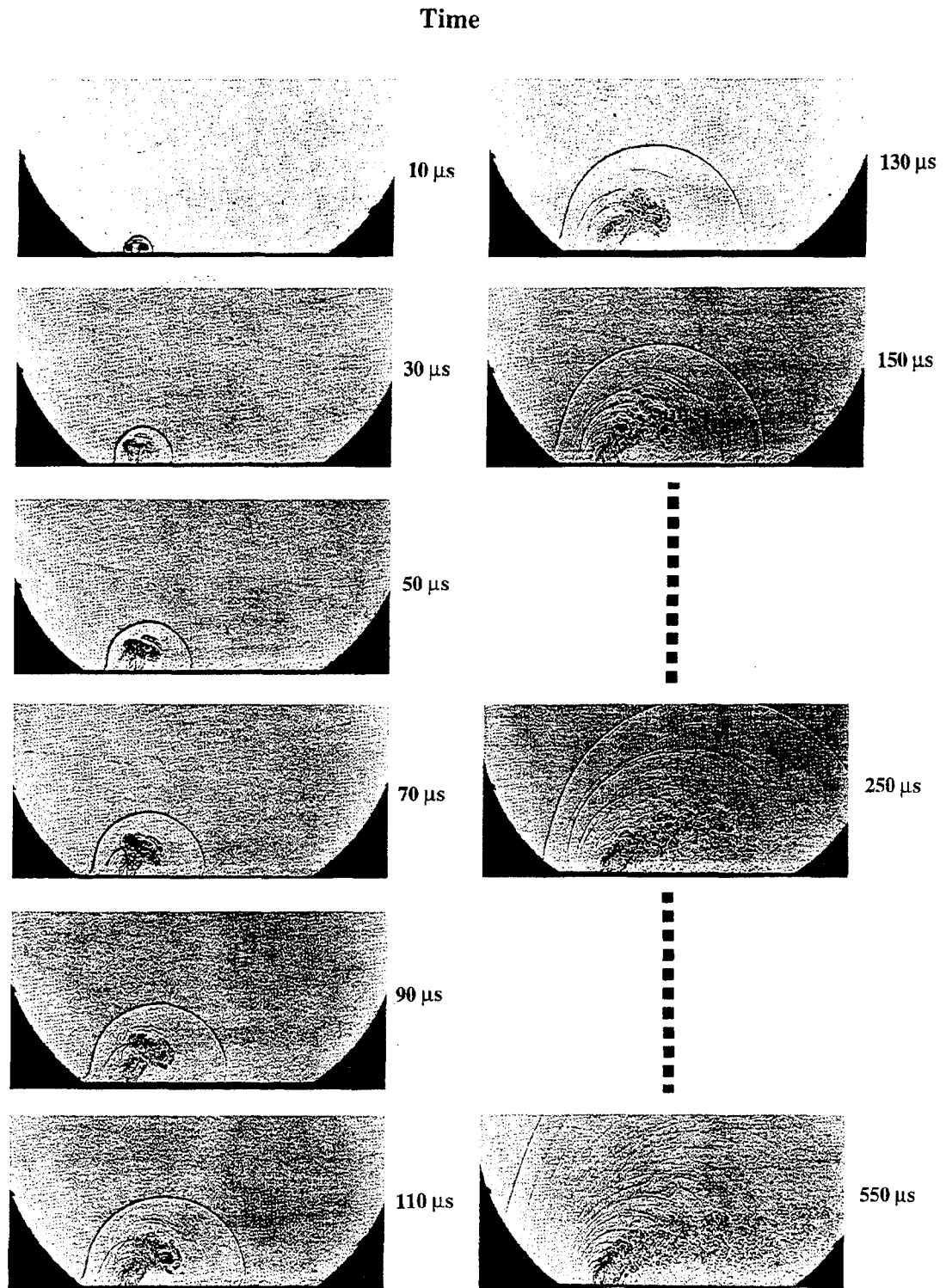


Fig. 8.9 - ULTRA-HIGH-SPEED SHADOGRAPH VISUALISATIONS

(Balance + Accelerometers)

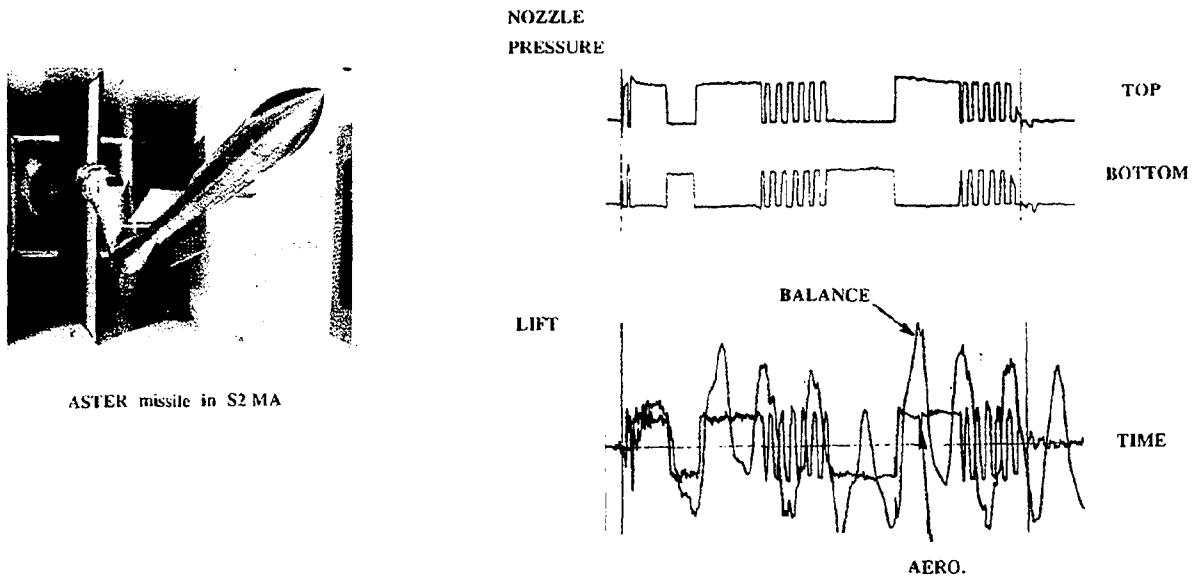


Fig. 8.10 - UNSTEADY FORCE MEASUREMENTS - ASTER MISSILE

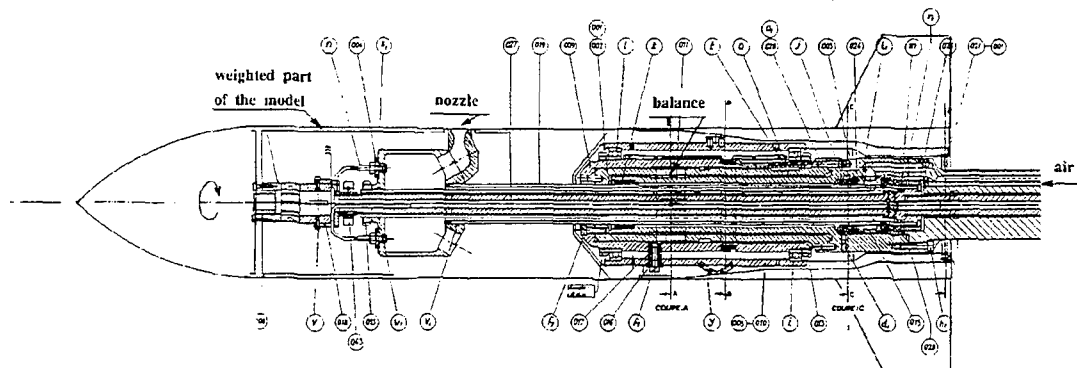
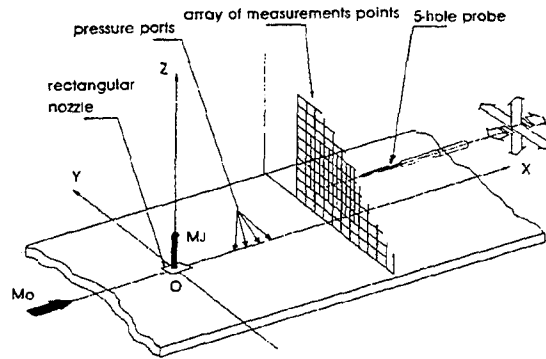


Fig. 8.11 - TEST SET UP FOR FORCE MEASUREMENTS ON SPINNING CONFIGURATION



EXPERIMENT

- Schlieren visualization
- Surface pressure
- Probe in a plane (X = Constant)

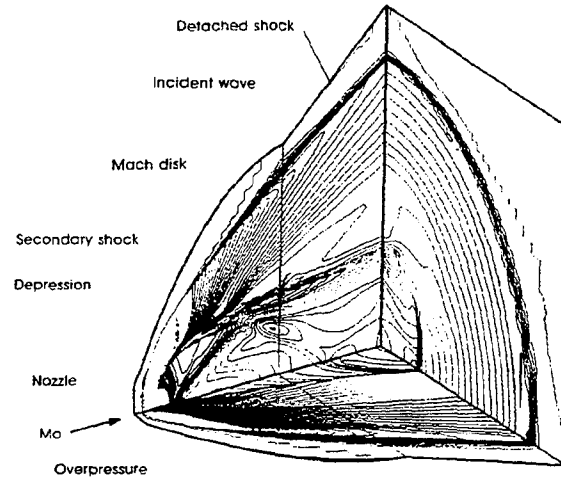
COMPUTATION

- Half domain $Y \geq 0$
- 135 x 70 x 75 mesh points
- 175 mesh points in the nozzle exit area

FUNDAMENTAL VALIDATION : FLAT PLATE

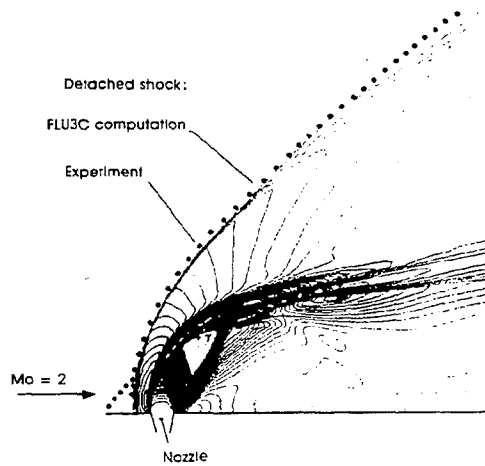
$Mo = 2$ $MJ = 2.5$ $P_{1J}/P_{10} = 14.3$

Fig. 9.1



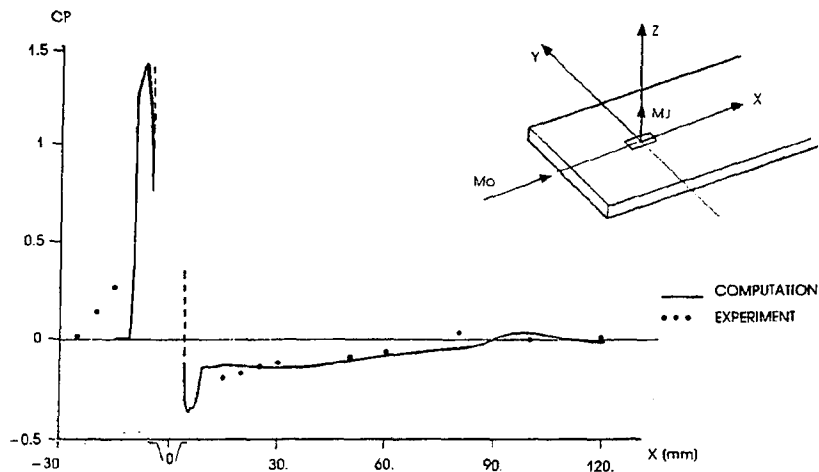
**FLAT PLATE ($Mo = 2 - MJ = 2.5 - P_{1J}/P_{10} = 14.3$)
PRESSURE COEFFICIENT CONTOURS - FLU3C COMPUTATION**

Fig. 9.2



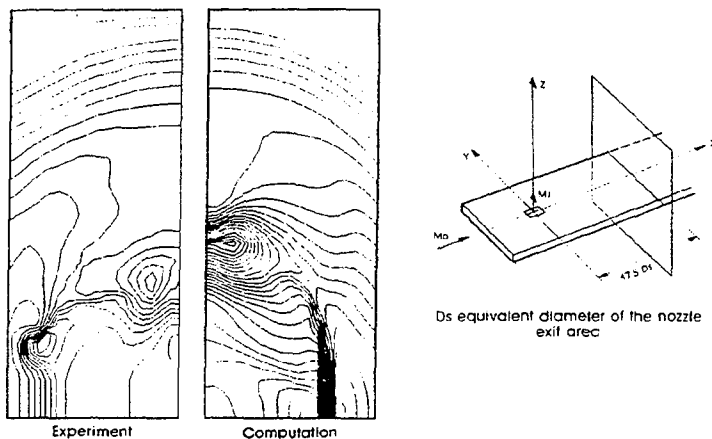
**FLAT PLATE ($Mo = 2 - MJ = 2.5 - P_{1J}/P_{10} = 14.3$)
MACH NUMBER CONTOURS IN THE PLANE OF SYMMETRY - FLU3C COMPUTATION**

Fig. 9.3



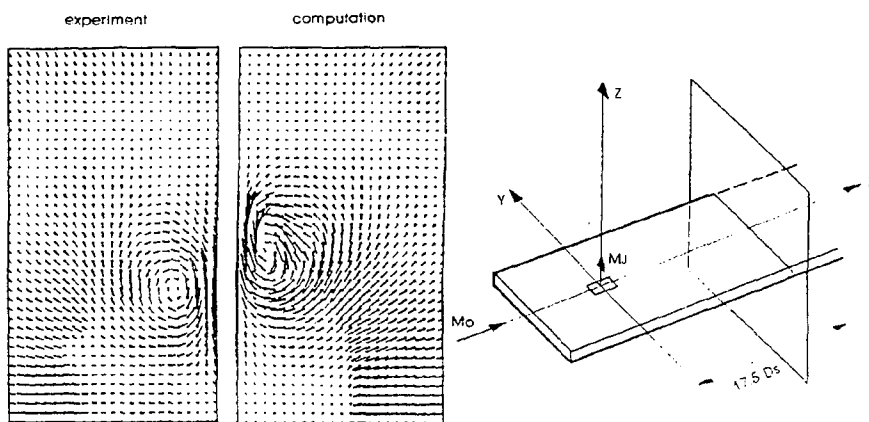
**FLAT PLATE ($M_o = 2 - M_J = 2.5 - P_{1J}/P_{1O} = 14.3$)
 VARIATION OF SURFACE PRESSURE COEFFICIENT DISTRIBUTION ALONG X**

Fig. 9.4



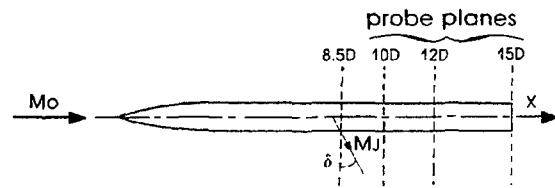
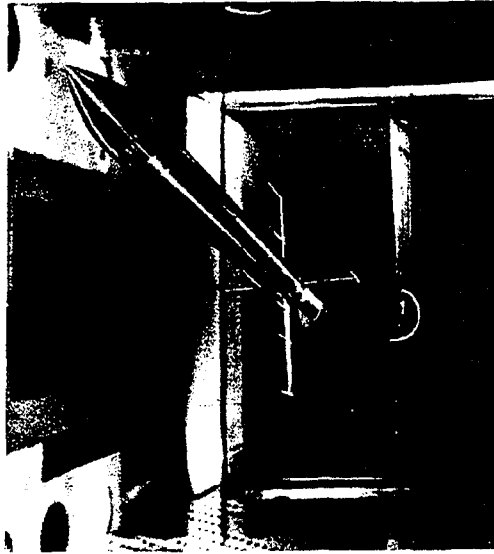
**FLAT PLATE ($M_o = 2 - M_J = 2.5 - P_{1J}/P_{1O} = 14.3$)
 PRESSURE COEFFICIENT CONTOURS IN THE TRANSVERSE PLANE LOCATED 17.5 D_s
 BEHIND THE NOZZLE**

Fig. 9.5



**FLAT PLATE ($M_o = 2 - M_J = 2.5 - P_{1J}/P_{1O} = 14.3$)
 VORTICITY CONTOURS IN THE TRANSVERSE PLANE LOCATED 17.5 D_s
 BEHIND THE NOZZLE**

Fig. 9.6



EXPERIMENT

- Probe in 3 planes (X = constant)

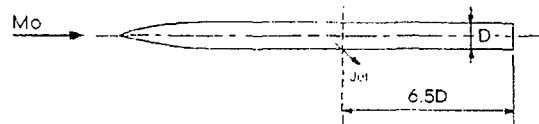
COMPUTATION

- Half domain
- 190 000 mesh points
- 153 mesh points in the nozzle exit area
- 1 CPU hour on CRAY XMP

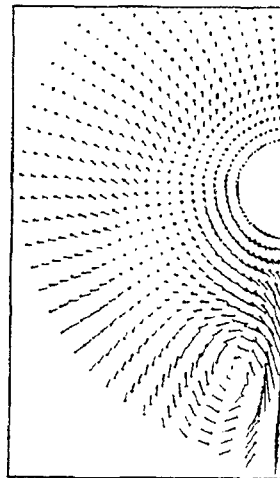
FUNDAMENTAL VALIDATION : FUSELAGE

$\alpha = 0^\circ$ $Mo = 2$ $MJ = 2.5$ $\delta = 30^\circ$ $P_{1J}/P_{10} = 28$

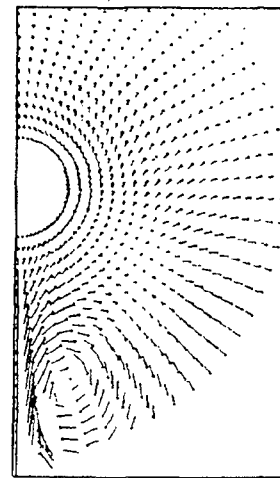
Fig. 9.7



Upstream flow velocity magnitude



Experiment

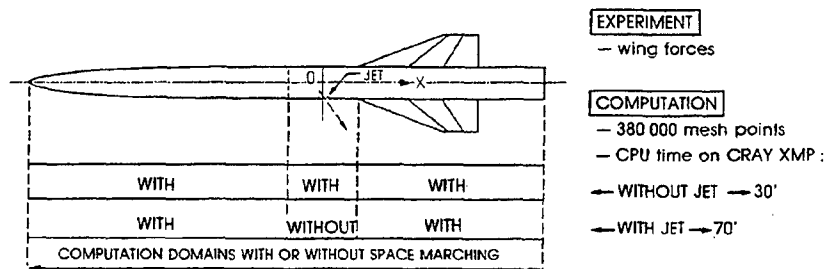


Computation

**LATERAL JET IN AN EXTERNAL SUPERSONIC FLOW
VELOCITY VECTORS IN THE TRANSVERSE PLANE LOCATED 6.5 D
BEHIND THE NOZZLE**

Fig. 9.8

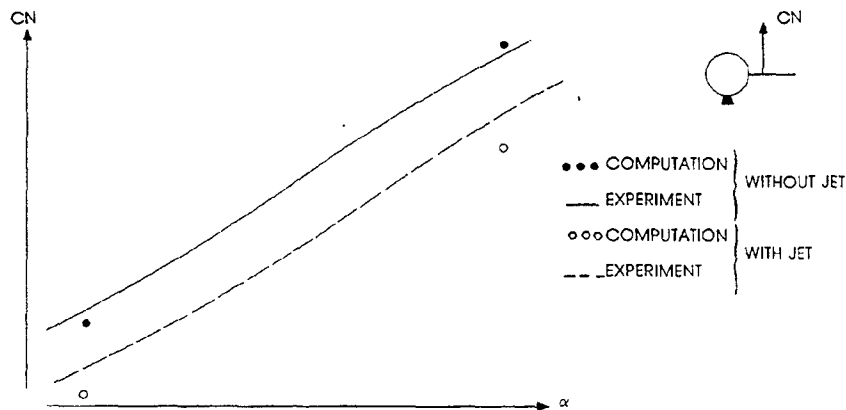
2 CRUCIFORM WINGS CONFIGURATIONS: "+" SHAPED WINGS AND "X" SHAPED WINGS



INDUSTRIAL VALIDATION : "ONERA" MODEL

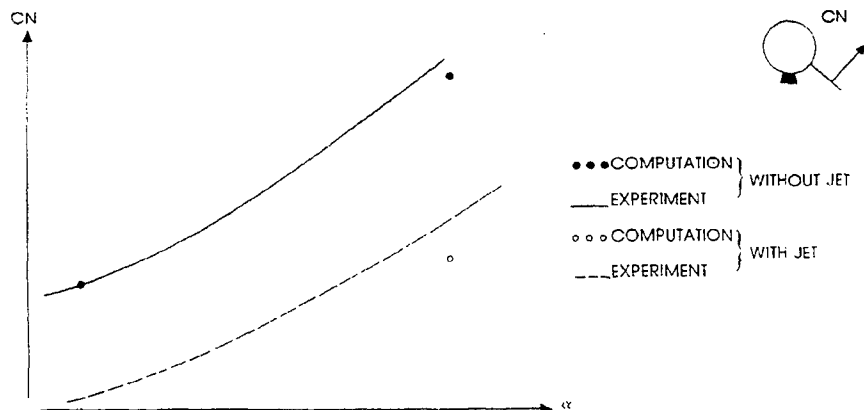
$M_0 = 2$ $M_J = 2.5$ $P_{tj}/P_{t0} = 13.9$

Fig. 9.9



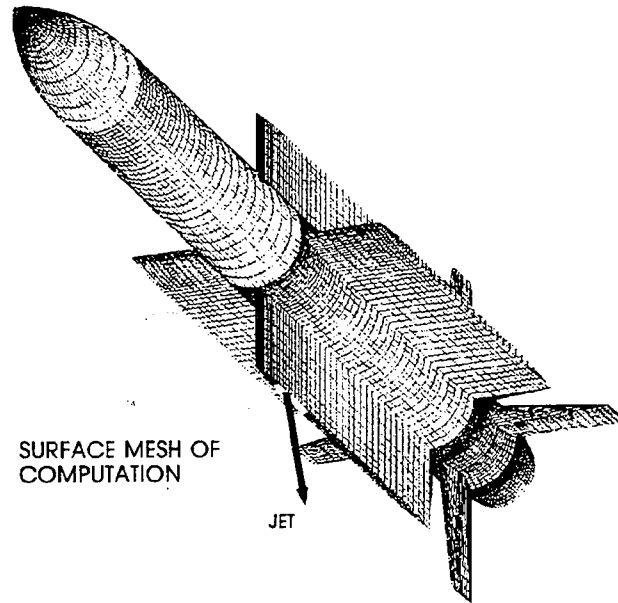
WING-BODY MODEL ("+" SHAPED WINGS - $M_0 = 2$)
NORMAL FORCE COEFFICIENT OF A HORIZONTAL WING

Fig. 9.10



WING-BODY MODEL ("x" SHAPED WINGS- $M_0 = 2$)
NORMAL FORCE COEFFICIENT OF LEEWARD WING

Fig. 9.11



EXPERIMENT

- Schlieren visualizations
- Overall forces

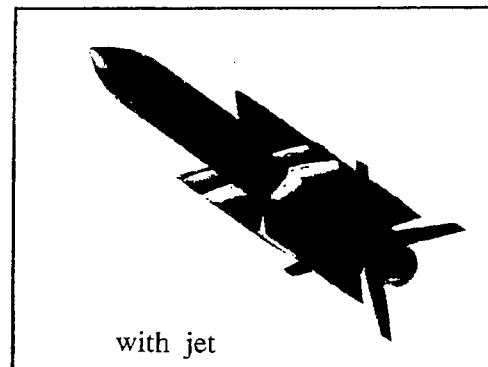
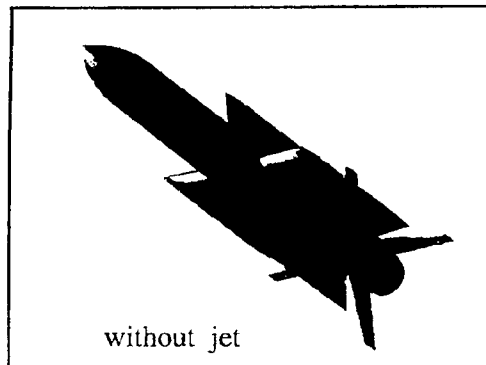
COMPUTATION

- 300 000 mesh points
- CPU time on CRAY XMP :
Without Jet. - 35'
- With Jet - 1 h 45'

INDUSTRIAL VALIDATION : ASTER MISSILE

$M_o = 2 \quad \alpha = 12^\circ$

Fig. 9.12



**EULER Code - Pressure distribution
ASTER MISSILE - MACH = 2 - $\alpha = 12^\circ$**

Fig. 9.13

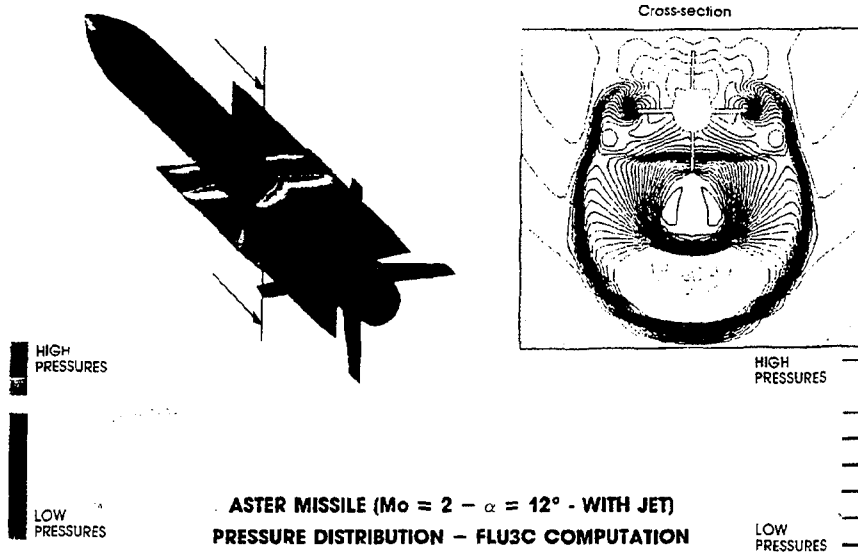
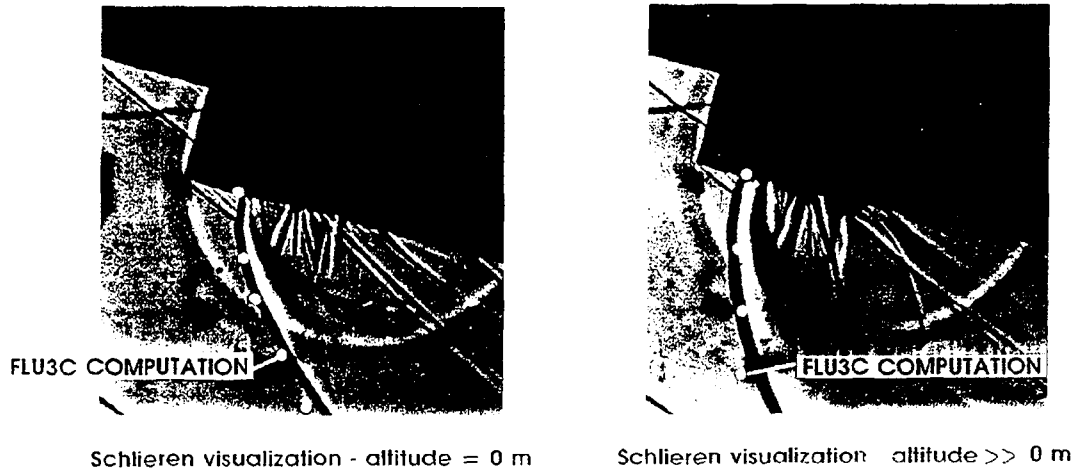


Fig. 9.14



ASTER MISSILE ($M_0 = 2 - \alpha = 12^\circ$ - WITH LATERAL JET)
DETACHED SHOCK LOCATION - COMPARISON BETWEEN
FLU3C COMPUTATION AND EXPERIMENT

Fig. 9.15

	WITHOUT LATERAL JET	WITH LATERAL JET	
		ALTITUDE = 0 m	ALTITUDE >> 0 m
$\frac{\Delta C_N}{C_N}$	7%	4%	4%
$\frac{\Delta X_{cp}}{D}$	0.23	0.14	0.10

D missile diameter

ASTER MISSILE ($M_0 = 2 - \alpha = 12^\circ$)
RELATIVE ERRORS ON THE AERODYNAMIC COEFFICIENTS
PREDICTED BY THE FLU3C CODE

Fig. 9.16

AERODYNAMIC CONFIGURATIONS

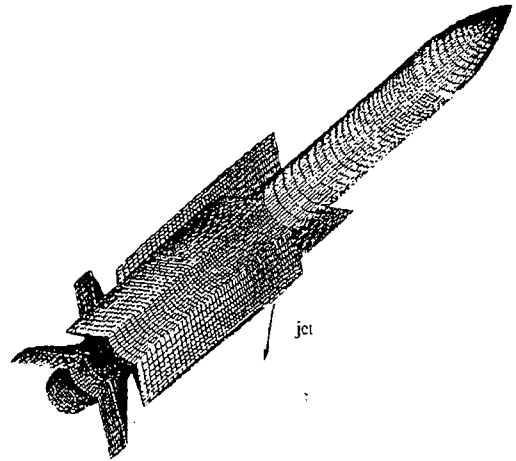
Upstream Conditions

$M_0=1.6, \alpha=8^\circ$

- without jet
- with a cold air jet
- with a hot air jet
- with a powder gas jet modelised as a perfect gas

MESH

Surface Mesh for Computations



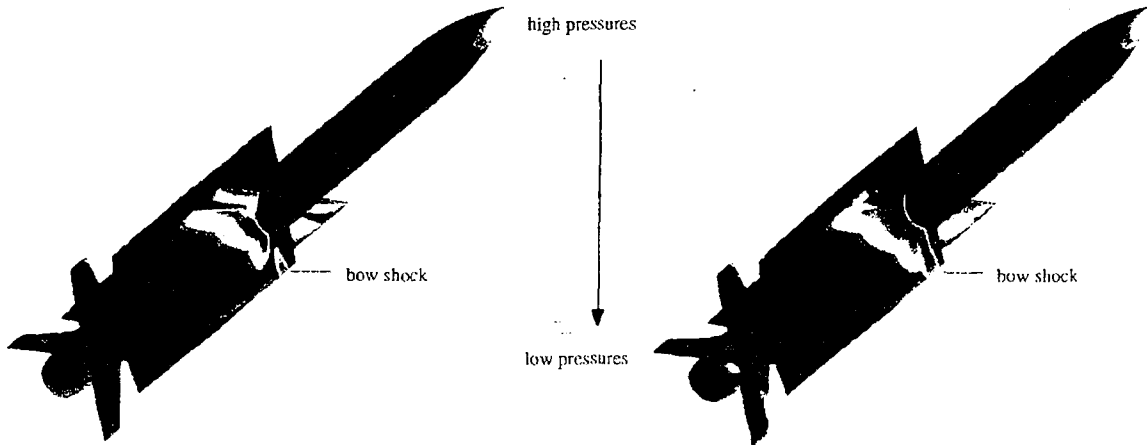
400000 mesh points (8 domains)

**ASTER MISSILE
AERODYNAMIC CONFIGURATIONS AND MESH**

Fig. 9.17

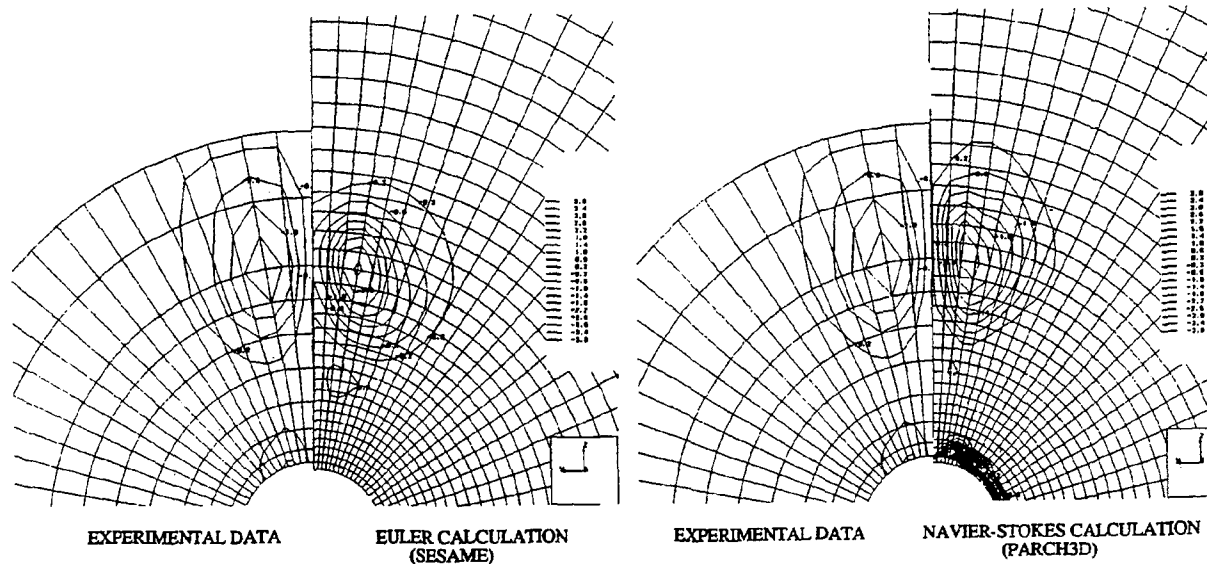
COLD AIR JET

POWDER GAS JET MODELISED
AS A PERFECT GAS



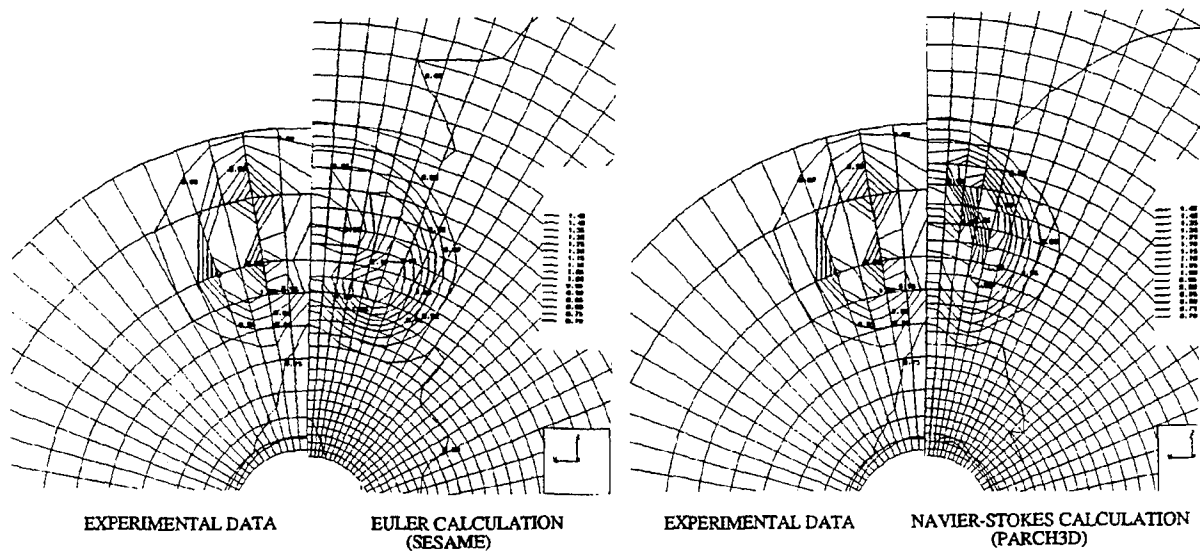
**ASTER MISSILE
COMPUTED WALL PRESSURE DISTRIBUTION**
($M_0=1.6, \alpha=8^\circ$)

Fig. 9.18



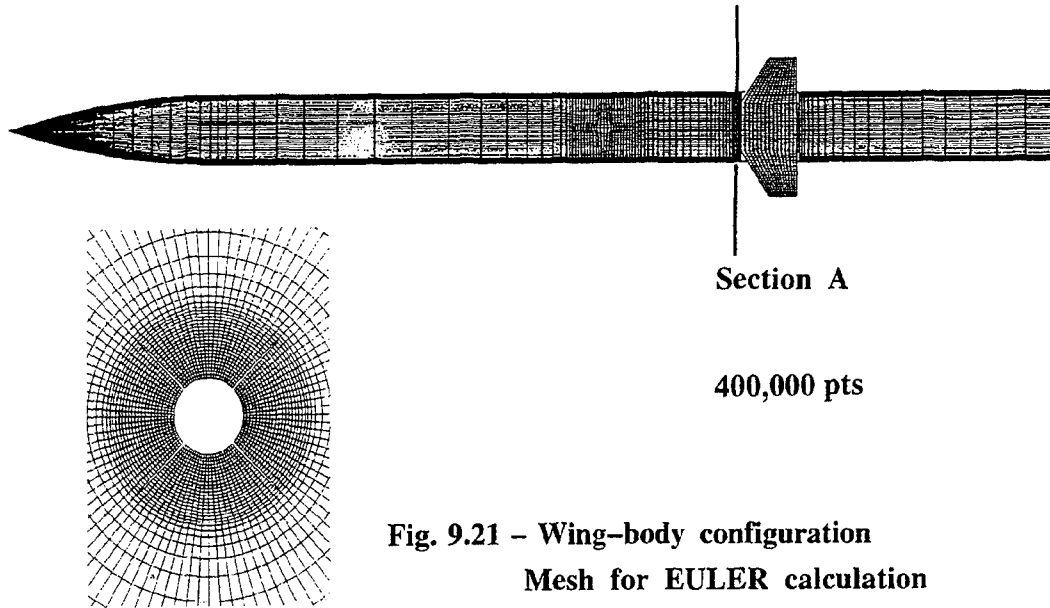
**OGIVE-CYLINDER MISSILE:
 Ω_x CONTOURS IN THE CROSS PLANE AT X=12 D**

Fig. 9.19



**OGIVE-CYLINDER MISSILE:
MACH NUMBER CONTOURS IN THE CROSS PLANE AT X=12 D**

Fig. 9.20



**Fig. 9.21 - Wing-body configuration
Mesh for EULER calculation**

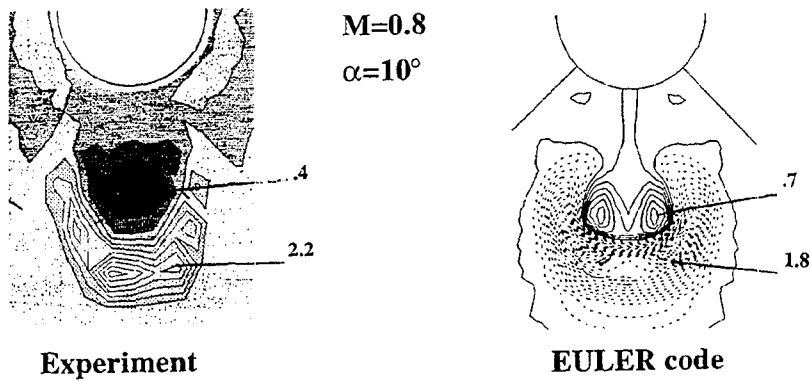


Fig. 9.22 - Total pressure contours in section A

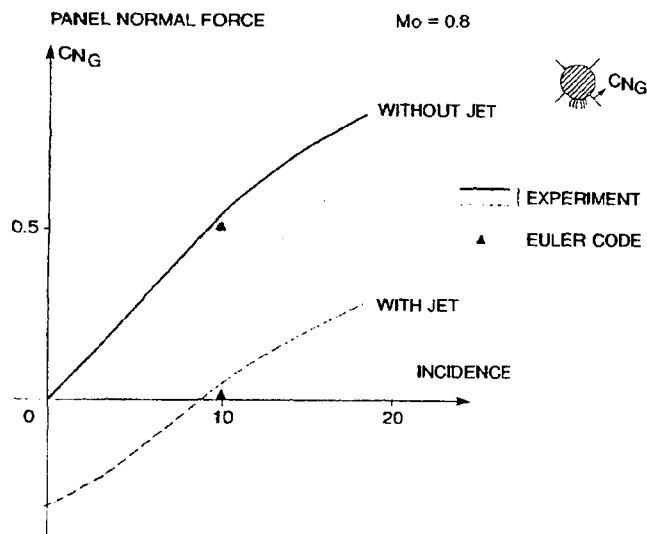
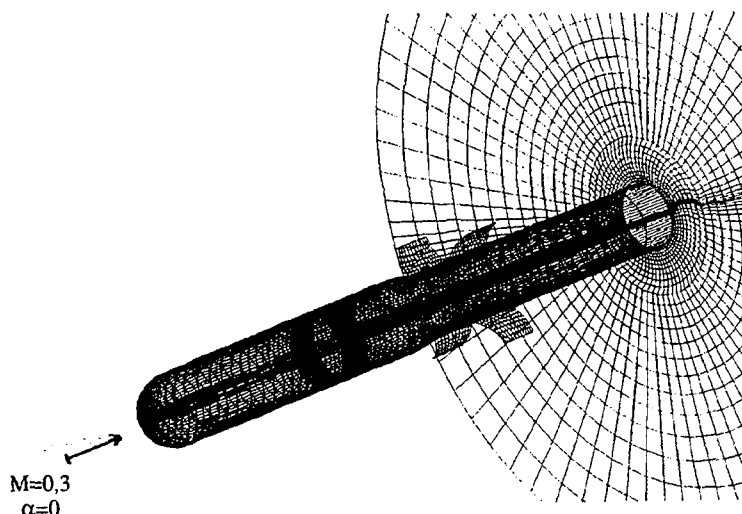


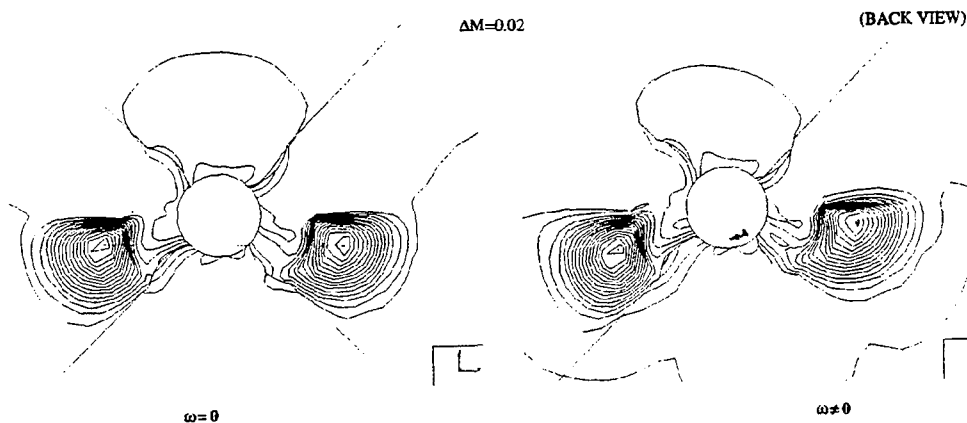
Fig. 9.23 - Induced normal force on wing panel



GRID FOR EULER CALCULATIONS

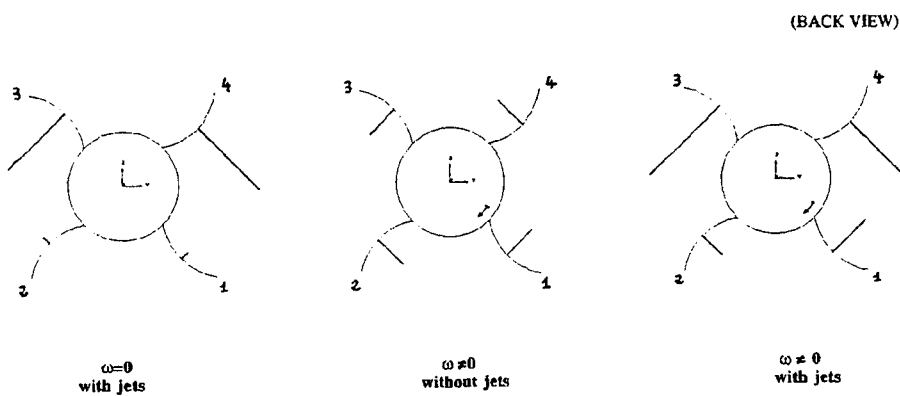
ANTITANK MISSILE

Fig. 9.24



ANTITANK MISSILE:
MACH NUMBER CONTOURS IN A CROSS PLANE
(EULER CALCULATIONS)

Fig. 9.25



ANTITANK MISSILE:
NORMAL FORCE COEFFICIENTS ON THE WINGS
(EULER CALCULATIONS)

Fig. 9.26

MISSILE INFRARED RADIATION ANALYSIS

Michel Engelhardt
Grumman Corporation
1111 Stewart Avenue (B46-35)
Bethpage, NY 11714 USA

1

Modern Trends in Electro-Optical Technology for Use in Missile Detection

SUMMARY

Modern trends in electro-optical/infrared (E-O/IR) technology for use in missile detection is presented as part of the NATO Advisory Group for Aerospace Research & Development (AGARD) special course on "Missile Aerodynamics." The course focuses on the operations of E-O/IR systems. The functions of the components of an E-O/IR system are summarized along with the missile source, background, contrast, and IR detection range equation.

NOMENCLATURE

- A_p = Area of the pixel, m^2
 $A_{s,j}$ = Projected area of the missile's j th facet in the line-of-sight of the E-O/IR system, m^2
 the system can observe different areas in the FOV
 $I_{1,\lambda}$ = Spectral intensity of pixel 1, $W/sr-\mu m$
 $I_{2,\lambda}$ = Spectral intensity of pixel 2, $W/sr-\mu m$
 $I_{c,\lambda}$ = Spectral contrast intensity, $W/sr-\mu m$
 $L_{B,1,\lambda}$ = Spectral radiance of the background seen in pixel 1, $W/sr-\mu m-m^2$
 $L_{B,2,\lambda}$ = Spectral radiance of the background seen in pixel 2, $W/sr-\mu m-m^2$
 $L_{T,\lambda}$ = Spectral radiance of the foreground between the missile and the E-O/IR system, $W/sr-\mu m-m^2$
 NEI = Noise Equivalent Irradiances, W/m^2
 R = Range between the missile and the E-O/IR system, m

S/N = Signal-to-noise ratio of the E-O/IR system

λ = Wavelength, μm

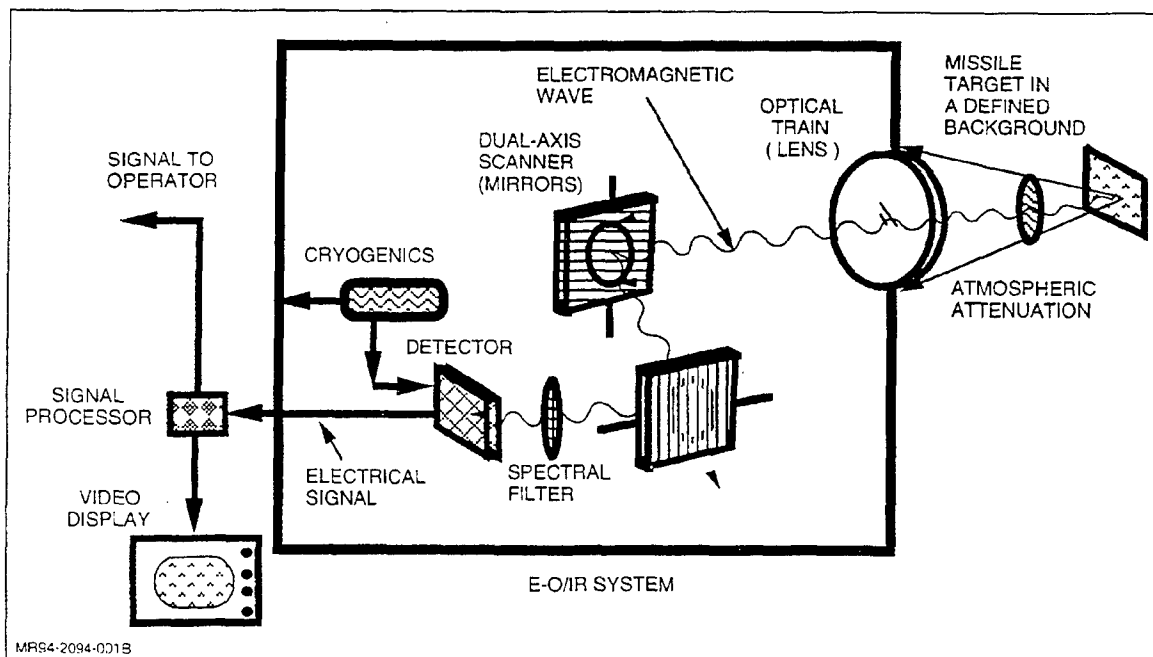
τ_λ = Spectral atmospheric transmittance between the missile and the E-O/IR system

INTRODUCTION

There are many different types of E-O/IR systems that are used for missile detection. The E-O/IR systems that detect missiles are integrated into commercial and military products. These systems include aircraft forward-looking IR systems and IR search and track systems, and even missile seeker systems integrated into missiles.

E-O/IR systems used to detect missiles are either imaging or non-imaging types. These systems are designed to detect missiles passively at moderate ranges and are limited in detection range by atmospheric attenuation.

As shown in Fig. 1, the optical train of a typical E-O/IR system focuses the radiant energy to a detector in a given field-of-view (FOV). A typical system consists of two mirrors. One mirror is used for horizontal scanning of the FOV and another for vertical scanning. By tilting the mirrors in horizontal and vertical directions, the system can observe different areas in the FOV. The electromagnetic energy that is incident on the detector is converted to an electric current. A signal processor is then used to determine whether or not the missile is in the FOV. This signal



MR94-2094-001B

Fig. 1 Components of a Typical E-O/IR System

© M. Engelhardt, 1994

Presented at an AGARD Special Course on 'Missile Aerodynamics', June 1994.

can be displayed to show the strength of the missile radiant intensity in the FOV. A spectral filter (or a circular variable filter) can be integrated into an E-O/IR system to filter out undesired wavelengths.

The head of a typical E-O/IR system is composed of an optical train, a detector array, and a cryogenic system. The cryogenic system is needed to reduce the amount of photon noise from the housing onto the detector array. The less thermal noise that is incident by internal photons from the system housing onto the detector, the more efficient the system operates. Detector systems are usually cooled by nitrogen at 77K.

The signal processor may contain a video processor, a discriminator, and/or a track processor. In these processors, the electronic signals that are transferred from the sensor head are processed to obtain information for the operator. The processed information can also be transferred to a computer for further processing with additional information from radar and/or visual tracks.

An E-O/IR system is analogous to a person's skin exposed to a thermal source of energy such as the sun. The tissues in the skin sense the sun's energy and convert thermal energy into an electrical signal via the nervous system to the brain. The brain is equivalent to a computer that processes the thermal source.

In a typical E-O/IR system, the detector material is composed of p-type and n-type crystals (see Fig. 2). These crystals are semiconductor materials including lead sulfide, indium antimonide, and mercury cadmium telluride. When photons are incident on semiconductor materials, they create a flow of electrons. This is known as the photovoltaic process and is done by creating whole-electron pairs. A photon excites and dislodges an electron in the detector's crystal structure. The electron then moves to the electrode in the n-type crystal layer. The "hole" (created by transferring the electron to the n-type crystal) moves to the p-type crystal layer. This creates a current flowing from the n-type to the p-type electrodes.

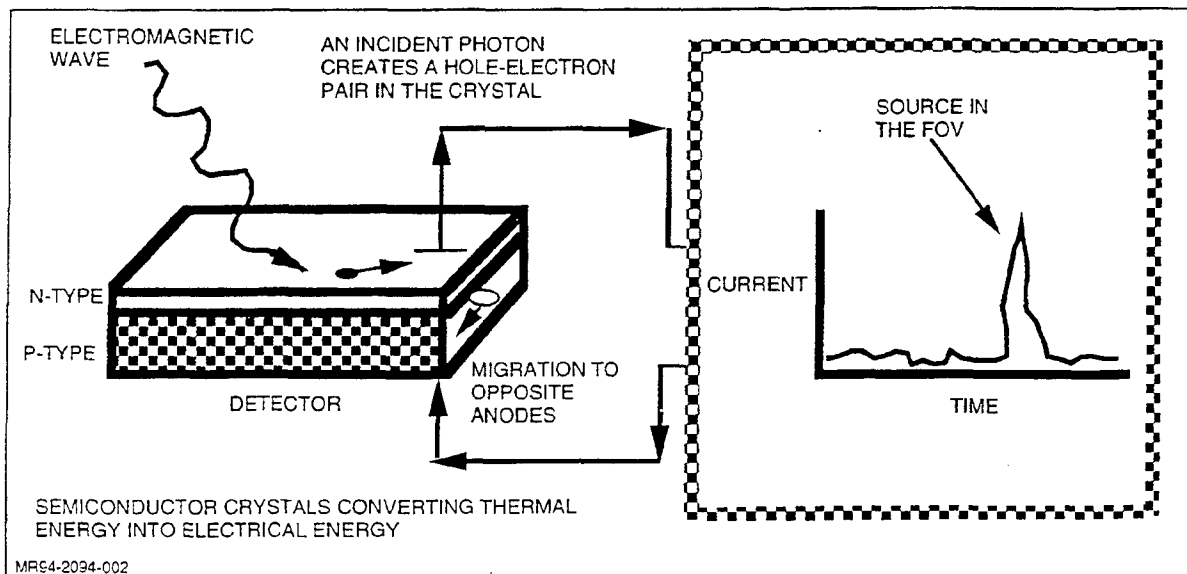


Fig. 2 Conversion of Thermal Energy into an Electrical Signal

THE ELECTROMAGNETIC SPECTRUM

As illustrated in Fig. 3, modern E-O/IR systems operate between the ultraviolet (UV) portion to the far IR portion of the electromagnetic spectrum. The IR portion of the spectrum (which is the subject of this course) is conventionally divided into five bands. These bands are the short-wave IR (SWIR) band, the mid-wave IR (MWIR) band, the water vapor absorption band, the long-wave IR (LWIR) band, and the low-temperature IR band.

The SWIR band ranges between 0.7-to-3 micrometers. The significance of the SWIR portion is that it is near the visual portion of the electromagnetic spectrum. Consequently, many E-O systems that operate in the visible portion extend into the SWIR. The SWIR is the portion of the spectrum that includes solar reflections from sources (98% of the integrated solar radiance is under 3 micrometers). It also includes high-temperature thermal emissions (resulting from heat exchangers and engine emissions.) Typical high temperatures are above 200 C.

The MWIR band ranges between 3-to-5 micrometers. The MWIR portion of the spectrum is sometimes referred to as the plume band since most conventional fuel combustion products (such as kerosene) emit in bands centered at 2.7 and 4.3 micrometers. This is due to water vapor (spiking at 2.7 micrometers) and the carbon dioxide (spiking at 2.7 and 4.3 micrometers) combustion products that emit strongly in these band centers. This band is also significant in detecting both missile emissions and reflections.

The water vapor absorption band lies between 5-to-8 micrometers. Water vapor in the atmosphere absorbs most of the radiation emitted by a missile in the 5-to-8 micrometer band. At low altitudes (under 10 km), coupled with an observer viewing aspect angle at ranges greater than 2 km, the attenuation due to the atmosphere is extremely severe. Consequently, airborne E-O/IR systems are usually not designed to operate in this portion of the spectrum. When the range is less than a kilometer

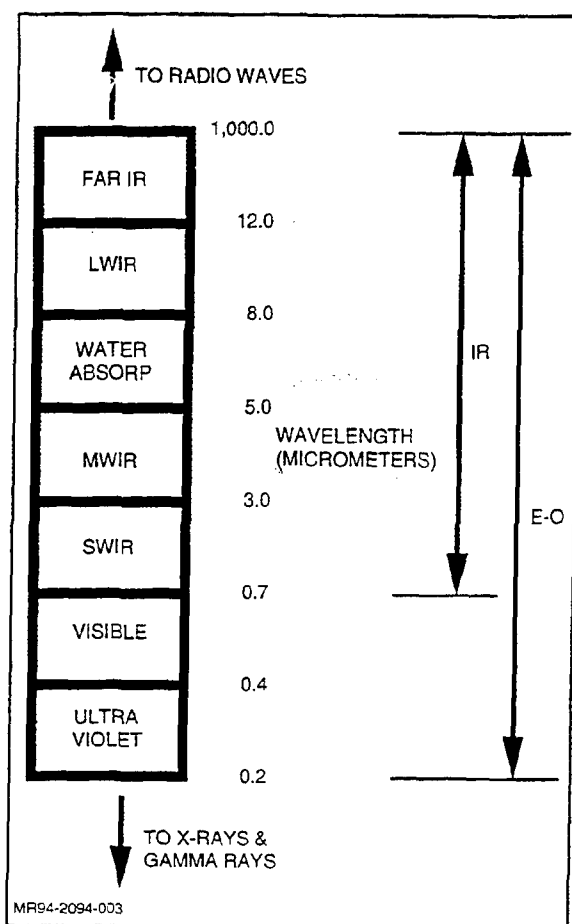


Fig. 3 The Electromagnetic Spectrum

and the water vapor concentration in the atmosphere is diminished (usually, at altitudes greater than 10 km), then it may be desirable to consider designs in this wavelength band.

The LWIR band is defined either between 8-to-12 or 8-to-14 micrometers. In the LWIR wavelength band, atmospheric absorption is not very severe. As a rule of thumb, approximately 80 percent of the total emitted energy from a missile airframe will be transmitted through the atmosphere at distances less than 25 km. As a result, designers of modern E-O/IR systems take advantage of this part of the spectrum by designing E-O/IR systems to detect missile emissions resulting from moderate temperatures (approximately, between 0 C and 100 C).

The low-temperature IR band of the spectrum is defined above 12 or 14 micrometers, and is sometimes used for detecting relatively cold missiles against space backgrounds.

INFRARED RADIATION FROM MISSILES AND BACKGROUNDS

As shown in Fig. 4, IR radiation from missiles consists of two components: source emissions and the reflections of background radiances. For a missile airframe, the source emission includes the following components:

- Aerodynamic heating
- Solar heating

- Backside "sources" that may heat or cool the missile structure
- Heat exchanger exhaust dumps
- Engine internal hot parts
- Engine compressor fan blades and inlets
- Exhaust plume heating
- Internal and exhaust plume emission.

Natural reflections from sources include the following components:

- Direct solar reflections
- Indirect solar reflections from the atmosphere, clouds, and the earth
- Earth shine
- Sky shine
- Cloud shine
- Re-reflections of natural reflections from the missile itself.

Both the emitted and reflected intensities from missile surfaces are attenuated by the atmospheric path between the missile and the E-O/IR system that is observing the missile. The attenuation is a result of atmospheric constituents, aerosols, clouds, and precipitation that absorb energy in a defined path.

INFRARED CONTRAST INTENSITY

An E-O/IR sensor detects a missile based on a contrast difference calculation. The E-O/IR detector views two different FOV (or two different pixels) and measures the intensity in each. To determine the contrast, the E-O/IR system processor subtracts the intensity in one pixel from that in another pixel and compares the differences.

Two pixels are illustrated in Fig 5; one pixel contains a missile intensity while the other does not. In pixel 2-3, the intensity is computed by multiplying the atmospheric path radiance plus the earth (or cloud) radiance by the area in the pixel. This intensity is represented as

$$I_{1,\lambda} = L_{B,\lambda} A_p \quad (1)$$

In pixel 3-4 (in Fig. 5), the IR intensity is computed by considering the following three components:

- *The source intensity* – The missile source intensity includes reflected and emitted source intensity components. The source intensities are then multiplied by the atmospheric transmittance which lies in the FOV of the E-O/IR sensor
- *The unaccounted background intensity* – The unaccounted (or unblocked) background intensity includes the atmospheric path radiance (including earth or cloud radiances) multiplied by the unaccounted area in the FOV. A typical missile is usually divided into planar surfaces known as facets that are summed as projected areas into the line-of-sight of the E-O/IR system. The projected area of a facet is obtained by multiplying the planar area of the facet by the dot product of the outward normal from the facet and the E-O/IR system
- *The foreground intensity* – The foreground intensity is the product of the atmospheric foreground radiance (between the missile and the E-O/IR system) and the projected area of the missile in a given line-of-sight.

The intensity for pixel 2 is:

$$I_{2,\lambda} = \tau_{\lambda} \sum_i I_{i,\lambda} + L_{B,\lambda} \left(A_p - \sum_{j=1}^n A_{s,j} \right) + L_{F,\lambda} \sum_{j=1}^n A_{s,j} \quad (2)$$

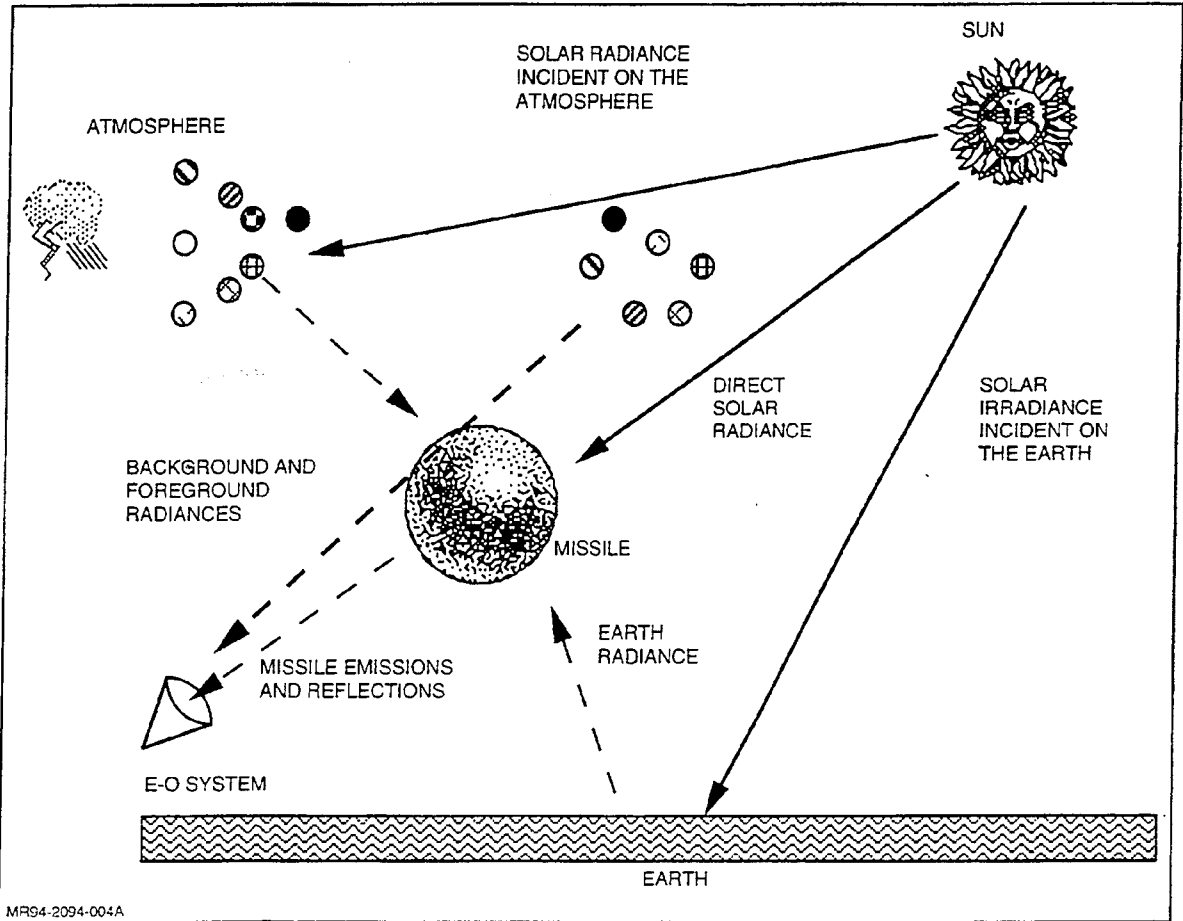


Fig. 4 IR Radiation from Missiles

The intensities computed in pixels 1 and 2 are then subtracted from one another (Eq 2 minus Eq 1) to obtain the following contrast difference:

$$I_{c,\lambda} = \tau_{\lambda} \sum_i I_{i,\lambda} - (L_{B,\lambda} - L_{F,\lambda}) \sum_{j=1}^n A_{s,j} - (L_{B',\lambda} - L_{B,\lambda}) A_p \quad (3)$$

In Eq 3, the prime superscript represents the background radiance related to pixel 2-3. In Eq 3, the IR contrast can either be positive, negative, zero, or any combination in the spectrum. This depends on the magnitude of the missile intensity and the difference between the background and foreground intensities. In Eq 1 and 2, if the background radiances are equal to one another, then Eq 3 becomes

$$I_{c,\lambda} = \tau_{\lambda} \sum_i I_{i,\lambda} - (L_{B,\lambda} - L_{F,\lambda}) \sum_{j=1}^n A_{s,j} \quad (4)$$

MISSILE TO SENSOR INFRARED RANGE EQUATION

To obtain the detection range of an E-O/IR system, three E-O/IR system parameters must be known. These parameters are the detector's wavelength band of operation, the system's signal-to-noise (S/N) ratio, and the system's noise equivalent irradiance (NEI). The detection range (or E-O/IR system lock-on range) is obtained from spherical geometry. Consider a missile in the

center of a spherical enclosure. The missile emits an exitance to the spherical enclosure equal to

$$4\pi \int_{\lambda_1}^{\lambda_2} I_{c,\lambda} d\lambda$$

The exitance that is received by the inner portion of the spherical area (with inner radius, R) is known as the irradiance and can be expressed as

$$\frac{4\pi \int_{\lambda_1}^{\lambda_2} I_{c,\lambda} d\lambda}{4\pi R^2}$$

The irradiance can be equated to the E-O/IR system's detection equivalent irradiance which is the product of the S/N and NEI. Solving for the range yields the following IR range equation

$$R = \sqrt{\frac{\int_{\lambda_2}^{\lambda_1} I_{c,\lambda} d\lambda}{S/N (NEI)}} \quad (5)$$

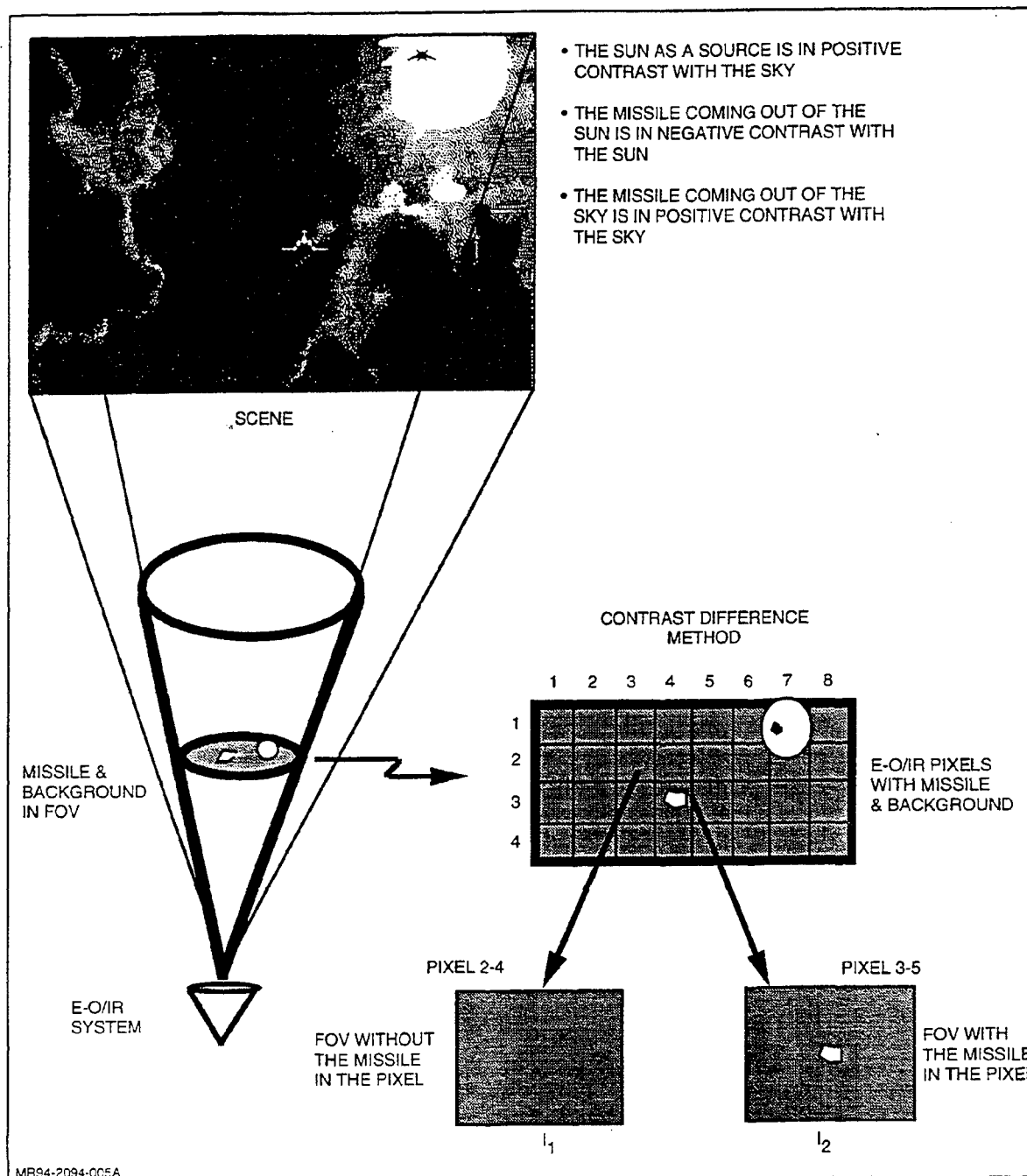


Fig. 5 IR Contrast Intensity

In Eq 5, the contrast intensity can be positive, zero, or negative. Therefore, the range can be positive, zero, or imaginary. When an imaginary solution occurs, the E-O/IR system logic (processor) determines that the lock-on range is being determined under a negative contrast. A negative contrast occurs when the missile is viewed against a background whose intensity is higher than the

missile. This occurs when a missile is being viewed against a relatively warm earth background. It should be noted that in Eq 5 the contrast intensity is a function of atmospheric transmittance and radiance. Since both atmospheric transmittance and radiance are a function of range, Eq 5 needs to be solved by iteration (since range is also on the left-hand-side of the equation).

Infrared Radiation Laws and Missile Characteristics

SUMMARY

Infrared radiation laws as applied to missile intensities are presented as part of the NATO Advisory Group for Aerospace Research & Development (AGARD) special course on "Missile Aerodynamics." This course focuses on radiative heat transfer laws with a discussion of the IR conservation principles and black body radiative laws.

NOMENCLATURE

A_1	= A dimensionless variable defined by Eq 5
A_2	= A dimensionless variable defined by Eq 5
C_1	= Planck's first constant (defined in Table 1), $W \cdot \mu m^5 / m^2$
C_2	= Planck's second constant (defined in Table 1), $\mu m \cdot K$
C_3	= Wein's constant (defined in Table 1), $\mu m \cdot K$
C_p	= Wein-Planck's constant (defined in Table 1), $W / m^2 \cdot \mu m \cdot K^5$
C_c	= $(C_3)^5 C_p$ (defined in Table 1), $W \cdot \mu m^4 / m^2$
d	= Thickness, m
I_λ	= Spectral intensity, $W / sr \cdot \mu m$
L	= Broadband black-body radiance, $W / sr \cdot m^2$
L_λ	= Spectral black-body radiance, $W / sr \cdot \mu m \cdot m^2$
$L_{MAX,\lambda}$	= Maximum spectral black-body radiance, $W / sr \cdot \mu m \cdot m^2$
m	= A number that varies from 1 to infinity
T	= Temperature of the missile skin, K
α_λ	= Spectral absorptivity
λ	= Wavelength, μm
ρ_λ	= Spectral reflectivity
τ_λ	= Spectral transmissivity
σ	= Stefan-Boltzmann's constant (defined in Table 1), $W / m^2 \cdot K^4$

INTRODUCTION

To compute the IR intensity from missiles and backgrounds, it is important to understand the basic IR radiation laws. IR radiation from missiles are a function of the following four basic parameters:

- **Geometry** – For emission, the missile projected area needs to be computed. This is the projected area into the line-of-sight of an electro-optical (E-O) system which is detecting the missile. For reflection, the surface structure of the missile needs to be computed, including curvature effects in the directions of both the background radiating source and the E-O system that detects the missile
- **Temperature** – The temperature of the missile needs to be computed. This is the temperature resulting from an energy balance due to aerodynamic heating; environmental parameters that interact among conduction, convection, and radiation heat transfer; and structural heat transfer via cold and hot sources of energies

- **Optical Parameters** – The surface emissivity (the emissivity affects the radiant intensity exiting the surface) and reflectivity (the reflectivity affects the amount of background intensity which is incident on the missile and reflected into the line-of-sight of the E-O/IR sensor) need to be measured for each different missile surface. Other optical parameters that need to be measured include the index of refraction of the medium that the missile is traveling in. The index of refraction affects the intensity being emitted by the surface. The surface absorptivity affects the missile's structure in terms of absorbing solar energy and radiant emission from the exhaust plume
- **Incident Background Sources of Radiation** – There are several intensities from background sources that are incident on a missile's surface. These background intensities include solar irradiance, earth shine, cloud shine, and sky shine. These irradiances are reflected from the missile's surface via the reflectivity of the surface.

PREVOST'S LAW

The most fundamental law in radiative transfer is Prevost's Law. This law states that a missile must continue to emit radiation even when in thermal equilibrium with its surroundings. At thermal equilibrium, the energy absorbed by the missile is equal to the energy emitted by the missile. The significance of this law is that every object (or missile) in the universe continually radiates and absorbs electromagnetic waves. This occurs even when the missile's thermal energy is forced to be identical to the surrounding energy.

CONSERVATION OF ENERGY

The next fundamental law is the Law of Conservation of Energy applied to a missile or medium. Referring to Fig. 1, the energy (or intensity) incident on a medium will be partially reflected, absorbed, and transmitted. An energy balance to account for the energy transfer yields,

$$I_\lambda = \alpha_\lambda I_\lambda + \rho_\lambda I_\lambda + \tau_\lambda I_\lambda \quad (1)$$

where, I is the spectral (as designated by the wavelength, λ) flux of radiant intensity incident on a surface of the medium. The fractions of intensity entering and leaving the medium are specified as α for absorptivity, ρ for reflectivity, and τ for transmissivity.

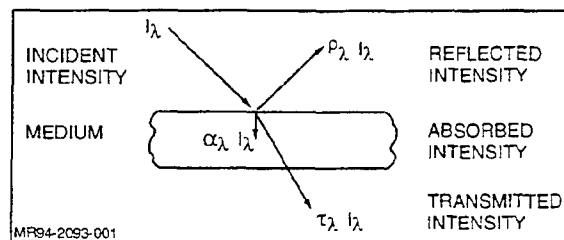


Fig. 1 Intensity Components Applied to a Medium

Upon dividing through by the spectral intensity, Eq 1 reduces to

$$\alpha_\lambda + \rho_\lambda + \tau_\lambda = 1 \quad (2)$$

For nontransparent (or opaque) solids, $\tau = 0$. Consequently,

$$\alpha_\lambda + \rho_\lambda = 1 \quad (3)$$

The following three ideal cases are readily observed from Eq 2:

- **Case 1: Perfect Absorber** $\alpha = 1$. A perfect absorber is often referred to as a black body. In nature, there are no real black bodies. Nevertheless, there are many substances that approach the ideal black body case: a real body (known as a grey body) has an absorptivity varying between 0 and 1. A missile fuselage can be made to approach a perfect absorber by painting the missile body with a paint whose absorptivity is high
- **Case 2: Perfect Reflector** $\rho = 1$. A perfect reflector is an ideal case. A highly polished (or mirrored) surface usually has properties that approach the perfect reflector. The definition of reflectivity is much more complex than absorptivity. This is because reflectivity is a function of the reflected intensity as well as the incident intensity. The reflectivity of a missile is quite complex due to the many different kinds of materials and coatings that are used in the construction of the missile's structure
- **Case 3: Perfect Transmitter** $\tau = 1$. In this ideal case, all of the energy incident on the surface of a transparent object enters through it and leaves unchanged. This is approximately analogous to light (in the visual part of the spectrum) passing through window glass. Caution should be made not to overextend this analogy into the IR spectrum. At different wavelength bands, glass absorbs and reflects different amounts of energy. Many glass domes that are used in E-O/IR seekers are good transmitters of IR irradiance.

There are two different endings used in specifying the above properties --ivity and --ance (such as reflectivity and reflectance). The "ivity" ending is used when referring to optically smooth and uncontaminated surfaces, therefore representing an ideal case. The "ance" ending refers to measured properties where there is a need to specify the surface conditions of the coupon or substance. Consequently, an absorptance of 0.85 for a missile skin would mean that the missile structural surface absorptivity was measured.

PLANCK'S LAW

The most significant law that governs the radiative IR intensity of missiles is Planck's Law. For the black body radiance leaving a missile surface Planck's Law is a function of three fundamental variables: temperature, index of refraction, and wavelength. To obtain the black body intensity, the radiance is multiplied by the projected area in the line-of-sight of the observer. For a missile, representing a grey body intensity, Planck's Law is multiplied by the emissivity at the surface of the missile.

Figure 2 illustrates the fundamental variables associated with Planck's Law. Each of these variables are discussed below:

- **Temperature** – In radiative heat transfer, temperature is defined as the absolute temperature on the surface of a missile. For example, referring to Fig. 2, consider the wall of a missile with a linear temperature gradient. The missile is detected by an E-O/IR system vis-a-vis the absolute temperature of the missile's outer extreme wall. For many missiles, the thermal

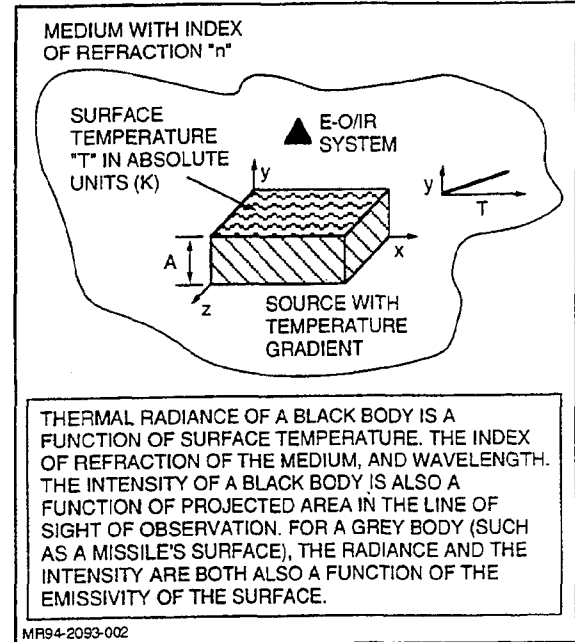


Fig. 2 Parameters Used in Planck's Law

gradient through the missile structure is often insignificant and consequently neglected. For example, this is usually the case for heated thin aluminum (less than 0.003 m thick). However, other missile structures are detected by E-O/IR systems, where material properties require a thermal analysis. Some missile structures have large thicknesses and/or low thermal conductivities, giving rise to thermal gradients in the missile structure. (When considering the significance of thermal gradients in missiles, the Biot number needs to be evaluated)

- **Index of Refraction** – Planck's Law is also a function of the index of refraction of the medium of propagation. The index of refraction is part of Planck's first and second constants. These constants are a function of the speed of light through the medium which the solid surface (or source) is emitting. When the missile is immersed in either water or a fluid whose index of refraction is not 1.0, then the index of refraction effect must be accounted for in Planck's Law. Usually, in air or in "empty space", the index of refraction of the medium can be assumed to be equal to 1.0. However, for missiles launched under water by submarines or for missiles where engine plumes flow past the fuselage, a correction for the index of refraction of the medium near the surface of emission must be accounted for in Planck's Law
- **Wavelength** – The wavelength dependency of radiation is very complex. For missile structures, however, the wavelength dependency is usually a function of temperature. As the temperature of a missile increases, the wavelength at which the intensity peaks becomes shorter. Assuming a constant missile temperature, the missile will have a different black body radiance value at each wavelength. In the Short Wave IR (SWIR) band (0.7 to 3 micrometers), solar reflections from missiles are significant. This band also includes high-temperature thermal emissions resulting from high-temperature heat exchangers and engine emissions. In the Mid Wave IR

(MWIR) band (3 to 5 micrometers), both missile emissions and reflections are significant. Also of significance in the MWIR band is the exhaust plume combustion constituents resulting from water vapor, carbon dioxide, and other constituents. In the Long Wave IR (LWIR) band (8 to 12 or 8 to 14 micrometers), the emitted energy from a missile airframe is significant.

To analytically determine the radiance and the spectral shape of the black body curves, Planck's Law is used. Planck's Law is

$$L_{\lambda} = \frac{2C_1 \lambda^{-5}}{\exp\left(\frac{C_2}{\lambda T}\right) - 1} \quad (4)$$

where, C_1 and C_2 are Planck's first and second constants, respectively. These constants are both a function of the medium that the missile is propagating into.

Table 1 lists the constants in Planck's Law for a missile structure that approaches a black body radiating into a medium whose index of refraction is not 1.0. Figure 3 is a plot of Planck's Law (for $n = 1.0$) for different temperatures. As indicated by Eq 4 and shown in Fig. 3, as the temperature increases the peak in radiance shifts to shorter wavelengths.

Planck's Law may be integrated over a wavelength band to produce the broadband radiance from either a missile or a background component. Upon integrating Eq 4 between λ_1 and λ_2 , the following expression results:

$$L = \int_{\lambda_1}^{\lambda_2} L_{\lambda} d\lambda$$

$$= 2C_1 \left(\frac{T}{C_2}\right)^4 \sum_{m=1}^{\infty} m^{-4} \left\{ \exp(-mx_2) A_2 - \exp(-mx_1) A_1 \right\} \quad (5)$$

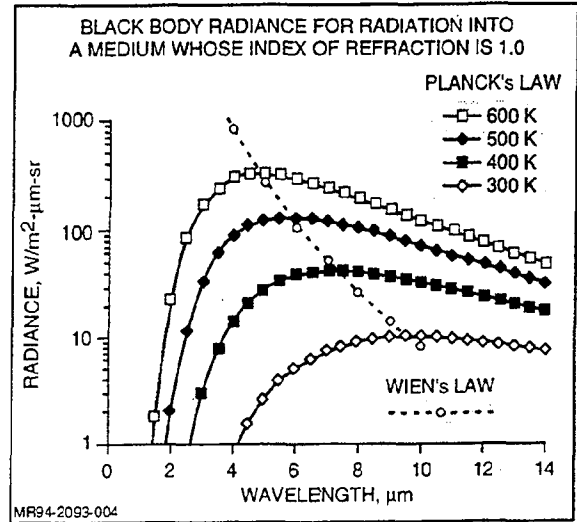


Fig. 3 Spectral Radiance from Planck's Law & Wien's Law

where

$$A_2 = (mx_2)^3 + 3(mx_2)^2 + 6(mx_2) + 6$$

$$A_1 = (mx_1)^3 + 3(mx_1)^2 + 6(mx_1) + 6$$

$$x_2 = \frac{C_2}{\lambda_2 T} \quad x_1 = \frac{C_2}{\lambda_1 T}$$

The significance of this integration is that E-O/IR systems operate in distinct wavelength bands. Therefore, it becomes important to know how much radiance is emitted from a missile over an E-O/IR system's spectral bandwidth ($\Delta\lambda$).

Table 1 Radiation Constants

THESE NUMERICAL CONSTANTS ARE FOR A BLACK BODY RADIATING IN A MEDIUM WHOSE INDEX OF REFRACTION IS n . FOR CLEAN AIR, n IS APPROXIMATELY 1.0.

CONSTANT	SYMBOL	VALUE	UNITS
PLANCK'S FIRST	C_1	$\frac{0.5954 \times 10^8}{n^2}$	$W-\mu m^4/m^2$
PLANCK'S SECOND	C_2	$\frac{14,388}{n}$	$\mu m-K$
STEFAN-BOLTZMANN'S	σ	$5.670 \times 10^{-8} n^2$	W/m^2-K^4
WIEN'S	C_a	$\frac{2,898}{n}$	$\mu m-K$
	C_b	$4.095 \times 10^{-12} n^3$	$W/m^2-\mu m-K^5$
	C_c	$\frac{836,700}{n^2}$	$W-\mu m^4/m^2$

STEFAN-BOLTZMANN'S LAW

When Planck's Law (Eq 4) is integrated over the entire spectrum from minus to plus infinity, the resulting equation is known as Stefan-Boltzmann's Law. Stefan-Boltzmann's Law accounts for the total radiance that is emitted from a missile. Upon integrating Eq 4 between minus and plus infinity, the following expression results:

$$L = \sigma T^4 \quad (6)$$

Stefan-Boltzmann's Law yields the total intensity over the spectrum for a given temperature. The value of Stefan-Boltzmann's constant is given in Table 1.

WIEN'S LAW

Wien's Law yields the maximum radiances from Planck's Law. From Wien's Law, three useful relationships can be obtained: (1) the wavelength at which the peak radiance occurs; (2) the temperature at which the peak radiance occurs; and (3) the maximum radiance that occurs at any given wavelength or temperature. Wien's Law is obtained when Eq 4 is maximized:

$$\frac{dL}{d\lambda} = 0$$

By solving the resulting equation, Wien's Law is obtained as:

$$C_2 = \lambda T \quad (7)$$

In Eq 7, C_2 is Wien's constant given in Table 1. Wien's Law is plotted in Fig. 3 as the locus of all points that form a maxima on the radiance curves obtained from Planck's Law. Wien's Law is also plotted in Fig. 4 for a black body radiating into a medium whose index of refraction is 1.0. In Fig. 4, Wien's Law is presented in its three different forms: temperature versus wavelength, maximum radiance versus temperature, and maximum radiance versus wavelength.

The maximum spectral radiance for a given temperature is obtained by substituting Eq 7 into Eq 4. This results in

$$L_{\max} = \frac{2C_1 T^5}{C_2^5 \left[\exp\left(\frac{C_2}{C_2}\right) - 1 \right]} \quad (8)$$

Evaluating the constants in the SI units for the propagation of a missile that approaches a black body radiance reduces Eq 8 to

$$L_{\max} = C_b T^5 \quad (9)$$

Table 1 defines the value of C_b . Equation 9 is plotted in Fig. 4 to illustrate the fifth power effect of temperature on black body radiance when radiating into a medium whose index of refraction is 1.0.

To obtain the maximum radiance for a specific wavelength, Eq 7 is again substituted into Eq 4, except this time the wavelength dependency is conserved. This results in the following equation:

$$L_{\max} = \frac{2C_1 \lambda^{-5}}{\exp\left(\frac{C_2}{C_2}\right) - 1} \quad (10)$$

Equation 10 reduces to

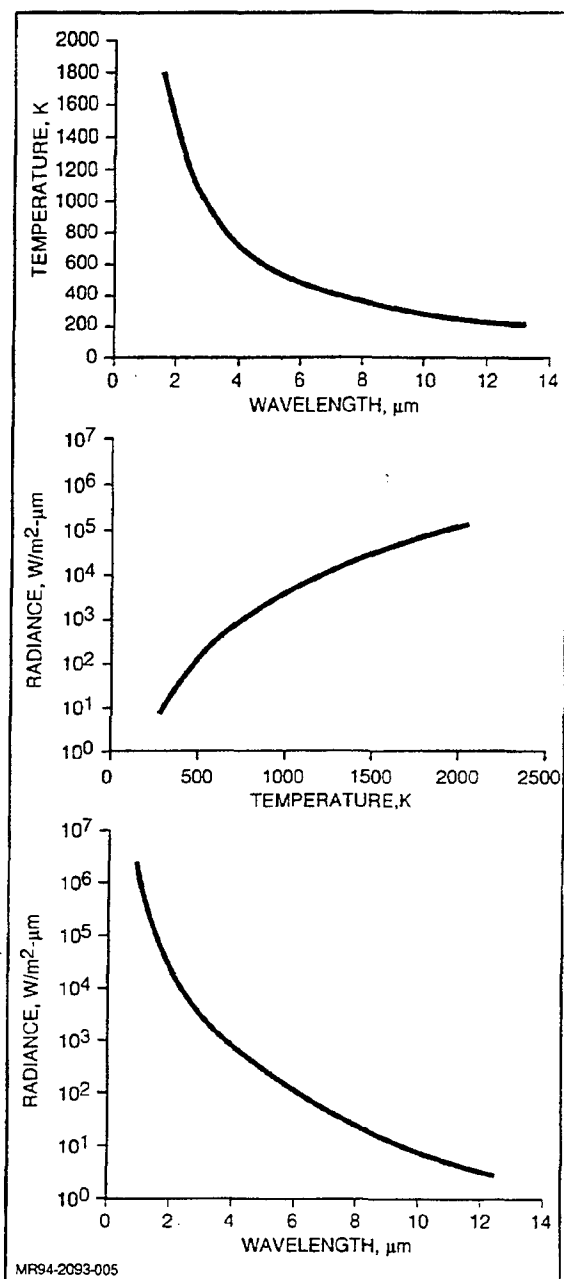


Fig. 4 Wien's Law

$$L_{\max} = C_c \lambda^{-5} \quad (11)$$

where, C_c is given in Table 1. The maximum radiance versus wavelength is plotted in Fig. 4. In Eq. 9 and 11, the maximum radiances are equal to one another. Equating these two equations also yields Eq 7.

The above maximum radiances can be converted to the following intensities:

- *Black body intensities* by multiplying the radiance by the projected area of the missile
- *Missile (grey body) intensities* by multiplying the black body intensity by the emissivity at the missile's surface.

Missile Infrared Radiative Properties

SUMMARY

The radiative properties of missiles is presented as part of the NATO Advisory Group for Aerospace Research & Development (AGARD) special course on "Missile Aerodynamics." This course focuses on the radiative properties of missile structures including the emissivity, absorptivity, and reflectivity. With a knowledge of these properties, the missile designer can determine the thermal balance of missile structures, the radiative intensity of missiles, and the impact of the irradiance from environment sources on the total intensity of the missile.

NOMENCLATURE

- A = Area of the missile used for absorbing incident thermal energy in the line-of-sight of the incident source, m²
 A_p = Projected area in the line-of-sight of the missile, m²
 C₁ = Planck's first constant, W-μm⁴/m²
 C₂ = Planck's second constant, μm-K
 E_i = Irradiance on the surface of a missile, W/m²
 I_a = Absorbed intensity, W/sr-μm
 I_b = Black body intensity, W/sr-μm
 I_i = Incident intensity, W/sr-μm
 I_r = Reflected intensity, W/sr-μm
 I_λ = Spectral intensity, W/sr-μm
 R = Radius of the hemisphere
 T = Temperature of the missile structure, K
 α = Absorptivity
 α_λ = Hemispherical spectral absorptivity
 ε_λ = Hemispherical spectral emissivity
 θ_c = Zenith angle of emitted intensity (or Exittance)
 θ_i = Zenith angle of incident intensity
 θ_r = Zenith angle of reflected intensity
 λ = Wavelength, μm
 π = 3.14...
 π' = 180 degrees
 ρ = Bidirectional reflectivity, 1/sr
 ρ_d = Diffuse reflectivity
 ρ_λ = Spectral reflectivity
 φ_e = Azimuth angle of emitted intensity (or Exittance)
 φ_i = Azimuth angle of incident intensity
 φ_r = Azimuth angle of reflected intensity

INTRODUCTION

In radiative heat transfer, there are two properties that influence the emission and reflection from missiles structures. These properties are the emissivity and reflectivity, respectively. Another property, the absorptivity, is defined as the ability of the structure to absorb incident irradiances from the environment and from other parts of the radiating structure or exhaust plume. This absorbed energy manifests itself into thermal emission and results in a temperature change within the missile structure.

The emissivity is the ratio of the "true" (or measured) intensity emitted by a missile to the intensity emitted by a black body. The

radiant intensity emitted from a missile is obtained by multiplying the missile's emissivity by Planck's Black Body Law, using the temperature of the missile structure. With respect to an energy balance on the missile, this is the term that results in a decrease in missile temperature since energy is being radiated out of the missile structure. The "true intensity" emitted by a missile is called the gray body intensity and has units of W/sr. The intensity is the product of the projected area of the missile into the line-of-sight of an observer, the missile's surface emissivity, and Planck's Black Body Law. This results in the following equation for the hemispherical spectral intensity:

$$I_{\lambda} = A_p \epsilon_{\lambda} \frac{2C_1 \lambda^{-5}}{\exp\left(\frac{C_2}{\lambda T}\right) - 1} \quad (1)$$

where, C₁ and C₂ are Planck's first and second constants, respectively. These constants are a function of the medium that the missile is propagating into. The temperature of the missile, T, may also influence the emissivity of the missile's structure.

The absorptivity is the ratio of radiant energy absorbed by the missile to the irradiance that is incident on the missile. The irradiance can either come from external or internal sources of energy which are incident on the missile's outer or inner surfaces, respectively. Examples of absorption include solar and laser irradiances incident on missiles. The absorption of energy by a missile results in an increase in the missile's temperature. The product of the area, absorptivity, and the sum of incident energies (or irradiances) on the surface results in the following equation for the hemispherical spectral absorption of thermal energy:

$$I_{\lambda} = A \alpha_{\lambda} \sum E_i \quad (2)$$

The reflectivity is the ratio of radiant intensity reflected from the missile to the intensity incident on the missile. Reflected natural energy sources include:

- Direct solar reflections
- Earth thermal energy reflected from the missile's structure
- Cloud and sky thermal energies reflected from a missile
- Scattered solar (or reflected) energy from the earth, clouds, and sky in the line-of-sight of the missile.

Manmade energies that are reflected from missiles include laser energy and thermal energies emitted from one missile structural component and then reflected by another. The product of the area, reflectivity, and incident irradiances results in the following equation for the diffuse reflection component from a missile:

$$I_{\lambda} = A \rho_{\lambda} \sum E_i \quad (3)$$

DEFINITION OF PROPERTIES

There are four categories of properties that define both emissivity and absorptivity: directional spectral, directional total, hemi-

spherical spectral, and hemispherical total. Table 1 lists these properties and their functional form.

In addition, reflective properties are defined as bidirectional, specular, hemispherical-directional-spectral, hemispherical-directional-total, directional-hemispherical-spectral, directional-hemispherical-total, and diffuse. These properties are also presented in Table 1.

There is also a special property defined as selective. This property is related to emissivity, absorptivity, and reflectivity. Selective surfaces are surfaces whose properties are either a function of wavelength, temperature, or both wavelength and temperature.

EMISSIVITY

Properties that define the emissivity are discussed below (these properties are unitless).

Directional Spectral Emissivity

A material that exhibits a directional spectral emissivity is a function of wavelength (spectral); solid angle (directional) of emission (exitance angles); and missile temperature. As shown in Fig. 1, the directional spectral emissivity is defined as the ratio of the measured intensity emitted by a missile (or small sample

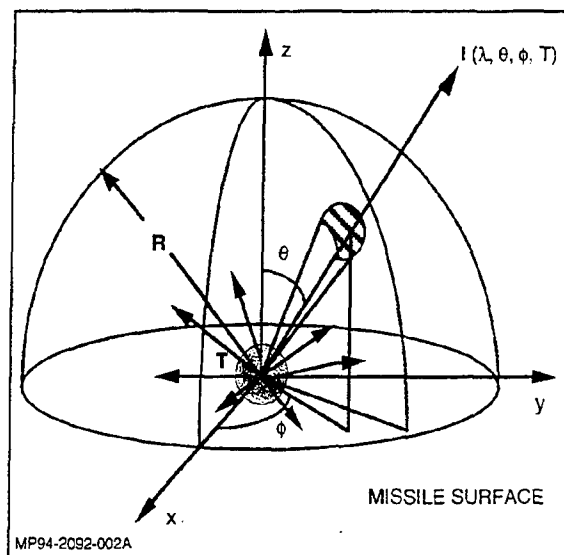


Fig. 1 Directional Spectral Emissivity from a Surface

Table 1 Functional Forms of Radiative Properties

PROPERTY	EMISSIVITY	ABSORPTIVITY	REFLECTIVITY
DIRECTIONAL SPECTRAL	$\lambda, \theta_e, \phi_e, T$	$\lambda, \theta_i, \phi_i, T$	
DIRECTIONAL TOTAL	θ_e, ϕ_e, T	θ_i, ϕ_i, T	
HEMISPHERICAL SPECTRAL	λ, T	λ, T	
HEMISPHERICAL TOTAL	T	T	
BIDIRECTIONAL			$\lambda, \theta_i, \phi_i, \theta_r, \phi_r, T$
SPECULAR			$\lambda, \theta_i = \theta_r$ $\phi_i = \phi_r - \pi, T$
HEMISPHERICAL DIRECTIONAL SPECTRAL			$\lambda, \theta_r, \phi_r, T$
HEMISPHERICAL DIRECTIONAL TOTAL			θ_r, ϕ_r, T
DIRECTIONAL HEMISPHERICAL SPECTRAL			$\lambda, \theta_i, \phi_i, T$
DIRECTIONAL HEMISPHERICAL TOTAL			θ_i, ϕ_i, T
DIFFUSE			$\lambda, \theta_i, \phi_i, T$
SELECTIVE	λ, T	λ, T	$\lambda, \theta_i, \phi_i, T$

MR94-2092-001A

of the missile for use in laboratory measurements) to the intensity emitted by a black body at the same temperature of the missile. The directional spectral emissivity is defined as:

$$\varepsilon(\lambda, \theta_e, \phi_e, T) = \frac{I(\lambda, \theta_e, \phi_e, T)}{I_b(\lambda, T)} \quad (4)$$

The intensity emitted by the missile is a function of wavelength, solid angle (defined by zenith and azimuth angles in a hemisphere) and temperature. The black body intensity is not a function of solid angle since its intensity is uniform at all observer viewing angles; this is known as a Lambertian or diffuse surface. Measurements of directional spectral emissivity are often made on rough surfaces where the surface roughness of the missile will result in different angular emissions. Examples of directional surfaces include painted substrates, and missiles whose surfaces are oxidized.

Directional Total Emissivity

When the directional spectral emissivity is integrated over the wavelengths from minus to plus infinity, it is referred to as the directional total emissivity. The directional total emissivity is a function of its exitance solid angles and missile temperature. Consequently, from Eq 4, averaging the emissivity over all wavelengths yields the following equation for the directional total emissivity:

$$\varepsilon(\theta_e, \phi_e, T) = \frac{\pi}{\sigma T^4} \int_0^{\infty} \varepsilon(\lambda, \theta_e, \phi_e, T) I_b(\lambda, T) d\lambda \quad (5)$$

Hemispherical Spectral Emissivity

Integrating the directional spectral emissivity over the solid angle yields the hemispherical spectral emissivity which is a function of wavelength and missile temperature. For the hemispherical spectral emissivity, the exitance solid angle is used in the integration. The hemispherical spectral emissivity is defined in Fig. 2. In this definition, the emissivity is not a function of solid angle. This results in a uniform (or Lambertian) emissivity in all directions. This is associated with smooth surfaces such as unpainted composite materials. From Eq 4, the hemispherical spectral emissivity is:

$$\varepsilon(\lambda, T) = \frac{1}{\pi} \int_{\phi_e=0}^{\pi} \int_{\theta_e=0}^{\pi/2} \varepsilon(\lambda, \theta_e, \phi_e, T) I(\lambda, T) \cos\theta_e \sin\theta_e d\theta_e d\phi_e \quad (5)$$

Hemispherical Total Emissivity

The hemispherical total emissivity is determined when integrating the directional spectral emissivity over both wavelength and solid angle. In this case, the hemispherical total emissivity is only a function of the missile temperature.

$$\varepsilon(T) = \frac{1}{\sigma T^4} \int_{\lambda=0}^{\infty} \left[I(T) \int_{\phi_e=0}^{\pi} \int_{\theta_e=0}^{\pi/2} \varepsilon(\lambda, \theta_e, \phi_e, T) \cos\theta_e \sin\theta_e d\theta_e d\phi_e \right] d\lambda \quad (6)$$

As a rule, when the ratio of surface roughness (usually taken as the root-mean-square (RMS) value of the roughness) to the

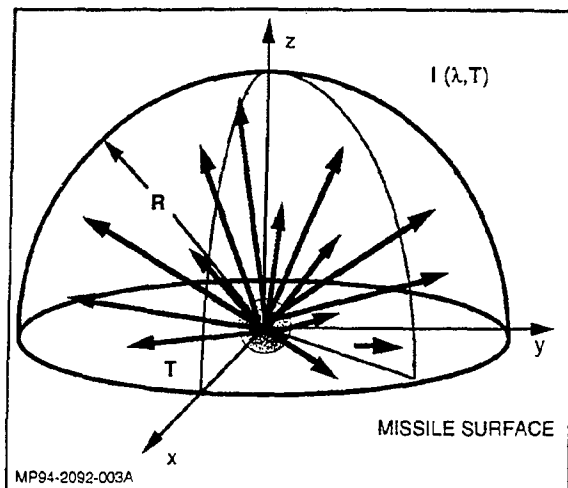


Fig. 2 Hemispherical Spectral Emissivity from a Missile Surface

wavelength is less than one, then the surface behaves as a hemispherical surface. When the ratio of surface roughness to the wavelength is greater than one, then the surface behaves as a directional surface. This is not always the case, since impurities and design of nonhomogeneous surfaces result in deviations from this rule. Since the surface temperatures of materials are not always in steady state, and since the emissivity of materials is a function of temperature, then the emissivity of materials will change during a transient change in temperature. This is often the case where the surface is relatively rough allowing for microstructural changes in the geometry of the rough surface. Consequently, Eq 4, 5, and 6 may require an averaging over time.

Typical emissivities of materials are as follows (these properties are general rules of thumb; however, for certain materials, these properties may deviate from the rule):

- Metals
 - Spectral emissivity decreases with increasing wavelength
 - Emissivity depends strongly on surface conditions. For example polished metals have emissivities less than 0.2, whereas oxidized metals have emissivities greater than 0.8
 - Directional emissivity increases with increasing angle of emission
 - Total hemispherical emissivity increases with increasing temperature
- Nonmetals
 - Spectral emissivities increase with increasing wavelength
 - Emissivity increases slightly with impurities and surface roughness
 - Directional emissivity decreases with increasing angle of emission
 - Total hemispherical emissivity increases or decreases as temperature increases—very material-dependent
- Semiconductors
 - Generally the same as metals
 - Spectral emissivity changes at approximately 4 micrometers when heated or cooled.

ABSORPTIVITY

The terminology for absorptivity is analogous to that of emissivity. Properties that define the absorptivity are defined below (these properties are unitless).

Directional Spectral Absorptivity

A material that exhibits directional spectral absorptivity is a function of wavelength (spectral), solid angle (directional) of absorption angles (incident angles), and missile temperature. As shown in Fig. 3, the directional spectral absorptivity of a coupon is defined as the ratio of the absorbed energy from a "directed outside source" to the irradiance of the "directed outside source" (an example of a directed outside source is a laser). For directional absorptivity, both the radiating "directed outside source" and the energy absorbed by the coupon are dependent on the solid angle between them. Under steady state conditions without thermal changes, measurements of absorptivity and emissivity should yield the same results. However, different methods of measuring the absorptivity and emissivity are used yielding small percent (usually under 5%) differences when compared. Consequently, the directional spectral absorptivity is the ratio of the absorbed to the incident energy and is defined as follows:

$$\alpha(\lambda, \theta, \phi, T) = \frac{d^2 I_a(\lambda, \theta, \phi, T)}{I_i(\lambda, \theta, \phi) dA \cos \theta \sin \theta d\theta d\phi d\lambda} \quad (7)$$

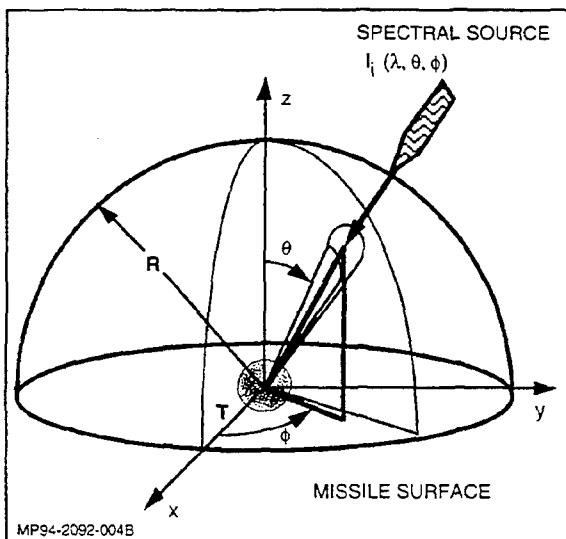


Fig. 3 Directional Spectral Absorptivity of a Missile Surface

Directional Total Absorptivity

From Eq 7, when the directional spectral intensity is integrated over the wavelengths from zero to infinity, it is referred to as the directional total intensity. (The directional total absorptivity is a function of incident solid angle and missile temperature.)

The ratio of the absorbed to incident intensity is then the directional total absorptivity, or

$$\alpha(\theta, \phi, T) = \frac{\int_0^{\infty} \alpha(\lambda, \theta, \phi, T) I_i(\lambda, \theta, \phi) d\lambda}{\int_0^{\infty} I_i(\lambda, \theta, \phi) d\lambda} \quad (8)$$

Hemispherical Spectral Absorptivity

Integrating the directional spectral absorptivity over the solid angle yields the hemispherical spectral absorptivity, which is a function of wavelength and missile temperature. For the hemispherical spectral absorptivity, the solid angle of incidence is used in the integration. When a coupon is illuminated uniformly about a hemispherical field of view, there is no solid angle dependency. Referring to Fig. 4, the hemispherical spectral absorptivity is defined as the ratio of the coupon absorbed energy to the uniform irradiance over the surface of the missile:

$$\alpha(\lambda, T) = \frac{\int_{\phi=0}^{2\pi} \int_{\theta=0}^{\pi/2} \alpha(\lambda, \theta, \phi, T) I_i(\lambda, \theta, \phi) \cos \theta \sin \theta d\theta d\phi}{\int_{\phi=0}^{2\pi} \int_{\theta=0}^{\pi/2} I_i(\lambda, \theta, \phi) \cos \theta \sin \theta d\theta d\phi} \quad (9)$$

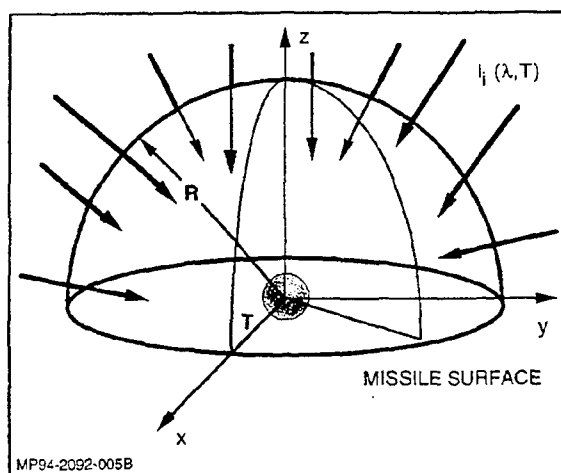


Fig. 4 Hemispherical Spectral Absorptivity of a Missile Surface

Hemispherical Total Absorptivity

The hemispherical total absorptivity is determined when integrating the directional spectral absorptivity over both wavelength and solid angle. In this case, the hemispherical total absorptivity is only a function of the missile temperature.

$$\alpha(T) = \frac{\int_0^{\infty} \left[\alpha(\lambda, T) \int_{\phi=0}^{2\pi} \int_{\theta=0}^{\pi/2} I_i(\lambda, \theta, \phi) \cos\theta \sin\theta d\theta d\phi \right] d\lambda}{\int_0^{\infty} \int_{\phi=0}^{2\pi} \int_{\theta=0}^{\pi/2} I_i(\lambda, \theta, \phi) \cos\theta \sin\theta d\theta d\phi d\lambda} \quad (10)$$

REFLECTIVITY

In comparison with emissivity and absorptivity, reflectivity is more complex in that two solid angles need to be considered. These are the incident and the reflected angles. The following paragraphs summarize the major reflectivities that need to be measured or input into IR intensity analyses of missiles:

Bidirectional Reflectivity

As illustrated in Fig. 5, the bidirectional (incident and reflected directions) reflection is defined as the ratio of the reflected intensity to the incident intensity integrated over the solid angle of incidence. This results in units of inverse steradian.

$$\rho(\lambda, \theta_r, \phi_r, \theta_i, \phi_i, T) = \frac{I_r(\lambda, \theta_r, \phi_r, \theta_i, \phi_i, T)}{I_i(\lambda, \theta_i, \phi_i) \cos\theta_i \sin\theta_i d\theta_i d\phi_i} \quad (11)$$

The bidirectional reflectivity is a function of the missile surface temperature. This is because the temperature will effect the surface "granularity" causing a variation in the bidirectional reflection as microcavities expand and contract.

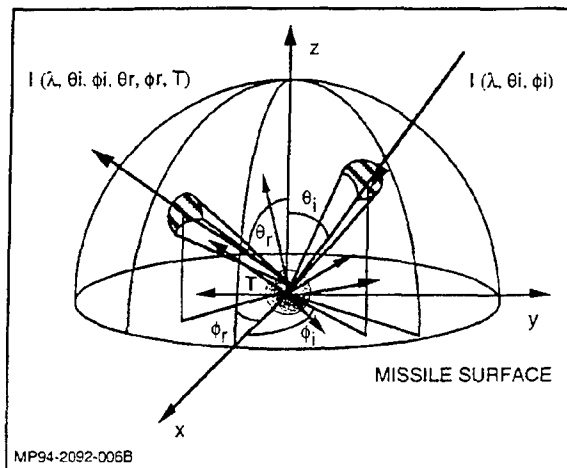


Fig. 5 Bidirectional Reflection from a Missile Source

Specular Reflectivity

The specular reflectivity is a special case of the bidirectional reflectivity. This occurs when the incident and reflected zenith angles are equal and have corresponding azimuth angles 180° apart.

Diffuse Reflectivity

The bidirectional reflectivity can be integrated over a solid angle to produce reflectivities that are unitless. Unitless properties of reflectivity include hemispherical-directional, directional-hemispherical, and diffuse reflectivities. Detail discussions of these properties can be found in Ref 1. These properties are obtained by integrating the bidirectional reflectivity over either incident or reflected solid angles. The diffuse reflectivity is obtained from Eq 11 and is defined as follows (this property is unitless):

$$\rho_D(\lambda, \theta_i, \phi_i, T) = \rho(\lambda, \theta_i, \phi_i, T) \int_{\phi_r=0}^{2\pi} \int_{\theta_r=0}^{\pi/2} \cos\theta_r \sin\theta_r d\theta_r d\phi_r \quad (12)$$

Equation 12 can be integrated over the limits imposed yielding:

$$\rho_D(\lambda, \theta_i, \phi_i, T) = \pi \rho(\lambda, \theta_i, \phi_i, T) \quad (13)$$

KIRCHHOFF'S LAW

Kirchhoff's Law is valid for a missile in thermodynamic equilibrium and located in an isothermal enclosure. Kirchhoff's Law basically states that at steady state, at a given wavelength λ , and at a defined solid angular direction (defined by θ and ϕ), the absorptivity and emissivity of a material are equal to one another:

$$\alpha(\lambda_i, \theta_a, \phi_a, T) = \epsilon(\lambda_i, \theta_e, \phi_e, T) \quad (14)$$

only when $\theta_a = \theta_e$ and $\phi_a = \phi_e$

In Eq 14, θ and ϕ represent the solid angle for both emission and absorption. Equation 14 is applicable only when the absorption and emission angles are defined as $\theta_a = \theta_e$ and $\phi_a = \phi_e$.

For the transient case, Kirchhoff's Law must be applied with caution. Consequently, the absorptivity and emissivity of materials need not be equal to one another. For many materials, the absorptivity and emissivity are close enough to one another for Kirchhoff's Law to be applicable. However, Kirchhoff's Law may not always be applicable to a real body undergoing a transient and/or having a thermal control system.

REFERENCES

1. Siegel, R. and Howell, J.R., Thermal Radiation Heat Transfer, 2nd Ed. Hemisphere Publishing Co., 1981.

Introduction to Missile Thermal Analysis

SUMMARY

The thermal analysis of missiles is presented as part of the NATO Advisory Group for Aerospace Research & Development (AGARD) special course on "Missile Aerodynamics." This course focuses on the thermal balance of missile structures, including the radiative heating/cooling, convective, and conduction heat transfer, as well as the internal energy of a missile structure. With a knowledge of the surface temperature of a missile, the missile designer can determine the radiative intensity of missiles.

NOMENCLATURE

A	= Surface area of the control volume, m^2
A_m	= Heat flow area for conduction heat transfer, m^2
A_p	= Projected area of the missile, m^2
c	= Speed of sound in air, m/s
C_p	= Specific heat under constant pressure, $W-s/kg-K$
C_v	= Specific heat under constant volume, $W-s/kg-K$
F	= Configuration factor relating the geometric orientation of the missile with respect to either its background or its internal compartment
h	= Convective heat transfer coefficient, W/m^2-K
H	= Solar irradiance, W/m^2
H_{si}	= Solar irradiance incident on the outer surface of the control volume, W/m^2
k	= Thermal conductivity of the missile structure, $W/m-K$
k^*	= Thermal conductivity of air, $W/m-K$
L	= Characteristic length from the leading edge, m
m	= Mass of the control volume, kg
M_∞	= Mach number of the missile
n_{cv}	= Unit normal vector from the control volume
n_s	= Unit normal vector from the sun
Nu	= Nusselt number
Pr	= Prandtl number
Q_c	= Energy either gained or lost by the control volume due to convective heat transfer between the control volume and the thermal boundary layer near its surface, W
Q_m	= Energy conducted either away, into or through the control volume by conduction, W
$(Q_r)_i$	= Energy either lost or gained by the control volume and its backside (compartment) surrounding, W
$(Q_r)_o$	= Energy lost by the control volume due to radiative transfer between the control volume and its ambient surrounding (energy is usually lost to the cold sky by the relatively hot missile surface), W
Q_s	= Solar absorbed energy (incident solar irradiance multiplied by the absorptivity at the outer surface of the control volume), W

Q_{si}	= Energy transferred from the inner surface of the control volume to internal heat sinks, W
Q_{so}	= Energy transferred by heat sources to the inner surface of the control volume, W
r	= Recovery factor
Re	= Reynolds number
t	= time, hr
T	= Temperature of the missile structure, K
T^*	= Reference temperature, K
T_r	= Recovery temperature, K
T_s	= Stagnation temperature, K
T_{sky}	= Temperature of the ambient sky, K
T_∞	= Ambient temperature at the elevation of the missile, K
u	= Internal energy of the control volume per unit mass, kJ/kg
V	= Velocity of the missile, m/s
α	= Absorptivity
γ	= Ratio of the specific heats
ϵ	= Thermal emissivity of the missile structure
θ	= Angle made between the sun unit normal and the control volume normal vector when a ray is drawn between the two
λ	= Wavelength, μm
μ	= Viscosity of the air, $kg/m-s$
ρ	= Air density, Kg/m^3
σ	= Stefan-Boltzmann's constant, W/m^2-K^4

INTRODUCTION

The temperature of a missile needs to be determined accurately, since the radiance from a missile will be strongly influenced by its temperature. To determine the temperature of a missile, the conservation of energy (or the energy balance method) is required. The energy balance method includes Fourier's Law to determine the conduction heat transfer through missile materials; Newton's Law of Cooling to determine the amount of heat transfer between the missile and the ambient air by convection; and Stefan-Boltzmann's Law to determine the radiant energy lost to the sky and/or to another missile structural parts. If the energy balance is properly computed, then the resulting missile temperature should be within $\pm 10\%$ of the true or measured temperature of the missile.

CONSERVATION OF ENERGY

To calculate the temperature of a missile that is either stationary or in motion, an energy balance is made on a missile control volume. The control volume is defined as an element or a node on the missile's structure where the energy balance is performed. To obtain a detailed temperature distribution of a missile, many small control volumes are used—yielding a spatial temperature distribution on the missile. (The spatial temperature distribution can be coupled with the spatial emissivities of the missile to yield the spatial emitted radiance of the missile.) The control volume allows for energy to be transferred either into or out of a missile

structure. As shown in Fig. 1, a section of a missile structure is isolated with the inclusion of energy sources and sinks. The energy either gained or lost by the control volume will result in either an increase or a decrease in temperature from the control volume.

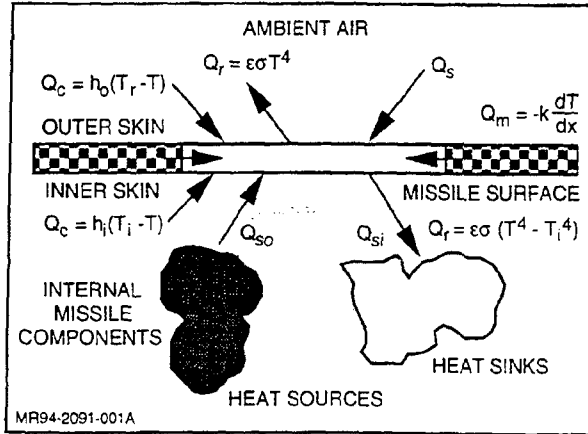


Fig. 1 Energy Balance on a Control Volume of a Missile Structure

Heat sources are those external (external to the control volume) energies that increase the temperature of the control volume. Heat sinks act to take energy away from the control volume, thereby decreasing the temperature of the control volume. Heat sources include solar heating, aerodynamic heating for missiles in flight, backside heat sources such as spars and compartments either conducting, radiating or convecting heat to the missile structure, and heat exchanger dumps. Heat sinks include convective cooling to the ambient air or fluid, radiant cooling to the ambient sky, and backside cooling through spars and compartments to thermal sinks that are cooler than the structural casing temperature of the control volume. Irradiances incident on the control volume are partially absorbed by the missile. The irradiances include solar, laser, or other missile structural components that radiate their energies into the line-of-sight of the control volume. Energy can either be lost or gained to the local ambient and to other sources through both convection and radiation.

For the control volume shown in Fig. 1, the energies leaving the control volume are summed and subtracted from the sum of energies entering the control volume. This is done for both the internal and external surfaces of the control volume, as well as for surrounding surfaces that conduct heat to or away from the control volume. This difference is then equated to the rate of change of the energy in the control volume, resulting in the following energy balance considering the inner and outer surfaces as well as surrounding structures for conduction:

$$(\pm Q_r \pm Q_c + \sum_j Q_{soj} - \sum_k Q_{slk}) + (-Q_r + Q_c + Q_s)_{in} \pm Q_m = \frac{d(mu)}{dt} \quad (1)$$

In Eq 1, each of these energy terms needs to be replaced by an equivalent expression to allow for the calculation of either the

transient or steady state temperature of the control volume. Each of these terms will be defined with an associated expression related to the temperature of the control volume.

INTERNAL ENERGY

On the right-hand side of Eq 1, the rate of energy change in the control volume is defined as the time rate of change of the mass in the control volume multiplied by the internal energy per unit mass. From thermodynamics, the temperature within the control volume is related by the following expression:

$$C_v = \left(\frac{\delta u}{\delta T} \right)_v \quad (2)$$

where, C_v is the specific heat under constant volume. For solids not undergoing any changes in phase, the specific heat under constant pressure, C_p , is approximately equal to C_v . Equation 2 can be substituted into the right-hand side of Eq 1 to obtain

$$\frac{d(mu)}{dT} = mC_v \frac{dT}{dt} + TC_v \frac{dm}{dt} \quad (3)$$

For many analyses related to missile structures, where the mass of the control volume remains unchanged, the rate of energy within the control volume is defined as follows:

$$\frac{d(mu)}{dT} = mC_v \frac{dT}{dt} \quad (4)$$

FOURIER'S LAW OF CONDUCTION

Heat transfer by conduction is the transfer of energy through the movement of molecules in solids, liquids, or gases. As shown in Fig. 2, when a structure is heated at one end, a temperature profile along the structure can be predicted using Fourier's Conduction Law. Fourier's Law is:

$$Q_m = -kA_m \frac{dT}{dx} \quad (5)$$

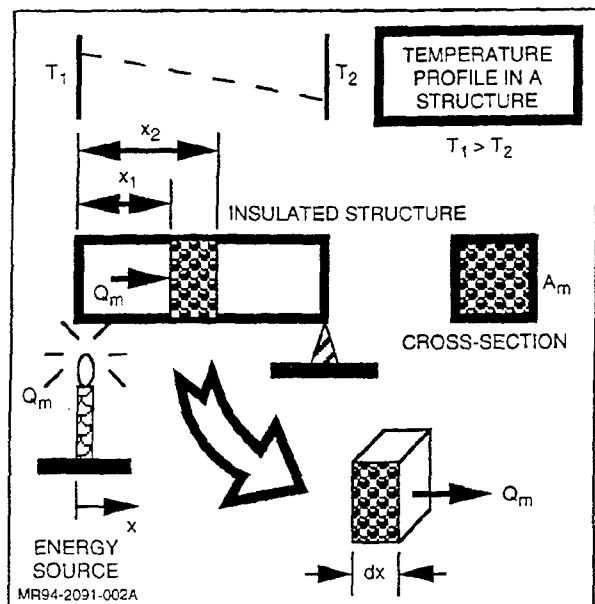


Fig. 2 Conduction Heat Transfer Through a Structure

The minus sign is due to the convention that the heat flow is positive in the direction of heat flow.

Typical values for the thermal conductivity of metals, nonmetals, liquids, and gases are given in Table 1. The thermal conductivity of specific materials can be found in Ref. 1.

Table 1 Typical Values for Thermal Conductivities

TYPE	MATERIAL AT 300 K	THERMAL CONDUCTIVITY, W/m-K
METALS	ALUMINUM	200
	STEEL	55
NONMETALS	GLASS	0.8
	PLASTICS	0.2
LIQUIDS	WATER	0.6
	HYDRAULIC OIL	0.2
GASES	HYDROGEN	0.2
	AIR	0.03

MR94-2091-006

RADIATIVE HEAT TRANSFER

In radiative heat transfer, energy is transferred by electromagnetic emission and does not require a medium to exchange energy with. The energy emitted from a missile surface is obtained by Stefan-Boltzmann's Law:

$$Q_r = \epsilon \sigma A_p T^4 \quad (6)$$

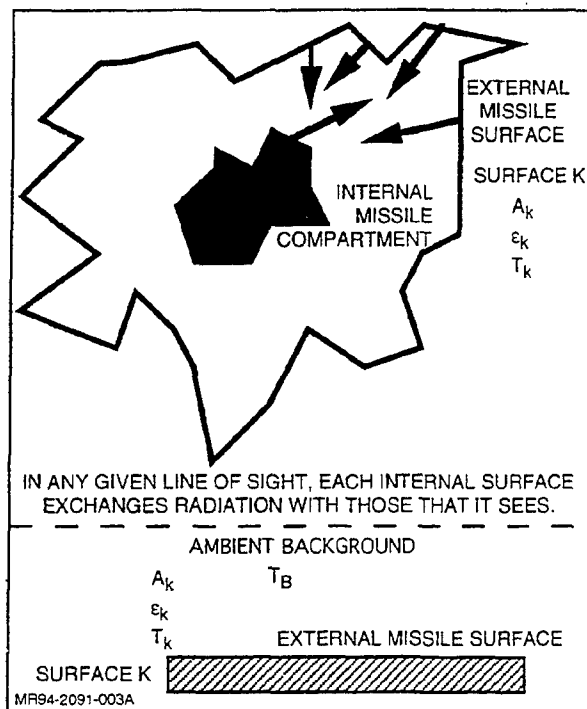
If a missile source is exchanging radiant energy with another missile source, then the geometric orientation between the sources needs to be considered. As illustrated in Fig. 3, two sources are exchanging energy with one another.

Radiative heat transfer is governed by Stefan-Boltzmann's Law. The exchange of radiant emission between two missile structures or between a missile and its background is governed by the following equation:

$$Q_r = F A_p \sigma (T^4 - T_B^4) \quad (7)$$

where, the script F is the configuration factor relating the geometric orientation of the missile with respect to its background, coupled with the respective missile and background emissivities (or reflectivities). For tables of configuration factors for different geometry, refer to Ref. 2. The temperatures of both the missile and the background are in degrees Kelvin.

The solar irradiance incident on the surface of a missile is obtained through tables of solar irradiance (or insolation). Figure 4 shows typical values of solar irradiance for various portions of the earth. Reference 3 contains a detail discussion of solar effects as well as tables of irradiances. The solar energy absorbed by a control volume is obtained by multiplying the incident solar irradiance at altitude by the absorptivity of the outer surface of the control volume. This product is then multiplied by the dot product of the two unit normal vectors of the sun and the control volume:



MR94-2091-003A

Fig. 3 Exchange of Energy by Radiation

$$Q_s = \alpha H_{si} (\bar{n}_s \cdot \bar{n}_{cv}) A \quad (8)$$

where, $\bar{n}_s \cdot \bar{n}_{cv} = \cos \theta$ between the sun and the control volume.

The effect of solar heating can be evaluated using the amount of solar irradiance incident on a missile. Since different coatings can be used on missiles, the effects of solar absorptivity and long wave thermal emission often need to be evaluated at the same time.

NEWTON'S LAW OF COOLING/HEATING—CONVECTION

The heat transferred by convection is defined as the transfer of thermal energy by virtue of the motion of a gas over a missile. To analyze the rate of heat transfer by convection, Newton's Law of Cooling/Heating is used. Referring to Fig. 5, Newton's Law is as follows:

$$Q_c = hA (T - T_r) \quad (9)$$

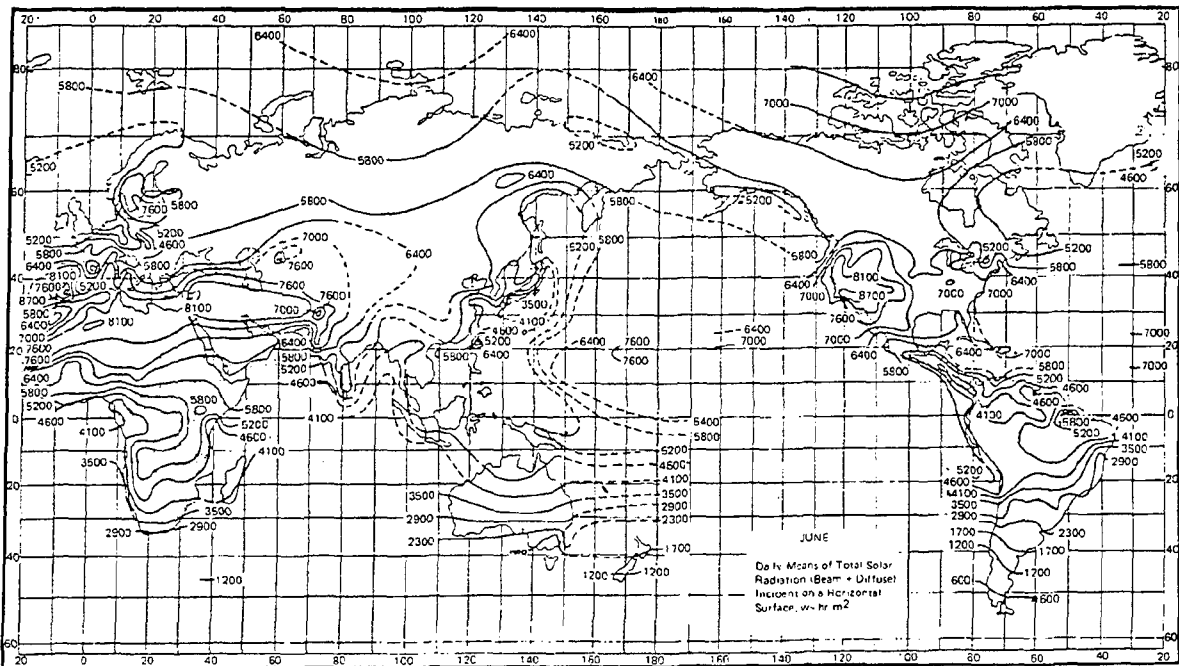
where, the recovery temperature, T_r , is defined as follows:

$$T_r = T_\infty \left[1 + r \left(\frac{\gamma - 1}{2} \right) M_\infty^2 \right] \quad (10)$$

The Mach Number is defined as the ratio of the missile velocity to the local acoustical velocity of the air. The Mach Number is defined as:

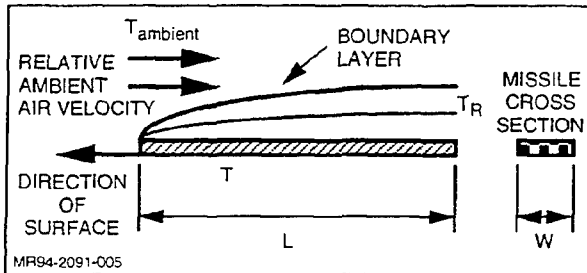
$$M_\infty = \frac{V}{c} \quad (11)$$

The plus sign in front of the convective heat transfer coefficient, h , in Eq 9, indicates that the heat flow is in the direction out of the surface of the missile. If the direction of the heat flow is into the



MR94-2091-004

Fig. 4 Mean Solar Irradiance for the Month of June



MR94-2091-005

Fig. 5 Newton's Law of Cooling

missile, then the sign is negative. (This case occurs when T_r is greater than T .)

The convective heat transfer coefficient is obtained through dimensionless numbers and correlations from test data. Typical heat transfer coefficients are presented in Table 2.

Table 2 Range of Convective Heat Transfer Coefficients

MODE OF CONVECTION	APPROXIMATE RANGE OF CONVECTIVE HEAT TRANSFER COEFFICIENTS, W/m^2-K
FREE CONVECTION OF AIR	5 - 30
FORCED CONVECTION OF AIR	30 - 350

MR94-2091-007

The altitude affects both ambient air temperature and the physical properties of the air (density, viscosity, and Prandtl number).

For ambient air,

$$\gamma = 1.4$$

Turbulent and laminar flow requires

$$\text{Turbulent flow: } r = (Pr)^{1/3}$$

$$\text{Laminar flow: } r = (Pr)^{1/2}$$

For Mach numbers less than 1.2, the missile fuselage temperature can be approximated by the recovery temperature (Eq 10). For higher Mach numbers, the heat transfer coefficient must be calculated and an energy balance for the fuselage wall must be computed. The following procedure can be used to determine the heat transfer coefficient from a flat plate (a flat plate is presented for simplicity; for other geometries refer to Ref. 1).

1. Atmospheric Temperatures and Properties

Typical ambient temperatures as a function of altitude are presented in Table 3 (Ref. 4). Air properties as a function of temperature are presented in Table 5 (Ref. 4).

2. The Reference Temperature

The reference temperature at which the boundary layer properties are evaluated is given by

$$T^* = T_\infty + 0.5(T - T_\infty) + 0.22(T_r - T_\infty) \quad (12)$$

Since this procedure involves an iterative solution, an initial estimate of the missile wall temperature needs to be made. A good first approximation for the missile wall temperature is as follows:

$$T \cong 0.9T_r + 0.1T_\infty \quad (13)$$

Table 3 Selected Properties of the Standard Atmosphere

ALTITUDE, km	TEMP, C	SPEED OF SOUND, m/s	PRESSURE $\times 10^{-4}$, N/m ²	DENSITY, kg/m ³	VISCOSITY $\times 10^{-5}$, kg/m-s
0	15.00	340	10.132	1.226	1.780
1	8.50	336	8.987	1.112	1.749
2	2.00	332	7.948	1.007	1.717
3	-4.50	329	7.010	0.909	1.684
4	-11.00	325	6.163	0.820	1.652
5	-17.50	320	5.400	0.737	1.619
6	-24.00	316	4.717	0.660	1.586
7	-30.50	312	4.104	0.589	1.552
8	-37.00	308	3.558	0.526	1.517
9	-43.50	304	3.073	0.467	1.482
10	-50.00	299	2.642	0.413	1.447
11	-56.50	295	2.261	0.364	1.418
12	-56.50	295	1.932	0.311	1.418
13	-56.50	295	1.650	0.265	1.418
14	-56.50	295	1.409	0.227	1.418
15	56.50	295	1.203	0.194	1.418
16	-56.50	295	1.027	0.163	1.418
17	-56.50	295	0.785	0.141	1.418
18	-56.50	295	0.749	0.121	1.418
19	-56.50	295	0.640	0.103	1.418
20	-56.50	295	0.546	0.088	1.418
30	-56.50	295	0.117	0.019	1.418
45	40.00	355	0.107	0.002	1.912
60	70.80	372	0.003	3.9×10^{-4}	2.047
75	-10.00	325	0.0005	8×10^{-5}	1.667

MRS4-2091-008

Air properties are established at the reference temperature using Table 4. The accuracy of the recovery factor assumption is then checked and the recovery temperature recalculated if necessary.

3. The Reynolds Number

The boundary layer Reynolds number is then calculated:

$$Re^* = \frac{\rho^* VL}{\mu^*} \quad (14)$$

where, the density and viscosity are evaluated at the reference temperature.

4. The Nusselt Number

The average Nusselt number for a flat plate is then calculated

based on the following correlations. For other geometries, refer to Ref. 1:

$$Re^* \leq 10^7: Nu^* = 0.036 Re^{*0.8} Pr^{*0.333}$$

$$10^7 \leq Re^* \leq 10^9: Nu^* = \frac{0.277 Re^* Pr^{*0.333}}{(\log_{10} Re^*)^{2.584}} \quad (15)$$

5. The Overall Heat Transfer Coefficient

The overall heat transfer coefficient is obtained from the Nusselt number:

$$h = Nu^* \left(\frac{k^*}{L} \right) \quad (16)$$

Table 4 Air Properties at Sea Level

TEMP, K	DENSITY, kg/m ³	SPECIFIC HEAT, W-s/kg-K x10 ³	VISCOSITY, kg/m-s x10 ⁻⁵	THERMAL CONDUCTIVITY, W/m-K	Pr
200	1.7684	1.0061	1.3289	0.01809	.739
250	1.4128	1.0053	1.5990	0.02227	.722
300	1.1774	1.0057	1.8462	0.02624	.708
350	0.9980	1.0090	2.0750	0.03003	.697
400	0.8826	1.0140	2.2860	0.03365	.689
450	0.7833	1.0207	2.4840	0.03707	.683
500	0.7048	1.0295	2.6710	0.04038	.680
550	0.6423	1.0392	2.8480	0.04360	.680
600	0.5879	1.0551	3.0180	0.04659	.682
650	0.5430	1.0635	3.1770	0.04953	.682
700	0.5030	1.0752	3.3320	0.05230	.684
750	0.4709	1.0856	3.4810	0.05509	.686
800	0.4405	1.0978	3.6250	0.05779	.689
850	0.4149	1.1095	3.7650	0.06028	.692
900	0.3925	1.1212	3.8990	0.06279	.696
950	0.3716	1.1321	4.0230	0.06525	.699
1000	0.3524	1.1417	4.1520	0.06752	.702

MR94-2091-009

6. The Missile Skin Temperature

The missile temperature can be solved by an energy balance among heat sources, sinks, viscous dissipation, and radiation. An example of an energy balance on a missile structure is as follows:

$$\begin{aligned} \Sigma Q_i - \Sigma Q_o + \alpha H A_2 + h A (T_r - T) - \sigma \epsilon A_p (T^4 - T_{sky}^4) \\ = m C_v \frac{dT}{dt} \end{aligned} \quad (17)$$

where, ΣQ_i and ΣQ_o represents the heat into and out of the missile structure, respectively, from internal compartment heating and cooling. $\alpha H A_2$ is the energy absorbed by the missile structure. $h A (T_r - T)$ represents the aerodynamic heating of the missile. $\sigma \epsilon A_p (T^4 - T_{sky}^4)$ is the radiative cooling to the ambient sky temperature. Finally, $m C_v \frac{dT}{dt}$ is the energy storage term. If the right hand side of Eq 17 is set to zero, then a steady state solution is obtained.

Having calculated the wall temperature, the reference temperature, T^* , is then checked using Eq 12 and another iteration is performed, if necessary.

The procedure outlined above used a semi-infinite flat plate approximation for wall temperature calculation. The temperature calculated is the average missile temperature for the length of the missile. It should be noted that, if the leading surfaces of the missile are highly blunted, the wall temperature on the forward surface approaches the stagnation temperature. The stagnation temperature is given by:

$$T_s = T_\infty \left[1 + \left(\frac{\gamma - 1}{2} \right) M_\infty^2 \right] \quad (18)$$

REFERENCES

1. Chapman, A., Heat Transfer, Macmillan Co., NY, 2nd ed., 1964.
2. Seigel, R. and Howell, J.R., Thermal Radiation Heat Transfer, Hemisphere Co., NY, 2nd Ed., 1981.
3. Kreith, S. and Kreider, J.F., Principles of Solar Energy, McGraw-Hill, 1981.
4. Handbook of Supersonic Aerodynamics, Dept of the Navy, 1953.

Infrared Intensities from Missiles

SUMMARY

Infrared (IR) intensities from missiles is presented as part of the NATO Advisory Group for Aerospace Research & Development (AGARD) special course on "Missile Aerodynamics." The course focuses on the IR intensity components from a scene, including the emission and reflections from a missile. Also included is the missile source intensity, background intensity, and contrast intensity equations as well as the atmospheric attenuation equation.

NOMENCLATURE

- A_p = Area of the pixel, m^2
 $A_{j,j}$ = Projected area of the missile's j th facet in the line-of-sight of the E-O/IR system, m^2
 C_1 = Planck's first constant, $W \cdot \mu m^4 / m^2$
 C_2 = Planck's second constant, $\mu m \cdot K$
 $E_{E,\lambda}$ = Earth radiance, $W / sr \cdot \mu m^2$
 $E_{s,\lambda}$ = Solar irradiance, $W / sr \cdot \mu m^2$
 e_s = Unit normal vector from the sun
 e_j = Unit normal vector from the missile facet
 $I_{1,\lambda}$ = Spectral intensity of pixel 1, $W / sr \cdot \mu m$
 $I_{2,\lambda}$ = Spectral intensity of pixel 2, $W / sr \cdot \mu m$
 $I_{c,\lambda}$ = Spectral contrast intensity, $W / sr \cdot \mu m$
 $I_{E,\lambda}$ = Spectral earth reflected intensity, $W / sr \cdot \mu m$
 $I_{e,\lambda}$ = Spectral earth emitted intensity, $W / sr \cdot \mu m$
 $I_{HS,\lambda}$ = Spectral intensity of the horizontal sky, $W / sr \cdot \mu m$
 $I_{v,\lambda}$ = Spectral intensity entering atmospheric control volume, $W / sr \cdot \mu m$
 $I_{LS,\lambda}$ = Spectral intensity of the lower sky, $W / sr \cdot \mu m$
 $I_{u,\lambda}$ = Spectral intensity leaving atmospheric control volume, $W / sr \cdot \mu m$
 $I_{s,\lambda}$ = Spectral solar intensity, $W / sr \cdot \mu m$
 $I_{US,\lambda}$ = Spectral intensity of the upper sky, $W / sr \cdot \mu m$
 $L_{B1,\lambda}$ = Spectral radiance of the background seen in pixel 1, $W / sr \cdot \mu m \cdot m^2$
 $L_{B2,\lambda}$ = Spectral radiance of the background seen in pixel 2, $W / sr \cdot \mu m \cdot m^2$
 $L_{F,\lambda}$ = Spectral radiance of the foreground between the missile and the E-O/IR system, $W / sr \cdot \mu m$
 $L_{HS,\lambda}$ = Spectral radiance of the horizontal sky, $W / sr \cdot \mu m$
 $L_{LS,\lambda}$ = Spectral radiance of the lower sky, $W / sr \cdot \mu m$
 $L_{US,\lambda}$ = Spectral radiance of the upper sky, $W / sr \cdot \mu m$
 S = Atmospheric path length, km
 T = Temperature, K
 α_s = Absorption coefficient for aerosol components, $1/km$
 α_m = Absorption coefficient for molecular components, $1/km$
 ϵ_λ = Spectral Emissivity
 λ = Wavelength, μm
 π = 3.14...
 $\rho_{E,\lambda}$ = Diffuse spectral reflectivity of the earth
 σ_s = Absorption coefficient for aerosol components, $1/km$
 σ_m = Scattering coefficient for molecular components, $1/km$

$\tau_{1,\lambda}$ = Spectral atmospheric transmittance between the missile and the E-O/IR system

$\tau_{2,\lambda}$ = Spectral atmospheric transmittance between the missile and the sun

$\tau_{3,\lambda}$ = Spectral transmissivity between the earth and the missile

$\tau_{4,\lambda}$ = Spectral transmissivity between the sun and the earth

INTRODUCTION

The components of the IR intensities from missiles include structural emissions and reflections. The emission is a function of missile temperature and emissivity. For a missile exposed to ambient conditions, the reflected components include direct solar reflections, earthshine (including both earth reflected solar intensity and earth self-emission), cloudshine, and skyshine. Each of these components will be discussed based on a diffuse reflectivity consideration.

For the missile's propulsion system, there are also emission components from engine exhaust plumes and cavities. These emissions are also reflected from the missile. The emissions and reflections from engines and plumes will not be discussed.

Since these IR intensity components will be propagated through the atmosphere to the E-O/IR sensor, an introduction to atmospheric transmittance will be presented. When an unresolved missile is viewed by an E-O/IR sensor, then foreground and background radiances enter into the sensor's view. Consequently, a discussion will be made of the influence of the background and foreground radiances vis-a-vis the IR contrast equation.

EMITTED MISSILE INTENSITIES

Emitted missile intensities are obtained from Planck's Law by multiplying the black body radiance with the emissivity and the projected area of the missile (refer to Fig. 1). The projected area of the missile is projected into the direction of the viewing electro-optical (E-O)/IR sensor. To obtain the missile projected area, the missile is divided into small planar or triangular facets. The areas of each facet are computed, along with each corresponding outward normal vector. Observer orientations are then specified, along with a normal vector for each orientation. The dot product of the missile facet unit normal vector and each observer unit normal vector are then multiplied by the area of each facet. This product results in the projected area of the missile in the line-of-sight of the observer. In certain specified lines-of-sight, part of a missile may block another missile part (for example, the tail may block part of the fuselage). In such cases, the parts of a missile that are hidden from the line-of-sight must be excluded from the calculation. Upon this exclusion, the resulting missile emitted intensity in a specified line-of-sight is as follows:

$$I_{e,\lambda} = \frac{\tau_{1,\lambda} \epsilon_\lambda A_s 2C_1}{\lambda^5 [\exp(C_2/\lambda T) - 1]} \quad (1)$$

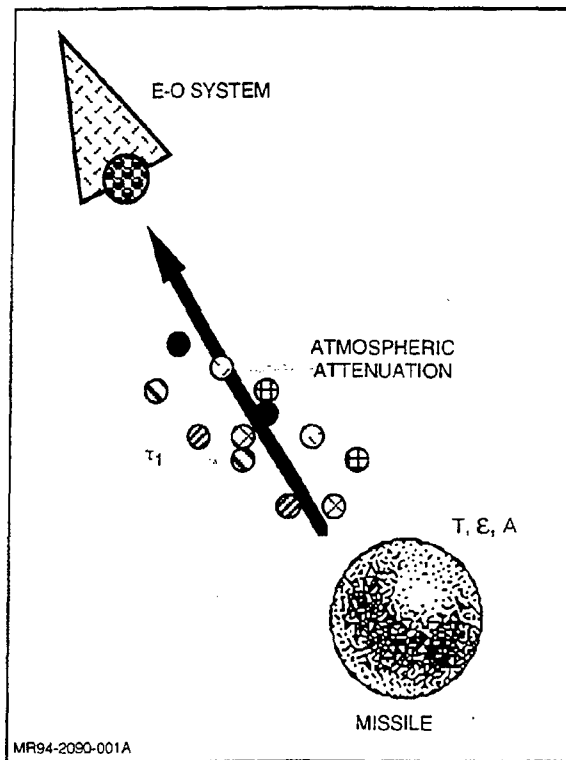


Fig. 1 Emitted IR Intensity from a Missile

Reflected Solar Intensity

Referring to Fig. 2, the reflected solar intensity is obtained by first propagating the solar irradiance through the atmosphere (the air between the edge of the atmosphere and the missile). The atmosphere will absorb part of the solar irradiance. The incident solar irradiance is then reflected by the missile. Once reflected, it is then partially absorbed by the atmosphere into the line-of-sight of the observer. Since the sun and the observer will both be oriented at different angular measurements to the missile, the dot products between the sun and the missile as well as between the missile and the observer need to be taken. The resulting solar reflection for the scenario results in the following equation:

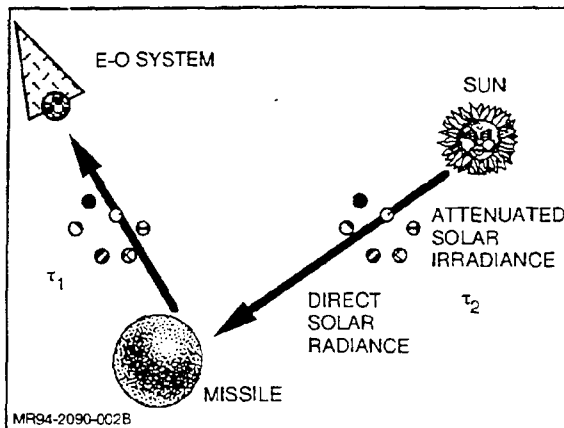


Fig. 2 Reflected IR Solar Intensity from a Missile

$$I_{s\lambda} = \tau_{1\lambda} \tau_{2\lambda} E_{s\lambda} A_s \frac{\rho_{d\lambda}}{\pi} (\hat{e}_s \cdot \hat{e}_j) \quad (2)$$

where $\hat{e}_s \cdot \hat{e}_j$ is the dot product between the solar unit vector and a missile facet unit normal vector.

Reflection of radiant solar energy from a missile surface in the direction of the observer is composed of both specular and diffuse reflections. The solar intensity reflected from the missile is the product of the solar irradiance at the edge of the atmosphere, the atmospheric path transmittance, the missile geometric configuration factor, and the missile skin spectral diffuse reflectivity.

For a typical airframe, the viewing aspects of interest with respect to solar reflections are the near nose-on, look-down and side-on. The directly reflected solar intensity is of significant interest under $3 \mu\text{m}$, because 98% of the total solar irradiance incident on the surface of the earth is under $3 \mu\text{m}$. (At $4 \mu\text{m}$, 99% of the total solar irradiance is incident on the earth's surface.)

Under many power flight conditions, solar heating effects are overwhelmed by aerodynamic heating effects. However, when thermal control devices are integrated into missile structures, the effect of solar heating needs to be accounted for in thermal heat balances (particularly for high-altitude subsonic missiles with a coating whose solar absorptivity is high).

REFLECTED EARTHSHINE AND CLOUDSHINE

Reflected earthshine and cloudshine consists of two components: the reflected direct thermal emission from either the earth or clouds, and the indirectly reflected solar irradiance from either the earth or clouds to the missile. Figure 3 illustrates these two components for the earth. The earth emission rate varies with season and latitude. The earth can be considered to be a uniform, diffuse emitter. The earth intensity is composed of the earth emitted and solar diffuse reflected energies. The emitted earth intensity reflected from the missile is the product of the black body (Planck's Law) earth emission, the earth emissivity, the missile's geometric factor, the missile's diffuse reflectivity from measured data, and the associated atmospheric transmissivity. The reflected solar energy from the earth is the product of the atmospheric-transmitted solar energy, the earth diffuse reflectivity, the missile geometric factor, the diffuse missile reflectivity, and the associated atmospheric transmissivity. The reflected earthshine from a surface is presented in the following equation:

$$I_{E\lambda} = \tau_{1\lambda} \tau_{3\lambda} \rho_{d\lambda} A_s \left\{ E_{e\lambda} \frac{\rho_{E,d,\lambda}}{\pi} \tau_{4\lambda} + E_{E\lambda} \frac{(1 - \rho_{E,d,\lambda})}{\pi} \right\} \quad (3)$$

The earth spectral reflectance varies significantly under $5 \mu\text{m}$ where earth solar reflections are significant, but varies less in the 8- to $12\text{-}\mu\text{m}$ band (except for rock and gravel) where thermal emission is significant. Water backgrounds must consider wave heights, salinity, and percent ice formation when measuring ocean spectral reflectance properties. Earth surface temperature variations have a more significant impact on background radiance than the earth's surface emissivity variations.

An analytical expression for cloudshine is analogous to Eq 3 except that the temperature of the cloud is assumed to be in equilibrium with its atmospheric surroundings. This atmospheric temperature is used in Planck's Law along with the cloud emissivity and area to obtain the intensity leaving the cloud.

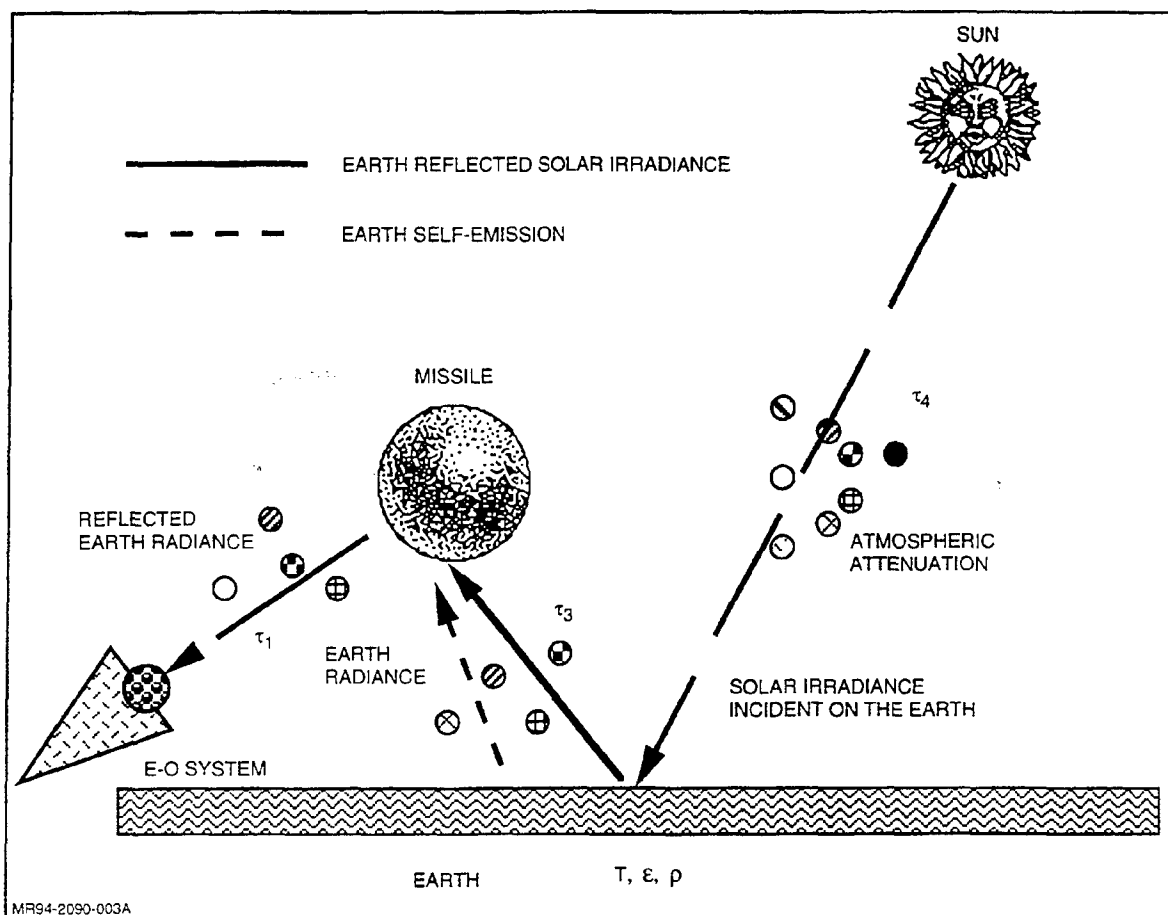


Fig. 3 Reflected Earthshine from a Missile

REFLECTED SKYSHINE

The reflected skyshine component is composed of scattered solar radiation and thermal emission from atmospheric constituents. The skyshine components can be categorized into solar and thermal spectral regions. The reflected skyshine intensity is the product of the atmospheric radiance, missile aspect-dependent geometric factor, atmospheric transmittance between the missile and observer, and the missile diffuse spectral reflectance.

Solar scattering is dominant under $3 \mu\text{m}$, whereas thermal emission dominates at wavelengths longer than $3 \mu\text{m}$. The skyshine radiance is incident upon the missile from all directions. To reduce the computing complexity of this incident radiance, each facet of the missile model is assumed to be isotropically irradiated by the sky radiance as viewed along the direction normal to the facet. The magnitude of the radiance viewed by any particular facet is approximated by a weighted average sky radiance in three standard, mutually orthogonal directions. These relations are as follows:

$$I_{LS,\lambda} = \rho_{d,\lambda} \tau_{1,\lambda} A_s L_{LS,\lambda} \quad (4)$$

$$I_{US,\lambda} = \rho_{d,\lambda} \tau_{1,\lambda} A_s L_{US,\lambda} \quad (5)$$

$$I_{HS,\lambda} = \rho_{d,\lambda} \tau_{1,\lambda} A_s L_{HS,\lambda} \quad (6)$$

If solar scattering is ignored, the atmospheric radiance is uniform in the horizontal plane. Consequently, only three directions are considered when calculating the orthogonal sky radiances: up, down, and a single horizontal direction. However, when solar scattering is included, all six orthogonal directions must be considered.

For sky radiance calculations, it can be assumed that the missile reflects diffusely. The resultant irradiance of all facets that can be seen is then reflected to the observer.

ATMOSPHERIC TRANSMISSION

With clouds in the FOV, the atmospheric transmittance is significantly degraded as compared to the atmospheric transmittance in a cloud-free line-of-sight (CFLOS) with aerosols.

The atmosphere is made-up of different molecules and aerosols that attenuate and radiate IR energies. Some of these molecules absorb and scatter energy as it travels through the atmosphere. The molecules that attenuate (absorb and scatter) and radiate (emit and scatter) electromagnetic energy include water vapor, carbon dioxide, ozone, nitric oxide, carbon monoxide, oxygen, methane, and nitrogen. Also, components such as dust and aerosols contribute to both atmospheric transmittance and radiance. Consequently, when a source emits energy, the surrounding atmosphere reduces that energy as the energy travels (propa-

gates) through the atmosphere. In general, the longer the atmospheric path, the more the source intensity will be attenuated. Also, the denser the atmosphere the lower the transmittance — depending on wavelength and the constituents found in the atmospheric path. Both the atmospheric attenuation and radiance are spatial (latitude, longitude, and altitude) and temporal (time) dependent quantities.

Figure 4 illustrates a control volume of atmospheric constituents. When energy propagates through this control volume, some of it is absorbed and scattered by the constituents or species. Through measurements, it has been determined that this attenuation of radiation can be determined from the following relation:

$$dI_{\lambda} = -[(\alpha + \sigma)_m + (\alpha + \sigma)_a] I_{\lambda} dS \quad (7)$$

where, the minus sign indicates a loss of energy as the energy propagates through the atmospheric path. In Eq 7, α and σ are the absorption and scattering coefficients, respectively, which are found experimentally. The subscripts m and a refer to molecular and aerosol components. The sum of the absorption coefficient and the scattering coefficient is often defined as the extinction coefficient, K . There are three forms of the extinction coefficient. The first form represents the total of the molecular and aerosol coefficients, the second represents the sum of the absorption and scattering coefficients due to molecular effects, and the third represents the sum of the absorption and scattering coefficients due to scattering effects.

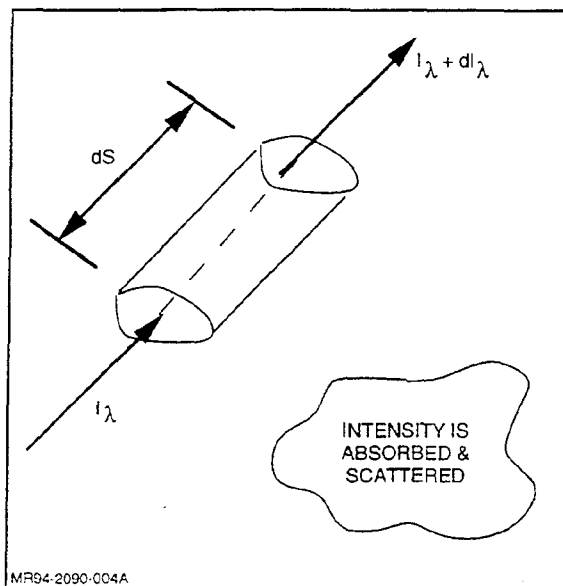


Fig. 4 Control Volume Used in Atmospheric Absorption & Scattering

Both the molecular absorption coefficient, α_m , and molecular scattering coefficient, σ_m , depend on the number density of molecules in the control volume. In addition, the molecular absorption is also a function of atmospheric temperature, pressure, and wavelength. The molecular scattering coefficient has been found to be approximately inversely proportional to the wavelength to the fourth power ($1/\lambda^4$).

The aerosol absorption coefficient, α_a , and aerosol scattering coefficient, σ_a are both functions of wavelength, the number density of aerosols in a control volume, the size distribution of the aerosols, and the complex index of refraction of the aerosols.

Since both molecules and aerosols vary in temperature and pressure, then altitude, latitude, and longitude will have an effect on the attenuation. In addition, since the atmosphere is dynamic in nature, both absorption and scattering coefficients are also time-dependent for both molecular and aerosol types.

There are two standard aerosol models used to determine the effects of aerosols on attenuation: the 23-km visibility model (or clear atmosphere) and the 5-km visibility model (or hazy atmosphere). Figure 5 illustrates these two models. For both atmospheric models, the aerosol size distribution at all altitudes is assumed to be the same. The difference between the two models is the particle density in the first 4 km of the atmosphere. Consequently, at altitudes of 5 km or greater, the particle density is the same.

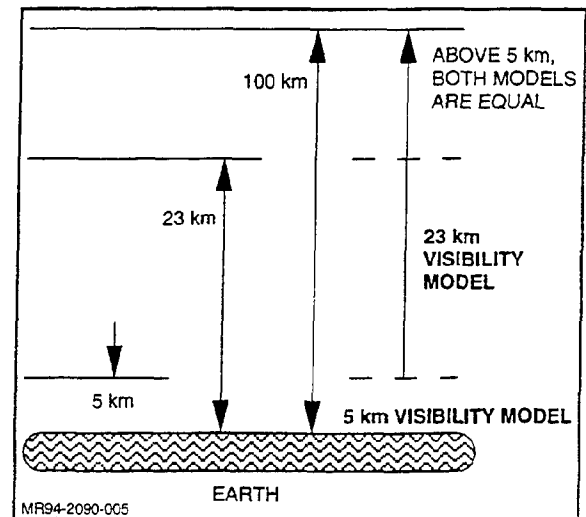


Fig. 5 Atmospheric Aerosol Models

Equation 7 is rearranged and integrated over the path length to yield Bouguer's Law.

$$I_{o,\lambda} = I_{i,\lambda} \exp \{ - [(\alpha + \sigma)_m + (\alpha + \sigma)_a] \Delta S \} \quad (8)$$

In Eq 8, $I_{i,\lambda}$ represents the intensity entering ('into') into the control volume, while $I_{o,\lambda}$ represents the intensity leaving ('out of') the control volume for a defined atmospheric path. ΔS is the path length. Bouguer's Law can be applied to any attenuating medium and states that, as radiation propagates along a defined path, it will be attenuated exponentially. The molecular and scattering coefficients are found experimentally for a defined atmospheric path.

To determine the atmospheric transmittance, three parameters must be known: the atmospheric path length, the spectrally dependent absorption and scattering coefficients, and the equivalent absorber density for a given atmospheric path. The last two parameters are determined empirically using measured data over a known path.

Atmospheric transmittance is defined from Bouguer's Law as the intensity leaving a specifically defined control volume to the intensity entering the control. By definition, the transmittance is obtained from Eq 8 as:

$$\tau_{\lambda} = \frac{I_{o,\lambda}}{I_{i,\lambda}} \quad (9)$$

In general, the atmosphere is divided into path lengths, each having measured properties as a function of altitude. Furthermore, to obtain the variation in latitude and longitude, the atmosphere is divided into defined regions. These regions include tropical, mid-latitude, polar, arctic, and specifically defined regions. To determine the quasi-transient effect, each region is further subdivided into winter and summer, e.g., tropical winter and tropical summer. Atmospheric data for specific days are usually recorded when performing outdoor measurements. In such measurements, the transmittance is measured between the source and the observer at multiple viewing aspect angles representing different atmospheric paths. The measured absorption and scattering coefficients are used in Bouguer's Law to determine the transmittance along a path length. A standard

computer code like LOWTRAN (Ref. 1) can be used to make these computations.

BACKGROUND AND FOREGROUND RADIANCES

The types of background radiances seen by an observer are dependent on the observer's position. An observer viewing in a direction below the horizon sees either the earth or a cloud layer in the background, along with atmospheric radiance occurring between either the earth or a cloud and the missile. The earth background spectral emission and reflection radiance components are computed as gray body earth emission and diffuse reflection of earth incident solar radiation, respectively. As shown in Fig. 6, (for a look-up viewing aspect angle) these components are attenuated through the atmosphere to the observer, and the atmospheric radiance contribution is added to produce the total background radiance. If either the earth or a cloud is not in the field-of-view (FOV), then the background radiance consists solely of atmospheric radiance.

Foreground radiance refers to the atmospheric radiance between the observer and the missile. The atmospheric foreground radiance is more important to consider in the 8- to 12- μm portion

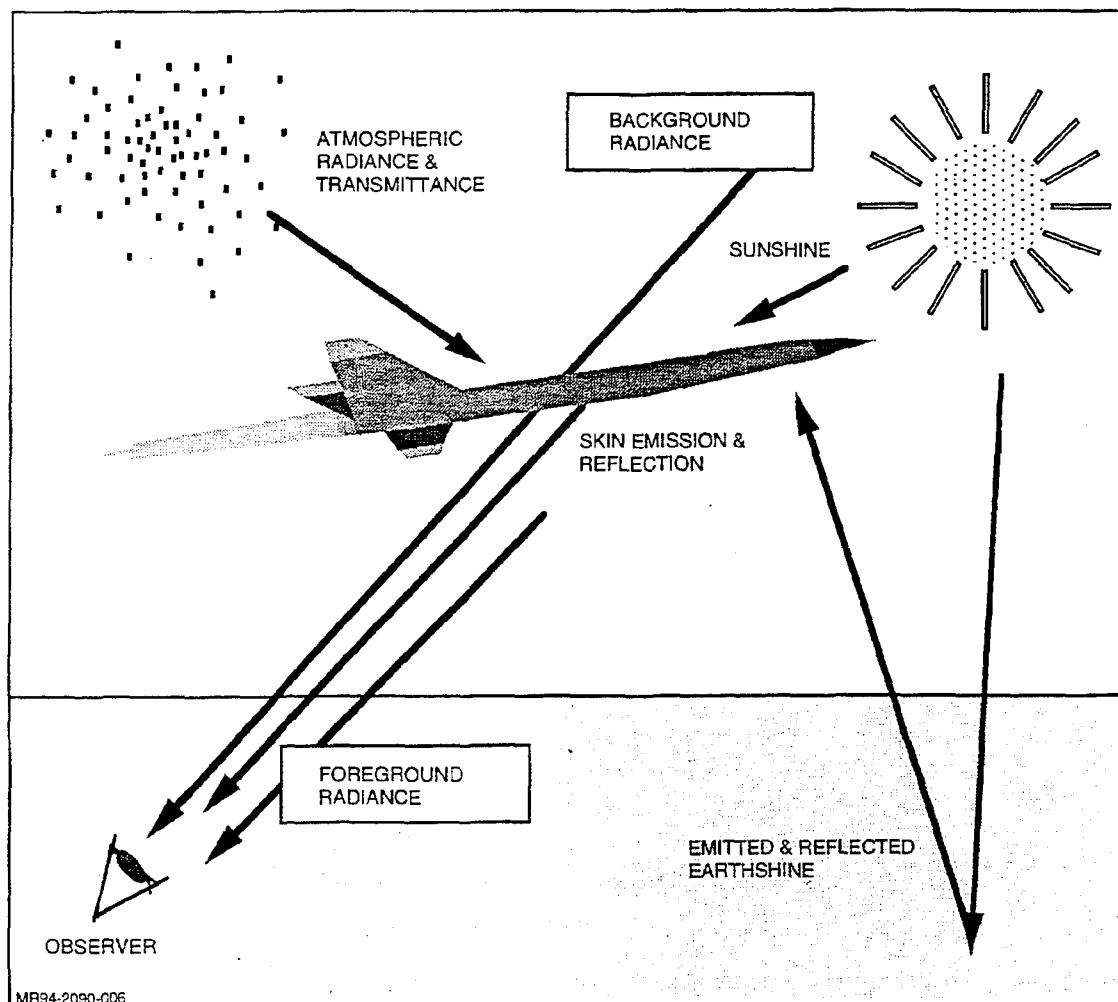


Fig. 6 Foreground & Background Radiances & Skin Emission & Reflection Components

than in the 3- to 5- μ m portion of the spectrum. Foreground atmospheric radiance is higher in the summer than in the winter due to the higher atmospheric temperatures along a line-of-sight (LOS) between the missile and sensor.

INFRARED CONTRAST INTENSITY

An E-O/IR sensor detects a missile based on a contrast difference calculation. The E-O/IR detector views two different FOV (or two different pixels) and measures the intensity in each. To determine the contrast, the E-O/IR system processor subtracts the

intensity in one pixel from that in another pixel and compares the differences.

Two pixels are illustrated in Fig. 7; one pixel contains a missile intensity while the other does not. In pixel 2-3, the intensity is computed by multiplying the atmospheric path radiance by the area of the pixel. This intensity is represented as:

$$I_{1,\lambda} = L_{B,\lambda} A_p \quad (10)$$

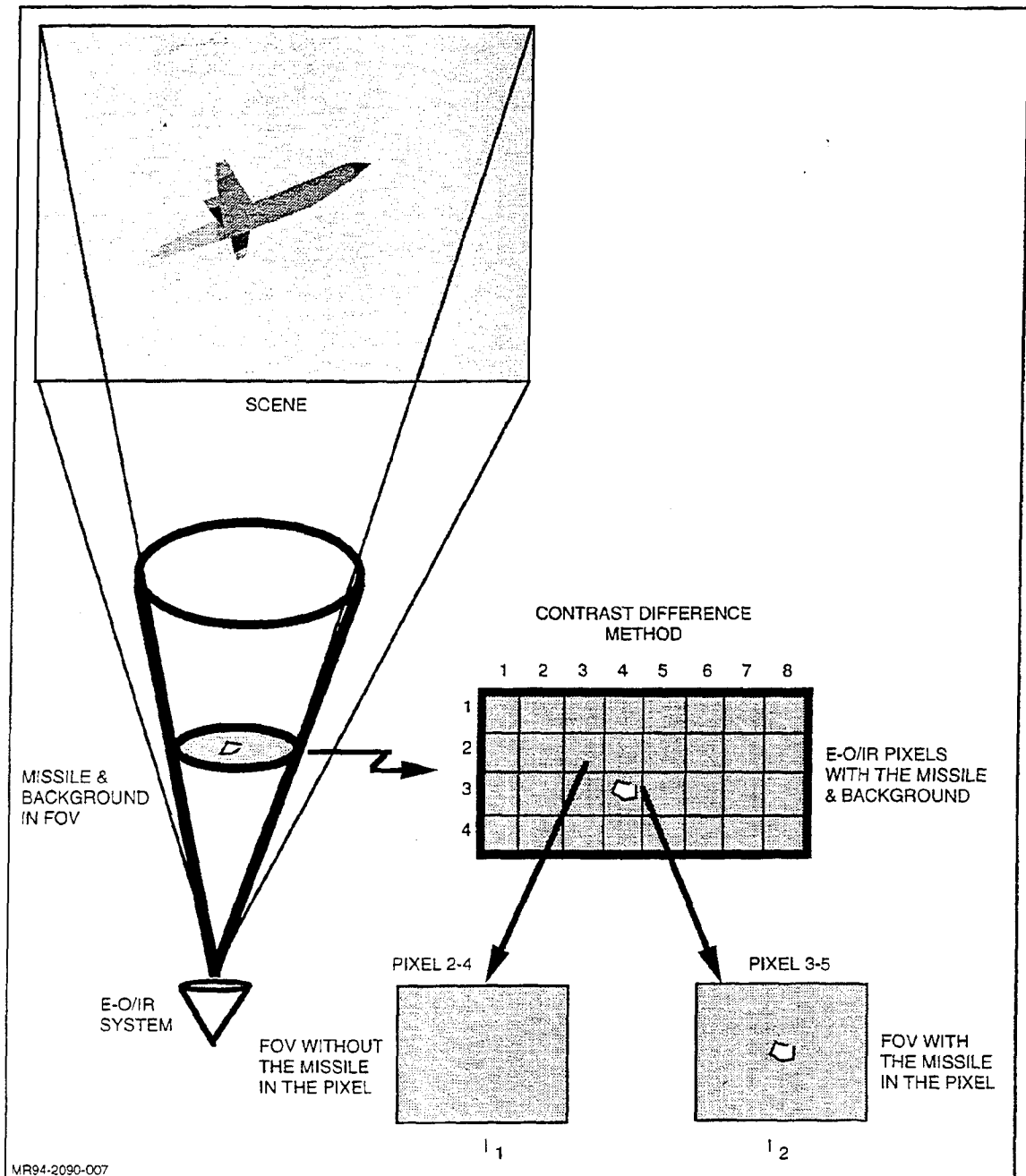


Fig. 7 IR Contract Intensity

In pixel 3-4, (in Fig. 7), the IR intensity is computed by considering the following three components:

- *The source intensity* – The missile source intensity includes reflected and emitted source intensity components that are attenuated by the atmosphere
- *The unacculted background intensity* – The unacculted background intensity includes the atmospheric path radiance (including earth or cloud radiances) multiplied by the unacculted area in the FOV. A typical missile is usually divided into planar surfaces known as facets that are summed as projected areas into the LOS of the E-O/IR system. The projected area of a facet is obtained by multiplying the planar area of the facet by the dot product of the outward normals from the facet and the E-O/IR system
- *The foreground intensity* – The foreground intensity is the product of the atmospheric foreground radiance (between the missile and the E-O/IR system) and the projected area of the missile in a given line-of-sight.

The intensity for pixel 2 is:

$$I_{2\lambda} = \sum_i I_{i,\lambda} + L_{B\lambda} \left(A_p - \sum_{j=1}^n A_{s,j} \right) + L_{F,\lambda} \sum_{j=1}^n A_{s,j} \quad (11)$$

In Eq 11, $I_{i,\lambda}$ includes the transmitted-emitted missile intensity as well as the transmitted-reflected solar, earthshine, and skyshine intensities (Eq 1 through 6).

The intensities computed in pixels 1 and 2 are then subtracted from one another (Eq 11 minus Eq 10) to obtain the following contrast difference:

$$I_{c,\lambda} = \sum_i I_{i,\lambda} - (L_{B\lambda} - L_{F,\lambda}) \sum_{j=1}^n A_{s,j} - (L'_{B,\lambda} - L_{B\lambda}) A_p \quad (12)$$

In Eq 12, the prime superscript represents the background radiance related to pixel 2-3. In Eq 12, the IR contrast can either be positive, negative, zero, or any combination in the spectrum. This depends on the magnitude of the missile intensity and the difference between the background and foreground intensities. In Eq 10 and 11, if the background radiances are equal to one another, then Eq 12 becomes

$$I_{c,\lambda} = \sum_i I_{i,\lambda} - (L_{B,\lambda} - L_{F,\lambda}) \sum_{j=1}^n A_{s,j} \quad (13)$$

REFERENCES

1. Kneizys, F.X., et al., "Atmospheric Transmittance/Radiance: Computer Code - LOWTRAN7," AF Geophysics Lab 1988.

HIGH ANGLE OF ATTACK AERODYNAMICS

P. CHAMPIGNY

Office National d'Etudes et de Recherches Aéropatiales (ONERA)
29, Avenue de la Division Leclerc - 92320 CHATILLON (FRANCE)

ABSTRACT

The demand for continually increased performance of missiles and aircraft leads to considering flight at very high angles of attack where control is very difficult.

This is mainly due to the shedding of asymmetric vortices from the forebody, producing side forces even at zero sideslip.

The purpose of this paper is not to make a review of missile aerodynamics at high angle of attack (for that, see for example [1]), but to focus on an understanding of the phenomena which give rise to asymmetric vortices, from an experimental as well as a theoretical point of view.

1. INTRODUCTION

The demand for increased maneuverability of fighter aircraft and missiles leads to considering flights at much higher angles of attack than before.

For instance, during fighter aircraft dogfights or the tilting sequence of a vertically launched missile, the angles of attack can be up to 50 degrees or even more (fig. 1).

In this flight domain, the flow around missiles or aircraft is very complex. It is characterized by the presence of very large separated regions with strong vortex sheets propagating from the nose of the vehicle.

Above a certain angle of attack, these forebody vortices develop asymmetrically (fig. 2) even on a symmetric configuration at zero sideslip. They give rise to spurious aerodynamic forces and moments that are difficult to control.

To illustrate this problem, figure 3 shows that side forces appear at angles of attack of more than 20 degrees on a simple body of revolution and can exceed the lift at around 50 degrees, even with zero sideslip.

If there are wings attached to the fuselage, the asymmetric vortices generate on the wings even larger spurious forces and moments. For instance, for a missile type configuration, figure 4 shows that the induced roll moments are so strong that the control surfaces are incapable of controlling them.

Similarly, figure 5 demonstrates the importance of yawing moment induced on a fighter aircraft

configuration compared with that created by deflection of the rudders.

Furthermore, for those who have doubts about the real existence of such asymmetric flows on symmetric configurations and believe that they only occur in wind-tunnels, it should be pointed out that the same types of problems were identified in flight, for instance on the NORTHROP F5F aircraft in the mid-1970s [1], figure 6.

The existence of asymmetric flows at high angles of attack has been known for nearly 40 years [2], but it is only in the last 25 years, after wind-tunnel testing on realistic missile and fighter aircraft configurations showed that flight control at high angles of attack became very difficult or even impossible, that a large amount of work has been conducted on the problem.

Initially, the work was experimental and was first aimed at quantifying the phenomena. Then it was attempted to gain a better understanding of them, minimize their effects and finally control them.

Theoretical work (in particular Navier-Stokes computations) has only been undertaken in the last few years, again for the purpose of understanding these complex flows.

The literature on the subject is very abundant. In particular can be mentioned the synopsis documents of ERICSSON and REDING [3], [4] and MALCOM [5].

Based on all this work, we propose herein in a first part to at least partially answer three basic questions:

- WHY does the flow become asymmetric?
- WHEN do these phenomena occur?
- HOW can their effects be minimized or controlled?

In a second part, the situation relative to prediction methods and especially to numerical simulations of such flows will be reviewed.

2. BACKGROUND

First of all, it should be noted that we will essentially be concerned here with flows around bodies of revolution, representing missile or fighter aircraft forebodies. In effect, as we surmised and as will be developed below, the spurious side forces are generated by vortices shed from the fuselage nose, i.e. on shapes that are axisymmetric in the case of missiles and very nearly so (rounded shapes with a plane of symmetry) for aircraft.

Before analyzing these complex phenomena related to high angles of attack in detail, the flows occurring on a body of revolution according to its angle of attack should be recalled (fig. 7).

At very low angles of attack ($\alpha \leq 5$ degrees), the flow remains attached to the fuselage and the axial component of the flow predominates, although the transverse component is already responsible for thickening of the boundary layer on the leeward side. The potential flow theory generally accounts satisfactorily for this first flow state and the forces that develop, such as for instance a lift that varies linearly with the angle of attack.

At moderate angles of attack ($5 \text{ degrees} \leq \alpha \leq 25$ degrees), the crossflow becomes increasingly important, and, under the effect of positive transverse pressure gradients, the boundary layer separates on the leeward side of the fuselage to give rise to two symmetric vortex sheets. The lift then increases nonlinearly with a so-called vortex lift term.

For even higher angles of attack up to around 60 degrees, the leeward vortices develop asymmetrically giving rise to spurious side forces. We will see below why these vortices are asymmetric.

For very long bodies, there can be several pairs of asymmetric vortices. This is because one of the first two asymmetric vortices moves faster away from the fuselage than the other, until the vortex sheet separates to give a free vortex. A new vortex sheet then forms along the fuselage. This process is repeated alternately all along the fuselage. Seen from the rear, this vortex structure resembles the well-known Karman vortex street. However, the influence of the axial flow is still strong enough to ensure that this complex structure

remains stable over time. The distribution of side forces therefore is sinusoidal (fig. 8), and each maximum corresponds to the detachment of a vortex sheet.

On pointed bodies, the vortex asymmetry usually begins at the nose, and the rate at which the vortices are shed increases with the angle of attack. This can be seen figure 9, which presents local side force distributions. When α increases, the alternating side force cells are smaller and smaller which corresponds to an increase of the vortex shedding frequency.

To describe this vortex shedding process, a time-space equivalence between the Von-Karman unsteady asymmetric wake in 2D flow and the steady asymmetric vortex pattern in 3D flow can be made [23].

According to the definition of the Strouhal number, and to the sketch of flow pattern illustrated in figure 10, this yields for the distance between two successive peaks of the side force distribution to the relation:

$$\Delta x_{\max} / D = 1 / (2.S.\tan\alpha)$$

where S is the Strouhal number.

Figure 11 shows that this analogy is quite in a good agreement with experimental results obtained at ONERA on a pointed ogive-cylinder and that it gives the correct trend.

It should be noticed that for blunted nose bodies, a second type of vortex shedding occurs (figure 12). The asymmetric vortices develop first at the rear of the body, and the alternating vortex shedding does not occur as readily; thus the side force cells are much larger and can cover the entire cylindrical aft body.

Finally, for very large angles of attack, the flow become disorganized and turns into an unsteady flow of the wake type, like that found on a cylinder in crossflow.

3. WHY DOES THE FLOW BECOME ASYMMETRIC?

Several mechanisms were suggested as being responsible for the asymmetric vortices on axisymmetric bodies in recent years. They are investigated below.

The first, fully viscous in origin, is based on the fact that when the angle of attack increases, the vortices, initially symmetric, degenerate into asymmetric vortices because the separation lines on either sides of the fuselage become asymmetric. It is as if there were a laminar type separation on one side and a transitional or turbulent separation on the other. It is well known

that on a cylinder in a crossflow, this leads to variations of around 50 degrees in the angular position of the separation line.

However, this hypothesis is not consistent with the effect of the Reynolds number, which has been investigated experimentally. In effect, according to this hypothesis, it is in the region where the Reynolds numbers are critical (i.e. at the transition of the flow from laminar to turbulent) that these phenomena should be the most pronounced. But the many experiments conducted in this range, such as the work of LAMONT [6] shows that the side forces are smallest in this region (fig. 13) whereas they are very large at low Reynolds numbers where the flow is completely laminar.

In addition, by simple inviscid fluid computations (potential flow + vortex line model), FIDDES [8] showed that with this hypothesis of asymmetric separation lines, it was not possible to generate induced side forces of the same order of magnitude as those measured in wind-tunnels. The forces generated are too small.

The second mechanism suggested, which currently seems the most plausible, is of inviscid origin and is related to the unstable character of the flow.

More specifically, it is assumed that above a certain angle of attack, it is no longer possible for two strong contrarotating vortices to coexist symmetrically. A very small perturbation (inhomogeneous upstream flow, slight geometrical defect, etc.) is then sufficient to cause the vortex system to go from an unstable symmetric state to a stable asymmetric state.

This flow instability mechanism was revealed numerically by FIDDES, again in reference [8]. In particular, he showed that solutions of the second family (by contrast with the first, corresponding to an asymmetric state of the separation lines) appeared above a certain angle of attack and led to very large side forces of the same order of magnitude as those measured in wind-tunnels (fig. 14).

Similarly, several recent papers [9], [10] and [11], discuss stable asymmetric solutions in Navier-Stokes computations.

It should also be noted that asymmetric vortex sheets on symmetric configurations are also encountered on delta wings at high angles of attack [12], whereas the separation lines are symmetric (sharp leading edges of the wing).

So, we may conclude that it is not an asymmetry in the separation lines that is responsible for the formation of asymmetric vortices, but rather an instability in the flow. However, this has the consequence that the separation lines will not necessarily remain symmetric

(fig. 8).

The mechanism triggering these phenomena may originate mainly from two sources: the upstream flow and/or the forebody.

Concerning the upstream flow, a global defect in flow symmetry can first be imagined, i.e. a slight sideslip. Firstly, it is not this sideslip, which does not exceed a few degrees in standard wind-tunnels, that is responsible for the side forces. As we saw above, the side forces may exceed the lift on a body of revolution, at an angle of attack of around 50 degrees. Secondly, experiments [5] showed that the sign of the side forces is not altered by either a positive or a negative sideslip (fig. 15), at high angle of attack.

Another source of upstream flow irregularity is the turbulence.

According to the experiments conducted by HUNT and DEXTER [13] in two wind-tunnels, one highly turbulent (0.7%) and the other rather quiet (0.01%), it was observed that turbulence could in certain cases cause an asymmetry of the flow, but only randomly with no stability (fig. 16a, $\alpha = 30$ degrees) or that it could destroy the stable character of the asymmetric flow (fig. 16b, $\alpha = 50$ degrees).

This means that the upstream flow is clearly not responsible for these asymmetries, and it is now generally accepted that microscopic irregularities of the forebody geometry are what trigger this process of asymmetric vortices.

This was shown experimentally by various authors [6], [7], [14], [15] and [16] when investigating the effect of roll orientation of the model. In effect, when the model rotates about its axis of symmetry, the side forces are generally observed to oscillate about two extreme symmetric values ($\pm |C_{Y_{max}}|$).

More specifically, it was demonstrated by the author [16] that on a very smooth model (mean roughness $Ra = 0.1 \mu m$), the side forces alternated between $\pm |C_{Y_{max}}|$ during a complete revolution of the model (fig. 17a). This means that even on this almost perfect model, there must have been a microscopic irregularity that caused the asymmetric vortex system to arise in one direction or in the symmetrically opposite direction. In addition, this figure shows the stable character of the asymmetric flow through ranges of about 180 degrees, which may correspond to a location of the microscopic irregularity either on the right or on the left side.

By contrast, on a very rough model (fig. 17b), there are an infinity of "triggers", and for this reason, the flow seems less stable and the side force versus the roll orientation varies much more randomly even though it

is relatively reproducible.

To stabilize the flow in a given asymmetric position, a small excrescence can be added on the model nose [14]. However, this excrescence should be placed in the vicinity of the very tip of the nose, since that is this region which controls the flow (fig. 18).

When numerically simulating these flows [9], [10] and [11], stable asymmetric solutions are obtained by adding a small surface imperfection which does not moreover disturb the flow at moderate angles of attack (stable symmetric solution).

It should be emphasized that although it is not possible a priori to predetermine the direction of these side forces, they are fully reproducible as is shown in figures 17 and 19 giving the measurements made in fixed positions or variable positions of the model.

As was seen above in highly turbulent wind-tunnels, and as is also the case for very rough models, a certain flow instability can be observed, in particular in the vicinity of the critical Reynolds numbers. This may be explained by the fact that these two parameters (turbulence, roughness) play a basic role in transition of the boundary layer and the side forces are then strongly dependent on its nature.

However, even under stable flow conditions, a certain fluctuation is always observed in wind-tunnel, especially when the model support system is flexible. This is particularly true when measuring the overall forces with a balance (fig. 20). It should however be noted from this figure that the force oscillations never cause the flow to go from one state of equilibrium to the symmetrically opposite state.

4. WHEN DO THESE PHENOMENA OCCUR?

After analyzing the mechanisms leading to the appearance of side forces at high angles of attack, we must now examine whether these phenomena always occur according to the flight domain considered, i.e. according to the values of:

- angle of attack,
- Mach number,
- Reynolds number.

As we already saw, the angle of attack has to reach a certain level ($\alpha_0 \approx 25^\circ$) for asymmetric vortices to occur.

More precisely, this angle of attack depends on the shape of the forebody and the length of the fuselage [17], [18]. It is therefore generally observed that the slenderer the ogive or the longer the fuselage is, the lower α_0 is (fig. 21).

In addition, this limit angle of attack appears to be lower in a turbulent flow (with a high Reynolds number) than in a laminar flow or, which is equivalent, on very rough surfaces (fig. 22).

As concerns the Mach number, it is generally observed that side forces only occur for subsonic Mach numbers [19], [20], which is unfortunately the flight domain in which maneuvers at very high angles of attack are required.

For instance, figure 23 shows that although the side force is very large up to Mach 0.5, it is already much lower at Mach 0.8 and has almost disappeared at Mach 1.15.

The near absence of asymmetric flows at supersonic speeds is explained by the fact that the crossflow Mach numbers are high at the angles of attack considered and are such that shocks appear on the leeward side of the fuselage, making flow separations symmetric. This is shown in figure 24 containing many experimental results presented as maximum side force versus crossflow Mach number. A drop in $C_{Y_{max}}$ above Mach 0.5 is clearly visible.

Referring to the diagram showing the angle of attack versus the Mach number in figure 25, it is clear that the range of appearance of side forces is limited to subsonic Mach numbers, for the angle of attack range considered and the limit $Mo \sin \alpha \leq 0.5$.

The third major parameter for these phenomena is the Reynolds number. Its influence was mainly investigated by LAMONT [6], [21], [22] and the author [23]. Their results showed that large side forces occurred just as well at low Reynolds numbers (laminar flow) as at high Reynolds numbers (turbulent flow), figures 13 and 26.

However, there is an intermediate range where the side forces are very small or even disappear, corresponding to Reynolds numbers of around 0.5 to 1×10^6 , i.e. when the boundary layer is in a transitional state. The shape of the C_Y curve versus the Reynolds number (fig. 27) is then similar to that of the drag coefficient of a cylinder in a crossflow.

The absence of significant side forces at critical Reynolds numbers is explained by the fact that since the boundary layer separates so late on the leeward side, firstly the vortex sheets are not well formed and are weak, but secondly, the separation asymmetry only affects the pressures in a region ($\phi > 140^\circ$) where they are relatively ineffective in producing a side force. This also explains why the lift is low in this range of Reynolds numbers.

Figure 27 also shows that the maximum side force occurs around $Re_D = 0.45 \times 10^6$ i.e. within the limit of subcritical and critical Reynolds numbers. In this case,

the boundary layers on the two sides of the fuselage are probably not in the same state (laminar on one side and transitional on the other). Although this does not cause the asymmetry, as we saw above, it provides the maximum differential in the separation location ($\phi \approx 80^\circ$ to 140°) and so the maximum pressure differential on opposite sides of the body.

In addition, observing the longitudinal distribution of local side forces (fig. 28), it can be seen that for this Reynolds number ($Re_D \approx 0.44 \times 10^6$) it has a shape somewhat different from the others. That is, the $C_{Y_{local}}$ is generally sinusoidal (because of vortex shedding) whereas it never changes sign at this Reynolds number. This gives a very large total force integrated along the length of the fuselage. According to ERICSSON [4], this phenomenon may be due to a moving wall effect, particularly pronounced at critical Reynolds numbers.

This phenomenon is well known for a rotating cylinder in a crossflow [34]. A Magnus force is created by the spin, due to the asymmetry of the separation points. However, in the critical flow regime, this force has the opposite sign and is much higher than what occurs in a subcritical or a supercritical flow, because of a change in the type of separation (fig. 29).

For the experiment considered, it is sufficient for the model to have a slight conical motion in wind-tunnel (a setup not entirely rigid, excited by aerodynamic effects) for the boundary layer separations to be greatly altered and to occur asymmetrically and continuously over the full length of the fuselage.

5. HOW CAN THE ASYMMETRIC VORTEX EFFECTS BE REDUCED OR CONTROLLED?

Because of the flight conditions (angle of attack, Mach number, Reynolds number) for which maneuvers at high angles of attack are considered, such spurious forces caused by asymmetric vortices will always exist.

To allow control, it is necessary to find a favorable geometry to minimize these effects.

At the same time, it could be attempted to put these phenomena to use for flight control.

These two points are developed below.

5.1. How Can the Effects of Asymmetric Vortices Be Reduced?

As was seen above, asymmetric vortices arise on the fuselage nose, which means that the shape of the forebody has a large influence on these phenomena [20], [24].

To reduce the side forces, the ogive should be short and slightly blunted (fig. 30). Moreover the angle of

attack at which they appear will be greater.

Another way of reducing the effects of asymmetric vortices could be to make them symmetric or to destabilize them.

In the first case, strakes [4], [24] or trips [25] can be added on either sides of the fuselage (fig. 31). But they must be located as close as possible to the tip and must be symmetric with respect to the plane of incidence. Otherwise, the side forces could be even larger than on a smooth ogive. This requires accurate control of the aircraft or missile and is therefore generally not possible for a missile which must be able to maneuver in any direction (bank to turn).

Among the devices that could destabilize the vortex sheets can be mentioned:

- . nose booms [24],
- . vortex generators on the ogive [26],
- . jet blowing [5], [27], [28],
- . spinning nose with strips [29].

The first three devices are not very effective and the third is too sensitive to flight conditions. Only the last device (fig. 32) appears able to substantially reduce the side forces, but it is more complicated technologically (spinning of the nose).

When attempting to optimize the global configuration of an aircraft, and even more especially for a missile, some wing configurations appear preferable from the standpoint of side forces at high angles of attack. This is true, for instance, of a configuration with wings located very far forward (fig. 33). In this case, the forebody vortices do not have time to develop before encountering the wings which make the flow symmetric again.

5.2. How Can the Vortices Be Controlled?

As we already saw, the presence of asymmetric vortices developing on the forebody means that many aircraft or missiles required to operate at high angles of attack are uncontrollable. This gave the idea of using these vortices, responsible for the problem, to control the vehicle, in particular aircraft.

Several techniques for "manipulating" or controlling the forebody vortices have been considered and tested in wind-tunnels [5]. They are all based on modifying the fuselage nose to control separation.

The following can be mentioned in particular:

- . strakes that are retractable or rotatable [5], [31], [33],
- . blowing or suction through holes or slots [5], [30].

5.2.1. Strakes

Strakes may have a dual purpose:

- . they can cause asymmetric vortices to form naturally in a given direction, which is the case for very small strakes;
- . they can force the direction of asymmetry by action on the separations and additional vortex energy which is the case of larger strakes.

Both these mechanisms are involved in retractable strakes (variable span) whereby the same pair of strakes is used to cancel the side forces or, to control the direction and, to a certain extent, the intensity of the side forces and moments (fig. 34).

Another solution consists of using a single strake or a pair of strakes with a fixed span but rotatable (fig. 35). This solution is more flexible as regards its efficiency over a wide range of angles of attack and sideslip.

The drawback of these devices resides in the fact that they modify the external shape of the forebody (interference with the radar?) and require moving devices.

5.2.2. Blowing - Suction

Blowing on a forebody at a high angle of attack may have various effects, depending on how it is done.

If blowing is tangential to the wall and upstream of the separation, it gives energy to the boundary layer and thereby delays its separation.

If it is performed under a vortex sheet, it will modify the vortex position by an entrainment effect.

So we can see that it is possible to control the vortex asymmetries in both cases and therefore the induced forces.

For instance, figure 36 shows how the yawing moment can be modulated by combining two blowings, one on either side of the ogive.

It should however be noted that the experiments conducted have shown that it might prove difficult to keep a flow symmetric at a high angle of attack by blowing and that it may prove necessary to add strakes.

Furthermore, as is the case for strakes, it is difficult to control the level of the induced forces because the efficiency depends on a number of parameters, in particular the angle of attack, the sideslip, and the Reynolds number.

On the same principle of "manipulating" the boundary

layer and the separations, a suction device can also be used. However, the possibilities of such a device have not so far been investigated as much the previous device.

More practical to use, these two devices are also easier to implement than strakes: fewer changes in the external shapes, pneumatic rather than mechanical parts; however, integration of such devices in the aircraft nose must be compatible with the presence of a homing system.

6. PREDICTION METHODS

6.1. Empirical methods

The earliest methods considered were based upon inviscid flow modeling of the vortices. These methods used either the impulsively started cylinder flow analogy or the time-space equivalence between the Von-Karman unsteady asymmetric vortex wake in 2D flow and the steady asymmetric vortex wake in 3D flow.

Thus they are applicable only to the cylindrical aft body, and so, not for the case when asymmetric vortex shedding starts on a pointed nose which is the most common case.

They can give qualitative informations about the angle of attack for incipient asymmetric vortex shedding but they can not predict the experimentally obtained asymmetric loads, neglecting the dominating influence of the nose.

A method of practical use for the prediction of maximum possible $C_{y_{max}}$ on body of revolution was developed assuming the analogy between the peak unsteady lift on a 2D cylinder and the steady side force on an inclined body [3].

This technique is of course valid only for bodies dominated by a single asymmetric vortex pair, but its corresponds to the case which gives the maximum side load.

Thus, the overall vortex-induced side force to normal force ratio can be bounded by:

$$|C_{y_{max}}| / C_N = 0.5 C_{lp} / C_d$$

where C_{lp} / C_d is the peak unsteady lift to drag ratio of a cylinder in 2D flow, function of the Reynolds number (figure 37).

6.2. Navier-Stokes simulations

Progress in numerical methods has been such that Navier-Stokes computations, which are the only ones capable of providing realistic simulations, are

beginning to be used to gain a better understanding of these flows.

The results obtained by DEGANI [9] and SCHIFF [36] for laminar flows ($Re_D = 0.2 \cdot 10^6$), demonstrate the marked asymmetry which has been observed in experiments. But they found that it is essential to introduce a space-fixed, time invariant perturbation (a small geometrical bump or a small jet blowing normal to the body) into the computation to simulate asymmetric flows.

Apparently, for laminar flows, the most sensitive circumferential angles to place a disturbance are between 90 to 140° from the windward plane of symmetry.

Time-accurate solutions of a thin layer Navier-Stokes code are presented in figure 38 for $\alpha = 40^\circ$. We can observe that these solutions present a high level of unsteadiness and are highly dependent on the size of disturbance. Moreover it was noted that the flow relaxes back to its initial symmetric state when the perturbation is removed.

At an angle of attack of 20° , the flow was steady and symmetric, and the presence of a perturbation made only a small change.

So it is suggested that the asymmetric flow which exists for high angle of attack is the result of disturbing a convectively unstable symmetric flow.

For turbulent flow conditions often existing in full-scale flight, computations have also been attempted [10], [11].

DEGANI and LEVY [11], found again that in order to reproduce any one of the experimentally observed flowfield, it was necessary to add a small geometrical disturbance near the body apex (figure 39).

They also found that when the disturbance is removed, the flowfield returns to its original symmetric shape (figure 40).

By determining an appropriate size of the disturbance, it seems possible to obtain excellent agreement between experiments and numerical results (figure 41), but this problem becomes more tricky if it is desired to predict the asymmetric flow around a given configuration. And even if we knew the exact geometry of the body, would it be possible to have a sufficient grid resolution to reproduce the shape of small imperfections on the nose?

About the necessity of introducing a small disturbance, HARTWICH and all [10] found that asymmetric solutions could be obtained with axisymmetric body, triggered by machine accuracy, but the asymmetry is

low compared to experimental results (figure 42).

This behavior is reinforced by SICLARI and MARCONI results [35]. Computations were carried out with the assumption of conical flow, for a 5° circular cone at Mach 1.8.

These calculations demonstrate the existence of asymmetric solutions for high angles of attack as shown by FIDDES with his vortex sheet modeling.

An example of the convergence history of such calculations is shown figure 43. Computations are started with symmetric freestream conditions, and the solution seems first to converge toward a symmetric flowfield, but then the residuals increase to about their original level and then, decline again to reach machine zero, and the solution is therefore asymmetric. It must be concluded that the symmetric state is unstable since machine zero cannot be maintained, and this was verified for any angles of attack in the range $2.5 \leq \alpha/O \leq 5.0$ (figure 44). This figure shows that the Navier-Stokes solutions compare remarkably well with the experimental data.

Moreover, it should be noted that a monotomic convergence to the asymmetric solution could be achieved if a small asymmetry was introduced into the initial conditions.

In conclusion, all these calculations reinforce the assumption that at high angles of attack the flow is unstable, and that asymmetric flows are the result of disturbing a convectively unstable symmetric flow.

7. CONCLUSIONS - RECOMMENDATIONS

This review of flows at high angles of attack identified the problems related to the existence of asymmetric vortices on symmetric configurations. In this respect, it was seen that:

- . the asymmetric vortices are probably due to a flow instability and the phenomena are triggered by microscopic irregularities on the nose, making the influence of the forebody predominant;
- . asymmetric separations on the nose are not the cause but rather a consequence of the phenomenon;
- . stable, reproducible side forces and moments occur in the flight domain: $20 \text{ degrees} \leq \alpha \leq 60 \text{ degrees}$ and $\text{Mach} \leq 1$;
- . these forces and moments are highly dependent on the Reynolds number.

Considering the very strong influence of the forebody geometry, it is generally impossible to make a preliminary estimate of the forces and moments

induced on a given configuration. Currently, only wind-tunnel testing can give the order of magnitude of their level, but certain precautions are required:

- . the tests must be conducted over the complete range of angles of attack (0 to 90 degrees) and roll of the forebody (0 to 360 degrees) to be sure that the maxima of side forces and moments have been measured;
- . if possible, the tests must be performed in the flight Reynolds number range. Otherwise, it is preferable to remain at a low Reynolds number ($Re_D \leq 0.3 \times 10^6$) rather than at the maximum Reynolds number of the wind-tunnel which could correspond to a critical Reynolds number for which the induced effects are small. In addition, it is pointless to use boundary layer transition devices which cannot simulate a turbulent boundary layer over the full range of angles of attack, but which would lead to very different flows because of the influence of surface roughnesses on the induced forces;
- . similarly, during laminar tests, it must be made sure that the turbulence in the wind-tunnel is low ($\leq 0.1\%$) otherwise the phenomena may disappear [32];
- . insofar as possible, the setup used should be rigid to prevent coupling between the model motion and the flow; although this does not raise any particular problems for pressure measurements, the same is not true for force measurements with a balance;
- . the model support must be as unobtrusive as possible and far from the vortex wakes;
- . for measurements, it should be emphasized that:
 - . the use of probes to survey the flow is prohibited,
 - . the pressure taps must be distributed all around the fuselage and not on a single meridian with a rotatable body,
 - . the viscous coatings used for surface flow visualizations strongly alter the flow;
- . in addition to static tests, dynamic tests are generally necessary to satisfactorily quantify the maxima of the induced forces and moments (body spin and coning effect).

As concerns the devices that could minimize asymmetric vortex effects, it can be recommended to use:

- . a slightly blunted ogive or/with a low fineness ratio,
- . trips or strakes located as close to the tip as possible,
- . a spinning nose with strips.

To control and use the induced forces and moments for flight control, the most efficient devices seem to be:

- . strakes that are retractable or rotatable,
- . blowing.

However, the efficiency of such devices has been measured only at low Reynolds numbers and has practically never been demonstrated in turbulent flow.

Progress on numerical methods means that Navier-Stokes calculations, the only ones capable of producing realistic simulations, are beginning to be used to gain a better understanding of these flows. However, several problems arise:

- . disturbances must generally be introduced (but not always [35]) to obtain asymmetric numerical solutions on symmetric configurations. Certain authors ([9], [10], [11]) show that they must be permanent (e.g. asymmetric nose) and others [35] that it is sufficient to disturb the initial conditions;
- . the solutions obtained are not always very stable [9] and are highly sensitive to the disturbance introduced.

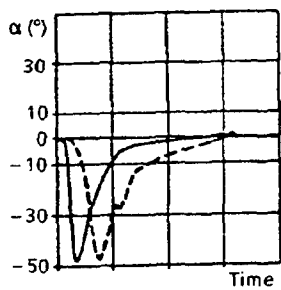
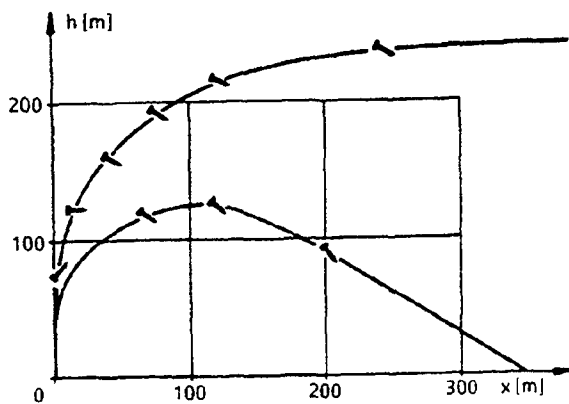
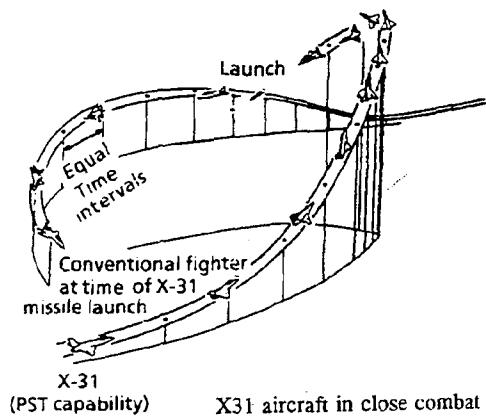
In addition, it can be wondered whether there is a steady numerical solution and, if so, whether it is unique. This problem is certainly even more complex for the simulation of turbulent flows with averaged Navier-Stokes equations.

REFERENCES

- [1] Lecture series on "High Angle of Attack Aerodynamics".
AGARD LS 121. March 1982.
- [2] W. LETKO
A low-speed experimental study of the directional characteristics of a sharp nosed fuselage through a large angle of attack range at zero angle of sideslip.
NACA TN 2911, 1953.
- [3] L.E. ERICSSON, J.P. REDING
Vortex-induced asymmetric loads in 2D and 3D flows.
AIAA paper 80-0181.
- [4] L.E. ERICSSON, J.P. REDING
Asymmetric vortex shedding from bodies of revolution.
In "Tactical Missile Aerodynamics", vol. 104.
Progress in Astronautics and Aeronautics Series.
1986.

- [5] G.N. MALCOLM
Forebody vortex control.
AGARD R-776. 1991.
- [6] P.J. LAMONT
The complex asymmetric flow over a 3.5D ogive nose and cylindrical afterbody at high angles of attack.
AIAA paper 82-0053.
- [7] E.R. KEENER, G.T. CHAPMAN, L. COHEN, J. TALEGHANI
Side forces on a tangent ogive forebody with a fineness ratio of 3.5 at high angles of attack and Mach numbers from 0.1 to 0.7.
NASA TMX 3437, Feb. 1977.
- [8] S.P. FIDDES, J.H.B. SMITH
Calculations of asymmetric separated flow past circular cones at large angles of incidence.
AGARD CP 336 (Missile Aerodynamics), 1982, paper N° 14.
- [9] D. DEGANI
Numerical investigation of the origin of vortex asymmetry.
AIAA paper N° 90-0593.
- [10] P.M. HARTWICH, R.M. HALL, M.J. HEMSCH
Navier-Stokes computations of vortex asymmetries controlled by small surface imperfections.
AIAA paper N° 90-0385.
- [11] D. DEGANI, Y. LEVY
Asymmetric turbulent vortical flows over slender bodies.
AIAA paper N° 91-3296 CP.
- [12] E.R. KEENER, G.T. CHAPMAN
Similarity in vortex asymmetries over slender bodies and wings.
AIAA Journal vol. 15, N° 9, Sept. 1977.
- [13] B.L. HUNT, P.C. DEXTER
Pressures on a slender body at high angle of attack in a very low turbulence level air stream.
AGARD CP 247, paper 17, 1979.
- [14] P.C. DEXTER
A study of asymmetric flow over slender bodies at high angles of attack in a low turbulence environment.
AIAA paper 84-0505.
- [15] P.C. DEXTER, B.L. HUNT
The effect of roll angle on the flow over a slender body of revolution at high angles of attack.
AIAA paper 81-0358.
- [16] P. CHAMPIGNY
Stability of side forces on bodies at high angle of attack.
AIAA paper 86-1776.
- [17] E.R. KEENER, G.T. CHAPMAN, R.L. KRUSE
Effects of Mach number and afterbody length on onset of asymmetric forces on bodies at zero sideslip and high angles of attack.
AIAA paper 76-0066.
- [18] I.R.M. MOIR
An experimental investigation of the effect of fineness ratio on lateral forces on a pointed body of revolution.
AGARD CP 494. Paper N° 19. 1990.
- [19] A.B. WARDLAW, A.M. MORRISON
Induced side forces at high angle of attack.
Journal of spacecraft and Rockets. Vol. 13, nb. 10. 1976.
- [20] G.S. PICK
Investigation of side forces on ogive-cylinder bodies at high angles of attack in the $M = 0.5$ to 1.1 range.
AIAA paper 71.0570.
- [21] P.J. LAMONT
Pressure measurements on an ogive-cylinder at high angles of attack with laminar, transitional or turbulent separation.
AIAA paper 80-1556.
- [22] P.J. LAMONT
The effect of Reynolds number on normal and side forces on ogive cylinders at high incidence.
AIAA paper 85-1799.
- [23] P. CHAMPIGNY
Reynolds number effect on the aerodynamic characteristics of an ogive-cylinder at high angles of attack.
AIAA paper 84-2176.
- [24] E.R. KEENER, G.T. CHAPMAN
Onset of aerodynamic side forces at zero sideslip on symmetric forebodies at high angles of attack.
AIAA paper N° 74-770.
- [25] D.M. RAO
Side force alleviation on slender, pointed forebodies at high angles of attack. AIAA paper 78-1339.

- [26] W.H. CLARK, J.R. PEOPLES, M.M. BRIGGS
Occurrence and inhibition of large yawing moments during high-incidence flight of slender missile configurations.
AIAA paper 72-968.
- [27] D. ALMOSNINO, J. ROM
Lateral forces on a slender body and their alleviation at high incidence.
AIAA paper 80-1558.
- [28] D.J. PEAKE, F.K. OWEN, D.A. JOHNSON
Control of forebody vortex orientation to alleviate side forces.
AIAA paper 80-0183.
- [29] J.E. FIDLER
Active control of asymmetric vortex effects.
AIAA paper 80-0182.
- [30] T.T. NG, C.J. SUAREZ, G.N. MALCOLM
Forebody vortex control using slot blowing.
AIAA paper 91-3254.
- [31] C.A. MOSKOVITZ, R.M. HALL, F.R. DEJARNETTE
New device for controlling asymmetric flowfields on forebodies at large alpha.
Journal of Aircraft. Vol. 28, N° 7. July 1991.
- [32] R.M. HOWARD, M.P. RABANG, D.P. ROANE
Aerodynamic effect of a turbulent flowfield on a vertically launched missile.
Journal of Spacecraft and Rockets. Vol. 26, N° 6, Nov. 1989.
- [33] C. QUEMARD, D. REGARD, D. TRISTRANT
Ecoulement sur la pointe avant d'un avion de combat à grande incidence.
Colloque ONERA 1993.
- [34] W.H. SWANSON
The magnus effect. A summary of investigations to date.
Journal of Basic Engineering. Supt. 1961.
- [35] M.J. SICLARI, F. MARCONI
Computation of Navier-Stokes Solutions Exhibiting Asymmetric Vortices.
AIAA Journal Vol. 29 N° 1. January 1991.
- [36] D. DEGANI, L.B. SCHIFF
Numerical simulation of the effect of spatial disturbances on vortex asymmetry.
AIAA paper N° 89-0340.



Missile fired vertically

Fig. 1 - EXAMPLES OF FLIGHT AT HIGH ANGLES OF ATTACK.

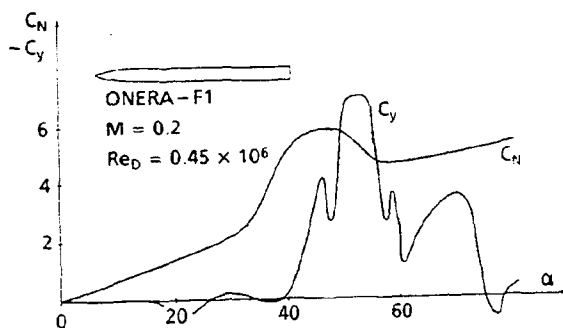


Fig. 3 - LIFT AND SIDE FORCE ON A BODY OF REVOLUTION.

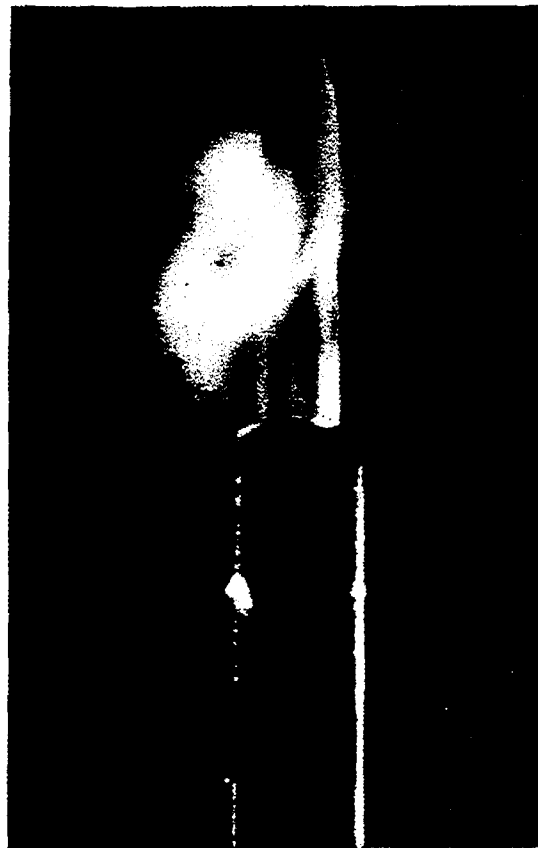


Fig. 2 - VISUALIZATION OF ASYMMETRICAL FLOW AT $\alpha = 50^\circ$.

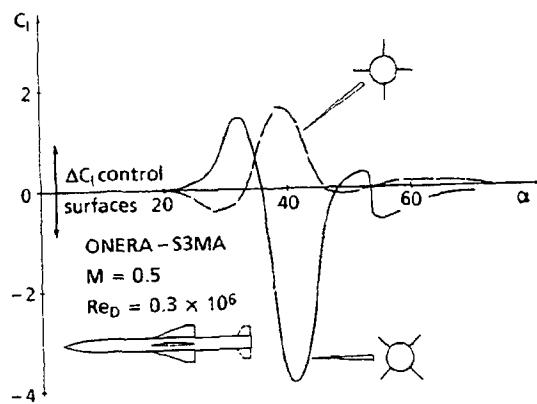


Fig. 4 - ROLL MOMENT ON A MISSILE CONFIGURATION.

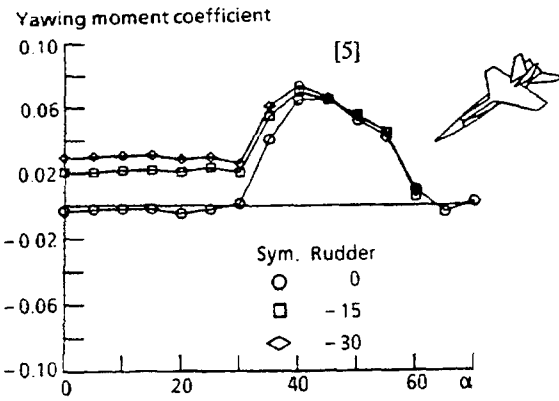


Fig. 5 - YAWING MOMENT ON A FIGHTER PLANE CONFIGURATION.

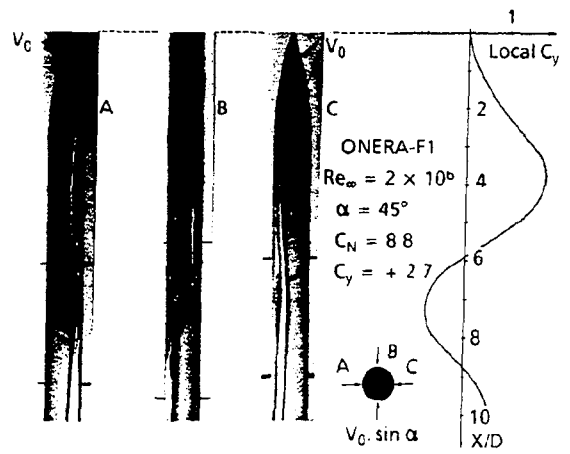


Fig. 8 - SIDE FORCES DISTRIBUTION AND OIL-FLOW VISUALIZATIONS.

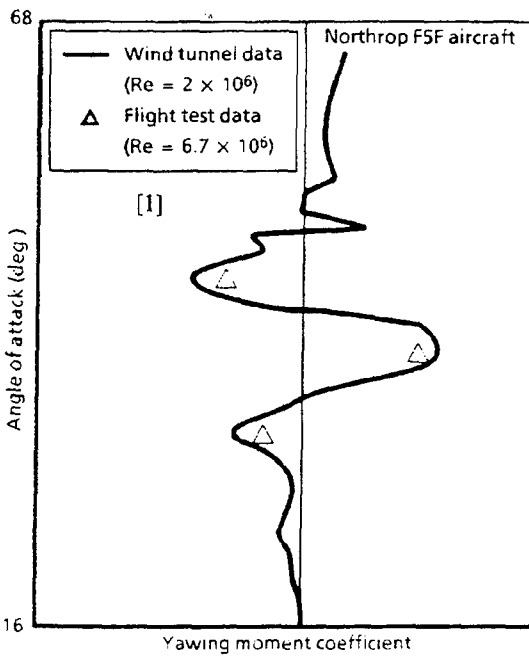


Fig. 6 - YAWING MOMENT AT HIGH ANGLE OF ATTACK. COMPARISON OF FLIGHT AND WIND TUNNEL DATA.

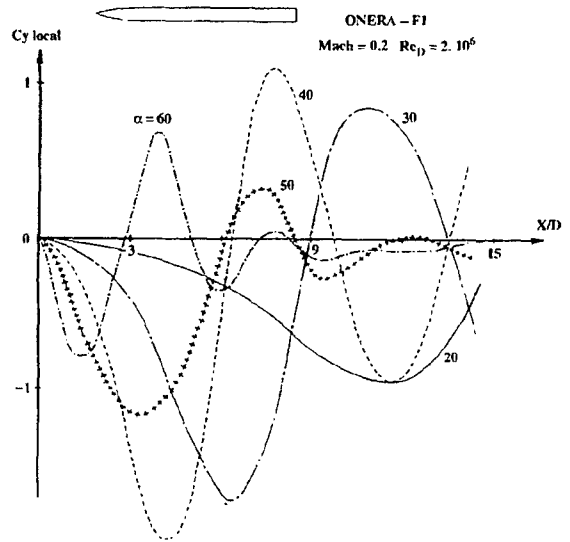


Fig. 9 - EFFECT OF ANGLE OF ATTACK ON LOCAL SIDE FORCE DISTRIBUTIONS.

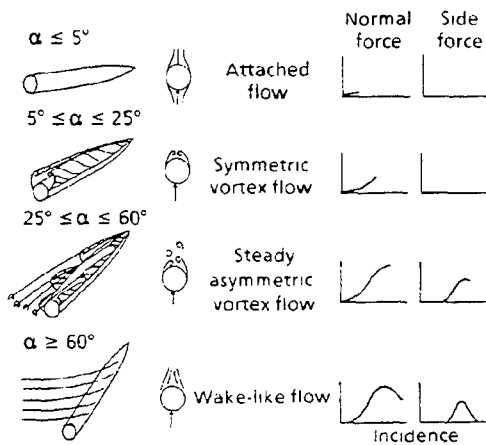


Fig. 7 - EFFECT OF ANGLE OF ATTACK ON LEFTSIDE FLOWFIELD.

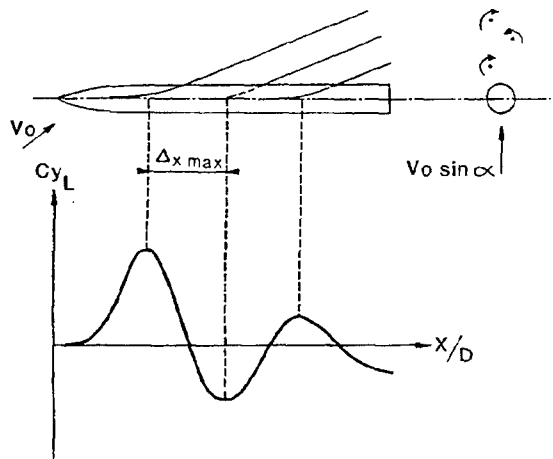


Fig. 10 - SKETCH OF FLOW PATTERN AND SIDE FORCE DISTRIBUTION.

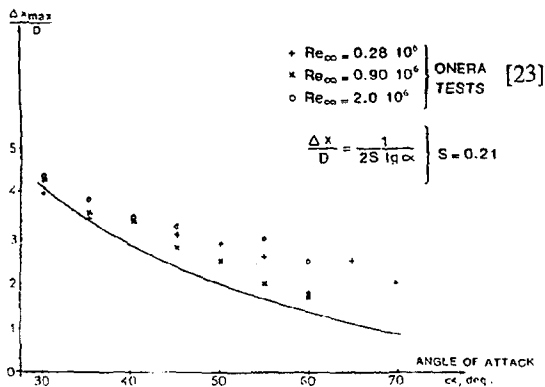


Fig. 11 - SPACING IN LOCAL SIDE FORCE PATTERN.

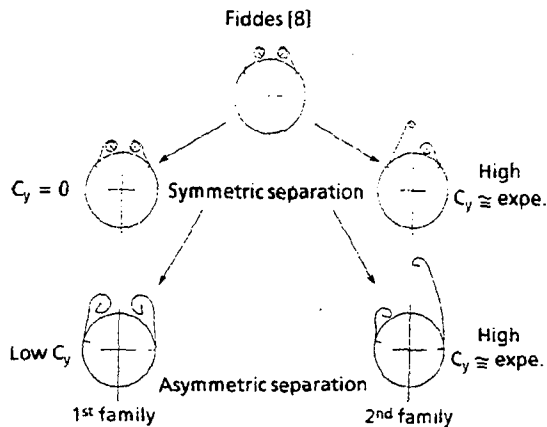


Fig. 14 - DIAGRAMS OF FLOWS AT HIGH ANGLES OF ATTACK.

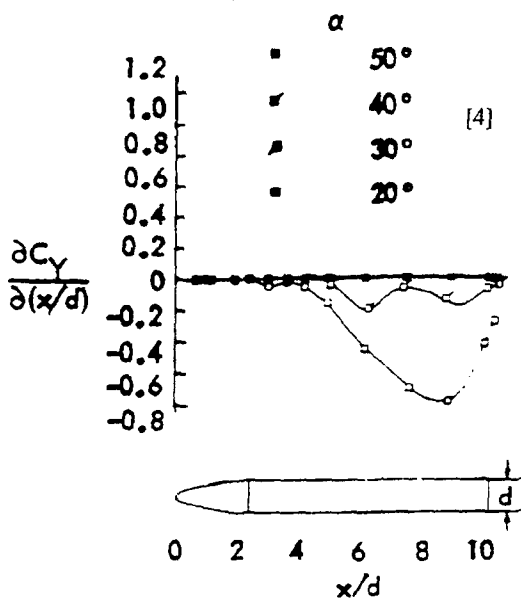


Fig. 12 - LOCAL SIDE FORCE DISTRIBUTION ON BLUNTED OGIVE-CYLINDER BODY.

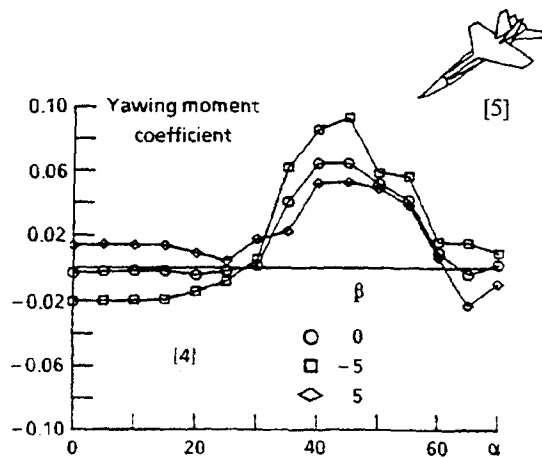


Fig. 15 - EFFECT OF SIDESLIP ON YAWING MOMENT AT HIGH ANGLES OF ATTACK.

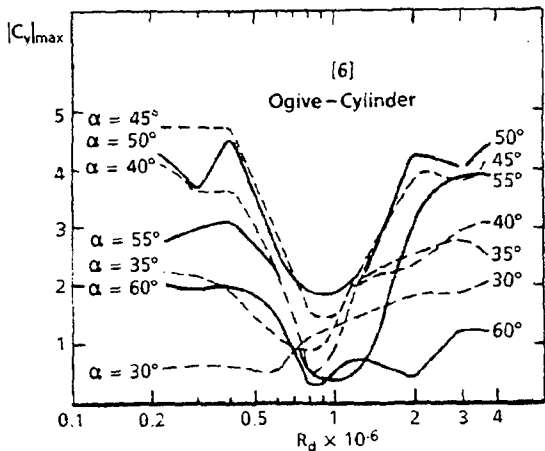


Fig. 13 - EFFECT OF REYNOLDS NUMBER ON MAXIMUM SIDE FORCE.

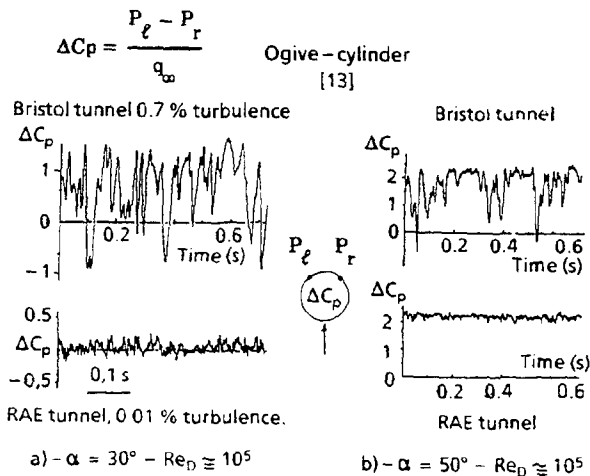


Fig. 16 - EFFECT OF TURBULENCE.

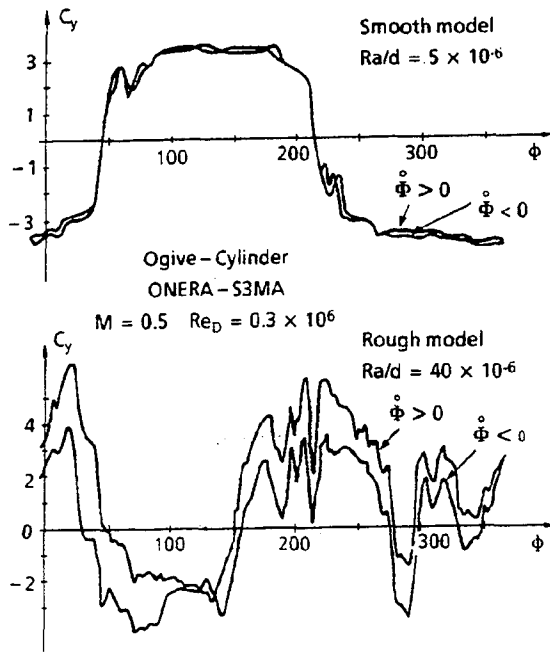
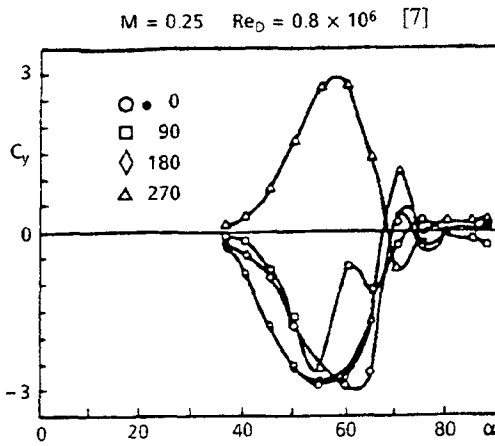
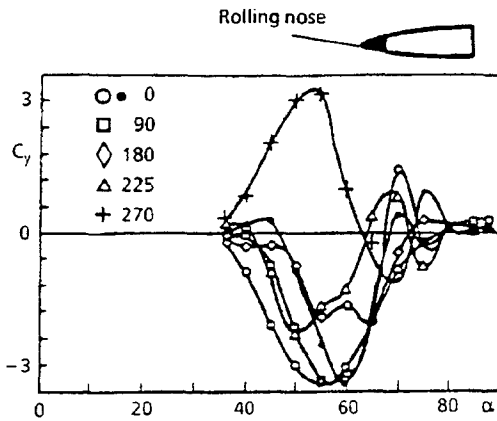


Fig. 17 - EFFECT OF ROLL ANGLE.



a) - Effect of body roll angle



b) - Effect of nose roll angle

Fig. 18 - EFFECT OF ROLL ANGLE.

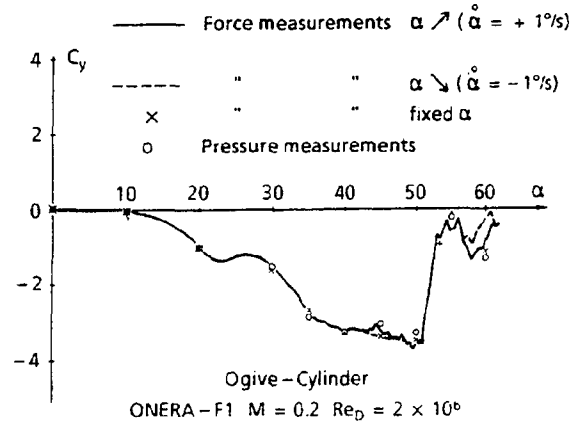


Fig. 19 - MEASUREMENTS REPEATABILITY.

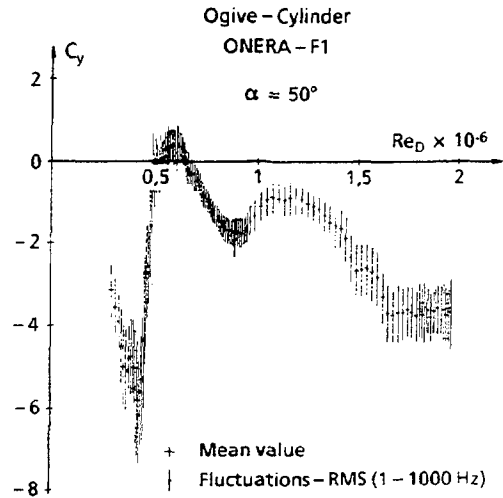


Fig. 20 - MEAN SIDE FORCE AND FLUCTUATIONS.

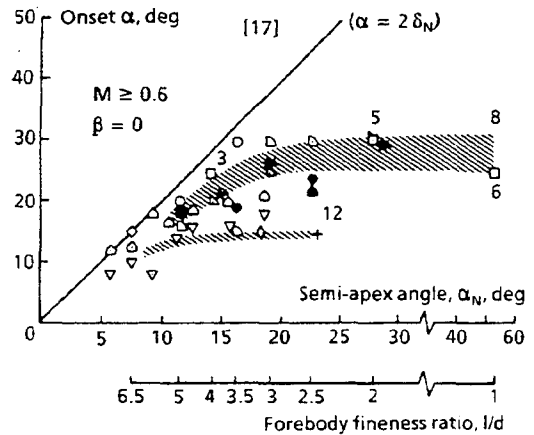


Fig. 21 - ANGLE OF ATTACK AT WHICH SIDE FORCES APPEAR. PLOTTED OGVES.

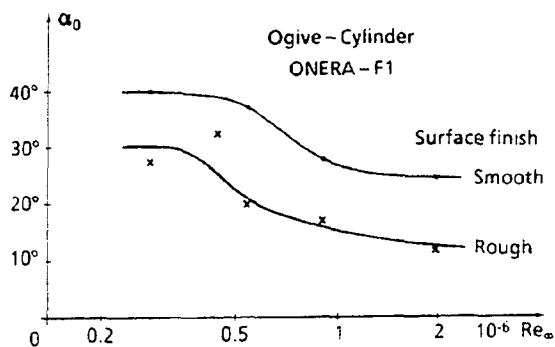


Fig. 22 - ANGLE OF ATTACK AT WHICH SIDE FORCES APPEAR. ROUGHNESS AND REYNOLDS NUMBER EFFECTS.

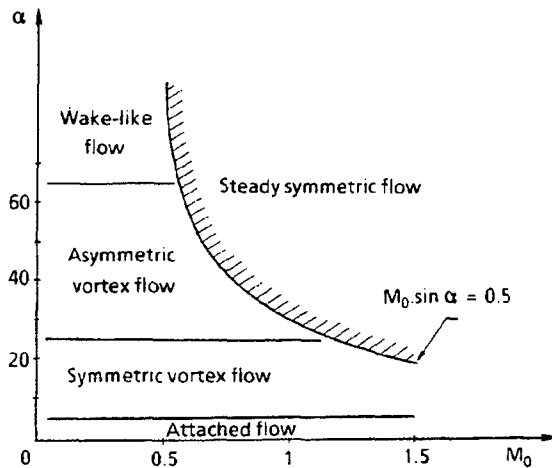


Fig. 25 - CLASSIFICATION OF FLOWS IN A (α , MACH) DIAGRAM.

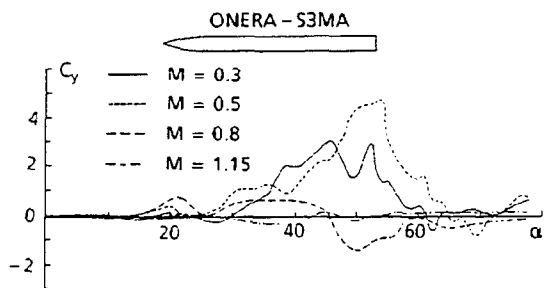


Fig. 23 - EFFECT OF MACH NUMBER ON SIDE FORCES.

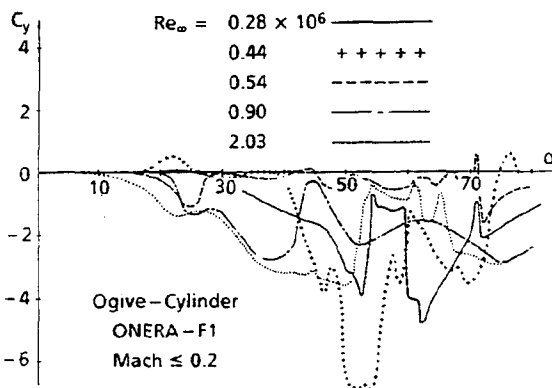


Fig. 26 - EFFECT OF REYNOLDS NUMBER ON SIDE FORCES.

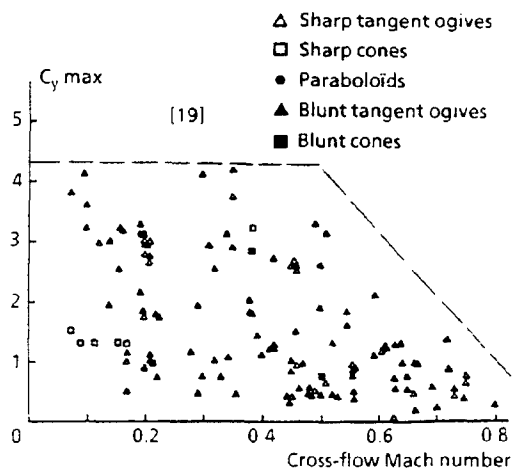


Fig. 24 - MAXIMUM SIDE FORCES AS A FUNCTION OF CROSSFLOW MACH NUMBER.

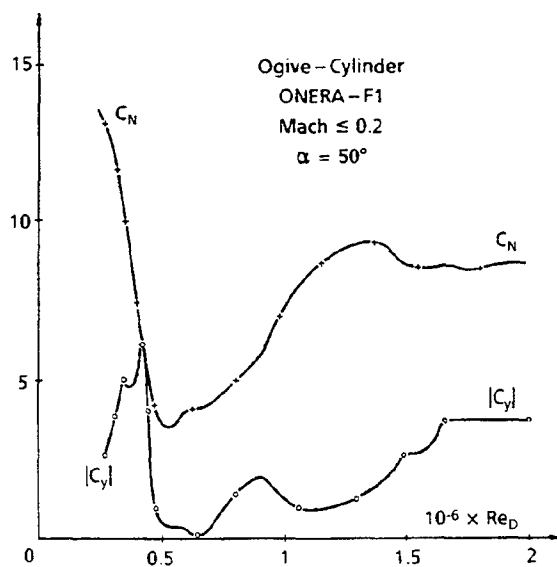


Fig. 27 - REYNOLDS NUMBER EFFECT AT $\alpha = 50^\circ$.

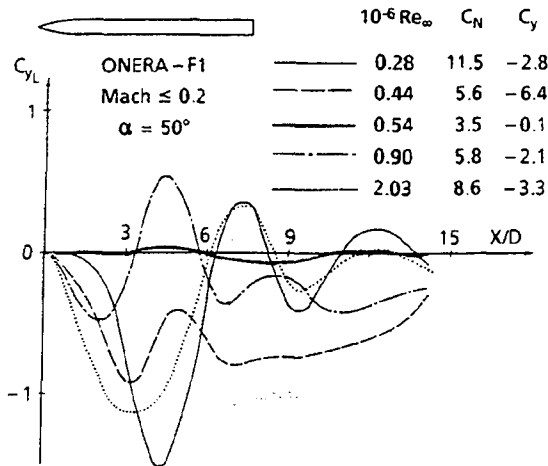


Fig. 28 - LOCAL SIDE FORCES AS A FUNCTION OF REYNOLDS NUMBER.

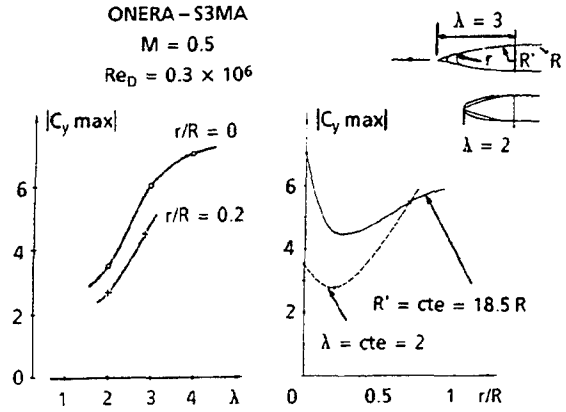


Fig. 30 - EFFECT OF OGI VE GEOMETRY ON MAXIMUM SIDE FORCES.

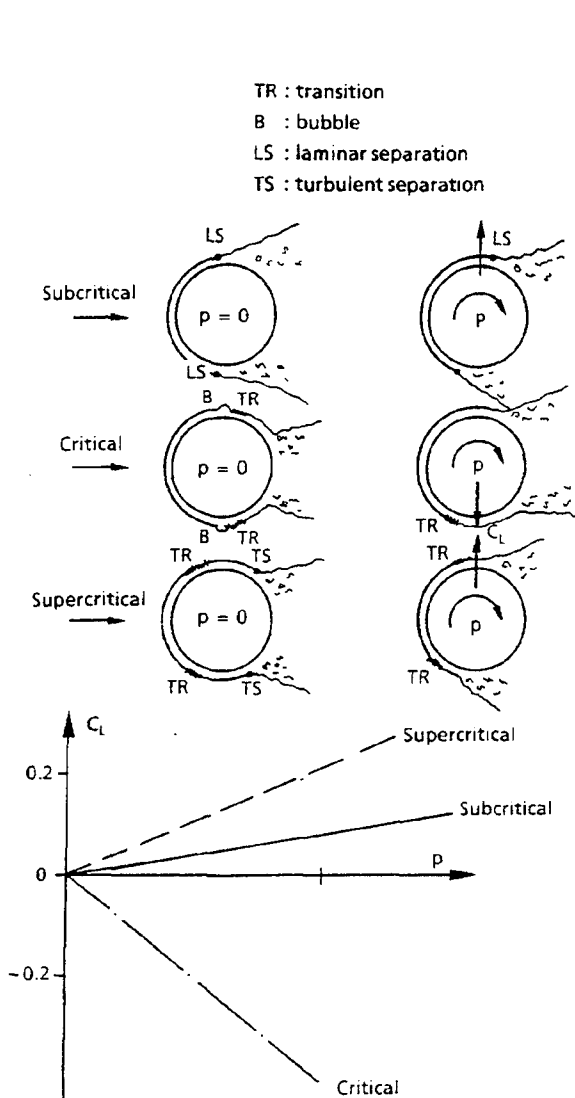


Fig. 29 - MAGNUS COEFFICIENT AT LOW SPIN RATE FOR DIFFERENT FLOW REGIMES.

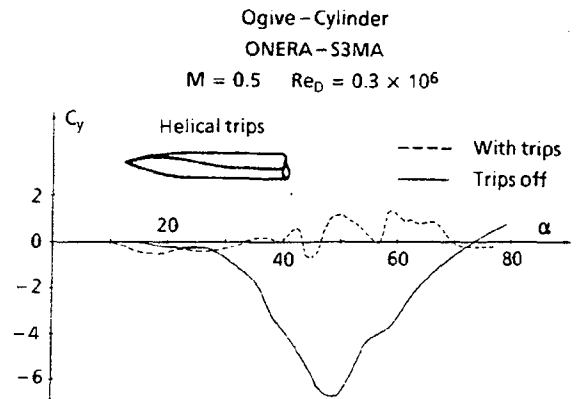


Fig. 31 - EFFECT OF STRAKES ON SIDE FORCES.

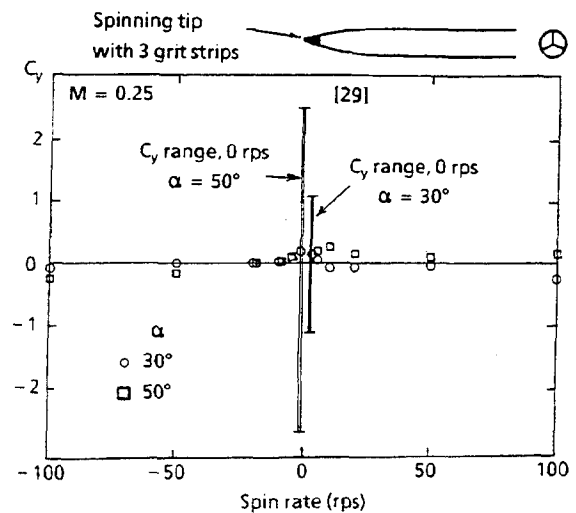


Fig. 32 - EFFECT OF NOSE SPIN ON SIDE FORCES.

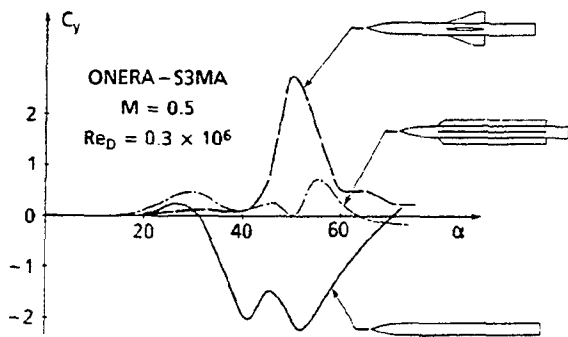


Fig. 33 - EFFECT OF WINGS ON SIDE FORCES.

Sym	Run	CMU-L	CMU-R
○	454	0.03	0.03
□	453	0	0.03
◇	420	0.03	0
△	456	0.03	0

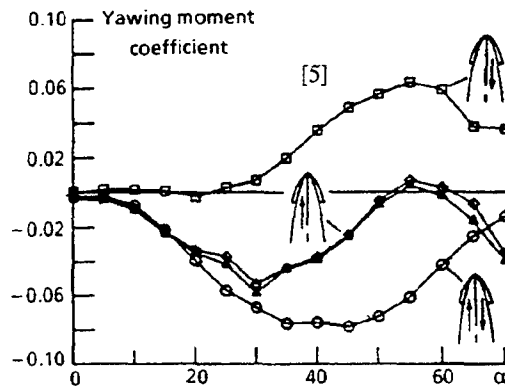


Fig. 36 - YAWING MOMENT CONTROL BY BLOWING.

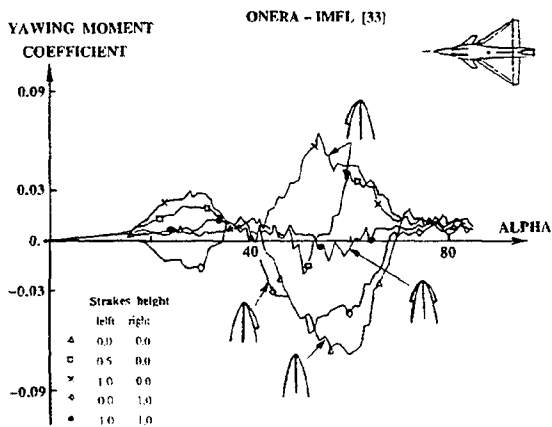


Fig. 34 - YAWING MOMENT CONTROL WITH RETRACTABLE STRAKES.

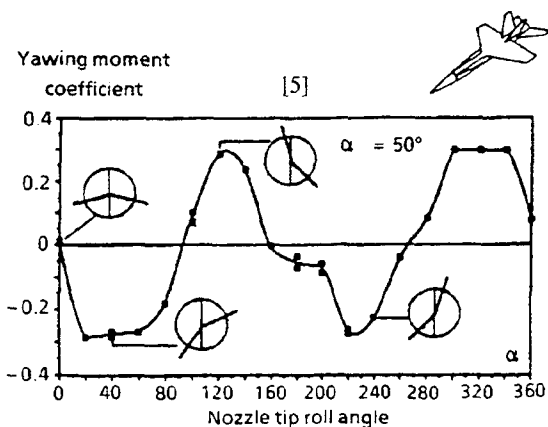


Fig. 35 - YAWING MOMENT CONTROL WITH ROTATABLE STRAKES.

- 2D CYLINDER - C_l/C_d
- 3D SLENDER BODY - C_{Ymax}/C_N
- LAMONT - $l/d = 3.5$ Ogive - $\alpha = 40^\circ$
- KEENER - $l/d = 3.5$ Ogive - $\alpha = 40^\circ$
- △ KEENER - $l/d = 3.5$ Ogive - C_{Ymax}/C_N
- × CHAMPIGNY - $l/d = 3.0$ Ogive - $\alpha = 50^\circ$

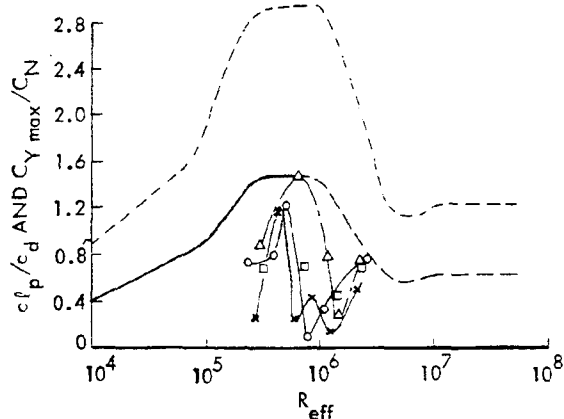


Fig. 37 - PREDICTED AND MEASURED MAXIMUM TOTAL SIDE FORCE TO NORMAL FORCE RATIO.

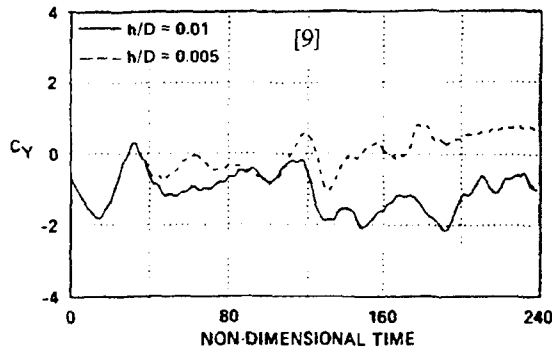


Fig. 38 - SIDE FORCE COEFFICIENT HISTORY.
OGIVE-CYLINDER, $\alpha = 40^\circ$, $M = 0.2$, $Re_p = 0.2 \times 10^6$.

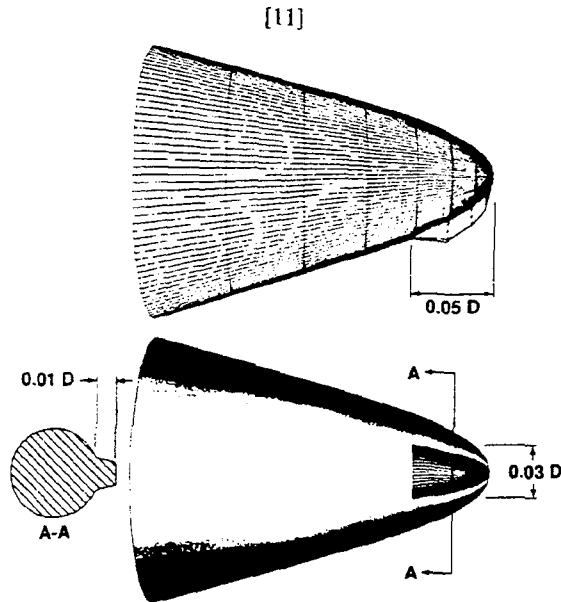


Fig. 39 - DETAILED GEOMETRICAL DISTURBANCE.

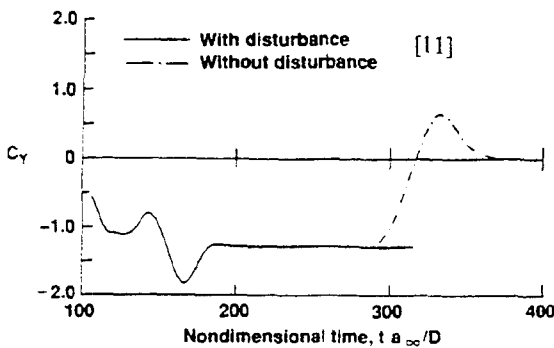


Fig. 40 - SIDE FORCE COEFFICIENT HISTORY.
OGIVE-CYLINDER, $\alpha = 30^\circ$, $M = 0.2$, $Re_p = 4.0 \times 10^6$.

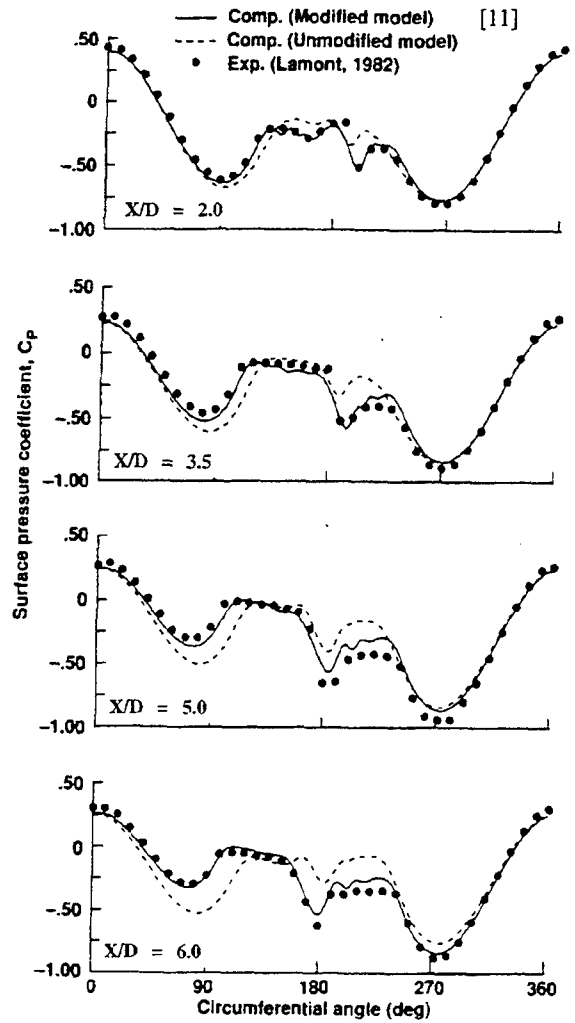


Fig. 41 - COMPUTED AND MEASURED PRESSURE DISTRIBUTIONS
OGIVE-CYLINDER, $\alpha = 30^\circ$, $M = 0.2$, $Re_p = 4.0 \times 10^6$.

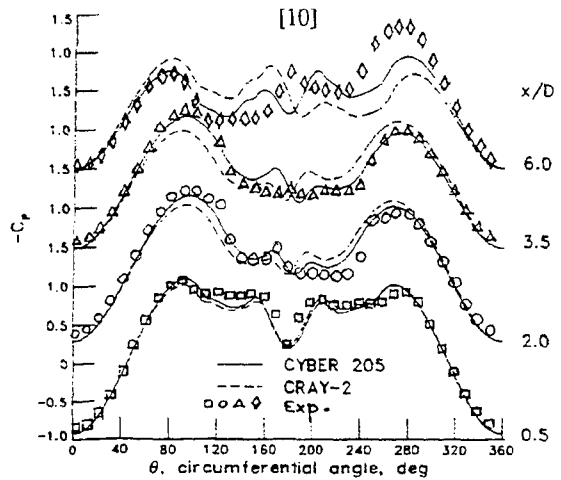


Fig. 42 - COMPUTED AND MEASURED PRESSURE DISTRIBUTIONS.
EFFECTS OF MACHINE ACCURACY
OGIVE-CYLINDER, $\alpha = 40^\circ$, $Re_p = 0.8 \times 10^6$.

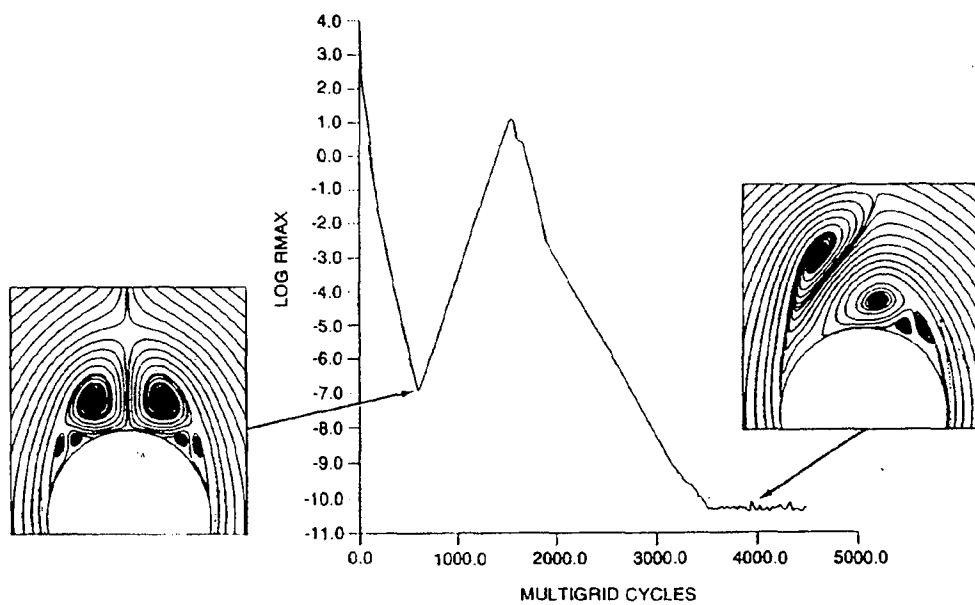


Fig. 43 - CONVERGENCE HISTORY.
 5-DEG. CONE, $M = 1.8$, $\alpha/\theta = 4$, $Re = 10^5$. [35]

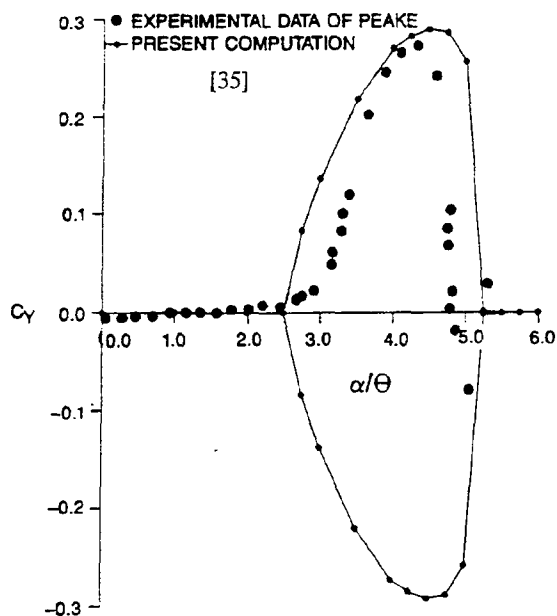


Fig. 44 - COMPARISON OF COMPUTED SIDE FORCE COEFFICIENT
 TO EXPERIMENTAL MEASUREMENTS.
 5-DEG. CONE, $M = 1.8$, $Re = 10^5$.

NAVIER-STOKES PREDICTIONS OF MISSILE AERODYNAMICS

Paul Weinacht
Jubaraj Sahu
Propulsion and Flight Division, WTD
U.S. Army Research Laboratory
Aberdeen Proving Ground, Maryland 21005-5066

1. SUMMARY

This paper discusses the application of Navier-Stokes computational methods to the prediction of the aerodynamics of missile configurations. The governing equations, turbulence models and numerical approaches used to solve these equations are briefly described. The paper focuses mainly on aerodynamic coefficient prediction. Static and dynamic aerodynamic derivative prediction methods and applications are presented for axisymmetric and finned bodies and comparisons are made with experimental data. Results of validation studies are also presented for the purpose of demonstrating the accuracy as well as potential shortcomings of these techniques. The paper also discusses the application of Navier-Stokes methods in the prediction of base flow. Application of these techniques to unpowered, base bleed and powered configurations are shown.

2. LIST OF SYMBOLS

a_∞	freestream speed of sound
C_{A_v}	viscous axial force coefficient
C_{D_0}	zero yaw drag coefficient
C_{l_0}	roll producing moment coefficient
C_l	net roll moment coefficient
C_{l_0}	roll producing moment coefficient
C_{l_p}	roll damping moment coefficient
C_m	pitching moment coefficient
C_{m_α}	slope of the pitching moment coefficient with angle of attack
$C_{m_q} + C_{m_\dot{\alpha}}$	pitch damping moment coefficient
C_n	side moment coefficient
C_{n_α}	slope of the side moment coefficient with angle of attack
$C_{n_\dot{\alpha}}$	slope of the side moment coefficient with coning rate
$C_{n_{p\alpha}}$	Magnus moment coefficient
C_{N_α}	slope of the normal force coefficient with angle of attack
$C_{N_q} + C_{N_\dot{\alpha}}$	pitch damping force coefficient
$C_{Y_{p\alpha}}$	Magnus force coefficient
D	projectile diameter
e	total energy per unit volume
$\hat{E}, \hat{F}, \hat{G}$	flux vectors in transformed coordinates
\hat{H}	source term in Navier-Stokes eqs.
J	Jacobian
l	characteristic length, typically D
M	Mach number
p	pressure, as used in N-S eqs.
\dot{p}	spin rate, as used roll equations
Pr	Prandtl number
Re	Reynolds number, $a_\infty \rho_\infty l / \mu_\infty$

s	distance downrange
s_{cg}	center of gravity shift, calibers
\vec{S}	viscous flux vector
S_{ref}	reference area of projectile, $\pi D^2/4$
t	time
u, v, w	velocity components in x,y,z directions
V	freestream velocity
x, y, z	Cartesian coordinates w.r.t. body

Note: Force coefficients are scaled, $F/\frac{1}{2}\rho_\infty a_\infty^2 M_\infty^2 S_{ref}$;
Moment coefficients are scaled, $M/\frac{1}{2}\rho_\infty a_\infty^2 M_\infty^2 D S_{ref}$

Greek Symbols

α, β	vertical and horizontal components of angle of attack in non-rolling coordinates
α_t	total angle of attack, $\sqrt{\alpha^2 + \beta^2}$
γ	ratio of specific heats, in N-S eqs.
γ	cosine of the angle of attack, as used in aerodynamic force and moment eqs.
δ	sine of the angle of attack
μ, μ_t	laminar and turbulent viscosity
ξ, η, ζ	transformed coordinates in N-S eqs.
ξ	complex angle of attack
ρ	density
$\dot{\phi}$	coning rate of projectile
$\frac{\dot{\phi} D}{V}$	nondimensional coning rate
Ω_c	angular rate of rotating coordinate frame

Superscripts

$()$	rate of change with respect to time
$()'$	rate of change with respect to space
$()$	referenced to non-rolling coordinate frame

Subscripts

(∞)	denotes freestream value of variable
------------	--------------------------------------

3. INTRODUCTION

This paper will address the application of computational techniques based on the solution of the Navier-Stokes equations to the field of missile aerodynamics. Other papers in the course have addressed other methods which are based on simpler theories or empirical methods. These methods can be quite powerful because the effect of design parameters on the vehicle's aerodynamics can be rapidly predicted and optimized. As with any model, if these models are applied beyond their range of applicability or if the simplifying assumptions are violated, the accuracy of the results may be suspect.

In contrast to these "engineering" methods, Navier-Stokes techniques have the potential of being able to

model the flow physics at a more fundamental level because the relevant equations are based on "first principles". Navier-Stokes techniques can provide an advantage over simpler theories for a number of reasons. First, because the physical models are based on "first principles", the results may be more accurate than the results obtained by simpler theories because fewer approximations may be required. Secondly, these models can provide a high level of detail that may help the aerodynamicist to predict not only how the performance of a flight vehicle will be affected by design changes but also why the flow physics produces a certain type of aerodynamic behavior.

The claim that Navier-Stokes methods are based on "first principles" is arguably an over-simplification, particularly for the case of turbulent flow. Although the governing equations require the conservation of mass, momentum and energy, for the case of turbulent flow, closure of the equations requires some level of approximation or empiricism. Turbulence modeling (including predicting the transition from laminar to turbulent flow) is probably the "Achilles Heel" of Navier-Stokes modeling. Fortunately, for many problems adequate turbulence models can be found which provide proper modeling of the flow physics.

Navier-Stokes methods also suffer from the fact that they tend to be computationally intensive. This is probably the major reason that these methods have not been as widely used as simpler theories. However, the rapid pace of developments in computers promises to remove this barrier in the near future. Indeed, it has only been in the last decade and a half that significant progress has been made in the development and application of Navier-Stokes techniques in the field of missile aerodynamics.

This paper focuses on the use of Navier-Stokes techniques for aerodynamic coefficient prediction, although it is important to realize that these techniques can also be employed to examine other flow related phenomenon which may be important in missile aerodynamics such as surface heat transfer due to aerodynamic heating. The paper provides a brief description of the governing equations and computational techniques typically used in applying Navier-Stokes techniques to missile aerodynamics. Several sections of the paper are devoted to applications of these techniques for the prediction of static aerodynamics, aerodynamics in pure rolling motion and dynamic derivative prediction. The last section of the paper discusses the application of these methods to base flows, both with and without mass injection.

4. THEORETICAL BACKGROUND

4.1 Governing Equations

The governing equations which are the basis of Navier-Stokes techniques are the Navier-Stokes equations. This set of equations states that mass, momentum and energy are conserved. These equations are often written in vector form as in Equation 1. For convenience, the equations are cast in Cartesian coordinate form, although it is noted that for many missile applications the cylindrical coordinate form of the equations can provide better accuracy for the same number of grid

points.

$$\frac{\partial q}{\partial t} + \frac{\partial E}{\partial x} + \frac{\partial F}{\partial y} + \frac{\partial G}{\partial z} + H = \frac{1}{Re} \left(\frac{\partial E_v}{\partial x} + \frac{\partial F_v}{\partial y} + \frac{\partial G_v}{\partial z} \right) \quad (1)$$

These five equations are statements of the conservation of mass and energy and conservation of momentum in the x, y and z direction. This form of the equations assumes that the fluid may be compressible and that heat generation and body forces (except for those which might be included in the source term, H) can be ignored. This vector equation states that the time rate of change in the dependent variables q is equal to the spatial change in the inviscid fluxes, E , F and G , and viscous fluxes, E_v , F_v and G_v . A source term, H , is included to account for the centrifugal and Coriolis force terms which appear if the coordinate frame is rotating. The use of the rotating coordinate frame will be discussed in a later section. The presence of the Reynolds number, $Re = \bar{\rho} \bar{u} \bar{L} / \bar{\mu}$, implies that the governing equations have been non-dimensionalized; with $\bar{\rho}$ and \bar{u} often chosen as the freestream density and velocity, \bar{L} chosen as the reference length of the body and $\bar{\mu}$ evaluated at the freestream static temperature. The vector of dependent variables, the inviscid and viscous flux terms are shown below.

$$q = \begin{bmatrix} \rho \\ \rho u \\ \rho v \\ \rho w \\ e \end{bmatrix} \quad E = \begin{bmatrix} \rho u \\ \rho u^2 + p \\ \rho uv \\ \rho w u \\ (e + p)u \end{bmatrix}$$

$$F = \begin{bmatrix} \rho v \\ \rho uv \\ \rho v^2 + p \\ \rho vw \\ (e + p)v \end{bmatrix} \quad \hat{G} = \begin{bmatrix} \rho v \\ \rho vw \\ \rho v^2 + p \\ (e + p)v \end{bmatrix}$$

$$\hat{E}_v = \begin{bmatrix} 0 \\ \tau_{xx} \\ \tau_{xy} \\ \tau_{xz} \\ u\tau_{xx} + v\tau_{xy} + w\tau_{xz} - q_x \\ 0 \end{bmatrix}$$

$$\hat{F}_v = \begin{bmatrix} \tau_{xy} \\ \tau_{yy} \\ \tau_{yz} \\ u\tau_{xy} + v\tau_{yy} + w\tau_{yz} - q_y \\ 0 \end{bmatrix}$$

$$\hat{G}_v = \begin{bmatrix} \tau_{xz} \\ \tau_{yz} \\ \tau_{zz} \\ u\tau_{xz} + v\tau_{yz} + w\tau_{zz} - q_z \end{bmatrix} \quad (2)$$

Here ρ is the fluid density; u , v and w are the fluid velocities in the x, y and z coordinate directions, and e is the total energy per unit volume. The viscous flux terms are functions of the local fluid velocities, the shear stresses, τ_{xx} , ..., and heat conduction terms, q_x , q_y and q_z .

The pressure, p , which appears in the inviscid flux terms, is related to the dependent variables through an appropriate equation of state. In this paper, the pressure is related to the dependent variables by applying the ideal gas law.

$$p = (\gamma - 1) \left[e - \frac{1}{2} \rho (u^2 + v^2 + w^2) \right] \quad (3)$$

The shear stresses are related to the velocity gradient of the fluid, assuming a Newtonian fluid. For turbulent flow, a Reynolds-averaged form of the equations is used where the dependent variables represent the mean flow contribution. The Boussinesq assumption is applied, permitting the apparent turbulent stresses to be related to the product of the mean flow strain rate and an apparent turbulent viscosity. The shear stress tensor has the following form;

$$\tau_{ij} = (\mu + \mu_T) \left[\left(\frac{\partial u_i}{\partial x_j} + \frac{\partial u_j}{\partial x_i} \right) - \frac{2}{3} \delta_{ij} \frac{\partial u_k}{\partial x_k} \right] \quad (4)$$

The heat conduction terms, when Reynolds-averaging and the Boussinesq assumption are applied, are proportional to the local mean flow temperature gradient;

$$q_i = \frac{-1}{(\gamma - 1) Pr M_\infty^2} (k + k_T) \frac{\partial T}{\partial x_i} \quad (5)$$

Here, γ represents the ratio of specific heats, Pr is the Prandtl number and M_∞ is the free stream Mach number.

To determine the effective turbulent conductivity, k_T , Reynolds analogy is applied and the turbulent conductivity is related to the turbulent viscosity as follows;

$$k_T = \frac{Pr}{Pr_T} \mu_T \quad (6)$$

Here, and in the equations above, the conductivity and viscosity are non-dimensionalized by their representative (laminar) values evaluated at the freestream static temperature. A turbulent Prandtl number, $Pr_T = 0.9$ is often used.

In many CFD applications, it is desirable to solve the governing equations in a domain which has surfaces which conform to the body rather than in a Cartesian coordinate domain. A transformation is applied to the original set of equations to obtain a "generalized geometry" form of the governing equations. This allows the irregularly shaped physical domain to be transformed into a rectangular shaped computational domain which allows the numerics to be simplified somewhat. The transformed equations are shown below.

$$\frac{\partial \hat{q}}{\partial t} + \frac{\partial \hat{E}}{\partial \xi} + \frac{\partial \hat{F}}{\partial \eta} + \frac{\partial \hat{G}}{\partial \zeta} + \hat{H} = \frac{1}{Re} \left(\frac{\partial \hat{E}_v}{\partial \xi} + \frac{\partial \hat{F}_v}{\partial \eta} + \frac{\partial \hat{G}_v}{\partial \zeta} \right) \quad (7)$$

Here, it is assumed that the transformation is time-invariant (i.e., the computational grid does not change with time), although it is possible to develop a transformation in which the grid is allowed to change with time. Typically, the physical domain is oriented in such a way that the coordinate directions in the computational domain, ξ , η and ζ , may correspond to directions relative to the body. In many of the applications discussed here, ξ corresponds to the direction along the body, η corresponds to the circumferential direction and ζ corresponds to the outward direction from the body surface.

The transformed fluxes are functions of the original Cartesian flux terms and have a similar form. After

rearranging, the vector of dependent variables and inviscid flux terms take the following form. (Due to space limitations, the viscous term are not shown but can be easily found in the literature¹.)

$$\hat{q} = \frac{1}{J} \begin{bmatrix} \rho \\ \rho u \\ \rho v \\ \rho w \\ e \end{bmatrix} \quad \hat{E} = \frac{1}{J} \begin{bmatrix} \rho U \\ \rho u U + \xi_x p \\ \rho v U + \xi_y p \\ \rho w U + \xi_z p \\ (e + p) U \end{bmatrix} \\ \hat{F} = \frac{1}{J} \begin{bmatrix} \rho u V + \eta_x p \\ \rho v V + \eta_y p \\ \rho w V + \eta_z p \\ (e + p) V \end{bmatrix} \quad \hat{G} = \frac{1}{J} \begin{bmatrix} \rho W \\ \rho u W + \zeta_x p \\ \rho v W + \zeta_y p \\ \rho w W + \zeta_z p \\ (e + p) W \end{bmatrix} \quad (8)$$

where

$$U = u\xi_x + v\xi_y + w\xi_z \quad (9)$$

$$V = u\eta_x + v\eta_y + w\eta_z \quad (10)$$

$$W = u\zeta_x + v\zeta_y + w\zeta_z \quad (11)$$

In addition to the original Cartesian variables, additional terms (J , ξ_x , η_y , ζ_z , ...) appear in the equations. These terms, referred to as the metric terms, result from the transformation and contain the purely geometric information which relates the physical space to the computational space.

Further simplification of the governing equations shown above is often desirable and physically justified. In many missile applications, the viscous effects are limited to the boundary layers near the body surfaces or along shear layers which are normal to a single grid direction. In such cases, it may be desirable to include only the most dominant viscous terms in similar fashion as the boundary layer equations. Indeed, from a computational perspective, for viscous effects to be properly modeled, the relevant viscous terms must be included in the governing equations and the flow field gradients must be resolved with sufficient accuracy on the computational mesh. For these reasons, a simplified form of the governing equations is often applied. This set of equations is often referred to as the "thin-layer" Navier-Stokes equations. In a fashion similar to the boundary layer length scale analysis, only viscous terms which involve derivatives along a single coordinate direction (typically normal to the body surface) are retained and the other viscous terms are dropped. At this point only a single vector of viscous terms remains.

$$\frac{\partial \hat{q}}{\partial t} + \frac{\partial \hat{E}}{\partial \xi} + \frac{\partial \hat{F}}{\partial \eta} + \frac{\partial \hat{G}}{\partial \zeta} + \hat{H} = \frac{1}{Re} \frac{\partial \hat{S}}{\partial \zeta} \quad (12)$$

This form of the equations has the nice feature that the cross-derivatives in the viscous terms have been eliminated and are now in a form which is amenable to solution by direct implicit numerical techniques such as the Beam-Warming algorithm². Additionally, some solution methods such as the Parabolized Navier-Stokes technique may require the streamwise diffusion terms to be neglected as a condition for stable marching.

4.2 Turbulence Modeling

The form of the Reynolds-averaged Navier-Stokes equations discussed previously requires a model for the

apparent turbulent viscosity which appears in the viscous and heat conduction terms. There are numerous approaches for determining the turbulent viscosity. These range from simple algebraic models, which are evaluated based on the local flow field properties, to models which involve the solution of partial differential equations which have a form similar to the governing equation.

One of the most widely used approaches used for missile applications is the algebraic model of Baldwin and Lomax³. The Baldwin-Lomax model, which is patterned after the model of Cebeci⁴, is relatively easy to implement and computationally inexpensive. Because some of the details of the model are discussed later, a brief description of the model is given here.

The Baldwin-Lomax model is a two-layer model where the turbulent viscosity is evaluated using two parts, an inner and outer model. The inner model is applied between the body surface and a cross-over point where the inner viscosity exceeds the viscosity evaluated using the outer model. The outer model is applied outward from the cross-over point.

The inner model utilizes Prandtl-Van Driest mixing length approach and takes the following form;

$$(\mu_t)_{inner} = \rho l^2 |\omega| \quad (13)$$

where

$$l = k y [1 - \exp(-y^+ / A^+)] \quad (14)$$

Here, y is the coordinate normal to the surface and $|\omega|$ is the magnitude of the local vorticity. The constants, k and A^+ , were assigned the following values by Baldwin and Lomax; $k = 0.4$ and $A^+ = 26$. The non-dimensional boundary layer coordinate, y^+ , is defined below and is a function of the fluid viscosity, ν_w , fluid density, ρ_w , shear stress, τ_w , and the dimensional distance from the wall, y . The subscript, w , indicates that the quantities are to be evaluated at the body surface. For wake flows, the exponential term shown above is set to zero.

$$y^+ = \frac{y u_*}{\nu_w} \quad (15)$$

$$u_* = \sqrt{\tau_w / \rho_w}$$

The model in the outer region takes the following form

$$(\mu_t)_{outer} = \rho K C_{cp} F_{wake} F_{KLEB}(y) \quad (16)$$

$F_{KLEB}(y)$ is the Klebanoff intermittency factor which takes the following form;

$$F_{KLEB}(y) = \left[1 + 5.5 \left(\frac{C_{KLEB} y}{y_{max}} \right)^6 \right]^{-1} \quad (17)$$

where the constants K , C_{cp} , C_{KLEB} are assigned the following values by Baldwin and Lomax; $K = 0.0168$, $C_{cp} = 1.6$, $C_{KLEB} = 0.3$.

The parameter, F_{WAKE} , is evaluated as shown below.

$$F_{WAKE} = \text{smaller of } \left[\begin{array}{cc} y_{max} F_{max} & \\ C_{WK} y_{max} u_{DIF}^2 / F_{max} & \end{array} \right] \quad (18)$$

where u_{DIF} is the total velocity difference across the boundary layer or wake and C_{WK} is a constant. C_{WK} was originally assigned a value of 0.25 by Baldwin and Lomax, although there are indications that a value of 1.0 may be more appropriate^{5, 6}.

F_{max} is determined from the maximum value of the function $F(y)$, shown below, and y_{max} is the location where the maximum occurs.

$$F(y) = y |\omega| [1 - \exp(-y^+ / A^+)] \quad (19)$$

A key feature of the Baldwin-Lomax model is the evaluation of the parameter F_{WAKE} which removes the necessity of determining the displacement thickness or wake thickness in the first and second equations in the outer model. For attached boundary layers, the first part of the model $F_{WAKE} = y_{max} F_{max}$ is usually applied. For wake flows and separated boundary layers, some discretion is required in applying the model, as the normal direction, y , must be appropriately determined^{5, 6}.

4.3 Numerical Algorithms

In this paper, two basic approaches for solving the Navier-Stokes equations will be discussed. The first approach can be referred to as the time-dependent or unsteady approach. Here, the time-dependent Navier-Stokes equations are solved by marching the solution forward in a time-like fashion. The goal may be to determine the time-evolution of the flow physics from one state to another. Alternatively, this approach may be used to predict the steady flow over a flight vehicle where an initial "guessed" solution is iterated until a final converged solution is obtained.

The second approach assumes from the outset that the flow field does not vary in time and the steady flow equations can be solved. In the field of missile aerodynamics, probably the most popular method for solving the steady Navier-Stokes equations is the Parabolized Navier-Stokes (PNS) approach. Using the PNS approach, the flow field about the missile geometry is obtained by computing the solution over the missile body starting at the nose of the missile and "marching" to the tail. Only a single pass through the grid is required to obtain the solution, and for this reason, the PNS method is at least an order of magnitude more efficient than a comparable calculation performed using a time-dependent approach. Additionally, since only a few "planes" of data are required to be stored in memory at any given time, the PNS technique also requires much less computer memory compared with the time-dependent approach. Further details of the PNS approach are discussed below.

4.3.1 The PNS Approach

The governing equations for the PNS approach are based on the steady thin-layer Navier-Stokes equations which are obtained by dropping the temporal term from the unsteady thin-layer equations (Equation 12). In this form, the equations do not exhibit the proper characteristics for marching the solution downstream (taken here as the ξ direction) in a stable manner. It can be demonstrated that stable marching in the ξ direction will require that the eigenvalues of the Jacobian matrix of E (Jacobian matrix, $A = \delta E / \delta q$) to be positive and real^{7, 1}.

This will be satisfied as long as the local flow velocity in the marching direction is positive and greater than the local sound speed. Unfortunately, the condition of no-slip at the body surface due to the viscous boundary layer will produce local velocities which are less than the local sound speed. For this reason, the matrix of streamwise fluxes, E , must be modified.

A physical interpretation that can be applied here is that when the flow is supersonic, the state of the flow depends on conditions upstream; there is no "upstream influence". Close to the body surface where the flow becomes subsonic, the flow exhibits an elliptic nature where disturbances can propagate both upstream and downstream. The streamwise flux vector is modified in a way to eliminate the upstream influence within the subsonic region.

A key feature of PNS schemes is the treatment of the streamwise flux vector in the subsonic region close to the body surface (called the sublayer region). These "sublayer models" typically attempt to remove the explicit dependence of the pressure on the local flow field variables such as that which exists in the ideal gas law. Simple approaches have included eliminating the pressure gradient term within the subsonic region or backward differencing the pressure gradient term which has the effect of lagging the pressure gradient by one marching step. Two of the most commonly used sublayer models are those proposed by Schiff and Steger⁷ and Vigneron, Rakich and Tannehill⁸. These models are briefly described below.

The Schiff-Steger sublayer model makes use of the observation that the pressure gradient across the thickness of the boundary layer is zero. In their model, the sublayer region extends from body surface to a position several grid points beyond the point where the local streamwise velocity exceeds the sonic velocity. The pressure across the sublayer region is constant and is determined by evaluating the pressure at the edge of the sublayer region.

Another common sublayer model developed by Vigneron, et al., takes advantage of the fact that within the subsonic region, a portion of the pressure term can have a direct dependence on the local flow field variables (as it does in the supersonic regime) and still have the eigenvalues be real and positive. In this approach, the pressure gradient term has the following form;

$$\frac{\delta p}{\delta \xi} = \omega \frac{\delta \hat{p}}{\delta \xi} + (1 - \omega) \frac{\delta \bar{p}}{\delta \xi} \quad (20)$$

$$\omega = \sigma \gamma M_x^2 / (1 - (\gamma - 1) M_x^2); \quad M_x^2 < \frac{1}{\gamma(\sigma - 1) + 1}$$

$$\omega = 1; \quad M_x^2 \geq \frac{1}{\gamma(\sigma - 1) + 1}$$

Here, the pressure term, \hat{p} , is evaluated from the local flow field variables and the pressure term, \bar{p} , is evaluated by alternate means which might include backward differencing or by applying the condition of zero normal pressure gradient. The weighting function, ω , is a function of the local streamwise Mach number, M_x , and increases from zero at the body surface to one near the edge of the subsonic region. A safety factor, σ , is used to ensure stable marching. This approach allows a portion of the pressure gradient term to be evaluated from

the local flow field variables, while still satisfying the conditions for stable marching.

It should be clear that the constraints on stable marching limit the flow regimes where the PNS code can be applied. These constraints require the external flow to be supersonic and free from regions where the flow separation produces reverse flow in the streamwise or marching direction. It should be emphasized that crossflow (circumferential) flow separation such as that produced by lee side vortices can be handled by the PNS approach. In practical terms, most PNS codes will fail to run for freestream Mach numbers below about Mach 1.5-1.7, even though the flow could still be considered supersonic. As well, many flight bodies possess discontinuities in body geometry which would produce axial flow separation. Often discontinuities can be handled using fillets without affecting the results significantly. If the flow separation has a strong effect on the aerodynamics, the region of flow separation should probably be treated using a time-dependent code.

Because the PNS technique advances the solution by marching downstream, an initial solution near the nose of the projectile is required. Several approaches have been devised to obtain this initial solution. For missiles with sharp nosetips, a conical step-back procedure is often used. Here the actual nosetip is replaced by a conical extension near the nose tip. The assumption of conical flow is applied; that is, the flow along rays emanating from the cone vertex is assumed to be self-similar. Grids at successive streamwise stations are formed which are also conical in nature. The solution is advanced downstream by one marching step. Using conical flow assumption, the new solution is scaled back to the initial streamwise plane. The process of advancing the solution forward one step and scaling the solution back is performed successively until a converged solution is obtained.

If details of the flow in the vicinity of the nosetip are important or have impact on the flow field downstream, auxiliary codes can be applied to more accurately determine the flow field in the nosetip region. Flow field data from these codes can be used to construct a starting plane of data downstream from this region for use by the PNS code. This type of approach may be required if the missile geometry has a blunt nose cap. In the flowfield in front of the nose cap and behind the bow shock, the flow will be locally subsonic. The flow in this region can be computed using a time-dependent Navier-Stokes code.

4.4 Gridding

The gridding strategies used in Navier-Stokes computations require that both the inviscid effects (such as expansions, shocks) and the viscous effects (within the boundary or shear layers) are adequately resolved. For missile applications, a typical inviscid grid might be fairly uniformly distributed throughout the flow field with some mild clustering of the grid points near the body. Due to the presence of the thin boundary layers near on the body surface, a grid for a viscous calculation will require a fairly fine grid within this region so that the viscous gradients will be adequately resolved. Outside the boundary layer, the grid should transition back to the level of resolution required to resolve the inviscid

effects. To obtain a suitable grid, the analyst will have to balance the need for a fine grid within the viscous regime with the need to use adequate grid points in the inviscid region. The resulting grid will characteristically require a significant level of stretching as the grid transitions from a fine grid at the body surface to the inviscid grid further away from the body.

The stretching of the grid should be controlled to some extent because of accuracy (truncation error) considerations. One rule of thumb is to limit the stretching within the grid to 15 to 20 percent. For example, proceeding away from the body, the radial height of each successive grid point should not increase by more than 15 to 20 percent of the radial height of the previous grid point.

Within attached boundary layers, it is possible to define an additional requirement which controls the resolution of the grid within the boundary layer. This approach utilizes the non-dimensional boundary layer coordinate, y^+ , which is defined in Equation 15. The value of y^+ at the first grid point above the wall can be monitored and an acceptable range of values can be determined by numerical experimentation. For turbulent boundary layers where the body surface temperatures are close to the ambient temperature, it appears that the viscous effects can be properly resolved when at least the first grid point above the wall is located at a y^+ of about three. This requirement seems to hold over a wide range of Mach numbers, from subsonic to supersonic. Placing the grid point in this location, allows at least one point within the "laminar sublayer" (also termed the "viscous sublayer") where the velocity profile varies in a fairly linear manner with distance from the wall.

As a demonstration of the effect of resolution on the solution, PNS calculations were performed on an eight degree cone-cylinder body at a flight Mach number of 4, zero degree angle of attack and at a Reynolds number based on diameter of 3.2×10^6 . The calculations were performed by adapting the grid so that y^+ at the first point above the wall was close to a specified value over the entire body. Thus, the physical grid had a finer spacing near the nose and gradually increased as the boundary layer thickened. Table 1 shows the viscous axial force component for the various levels of grid resolution over ten calibers of body length. A three-point stencil (second-order accurate) was used to evaluate the velocity gradient at the wall. The results show that as the spacing at the wall is decreased, the results approach a uniform value in an asymptotic fashion. If a two-point stencil (first-order accurate) is used to evaluate the velocity gradient, the effect of wall spacing will be more pronounced.

y^+	C_{A_v}	% Difference
1.	.0642	-
2.	.0643	0.2 %
3.	.0648	0.9 %
6.	.0689	7.3 %
10.	.0730	13.7 %

Table 1. Viscous Component of Axial Force Coefficient as a Function of Grid Resolution

The sensitivity of viscous drag to grid resolution is related to two effects; (1) the effect of grid resolution on the prediction on the velocity gradient from the velocity profile and (2) the effect of grid resolution on the prediction of the velocity profile itself. These effects are illustrated in Figure 1 which shows a portion of the longitudinal velocity profile close to the wall at an axial location 6.2 calibers down from the nose. The $y^+ = 1$, $y^+ = 2$ and $y^+ = 3$ results are practically identical, although as the wall spacing is increased ($y^+ = 6$ and 10), the velocity profile deviates from the fine grid result. Close to the wall, the $y^+ = 6$ result closely matches the fine grid velocity profile although the skin friction drag is over-predicted by seven percent for this case. In this case, much of the over-prediction can be attributed to the evaluation of the velocity gradient. This can be demonstrated by evaluating the velocity gradient from the $y^+ = 1$ solution based on three grid nodes which are close to the location of the first three grid nodes of the $y^+ = 6$ solution, and comparing the result with the gradient evaluated directly from the $y^+ = 6$ solution. When this is done, the gradient from both cases differ by less than one percent demonstrating that the problem here is the evaluation of the gradient rather than the prediction of the velocity profile. As the grid spacing at the wall is increased above $y^+ = 6$, the velocity profile deviates further from the fine grid result resulting in a less accurate evaluation of the skin friction.

Once the maximum radial extent of the computational domain has been established, the constraints on wall spacing and grid stretching can be used to determine the number of points required to cover the region between the body and the outer boundary. If the number of grid points is limited (by available computer memory for instance), one of the two constraints may have to be relaxed, though problems with the accuracy of the results may result. On the other hand, use of an overly fine grid adds an additional computational burden because of the increase in the number of points and because a smaller time-step or marching step size will typically be required.

With the PNS approach, the computational grid is typically generated within the code as the calculation proceeds down the body. By monitoring the y^+ at the first grid point above the wall at each successive step, an adaptive grid approach can be implemented which allows the grid spacing near the wall to be adjusted based on the boundary layer growth. It has been found that problems may arise if the grid spacing is adjusted at each point based on the local value of y^+ . It is often better to increase or decrease the grid spacing by a certain percentage if the y^+ at the first point above the wall falls outside a specified value. This reduces the possibility that numerical oscillations in the flow field will produce undesirable spikes and kinks in the grid which can lead to further instability. For similar reasons, it is also desirable to vary the circumferential distribution of the grid spacing at the wall in a uniform fashion. For axisymmetric bodies, this might be accomplished by monitoring the value of y^+ at the first point above the wall on the wind and lee sides of the body and adjusting the grid uniformly around the body. For more complicated geometries, other strategies can be devised to appropriately refine the grid in regions of high gradients.

Grid generation with the time-dependent codes is performed before the start of the calculation and before the flow characteristics are known. Often for particular classes of problems, it is possible to use past experience as a guide in determining the proper level of grid refinement before performing the grid generation process.

5. FOREBODY STATIC AERODYNAMICS

5.1 Validation

This section addresses computational studies where details of flow field predictions have been compared with experimental data for the purposes of benchmarking the computational technique. The missile designer, being typically interested in the integrated effect of the flow field, is not usually concerned with the flow details at the level discussed here. However, the accuracy of the integrated effect generally depends on the accuracy of the important flow details. Because of this, it is useful to present a sampling of results which seek to benchmark the accuracy of the predicted flow details.

One early validation of the Schiff-Steger PNS code was performed by Schiff and Sturek⁹. Calculations were performed for a conical body and for a secant ogive-cylinder-boattail (SOCBT) configuration. A schematic of the SOCBT configuration is shown in Figure 2. The SOCBT configuration models many of the geometric features found on an artillery projectile although nose bluntness and the rotating band are not simulated. Calculations were performed at Mach 3 and over a range of angles of attack up to about ten degrees. The computational results were benchmarked with wind tunnel measurements^{10, 11, 12, 13} and included aerodynamic force and moment measurements as well as pressure and boundary layer surveys. This work was followed by related computational study by Sturek and Schiff¹⁴ which focused on the Magnus effect for spinning axisymmetric projectile geometries. As part of this study, further validations were performed for a spinning SOCBT geometry. The configurations examined in both studies had sharp nosetips and the conical step-back procedure was used to generate the starting solution near the nose of the projectile. Since a boundary layer trip had been used in the experiment, the PNS calculations simulated a turbulent boundary layer over the complete configuration using the Baldwin-Lomax turbulence model. Discussion of the important validation results from these two studies is provided below.

Comparisons of the axial and circumferential distributions of surface pressure were made for the non-spinning SOCBT geometry over a range of angles of attack. Figure 3 shows the wind and lee side pressure distribution for the SOCBT body at Mach 3 and an angle of attack of 6.3 degrees. This figure shows a comparison between PNS and inviscid computation and experimental data. The biggest differences between the PNS and inviscid calculations appear on the boattailed region of the projectile. On this scale, both the PNS and inviscid calculation appear to be in good agreement with the experimental data. The circumferential distribution of pressure, shown in Figure 4, reveals bigger differences between PNS and inviscid calculations with the PNS results providing better agreement with the experimental data than the inviscid calculations, particularly on the boattailed section of the body. At higher angles of at-

tack, the comparisons between the PNS results and the experimental results were less favorable, particularly on the lee-side of the boattailed portion of the body where a region of crossflow separation was present. The PNS results were, however, in better agreement with the experimental data than were the inviscid computations.

Comparisons between axial velocity profiles obtained from the computation and from wind tunnel data were also performed in both studies. Two such comparisons are shown in Figures 5 and 6. The computations are in reasonable agreement with experimental data with velocity deficit in the lee-side ($\phi = 180^\circ$) wake region being generally well represented in the computation. Sturek and Schiff did note some small differences in the velocity profiles in the lee-side wake region which could be attributed to the vortices in the region of crossflow separation.

A later study by Degani and Schiff¹⁵ revealed that within the region of crossflow separation, the Baldwin-Lomax turbulence model tended to over-predict the turbulent length scale causing inaccuracies in the flow field predictions. Degani and Schiff proposed a modification to the original Baldwin-Lomax model which considerably improved the predictions in the crossflow region. In particular, the authors found that the value of y_{max} used in the outer region portion of the turbulence model was being over-predicted. (y_{max} is determined from the location where $F(y)$ reaches a maximum. $F(y)$ is essentially the moment of vorticity.) Outside the region of crossflow separation, the moment of vorticity typically had a well defined maximum and the value of y_{max} could be determined without any ambiguity. However, in the region of crossflow separation, the moment of vorticity was observed to have a number of local maxima because of the shape of the velocity profile in the leeward wake. The unmodified Baldwin-Lomax model tended to select a y_{max} which was an order of magnitude greater in the region of lee-side crossflow separation than the y_{max} on the windward side. Degani and Schiff proposed that the proper determination of y_{max} could, in most cases, be obtained by finding the first local maximum in y_{max} when sweeping out from the body surface. Near the circumferential location of the primary crossflow separation, Degani and Schiff noted that problems in determining an appropriate value of y_{max} could still occur. To deal with this situation, at each axial location, the determination of y_{max} proceeded from the windward to the leeward side. The radial search for the maximum vorticity was limited to the region between the body and a radial location of 1.5 times the y_{max} at the previous location. If no local maximum was found in this region, the value of y_{max} (and F_{max}) from the previous circumferential location was used.

To validate their modifications to the Baldwin-Lomax model, Degani and Schiff performed calculations for a number of conical bodies at angles of attack which were two to three times the cone half-angle and for a six-caliber secant ogive-cylinder (SOC) geometry at angles of attack of six and ten degrees. In each case, the large angles of attack produced regions of crossflow separation on the lee side of the body. The computational results for the conical body showed much improved agreement with pressure data and circumferential and axial velocity profile data. In fact, for some of the conical bodies, the

computational results with the modified model showed a wider region of crossflow separation with three vortices present, compared to the results obtained with the original Baldwin-Lomax model which showed only a single crossflow vortex.

For the SOC geometry, Degani and Schiff also demonstrated improved agreement with the pressure and velocity profile data through the use of their modified model. Figures 7 and 8 show the circumferential pressure distribution near the aft end of the model for angles of attack of 6.3° and 10.4° degrees. The results show improved agreement on the lee side of the body compared with the original Baldwin-Lomax model, particularly at the higher angle of attack. The modified model also improved the agreement in the velocity profiles, particularly near the edge of the region of crossflow where the largest differences between experiment and the unmodified Baldwin-Lomax computational results were observed. This is demonstrated in Figure 9 which shows a comparison of the original and modified Baldwin-Lomax results with experimental results near the edge of the crossflow region.

The effect of nose bluntness on pressure and velocity fields over a nine caliber body of revolution was examined computationally by Guidos, et al.¹⁶ The computations were validated using a comprehensive set of wind tunnel data obtained by Dolling and Gray¹⁷. Both the computational and experimental studies examined sharp, hemispherically blunted and flat nosetips for several bluntness ratios (nose tip radius/body radius) with the largest bluntness ratios of 25% providing the significant effect compared with the sharp nosetip. Results were obtained at Mach 3 and at an angle of attack of 2.9 degrees. A schematic of the tangent ogive nosetip geometry is shown in Figure 10.

The PNS approach was used to predict the flow downstream of the nosetips. Starting solutions for the sharp nosetip geometry were obtained using a conical step-back procedure. For the blunted geometries, a time-dependent thin-layer Navier-Stokes code^{18, 19, 20, 21} was used to obtain the flow field in the vicinity of the nose cap. Sample grids for the time-dependent calculations are shown in Figures 11 and 12. For the blunted geometries, the starting plane for the PNS calculation was obtained using a plane of data which was several planes upstream of the downstream boundary of the computational domain. Since the flow field variables at the downstream boundary are obtained by extrapolating the values from the interior of the domain (supersonic outflow boundary condition), the use of a plane of data from the interior of the computational domain was thought to minimize the errors associated with using the downstream boundary as the starting plane.

Evidence from the experiment indicated that the flow on the nosetip was laminar and transitioned to turbulent on the ogive. Laminar solutions were obtained in the nosetip region. The PNS approach utilized an effective viscosity which allowed the transition from laminar to turbulent flow to be modeled. The location of transition was specified in the computation using the spark shadowgraphs as a guide.

Figures 13 and 14 show the computed Mach contours on the wind and lee sides of the flat nosetip. Also

shown are the locations of the bow shock and the imbedded recompression shock obtained from the experiment. The computed location of the bow shock corresponded to the outer boundary of the computational domain which was shock fit. The location of the imbedded shock which was "captured" within computational domain was determined after the completion of the calculation using a post-processing algorithm. The location of the recompression shock is well predicted in the computation and appears to be influenced by the location of the separation bubble at the corner of the nosetip.

The computed pressures were in good agreement with the experimental results for all three nosetip geometries. The pressure distributions on the wind and lee sides of the flat nosetip are shown in Figures 15 and 16. The agreement between computation and experiment is good with the low pressure region associated with the separation bubble downstream of the nose corner well modeled. Lee side velocity profiles for the pointed, hemispherically blunted and flat nosetips are shown at three downstream locations in Figures 17 and 18. For the purposes of comparison, the pointed nosetip results are shown in both figures. The velocity deficit produced by the nose bluntness is evident for both nosetips with the flat nosetip having the biggest effect.

5.2 Pitch Plane Static Coefficient Predictions

In this section the prediction of the static pitch-plane aerodynamics will be discussed. Predictions for both axisymmetric bodies and finned bodies will be presented.

For a large class of vehicles, the accurate prediction of the static pitch-plane derivatives can be obtained without the need of predicting the flow in the base region of the projectile. This is particularly true for flight bodies with flat bases flying at supersonic velocities. In the supersonic regime, the flow over the forebody is usually unaffected by the flow in the base area because of the lack of upstream influence. As well, for vehicles with flat bases, the normal force contribution from the base is due only to the shear stresses acting on the base surface which yield a very small integrated effect. The pitching moment can also have an additional pressure effect from the base due to the wind side to lee side pressure gradient. This is typically small due primarily to the relatively small moment arm through which the pressure forces can act. One must be careful in analyzing bodies with base cavities because of potential for significant contributions to the pitch-plane aerodynamics due to these regions. Limited experimental evidence indicates that the base cavity will produce a stabilizing effect and will cause predictions which ignore this effect to be conservative.

Because the base region effect is limited, techniques which consider just the forebody, such as the PNS approach, can be used effectively to predict the static pitch-plane aerodynamics without the need for considering the base flow.

5.2.1 Pitch-plane predictions for axisymmetric bodies

Pitch-plane aerodynamic predictions were performed for six-caliber secant ogive-cylinder (SOC) and

secant ogive-cylinder-boattail (SOCBT) configurations by Sturek and Schiff¹⁴ as part of their study of the Magnus effect on spinning projectiles. The PNS predictions were made across a range of Mach numbers from Mach 2 to Mach 4 and compared with wind tunnel data¹³. Figures 19 and 20 show comparisons between computation and measurement for the pitching moment coefficient slope and normal force center of pressure for the SOCBT body. Excellent agreement is seen between the computation and experiment for both of these coefficients. Similar agreement was demonstrated for the SOC body as well.

The static aerodynamics predictions presented above were obtained at low angles of attack (2°). A follow-on study by Sturek and Mylin²² included aerodynamic coefficient predictions up to ten degrees angle of attack. Figure 21 shows a prediction of the normal force as a function of angle of attack at Mach 3 for the SOC and SOCBT bodies. The predictions are in good agreement with the experimental data even at the higher angles of attack where some non-linear behavior in the normal force coefficient is evident. The predictions shown here were obtained with the original Baldwin-Lomax turbulence model. As seen previously, at the higher angles of attack, the unmodified turbulence model will produce inaccuracies in the flow details such as the surface pressure distribution. However, the effect on the integrated force coefficient appears to be small for these bodies.

Presumably the prediction of pitch plane aerodynamics of short bodies such as those discussed above can be performed accurately at supersonic velocities and small angles of attack with good accuracy using inviscid procedures. However, the computing times required to perform the viscous calculation are relatively small (20 CPU minutes on a Cray X-MP computer) and it may be possible to obtain additional coefficients from a single run such as forebody drag and pitch damping or Magnus coefficients.

For higher length-to-diameter (L/D) ratio bodies, viscous effects can show a bigger effect on the pitch plane coefficients. Comparisons of PNS and inviscid code results with wind tunnel data for high L/D bodies were made by several researchers and compiled in the paper by Jones, et al.²³ The study showed that the PNS results, which were performed using the Baldwin-Lomax turbulence model, gave good agreement with experimental data for long axisymmetric bodies up to angles of attack of about five degrees. Beyond five degrees, the problems in computing the lee side crossflow separation resulted in an under-prediction of the normal force. Figure 22 shows a schematic of one of the bodies examined in the study. Figures 23-26 show the normal force loading distribution and the normal force coefficient as a function of distance from the nose for angles of attack of three and seven degrees at Mach 3.5. The three degree angle of attack results show good agreement with wind tunnel data^{24, 25} for both the normal force and loading distribution. At seven degrees angle of attack, the experimental loading distribution (and hence the normal force) shows a consistently higher value over the rear half of the body than does the PNS result. This results in an over-prediction in the normal force of about 15%-20% at the higher angle of attack. Examination of the pressure distribution for the seven degree case shows

good agreement with the experiment data on the nose and on the windward side of the body. At the aft end of the body on the leeward side, differences exist in the region of recirculation. The differences between computation and experiment may be due to problems with the turbulence model. Application of the Degani and Schiff modifications to the Baldwin-Lomax turbulence model improved the results only slightly.

Other studies have addressed prediction of the aerodynamics of axisymmetric bodies at higher angles of attack. Hartwich and Hall²⁶ computed the low speed symmetric vortical flow over a tangent-ogive cylinder at angles of attack of 20° and 30° . Their results showed good agreement with the experimental surface pressure data over six calibers of body length. Degani and Levy²⁷ computed the low speed asymmetric vortical flow about a tangent-ogive cylinder with a small surface imperfection located near the nose. The comparison of the experimental and computation circumferential pressure distributions were quite good over six calibers of body length. A key feature of both of these studies was the application of modified forms of the Baldwin-Lomax turbulence model.

The transonic pitch-plane aerodynamics of axisymmetric vehicles has been examined in a number of studies over the past decade. This problem is of interest because the pitch-plane aerodynamic coefficients exhibit a "critical behavior" (a rapid change in magnitude with flight velocity). Early studies of this problem²⁸ demonstrated that many of the flow features could be captured using Navier-Stokes methods, though improvements in the accuracy of the integrated aerodynamic coefficients was still desired. Subsequently, Sahu²⁹ was able to demonstrate a computational capability for predicting the pitch-plane aerodynamics for boattailed projectiles by exploiting improvements in CFD algorithms and computer hardware.

Sahu²⁹ performed a series of computations for a secant ogive cylinder boattailed body (SOCBT) similar to that shown in Figure 2. The calculations were performed at 4° angle of attack and spanned a range of transonic Mach numbers ($M_\infty = 0.9-1.2$). The computational requirements for each calculation was about 16 million words of memory and about 20 hours of CPU time on a Cray-2 computer. Figure 27 shows a comparison of experimental and computed surface pressures on the wind and lee sides of the body at Mach 0.96. The computed results are in good agreement with the experimental pressure data. The comparisons at other transonic Mach numbers showed similar agreement.

In the same study, Sahu also performed calculations for an artillery shell configuration (see Figure 28) which had been tested in an aerodynamics range. Figure 29 shows the predicted and experimental pitching moment coefficient across the range of transonic Mach numbers. The predicted values, which shows the "critical behavior" in the pitching moment, is in good agreement with the range data.

A later study by Sahu and Nietubicz³⁰ utilized this capability to examine the pitch-plane aerodynamic behavior of a projectile with a base cavity. Figure 30 shows a side view of the projectile geometry. The projectile was originally designed with an indented base as

shown in Figure 31. Later, a dome base was proposed for the purpose of improving the structural integrity of the shell. Firing tests of the dome base revealed differences in the flight performance, particularly in the trajectory "drift" which is related to the lift of the projectile. This was subsequently confirmed by the computation. Figure 32 shows the predicted normal force coefficient for both configurations. The dome projectile is seen to have about ten percent more normal force at the low transonic velocities though at the higher velocities, the differences are relatively small. The pitching moment coefficient is also affected by the base configuration as shown in Figure 33. Both the computation and the range data show a similar effect of base configuration across the range of Mach numbers. Detailed examination of the flow field data revealed that at the lowest Mach number about 25% of the difference between the standard and dome base was due to the lift generated in the base cavity with the remainder of the lift difference being produced by the upstream influence of the wake on the flow over the projectile body.

In general, the results seem to indicate that the low angle of attack flow over axisymmetric bodies can be accurately computed using Navier-Stokes approaches. At higher angles of attack where crossflow separation plays an important role, the accuracy of the results appears to be dependent on the turbulence modeling. Accurate high angle of attack results at low speed and moderate length to diameter ratios have been demonstrated. Further research at high speed and high L/D s is still required.

5.2.2 *Pitch-plane predictions for finned bodies*

Prediction of the pitch-plane aerodynamics for finned bodies has also been made using Navier-Stokes approaches. In this section examples of predictions made with both PNS and time-marching approaches are discussed.

For PNS calculations of flight vehicles with highly swept fins, the most commonly used gridding strategy utilizes a single grid which is wrapped around the projectile geometry. In some ways, this approach is simpler to implement for viscous flows than the zonal grid approach often applied for finned geometries using inviscid codes. However, it often requires more grid points and tends to be less flexible because it is generally applicable to a more restrictive class of fin geometries (highly swept fins). Because there is a single direction which is nearly normal to the body surface across the projectile geometry, the thin-layer assumption can be applied in a straight forward manner. Normally, this approach requires the geometry to be fairly smooth; that is, local slope of the body surface is continuous. Thus, the leading edge is typically rounded and the fin-body junction is often filleted.

Rai, Chaussee and Rizk³¹ utilized this approach to compute the flow over a cone-cylinder-finned body. They adapted an elliptic grid generation approach to obtain the grid over the finned portion of the body. Through appropriate controls in grid generation approach, a smooth grid is generated which has the important characteristic that the grid lines are nearly normal to the body surface in the circumferential plane. Figure 34 shows a circumferential plane of grid on a finned body which was generated using the approach described above.

The approach of Rai, et al.³¹ was later applied by Weinacht, et al.^{32, 33} to compute the static pitch-plane aerodynamics for a similar class of projectile shapes such as that shown in Figure 35. The computational requirements for PNS calculations for this body is modest; about 1-2 hours of CPU time and about 0.5 million words of memory on a Cray X-MP computer.

The computational model for this projectile includes several geometric simplifications. Because the nose bluntness on the actual flight body is small, the computations were performed assuming a sharp conical nose and the conical step-back procedure employed to generate the starting solution. Secondly, the actual geometry has a number of sub-caliber circumferential grooves which cover much of the cylindrical surface. These grooves are required to mate the projectile with the rest of the launch package. These grooves produce a roughness effect which can thicken the boundary layer somewhat, producing a small increase in drag and potentially reducing the fin effectiveness. The geometry is currently modeled as a smooth surface and the effect of the grooves is not modeled.

Figure 36 shows the development of the normal force coefficient over the body of the M735 body at Mach 4 and two degrees angle of attack. Comparison is made between PNS results and results obtained using the inviscid code, SWINT³⁴. Also shown is the total normal force coefficient obtained from aerodynamic range data. The results are generally in good agreement and indicate that the viscous effects are small for this geometry.

Figure 37 and 38 show the zero-degree normal force and pitching moment coefficient slope for the M735 geometry across a range of supersonic Mach numbers. The PNS results are compared with data obtained from aerodynamics range firings. (The range value of the pitching moment is determined from the frequency of the yawing motion which can be accurately determined. The range value of the normal force is obtained from the amplitude of the center of gravity motion which tends to be small, decreasing the accuracy of the measurement. Thus, the pitching moment tends to be a more critical comparison.) The normal force predictions fall within the scatter of the aerodynamics range data. The pitching moment predictions show a slight over-prediction compared with the range data. The over-prediction in the pitching moment is thought to be due to the fact that the modeled geometry does not incorporate the effect of the grooves which might produce a reduction in the fin effectiveness. If the differences between computation and experiment is due to the groove effect, the results indicate that the grooves produce a loss of fin effectiveness of several percent. The results indicate that the center of pressure is predicted to within about one quarter of a body diameter (two percent of the body length). Also shown in Figure 38 are inviscid predictions made using an inviscid option in the Schiff-Steger PNS code. The inviscid results show an over-prediction of the pitching moment by about ten percent compared with the viscous results.

This configuration was later examined by Giolda and McRae³⁵ using an explicit PNS approach based on the explicit MacCormack algorithm. Their predicted normal force coefficient was within five percent of the predictions discussed above.

Similar predictions have been made for a longer length-to-diameter finned body shown in Figure 39. As for the previous body, the computational model assumes a sharp nosetip and ignore the grooves on the cylindrical portion of the body. The configuration also has fins which overhang the cylindrical base of the projectile. To model this portion of the body, the computations are performed as if the base of the projectile was aligned with the trailing edge of the fins. When the forces are computed, the "fictitious" part of the body is ignored. Because the flow is supersonic, and the effect of the baseflow on the fins is small, the forces acting on the fin surfaces are thought to be accurately predicted. A comparison of the predicted pitching moment coefficient with range data for a range of supersonic Mach numbers is shown in Figure 40. The results also show a slight overprediction compared with the range data. Again, this difference between experiment and computation may be associated with a small loss in fin effectiveness from the circumferential grooves which are not modeled in the computational approach.

Time-marching approaches have also been used to predict the aerodynamics of missile configurations at angle of attack. Priolo and Wardlaw³⁶ performed Navier-Stokes calculations for a delta wing configuration and for a canard-body-tail configuration at supersonic velocities. The delta wing configuration calculations included both inviscid and viscous (laminar) results. The viscous results were generally in better agreement with the experimental data than the Euler results. Results for the canard-body-tail configuration, shown in Figure 41, were also presented. The computations were performed at Mach 2.5 and 20° angle of attack. This calculation was performed using a zonal grid strategy with 11 blocks and contained over 750,000 points. Turbulent viscous solutions for this configuration were obtained using over 50 hours of computer time on a Cray Y-MP computer. Figures 42 and 43 show pressure contours and simulated oil flow visualizations on the body surfaces. The oil flow visualizations show the presence of the primary (body) vortices and secondary (tip) vortices on the fin surface. No force or moment comparison were presented for this configuration.

It is interesting to note that Euler space-marching computations for the canard-body-tail configuration have been performed previously³⁷. The static force and moments predicted using the inviscid technique, SWINT³⁴, were in good agreement with wind tunnel data particularly at low angles of attack. Obviously, the inviscid predictions were obtained at a small fraction of the computational cost of the viscous results presented here. Viscous calculations for this type of vehicle appears to be more amenable to solution using time-marching rather than space-marching approaches because the vehicle geometry includes a canard. Even for the case where the canard has a sharp trailing edge, modeling of the flow in the wake behind the canard is difficult using the PNS approach. The no-slip condition on the fin surface and at the trailing edge implies that at least some portion of the trailing edge wake will be subsonic and a sub-layer model will be required. Sublayer modeling in the wake of lifting surfaces has been addressed in the literature³⁸. Although techniques may exist for treating forward mounted lifting surfaces using PNS techniques, it is clear that such modeling has not seen wide spread usage compared to

inviscid techniques.

6. AERODYNAMICS IN PURE ROLLING MOTION

The spin history of the projectile can be determined from the following ordinary differential equation³⁹,

$$I \frac{dp}{dt} = \frac{1}{2} \rho_{\infty} a_{\infty}^2 M_{\infty}^2 D S_{ref} C_l \quad (21)$$

where p is the spin rate, t is time, I is the axial moment of inertia, C_l is the net aerodynamic roll moment coefficient acting on the projectile, and ρ_{∞} , a_{∞} , M_{∞} , D , and S_{ref} are, respectively, the reference density, speed of sound, Mach number, diameter, and area.

The net aerodynamic roll moment is composed of two components, the roll producing moment and the roll damping moment. The roll producing moment, which induces spin on the projectile, results from the aerodynamic loads produced by either asymmetries in the fin or body geometry or by the fin cant, while the roll damping contribution consists of pressure and viscous forces that oppose the spin. The relationship of these contributions to the net aerodynamic roll moment is expressed below in non-dimensional form,

$$C_l = C_{l_0} + C_{l_p} \frac{pD}{V} \quad (22)$$

where C_{l_0} is the roll producing moment coefficient, C_{l_p} is the roll damping moment coefficient and $\frac{pD}{V}$ is the non-dimensional spin rate. The roll damping coefficient will differ in sign with the roll producing moment coefficient and will be negative if the direction of positive roll moment is in the direction of positive spin.

In the computational frame work, where the projectile is flying at constant velocity, Equation 22 shows that the roll producing moment can be obtained by computing the net aerodynamic roll moment at zero spin rate. Likewise, the roll damping moment is obtained by computing the net aerodynamic roll moment on the projectile at a fixed spin rate, subtracting the roll producing moment from it and dividing by the spin rate. The equilibrium spin rate, which occurs when the net aerodynamic roll moment is zero, is obtained by dividing the roll producing moment by the roll damping moment. Schematically, the various components of the rolling motion are shown in Figure 44.

6.1 Axisymmetric bodies

For axisymmetric bodies, the body symmetry requires that the roll producing moment be zero and the roll damping moment is produced by viscous shear stresses acting on the body surface. Prediction of the roll damping moment for axisymmetric bodies is easily accomplished because a spin boundary condition can be imposed at the body surface without introducing any time-dependency. The spin boundary condition simply requires that the usual no-slip boundary condition be modified so that the circumferential component of velocity tangent to the surface is equal to the product of the local radius and the spin rate. If angle of attack effects are thought to be small, the calculation can be performed at zero degrees angle of attack. For this case, the flow

will be axisymmetric and a two-dimensional calculation can be performed.

Sturek⁴⁰ obtained prediction of the roll damping of axisymmetric projectiles at supersonic velocity. His results were compared with design code results and the two set of results compared to within about 25 percent. More recently, Weinacht⁴¹ obtained results for the roll damping of axisymmetric bodies at supersonic velocities for a family of axisymmetric bodies. Figure 45 shows a schematic of the body geometry. In the range tests⁴², three body lengths were tested; 5, 7 and 9 calibers in total body length. The predictions of the roll damping versus body length is shown in Figures 46 and 47 for Mach numbers of 1.8 and 2.5. The computations show a slight over-prediction in the roll damping moment. The computational results, which were obtained using a fully turbulent boundary layer, might be improved by accounting for the region of laminar flow on the nose which was observed in the experiment. The increase in the coefficient with decreasing Mach number is reflected in both the computation and the experiment.

6.2 Finned bodies

Predicting the rolling motion of non-axisymmetric bodies is complicated by the fact that in the typical reference frame, the flow is time-dependent. At zero degrees angle of attack, it is possible to use a rotating coordinate frame to remove the time dependency from the problem. This coordinate frame is fixed to the body and thus rotates at the roll rate of the flight vehicle. In this coordinate frame, at a constant spin rate, the unsteady nature of the flow which is produced by the roll will be removed. Use of the rotating coordinate frame will require that the Coriolis and centrifugal force terms be added to the governing equations.

This approach has been applied by Weinacht and Sturek^{43, 44} to predict the roll characteristics of finned projectiles. Sample results for the M829 finned body (see schematic in Figure 39) are presented here. The roll characteristics for this body were obtained by performing the computations over a range of Mach numbers ($M = 3.0$ to 5.5) and non-dimensional spin rates ($pD/V = 0$ to $.015$) for free-flight (sea-level) atmospheric conditions. The computations were compared with data obtained from range firings.

Figure 48 shows the comparison of the steady-state spin rate as a function of Mach number. The computed results are bracketed by the range data, demonstrating that the predictions of the steady-state spin rate are within the accuracy of measurements.

Comparisons of the roll producing and roll damping moment coefficients are shown in Figures 49 and 50. The computed results for both coefficients lie somewhat above the range data. At Mach 5.25, the range values of the roll producing moment coefficient are 4 to 35 percent below the computed result, while the range values of the roll damping moment coefficient are 10 to 38 percent below the computed value. The result that both coefficients show similar comparisons between range and computed values is a reflection of the fact that the steady-state spin rate is approximately the ratio of the roll producing moment coefficient to the roll damping moment coefficient. As was shown in Figure 48, this

ratio is accurately predicted. It should be noted that the range data were obtained by measuring the roll rate at only two stations and assuming that the spin rate at launch was zero. Additional measurement stations are obviously desirable.

Using the computed roll producing and roll damping moment coefficients, spin histories of the projectile were determined by solving the roll equation (Equation 21). A representative trajectory (launch Mach = 5.25) is shown in Figure 51. The computed spin history falls within the range of the range data at both of the measurement locations. This type of comparison may be a better indicator of the accuracy of the computational approach than the comparisons with the individual coefficients given the limited number of data stations. The computed trajectories show that at the second measurement station, the projectile is within 3 percent of the steady-state spin rate.

This approach for predicting the roll producing and roll damping moments has also been utilized by Daywitt, Prats and Chan⁴⁵ to determine the roll characteristics of a finned projectile with low aspect ratio canted fins. The authors benchmarked PNS calculations with wind tunnel data for fin cant angles of 0.1° and 0.5° degrees. The PNS predictions of the roll producing moment showed good agreement with the wind tunnel data and appeared to show the correct variation of the roll producing moment with cant angle. The PNS predictions of the roll damping coefficient were within 10% - 20% of predictions made with the NAVY Aero-Prediction code⁴⁶. A comparison of the roll history over the first 0.5 seconds of flight showed reasonable agreement with the experimental data.

The computational study of Edge⁴⁷ which examined the roll characteristics of a missile with "wrap-around" fins serves as a final example in this section. For several decades, missile designers have used wrap-around fins as a method of providing aerodynamic stabilization for tube-launched munitions. These fins are folded down around the aft end of the body so that the flight body maintains a circular cross section while inside the launcher, hence the term "wrap-around fins". After launch, the fins are deployed using dynamic or mechanical means. Because the fins conform to the body prior to launch, the cross section of each fin blade is a circular arc when deployed.

While wrap-around fins have obvious advantages for launching munitions from circular cross-section launchers, aerodynamic problems have been associated with their use. Because the fin blades are curved, the air flow on adjacent sides of the fins is not symmetric. The asymmetric flow of air across the fins will produce aerodynamic loads on the fins that cause the projectile to roll. The magnitude and, more importantly, the direction of the roll moment are dependent on the flight velocity. Typically, munitions which are launched at supersonic velocity have been observed to roll in the direction away from the fin's center of curvature. As the velocity of the projectile slows due to aerodynamic drag, the roll of the projectile decreases and may eventually change direction at low supersonic or transonic velocities. This type of behavior can cause poor flight dynamics performance for the projectile. A simple model of the roll reversal mechanism does not appear possible. Instead the phe-

nomenon appears to involve complicated flow physics such as the pressure field on the fin planform which is produced by the impingement of shock waves from adjacent fins. Thus, engineering design codes may not be fully capable of addressing this problem.

Edge⁴⁷ utilized a time-dependent full Navier-Stokes approach to predict the roll behavior of a missile configuration with four unswept wrap-around fins. The missile geometry is shown in Figure 52. Because of the rectangular nature of the fin geometry, a zonal grid topology was utilized. Utilizing the periodic symmetry which exists at zero degrees angle of attack, seven computational zones were employed in gridding a 90° circumferential sector around the body. The computational grid employed clustering normal to the body and the fins to resolve the viscous effects on both surfaces. The resulting grid contained nearly one million grid points.

Figure 53 shows a comparison of the computed roll producing moment with free-flight data across a range of supersonic Mach numbers. Computational data was obtained for two sets of free-stream Reynolds numbers, one corresponding to wind tunnel Reynolds number (17 to 23 million) and the second corresponding to free-flight Reynolds numbers (30 to 69 million). Both the computation and experiment show a reversal in the roll producing moment at about Mach 1.7. Here, positive roll moment corresponds to a moment in the direction of fin's center of curvature. The computational results compare reasonably well with the experimental data across the range of Mach numbers and appear to be relatively insensitive to Reynolds number.

Detailed examination of the pressure field indicates that the roll producing moment on this configuration results from two phenomenon. The first is the leading edge shocks which impinge on adjacent fins produce an asymmetric pressure field on the fin surface giving rise to a roll producing pressure differential across each fin blade. Because the shock angle and strength is a function of Mach number, the roll producing moment may vary accordingly. Secondly, there appears to be a large pressure differential near the leading edge; the position and strength of which shows a strong dependence on Mach number. Clearly, the complicated pressure fields which give rise to the roll moment indicate that it may be difficult to develop simple theories which can be applied in a "fast" design code approach. Whether or not inviscid codes can accurately predict roll reversal for missiles with wrap-around fins is still an open issue, though it is clear that accurate geometric modeling of the fins, especially fin thickness, is important⁴⁸.

7. DYNAMIC DERIVATIVE PREDICTION

7.1 Magnus Coefficients

One of the pacing problems in computational projectile aerodynamics is the prediction of the Magnus force and moment. The Magnus force and moment result from the cross-coupling of spin and angle of attack. For axisymmetric geometries, asymmetric boundary layers will be produced on each side of the pitch plane if the body is spinning. These boundary layers can affect the pressure field on the body surface through the boundary layer displacement effect and produce a side force and moment that can ultimately affect the dynamic stability

of the flight vehicle.

Clearly, the viscous effects must be determined to accurately predict this phenomenon. In the late 1970's, some success in predicting the Magnus effect at supersonic velocities was attained using coupled inviscid and boundary layer techniques⁴⁹. The technique did not appear to offer a satisfactory capability for some body shapes, particularly those with an aft boattail. Sturek and Schiff¹⁴ later demonstrated a more widely applicable capability for the supersonic Magnus problem using the PNS technique. Sturek and Schiff obtained Magnus predictions for a conical body and for a secant ogive cylinder body with and without an aft boattail (SOC/SOCBT). (SOCBT body show in Figure 2). Figures 54 and 55 show comparisons of the predicted Magnus force and moment for the SOCBT body with wind tunnel data over a range of supersonic Mach numbers. The agreement with the experimental data is quite good. Similar good agreement was obtained for the SOC and conical bodies.

Prediction of the Magnus effect at supersonic velocities has been performed for other bodies. Several examples are cited in a later section as part of the discussion on pitch damping prediction.

Computation of the Magnus effect at transonic velocities has been a subject of research for over a decade^{50, 51}. Like the predictions of the transonic "critical" behavior of the pitching moment, the Magnus problem at transonic velocity is very computationally intensive. Since the spin removes the symmetry across the pitch plane, the computational requirements are about twice that required for the prediction of the static pitch plane aerodynamics. Recently, Sahu⁵¹ obtained predictions of the transonic Magnus effect at Mach 0.94 over a 5.5 caliber SOCBT configuration with a half caliber seven degree boattail. The computational predictions were benchmarked against detailed surface pressure measurements as well as force and moment coefficients from the wind tunnel. Figure 56 shows the development of the Magnus force over the body at four and ten degrees angle of attack. The predictions are compared to data obtained from the integration of the surface pressure measurements and with the force balance measurements. At four degrees angle of attack, the experimental results are in reasonable agreement with the experimental data. At ten degrees angle of attack, the computational results and force balance measurements are in reasonable agreement. Comparisons with the force distribution obtained from the pressure measurements at the higher angle of attack are inconclusive since this data is not confirmed by the force balance measurement. The results indicate low angle of attack prediction of the Magnus effect is possible at transonic velocity although the large computational requirements (82 million words of memory and 40 hours of CPU time on a Cray-2 computer) demonstrate that it may be some time before this type of calculation can be routinely performed.

While progress has been made in Magnus prediction, some areas still need to be addressed including the geometry effects (rotating band, rounded base corners) and non-linear effects. A capability for predicting side force and moment on a spinning finned body (fin Magnus effect) still remains a challenge because the

combination of spin and angle of attack will produce a time-dependent flow field.

7.2 Pitch Damping Prediction

7.2.1 Pitch Damping Theoretical Background

The prediction of the pitch damping coefficients is often thought to be a difficult problem because the pitch damping forces and moments are produced by the time-dependent motion of the body. It is, however, possible to devise steady motions which can be used to predict the pitch damping coefficients for symmetric missiles. This approach was first applied by Schiff⁵² to conical bodies in supersonic flight using an Euler space-marching code. Later studies of conical bodies were performed by Lin⁵³ using an inviscid/boundary layer approach and by Agarwal and Rakich⁵⁴ using a PNS approach. This approach was further developed by Weinacht, Sturek and Schiff⁵⁵ and applied to compute the viscous flow about axisymmetric bodies using a PNS approach. Later, Weinacht and Sturek⁵⁶ applied this approach to compute the pitch damping of finned bodies.

As a way of introduction, the moment expansion for a symmetric missile in the non-rolling coordinate frame is shown below³⁹. The moment formulation makes use of complex variables to separate the moment components, \tilde{C}_m and \tilde{C}_n which produce rotations in the vertical and horizontal planes, respectively.

$$\tilde{C}_m + i\tilde{C}_n = \left\{ \left(\frac{pl}{V} \right) C_{n_{\rho\alpha}} - iC_{m_\alpha} \right\} \tilde{\xi} - \frac{i}{\gamma} [C_{m_q} + \gamma C_{m_\alpha}] \tilde{\xi}' \quad (23)$$

In the moment formulation, the pitching moment coefficient, C_{m_α} , and pitch damping moment coefficient, $C_{m_q} + \gamma C_{m_\alpha}$, produce moments proportional to the complex angle of attack, $\tilde{\xi}$, and angular rate, $\tilde{\xi}'$, respectively. The Magnus moment coefficient, $C_{n_{\rho\alpha}}$, accounts for a side moment due to flow asymmetries from a combination of spin and angle of attack. This form of the moment expansion assumes that the missile undergoes small amplitude motions. In this case, q is approximately equal to $\dot{\alpha}$ and the effect of q and $\dot{\alpha}$ are represented by a "single" coefficient represented by the sum $C_{m_q} + \gamma C_{m_\alpha}$.

Equation 23 seems to imply that an unsteady motion is required to produce a pitch damping moment contribution because of the presence of the angular rate, $\tilde{\xi}'$. However, it is possible to devise motions that are steady and still result in a non-zero angular rate. One such motion is steady "coning" motion. Steady coning motion is defined as the motion performed by a missile flying at a constant angle with respect to the free stream velocity vector (angle of attack) and undergoing a rotation at a constant angular velocity about a line parallel to the freestream velocity vector and coincident with the projectile center of gravity. This is shown schematically in Figure 57. The longitudinal axis of the flight body will sweep out a conical surface with the vertex located at the center of gravity. With respect to a non-rolling coordinate frame, the vertical and horizontal components of the angle of attack, α and β , vary in a sinusoidal fashion as the projectile rotates about the free-stream velocity vector, but differ in phase by a quarter of a cycle. The

total angle of attack, $\alpha_t = \sqrt{\alpha^2 + \beta^2}$ is constant, however.

For the case of steady coning motion, the angle of attack and angular rate can be written as follows:⁵⁷

$$\begin{aligned} \tilde{\xi} &= \delta e^{i\gamma\phi t} \\ \tilde{\xi}' &\equiv \frac{d\tilde{\xi}}{d\left(\frac{t}{\tau}\right)} = i\delta\gamma \frac{\phi l}{V} e^{i\gamma\phi t} \end{aligned} \quad (24)$$

Here, ϕ represents the coning rate, δ is the sine of the total angle of attack, γ is the cosine of the angle of attack and l and V are, respectively, a reference length and velocity. $\frac{\phi l}{V}$ is the non-dimensional coning rate.

In the non-rolling coordinate frame, the complex angle of attack and angular rate show a dependence on time, t , in the complex exponential function, e . It is convenient to consider an additional coordinate frame called the coning coordinate frame. In the coning frame, missile longitudinal axis (x axis) and the z axis remain in the plane of the angle of attack (pitch plane) while the y axis is normal to the pitch plane. In steady coning motion, the coning coordinate frame rotates in a periodic fashion about the non-rolling coordinate frame.

By using the coning frame, the time-dependence which exists in the non-rolling frame can be removed, as seen below.

$$\begin{aligned} C_m + iC_n &= ie^{-i\gamma\phi t} (\tilde{C}_m + i\tilde{C}_n) \\ &= C_{m_\alpha} \delta \\ &\quad + i \left\{ \left(\frac{pl}{V} \right) C_{n_{\rho\alpha}} \delta + \delta \left(\frac{\phi l}{V} \right) [C_{m_q} + \gamma C_{m_\alpha}] \right\} \end{aligned} \quad (25)$$

In the coning frame, C_m represents the "in-plane" moment which cause rotations of the body in the pitch plane and C_n represents the moment which causes the body to rotate out of the pitch plane and is often referred to as the side moment. The in-plane moment (real part) results only from the pitching moment, while the total side moment (complex part) consists of contributions from the Magnus moment and pitch damping moment.

7.2.1.a Lunar Coning Motion

In the current study, there are two particular types of coning motion of interest. The first motion is described as lunar coning motion. In lunar coning motion, the coning coordinate system becomes a body fixed axis system. Lunar coning motion will cause the body to undergo a rotation at a rate which is proportional to the coning rate of the projectile. This motion is spinning motion in the non-rolling coordinates.

$$p = \gamma\phi \quad (26)$$

For this type of coning motion, the side moment can be written as shown below.

$$C_n = \delta \left(\frac{\phi l}{V} \right) (\gamma C_{n_{\rho\alpha}} + [C_{m_q} + \gamma C_{m_\alpha}]) \quad (27)$$

The notation can be simplified by noting that the right hand side of Equation 27 is simply the variation of

side moment with coning rate, valid for linear variations of side moment with coning rate.

$$C_{n_{\dot{\phi}}} \equiv \frac{\partial C_n}{\partial(\frac{\dot{\phi}}{V})} = \delta(\gamma C_{n_{p\alpha}} + [C_{m_q} + \gamma C_{m_{\dot{\alpha}}}] \quad (28)$$

This relation is identical to that presented by Schiff and Tobak⁵⁸ for bodies of revolution. This equation relates the variation of the side moment with coning rate, $C_{n_{\dot{\phi}}}$, to the pitch damping coefficient, $[C_{m_q} + \gamma C_{m_{\dot{\alpha}}}]$, and the Magnus moment coefficient, $C_{n_{p\alpha}}$. Assuming that the side moment due to coning and the Magnus moment can be determined, this relation will allow the pitch damping coefficient to be determined.

Despite the fact that lunar coning motion requires that the Magnus moment be determined (or assumed negligible) in order to determine the pitch damping coefficient, this motion is useful. Because the body does not rotate with respect to the pitch plane while undergoing coning motion, the flow, when observed in the coning coordinate frame, will be steady for axisymmetric and non-axisymmetric bodies. In many cases, particularly in supersonic flow, the contribution of the Magnus moment to the side moment may be neglected and the pitch damping moment can be determined directly from the side moment without any appreciable loss of accuracy. For axisymmetric bodies, a second type of coning motion avoids the need to neglect the Magnus moment and is discussed below. For non-axisymmetric bodies, the use of lunar coning motion can give an accurate determination of the pitch damping coefficient without resorting to a time-accurate approach. This approach has been recently applied to predict the pitch damping for six-finned bodies⁵⁶ and straked flare bodies⁵⁹. It should be noted that non-axisymmetric bodies with aerodynamic coefficients which exhibit a significant dependence on roll angle may need to be treated with a more general aerodynamic formulation^{60, 61} than is presented here.

7.2.1.b Combined Spinning and Coning Motion

A second type of coning motion can be formulated which allows the side force and moment to be directly related to the pitch damping force and moment. In this motion, the body does not spin with respect to the non-rolling coordinate frame. In other words, both the non-rolling coordinates and the body fixed coordinates do not rotate with respect to each other. Thus, the spin rate, as observed from the non-rolling coordinates, is zero.

$$p = 0. \quad (29)$$

It should be noted, however, that the coning coordinate frame rotates with respect to the non-rolling coordinate frame and the body-fixed coordinate frame. In the coning coordinate frame, then, the body appears to perform a spinning motion since the body-fixed coordinate system rotates with respect to the coning coordinate frame. The spin rate in the coning coordinate frame will be $p_{cf} = -\gamma\dot{\phi}$. In this report, this motion is called combined spinning and coning motion because in the coning frame (which is the coordinate frame in which the computations are performed) the motion is a specific combination of spinning and coning motion. In the coning frame, this motion is a steady motion for axisymmetric bodies only. The presence of spin and angle of

attack produces a periodic motion for non-axisymmetric bodies, thereby eliminating steady flow computational approaches from consideration.

For this type of coning motion, the side moment can be written as shown below.

$$C_n = \delta\left(\frac{\dot{\phi}l}{V}\right)[C_{m_q} + \gamma C_{m_{\dot{\alpha}}}] \quad (30)$$

In this type of coning motion, the side moment is directly proportional to the pitch damping moment coefficient. Despite the simplicity of this expression, the Magnus problem has not been entirely removed from the problem, however. This is because the motion in the coning coordinate frame involves coning and spinning motions. Thus, any approach, whether computational or experimental, which uses this motion must be capable of modeling both of these effects. For example, a coarse grid CFD computation which does not resolve the viscous effects sufficiently to properly model the Magnus problem will produce pitch damping results which will be in error by the degree to which the Magnus moment is improperly determined.

Similar expressions relating side force due to coning to the pitch damping force and Magnus force for the cases of lunar coning and combined spinning and coning can be developed using the same approach as discussed above.

7.2.2 Pitch Damping of Axisymmetric Bodies

The use of combined spinning and coning motion has been used to predict the pitch damping for the family of axisymmetric bodies shown in Figure 45. These projectiles were fired in an aerodynamics range and the aerodynamics determined from the projectile motion⁴². The projectiles consisted of a two caliber ogive nose with several different length cylindrical bodies. The total body lengths were five, seven, and nine calibers. For each body length, projectiles were fabricated and fired with three different center of gravity (CG) locations. This allowed the aerodynamic forces to be determined from the variation of the aerodynamic moments with CG location.

Figure 58 shows the variation of the pitch damping moment coefficient with CG location for the five, seven, and nine caliber bodies at Mach 1.8. Figure 59 shows a similar plot at Mach 2.5. In both of the figures, the computed results are compared with the experimental measurements. The computational results are in excellent agreement with the experimental data. The computational predictions were made by computing the flow field for each of the CG locations. This was performed because the coning motion produces a rotation about the CG, producing a different flow field in each case. These results are shown by the open triangular symbols. However, once the aerodynamics of a given configuration are determined, the CG translation relations³⁹ can be applied to predict the aerodynamic coefficients for the same configuration with a different CG location. The CG translation relation for the pitch damping moment coefficient is shown below.

$$\begin{aligned} \hat{C}_{m_q} + \hat{C}_{m_{\dot{\alpha}}} &= C_{m_q} + C_{m_{\dot{\alpha}}} - s_{cg}(C_{N_q} + C_{N_{\dot{\alpha}}}) \\ &+ s_{cg}C_{m_{\alpha}} - s_{cg}^2 C_{N_{\alpha}} \end{aligned} \quad (31)$$

This equation expresses the variation in the pitch damping moment coefficient with the center of gravity shift, s_{cg} , given that the aerodynamic coefficients for the baseline configuration are known (s_{cg} is in calibers and is positive for a CG shift towards the nose). Using this relation and the predicted aerodynamic coefficients for the middle CG position, the variation of the pitch damping moment coefficient with CG location was determined. This variation is shown in Figures 58 and 59 by the solid line. The difference between the pitch damping moment coefficients predicted from the CG translation relations and the pitch damping moment as determined from the direct computations is less than 0.1%. This serves as a consistency check for the computational approach.

Using Equation 31, it is also possible to determine the pitch damping force coefficient from the variation in the pitch damping moment coefficient with CG location given that the normal force and pitch moment are also known. While the computational approach can determine this directly, the pitch damping force has little effect on the free flight motion. This approach was used to determine the range values of the pitch damping force coefficient. Figure 60 shows the variation of the pitch damping force coefficient with body length for the middle center of gravity location. Note that, unlike the normal force coefficient, the pitch damping force varies with CG position. The agreement between the computational predictions and experimental results are within the experimental accuracy and show the correct variation with body length and Mach number.

As mentioned previously, the pitch damping predictions were obtained using the combined spinning and coning motion which allows the pitch damping force and moment to be determined directly from the side force and moment. The expected differences between applying combined spinning and coning motions, and lunar coning motion is reflected in the Magnus moment coefficient. In the current effort, the Magnus force and moment have been computed for the ANSR configuration and comparison made with range data obtained from the same series of firings as shown in Figures 61 and 62. The computed results were obtained for a fully turbulent boundary layer. (There is some evidence from the experimental program to indicate laminar flow over a portion of the body, particularly near the nose.) The computational results are in reasonable agreement with the experimental data. The predictions show that determining the pitch damping coefficient from the side moment due to lunar coning motion and completely ignoring the Magnus moment will result in errors of less than 5 percent for this configuration.

7.2.3 Pitch Damping of Finned Bodies

Pitch damping predictions for finned projectiles⁵⁶ were made using the lunar coning motion approach. Results are shown here for the M735 configuration shown previously in Figure 35.

The computed variation of the side moment coefficient with coning rate at Mach 4 and two degrees angle of attack is shown in Figure 63. The variation of the side moment coefficient with coning rate is seen to be linear across the range of coning rates examined here. This range of coning rates is representative of the pitching frequencies experienced by the M735 projec-

tile in flight. At Mach 4, the non-dimensional pitching frequency of the projectile is 0.004, where the form of the non-dimensionalization is the same as for the coning rate. The results also show the existence of a small non-zero side moment coefficient at zero coning rate. This side moment is due to bevels on the fins. The existence of this side moment at zero coning rate requires that computations be performed for at least two coning rates in order to evaluate the variation of the side moment coefficient with coning rate, $C_{n_{\dot{\delta}}}$.

Figure 64 shows $C_{n_{\dot{\delta}}}$ as a function of δ (the sine of the angle of attack) at Mach 4. The dashed line displayed on this figure is representative of a linear variation of $C_{n_{\dot{\delta}}}$ with δ across the range of angles of attack examined. The computed results show that, at small angles of attack, $C_{n_{\dot{\delta}}}$ varies linearly with δ , but departs from a linear variation as the angle of attack increases.

Figure 65 shows the development of $C_{n_{\dot{\delta}}}/\delta$ over the M735 kinetic energy projectile at Mach 4 and two degrees angle of attack. As discussed previously, $C_{n_{\dot{\delta}}}/\delta$ should be a reasonable representation of the pitch damping coefficient, $C_{m_q} + C_{m_{\dot{\alpha}}}$, in the linear aerodynamic regime. This figure shows that the fins contribute most of the side moment due to coning (and hence, the pitch damping) with a smaller contribution from the nose.

The Mach variation of $C_{m_q} + C_{m_{\dot{\alpha}}}$ for the M735, as determined from $C_{n_{\dot{\delta}}}/\delta$, is shown in Figure 66. The computed results are compared with range measurements of the pitch damping coefficient. Though the range data shown here are considered well-determined, some scatter is still evident because damping rates are typically difficult to measure. The experimental results do reflect the expected level of accuracy in determining this coefficient experimentally. The comparisons show that the computational results are within the accuracy of the experimental data and provide a measure of validation of the computational approach.

The lunar coning motion approach was also applied to predict the pitch damping of a family of flared flight bodies⁵⁹. These configurations have been investigated experimentally in aerodynamics range tests^{62, 63} and the data has been used for benchmarking purposes. A schematic of the baseline cone-cylinder-flare projectile configuration is shown in Figure 67. Each of the projectiles examined here has the same cone-cylinder forebody. The forebody has a slightly truncated conical nose. In the computations, the nose is modeled as a sharp tipped cone. The cylindrical portion of the body also has a number of sub-caliber grooves which permit the launch loads to be transferred from the sabot to the projectile during launch. These grooves are not modeled in the computations presented here.

Various afterbodies have been analyzed both experimentally and computationally. Schematics of the afterbodies are shown in Figure 68. The configurations CS-V4-2 through CS-V4-5 have a one caliber afterbody extension added to the baseline configuration, CS-V4-1. The angle of inclination of the conical extensions for configurations CS-V4-2 through CS-V4-5 are respectively 6° (simple extension of original flare), 0° (cylindrical skirt), 12° (steeper flare), and -6° (boattail). Configu-

ration CS-V4-6 consists of a 9.37 degree flare which has been machined to produce a square cross section over the last caliber of the body. Configuration CS-V4-7 is identical to the boattailed configuration CS-V4-5, except that four 12° degree fins have been added to the boattailed portion of the body. The fins are 0.153 calibers thick. The final configuration, CS-V4-8, is identical to the baseline configuration, except that four boundary layer strakes have been added to the flared portion of the body. The strakes are 0.153 calibers in height and width.

Figure 69 shows a comparison of the pitch damping moment coefficients for each of the eight configurations at Mach 4. Both the PNS predictions and the range data are shown. Each of the bodies with the conical extensions, configurations CS-V4-2 through CS-V4-5, have larger pitch damping coefficients compared with the baseline configuration CS-V4-1. Computational predictions show a consistent increase in the pitch damping for the bodies with the conical extensions with the boattailed configuration having the lowest pitch damping coefficient and the steepest flare having the highest pitch damping coefficient. These trends are, for the most part, reflected by the range data.

The finned configuration, which is identical to the boattailed configuration, except that four 12 degree swept fins have been added to the boattailed portion of the body, shows a modest increase in the damping over the boattailed configuration. The finned configuration, however, produces significantly less pitch damping than the configuration with the 12 degree flare extension. Again, these trends are reflected by the range data. The configuration with the boundary layer strakes also produces a modest increase in the damping compared with the baseline configuration which has no strakes. The square base configuration (CS-V4-6), which has the same base area as the baseline configuration (CS-V4-1) and the configuration with the cylindrical skirt (CS-V4-3), produces more damping than the baseline configuration and slightly more damping than the cylindrical skirt.

Determining the pitch damping coefficients from the side force and moment due to lunar coning motion requires that the Magnus force and moment be determined from another source or neglected. For the axisymmetric configurations (CS-V4-1 to CS-V4-5), the Magnus force and moment have been predicted using the PNS approach. These calculations were performed with the body spinning at angle of attack and in the absence of coning motion. Magnus predictions for the non-axisymmetric geometries could not be made because the combination of spin and angle of attack for these bodies produces a time-dependent flow field. Figure 70 shows a comparison of the Magnus moment coefficients by configuration at Mach 4. Range results are shown for each of the eight configurations, while computational results are shown for the axisymmetric configurations. The computational data are bracketed by the range data for each of the axisymmetric configurations, and similar trends are shown by the computational and experimental results. Both the computational and experimental results reveal that the Magnus moment is small in comparison to the pitch damping moment coefficient for the configurations examined here. The computational

predictions also confirm that the Magnus force is small in relation to the pitch damping force coefficient. This result demonstrates that, by ignoring the contribution from the Magnus coefficients, the pitch damping coefficients can be determined directly from the side force and moment due to lunar coning motion with little effect on the accuracy of the prediction.

8. BASE FLOW

One of the important parameters in the design of missiles is the total aerodynamic drag. The total drag can be thought to consist of three drag components: the pressure drag or the wave drag (excluding the base), the viscous drag, and the base drag. The base drag component is a large part of the total drag⁶⁴ and can be as high as 50% or more of the total drag. Of all these three components of drag, the most difficult one to predict is the base drag. The base drag depends on the pressure acting on the base which is usually much lower than that of the free stream. Therefore, it is necessary to determine the base pressure as accurately as possible.

The class of flows known as base flows has received significant attention since the early 1950's. Early studies of low speed flow around blunt based bodies tended to be over-shadowed by the phenomenon of vortex shedding. Research initiated since the advent of high speed flight resulted in a slow unravelling of the processes and mechanisms which control and establish these flows. The essentially inviscid free stream establishes and determines the major portion of the wake. On the other hand, the viscous flow processes such as mixing in the free shear layer, flow recompression at the end of the wake, and the ensuing process of flow redevelopment, establish and determine the "corresponding inviscid body geometry". Thus, a low base pressure is the result of the strong interaction between the inviscid and viscous flows; the latter being attached to the inviscid flow in the sense of the boundary layer concept.

Historically, the flow processes described above formed the basis for the development of analytical methods to predict the base region flow fields. The turbulent base flow theory of Korst⁶⁵(1956) and the theory of Chapman⁶⁶(1950) for laminar base flows were developed while working independently. Both theories divided the base region flow field into different regions, solved each region separately, and patched the solutions together at the respective boundaries. This so-called multi-component approach became known as the Korst-Chapman theory. The multi-component method is relatively simple and computationally inexpensive. However, these models depended on experimental information for some parameters and a significant number of experiments were carried out to provide the required information for the analytical models. Most of these experiments were taken on simple geometries to provide better insight into the separation, mixing, recompression, and redevelopment processes. Many of these experiments such as those conducted by Reid and Hastings⁶⁷(1959) and Badrinarayan⁶⁸(1961) did provide information on the base flow process. However, most of these experiments suffered from intrusive techniques and wind tunnel model interference. For power-off base flows, detailed information in the critical near wake region and detailed base pressure data were not available in these experiments. This prevented a more

complete understanding of the base flow process. Until recently, very little detailed non-intrusive experimental base flow field data existed for supersonic axisymmetric base flows. The advent of Laser Doppler Velocimeter (LDV) has begun to provide detailed velocity field data in the near wake region. Delery⁶⁹ (1983) presented a two-component LDV data for subsonic, axisymmetric base flows. More detailed experimental data has been recently obtained by Herrin and Dutton⁷⁰ (1991) for supersonic base flow over a cylindrical afterbody. Such detailed information provides both a better understanding of the complex fluid dynamic phenomenon associated with base flows and the data necessary for validating analytical and numerical models of these flows.

Analytical models based on multi-component techniques do offer an inexpensive way to predict the base pressure; however, these techniques are limited to simple planar or axisymmetric geometries. For practical three dimensional complex geometries, more sophisticated numerical procedures are needed. These advanced numerical procedures are based on the solution of the Reynolds-averaged Navier-Stokes equations. The greatest advance in the last decade has been the evolution of these numerical methods for computational study of the turbulent, axisymmetric base flows. These techniques offer the greatest hope of realistically predicting the base flow structure for complex configurations including afterbodies with fins, and base cavities. Several problems arise in the base flow computations due to the complex nature of the turbulent separated flow field. Two of the most important factors which affect the accuracy of the computed base flow results are grid resolution and turbulence modeling. The lack of sufficient grid resolution can introduce significant error. To reduce this error, a sufficient number of grid points must be placed in the regions of high flow gradients such as the free shear layer. This can be done by using a grid adaptation procedure. Another, perhaps a more significant problem encountered in base flow computations is that of turbulence modeling. The turbulence model used in the wake must capture the flow physics, and in particular the turbulent mixing process associated with base flow. These sources of errors need to be examined during the validation of CFD results on base flows. In the sections below, numerical examples are given for base flow for power-off conditions, followed by base flows with mass injection (base bleed and jet-on), and base flows with base cavities.

8.1 Base Flow for Power-Off Condition

The prediction of the axisymmetric base flow for unpowered configurations have been performed for over a decade. Sahu, Nietubicz, and Steger⁷¹ presented predictions of base flow behind a secant ogive cylinder configuration at transonic and low supersonic velocities. Their computational results were obtained using a time-marching Navier-Stokes approach and utilized the Baldwin-Lomax turbulence model. Figure 71 shows the predicted stream function contours for in the base region of the projectile. The recirculation region in aft of the base is evident. Predictions of the integrated base drag, shown in Figure 72, were also presented. The predicted base drag is in reasonable agreement with experimental data and design code results. In a subsequent study, Sahu⁷² presented additional results for boattailed projec-

tiles and considered a greater range of Mach numbers. These calculations again used the Baldwin-Lomax turbulence model. Figure 73 shows a comparison of the predicted total drag for the M549 configuration (previously shown in Figure 28) with design codes (MCDRAG⁷³ and NSWCAP⁷⁴) and experiment data (LCWSL). The computed results, design codes and experimental data are in good agreement. These studies seemed to indicate that base drag could be adequately computed using a simple turbulence model such as the Baldwin-Lomax model. However, due to the lack of detailed measurements in the base region, no detailed assessment of the accuracy of the predictive approach could be made.

Recently, an interesting validation case for the supersonic flow over a simple axisymmetric afterbody for the power-off condition was investigated by Sahu⁷⁵. Comparisons were made between computation and experiment using the detailed experimental data obtained by Herrin and Dutton⁷⁰. The data includes base pressure distribution, mean flow as well as turbulence quantities in the near wake. The numerical flow field computations were performed at $M_\infty = 2.46$ and at zero degree angle of attack using a time-dependent, Reynolds-averaged, thin-layer, Navier-Stokes computational technique⁷⁶. Typically, the thin-layer approximation implies retaining viscous terms in the normal direction only; however, for wake and base flows, the viscous terms involving velocity gradients in both the normal and streamwise directions are retained. In addition, this procedure uses a zonal or composite grid scheme which preserves the base corner and allows better modeling of the base region flow.

A schematic diagram showing the important features of supersonic base flow is shown in Figure 74. The approaching supersonic turbulent boundary layer separates at the base corner and the free shear layer region is formed in the wake. The flow expands at the base corner and is followed by the recompression shock downstream of the base which realigns the flow. The flow then redevelops in the trailing wake. A low pressure region is formed immediately downstream of the base which is characterized by a low speed recirculating flow region. Interaction between this recirculating region and the inviscid external flow occurs through the free shear mixing region. This is the region where turbulence plays an important role. Various turbulence models were used and included the algebraic models of Baldwin and Lomax, and Chow, as well as a two-equation $k - \epsilon$ model. A brief discussion of the turbulence models used is presented.

Baldwin-Lomax Model. This model has been described in detail in section 4.2. In the computational results described here, the distance, y , which appears in the Baldwin-Lomax model is measured from the center line of symmetry in the base or wake region. Additionally, in the wake formulation of the outer model, C_{wk} was set equal to 0.25.

Chow Model. Another algebraic model that has been used in some base flow computations is that due to Chow⁷⁷. This model is intended to be used in the base or wake region only. It is based on the simple exchange-coefficient concept. The turbulent eddy viscosity coeffi-

cient is usually given by

$$\mu_t = \frac{1}{4\sigma^2} x u_e \quad (32)$$

where x is the distance measured from the origin of the mixing region (i.e., the base), u_e is the velocity at the edge of the mixing region, and σ is the spread rate parameter. It is known that σ assumes a value of 12 for incompressible flow and it increases slightly with Mach number.

$$\sigma = 12 + 2.76 M_e \quad (33)$$

where M_e is given by

$$M_e^2 = \frac{2}{\gamma - 1} \left(\frac{1 + \frac{\gamma-1}{2} M_\infty^2}{\left(\frac{\bar{P}}{P_\infty}\right)^{\frac{\gamma-1}{\gamma}}} - 1 \right) \quad (34)$$

and \bar{P}_b/P_∞ is the average base pressure. The equivalent velocity u_e at the edge of the mixing region can be found from

$$u_e = M_e \sqrt{\left(1 + \frac{\gamma-1}{2} M_\infty^2\right) / \left(1 + \frac{\gamma-1}{2} M_e^2\right)} \quad (35)$$

As a first approximation the average value of μ_t is assumed to be same at all points for a constant x location. After reattachment, turbulence should decay. Since the interest in the base flow calculations is to obtain the correct base pressure, it is assumed that the eddy viscosity level at the reattachment stays the same at other locations downstream. For base flow with a jet, similar algebraic relations can be used for the jet shear layer.

Two-Equation $k - \epsilon$ Model. Both the Baldwin-Lomax and the Chow models are algebraic models which depend only on local information. Other models, such as the two-equation $k - \epsilon$ model, contain less empiricism and allow the flow history to be taken into account. The two-equation turbulence model used here is Chien's⁷⁸ $k - \epsilon$ model which is similar to that of Jones and Launder⁷⁹. In this model, two transport equations are solved for the two variables, k (turbulent kinetic energy) and ϵ (turbulent dissipation rate).

$$\rho \frac{Dk}{Dt} = \frac{\partial}{\partial X_j} \left[\left(\frac{\mu_t}{\sigma_k} + \mu \right) \frac{\partial k}{\partial X_j} \right] + \mu_t \frac{\partial u_i}{\partial X_j} \left(\frac{\partial u_i}{\partial X_j} + \frac{\partial u_j}{\partial X_i} \right) - \rho \epsilon - 2\mu \frac{k}{y_n^2} \quad (36)$$

$$\rho \frac{D\epsilon}{Dt} = \frac{\partial}{\partial X_j} \left[\left(\frac{\mu_t}{\sigma_\epsilon} + \mu \right) \frac{\partial \epsilon}{\partial X_j} \right] + c_1 \mu_t \frac{\epsilon}{k} \frac{\partial u_i}{\partial X_j} \left(\frac{\partial u_i}{\partial X_j} + \frac{\partial u_j}{\partial X_i} \right) - c_2 \rho \frac{\epsilon^2}{k} - 2\mu \frac{\epsilon}{y_n^2} \exp(-y^+/2) \quad (37)$$

Here, y_n is the distance normal to the surface. The coefficients in the k and ϵ equations are given by

$$\begin{aligned} c_1 &= 1.44 \\ c_2 &= 1.92[1 - 0.3 \exp(-R_t^2)] \\ c_3 &= 1.44, \quad \sigma_k = 1.0, \quad \sigma_\epsilon = 1.3 \\ c_4 &= 0.09[1 - \exp(-0.01y^+)] \end{aligned} \quad (38)$$

where $R_t = k^2/\nu\epsilon$.

The $k - \epsilon$ model employs the eddy viscosity concept and relates the turbulent eddy viscosity to k and ϵ by,

$$\mu_t = c_\mu \rho (k^2/\epsilon) \quad (39)$$

Following the same procedure used for the mean flow equations, the turbulence field equations can be written in conservative form and then transformed into generalized coordinates and solved using an implicit scheme⁸⁰. The model used is a low Reynolds number formulation of the $k - \epsilon$ model. Calculations are extended up to the wall itself, and exact values of the dependent variables at the wall are used as boundary conditions. Chien's model is better mathematically behaved near the wall and is used in the results presented here.

The model used in the experiment and in the computational study is shown in Figure 75. It is an axisymmetric cylindrical afterbody which has a diameter of 63.5 mm. This figure also shows the stations where mean and fluctuating velocity components were measured by Herrin and Dutton⁷⁰ using a LDV system.

Figure 76 shows an expanded view of the grid in the base region. The grid outer boundary has been placed 1 diameter away from the surface of the afterbody. The downstream boundary was placed at 10 diameters away from the base. Since the calculations are in the supersonic regime, the computational outer boundary was placed close to the body and a no-reflection boundary condition is used at that boundary. The full grid is split into two zones, one upstream of the base, and the other one in the base region or the wake. These grids consist of 22x60 and 95x119 grid points, respectively. Figure 76 shows the longitudinal grid clustering near the base corner. The grid points are also clustered near the afterbody surface to capture the viscous effects in the turbulent boundary layer. The clustered grid points are spread out downstream of the base in the wake to capture the free shear layer region.

A few qualitative results are presented next. Figure 77 shows the pressure contour plot for the base region. The features to observe are flow expansion at the base corner which is followed by the recompression shock downstream of the base (coalescence of contour lines). The computed Mach number contours in the base region of the flow field, displayed in Figure 78, also show the flow expansion at the base and the recompression shock downstream of the base. In addition, this figure shows the free shear layer in the near wake. Although not indicated in Figure 78, the flow in the near wake is primarily subsonic. Figure 79 shows the computed vectors in the base region. The recirculatory flow in the near wake is clearly evident. The flow reattachment occurs at about three base radii downstream. Also, as can be seen the magnitude of the velocity is quite small in the immediate vicinity of the base. The computed results shown in Figures 77, 78 and 79 were obtained using the two-equation $k - \epsilon$ model.

Figures 80 and 81 show the velocity components in the streamwise and normal directions, respectively. These velocity profiles are taken at four longitudinal positions in the wake or the base region ($X/D = 1.26, 1.42, 1.73, \text{ and } 1.89$). The computed velocity profiles

obtained using two algebraic turbulence models and the two-equation $k - \epsilon$ model are compared with the experimental data. Figure 80 shows the comparison of the u (streamwise) component of velocity. In general, the profiles obtained with the $k - \epsilon$ model are in much better agreement at the axial stations located at $X/D = 1.26$ and $X/D = 1.42$. The profiles are rather poorly predicted by both algebraic models at these two stations.

The reattachment point estimated from the experimental measurements is located about 1.4 base diameters downstream of the base. The computed value with the $k - \epsilon$ model is 1.5. This small disagreement is also seen in the flow redevelopment region downstream of the reattachment ($X/D = 1.73$ and 1.89). The algebraic turbulence models predict the reattachment point better than the $k - \epsilon$ model. The velocity profiles predicted with these models are in fairly good agreement with the experimentally obtained profiles at these two stations. Chow model predictions are slightly better than those by the Baldwin-Lomax model in this flow redevelopment region. Figure 81 shows the comparison of the w (vertical) component of the velocity. This component of velocity is better predicted by the $k - \epsilon$ model than the algebraic models both in the flow recirculation and redevelopment regions. The profiles by the algebraic models are in poor agreement with the experimental data especially for radial positions greater than half of the base radius.

Figure 82 shows the turbulent shear stress profiles in the wake. The computed values obtained by both the algebraic models and the $k - \epsilon$ model are compared with the experimental data. In general, a small improvement can be observed in the predicted values with the $k - \epsilon$ model over the algebraic models. Discrepancy exists between the experimentally obtained turbulent shear stress and the predicted shear stresses with all the turbulence models. This is true especially near the peaks at $x/D = 1.26$ and 1.42 . The magnitude of the peak predicted by the $k - \epsilon$ model is about the same as predicted by the Baldwin-Lomax model at these two positions; however, they both underpredict the experimental peak. The Chow model underpredicts the peak even more. As for the location of the peak, the $k - \epsilon$ model does better than the algebraic models. As x/D is increased from 1.26 to 1.42, the location of the peak predicted by the $k - \epsilon$ model moves closer to the center line similar to that observed in the experiment. This is not seen in the prediction by the algebraic models. The $k - \epsilon$ model predictions agree better than the predictions by the algebraic models at $x/D = 1.73$ and 1.89 .

Of particular interest is the accurate prediction or determination of base pressure and, hence, base drag. Figure 83 shows the base pressure distribution (along the base). The base pressures predicted by both the algebraic models and the two-equation $k - \epsilon$ turbulence model are compared with the experimental data⁷⁰. The experimental data is shown in dark circles and the computed results are shown in lines. Here, $z/D = 0.0$ corresponds to the center line of symmetry and $z/D = 0.5$ corresponds to the base corner. The base pressures predicted by both algebraic turbulence models show a big increase near the center line of symmetry. The experimental data shows almost no change (only 3%) in the base pressure distribution. The base pressures are

very poorly predicted by the algebraic models, not only near the center line but also near the base corner. A much improved base pressure distribution is predicted by the $k - \epsilon$ model and its agreement with the measured base pressure is quite good. The $k - \epsilon$ prediction shows a small increase in the base pressure near the center line which is not observed in the data.

The results above show that the algebraic turbulence models predict the mean velocity components poorly in the recirculatory flow region in the wake. In general, the velocity components predicted by the two-equation $k - \epsilon$ model are in better agreement with the experimental data than the algebraic models. The base pressures predicted by the algebraic models show a much larger variation and are in worse agreement with the data. The measured base pressures show a very small change along the base and is predicted rather well with the $k - \epsilon$ turbulence model. This perhaps suggests that for complex base flow problems one needs to consider using higher order turbulence models. The use of higher order turbulence models does add to the overhead and CPU time needed for the base flow computations and it is this reason that has prohibited the use of higher order models especially for complex 3D base flows. In the future, however, greater computer speed and power will become available and increased use of higher order advanced turbulence models will be found.

8.2 Base Flow with Base Cavities

The majority of the previous base flow computations^{71, 81, 82} and analytical studies considered the base of a projectile to be a flat surface. This was true even though many of the actual projectile configurations had some form of a base cavity. Until recently, the general opinion was that the internal base shape had very little or no effect on the overall flight performance parameters. Range firings of the M825 and M865, both of which have cavities, provided the evidence that the base configuration can indeed affect the base region flow and in turn, have a significant effect on the aerodynamics.

The M825 projectile originally had an aluminum/steel base which contained a flat (standard) cavity. As a result of a product improvement program, a new all steel base configuration was designed which contained a dome cavity. The flight body and the base cavity shapes were shown previously in Figures 30 and 31. As a result of range tests, it was found that differences in the aerodynamic performance (including drag) of the two bases existed. Sahu and Nietubicz⁸³ carried out a computational study to determine the ability of the present Navier-Stokes codes to predict these differences and to further understand the fluid dynamic behavior which can account for these changes. The Navier-Stokes computational technique was used to provide a detailed description of the flow field associated with the M825 configuration as well as the integrated aerodynamic coefficients.

Figures 84 and 85 show the velocity vectors in the base region for both base configurations at $M_\infty = 0.98$ and $\alpha = 0.0^\circ$. The recirculatory flow in the base region is evident and as expected, is symmetric. As shown in Figure 84, the recirculation region for the standard base extends to about one and a half caliber downstream of

the base corner. The back flow, upon reaching the cavity follows the contour of the cavity and leaves the cavity pushing the flow upwards. The shear layer leaving the base corner is displaced upwards weakening the expansion at the base. Figure 85 for the dome configuration shows a weak secondary bubble inside the cavity in addition to the primary bubble. The flow again follows the contour of the cavity and, upon leaving the dome cavity, is almost parallel to the streamwise direction. This flow, thus, has less effect on the free shear layer and does not weaken the expansion at the base corner as much compared to the standard base. The net effect is that the size of the primary bubble for the dome base is slightly smaller than that for the standard base. The reattachment point is therefore closer to the base and results in lower base pressure or higher base drag at this Mach number.

Comparison of the total aerodynamic drag is shown in Figure 86. As shown in this figure, the difference is very small near $M = .97$ and is somewhat larger at high transonic speeds ($1.1 < M < 1.5$) as well as at low transonic speeds ($M < .92$). This plot also shows the range data for both base configurations. The overall comparison of the computed drag with the range data is fair. The range data shows that the dome base has higher drag at higher transonic Mach numbers and this trend is seen in the computed results also. The computed drag data and well as the static aerodynamics coefficients shown previously (Figures 32 and 33) clearly showed a difference in the aerodynamics between the two configurations with different base cavities and were in general agreement with the trend of the data.

The effect of base cavities was also revealed in a computational study for the M865 projectiles. The M865 is a flare stabilized projectile which simulates the flight of a long L/D finned projectile for training purposes. This projectile contains a tracer in the base cavity. In firing tests, it was noticed that the tracer, which the gunner uses to detect the impact point of the round, was not visible for the full range of interest. In an effort to uncover a cause for this unsatisfactory performance, Sahu⁸⁴ performed a computational study with emphasis on the base region flow field. The objective was to find out if any flow irregularities occur in the base region and to correct for such behavior by making simple configuration changes in the afterbody/base cavity shape. Flow field computations for the M865 projectile were performed at various supersonic Mach numbers, $2 < M < 5$ and $\alpha = 0.0^\circ$. Figure 87 shows the computational mesh for the M865 projectile including the base region cavity. This figure shows the grid point clustering near the base corner and in the free shear layer region. This was done in an attempt to put more grid points in the regions where flow field gradients are large.

An analysis of the computed base flow results indicated the presence of a pressure spike located along the axis in the near wake region. Figure 88 is a plot of the center line pressure extending from the interior cavity downstream. With the exception of $M=5$, the jump in pressure can be seen for all Mach numbers with the largest peak occurring at $M = 3.0$. This rapid pressure change was considered as a potential reason for the premature tracer burnout. In an attempt to reduce or eliminate this problem, several modified base cavity con-

figurations were proposed and computations were performed. Figures 89 and 90 show pressure contours in the base region of the original configuration, as well as for one of the modified base configurations. The comparison between the original and a modified configuration shows that the original pressure spike has greatly been reduced. Based on these computational results, a new afterbody configuration was chosen. Subsequent firing tests were then conducted for the modified M865 projectile with the new cavity. The results did reveal some improvements in the visibility of the tracer when compared to the original configuration.

The base drag for all configurations including the original one is shown in Figure 91. Flow field computations were also made for a configuration with a flat base (without any base cavity) for comparison purpose. The base drag for this case is included in Figure 91. As seen in this figure, the base drag for the solid base is the largest and is reduced by the changes made in the afterbody configurations. The base drag for the case where the outer flare was clipped is the lowest and is less than half that of the flat base case. For the other configurations the outer flare remained unchanged and different base cavity shapes have been used. The base drag is reduced by 4% to 30% due to the various base cavities. The original base cavity configuration (second from the right) has the lowest base drag among the configurations where only base cavity was changed. The modified configuration 1 which showed the smoothest behavior in the base region flow field and the ARDEC configuration have slightly higher base drag than the original configuration. Also shown here is the result of another configuration with a rectangular base cavity. The base drag for this configuration is slightly less than that of the flat base case. A careful look at these results reveal larger reduction in base drag with larger reduction in the base height (or base area). It can also be noted that the effect due to change in the depth of the base cavity is rather small as can be seen with configurations 3,4, and 5. Although not shown here, the largest base drag reduction due to the base cavity alone compared to the flat base case corresponds to about a 12% reduction in the total drag.

8.3 Base Flow with Mass Injection

A strong motivation for studying base flows is the desire to control the flow field interactions which will allow higher base pressures and thus, lower base drag to be obtained. Several methods are employed for base reduction: afterbody boat-tailing, base bleed, base cavities, and base/external burning. One of the effective ways to reduce the base drag is to increase the base pressure through the base bleed. In this method, a relatively small amount of low velocity fluid is injected into the dead air region immediately behind the base (see Figure 92).

For increasing stagnation pressures of the bleeding jet issuing from the center portion of the base into the wake, three distinctly different flow regimes exist (Figure 93). As the stagnation pressure of base bleed increases (thus, increasing the mass flow rate gas injected), the base pressure increases. Under this condition, all the mass of the bleed is entrained into the mixing region along the wake boundary of the slip stream, and

this flow condition is indicated as Regime I. Typically Regime I corresponds to very small rates of mass injection, of the order of a few percent). The trend of increase in base pressure persists until a maximum is reached. Thereafter, as the stagnation pressure (or, the mass flow rate) increases, the momentum of the bleed gas is strong enough to overcome the high pressure prevailing at the end of the wake as a result of flow recompression, and the base pressure starts to decrease. This type of flow pattern occurs in Regime II. The base pressure would continue to decrease until a relative minimum is reached. Thereafter, for higher mass injection rates, the jet is so strong that it becomes a supersonic stream itself and the base pressure increases (Regime III). The interaction between the two supersonic streams is such that an equilibrium base pressure is reached. Under this situation, the slip stream pumps out a certain amount of fluid from the near wake while the jet stream feeds an equal amount of fluid into the wake. For unusually high mass injection rates or stagnation pressures, the base pressure may be higher than the free stream pressure, and the pluming jet may cause separation of the slip stream away from the wall ahead of the base. This is usually known as the plume-induced separation.

The above description of the effect of base bleed has been observed by many experimental investigations^{85, 86, 87} Sahu^{81, 82} has applied the Navier-Stokes computational technique and showed that the phenomenon of base injection in all of the three different flow regimes could be predicted simply by providing appropriate numerical boundary conditions in the base for the bleeding stream. Earlier work (Sahu⁸¹) used an iterative boundary condition procedure at the base bleed exit. This procedure was later modified by Nietubicz and Sahu⁸⁸ to include a non-iterative boundary condition. Computed results obtained by Sahu^{81, 82} have supported the observed influences of base bleed throughout all three different regimes. Figure 94 shows a typical computational grid used in the base region for a flow condition in Regime I. Here, an attempt was made to adapt the grid points to the free shear layer. The computed velocity vectors in the base region obtained with this grid are shown in Figure 95. This figure shows the detailed velocity vectors (streamline pattern) of the flow in Regime I, where all mass of the bleed has been entrained into the mixing region. This entrained mass weakens the expansion at the base corner and the recompression downstream of the base which results in a higher base pressure. Indeed, this increase in computed base pressure is also observed for small mass bleed parameters (see Figure 96). Figure 96 also shows a drop in base pressure with a further increase in the bleed parameter (or a larger stagnation pressure of the bleed gas). This corresponds to the flow conditions in Regime II. A velocity vector plot in the near wake for this regime is shown in Figure 97. It shows some of the bleed flow penetrating the downstream region of high pressure. With further increase in bleed parameter (for higher stagnation pressures), the bleed stream becomes a pluming jet (jet flow). The flow field in this case corresponds to Regime III where the base pressure increases with increase in the stagnation pressure of the jet. A velocity vector plot for this flow condition is shown in Figure 98. The interaction between the free stream and the jet results in a pair of counter rotating recirculating bubbles in the near wake. The effect of bleed is due to mass ad-

dition if the stagnation temperature of the jet equals to that of the free stream. If the stagnation temperature of the jet exceeds the free stream total temperature, then it involves both mass and energy additions into the wake.

In the past decade, an extensive computational effort has been devoted to the study of power-on (jet-on) base flows. Some of these numerical studies include the work by Deiwert⁸⁹, Wagner⁹⁰, Sahu^{82, 91}, Childs and Caruso⁹², and Peace⁹³. A variety of turbulence models (both algebraic and two-equation models) were applied with varying degrees of success. Sahu⁸² computed the supersonic flow over a missile afterbody containing a centered propulsive jet where the free stream Mach number was 2.0 and the jet exit Mach number was 2.5. The jet to free stream pressure ratio varied from 1 to 15 for a conical nozzle exit half angle of 20 degrees. The grids in the base region were adapted to the free shear layer as the solutions developed. Figure 99 shows a typical computational grid in the base region for a jet to free stream pressure ratio of 3. Computed results were obtained using this grid and the algebraic Baldwin-Lomax turbulence model. Comparison of the computed density contours and the experimental (Agrell and White⁹⁴) Schlieren picture for this case is shown in Figures 100 and 101. The flow features to be seen are the oblique shock at the end of the afterbody, the trailing shock system inside the plume and the slip line that emanates from the nozzle lip and defines the jet boundary. The trailing shocks inside the plume cross each other about 2 calibers downstream of the base. The agreement of these qualitative features between the computed results and the experiment are quite good. A plot of average base pressure as a function of exit pressure is shown in Figure 102. The base pressure increases as the stagnation pressure of the jet increases. This clearly corresponds to flow Regime III. The agreement of the computed base pressures with experiment is good for higher pressure ratios of 9 and 15, but falls off at the lower values.

Another experimental data set that has been used for computational validation is that obtained by Heltsley, et al.⁹⁵ for a free stream Mach number of 1.4 and a Mach 2.7 nozzle. Petrie and Walker⁹⁶ published comparisons of computational results from various research groups with this experimental data. It should be noted that the experimental data was not provided until after the computations were complete. The study indicated that the computed results suffered from grid resolution and turbulence modeling issues which prevented accurate predictions in the base flow region. It was also noted that the experimental data suffered from uncertainties in the measurements in the near wake region. Since then, the experimental results have become available and Child and Caruso⁹² and others have predicted these flows more accurately. They concluded that grid resolution and turbulence model deficiencies caused significant error in the numerical prediction of such flows. They obtained the computed results using a two equation $k - \epsilon$ turbulence model and adapted grid; however flow inside the nozzle was not included in their calculations. Sahu⁹⁷ has performed computations that includes the inside of the nozzle. In addition, a grid adaptation procedure was developed to adapt the base region grid to both the free and the jet shear layers using the temperature gradients. An example of two adapted grids for two pressure ratios (50 and 150) are shown in Fig-

ures 103 and 104. Computed velocity vectors and Mach contours for the low pressure ratio case are shown in Figures 105 and 106, respectively. Figure 105 shows the two counter rotating recirculating bubbles in the near wake. It also shows the flow in the nozzle itself. Figure 106 shows the qualitative features such as the flow expansion at the base corner, recompression shock downstream of the base, Mach disk inside the plume, and the two shear layers. Figure 107 and 108 show the corresponding base pressure distributions. For both pressure ratios, the new results are compared with experiment and previously computed results where grid adaptation was not used and flow inside the nozzle was not computed. In both these cases, the large kink in the pressure near the jet exit seen with the previous result has been eliminated in the new results, and a substantial improvement in the base pressure comparison has been achieved in the new results. These new results were obtained using an algebraic turbulence model. It appears that for jet flows, grid adaptation may be more critical than the turbulence modeling. Additional experimental data containing detailed information in the near wake for such flows is needed for further validation of computed results obtained with the Navier-Stokes computational techniques.

9. CONCLUSION

As evidenced by the results shown in this paper, Navier-Stokes methods have been successfully used to predict the aerodynamics of missile configurations. Methods currently exist for predicting both static and dynamic aerodynamic derivatives for these flight bodies. As demonstrated by a number of the applications, the computational requirements for applying these techniques can be considerable and represents the primary reason why these techniques have not experienced wider use. The results demonstrate that the accuracy of these techniques often depends on the accuracy of the turbulence model. In general, the results show that for low angle of attack flight, Navier-Stokes methods can provide accurate aerodynamic coefficient prediction with existing turbulence models for many flight vehicles. At higher angles of attack, shortcomings in turbulence modeling may affect the accuracy of the results, particularly for longer bodies.

The prediction of base flow, both with and without mass injections, can also be well predicted using Navier-Stokes techniques, provided adequate turbulence models and grid resolution are used. For the base flows in the absence of mass injection or for low mass injection rates, the accuracy of the details of the flow field appears to be dependent on the turbulence modeling, although the integrated effects are probably acceptable for aerodynamic coefficient prediction. For high mass injection, the accuracy of the flow field predictions depends strongly on grid resolution and grid adaptation appears to play an important role.

There is still much research work that needs to be performed before Navier-Stokes techniques can be routinely used for predicting the aerodynamics of complex missile shapes. From the computational side, improvements in algorithms, grid generation and turbulence modeling are obviously required. It should be clear from a number of examples cited in this paper, that one requirement for improving the computational modeling is continued detailed experimental testing.

References

1. Anderson, D.A., Tannehill, J.C., and Pletcher, R.H., "Computational Fluid Mechanics and Heat Transfer," Washington, DC, USA, Hemisphere Publishing Corporation, 1984 (ISBN 0-07-050328-1).
2. Beam, R., and Warming, R.F., "An Implicit Factored Scheme for the Compressible Navier-Stokes Equations," *AIAA Journal*, Vol. 16, No. 4, 1978, pp. 85-129.
3. Baldwin, B.S., and Lomax, H., "Thin Layer Approximation and Algebraic Model for Separated Turbulent Flows," *AIAA Paper 78-257*, 16th Aerospace Sciences Meeting, January 1978.
4. Cebeci, T., "Calculation of Compressible Turbulent Boundary Layers with Heat and Mass Transfer," *AIAA Paper 70-741*, *AIAA 3rd Fluid and Plasma Dynamics Conference*, Los Angeles, CA, June 29-July 1, 1970.
5. Danberg, J.E., and Patel, N.R., "An Algebraic Turbulence Model for Flow Separation Caused by Forward and Backward Facing Steps," *US Army Ballistic Research Laboratory Memorandum Report, BRL-MR-02813*, Aberdeen Proving Ground, MD, December 1989.
6. Renze, K.J., Buning, P.G., and Rajagopalan, R.G., "A Comparative Study of Turbulence Models for Overset Grids," *AIAA-92-0437*, 30th Aerospace Sciences Meeting and Exhibit, Reno, NV, January 1992.
7. Schiff, L.B., and Steger, J.L., "Numerical Simulation of Steady Supersonic Viscous Flow," *AIAA Journal*, Vol. 18, No. 12, December 1980, pp. 1421-1430. Also see, Schiff, L.B., and Steger, J.L., "Numerical Simulation of Steady Supersonic Viscous Flow," *NASA Technical Paper 1749*, May 1981.
8. Vigneron, Y.C., Rakich, J.V., and Tannehill, J.C., "Calculation of Supersonic Viscous Flow over Delta Wings with Sharp Subsonic Leading Edges," *AIAA Paper 78-1137*, Seattle, Washington, 1978.
9. Schiff, L.B., and Sturek, W.B., "Numerical Simulation of Steady Supersonic Flow over a Ogive-Cylinder-Boattail Body," *AIAA Paper 80-0066*, *AIAA 18th Aerospace Sciences Meeting*, January 1980.
10. Reklis, R.P., and Sturek, W.B., "Surface Pressure Measurements on Slender Bodies At Angle of Attack in Supersonic Flow," *U.S. Army Ballistic Research Laboratory/ARRADCOM Memorandum Report ARBRL-MR-02876*, Aberdeen Proving Ground, MD, November 1978. AD A064097.
11. Kayser, L.D., and Sturek, W.B., "Experimental Measurements in the Turbulent Boundary Layer of a Yawed, Spinning Ogive-Cylinder Body of Revolution at Mach 3.0. Part II: Data Tabulation," *U.S. Army Ballistic Research Laboratory/ARRADCOM Memorandum Report ARBRL-MR-02813*, Aberdeen Proving Ground, MD, March 1978. AD A053458.
12. Kayser, L.D., and Sturek, W.B., "Turbulent Boundary Layer Measurements on the Boattailed Section of a Yawed, Spinning Projectile Shape at Mach 3.0," *U.S. Army Ballistic Research Laboratory/ARRADCOM Memorandum Report ARBRL-MR-02880*, Aberdeen Proving Ground, MD, November 1978. AD A065355.
13. Nietubicz, C.J., and Opalka, K., "Supersonic Wind Tunnel Measurements of Static and Magnus Aerodynamic Coefficients for Projectile Shapes with Tangent and Secant Ogive Noses," *U.S. Army Ballistic Research Laboratory Memorandum Report ARBRL-MR-02991*, Aberdeen Proving Ground, MD, February 1980.
14. Sturek, W.B., and Schiff, L.B., "Computations of the Magnus Effect for Slender Bodies in Supersonic Flight," *U.S. Army Ballistic Research Laboratory, Aberdeen Proving Ground, Maryland, Technical Report No. 2384*, December 1981. (Also see, Sturek, W.B., and Schiff, L.B., "Computations of the Magnus Effect for Slender Bodies in Supersonic Flight," *AIAA Paper 80-1586-CP*, *AIAA Atmospheric Flight Mechanics Conference*, August 1980.
15. Degani, D., and Schiff, L.B., "Computation of Supersonic Viscous Flows Around Pointed Bodies at Large Incidence," *AIAA Paper 83-0034*, *AIAA 21th Aerospace Sciences Meeting*, January 1983.
16. Guidos, B.J., Weinacht, P., and Dolling, D.S., "Navier-Stokes Computations for Pointed, Spherical, and Flat Tipped Shell at Mach 3," *Journal of Spacecraft and Rockets*, Vol. 29, No. 3, May-June 1992, pp. 305-311.
17. Dolling, D.S., and Gray, W.K., "Experimental Study of Supersonic Turbulent Flow on Blunted Axisymmetric Body," *AIAA Journal*, Vol. 24, No. 5, 1986, pp. 793-799.
18. Pulliam, T.H. and Steger, J.L., "Implicit Finite-Difference Simulations of Three-Dimensional Compressible Flow," *AIAA Journal*, Vol. 18, Feb. 1980, pp. 159-167.
19. Rizk, Y.M. and Chaussee, D.S., "Three-Dimensional Viscous-Flow Computations using a Directionally Hybrid Implicit-Explicit Procedure," *AIAA Paper 83-1910*, July 1983.
20. Kutler, P., Pedelty, J.A., and Pulliam, T.H. "Supersonic Flow over Three-Dimensional Ablated Nostips using an Unsteady Implicit Numerical Procedure," *AIAA Paper 80-0063*, Jan. 1980.
21. Rizk, Y.M., Chaussee, D.S., and McRae, D.S., "Numerical Simulation of Viscous-Inviscid Interactions on Indented Nose Tips," *AIAA Paper 82-0290*, Jan. 1982.
22. Sturek, W.B., and Mylin, D.C., "Computational Parametric Study of the Magnus Effect on Boattailed Shell at Supersonic Speeds," *AIAA Atmospheric Flight Mechanics Conference*, *AIAA-81-1900*, Albuquerque, NM, August 1981.

23. Jones, D.L., Evans, J., Priolo, F., Sturek, W., and Wardlaw, A., "Application of Euler and Navier-Stokes Codes to Missile Type Bodies with High L/D Ratios," AGARD CP-493, April 1990, Paper 8.
24. Atraghji, E.G., "Pressure Distribution over a Family of Inclined Long Slender Bodies of Revolution at Mach=0.5, 2.0 and 3.5," National Research Council of Canada Report LTR-HA-5X5/0029, 1968.
25. Atraghji, E.G., "Influence of Mach Number, Reynolds Number, Semi-nose Angle and Roll Rate on the Development of the Forces and Moments over a Series of Long Slender Bodies of Revolution at Incidence," National Research Council of Canada Report LTR-HA-5X5/0020, 1967.
26. Hartwich, P.-M., and Hall, R.M., "Navier-Stokes Solutions for Vortical Flows over a Tangent-Ogive Cylinder," AIAA Journal, Vol. 28, No. 7, pp. 1171-1179, July 1990.
27. Degani, D., and Levy, Y., "Asymmetric Turbulent Vortical Flows over Slender Bodies," AIAA 9th Applied Aerodynamics Conference, AIAA Paper 91-3296-CP, September 1991.
28. Nietubicz, C.J., Sahu, J., and Lafarge, R., "Aerodynamic Coefficient Predictions for a Projectile Configuration at Transonic Speeds," U.S. Army Ballistic Research Laboratory, Aberdeen Proving Ground, Maryland, Memorandum Report BRL-MR-3639, December 1987.
29. Sahu, J., "Numerical Computations of Transonic Critical Aerodynamic Behavior," U.S. Army Ballistic Research Laboratory, Aberdeen Proving Ground, Maryland, Memorandum Report BRL-TR-2962, December 1988.
30. Sahu, J., and Nietubicz, C.J., "Three Dimensional Flow Calculations for a Projectile with Standard and Dome Bases," AGARD CP-493, April 1990, Paper 18.
31. Rai, M.M., D.S. Chaussee, and Y.M. Rizk. "Calculation of Viscous Supersonic Flows over Finned Bodies." AIAA Paper 83-1667. Paper presented at the AIAA Applied Aerodynamics Conference, Danvers, MA, July 1983.
32. Weinacht, P., Guidos, B.J., Sturek, W.B., and Hodes, B.A., "PNS Computation of Spinning Shell at Moderate Angles of Attack and for Long L/D Finned Projectiles," AIAA Paper 85-0273, AIAA 23th Aerospace Sciences Meeting, January 1985.
33. Weinacht, P., and Sturek, W.B., "Navier-Stokes Predictions of Static and Dynamic Aerodynamic Derivatives for High L/D Finned Projectiles," in "Missile Aerodynamics", AGARD CP 493, April 1990, Paper 20.
34. Wardlaw, A.B. Jr., Baltakis, F.P., Solomon, J.M., and Hackerman, L.B., "An Inviscid Computational Method for Tactical Missile Configurations," NSWC TR 81-457, December 1981.
35. Giolda, T.P., and McRae, D.S., "Explicit Parabolized Navier-Stokes Solutions for Secant-Ogive Cylinder-Boat-Tail and Finned Projectiles," AIAA Paper 87-2292, 1987.
36. Priolo, F.J., and Wardlaw, A.B. Jr., "Vortical Flowfields for Missiles Computed Using GRIDGEN and GASP," AIAA Paper 92-4351, AIAA Atmospheric Flight Mechanics Conference, Hilton Head Island, SC, August 1992.
37. Allen, J.M., and Townsends, J.C., "Application of the SWINT Code to Wing/Body/Tail Geometries," AIAA Paper 85-1811.
38. Wai, J.C., Blom, G., Yoshihara, H, and Chaussee, D., "PN/S Calculations for a Fighter Wing/Fuselage at High-Lift Yaw Conditions," AIAA-86-1829, AIAA 4th Applied Aerodynamics Conference, San Diego, CA, June 1986.
39. Murphy, C.H., "Free Flight Motion of Symmetric Missiles," U.S. Army Ballistic Research Laboratory, Aberdeen Proving Ground, Maryland, Report No. 1216, July 1963. (AD A442757)
40. Sturek, W.B., "Application of CFD to the Aerodynamics of Spinning Shell," AIAA Paper 84-0323, AIAA 22nd Aerospace Sciences Meeting, Reno, NV, January 1984.
41. Weinacht, P., "Unpublished computational results," Army Research Laboratory, Aberdeen Proving Ground, MD.
42. Murphy, C.H., and Schmidt, L.E., "The Effect of Length on the Aerodynamics Characteristics of Bodies of Revolution in Supersonic Flight," U.S. Army Ballistic Research Laboratory, Aberdeen Proving Ground, Maryland, Report No. 876, August 1953.
43. Weinacht, P., and Sturek, W.B., "Computation of the Roll Characteristics of Finned Projectiles," AIAA Paper 88-2540-CP, AIAA Applied Aerodynamics Conference, Williamsburg, VA, June 1988.
44. Weinacht, P., and Sturek, W.B., "Computation of the Roll Characteristics of a Long L/D Finned Projectile and Comparison with Range Data," AIAA Paper 89-3369-CP, AIAA Atmospheric Flight Mechanics Conference, Boston, MA, August 1989.
45. Daywitt, J.E., Prats, B.D., and Chan, Y.C., "Aerodynamic Analysis and Test of a Small Aspect Ratio Finned Projectile," AIAA Paper 93-3461-CP, AIAA Applied Aerodynamics Conference, Monterey, CA, August 1993.
46. Devan, L., and Mason, L., "Aerodynamics of Tactical Weapons to Mach Number 8 and Angle of Attack 180 degrees: Part II, Computer Program and User's Guide," Naval Surface Weapons Center, Dahlgren, VA, MSWC-TR-81-358, Sept. 1981.
47. Edge, H.L., "Computation of the Roll Moment Coefficient for a Projectile with Wrap-Around Fins," AIAA Paper 93-0499, AIAA 31st Aerospace Sciences Meeting, Reno, NV, January 11-14, 1993.

48. Abate, G.L., and Cook, T., "Analysis of Missile Configurations with Wrap-Around Fins using Computational Fluid Dynamics," AIAA Paper 93-3631-CP, AIAA Atmospheric Flight Mechanics Conference, Monterey, CA, August 9-11, 1993.
49. Sturek, W.B., Dwyer, H.A., Kayser, L.D., Nietubicz, C.J., Reklis, R.P., and Opalka, K.O., "Computations of Magnus Effects for a Yaw, Spinning Body of Revolution," AIAA Journal, Vol. 16, No. 7, July 1978, pp. 687-692.
50. Nietubicz, C.J., Sturek, W.B., and Heavey, K.R., "Computations of Projectile Magnus Effect at Transonic Velocities," US Army Ballistic Research Laboratory Technical Report, ARBRL-TR-02515, Aberdeen Proving Ground, MD, August 1983.
51. Sahu, J., "Transonic Navier-Stokes Computations for a Spinning Body of Revolution," Proceedings of the ASME Symposium on Advances and Applications in Computational Fluid Dynamics, Dallas, TX, November 1990.
52. Schiff, L.B., "Nonlinear Aerodynamics of Bodies in Coning Motion", AIAA Journal, Vol. 10, No. 11, November 1972, pp. 1517-1522.
53. Lin, T.C., "A Numerical Study of the Aerodynamics of a Reentry Vehicle in Steady Coning Motion", AIAA Paper 78-1358, AIAA Atmospheric Flight Mechanics Conference, Palo Alto, CA, August 1978.
54. Agarwal, R., and Rakich, J.V., "Computation of Supersonic Laminar Viscous Flow Past a Pointed Cone at Angle of Attack in Spinning and Coning Motion", AIAA Paper 78-1211, AIAA 11th Fluid and Plasma Dynamics Conference, Seattle, WA, July 1978.
55. Weinacht, P., Sturek, W.B., and Schiff, L.B., "Navier-Stokes Predictions of Pitch Damping for Axisymmetric Shell using Steady Coning Motion," AIAA Paper 91-2855, AIAA Atmospheric Flight Mechanics Conference, New Orleans, LA, August 1991.
56. Weinacht, P., and Sturek, W.B., "Navier-Stokes Predictions of Pitch Damping for Finned Projectiles Using Steady Coning Motion," AIAA Paper 90-3088, AIAA 8th Applied Aerodynamics Conference, Portland, OR, August 20-22, 1990.
57. Levy, L.L., and Tobak, M., "Nonlinear Aerodynamics of Bodies of Revolution in Free Flight", AIAA Journal, Vol. 8, No. 12, December 1970, pp. 2168-2171.
58. Schiff, L.B., and Tobak, M., "Results from a New Wind-Tunnel Apparatus for Studying Coning and Spinning Motions of Bodies of Revolution", AIAA Journal, Vol. 8, No. 11, November 1970, pp. 1953-1957.
59. Weinacht, P., "Navier-Stokes Predictions of Pitch Damping for a Family of Flared Projectiles," AIAA Paper 91-3339, AIAA 9th Applied Aerodynamics Conference, Baltimore, MD, September 23-25, 1991.
60. Tobak, M., and Schiff, L.B., "Generalized Formulation of Nonlinear Pitch-Yaw-Roll Coupling: Part I - Nonaxisymmetric Bodies," AIAA Journal, Vol. 13, No. 3, March 1975, pp. 323-326.
61. Tobak, M., and Schiff, L.B., "Generalized Formulation of Nonlinear Pitch-Yaw-Roll Coupling: Part II - Nonlinear Coning Rate," AIAA Journal, Vol. 13, No. 3, March 1975, pp. 327-332.
62. Celmins, I., "Aerodynamic Characteristics of Fin and Flare-Stabilized 25mm XM910 Prototypes," U.S. Army Ballistic Research Laboratory, Aberdeen Proving Ground, Maryland, Technical Report BRL-TR-2882, December 1987. (AD 191683)
63. Danberg, J.E., Sigal, A., and Celmins, I., "Aerodynamic Characteristics of a Family of Cone-Cylinder-Flare Projectiles," Journal of Spacecraft and Rockets, Vol. 27, No. 4, July-August 1990, pp 335-360. Also see, Danberg, J.E., Sigal, A., and Celmins, I., "Prediction and Comparison with Measurements of the Aerodynamic Characteristics of Flare-Stabilized XM910 Prototypes," U.S. Army Ballistic Research Laboratory, Aberdeen Proving Ground, Maryland, Technical Report BRL-MR-3752, May 1989. (AD 208099)
64. Rollstin, L., "Measurement of Inflight Base Pressure on an Artillery-Fired Projectile", AIAA Paper No. 87-2427, 1987.
65. Korst, H.H., "A Theory for Base Pressures in Transonic and Supersonic Flow," Journal of Applied Mechanics, Vol. 23, pp. 593-600, 1956.
66. Chapman, D.R., "An Analysis of Base Pressure at Supersonic Velocities and Comparison with Experiment," NACA TN 2137, 1950.
67. Reid, J. and Hastings, R.C., "Experiments on the Axi-Symmetric Flow Over Afterbodies and Bases at $M=2.0$," RAE Report Aero. 2628, Farnborough, England, 1959.
68. Badrinarayan, M.A., "An Experimental Investigation of Base Flows at Supersonic Speeds," Journal of the Royal Aeronautical Society, Vol. 65, pp. 475-482, 1961.
69. Delery, J., "ONERA Research on Afterbody Viscid/Inviscid Interaction with Special Emphasis on Base Flows," Proceedings of the Symposium on Rocket/Plume Fluid Dynamic Interactions, University of Texas at Austin, 1983.
70. Herrin, J.L., and Dutton, J.C., "An Experimental Investigation of the Supersonic Axisymmetric Base Flow behind a Cylindrical Afterbody," UILU 91-4004, University of Illinois at Urbana, Champaign, Urbana, IL, May 1991.
71. Sahu, J., C. J. Nietubicz, C.J., and Steger, J.L., "Navier-Stokes Computations of Projectile Base Flow With and Without Base Injection," BRL-TR-02532, U.S. Army Ballistic Research Laboratory, Aberdeen Proving Ground, MD, November 1983. (also see AIAA Journal, vol. 23, no. 9, pp. 1348-1355, September 1985)
72. Sahu, J., "Drag Predictions for Projectiles at Transonic and Supersonic Speeds," US Army Ballistic Research Laboratory Memorandum Report, BRL-MR-03523, Aberdeen Proving Ground, MD, June 1986.

73. McCoy, R.L., "McDrag - A Computer Program for Estimating the Drag Coefficient of Projectiles," US Army Ballistic Research Laboratory Technical Report, BRL-TR-02293, Aberdeen Proving Ground, MD, February 1981.
74. Moore, F.G., and Swanson, R.C., "Aerodynamics of Tactical Weapons to Mach Number 3 and Angle-of-Attack 15°, Part I - Theory and Application," NSWC/DL Tr-3600, March 1977.
75. Sahu, J., "Numerical Computations of Supersonic Base Flow with Special Emphasis on Turbulence Modeling," AIAA Paper AIAA-92-4352, AIAA Atmospheric Flight Mechanics Conference, Hilton Head Island, SC, August 1992.
76. Sahu, J., and Steger, J.L., "Numerical Simulation of Three-Dimensional Transonic Flows," AIAA Paper No. 87-2293, Atmospheric Flight Mechanics Conference, Monterey, California, August 1987.
77. Chow, W. L. "Improvement on Numerical Computation of the Thin-Layer Navier-Stokes Equation With Special Emphasis on the Turbulent Base Pressure of a Projectile in Transonic Flight Condition," Contract Report No. DAAG29-81-D-0100, University of Illinois, Urbana-Champaign, Urbana, IL, November 1985.
78. Chien, K. Y., "Predictions of Channel and Boundary-Layer Flows with a Low-Reynolds Number Turbulence Model," AIAA Journal, vol. 20, no. 1, pp.33-38, January 1982.
79. Jones, W.P., and Launder, B.E., "The Prediction of Laminarization With a Two-Equation Model of Turbulence." International Journal of Heat and Mass Transfer, vol. 15, 1972.
80. Sahu, J., and Danberg, J.E., "Navier-Stokes Computations of Transonic Flows with a Two-Equation Turbulence Model." AIAA Journal, vol. 24, no. 11, pp. 1744-1751, November 1986.
81. Sahu, J., "Supersonic Base Flow Over Cylindrical Afterbodies With Base Bleed," AIAA Paper No. 86-0487, Proceedings of the 24th Annual Aerospace Sciences Meeting, Reno, NV, January 1986.
82. Sahu, J., "Computations of Supersonic Flow Over a Missile Afterbody Containing an Exhaust Jet." AIAA Journal of Spacecraft and Rockets, vol. 24, no. 5, pp. 403-410, September-October 1987.
83. Sahu, J., and Nietubicz, C.J., "Three Dimensional Flow Calculation for a Projectile With Standard and Dome Bases." BRL-TR-3150, U.S. Army Ballistic Research Laboratory, Aberdeen Proving Ground, MD, September 1990, (Also see AGARD Conference Proceedings No. 493 on Missile Aerodynamics, 1990).
84. Sahu, J., "A Computational Study of the Base Region Flow Field for the M865 Projectile," ARL-TR-109, U.S. Army Research Laboratory, Aberdeen Proving Ground, MD, April 1993.
85. Bowman, J.E. and Clayden, W.A., "Cylindrical Afterbodies in Supersonic Flow with Gas Ejection," AIAA Journal, Vol. 5, No.8, pp. 1524-1525, 1967.
86. Clayden, W.A. and Bowman, J.E., "Cylindrical Afterbodies at $M=2$ with Hot Gas Ejection," AIAA Journal, Vol. 6, No. 12, pp. 2429-2431, 1968.
87. Schilling, H., "Experimental Investigation on the Base-Bleed-Effect for Body-Tail-Combinations," Proceedings of the 8th International Symposium on Ballistics, Amsterdam, Holland, 1984.
88. Nietubicz, C.J., and Sahu, J., "Navier-Stokes Computations of Base Bleed Projectiles," Proceedings of the First International Symposium on Special Topics in Chemical Propulsion: Base Bleed, Athens, Greece, November 1988.
89. Deiwert, G.S., "Supersonic Axisymmetric Flow over Boattails Containing a Centered Propulsive Jet," AIAA Journal, Vol. 22, No. 10, pp. 1358-1365, 1984.
90. Wagner, B., "Calculation of Turbulent Flow about Missile Afterbodies Containing an Exhaust Jet," AIAA Paper No. 84-1659, 1984.
91. Sahu, J., and Nietubicz, C.J., "Numerical Computation of Base Flow for a Missile in the Presence of a Centered Jet," AIAA Paper No. 84-0527, 1984.
92. Childs, R.E. and Caruso, S.C., "On the Accuracy of Turbulent Base Flow Predictions," AIAA Paper No. 87-1439, 1987.
93. Peace, A.J., "Turbulent Flow Predictions for Afterbody/Nozzle Geometries Including Base Effects," Journal of Propulsion and Power, Vol. 7, No. 3, pp. 396-403, 1991.
94. Agrell, J. and White, R.A., "An Experimental Investigation of Supersonic Axisymmetric Flow over Boattails Containing a Centered Propulsive Jet," The Aeronautical Research Institute of Sweden (FFA), TN AU-913, 1974.
95. Heltsley, F.L., Walker, B.J., and Nichols, R.H., "Transonic Nozzle-Afterbody Flowfield Measurements using a Laser Doppler Velocimeter," AGARD Conference Proceedings, No. 348, September 1983.
96. Petric, H.L. and Walker, B.J., "Comparison of Experiment and Computation for a Missile Base Region Flowfield with a Centered Propulsive Jet," AIAA Paper No. 85-1618, 1985.
97. Sahu, J., "Unpublished Computational Results on Base Flow with a Jet," 1989.

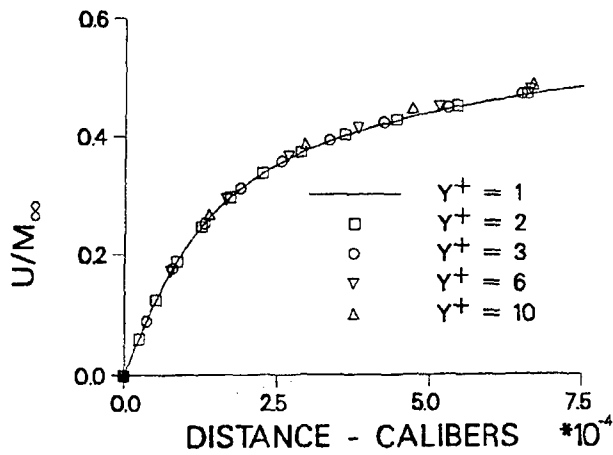
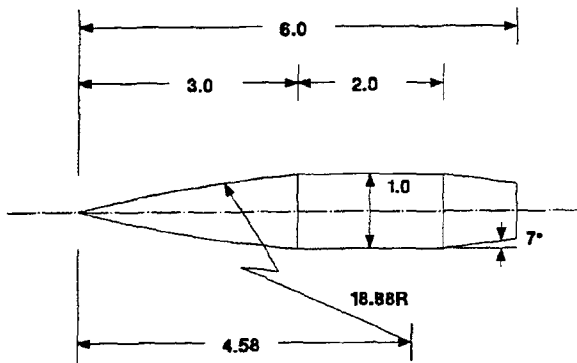


Figure 1. Longitudinal velocity profile for various grid spacings, Mach 4, cone-cylinder, $X/D = 6.2$



ALL DIMENSIONS IN CALIBERS (ONE CALIBER = 57.2 mm)

Figure 2. Schematic of the SOCBT configuration

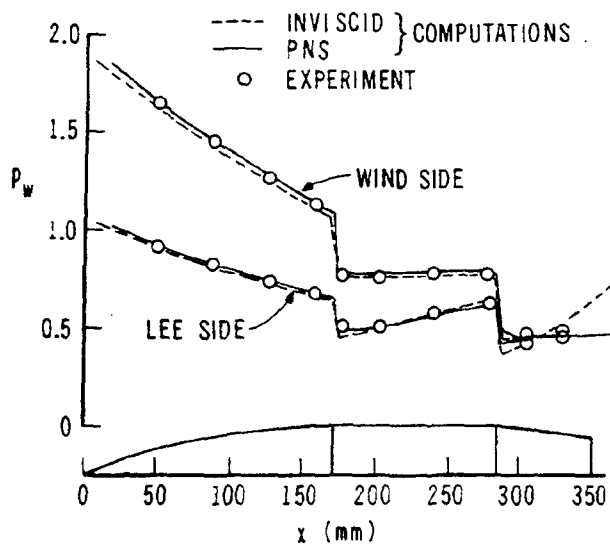


Figure 3. Longitudinal pressure distribution on SOCBT configuration, Mach 3, $\alpha = 6.3^\circ$, from Ref. [9].

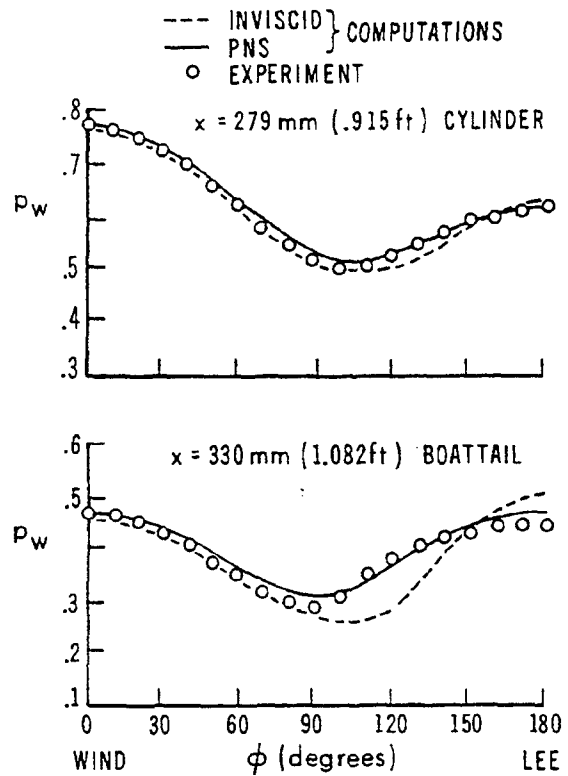


Figure 4. Circumferential pressure distribution on SOCBT configuration, Mach 3, $\alpha = 6.3^\circ$, (top) on cylinder, (bottom) on boattail, from Ref. [9].

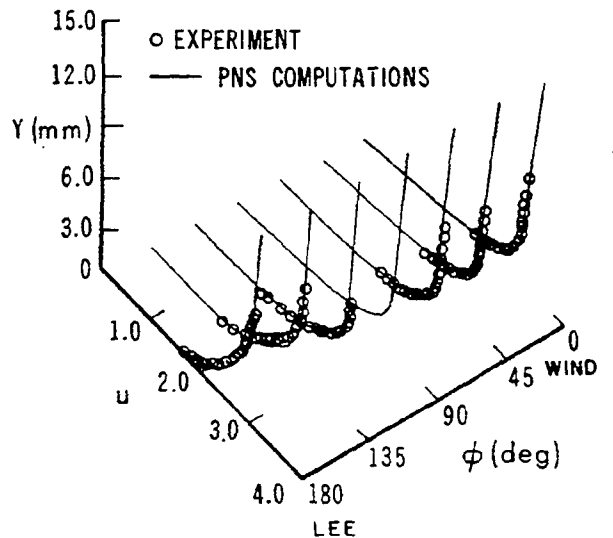


Figure 5. Velocity Profiles on SOCBT body, Mach 3, $\alpha = 6.3^\circ$, $X/D=4.44$ (on cylinder), from Ref. [9].

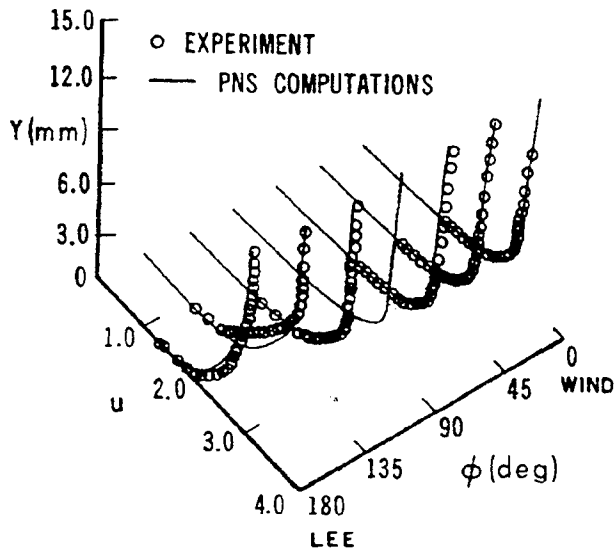


Figure 6. Velocity Profiles on SOCBT body, Mach 3, $\alpha = 6.3^\circ$, $X/D=5.56$ (on boattail), from Ref. [9]

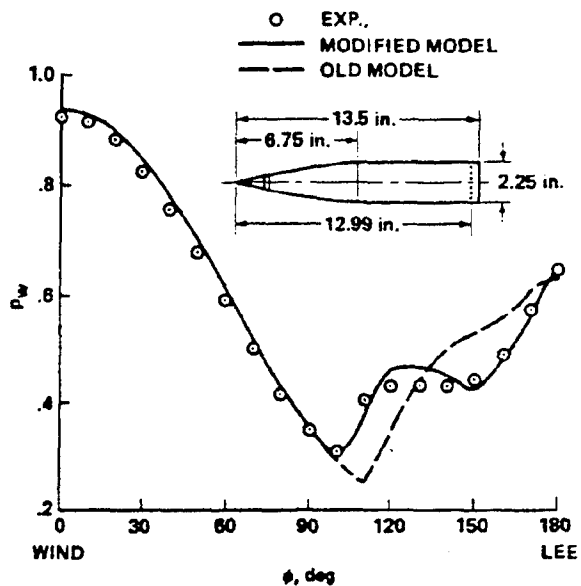


Figure 8. Circumferential pressure distribution near aft end of SOC body, Mach 3, 10.4° , from Ref. [15]

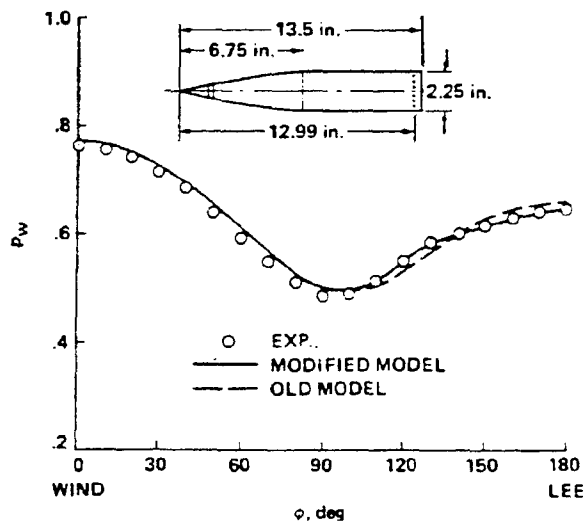


Figure 7. Circumferential pressure distribution near aft end of SOC body, Mach 3, 6.3° , from Ref. [15]

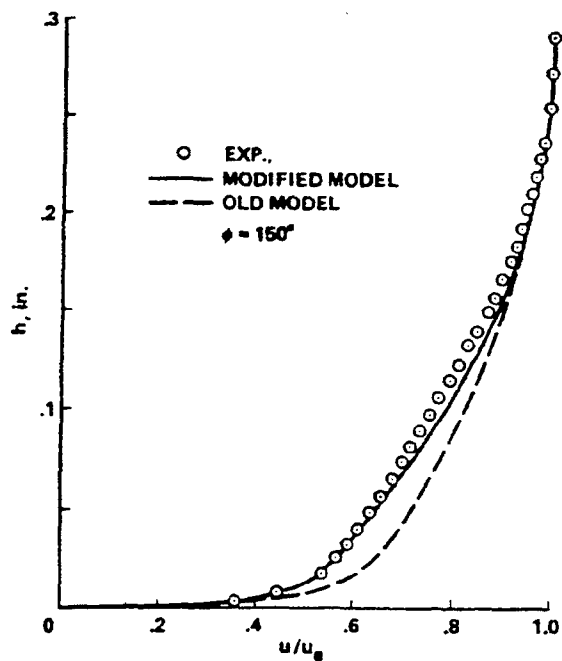


Figure 9. Velocity profile near aft end of SOC geometry, circumferential angle 30° from lee side, Mach 3, 6.3° , from Ref. [15]

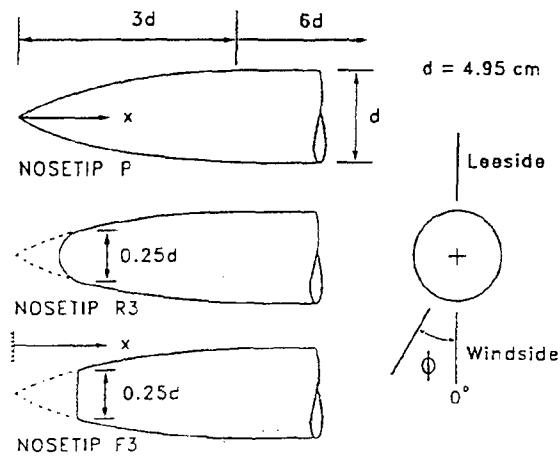


Figure 10. Schematic of nosetip shapes

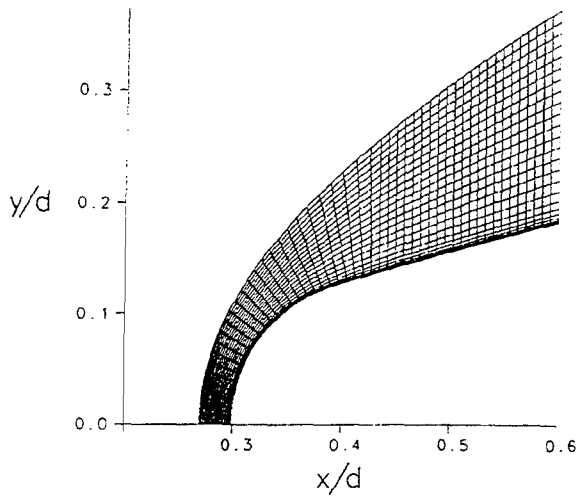


Figure 11. Grid used for hemispherical nosetip

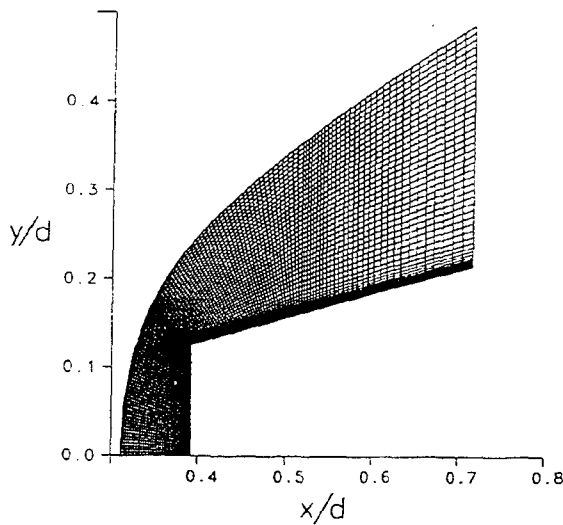


Figure 12. Grid used for flat nosetip

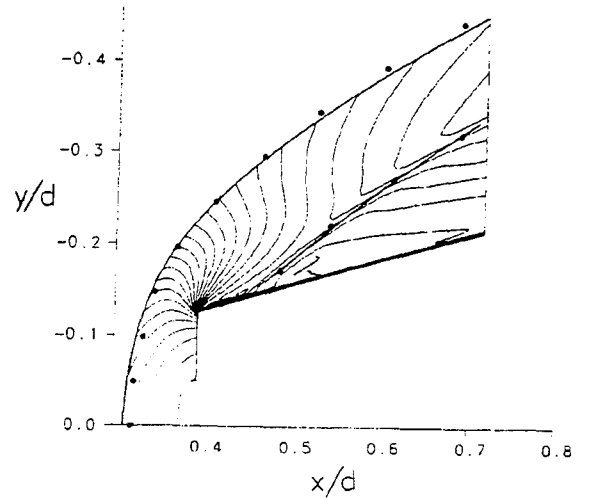


Figure 13. Mach contours on windward side of flat nosetip

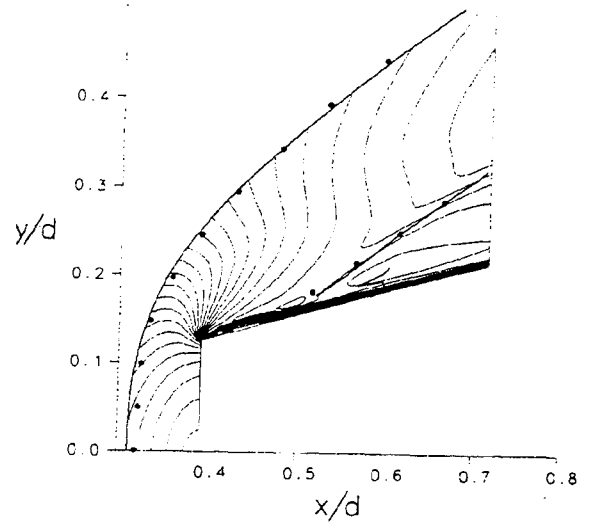


Figure 14. Mach contours on leeward side of flat nosetip

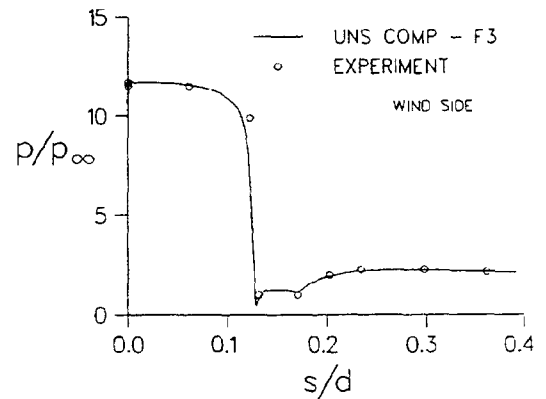


Figure 15. Surface pressure distribution on windward side of flat nosetip

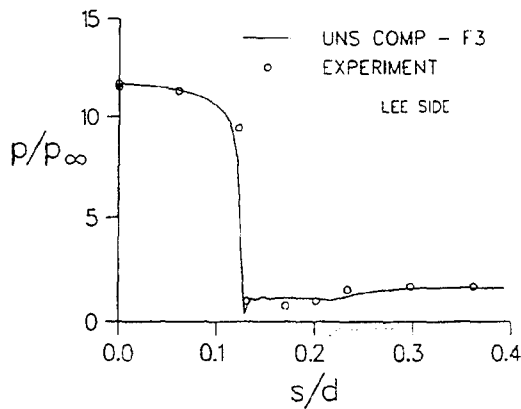


Figure 16. Surface pressure distribution on leeward side of flat nosetip

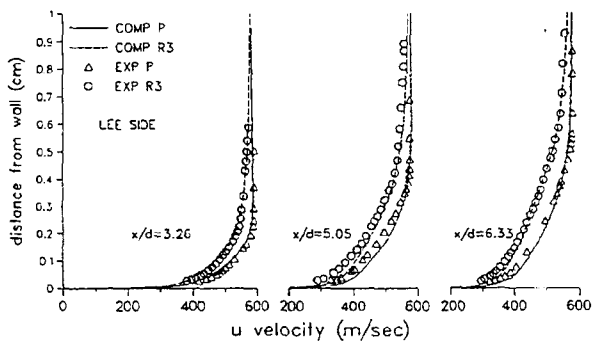


Figure 17. Velocity profiles at three axial stations downstream of round and pointed nosetip

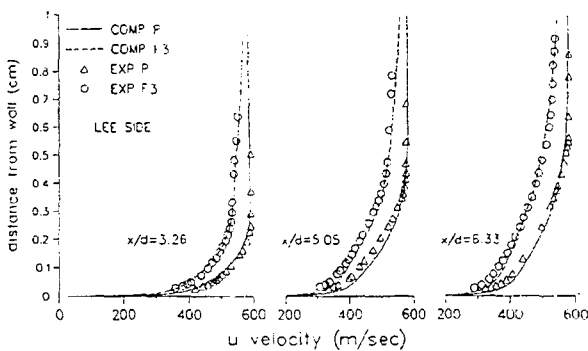


Figure 18. Velocity profiles at three axial stations downstream of flat and pointed nosetip

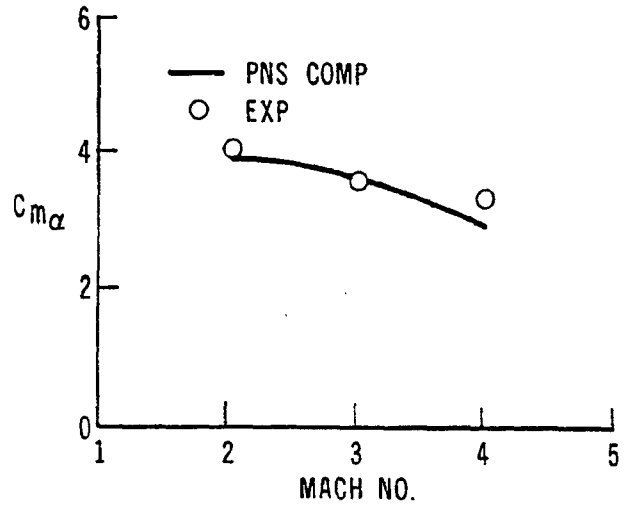


Figure 19. Pitching moment coefficient slope as a function of Mach number, SOCBT configuration, from Ref. [14]

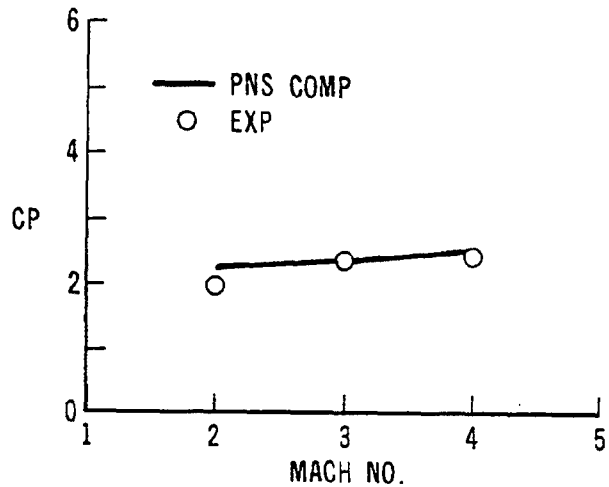


Figure 20. Normal force center of pressure as a function of Mach number, SOCBT configuration, from Ref. [14]

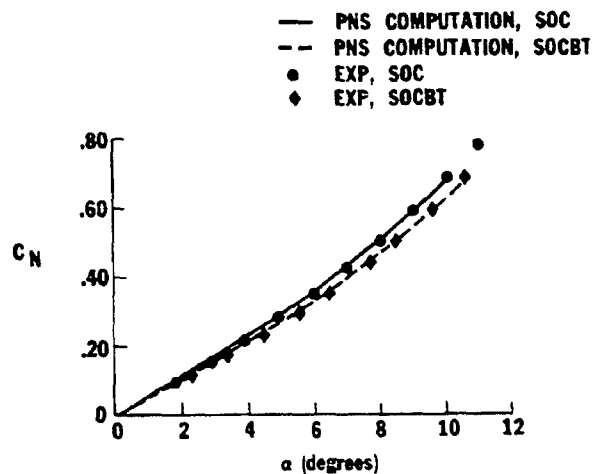


Figure 21. Normal force coefficient as a function of angle of attack, Mach=3, SOC and SOCBT bodies, from Ref. [22]

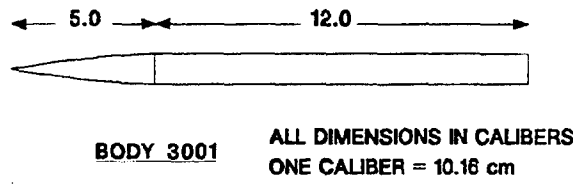


Figure 22. Schematic of high L/D body

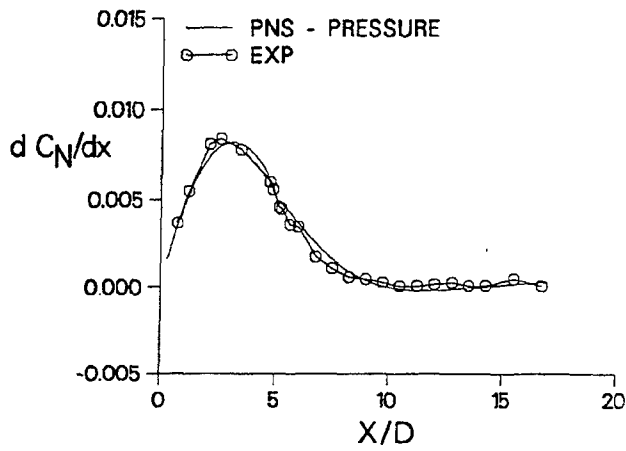


Figure 23. Normal force loading distribution on high L/D body, Mach 3.5, $\alpha = 3.06^\circ$

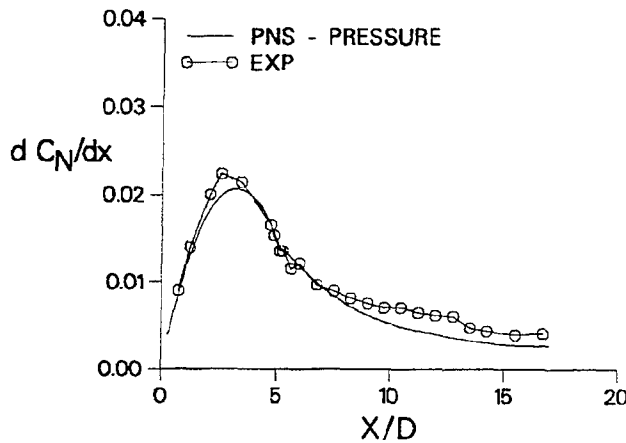


Figure 24. Normal force loading distribution on high L/D body, Mach 3.5, $\alpha = 7.13^\circ$

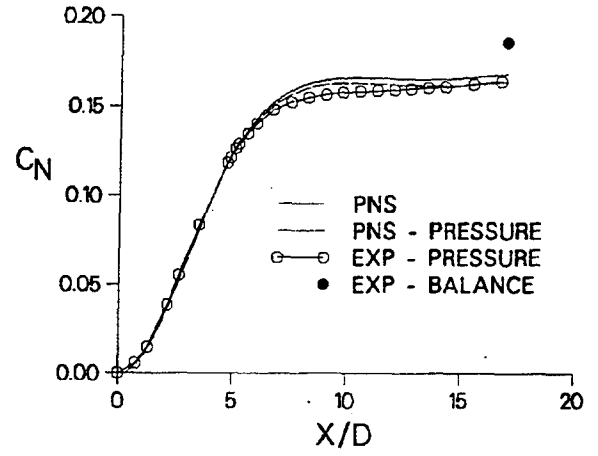


Figure 25. Normal force coefficient distribution on high L/D body, Mach 3.5, $\alpha = 3.06^\circ$

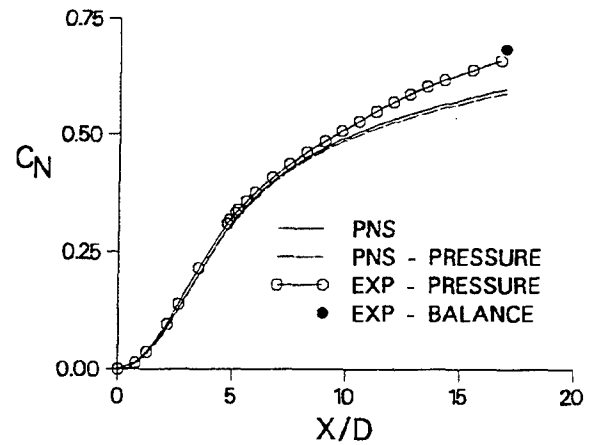


Figure 26. Normal force coefficient distribution on high L/D body, Mach 3.5, $\alpha = 7.13^\circ$

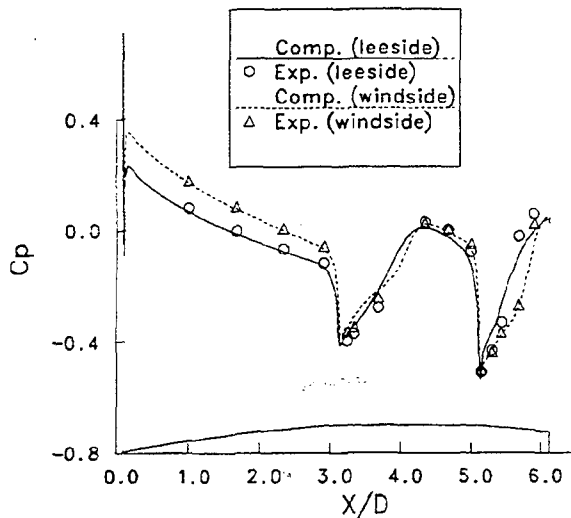


Figure 27. Surface pressure coefficient on wind and lee side of SOCBT, Mach 0.96, $\alpha = 4^\circ$

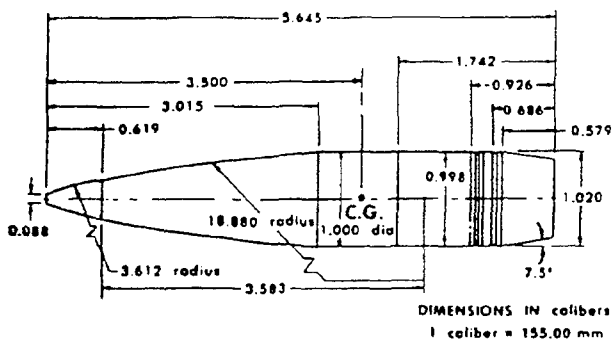


Figure 28. Schematic of M549 configuration

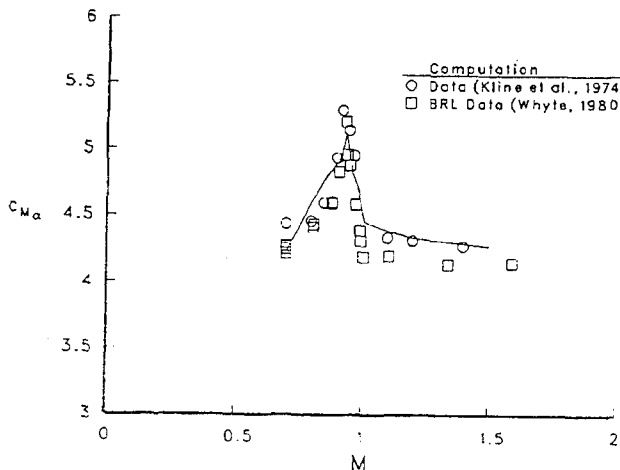


Figure 29. Pitching moment coefficient as a function of Mach number, M549 configuration

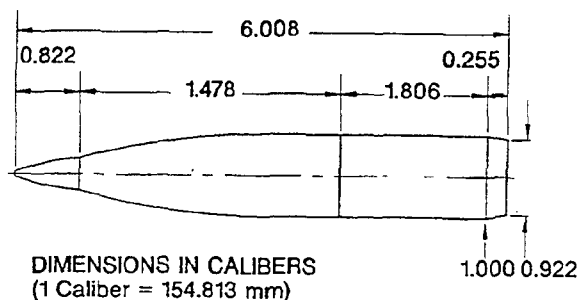


Figure 30. Schematic of M825 configuration

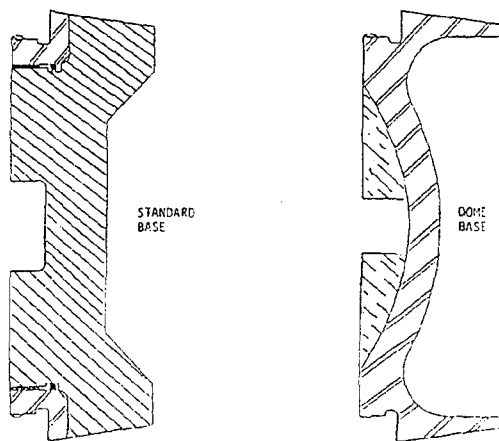


Figure 31. Schematic of M825 standard and dome base configurations

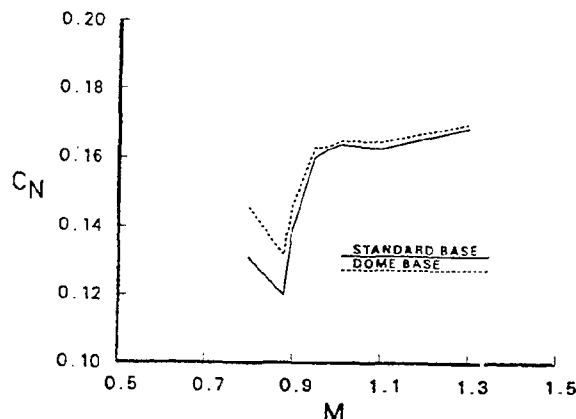


Figure 32. Normal force coefficient as a function of Mach number, M825 standard and dome bases, $\alpha = 4.0^\circ$

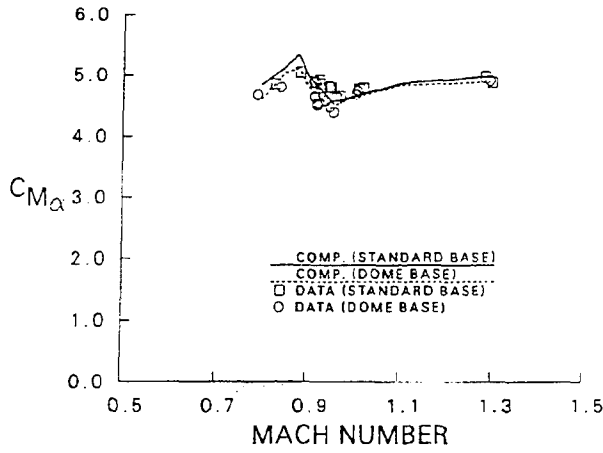


Figure 33. Pitching moment coefficient slope as a function of Mach number, M825 standard and dome bases

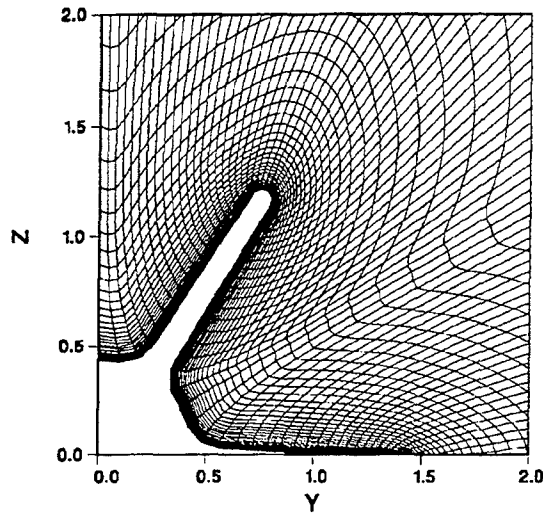
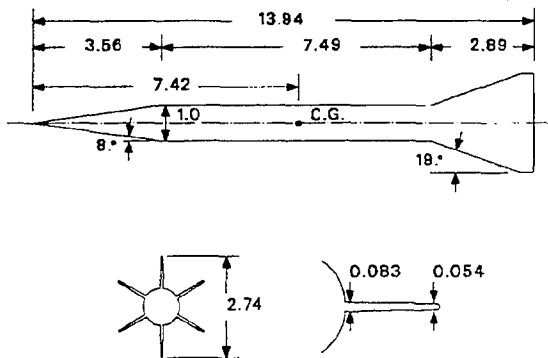


Figure 34. Circumferential plane of wrap-around grid for finned projectile



ALL DIMENSIONS IN CALIBERS (ONE CALIBER = 35.2 mm)

Figure 35. Schematic of M735 projectile

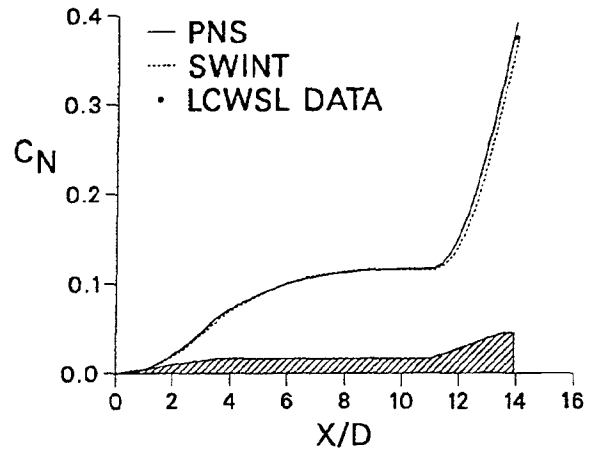


Figure 36. Development of normal force coefficient over M735 finned configuration, $M_\infty = 4$, $\alpha = 2^\circ$

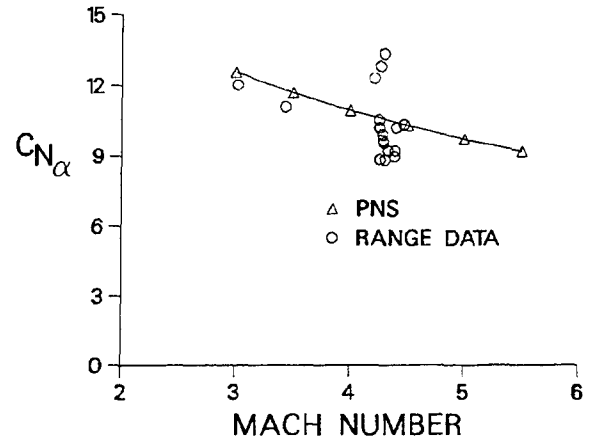


Figure 37. Normal force coefficient as a function of Mach number, M735

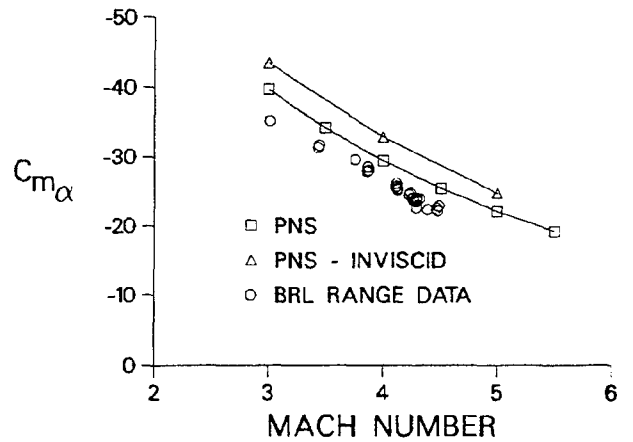
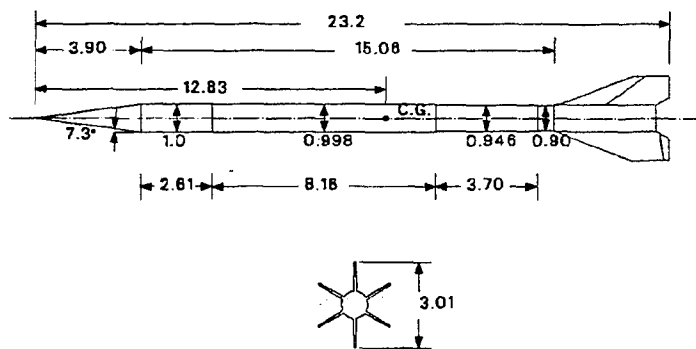


Figure 38. Pitching moment coefficient as a function of Mach number, M735



ALL DIMENSIONS IN CALIBERS (ONE CALIBER = 27.05 mm)

Figure 39. Schematic of M829 projectile

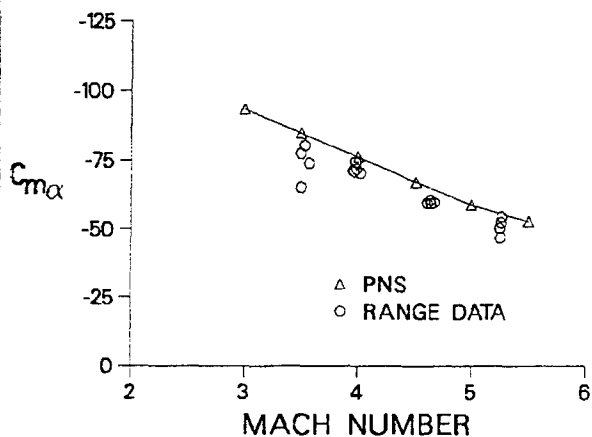


Figure 40. Pitching moment coefficient as a function of Mach number, M829

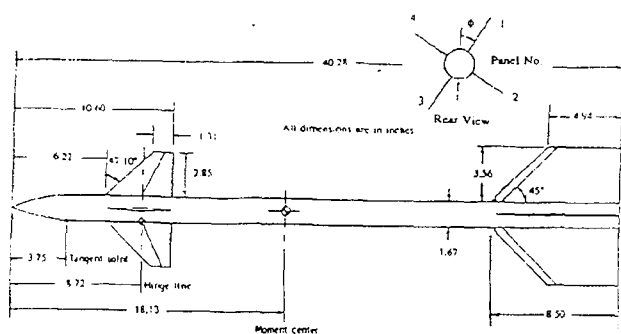


Figure 41. Schematic of Carnard-body-tail configuration, from Ref. [36]

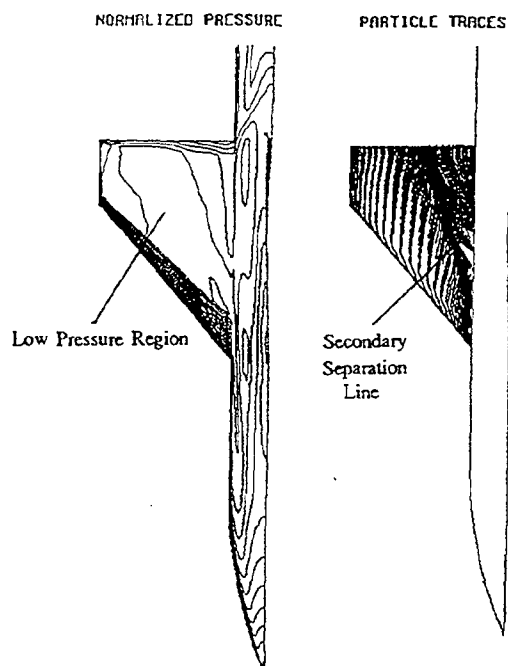


Figure 42. Oil flow and pressure contours on canard portion of canard-body-tail configuration, from Ref. [36]

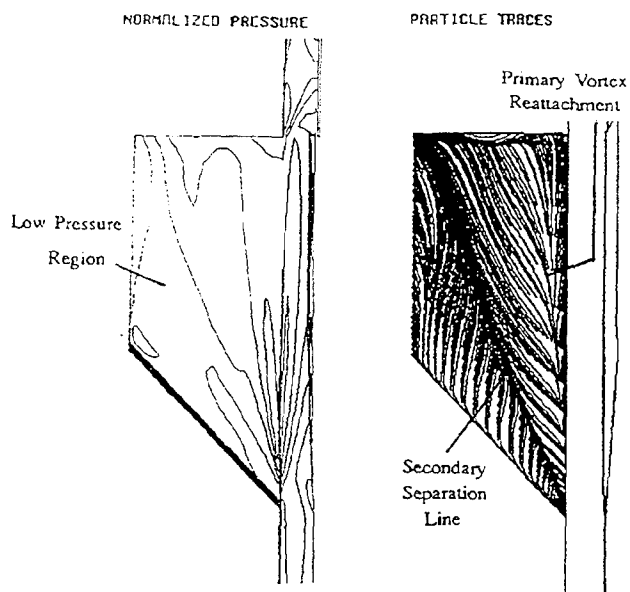


Figure 43. Oil flow and pressure contours on tail portion of canard-body-tail configuration, from Ref. [36]

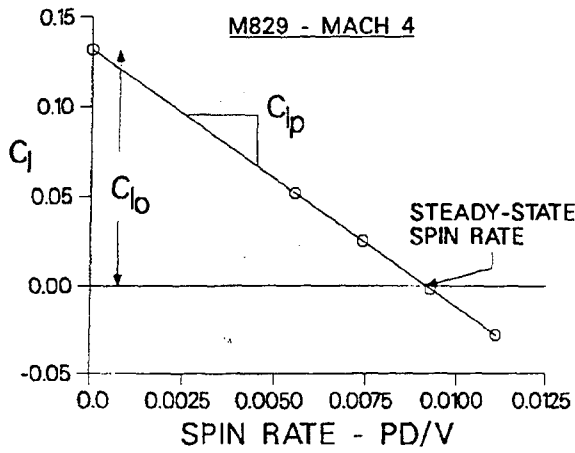


Figure 44. Schematic illustrating various roll coefficients

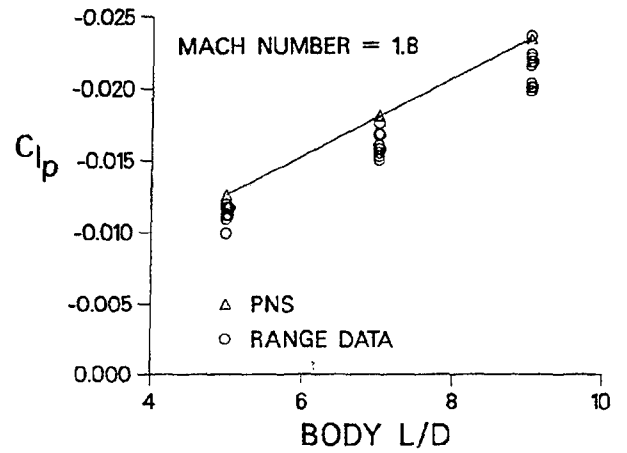


Figure 46. Roll damping coefficient versus body length, Mach 1.8, $\alpha = 0^\circ$, Army Navy spinner rocket

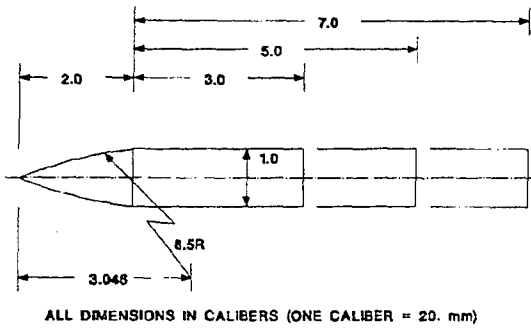


Figure 45. Schematic of the Army Navy spinner rocket

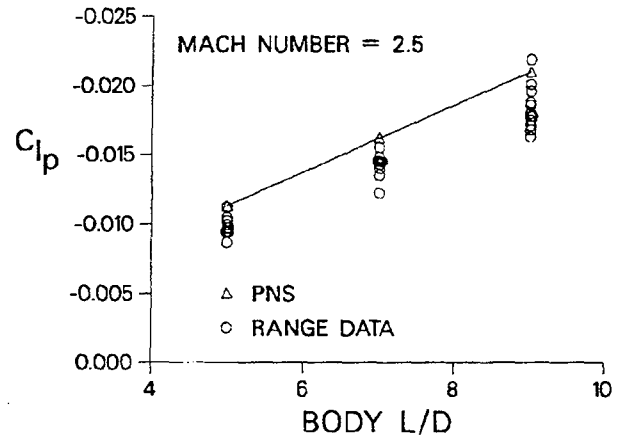


Figure 47. Roll damping coefficient versus body length, Mach 2.5, $\alpha = 0^\circ$, Army Navy spinner rocket

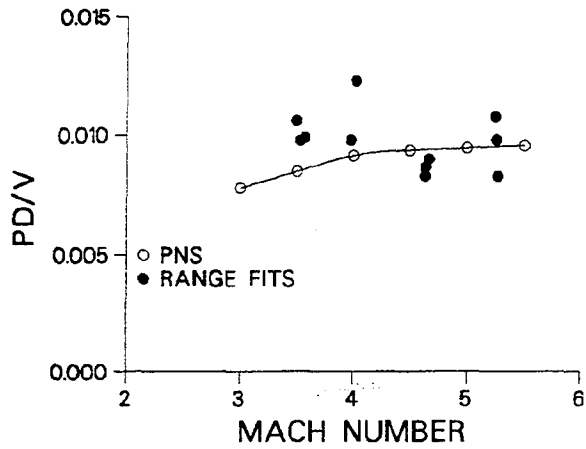


Figure 48. Comparison of computed Mach number variation of equilibrium spin rate with range data, M829

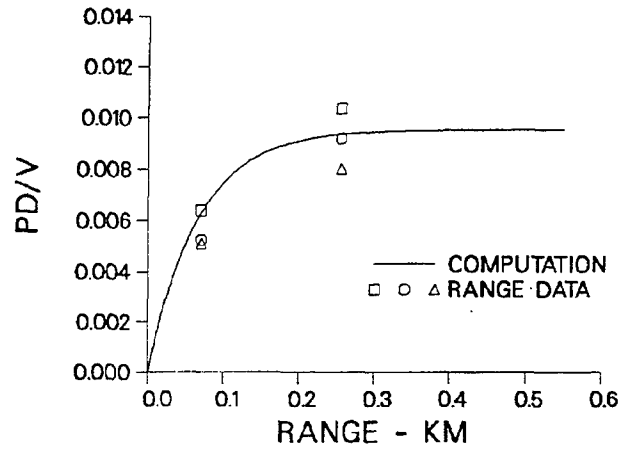


Figure 51. Comparison computed roll history with range data - Launch Mach number = 5.25, M829

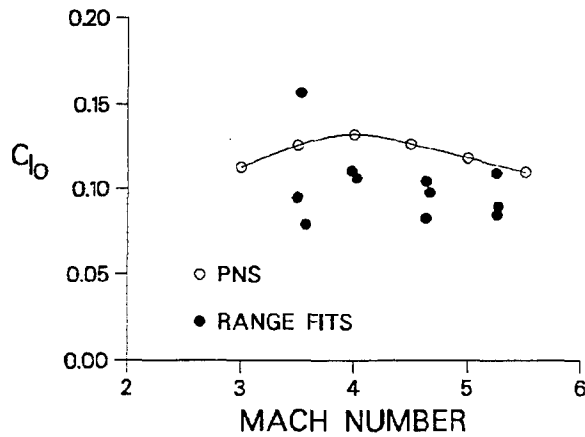


Figure 49. Comparison of computed Mach number variation of roll producing moment coefficient with range data, M829

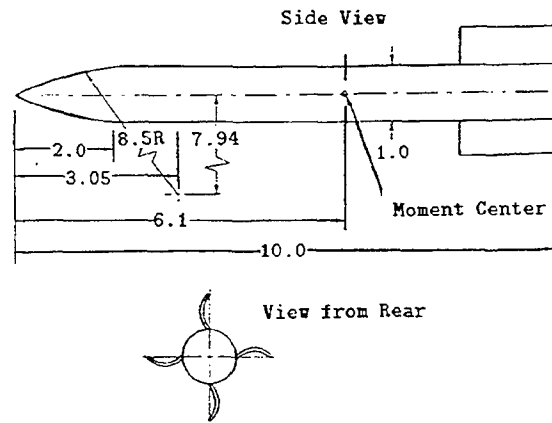


Figure 52. Schematic of wrap-around finned configuration, from Ref. [47]

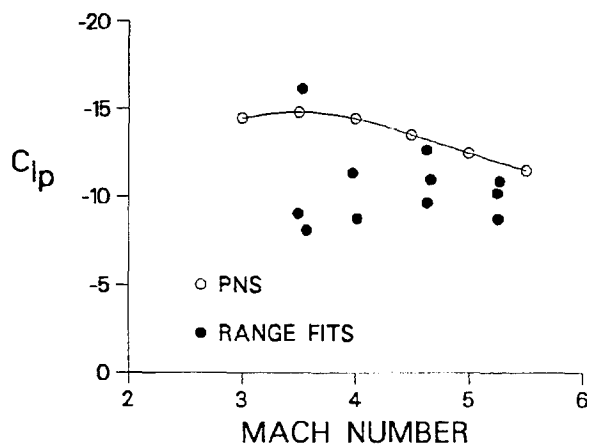


Figure 50. Comparison of computed Mach number variation of roll damping moment coefficient with range data, M829

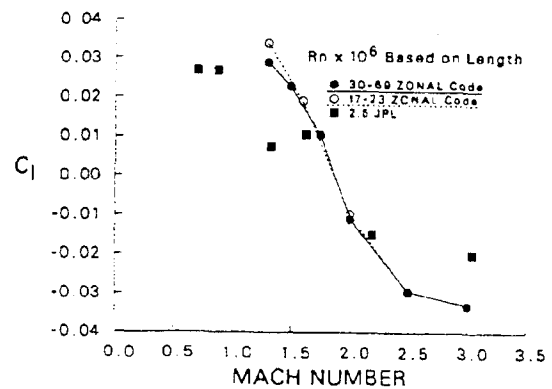


Figure 53. Variation of roll moment coefficient with Mach number for wrap-around fin configuration, from Ref. [47]

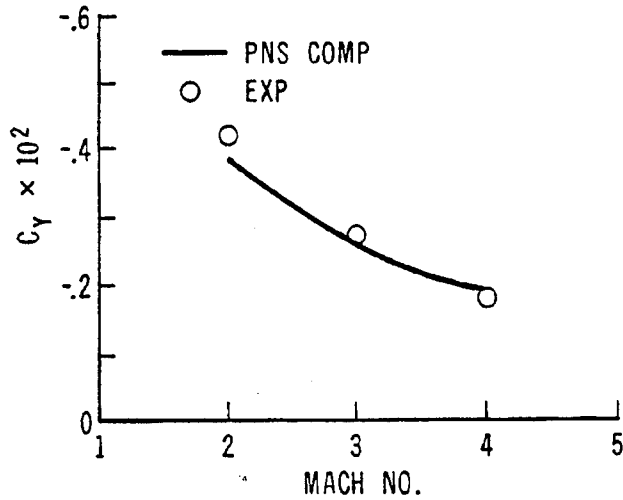


Figure 54. Magnus force coefficient versus Mach number, SOCBT, $\alpha = 2^\circ$, $p = 333RPS$, from Ref. [14]

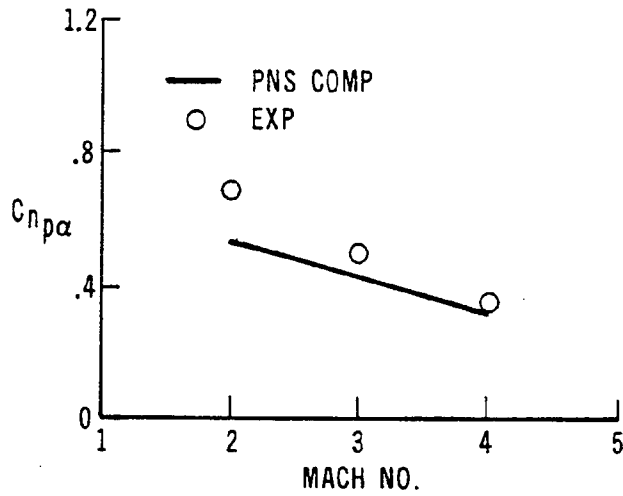


Figure 55. Magnus moment coefficient slope versus Mach number, SOCBT, from Ref. [14]

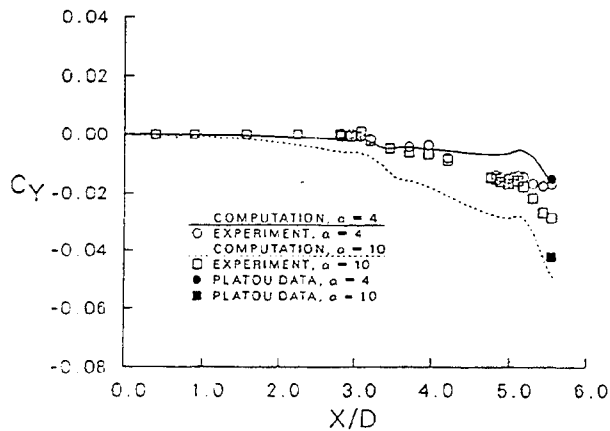


Figure 56. Distribution of Magnus force coefficient over SOCBT body with 0.5 caliber boattail, Mach=0.91

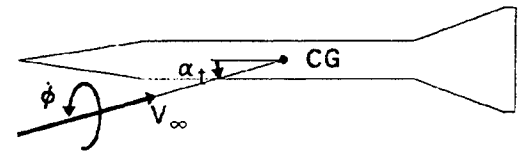


Figure 57. Schematic of coning motion

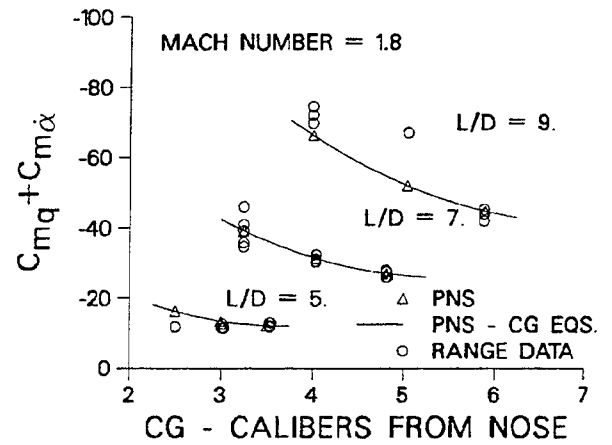


Figure 58. Pitch damping moment coefficient versus CG position, Mach 1.8, Army Navy spinner rocket

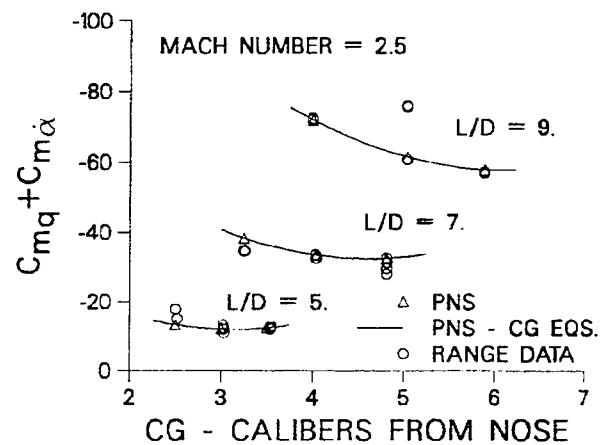


Figure 59. Pitch damping moment coefficient versus CG position, Mach 2.5, Army Navy spinner rocket

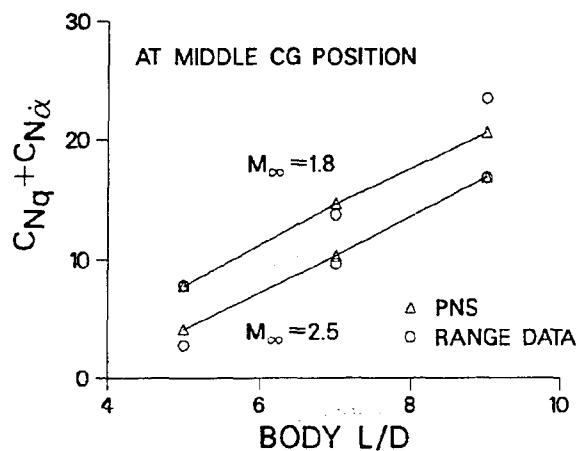


Figure 60. Pitch damping force coefficient versus body length, middle CG position, Army Navy spinner rocket

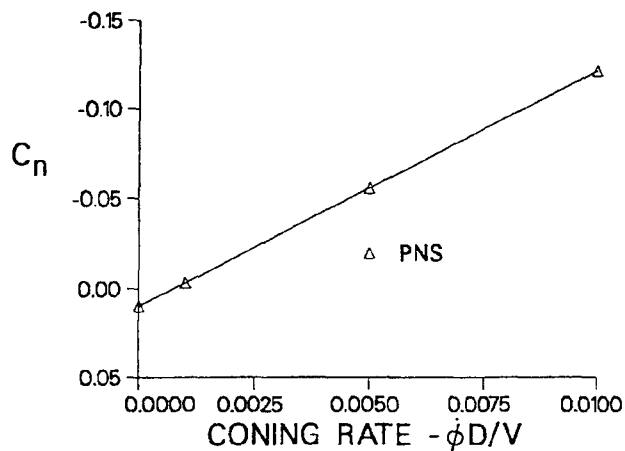


Figure 63. Variation of side moment coefficient with coning rate, M735, Mach 4, $\alpha = 2^\circ$

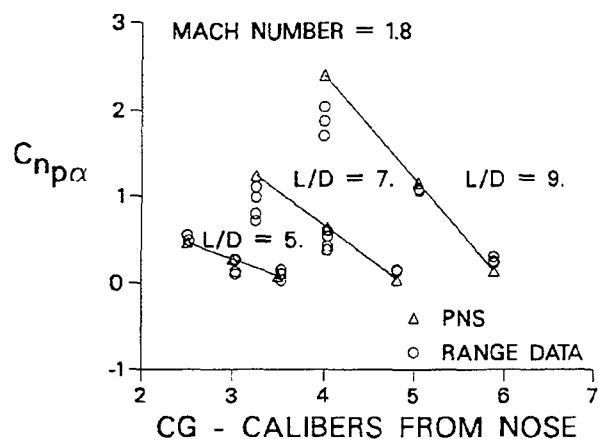


Figure 61. Magnus moment coefficient versus CG position, Mach 1.8, Army Navy spinner rocket

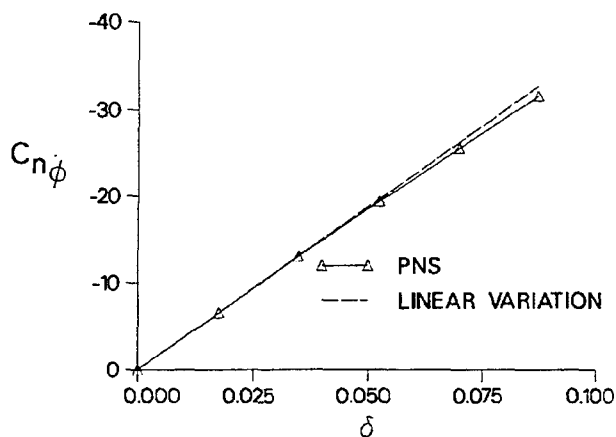


Figure 64. Variation of the slope of the side moment coefficient due to coning, $C_{n\dot{\phi}}$, as a function of the sine of the angle of attack, δ , M735, Mach 4

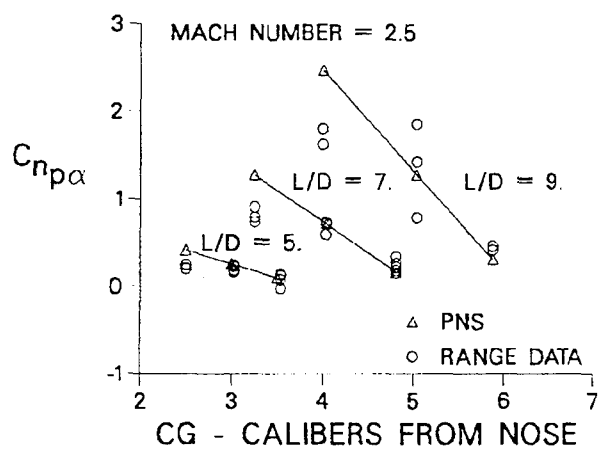


Figure 62. Magnus moment coefficient versus CG position, Mach 2.5, Army Navy spinner rocket

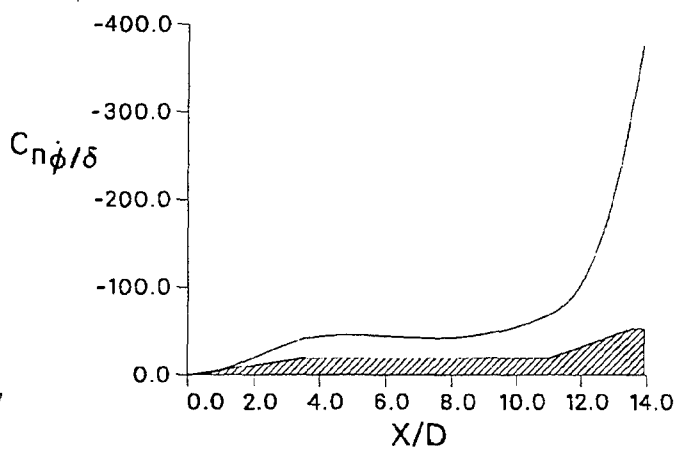


Figure 65. Development of normalized side moment slope due to coning, $\frac{C_{n\dot{\phi}}}{\delta}$, over M735 projectile, Mach 4

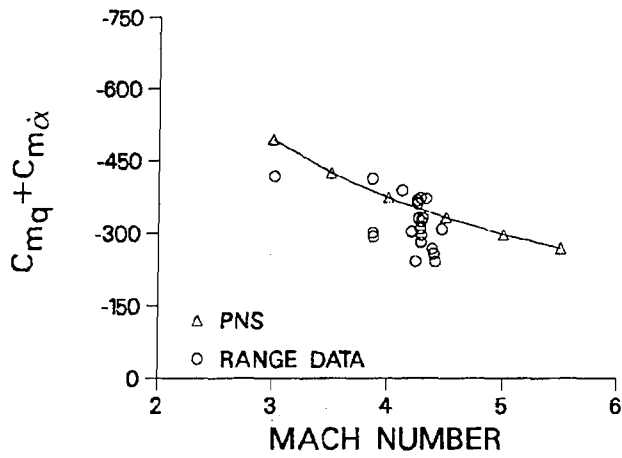


Figure 66. Mach number variation of computed normalized side moment slope due to coning compared with range measurement of pitch damping, M735

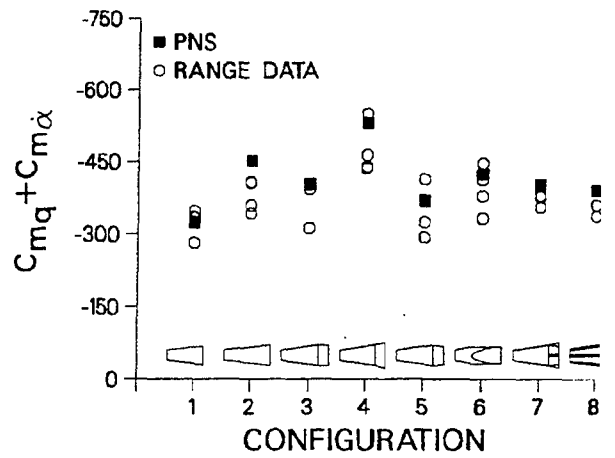


Figure 69. Pitch damping moment coefficient versus configuration, Mach 4

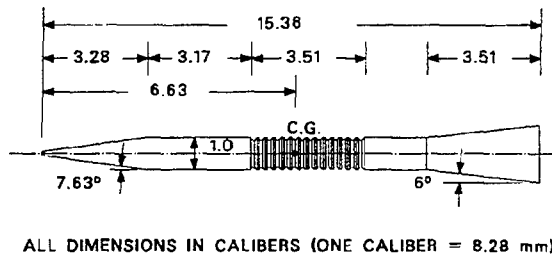


Figure 67. Schematic of baseline projectile configuration

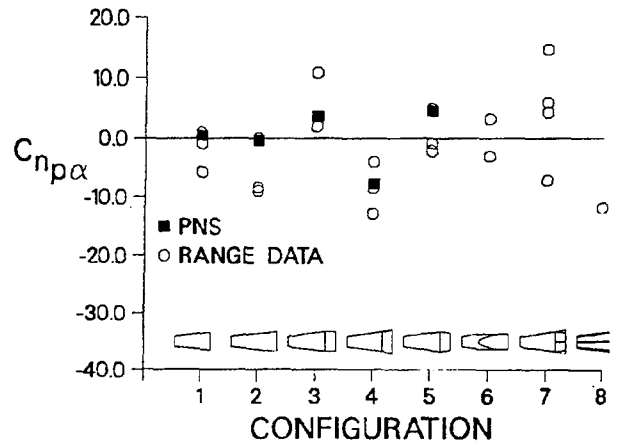


Figure 70. Magnus moment coefficient versus configuration, Mach 4

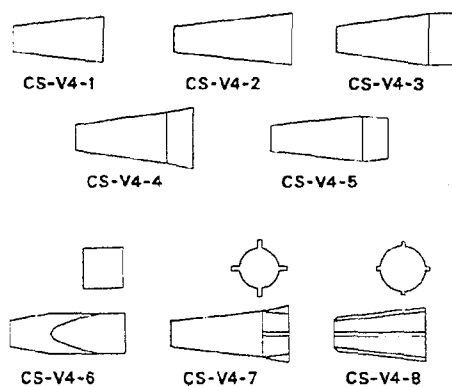


Figure 68. Schematic of projectile afterbodies

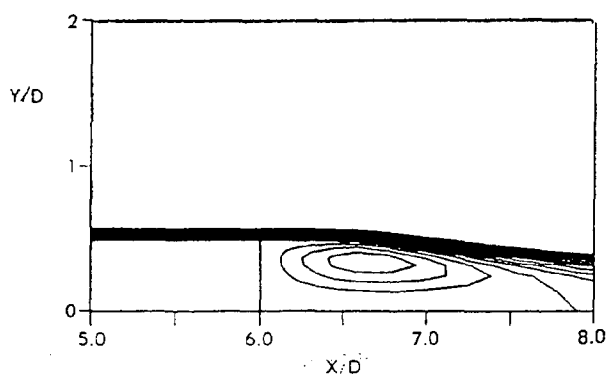


Figure 71. Stream function contour in base region of SOC, $M_\infty = 0.9$, $\alpha = 0$.

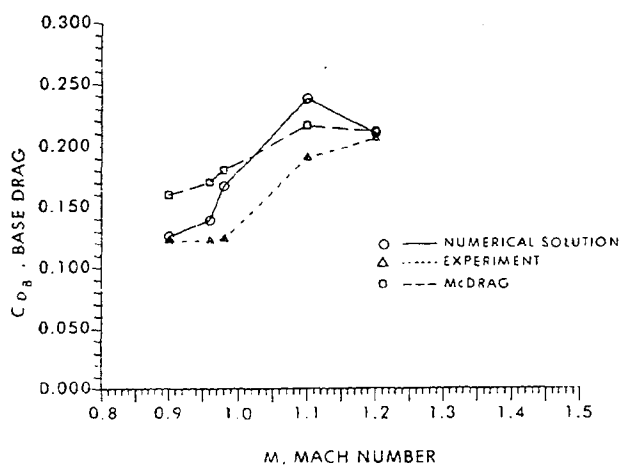


Figure 72. Base drag coefficient for SOC configuration, $\alpha = 0$.

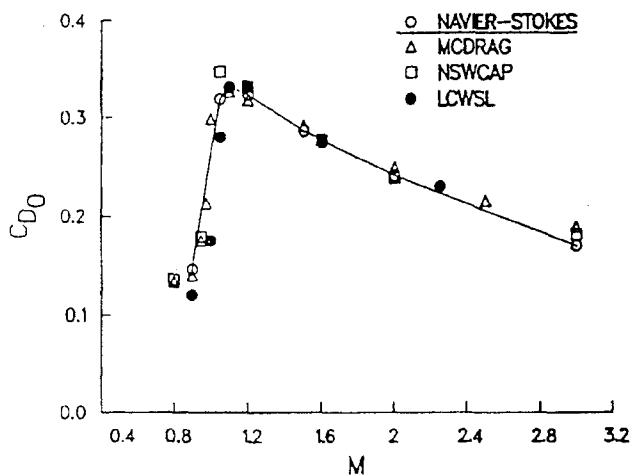


Figure 73. Zero yaw drag coefficient for M549 configuration, $\alpha = 0$.

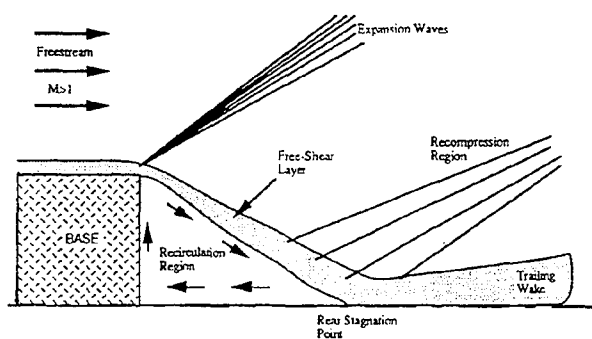


Figure 74. Schematic diagram of supersonic base flow

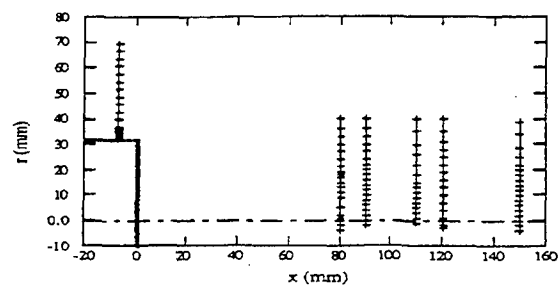


Figure 75. Afterbody measurement locations

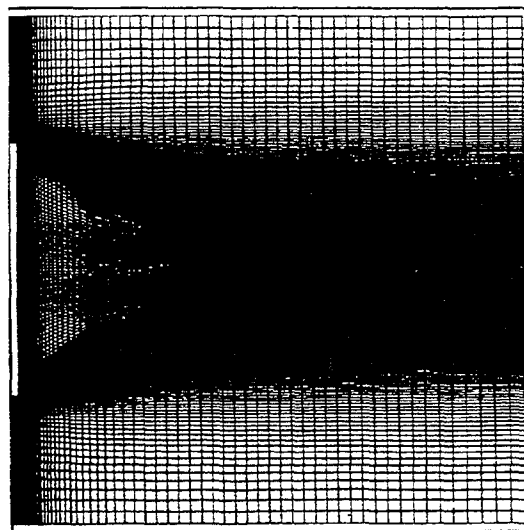


Figure 76. Base region computational grid

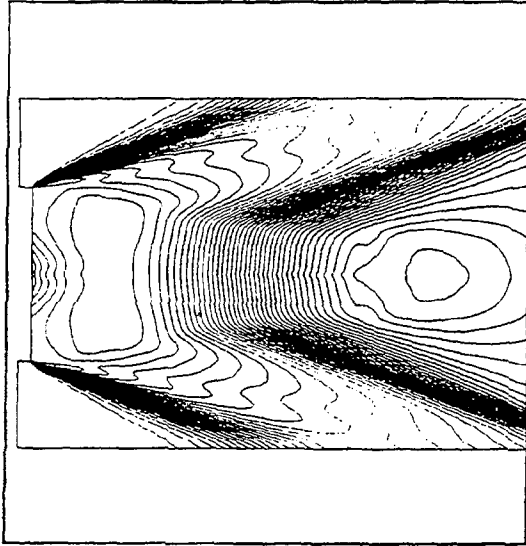


Figure 77. Computed pressure contours in the base region, $M_\infty = 2.46$, $\alpha = 0^\circ$, $k - \varepsilon$ model

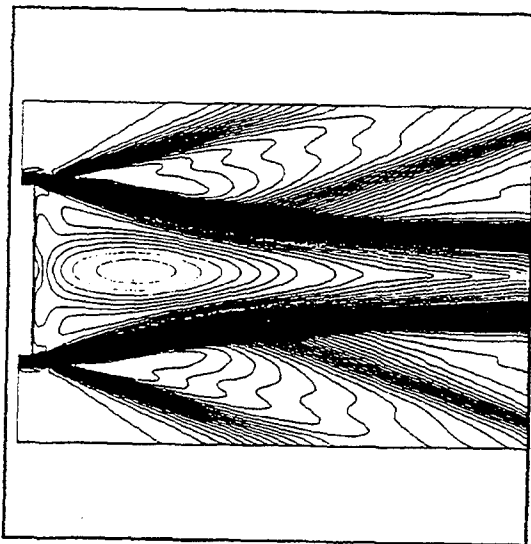


Figure 78. Computed Mach contours in the base region, $M_\infty = 2.46$, $\alpha = 0^\circ$, $k - \varepsilon$ model

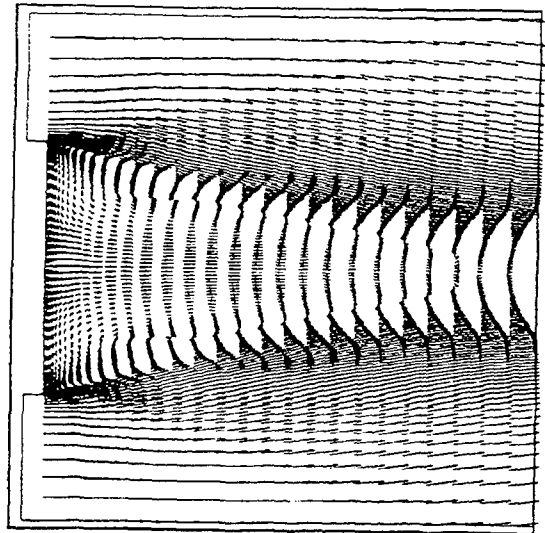


Figure 79. Computed velocity vectors in the base region, $M_\infty = 2.46$, $\alpha = 0^\circ$, $k - \varepsilon$ model

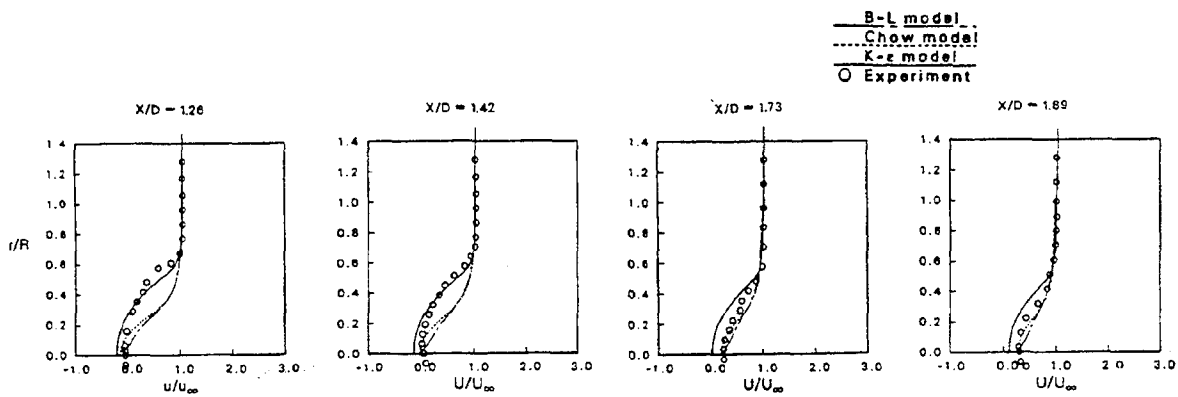


Figure 80. Streamwise velocity (u) profiles, $M_\infty = 2.46$, $\alpha = 0^\circ$

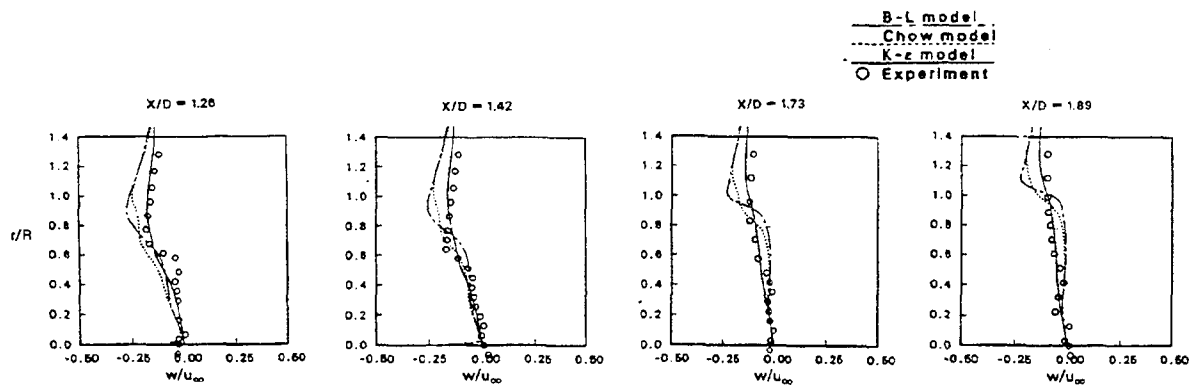


Figure 81. Normal Velocity (w) Profiles, $M_\infty = 2.46$, $\alpha = 0^\circ$

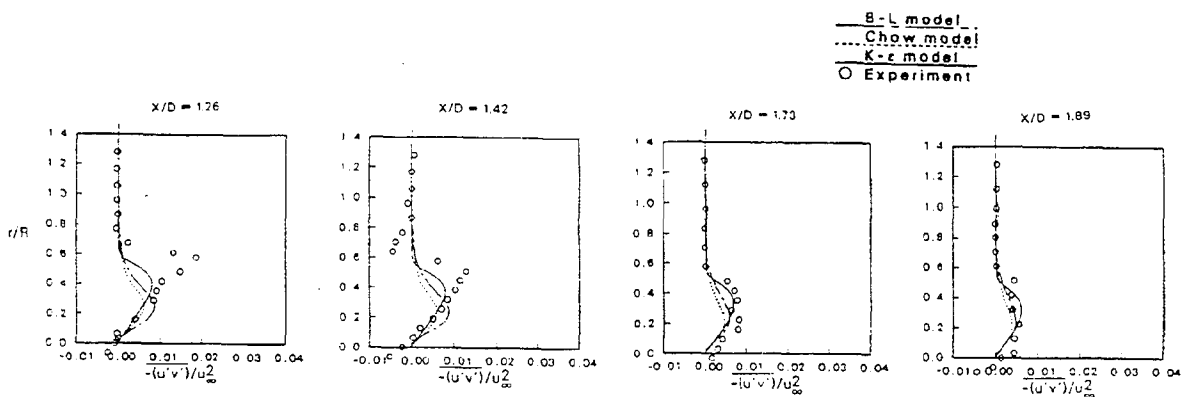


Figure 82. Turbulent Shear Stress Profiles, $M_\infty = 2.46$, $\alpha = 0^\circ$

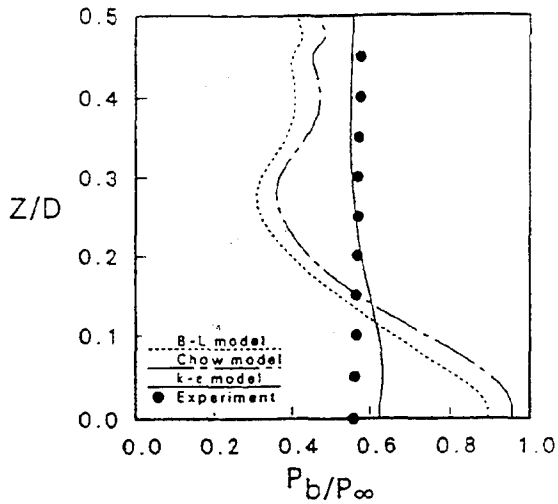


Figure 83. Base Pressure Distribution, $M_\infty = 2.46$, $\alpha = 0^\circ$

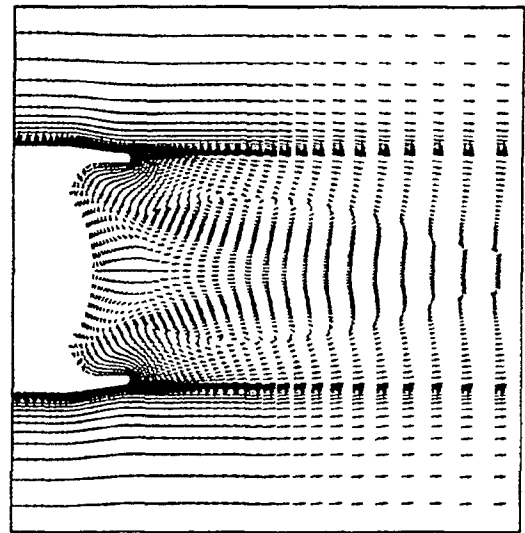


Figure 85. Velocity vectors in base region of M825 dome base, $M_\infty = 0.98$, $\alpha = 0^\circ$

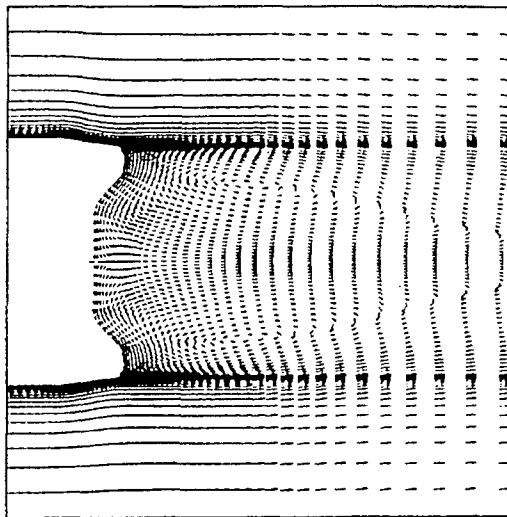


Figure 84. Velocity vectors in base region of M825 standard base, $M_\infty = 0.98$, $\alpha = 0^\circ$

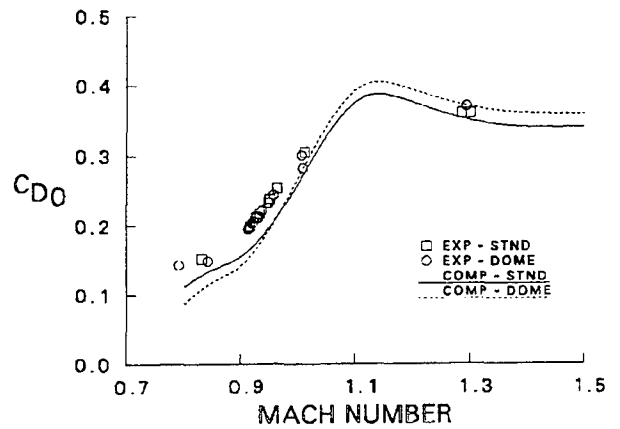


Figure 86. Predicted and experimental drag coefficient versus Mach number for M825 with standard and dome base

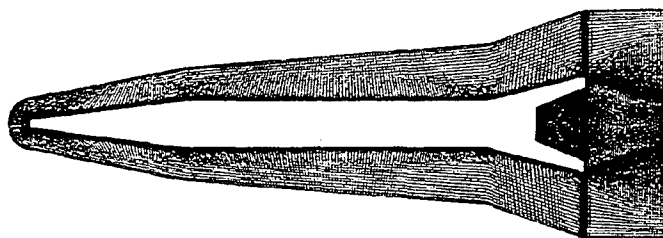


Figure 87. Grid for M865 configuration

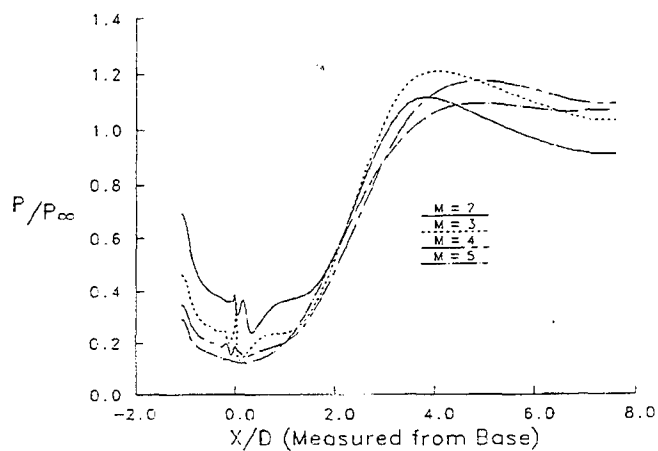


Figure 88. Predicted centerline pressure distribution in wake of M865

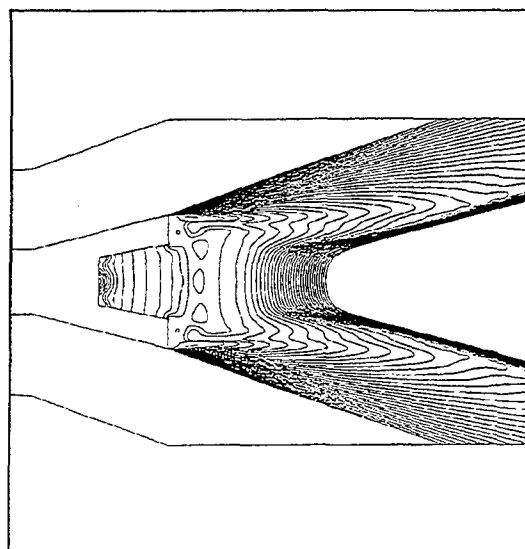


Figure 90. Pressure contours in base region of M865 with modified base, Mach 3

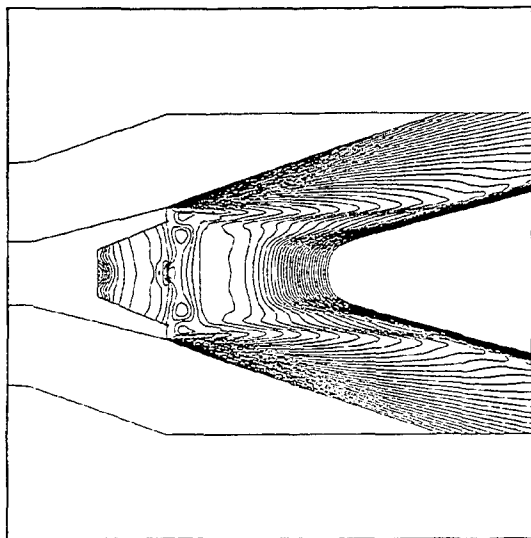


Figure 89. Pressure contours in base region of M865, Mach 3

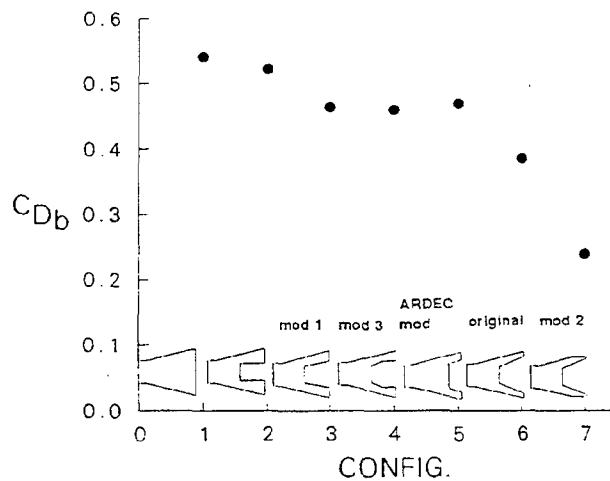


Figure 91. Computed drag coefficient for various base configurations for the M865, Mach 3

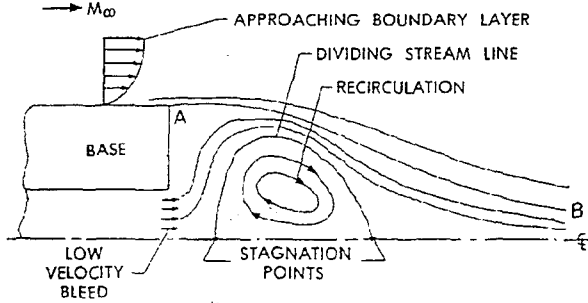


Figure 92. Schematic of illustration of base flow with base bleed

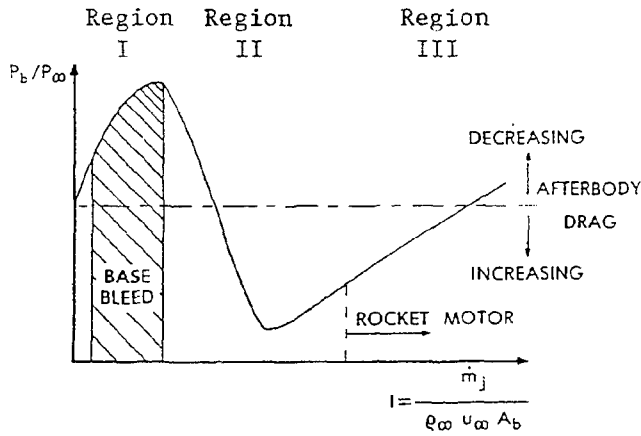


Figure 93. Base pressure versus mass flow rate of injection - base injection regimes

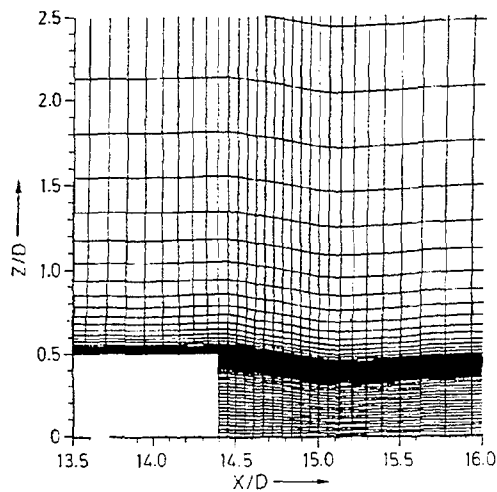


Figure 94. Computational grid in base region for base bleed case

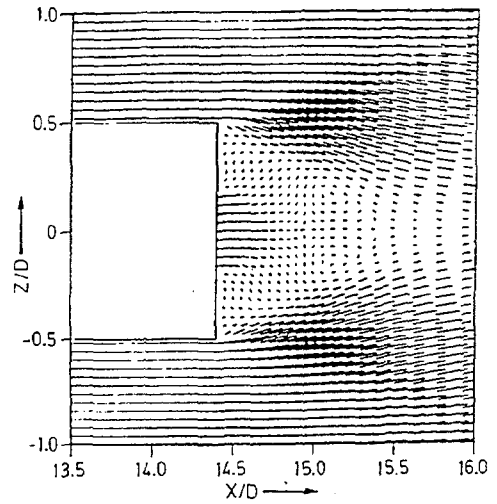


Figure 95. Velocity vectors in base region for base bleed, Regime I, $M_\infty = 2.5, \alpha = 0, I = 0.01$

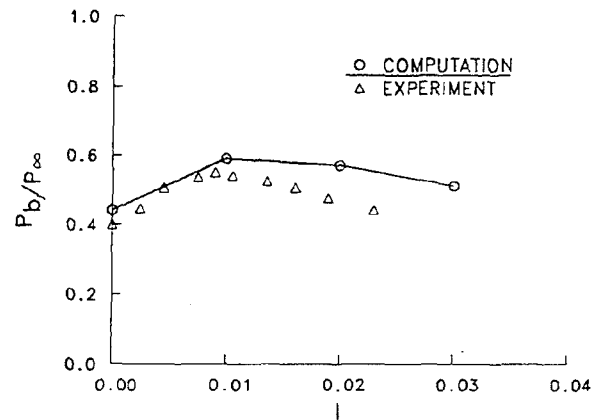


Figure 96. Base pressure versus base bleed injection parameter, Regimes I and II

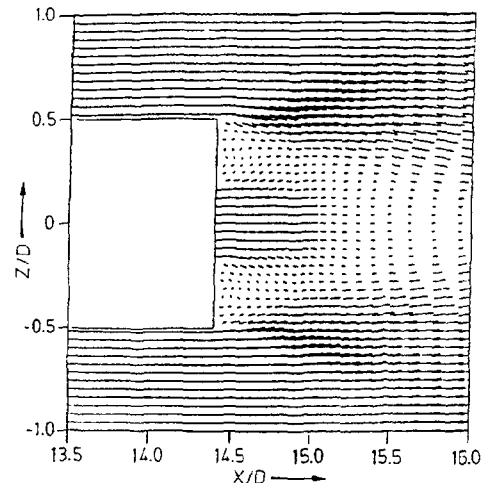


Figure 97. Velocity vectors in base region for base bleed, Regime II, $M_\infty = 2.5, \alpha = 0, I = 0.02$

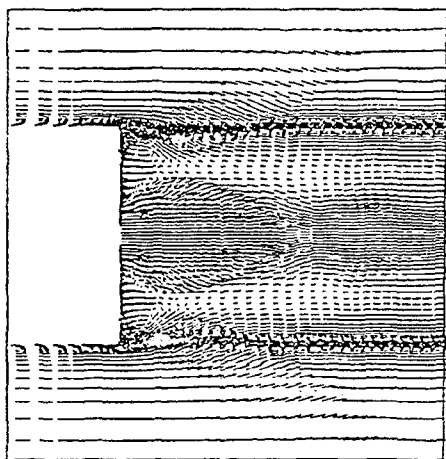


Figure 98. Velocity vectors in base region for base bleed, Regime III, $M_\infty = 3.0$, $\alpha = 0^\circ$

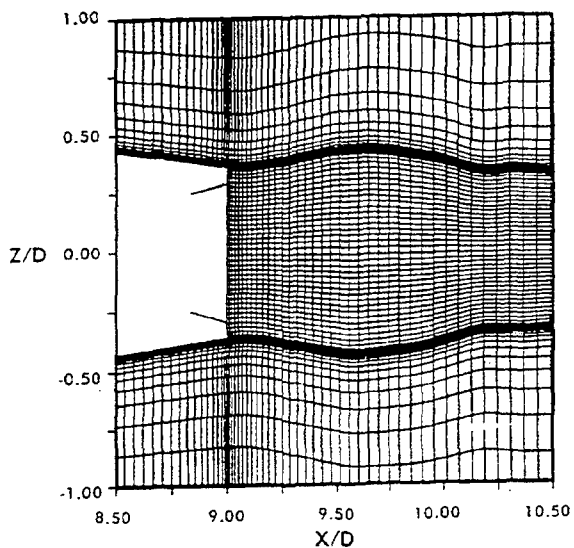


Figure 99. Computational grid in base region for jet case, $M_\infty = 2.0$, $M_j = 2.5$, $P_j/P_\infty = 3$

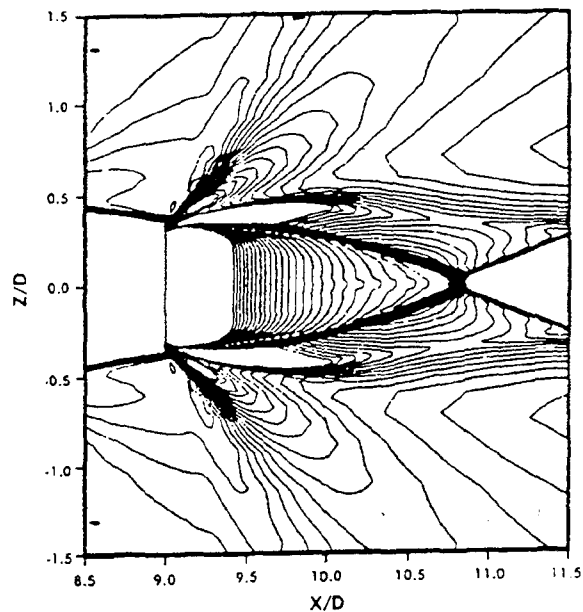


Figure 100. Pressure contours in base region for jet case, $M_\infty = 2.0$, $M_j = 2.5$, $P_j/P_\infty = 3$



Figure 101. Schlieren photograph of base region for jet case, $M_\infty = 2.0$, $M_j = 2.5$, $P_j/P_\infty = 3$

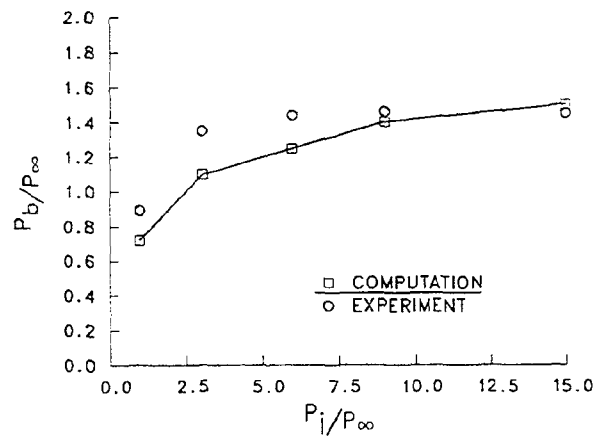


Figure 102. Average base pressure as a function of exit pressure

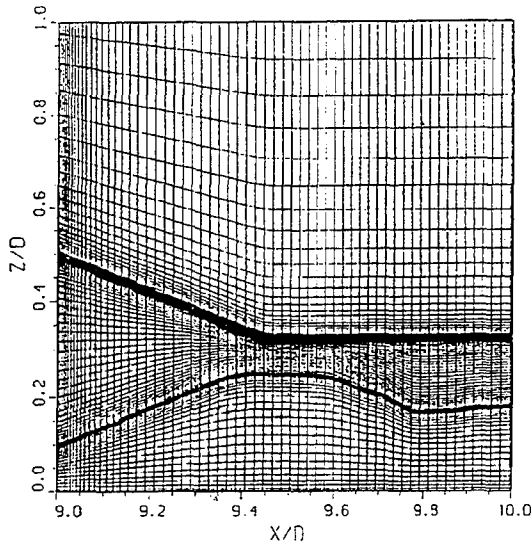


Figure 103. Computational grid for high pressure ratio jet case, $M_\infty = 1.4$, $M_j = 2.7$, $P_j/P_\infty = 50$

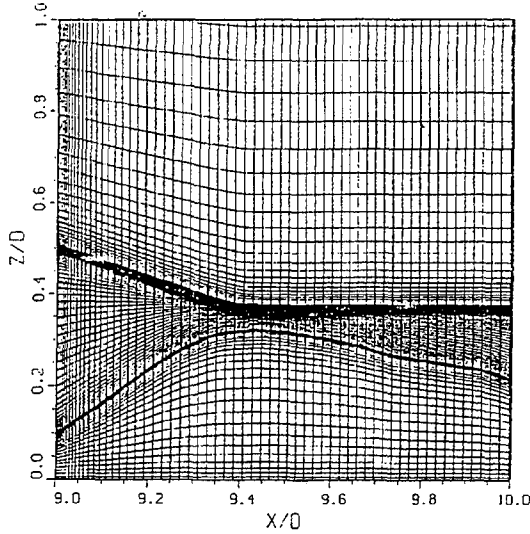


Figure 104. Computational grid for high pressure ratio jet case, $M_\infty = 1.4$, $M_j = 2.7$, $P_j/P_\infty = 150$

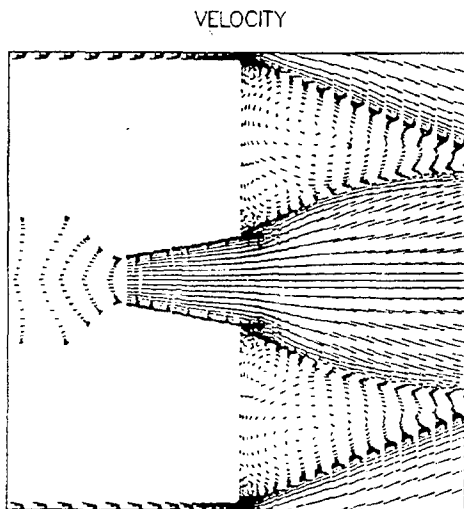


Figure 105. Velocity vectors for high pressure ratio jet case, $M_\infty = 1.4$, $M_j = 2.7$, $P_j/P_\infty = 50$

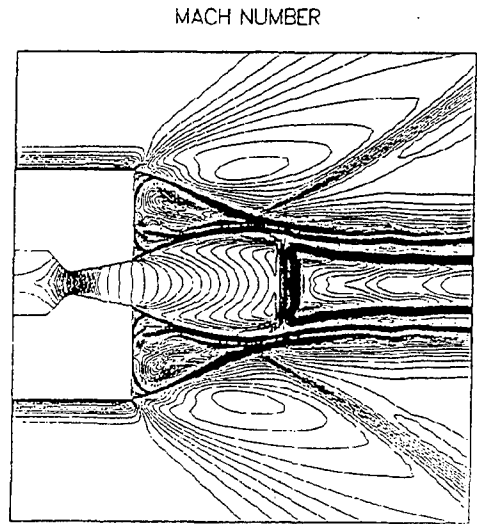


Figure 106. Mach contours for high pressure ratio jet case, $M_\infty = 1.4$, $M_j = 2.7$, $P_j/P_\infty = 50$

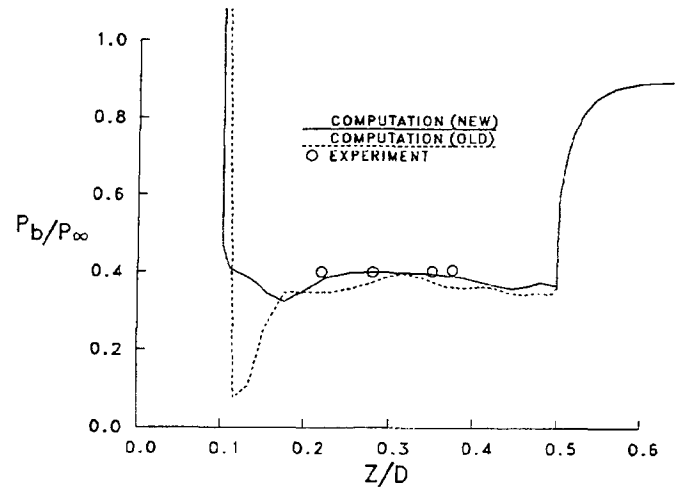


Figure 107. Pressure on base in presence of high pressure ratio jet, $M_\infty = 1.4$, $M_j = 2.7$, $P_j/P_\infty = 50$

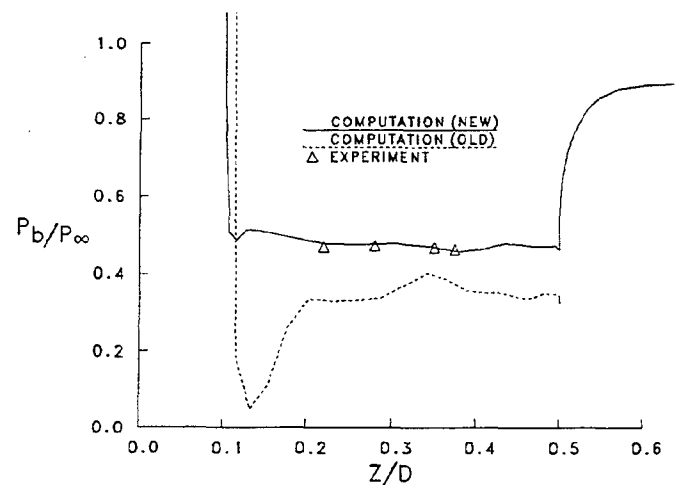


Figure 108. Pressure on base in presence of high pressure ratio jet, $M_\infty = 1.4$, $M_j = 2.7$, $P_j/P_\infty = 150$

COMPUTATION OF SUPERSONIC AIR-INTAKES

R.G. LACAU, P. GARNERO, F. GAIBLE
AEROSPATIALE MISSILES
91370 Verrières-Le-Buisson - FRANCE

1. INTRODUCTION

Air-breathing missiles are equipped with turbojet or ramjet engines which can only operate in the atmosphere.

The turbojet is well suited to subsonic missiles (APACHE, HARPOON, ...) and the ramjet, which is a simple engine, is well suited to supersonic missiles (ASMP, ANS, ...). With subsonic combustion ramjet engines, the possible flight Mach numbers range from about 2.0 to about 6.0. Above 6.0, a supersonic combustion is more advantageous and, below 2.0, additional propulsion means may be necessary to accelerate the missile (boost rocket).

Contrary to rocket propulsion for which propellant contains oxidizer, the air-breathing engine use the air atmosphere to burn the fuel. It follows that intakes are necessary to capture external flow.

The primary function of air-intakes is to decelerate air to subsonic combustion chamber, with the highest possible total pressure recovery and the required engine mass flow. Another function is to provide sufficiently uniform flow into the compressor or combustor for a good combustion process.

The achievement of these requirements is a very difficult task, more especially as the air-intakes are installed on a fuselage and therefore in a non-uniform flowfield.

In the past, air-intake studies were mainly based on long and expensive wind tunnel tests. The exclusive use of experimental facilities is no longer sufficient in terms of time and cost to define and optimize new configurations. So, thanks to computer hardware and numerical methods progress, the methodology has been adapted by using Computational Fluid Dynamics (CFD) tools (see figure 1.).

The aim of this paper is to present how some CFD tools can be used to compute external and internal flowfields involved in the design of supersonic air-intakes. These tools help the designer to better understand flow phenomena, to determine

favorable intake location and to predict air-intake performances such as pressure recovery and mass flow ratio.

As supersonic intakes are mainly used on ramjet missiles, we limit this paper to ramjet air-intakes.

After a brief overview of the existing types of air-intakes, we describe the way their performances are quantified. Then we present the CFD tools used to evaluate air-intake characteristics. Finally selected applications of these tools demonstrate how a comprehensive study of air-intake may be achieved through CFD. Both external and internal flowfield computations are presented, which allows to predict air-intake performances.

2. RAMJET MISSILE AND AIR-INTAKE CONFIGURATIONS [1 - 5]

We can distinguish three generations of ramjet missiles.

In the first one, the ramjet engine is positioned within a nacelle outside the missile dart. The intakes are axisymmetric and have good performances (low interference with fuselage flow field) but the missile is heavy and bulky and its drag is high. Such missiles were developed in the 1950's: BOMARC (USA), BLOODHOUND (GB), SIRIUS CT41 (France).

In the second generation, the engine is integrated in the dart, with the intake placed in the nose and with a jettisonable rocket booster located at the base. This configuration has several advantages as compactness and good intake performance, but has also some drawbacks as loss of volume for the payload and homing device, and excessive length. The main missiles developed are: TALOS (USA), SEA DART (GB), VEGA (France), STATALTEX (France).

In the third generation, which represents today's integration method, the air-intakes are placed on the sides of the fuselage and the rocket booster is integrated in the ramjet combustion chamber. This configuration avoid any loss of volume and therefore is optimum. Examples of such missiles

are: ASMP (France) equipped with two rectangular intakes, ANS (France-Germany) equipped with four axisymmetric intakes.

The number, shape and position of air-intakes are various and their choice depend on performance requirements: internal performance (thrust), external aerodynamics (drag, lift to drag ratio), operational constraints and control (skid to turn or bank to turn). We distinguish (figure 2) :

- single intake: nose, annular, chin, ventral or top mounted,
- two, three or four lateral intakes.

The shape may be (figure 3) : axisymmetric (full, half or quarter) or rectangular (conventional, inverted or lateral), and the longitudinal location is a compromise between: the flowfield around the fuselage, the diffuser length, the aerodynamic stability of the missile and the attachment points on the fuselage.

To compress the flow, multiwedge ramps are used. They may be completely external or mixed external-internal. For Mach numbers over about 3.0, mixed external-internal supersonic compression is a good process. It allows to limit the turning of the external flow ahead the cowl lip and so avoids steep cowl angle and therefore high cowl wave drag.

In order to improve supersonic air-intake efficiency we generally use external boundary layer bleed in order to evacuate as much forebody boundary layer as possible with moderate increase of external drag.

We also use internal boundary layer bleed which takes place at intake throat and catches some percentages of intake mass flow. This bleed has two main functions :

- improve air-intake efficiency by decreasing viscous losses i.e. boundary layer height at engine entry,
- stabilize and uniformize the flow at engine entry by reducing normal shock-boundary layer interaction at critical point.

It allows higher critical efficiency by delaying subcritical running.

Axisymmetric intakes have maximum performances at zero incidence with medium incidence sensitivity. Rectangular intakes have favourable incidence effects, but are highly sensitive to sideslip angle.

In the future, ramjet missile configurations will have non-circular cross sections for an optimum integration of the air-intakes in the fuselage flowfield, a low drag, a high lift to drag ratio, a

small radar cross-section and a good integration on carrier aircraft (figure 4).

3. DEFINITION OF THE MAIN INTAKE PERFORMANCE PARAMETERS [3, 18]

When we design an air-intake we need criteria in order to select the best geometry. These criteria are based on propulsion performances and on structural feasibility.

The best solution will provide the engine with the highest available energy at required engine Mach number and mass flow for the smallest size and weight.

In order to compare mass flows entering the engine, it is convenient to non-dimensionalise them by referring them to the mass flow that would pass through a characteristic area if it was placed in the freestream at flight conditions. For convenience, the air-intake entry area A_{int} is normally selected as the characteristic area (see figure 5 for a 2D representation):

$$\epsilon_{engine} = \dot{m}_{engine} / \dot{m}_{0 \text{ int}}$$

ϵ_{engine} = engine mass flow ratio

\dot{m}_{engine} = air mass flow at engine entry

$\dot{m}_{0 \text{ int}}$ = air mass flow through characteristic area at freestream conditions

$$\epsilon_{engine} = A_{0 \text{ engine}} / A_{int}$$

The mass flow ratio associated with boundary layer bleed may be defined in a similar manner :

$$\epsilon_{bleed} = \dot{m}_{bleed} / \dot{m}_{0 \text{ int}} = A_{0 \text{ bleed}} / A_{int}$$

The total intake capture mass flow ratio will be the sum of the engine and bleed mass flow ratios:

$$A_{0 \text{ total}} = A_{0 \text{ engine}} + A_{0 \text{ bleed}}$$

$$\epsilon_{total} = \epsilon_{engine} + \epsilon_{bleed}$$

Another important characteristic for an air-intake is its performance. This performance defines the characteristics of the flow at the end of the diffuser. The interesting features of this flow are: total pressure, kinetic energy, thermodynamic state, ... To measure performance or efficiency in the case of supersonic air-intakes, we commonly use total pressure recovery η_{02} (0 is in the freestream and 2 is at the engine face, see figure 5):

$$\eta_{02} = P_{T2} / P_{T0}$$

P_{T2} = mean total pressure at engine entry

P_{T0} = freestream total pressure

Thus, total pressure recovery is a measure of the available pressure energy at engine entry, compared with that existing in the flow at freestream conditions.

The internal performance of an air-intake may be described at each flight condition (Mach number, incidence and sideslip angles) by a single curve, the intake characteristic curve.

The common forms for intake characteristic curve are :

$$\eta_{02} = f(\epsilon_{\text{engine}}) \text{ or } \eta_{02} = f(\epsilon_{\text{total}})$$

A set of such curves are necessary to define air-intake performance over the flight envelope, taking into account, for example, the variation of flight Mach number and incidence.

The point at which the air intake operates on the characteristic curve is governed by conditions at downstream end of the intake duct, that is, by the engine airflow demand. This is known as the matched operating point.

On the characteristic curve, we can distinguish different air-intake runnings:

- Supercritical running

The normal shock which separates supersonic from subsonic flows in the duct, is downstream the cowl lip for external supersonic compression intake or downstream the throat (smallest internal section) for mixed supersonic compression air-intake.

- Critical running

The normal shock is located at the cowl lip for external compression intake or at the throat for mixed compression intake.

- Subcritical running

The normal shock is upstream the cowl lip for external compression intake or upstream the throat for mixed compression intake (in fact for this latter configuration we cannot have a steady normal shock between the throat and the cowl lip, so the steady location of the shock is also upstream the cowl lip).

Depending on the air intake type, we can use four types of characteristic curves:

- figure 6 presents the two common forms of a typical characteristic curve for an external supersonic compression intake with internal boundary layer bleed,
- figure 7 presents the two common forms of a typical characteristic curve for an mixed

supersonic compression intake with internal boundary layer bleed.

In addition to these performance data we need :

- internal pressure and heat fluxes distribution in order to verify structural feasibility and to estimate air-intake size and weight,
- flow profile at intake exit in order to verify air-intake/ engine compatibility.

Both external and internal flow fields predictions are required so as to obtain all these characteristics.

4. COMPUTATIONAL METHODS

Two types of computational methods are available : semi-empirical methods and numerical methods.

Semi-empirical methods are the simplest and the fastest methods to predict two-dimensional air-intake performances. They are based on shock wave theory for compression calculation and experimental results for internal loss calculation. They predict the intake efficiency and the mass flow ratio entering the combustor. Despite their limited accuracy, they are well suited to parametric studies.

Numerical methods are essential to determine favorable intake position and the mass flow captured by the intake, to predict the characteristic curve of the intake for all the possible operating conditions, from the supercritical to the subcritical one, and to provide with important insights into the understanding of complex flow mechanisms for the design studies.

The methods range from the Euler equations to the various forms of the Navier-Stokes equations.

The Euler equations represent the most complete set of equations modelling the evolution of a non-viscous and non-conducting fluid. They admit weak solutions with jumps, among which physical discontinuities are modelled such as shock waves.

In order to compute steady flows with Euler equations two main ways are used :

- solve the steady equations in case of supersonic flows. These equations are hyperbolic in space and a space-marching technique can be used.

- solve the unsteady equations. All flow variables are advanced in time until an asymptotic limit is reached. This procedure is valid for any speed range and is well suited to compressible internal flow calculation. But if the flow is supersonic as, for example, on the forebody, a pseudo-unsteady marching procedure can be used.

The boundary-layer equations are the simplest equations which include viscous effects. They are used to determine boundary layer thickness, transition location, separation lines. Boundary layer methods are inexpensive to use and therefore often part of a methodology loosely coupling Euler and boundary layer approaches. But this technique applies only to flow situations where the interaction between the viscous layer near the wall and the inviscid core region is weak. Now, if viscous effects become preponderant (flow separation around the forebody or in the duct, shock-boundary layer interaction, ...), we must use Navier-Stokes methods.

The unsteady Navier-Stokes equations should be capable of describing any flowfield over a forebody and in an air-intake. Predicted quantities include flow separation, vortical flow, turbulence, ... which are of prime importance.

Due to present computer limitations and incomplete understanding of the physics of turbulence, simplifications must be made to the full Navier-Stokes equations.

A first approximation is to resort to time-average rapidly fluctuating components. This yields to the Reynolds-Averaged Navier-Stokes equations (RANS) which require a turbulence model to provide closure for the solution. These equations should be used for the most complex industrial flows including large scale separations.

A second step of approximation is to neglect the viscous terms in the streamwise direction. This yields to the Thin-Layer Navier-Stokes equations (TLNS).

Finally, if in addition we neglect unsteady terms we obtain the Parabolized Navier-Stokes equations (PNS). These equations only apply to supersonic flows.

To demonstrate the ability of these predictive methods, we present in the following sections some practical examples. The computation codes used are :

- Semi-empirical code : OCEAS

This code, developed by AEROSPATIALE, predicts supersonic and hypersonic two-dimensional intake performances.

The main characteristics taken into account are:

- total pressure and Mach number losses due to oblique and normal shocks,
- the internal losses due to viscous effects,
- the boundary layers displacement effects.

As the flow is supposed to be two-dimensional and planar, the amount of flow spilled sideways is not taken into account. However, an estimate of these losses may be found in ref. 6 and 7.

OCEAS computes analytically, step by step, shock waves, expansion waves, slip lines and their interactions.

For supersonic intakes, the pressure recovery is computed for different normal shock wave positions in the intake. The highest value corresponds to a normal shock wave located at the cowl lip or at the smallest internal section (see §3).

Internal losses at the critical point (diffuser losses, ...) are determined by an empirical function F developed by ONERA from the compilation of many experimental results in the Mach number range 2 to 3.5 :

$$F = 1 / \cosh((Mach - 1)/3).$$

Above Mach number 3.5, pressure recovery may be much underestimated.

Total mass flow ratio ϵ_{total} , can be easily computed after the shock waves and the streamline which meets the cowl lip have been determined.

In supercritical regime, bleed mass flow ϵ_{bleed} is calculated as a function of the total pressure in the bleed and the sonic throat section of the bleed. The engine mass flow is then deduced according to:

$$\epsilon_{engine} = \epsilon_{total} - \epsilon_{bleed}$$

Boundary layer effects can be taken into account by wall displacements. The development of the boundary layer along the walls is obtained using semi-empirical formulas [8, 9]. It can be laminar or turbulent with a transition criteria. However these corrections are small and can be neglected for a preliminary design.

To visualize interactively the flowfields and the desired informations about the intake (average values, ...), a graphical environment has been developed. With this graphical environment, we can modify interactively the geometry and so

design and optimize geometries very rapidly (figure 8).

- Euler and Navier-Stokes code FLU3M [10.11]

For 3D external and internal transonic/supersonic flows, FLU3M code developed by ONERA in collaboration with AEROSPATIALE is used. It is a multi-block explicit or implicit Euler and Navier-Stokes solver. It is based on upwind schemes (Van Leer, Osher, Roe). Second order accuracy in space is obtained via MUSCL technique. For supersonic flows, a space-marching technique is available.

- Boundary layer code: 3C3D [12]

3C3D, developed by ONERA/CERT, solves the 3D boundary layer equations in direct mode. Equations are integrated along streamlines, in a space-marching method, taking into account characteristic surfaces, influence and dependence domains. The code includes semi-empirical transition criteria and turbulence models.

- Pseudo-PNS and PNS codes: FLU3PNS [13] and TORPEDO [14]

FLU3PNS, developed by AEROSPATIALE Space and Defence, is a 3D TLNS code with a space-marching strategy allowing pseudo-PNS computations. The TLNS equations are considered as unsteady equations and the space marching results of a time marching approach in each plane. Viscous fluxes are neglected in the marching direction. Baldwin-Lomax turbulence model is implemented with Degani-Schiff modification for vortical flows.

TORPEDO code, developed in collaboration between AEROSPATIALE Missiles, ENSAE and ONERA/CERT solves steady 3D PNS equations by means of a non iterative implicit Roe-Osher-Chakravarthy scheme. Upwinding is maintained in the subsonic layer.

- Navier-Stokes code : NS2D [15]

NS2D, developed by ONERA, is a 2D multi-block Reynolds-Averaged Navier-Stokes solver. It is based on a time explicit scheme, centered in space. The Baldwin-Lomax and MICHEL turbulence models are included for analyzing turbulent flows.

5. FUSELAGE FLOWFIELD COMPUTATION

Study of this flow is necessary to determine favorable intake position and the mass flow caught by the intake.

To achieve high intake performances, it is necessary to search low velocity fields and to avoid low energy fields (boundary layer and vortices) (figure 9).

So, local total pressure, Mach number, angle of attack, side slip angle, boundary layer height and vortex separation position have to be determined in several transverse planes. These computations will permit to determine favorable intake position, optimized geometry of the forebody and of the intake, position of the external boundary layer bleed and the mass flow caught by the intake.

The tools used for forebody studies include:

- Euler codes which are well suited to determine velocity fields,
- boundary layer codes giving information about the boundary layer thickness at the intake entrance section,
- Navier-Stokes codes for a better evaluation of the viscous effects around the forebody, taking into account flow separations which may appear for flights with manoeuvres.

At low incidence, boundary layer can be analysed relatively easily with the boundary layer code 3C3D. Figure 10 shows a typical turbulent boundary layer thickness computation on a fuselage. With incidence, the boundary layer on the leeward side becomes thicker and, under the positive pressure gradient effect, separates from the fuselage. This situation is much more difficult to predict. In the following we present different numerical applications concerning a 3 caliber tangent ogive cylinder experiment on which flow field and surface pressure measurements as well as skin friction patterns are available [16]. In this experiment, free stream angle of attack is 10° , temperature 183°K , Mach number 2, and Reynolds number, based on body diameter, 0.16×10^6 . In the computations, wall temperature is fixed at 307°K , which approximately corresponds to adiabatic wall conditions.

a) Laminar computation :

- Space-marching TLNS calculation with FLU3PNS

This computation begins with an explicit stepback procedure using local time step. Space-marching computations are then realized with an implicit algorithm and a global time step. CFL number varies from 40 to 100. The mesh has 86 points in the longitudinal direction, 80 in the radial direction and 40 in the circumferential direction. The grid in each transverse plane, issued from a 2D elliptic grid code, is clustered near the wall. Size of the first cell has been chosen to allow laminar and turbulent computations.

- PNS calculation with TORPEDO

This calculation is initialized by a stepback procedure. Fully upwind algorithm is used with

Van Leer limiter. In this case, the mesh has 4500 points in the longitudinal direction, 62 points in the radial direction and 31 in the circumferential direction.

- Unsteady Navier-Stokes calculation with FLU3M

RANS equations are solved on the same mesh as pseudo-PNS. Roe fluxes (explicit part) with Van Leer implicitation in the two transverse directions are used. Computations are made with a local time step and a CFL number of 5.

Figure 11 presents the computed Mach numbers evolution in several transverse planes (FLU3M calculation).

Figures 12 and 13 show total pressure and Mach number distributions in transverse plane located at $X/D=7$ (corresponding to a typical intake position on a fuselage). There is a good agreement between iterative solutions of FLU3M or FLU3PNS and experiments, but TORPEDO underestimates values of Mach number and total pressure.

b) Turbulent computation

A fully turbulent computation is realized with FLU3PNS, using Baldwin-Lomax turbulence model and Degani-Schiff modification, on the same mesh. The laminar step-back results are used to initialize the space-marching computation. CFL is fixed to 200. Results are compared with experiments made in the same conditions as the laminar ones, except the fact that transition is triggered at $X/D=1$.

Figures 14 and 15 present total pressure and Mach number distributions in the same transverse plane ($X/D=7$). The agreement between experiment and computation is excellent.

6. INTAKE FLOWFIELD COMPUTATION AND PERFORMANCE PREDICTION

Due to the complexity of intake geometries and flowfields, computations are usually splitted into two phases.

In the first one, intakes are computed alone, with an uniform upstream flowfield corresponding to the averaged flowfield entering the intake. This method is well suited for the design phase. But this simplified method is unperfect, and in a second phase it becomes necessary to take into account the real non uniform flowfield entering the air intake.

6.1. Intake with an uniform external flowfield

After the fuselage flow field has been computed, it is possible to calculate average values in the intake capture area (usually we consider a transverse plane located at the apex of the first compression ramp), for Mach number, total pressure, incidence and sideslip angles. Then, the intake can be considered located in this uniform flowfield as an isolated intake.

In this phase, the intake is considered 2D or axisymmetric.

The computation tools used are based on semi-empirical, Euler and Navier-Stokes methods.

To demonstrate the capabilities of these tools we will consider the two-dimensional intake presented in figure 16. This intake has two compression ramps and an internal boundary bleed, the freestream Mach number is 2.89.

- Semi-empirical calculation with OCEAS

Figure 17 presents the predicted characteristic curve. The comparison between experiment and computational results shows a quite good agreement. However, the efficiency at the critical point is underestimated. But, if we don't take into account the internal losses through the empirical function F (see §3), we overestimate the efficiency at this point.

- Euler calculation with FLU3M [7, 17]

Although Euler equations do not take into account viscous effects, they allow to analyse the flow in all the intake, and to estimate mass flow ratio, total pressure recovery and wall pressures.

To construct a structured grid in the intake, it is necessary to adopt a multi-block strategy. The grid we used contains about 30000 points and is subdivided into four domains (figure 16). The first one extends from the upstream boundary to the cowl lip plane, the second one from the cowl lip plane to the outer downstream boundary, the third one from the cowl lip plane to the diffuser end boundary and the fourth one represents the boundary layer bleed. For all these domains the grid is continuous except at the entry of the inner boundary layer bleed.

During the wind tunnel tests, the ramjet operation is simulated with an obstructer positioned at the end of the diffuser (see figure 16). In computations, we can use two possibilities to reproduce this :

- apply a static pressure in the downstream diffuser,

- use a variable throat in the downstream of the diffuser to simulate different sections and so different downstream static pressures.

The use of the first possibility is delicate. As explained in the ref. 7, it is not possible to initialize to a high value the static pressure in the downstream of the diffuser directly. It is necessary to first obtain a converged solution for a low static pressure, then to reinitialize another calculation with the results of the first one and with a static pressure slightly higher, and so on. If the step of the static pressure is too high, the calculation does not converge or give a solution which is not physical. In addition this procedure does not allow to compute the critical regime.

Figure 18 presents the iso Mach lines obtained with such a procedure. For this calculation we have applied the experimental static pressure in the downstream of the internal bleed. The solution presented corresponds to a critical regime. We can see the external compression shocks, the cowl shock and the downstream normal shock, near the internal boundary layer bleed entrance, which makes the separation between the supersonic part and the subsonic part of the flow.

Figure 19 shows the comparison between the computed iso Mach lines and schlieren photography obtained in wind tunnel. The comparison shows a good agreement between computation and experimental visualization for the shock wave positions.

Figure 20 presents the pressure distribution on upper and lower walls. Calculations have been performed with and without internal boundary layer bleed. The effect of representing the boundary layer bleed is to displace the normal shock wave upstream, which allows better results, especially the correct mass flow chamber, even if we use an Euler method.

Consider now the second possibility to represent the running of the internal bleed and of the ramjet. It consists in using a fixed throat downstream the internal boundary layer and a variable throat downstream the diffuser. The variable throat allows to simulate the different running regimes from the supercritical to the subcritical one (figure 21).

Figure 22 presents the characteristic curve obtained with this procedure. The comparison between experimental and computational results shows a good agreement. Computation near the critical point needs however some precaution due

to the normal shock instability, which is also observed experimentally as the shock moves upstream from a divergent duct to a convergent one.

- Navier-Stokes calculation with NS2D

Navier-Stokes calculations allow to take into account viscous effects like total pressures losses near the wall, shock-boundary layer interactions, vortical flow at bleed entrance,...

Figure 23 presents a comparison between Euler and turbulent Navier-Stokes computations. We can see that Navier-Stokes calculation provides a normal shock located slightly upstream from the one obtained with the Euler calculation. That is certainly due to the boundary layer displacement thickness in the diffuser which reduces the available cross section.

Figure 24 presents a Navier-Stokes calculation corresponding to a critical running. We observe the vortical flow in the boundary layer bleed and the separation of the boundary layer in the diffuser resulting from the shock-boundary layer interaction.

6.2. Intake with a non uniform external flowfield

The previous method is approximate as it does not take into account 3D effects due to forebody influence and also to compression ramp finite width or intake lateral walls. 3D air-intake calculations with the real non uniform flowfield around the fuselage are then necessary.

To perform these calculations, there are two ways :

- compute the intake placed in a non uniform flowfield,
- compute together external and internal flowfields (global computation).

a) Intake flowfield computation with a non uniform external flowfield

In this procedure the external flowfield is computed first. Depending on the intake geometry, this calculation is performed up to the apex of the first external compression ramp or up to the entry section of the intake.

Then, 3D external flow results are used as upstream boundary conditions for the internal flowfield calculation.

In order to obtain very fine results at the entry section of the intake, the internal computational domain is usually extended up to the apex of the first external compression ramp. In that case the multi-block grid used for the internal flow

calculation will include an external bloc delimited by the external ramps and the external flow previously computed (see figure 25). To obtain very fine results at the entry section of the intake, the mesh of this external block must be much finer than the one used for the external flow calculation.

This procedure applies only to supercritical and close critical regimes.

Figure 26 presents an application of such a method for the AEROSPATIALE ASMP type missile configuration (the grid on the whole missile is presented for a better understanding of the geometry).

b) Global computation

This procedure is more complex. It applies to all operating conditions, from the supercritical to the subcritical ones. Furthermore it allows to take into account the internal flow effects on external aerodynamics.

To illustrate this method, we will consider the forebody/intake configuration shown on figure 27. It corresponds to an aircraft of the F15 type with rectangular intakes.

We used 3D multi-block Euler code FLU3M to compute this configuration [18]. Calculation was performed without incidence and side slip, and with a freestream Mach number equal 2.2 corresponding to a critical regime. As the configuration is symmetric, only a half configuration has been computed.

Figures 28 and 29 present the topological decomposition used. The grid contains 882000 points and is subdivided into 11 domains covering all details: cockpit, external and internal boundary layer bleeds.

Figure 30 shows the mesh and the computed static pressures on the flow centerplane and the surface of the forebody and intake. The shock waves generated by the nose and cockpit are clearly indicated, as are the shocks generated by the intake compression ramps. It appears that an oblique shock has been generated by the diverter between the intake and the forebody and this shock is seen to pass under the fuselage. These are exactly the airframe/intake integration features which we would hope to model properly for improve performance.

Figures 31 and 32 illustrate the Mach number distribution on the body and intake surfaces. The compression in the intake can be seen with the

separation between the supersonic part and the subsonic part of the internal flow.

Figure 33 presents the Mach number distribution in the captation section. The comparison between experimental and computational results shows a quite good agreement even if the Mach numbers near the fuselage are underpredicted. The difference is about 2%.

6.3 Futur computational needs

We distinguish two main needs :

- develop robust and cost effective Navier-Stokes solvers with appropriate turbulence models,
- take into account real shape of the combustion chamber in final air-intake design.

For the first point, turbulence models have to increase their flexibility (ability to account for many walls for example) and their universality (reduction of user defined constants, validation on complex geometries).

The second need is to gather air-intake and combustion chamber computations. These simulations are currently only linked by the mean flowfield in the final plane of air-intake diffuser. Nevertheless, the extension of internal flowfield simulation up to the combustion is very important. It will allow a better simulation of the whole propulsive stream tube, taking into account the non uniform flow at the entry of the chamber and the flow interaction between the chamber and the diffuser. Such a simulation will be similar to the one performed on test benches.

7. CONCLUSION

A brief overview of CFD methods applied to supersonic intakes has been given.

Depending on the project phase, a large panel of methods are used. These range from the 2D semi-empirical one to 3D RANS equations resolution.

For preliminary design, semi-empirical tools are fairly well adapted for the test of a wide range of geometries. The selected concepts may then be fine tuned through Euler computations which give the main characteristics of the air intake. This computational methodology proved to be very efficient in terms of prediction and cost. Finally RANS computations usually allow a better understanding of flow behaviour (flow separation, ...) and an improved design.

To demonstrate the capabilities of these methods, we have presented three types of practical applications: external flow prediction around a fuselage at incidence, internal flow prediction in a isolated two-dimensional intake and global internal-external flow prediction for a three-dimensional intake mounted on a fuselage.

Further improvements of computational methodology for air-intakes will have to account for current design tendency: propulsion system tends to be more and more integrated to the airframe (mainly for stealth and compactness reasons). This trend will certainly emphasize the coupled external-internal approach (global computation) in order to predict critical and subcritical runnings up to buzz. Another numerical consequence of propulsion system integration will be the need to compute the largest part of the ramjet. In particular, integration of combustion chamber in air-intake simulation is the only way to correctly simulate heterogeneity and interaction existing between diffuser and combustor. This will be the next challenge for CFD.

ACKNOWLEDGEMENTS

We thank V. Le Gallo and C. Stylemans for their participation in the computations presented in this paper.

REFERENCES

1. - LARUELLE G., "Supersonic missile air-intakes: Design and development criteria", La Recherche Aérospatiale n° 1987-6.
2. - LARUELLE G., "Missile intakes", VKI Lecture Serie 1988-04 on Intake Aerodynamics, 1988.
3. - JELL C.S., "Air intake aerodynamics", AGARD/VKI Special course on Missile Aerodynamics, AGARD Report n° 754, 1987.
4. - THOMAS A.N., "Inlets", Tactical Missile Aerodynamics, Vol. 104, Progress in Astronautics and Aeronautics, AIAA, 1986.
5. - LAURENT J.M. and GARNERO P., "Propulsion par statoréacteur pour missiles dans le domaine Mach 3 à 4.5", AGARD Symposium: Airbreathing Propulsion for Missiles and Projectiles, AGARD-CP-526, 1992.
6. - GREGOR I. Mc., "Some theoretical parameters relevant to the performance of rectangular air intakes with double ramp compression surfaces at supersonic speed", RAE-TR-71232, 1971.
7. - DUVEAU P. and THEPOT R., "Prediction methods for supersonic inlets", Xth ISABE Symposium, 1991.
8. - COUSTEIX J., "Vol 1: Couches limites laminaires - Vol. 2: Turbulence et couches limites", Cours ENSAE.
9. - DAVIDENKO D., private communication, Russia
10. - GUILLEN P. and DORMIEUX M., "Design of a 3D multidomain Euler code", Computational Mechanics Institut, Supercomputing in Fluid Flows, Boston, 1989.
11. - DORMIEUX M., JOUET C. and BORREL M., "Simulations numériques d'écoulements non réactifs avec jet transversal au moyen de codes Euler et Navier-Stokes laminaire", 28ème Colloque d'aérodynamique appliquée, 1991.
12. - GAIBLE F., CARIOU R. and HOUEVILLE R., "Numerical simulation of three-dimensional supersonic flows using Euler and boundary layer solvers", AIAA 93-0531, 1993.
13. - CHAPUT E., DUBOIS F., LEMAIRE D., MOULES G. and VAUDESCAL J.L., "FLU3PNS a three dimensional thin layer and parabolized Navier-Stokes solver using the MUSCL upwind scheme", AIAA 91-0728, 1991.
14. - LAFON A., DENIAU H., MAMAN P. and MOSCHETTA J.M., "A fully upwind implicit PNS solver for the computation of 3D supersonic flows with crossflow separation", AIAA 94-0643.
15. - CAMBIER L., VEUILLOT J.P. and VUILLOT A.M., "Développement récents sur les méthodes de calcul d'écoulements internes par résolution des équations d'Euler ou de Navier-Stokes", Revue Française de Mécanique n°1988-4.
16. - PAGAN D., MOLTON P. and DELERY J., "Basic experiment on a supersonic vortex flow around a missile body", Journal of Spacecraft and Rockets, Vol. 29, n°3, May 1992.
17. - GARNERO P. and LACAU R.G., "Etudes aérodynamiques de prises d'air supersoniques", AGARD Symposium on Aerodynamic Engine/Airframe Integration for high Performance Aircraft and Missiles, AGARD-CP-498, 1992.
18. - AGARD Working Group 13 on Air-intakes for high speed vehicles, AGARD-AR-270, 1991.

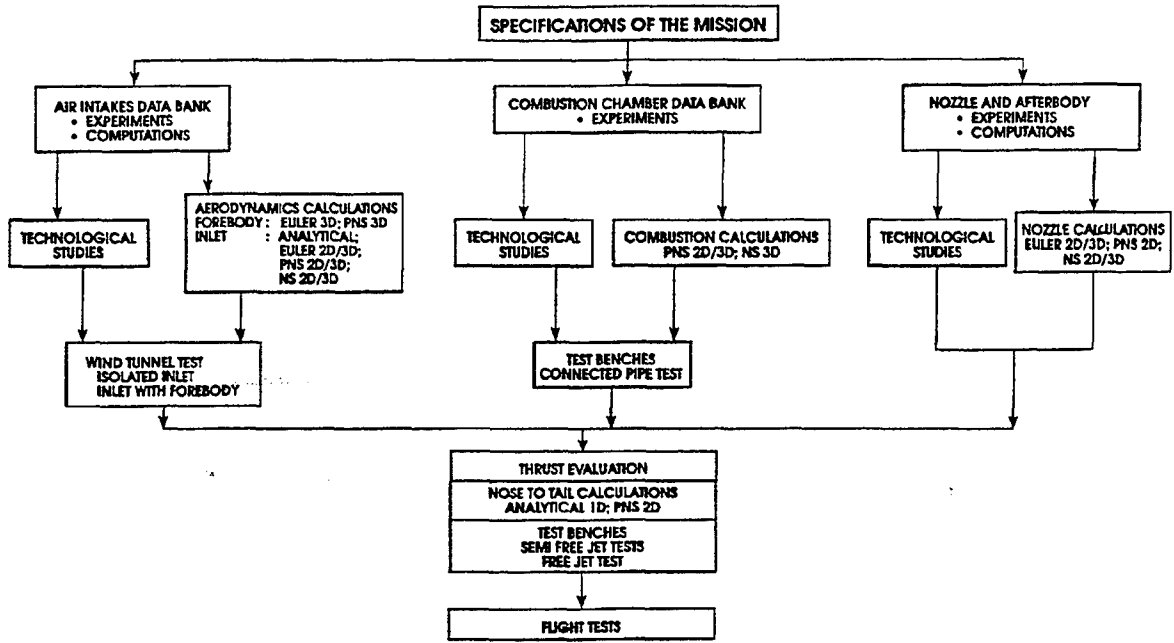


Figure 1 : Development Methodology of ramjet-scramjet/airframe integration

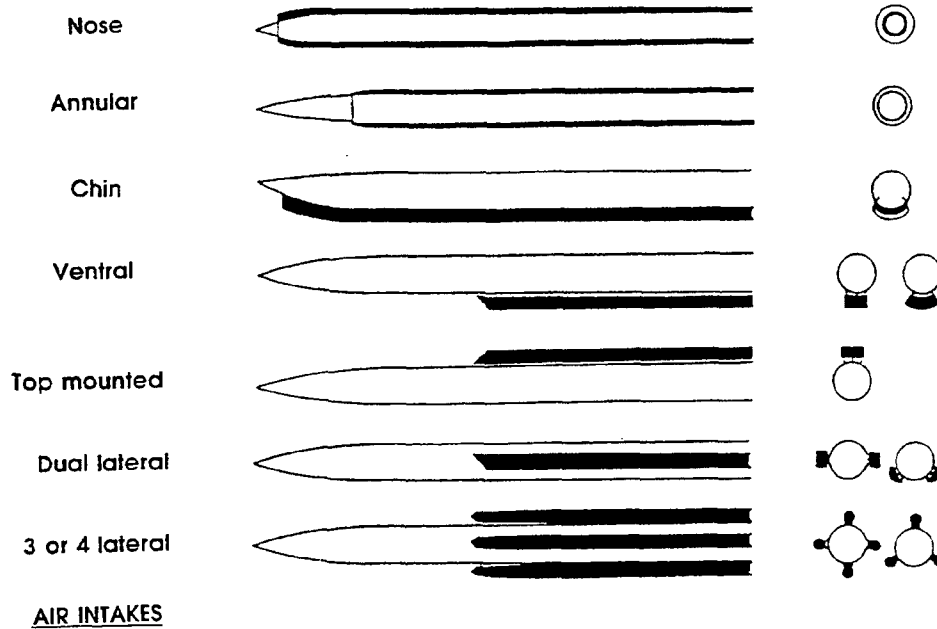


Figure 2 : Air-intake configurations [1]

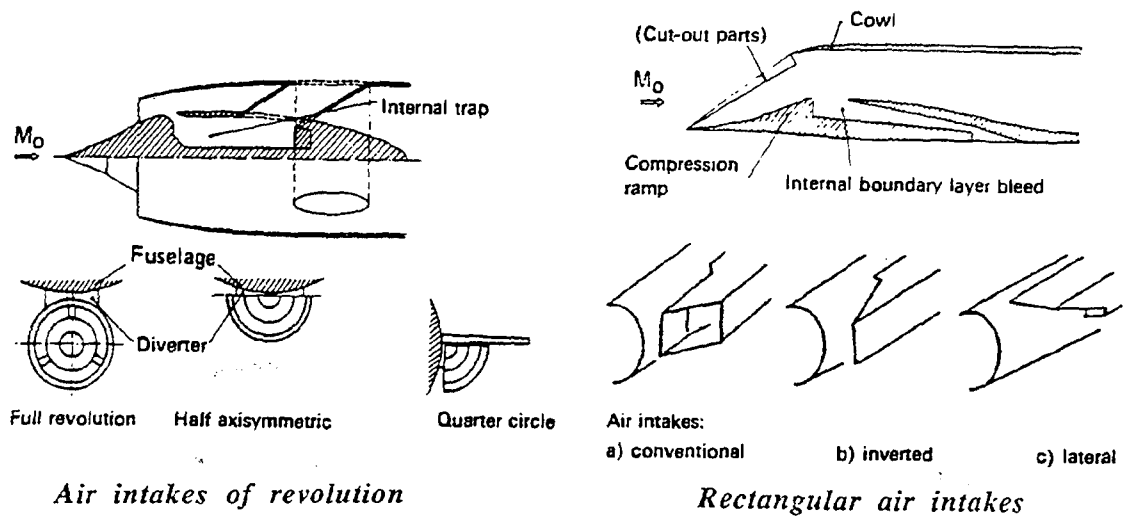


Figure 3 : Air-intake type [1]

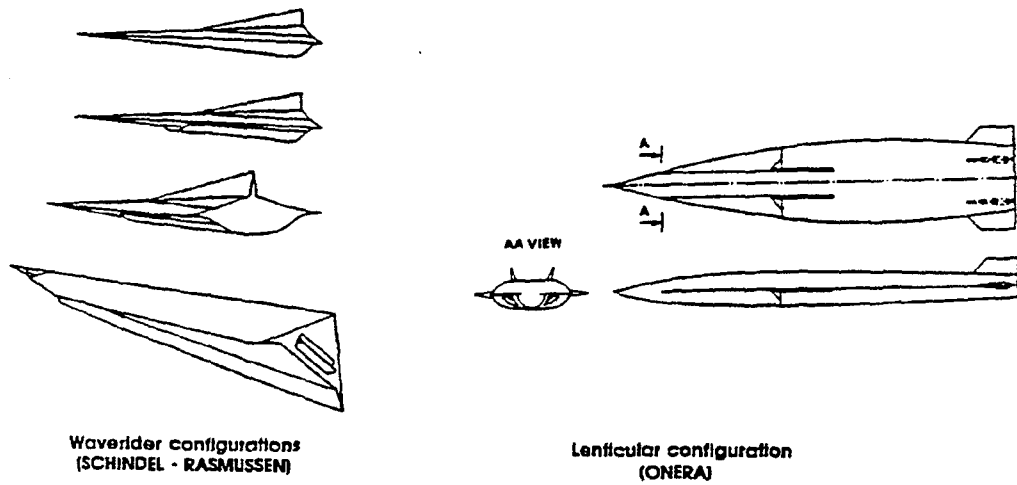


Figure 4 : Configurations with non circular cross sections

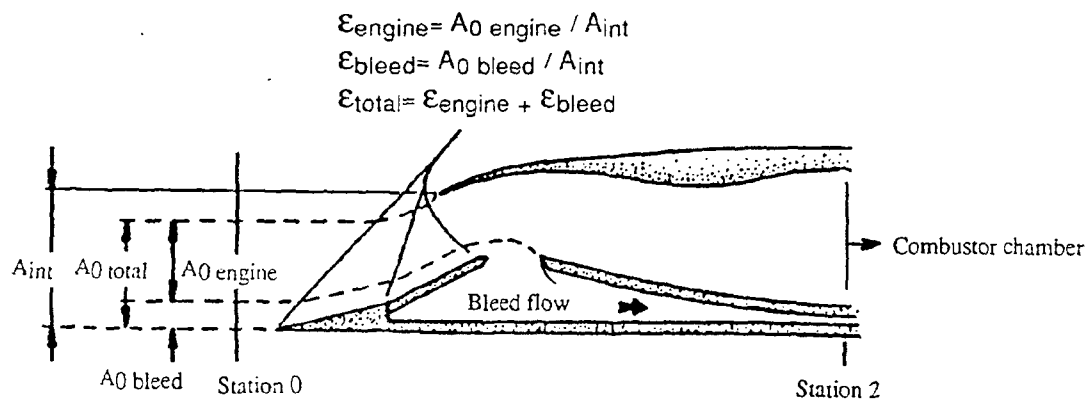


Figure 5 : Definition of air-intake mass flow ratio

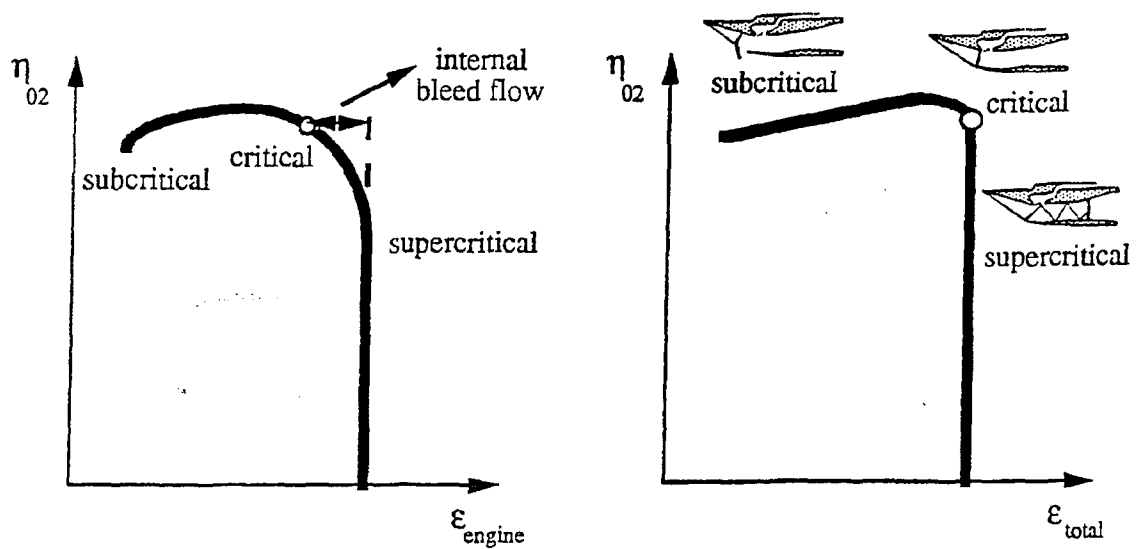


Figure 6 : Typical characteristic curves for external compression intake with internal boundary layer bleed

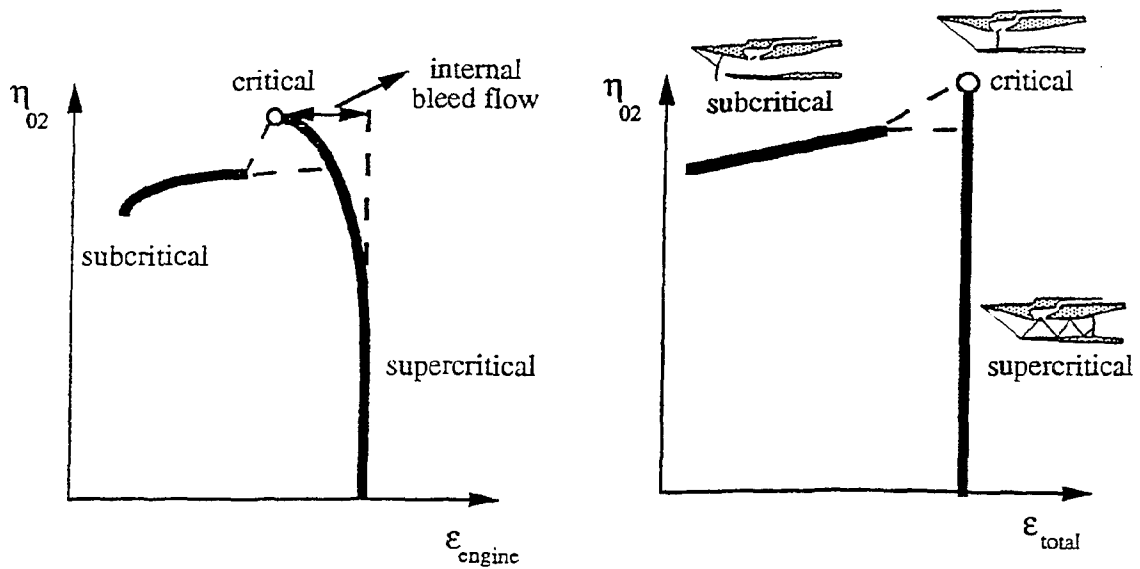


Figure 7 : Typical characteristic curves for mixed compression intake with internal boundary layer bleed

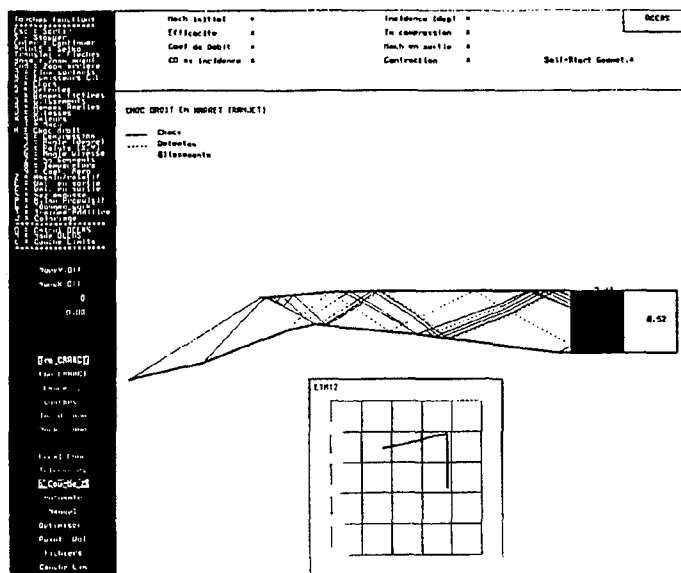


Figure 8 : OCEAS code - Graphical environment

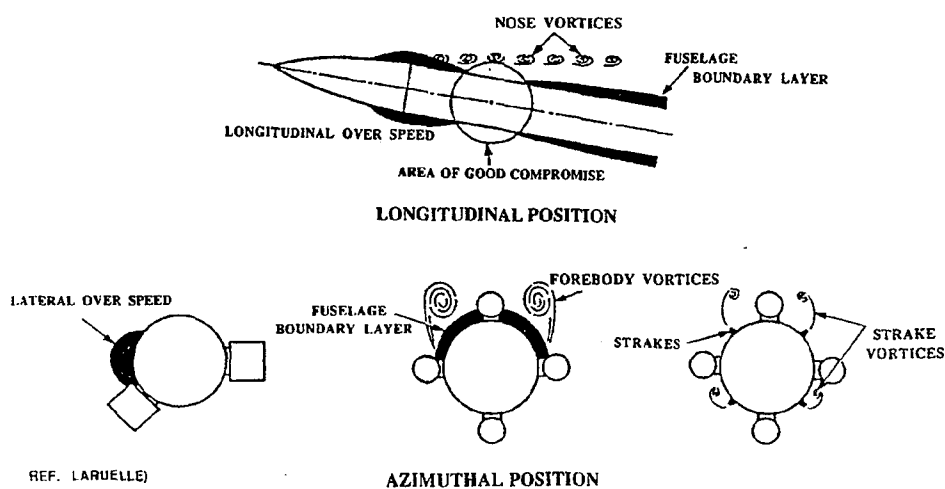


Figure 9: Air-intake position on fuselage

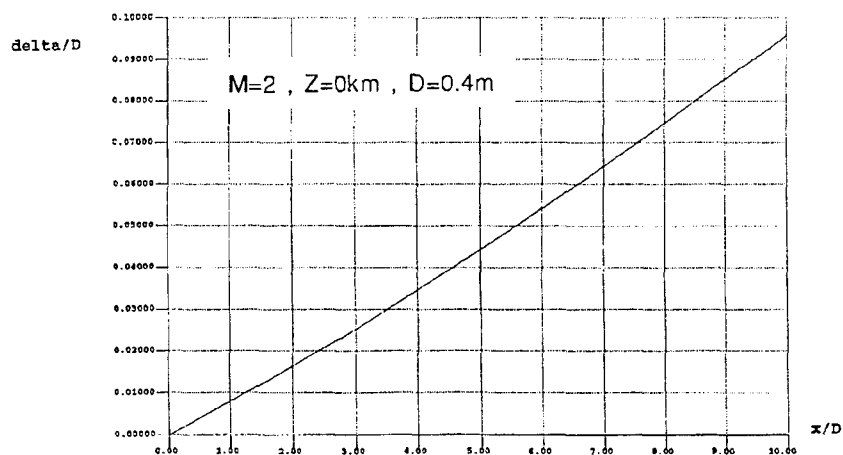


Figure 10 : Turbulent boundary layer thickness on a fuselage

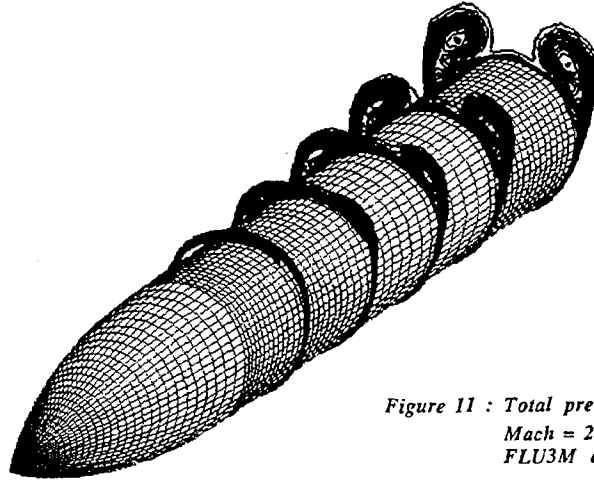


Figure 11 : Total pressure contours in crossflow planes.
Mach = 2, $\alpha=10^\circ$. Laminar boundary layer.
FLU3M computation

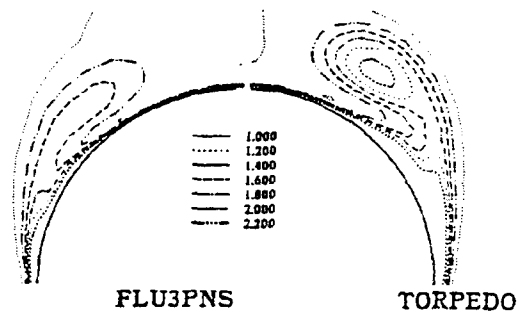
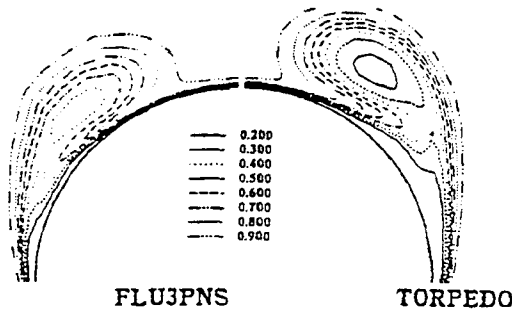
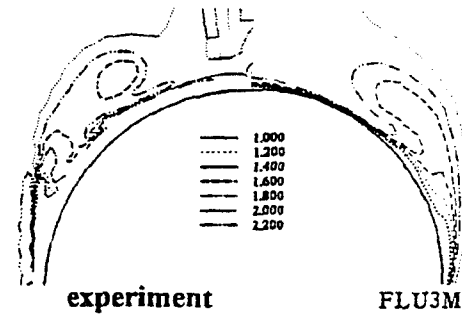
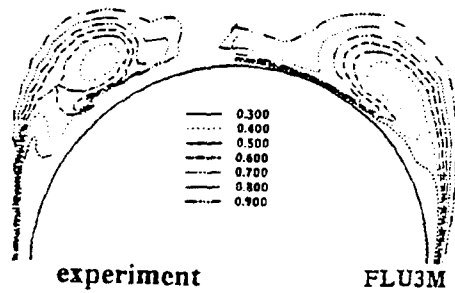


Figure 12 : Total pressure contours in the plane $X/D=7$.
Mach = 2, $\alpha=10^\circ$. Laminar boundary layer.

Figure 13 : Mach number contours in the plane $X/D=7$.
Mach = 2, $\alpha=10^\circ$. Laminar boundary layer.

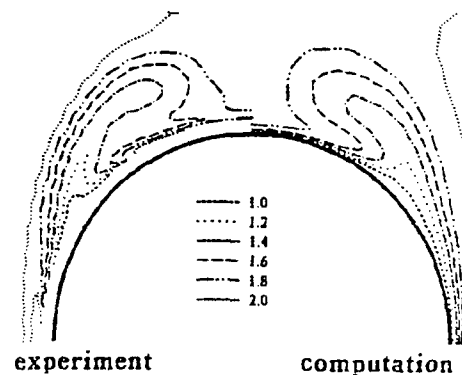
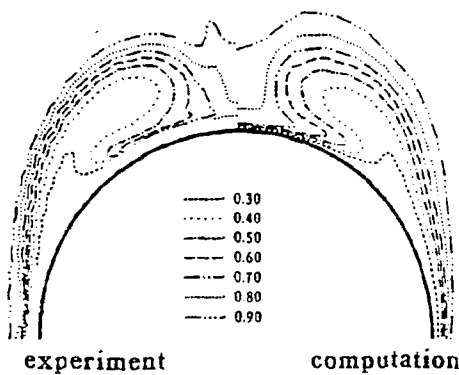


Figure 14 : Total pressure contours in the plane $X/D=7$.
Mach = 2, $\alpha=10^\circ$. Turbulent boundary layer.

Figure 15 : Mach number contours in the plane $X/D=7$.
Mach = 2, $\alpha=10^\circ$. Turbulent boundary layer.

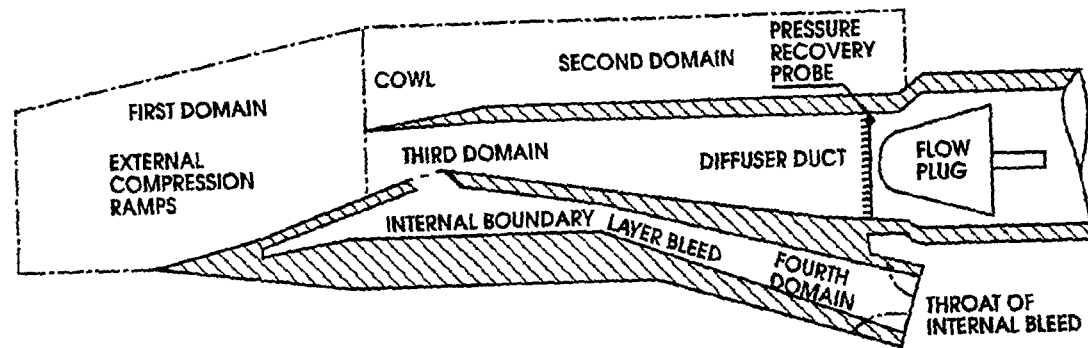


Figure 16 : Schematic drawing of the 2D air-intake. Mesh topology

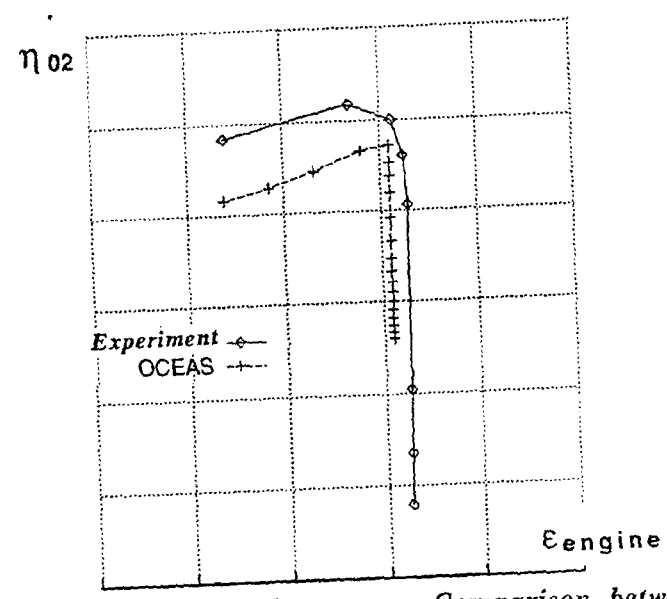


Figure 17 : 2D air-intake performance - Comparison between semi-empirical calculation (OCEAS) and experiment

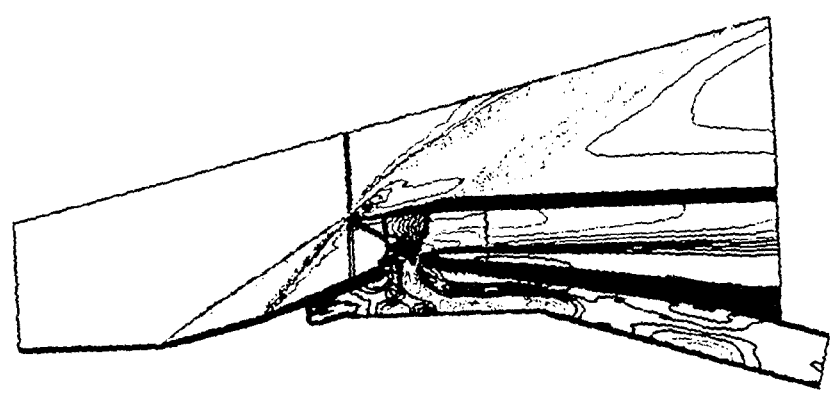


Figure 18 : 2D air-intake Mach number contours - Euler computation

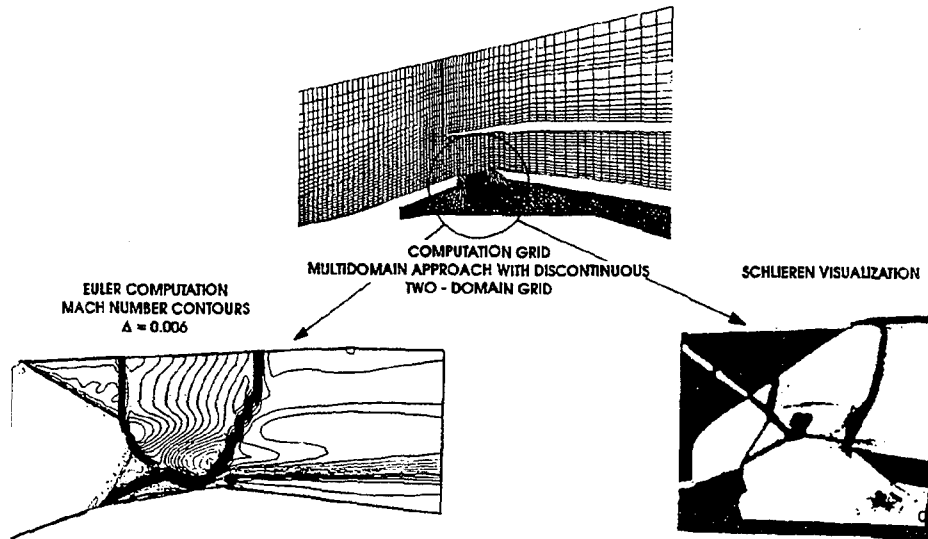


Figure 19 : 2D air-intake internal flowfield - Comparison between Euler computation and experiment

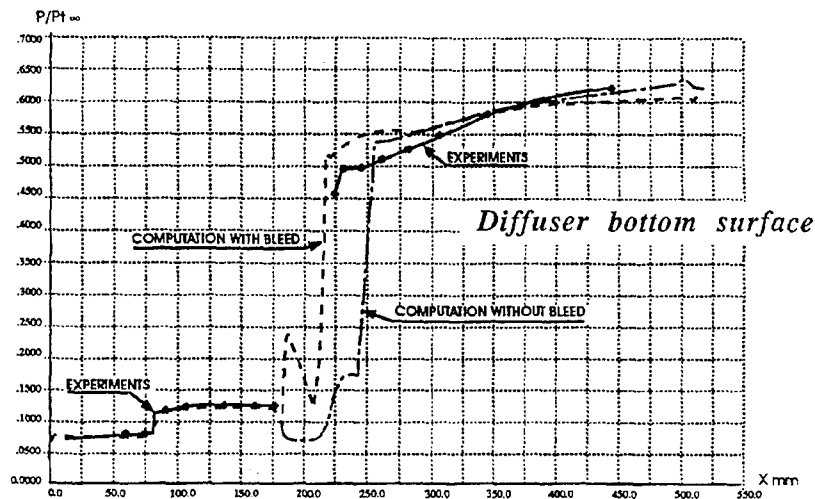
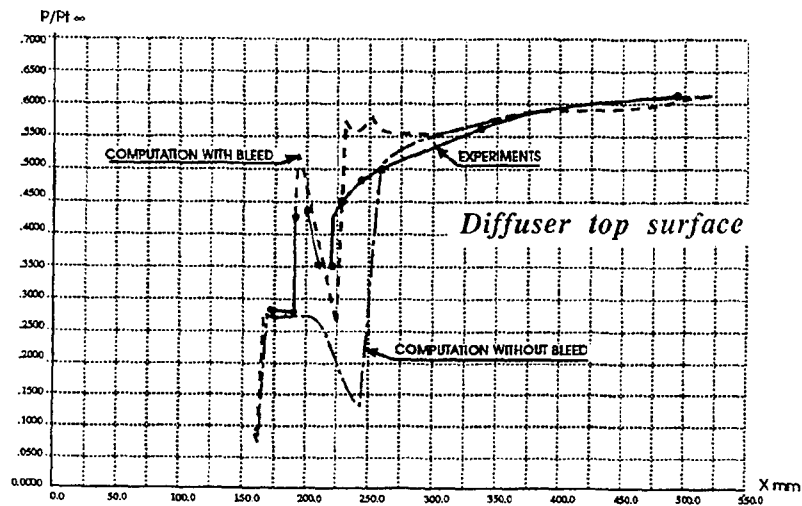


Figure 20 : 2D air-intake diffuser wall static pressure distribution. Comparison between Euler computation and experiment

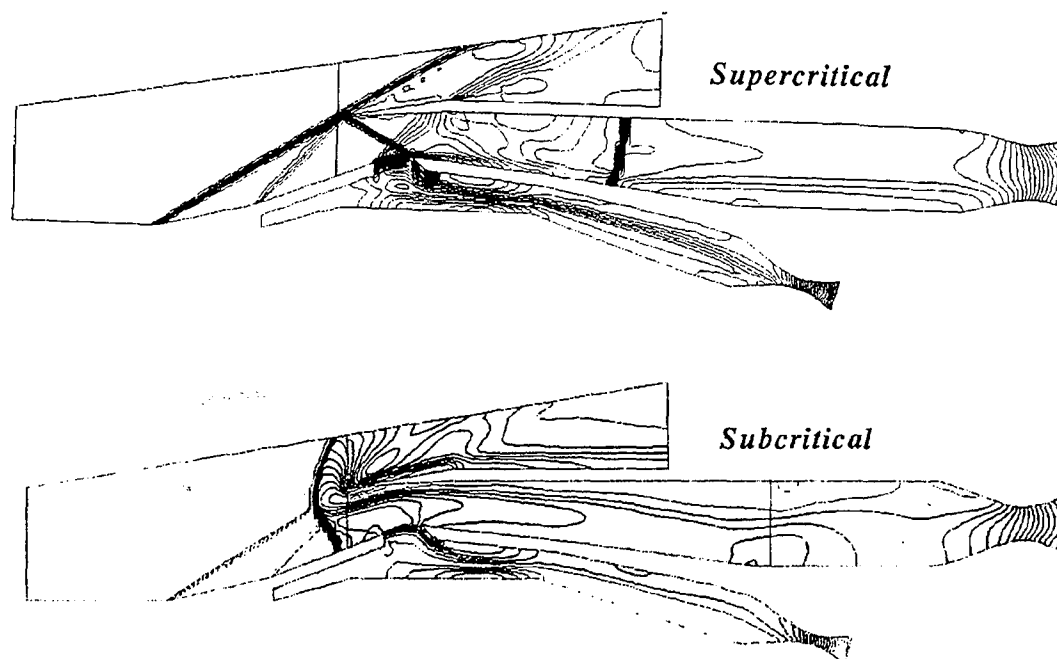


Figure 21 : 2D air-intake with diffuser throat and boundary layer bleed throat - Mach number contours - Supercritical and subcritical runnings Euler computation

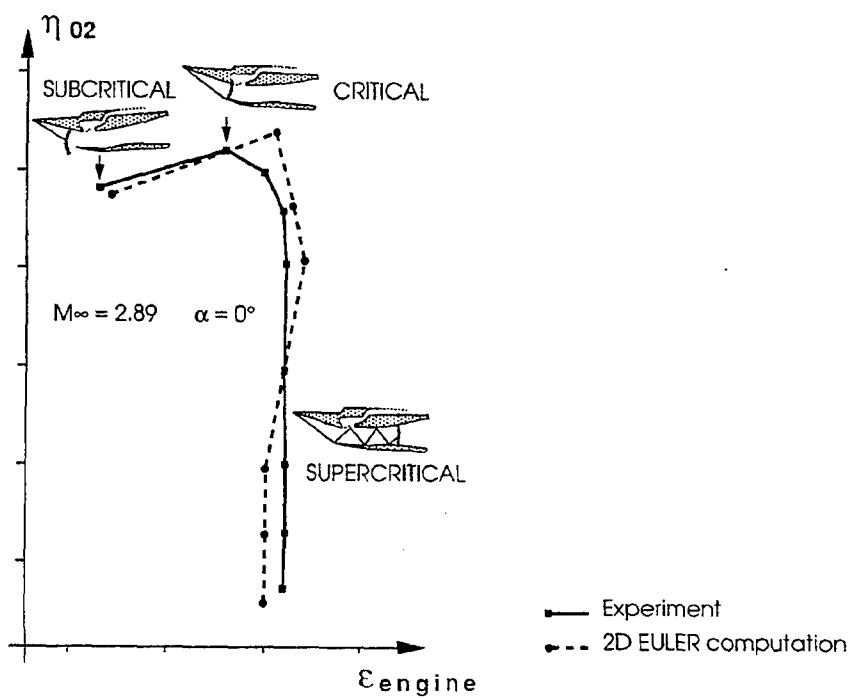
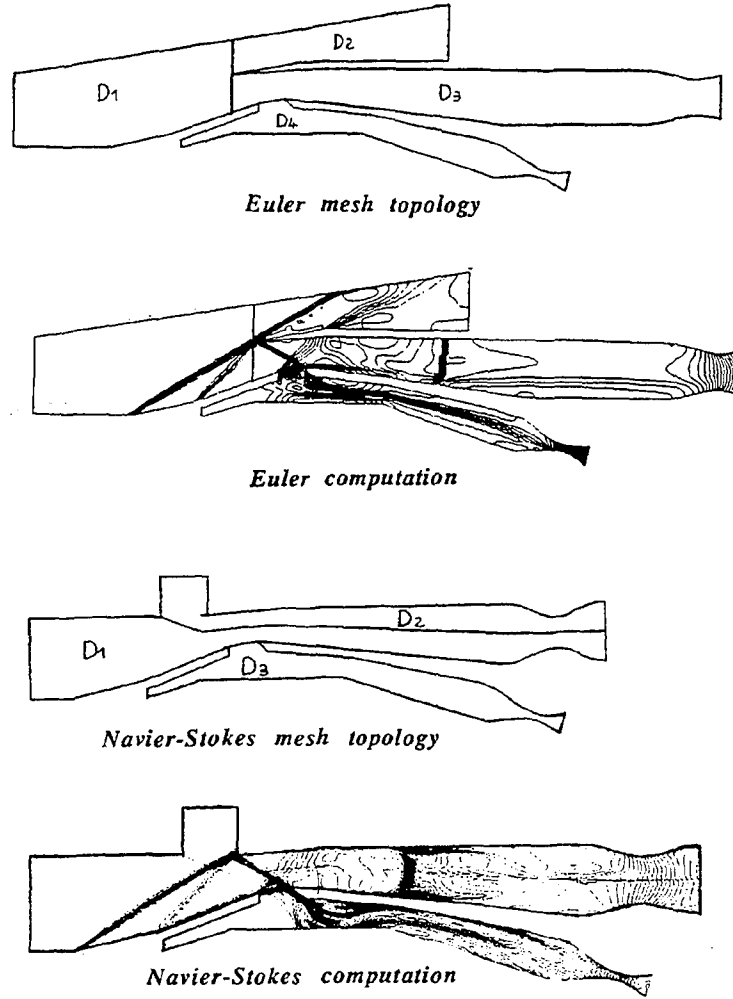
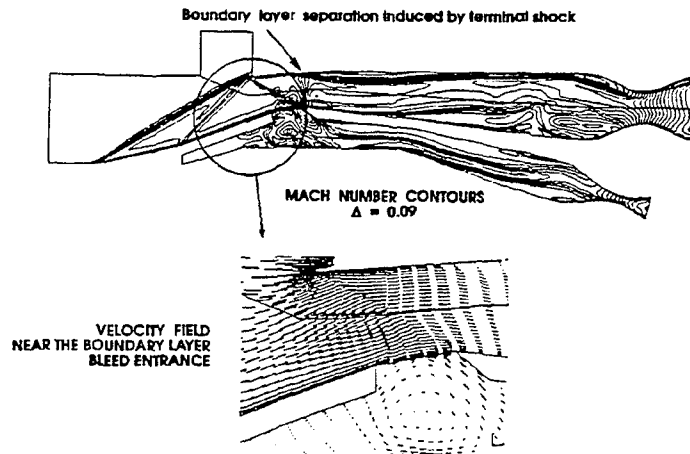


Figure 22 : 2D air-intake performance - Comparison between Euler computation and experiment



*Figure 23 : 2D air-intake Mach number contours.
Euler and Navier-Stokes computations*



*Figure 24 : 2D air-intake Mach number contours.
Navier-Stokes computation*

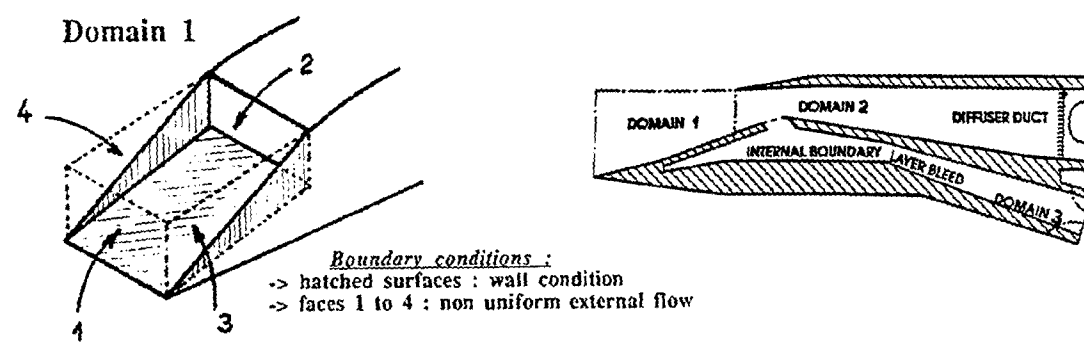


Figure 25 : Example of topology decomposition for a structured internal-external multi-block grid

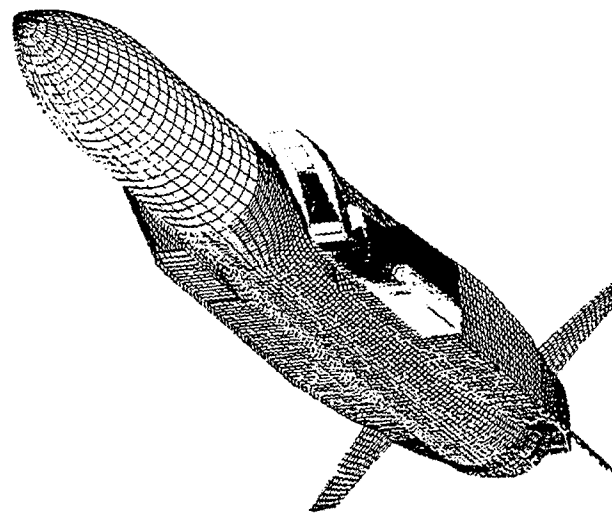
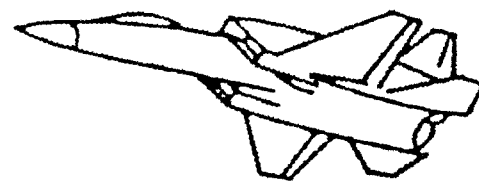


Figure 26 : ASMP type configuration - Internal flowfield computation taking into account non uniform external flowfield



$M_0=2.2$ $\alpha=0^\circ$ $\beta=0^\circ$

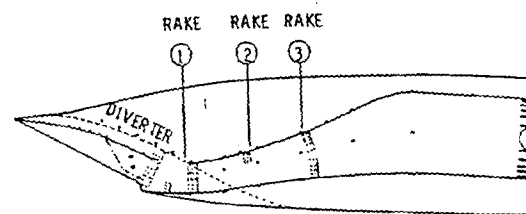


Figure 27 : 3D forebody/intake configuration

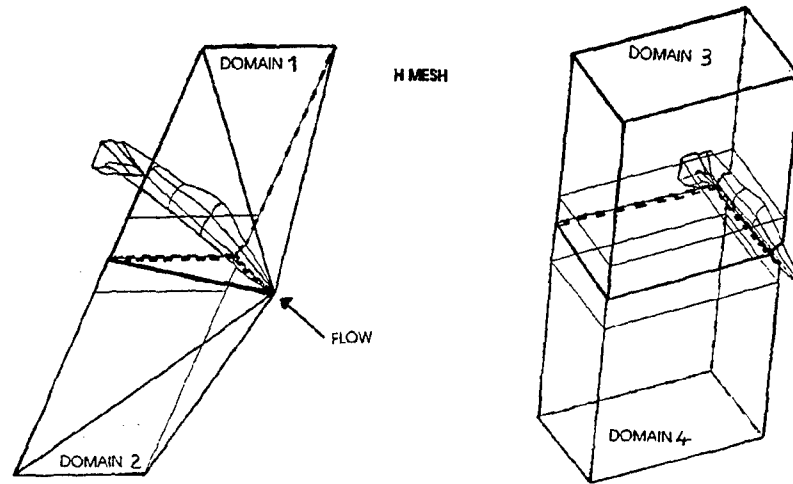


Figure 28 : Topologic decomposition for a structured multi-block mesh

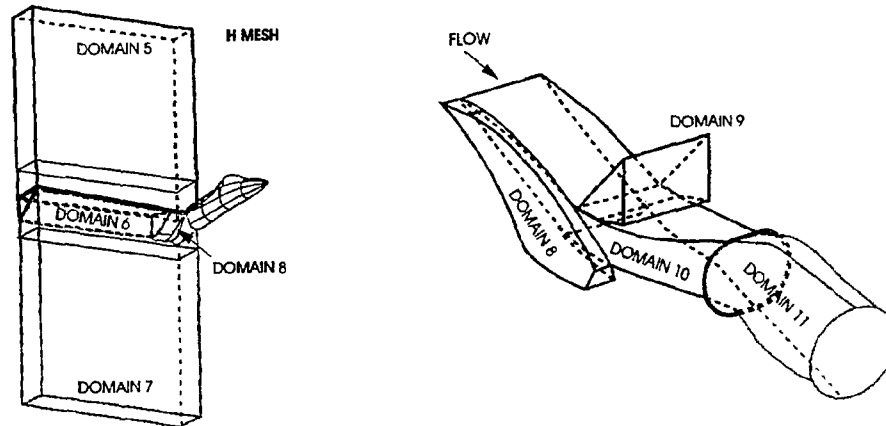


Figure 29 : Topologic decomposition for a structured multi-block mesh (continued)

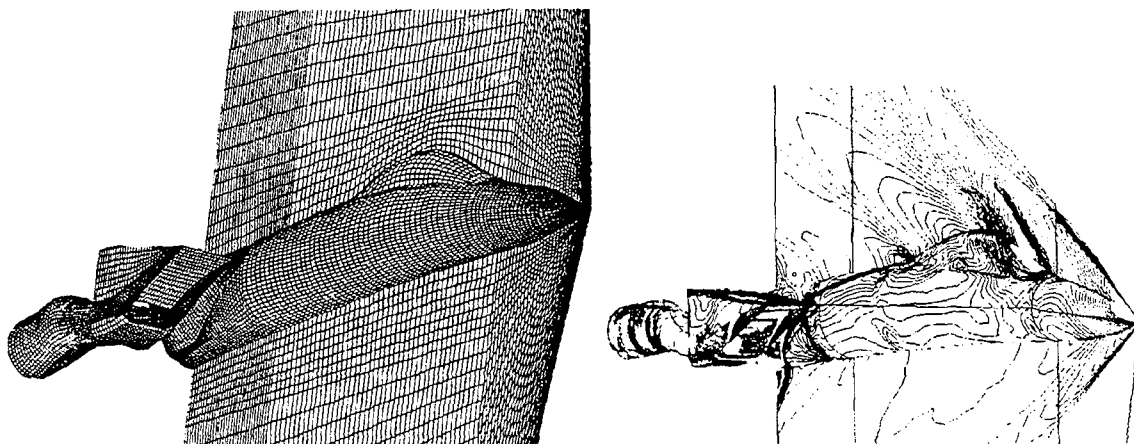


Figure 30 : Surface and symmetry plane grid.
Computed static pressure contours

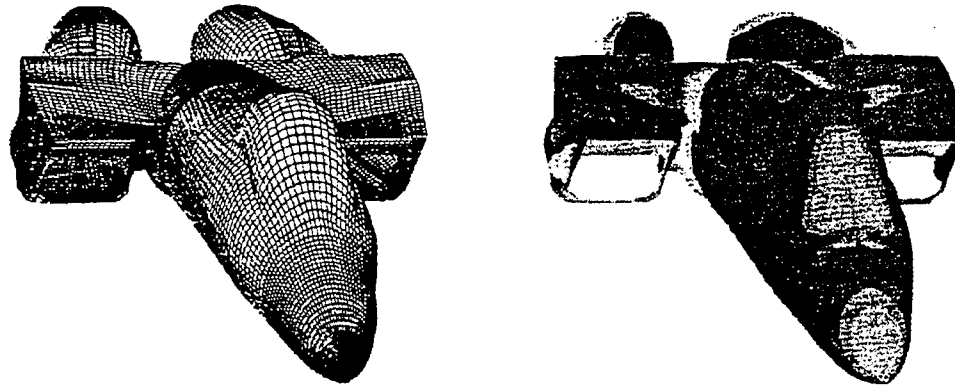


Figure 31 : Surface grid and computed Mach number distribution

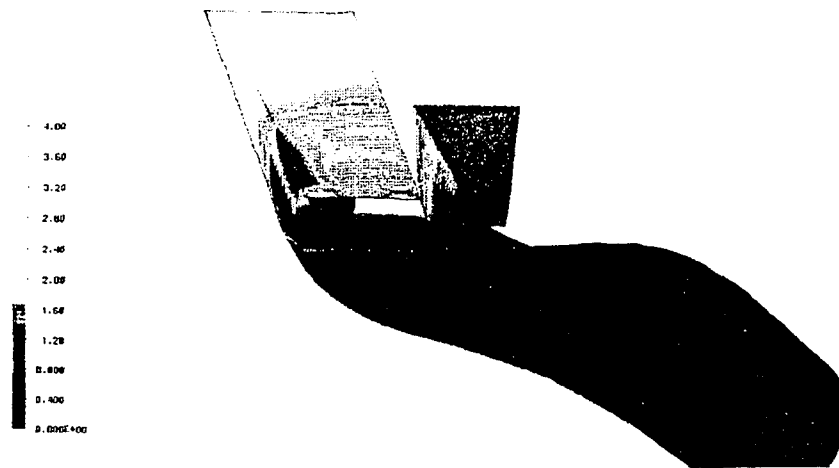


Figure 32 : Computed Mach number distribution on the intake internal surface

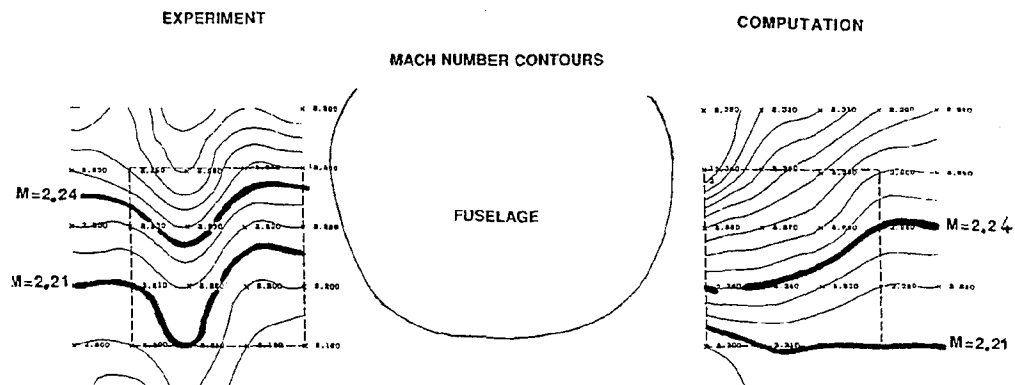


Figure 33 : Comparison between computed and measured Mach number distribution in the intake capture area

REPORT DOCUMENTATION PAGE

1. Recipient's Reference	2. Originator's Reference	3. Further Reference	4. Security Classification of Document								
	AGARD-R-804	ISBN 92-835-0752-5	UNCLASSIFIED/ UNLIMITED								
5. Originator	Advisory Group for Aerospace Research and Development North Atlantic Treaty Organization 7 rue Ancelle, 92200 Neuilly sur Seine, France										
6. Title	SPECIAL COURSE ON MISSILE AERODYNAMICS										
7. Presented at	an AGARD-FDP-VKI Special Course at the VKI, Rhode-Saint-Genèse, Belgium, 6th-10th June 1994 and at the Middle East Technical University, Ankara, Turkey, 13th-17th June 1994.										
8. Author(s)/Editor(s)	Various	9. Date	June 1994								
10. Author(s)/Editor's Address	Various	11. Pages	342								
12. Distribution Statement	There are no restrictions on the distribution of this document. Information about the availability of this and other AGARD unclassified publications is given on the back cover.										
13. Keywords/Descriptors	<table border="0"> <tr> <td>Aeromechanical design of modern missiles</td> <td>High angle-of-attack missile aerodynamics</td> </tr> <tr> <td>Missile aerodynamics</td> <td>Infrared radiation analysis</td> </tr> <tr> <td>Navier-Stokes predictions for missile configurations</td> <td>Lateral jet control for missiles</td> </tr> <tr> <td>Supersonic air intakes</td> <td></td> </tr> </table>			Aeromechanical design of modern missiles	High angle-of-attack missile aerodynamics	Missile aerodynamics	Infrared radiation analysis	Navier-Stokes predictions for missile configurations	Lateral jet control for missiles	Supersonic air intakes	
Aeromechanical design of modern missiles	High angle-of-attack missile aerodynamics										
Missile aerodynamics	Infrared radiation analysis										
Navier-Stokes predictions for missile configurations	Lateral jet control for missiles										
Supersonic air intakes											
14. Abstract	<p>Lecture notes for the AGARD Fluid Dynamics Panel (FDP) Special Course on "Missile Aerodynamics" have been assembled in this report. The aim and scope of this Course was to present the current state of the art on specific topics of tactical missile aerodynamics. Specifically, topics and methods covered include: Aeromechanical Design of Modern Missiles, Semi-empirical Predictive Tools, Lateral Jet Control, High Angle of Attack Aerodynamics, Analysis and Modelling of Missile Infrared Radiation, Navier-Stokes Computations for complete Missile Configurations, and Navier-Stokes and Euler Computations for Supersonic Air Intakes.</p> <p>The material assembled in this report was prepared under the combined sponsorship of the AGARD Fluid Dynamics Panel, the Consultant and Exchange Programme of AGARD, and the von Kármán Institute (VKI) for Fluid Dynamics.</p>										

<p>AGARD Report 804 Advisory Group for Aerospace Research and Development, NATO SPECIAL COURSE ON MISSILE AERODYNAMICS Published June 1994 342 pages</p> <p>Lecture notes for the AGARD Fluid Dynamics Panel (FDP) Special Course on "Missile Aerodynamics" have been assembled in this report. The aim and scope of this Course was to present the current state of the art on specific topics of tactical missile aerodynamics. Specifically, topics and methods covered include: Aeromechanical Design of Modern Missiles, Semi-empirical Predictive Tools, Lateral Jet Control, High Angle of Attack Aerodynamics, Analysis and Modelling of Missile Infrared Radiation, Navier-Stokes Computations</p> <p>P.T.O.</p>	<p>AGARD Report 804 Advisory Group for Aerospace Research and Development, NATO SPECIAL COURSE ON MISSILE AERODYNAMICS Published June 1994 342 pages</p> <p>Lecture notes for the AGARD Fluid Dynamics Panel (FDP) Special Course on "Missile Aerodynamics" have been assembled in this report. The aim and scope of this Course was to present the current state of the art on specific topics of tactical missile aerodynamics. Specifically, topics and methods covered include: Aeromechanical Design of Modern Missiles, Semi-empirical Predictive Tools, Lateral Jet Control, High Angle of Attack Aerodynamics, Analysis and Modelling of Missile Infrared Radiation, Navier-Stokes Computations</p> <p>P.T.O.</p>	<p>AGARD Report 804 Advisory Group for Aerospace Research and Development, NATO SPECIAL COURSE ON MISSILE AERODYNAMICS Published June 1994 342 pages</p> <p>Lecture notes for the AGARD Fluid Dynamics Panel (FDP) Special Course on "Missile Aerodynamics" have been assembled in this report. The aim and scope of this Course was to present the current state of the art on specific topics of tactical missile aerodynamics. Specifically, topics and methods covered include: Aeromechanical Design of Modern Missiles, Semi-empirical Predictive Tools, Lateral Jet Control, High Angle of Attack Aerodynamics, Analysis and Modelling of Missile Infrared Radiation, Navier-Stokes Computations</p> <p>P.T.O.</p>	<p>AGARD Report 804 Advisory Group for Aerospace Research and Development, NATO SPECIAL COURSE ON MISSILE AERODYNAMICS Published June 1994 342 pages</p> <p>Lecture notes for the AGARD Fluid Dynamics Panel (FDP) Special Course on "Missile Aerodynamics" have been assembled in this report. The aim and scope of this Course was to present the current state of the art on specific topics of tactical missile aerodynamics. Specifically, topics and methods covered include: Aeromechanical Design of Modern Missiles, Semi-empirical Predictive Tools, Lateral Jet Control, High Angle of Attack Aerodynamics, Analysis and Modelling of Missile Infrared Radiation, Navier-Stokes Computations</p> <p>P.T.O.</p>
<p>AGARD-R-804</p> <p>Aeromechanical design of modern missiles Missile aerodynamics Navier-Stokes predictions for missile configurations Supersonic air intakes High angle-of-attack missile aerodynamics Infrared radiation analysis Lateral jet control for missiles</p>	<p>AGARD-R-804</p> <p>Aeromechanical design of modern missiles Missile aerodynamics Navier-Stokes predictions for missile configurations Supersonic air intakes High angle-of-attack missile aerodynamics Infrared radiation analysis Lateral jet control for missiles</p>	<p>AGARD-R-804</p> <p>Aeromechanical design of modern missiles Missile aerodynamics Navier-Stokes predictions for missile configurations Supersonic air intakes High angle-of-attack missile aerodynamics Infrared radiation analysis Lateral jet control for missiles</p>	<p>AGARD-R-804</p> <p>Aeromechanical design of modern missiles Missile aerodynamics Navier-Stokes predictions for missile configurations Supersonic air intakes High angle-of-attack missile aerodynamics Infrared radiation analysis Lateral jet control for missiles</p>

<p>for complete Missile Configurations, and Navier-Stokes and Euler Computations for Supersonic Air Intakes.</p> <p>The Material assembled in this report was prepared under the combined sponsorship of the AGARD Fluid Dynamics Panel, the Consultant and Exchange Programme of AGARD, and the von Kármán Institute (VKI) for Fluid Dynamics. It was presented in an AGARD-FDP-VKI Special Course at the VKI, Rhode-Saint-Genèse, Belgium, 6th-10th June 1994 and at the Middle East Technical University, Ankara, Turkey, 13th-17th June 1994.</p>	<p>for complete Missile Configurations, and Navier-Stokes and Euler Computations for Supersonic Air Intakes.</p> <p>The Material assembled in this report was prepared under the combined sponsorship of the AGARD Fluid Dynamics Panel, the Consultant and Exchange Programme of AGARD, and the von Kármán Institute (VKI) for Fluid Dynamics. It was presented in an AGARD-FDP-VKI Special Course at the VKI, Rhode-Saint-Genèse, Belgium, 6th-10th June 1994 and at the Middle East Technical University, Ankara, Turkey, 13th-17th June 1994.</p>
<p>ISBN 92-835-0752-5</p>	<p>ISBN 92-835-0752-5</p>
<p>for complete Missile Configurations, and Navier-Stokes and Euler Computations for Supersonic Air Intakes.</p> <p>The Material assembled in this report was prepared under the combined sponsorship of the AGARD Fluid Dynamics Panel, the Consultant and Exchange Programme of AGARD, and the von Kármán Institute (VKI) for Fluid Dynamics. It was presented in an AGARD-FDP-VKI Special Course at the VKI, Rhode-Saint-Genèse, Belgium, 6th-10th June 1994 and at the Middle East Technical University, Ankara, Turkey, 13th-17th June 1994.</p>	<p>for complete Missile Configurations, and Navier-Stokes and Euler Computations for Supersonic Air Intakes.</p> <p>The Material assembled in this report was prepared under the combined sponsorship of the AGARD Fluid Dynamics Panel, the Consultant and Exchange Programme of AGARD, and the von Kármán Institute (VKI) for Fluid Dynamics. It was presented in an AGARD-FDP-VKI Special Course at the VKI, Rhode-Saint-Genèse, Belgium, 6th-10th June 1994 and at the Middle East Technical University, Ankara, Turkey, 13th-17th June 1994.</p>
<p>ISBN 92-835-0752-5</p>	<p>ISBN 92-835-0752-5</p>